# Fault controlled fluid flow and quartz cementation in porous sandstones.

Oliver F. Quinn


PhD
University of Edinburgh
2005

# Declaration

All of the material presented in this thesis is entirely my own work except where indicated otherwise:

Oliver F. Quinn

# Acknowledgements

I would like to thank Stuart Haszeldine for his guidance and support over the last few years, and for allowing me the freedom to develop the project in my own way. John Dixon is thanked for setting the foundations of the project and for many subsequent discussions. John Underhill is gratefully acknowledged for his help and input throughout, and for supplying seismic data.

I am indebted to Mark Wilkinson and Gavin England for their general guidance and for many useful discussions. I am also grateful to Kati Bodnar and Calum Macaulay for introducing me to the finer points of fluid inclusion analysis.

Many thanks are due to John Craven for instruction on the ion probe and for many early mornings spent helping me out. Nicky Cayzer, Paula McDade and Pete Hill are thanked for their guidance on the operation of the SEM and the carbon coating machine. Thanks also go to Mike Hall for making many thin sections, often at short notice

Ronald Bakker at the University of Leoben, Austria is gratefully thanked for expert advice and training in fluid inclusion analysis and for allowing use of their extensive inclusion laboratory.

Thanks to Michael Quinn for his assistance in the field spending some very long days drilling chunks of heavy sandstone, and for instantly learning the ropes of sample surveying.

Moray Stone Cutters are gratefully acknowledged for granting access and permission to sample at Clashach Quarry. NERC are acknowledged for funding the majority of the project. Additional funding from the AAPG Grant-in-Aid programme and sponsorship from Shell UK are also gratefully acknowledged.

I would also like to thank all of the people I have met in Edinburgh over the last few years who have made my time here very enjoyable, especially all the PG's in the 'mouse house'.

Most thanks go to Helen and to my parents, for all their moral and financial support.

# Abstract

Quartz cement is a major culprit of porosity and permeability loss in deeply buried sandstone hydrocarbon reservoirs. A major debate is whether quartz cement is entirely internally derived or if fluid flow and mass transfer can import silica for quartz cementation.

Two Late Jurassic normal faults are exposed within the aeolian (U. Permian) Hopeman Sandstone, onshore within the Inner Moray Firth basin, UK North Sea. The Clashach Fault has a throw <50m. The Burghead Fault has a throw of >100m. The faults crop out within the Hopeman Horst on the southern margin of the 50km wide, 5km deep, half-graben basin. Maximum burial depth of the Hopeman Sandstone within this horst block is 1.5-2.4km.

Quartz cementation is asymmetric across the fault planes. Moving through the footwall of the Clashach Fault toward the fault plane, quartz cement volume increases from 9% at 31.7m to a maximum of 26.5% at 13.8m from the plane. From 13.8m to 0.5m from the fault plane authigenic quartz volume decreases from 26.5% to 4.2% at 0.5m. In this zone carbonate cement, which later dissolved, reduced the space available for quartz precipitation. The hanging wall contains mean 4% authigenic quartz. Porosity displays an inverse relationship to quartz cement. Footwall porosity increases from 10% at 13.8m from the fault plane to 18.6% at 31.7m. From 13.8m-0.5m porosity varies inversely with the volume of quartz cement in each sample. Hanging wall mean porosity is 24.5%. Footwall intergranular volume decreases from a maximum of 32% at 13.8m to 28% at 31.7m.

At the Burghead Fault, footwall authigenic quartz volume increases moderately from 24.5% at 13m from the fault plane to 29% at 0.5m from the fault plane. Porosity displays an increase from 2.3% at 0.5m to 6.1% at 13m. Permeability decreases from 100-1000mD in poorly cemented hanging wall sandstone to <1mD in extensively quartz cemented sandstones in the footwalls of both faults. Footwall intergranular volume is consistently >30% in the Burghead Fault footwall.

Fluid inclusions within footwall quartz overgrowths are single phase, aqueous, indicating cement precipitation <60°C. Quartz cemented microfracture fluid inclusion trails, generated during fault movement, contain 2-phase (L+V) aqueous inclusions with mean homogenisation temperature of 166°C, recording the presence of hot fluids in the sandstone at the time of faulting. Ion microprobe analysis of quartz overgrowth oxygen isotope values for footwall cements around the Clashach Fault shows a linear increase of δ18O values with increasing distance from the fault plane from +17.9‰ at 4.2m to +20.8‰ at 30.8m. In quartz cements in the footwall of the Burghead Fault, δ18O rises from +17.5‰ at 0.1m from the fault plane to a consistent range of +19.1‰ to +19.5‰ up to 14m distant. Hanging wall cements have a mean δ18O +23.8‰ with range of δ18O +20.1‰ to +25.0‰. An isotopic profile across a single quartz cemented deformation band shows $\delta^{18}O$ is a minimum mean of +20.7‰.

Oxygen isotope and fluid inclusion data records quartz cementation from hot basinal fluids which entered the Hopeman Sandstone adjacent to fault planes. This fluid cooled and mixed with Jurassic meteoric porefluids, precipitating quartz cement at a burial depth of <1.25km. Siliceous fluids were sourced from sediment compaction following Late Jurassic extension in the basin and were expelled up-dip toward the basin margin. Fluid flow was locally focused through the Hopeman Horst, which acted as an exit point for regional fluid expulsion. Within the horst block advecting fluid flow was focused into basinward footwalls by the low permeability vertical fault planes. This was aided by an enhanced reduction in fault permeability by quartz cementation of deformation bands at shallow burial (500m-1km).

## TABLE OF CONTENTS

## LIST OF FIGURES

### CHAPTER 1



### CHAPTER 2



### CHAPTER 3



### CHAPTER 4

## CHAPTER 5

## CHAPTER 6

**CHAPTER 7**



## LIST OF PLATES

**CHAPTER 5**

This page left blank

# Chapter 1.

# Introduction, aims and techniques

---

The Hopeman Sandstone of the Inner Moray Firth Basin, UK North Sea has acted as a natural laboratory containing excellent exposures of faulted sandstone. Field, petrographic, structural and geochemical investigations have been combined to elucidate further understanding of diagenetic cementation, porosity and permeability evolution, development of fault seals, fluid flow and mass transfer in sedimentary basins.

## 1.1 Rationale

Oilfield reservoir quality is used as a way of stating how good or bad a sediment is at hosting oil and permitting its efficient and economic extraction. Reservoir quality is controlled by both the distribution and values of porosity and permeability. In a sandstone suitable as a hydrocarbon-bearing reservoir porosity and permeability initially reduces as burial depth increases. As the rock is buried physical grain compaction reduces porosity, and with progressive burial, cementation combined with chemical compaction, gradually occludes pores.

### 1.11 Quartz cementation

Quartz is usually the most abundant diagenetic cement in sandstones (e.g. Worden and Morad 2000), occurring in significant quantities (>2% vol.) at depths equivalent to a temperature of 70-90°C (Giles *et al.*, 2000), equivalent to 2.5 kilometres burial in the North Sea. A number of previous studies (e.g. Haszeldine *et al.*, 1984, Giles *et al.*, 1992, Fisher *et al.*, 2000) have focused directly on clastic reservoirs, unravelling the controls on quartz cementation and its prediction on a broad scale. In 1999 Lander and Walderhaug produced the first reasonably successful quantitative model of quartz cement in sandstones, based upon the assumptions that silica is locally supplied and the volume precipitated is linked to the rate

of precipitation. For clean sandstones this model generally predicts with good accuracy volumes of regional cementation.

By contrast the development and quantitative significance of more localised diagenetic cementation, in particular around structural features, and which may involve mass transfer and import of silica in an open fluid system, is less well known. This stems primarily from the restrictions of studying oilfields where samples are sourced from infrequently spaced drill cores whose locations are biased toward oil zones and thick sandstones. Although oilfields are rich in data in comparison to the surrounding subsurface, they are less rich than onshore exposures of equivalent rocks. Corbett *et al.* (1998) showed that the accuracy of up-scaling of rock properties measured in reservoir cores is partially dependent upon the scale of the property being measured, and that a strategy of higher resolution measurements of smaller volumes tends toward more accurate geological characterisation. Data sets with locally intense sampling are therefore necessary to be representative and significant in identifying, quantifying and unravelling 'localised' feature-related cementation. In this study, preliminary work indicated that quartz cement volume decreases in a linear pattern with increasing distance from certain exposed fault planes. This allowed a high resolution sampling programme in the zone of rapidly changing cement volume, with each sample located systematically further apart as the rate of change of cement volume decreases, up to distances of tens to hundreds of metres. Such sampling is not generally available from continuous oilfield core, which is limited in volume, and biased toward clean reservoir sands. The solution and focus of this thesis, is to study in statistically significant detail, exposed outcrops which can act as analogues for buried sandstones, and as accurate input data for the up-scaling of similar diagenetic patterns in less well constrained subsurface settings.

## 1.12 Permeability and porosity evolution

Understanding such feature related cementation by studying well exposed hydrocarbon reservoir analogues has important implications for predicting the distribution of porosity and permeability loss in hydrocarbon bearing sands. Absolute values of porosity and permeability dictate the volumes of oil or gas that a sand can hold, and the distribution of that porosity and permeability how easy it is to extract. As well as economic importance porosity and

permeability evolution exerts a strong control on patterns of sub-surface fluid flow and solute migration.

The extent of exposure allows a large data set of porosity, permeability, cement and compaction to be compiled, which can be used as input into models of buried sandstone evolution in order to predict hydrocarbon volumes, as well as patterns and rates of fluid flow. Documentation of cases of extensive shallow burial depth cementation, and fault related cementation, are also rare and little data exists which can be used to model the reservoir quality behaviour of sandstones where these processes are thought to have occurred in rocks now at deeper burial.

Permeability is a key parameter in the economic production of hydrocarbons, and is frequently reduced by cementation. A significantly large data set of samples from the same facies with the same burial history, but greatly differing amounts of cement allows the effect of increasing cement volume on permeability to be elucidated, and aids in understanding the amount of cement which may be critical in reducing permeability below economic values.

## 1.13 Faults as hydrocarbon traps

Fault planes can create traps for hydrocarbons in two different ways. The most understood mechanism is through juxtaposition of a low permeability non-reservoir unit against a high permeability reservoir unit, the porosity, permeability, and thickness of the non-reservoir unit controlling the potential volume of hydrocarbons trapped. A second set of hydrocarbon traps are formed by the creation of low permeability in the fault zone itself. Fulljames *et al.* (1997) classify such faults as 'fault gouge seals' and identify two types, clay smear and brittle deformation. Clay smear or shale gouge sealing faults are created when clay is forced into, and smeared along, a fault plane from surrounding clay layers. Modelling packages can in general predict with good accuracy the sealing potential of such clay smear faults by combining data on fault throw, clay type and number of clay layers. The second type of fault gouge seal, formed through brittle deformation, occurs within clean sandstones where no clay is available to form a smear, and the rock on both sides of the fault is high permeability reservoir sand. Behaviour of these faults in controlling fluid flow is less well known and difficult to predict. Grain crushing and the development of low porosity and permeability

cataclastic textures occurs within both millimetre scale deformation bands present in a zone around the main slip face, and within the major slip face, during faulting. The cataclastic rock in the deformation bands and fault slip face has lower porosity and permeability than the host sand, creating a barrier to fluid flow, but, as Fulljames *et al.* (1997) note, at shallow burial depths (<1km) the deformation bands may not have significantly lower permeability than the host sand, and consequently may not presently be predicted to act as traps for significant volumes of hydrocarbon. At deeper burial depth (>2.7km) the cataclastic bands may become preferentially cemented, enhancing the porosity and permeability loss, and trapping significant columns of hydrocarbons. However, no detailed studies are known which report the quantitative effects of interaction between brittle deformation faults and host rock, which generates significant quantities of cement within the adjacent reservoir sand. Identification, quantification and understanding of the genesis of cements precipitated from fault related fluids in sands surrounding such faults has important implications for understanding the permeability evolution of the fault and surrounding rock. Where such relationships are deduced in data intensive outcrop studies, such as this one, these may be extrapolated to offshore faults and used as data sets in basin models and for predictions of fluid flow pathways. Further, precipitation of cements in the reservoir rock may add to the sealing capacity of the fault at a shallow depth, and reduce the volume of hydrocarbons that can be stored in compartments between faults, due to porosity occlusion by cementation. Most studies of fault behaviour with respect to fluids concentrate on the fault structures and internal textures themselves, here the approach is reversed, the products of fault related fluid flow are investigated to deduce the role of the fault in controlling fluid flow and diagenesis.

## 1.14 Mass transfer and basinal fluid flow regimes

Diagenetic cements are the product of the interaction of fluids and solids in a sedimentary basin. Investigation of cements therefore provides an insight into the movement of solute, and is a powerful method of unravelling the roles played by fluid flow transporting solutes versus local material transport through static porefluids.

Major debate exists whether porefluids remain in stasis within sedimentary basins or whether open systems can prevail with advecting fluids transporting solute which precipitates as diagenetic cements. Evidence for porefluid stasis is primarily from studies of oilfield

sandstones which show significant silica cementation developing at 70-90°C in many different depositional facies, pointing toward slow burial and internally sourced cementation. Theoretical geochemists argue that silica is extremely insoluble at reasonable basinal temperatures, and so cannot be transported in the quantities observed by the volume of fluid available, and therefore must diffuse thorough static porefluids in a closed hydrologic system. The broadly good predictions of quartz cement volume obtained from the Lander and Walderhaug (1999) model of closed system diagenesis, with porefluid stasis and an internal silica source, favour localised solute diffusion and the domination of closed system hydrologic regimes in basins. However the bias of data from oilfield cores, which are aimed to avoid structural features and heterogeneities, means that the picture may be more complex with porefluid stasis the norm but occasionally punctuated by periods of fluid flow, reverting to an open hydrologic system. Large data sets from apparent open system cementation provide a window to investigate this process and importantly identify the conditions under which it can occur, and its importance as a basin process.

Mass transfer through advection of fluids may be constrained by temperatures and volumes of fluids in basins, but it may be locally significant around zones which can act as a focus and transport pathway for such fluids. Faults are known to act as transport pathways for hydrocarbons and other fluids, so it is reasonable to assume that products of open diagenesis may be preferentially associated with such structures. The scale of such deposits of cement may be small in relation to regional patterns of cementation, but locally significant. Study of the well-exposed faults within the Hopeman Sandstone allows statistically confident quantification of the amount of fluid required to transport the cement forming material into the sandstone, and consequently the scale of mass transfer processes associated with fault structures of different scales. Detailed isotopic and geochemical investigations allow the source of the fluid to be refined, adding understanding of the likely sources and mechanisms of advecting fluids to the understanding of the scale of fluid flow. The ability to quantify the scale of mass transfer also adds to understanding of how fluid volumes and temperatures in basins constrain solute transport.

In a wider scope, such mass transfer is not unusual in other basinal settings. Quartz veins are often observed in rift and significant mineral basins, where different temperature relationships and fluids exist. Elucidation of controls on large-scale mass transfer within the Inner Moray Firth can assist in bridging the link between these differing scenarios.

## 1.2 Study area

The Permian aeolian Hopeman Sandstone Formation (Warrington *et al.*, 1980) crops out on the southern coast of the Inner Moray Firth basin, Scotland. Stratigraphically the sandstone is partly equivalent in age to the Permian Rotliegend hydrocarbon reservoirs of the Southern North Sea (Glennie and Buller 1983) and is an excellent facies analogue for these deeply buried hydrocarbon-bearing sandstones (Fig. 1.1).

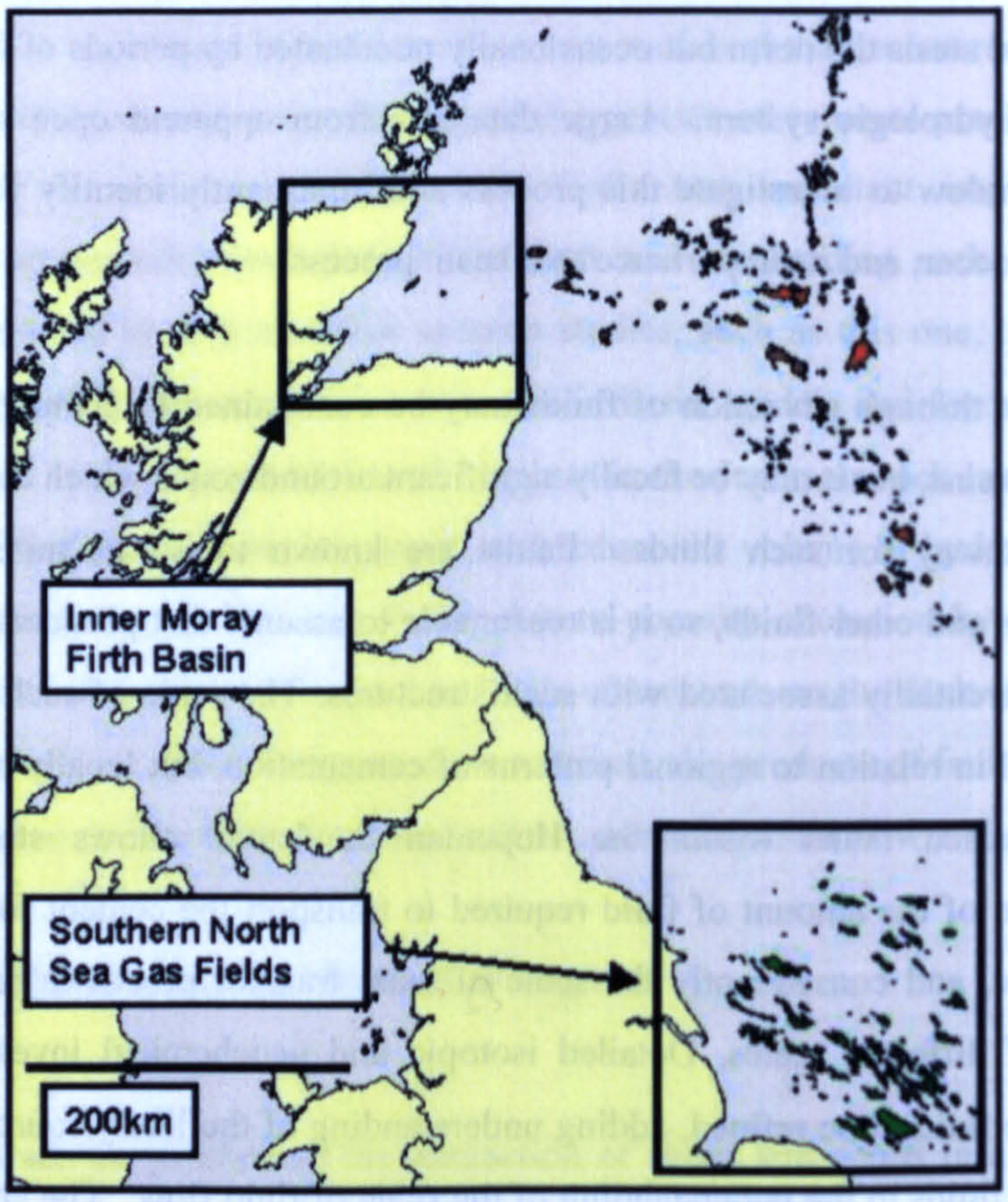


**Figure 1.1. Location of the Inner Moray Firth Basin, within which the Upper Permian Hopeman Sandstone crops out. The Hopeman Sandstone is a close sedimentological and age analogue to the aeolian Rotliegend gas reservoirs in the Southern North Sea.**

The exposures are visible for 8km along the coastline and also within adjacent quarries. Major (>100m) to minor (<10m) scale faults cut the Hopeman Sandstone, juxtapose it against the Triassic Burghead Sandstone, and crop out on the shore (Fig 1.2). The major faults are considered as equivalent size to faults identifiable on offshore seismic surveys, the minor

faults are below the threshold of seismic resolution. This allows the onshore faults to be classified as either seismic scale (>50m) or sub-seismic scale (<50m) (e.g. Kearey *et al.*, 2001) in terms of analogous offshore structures.

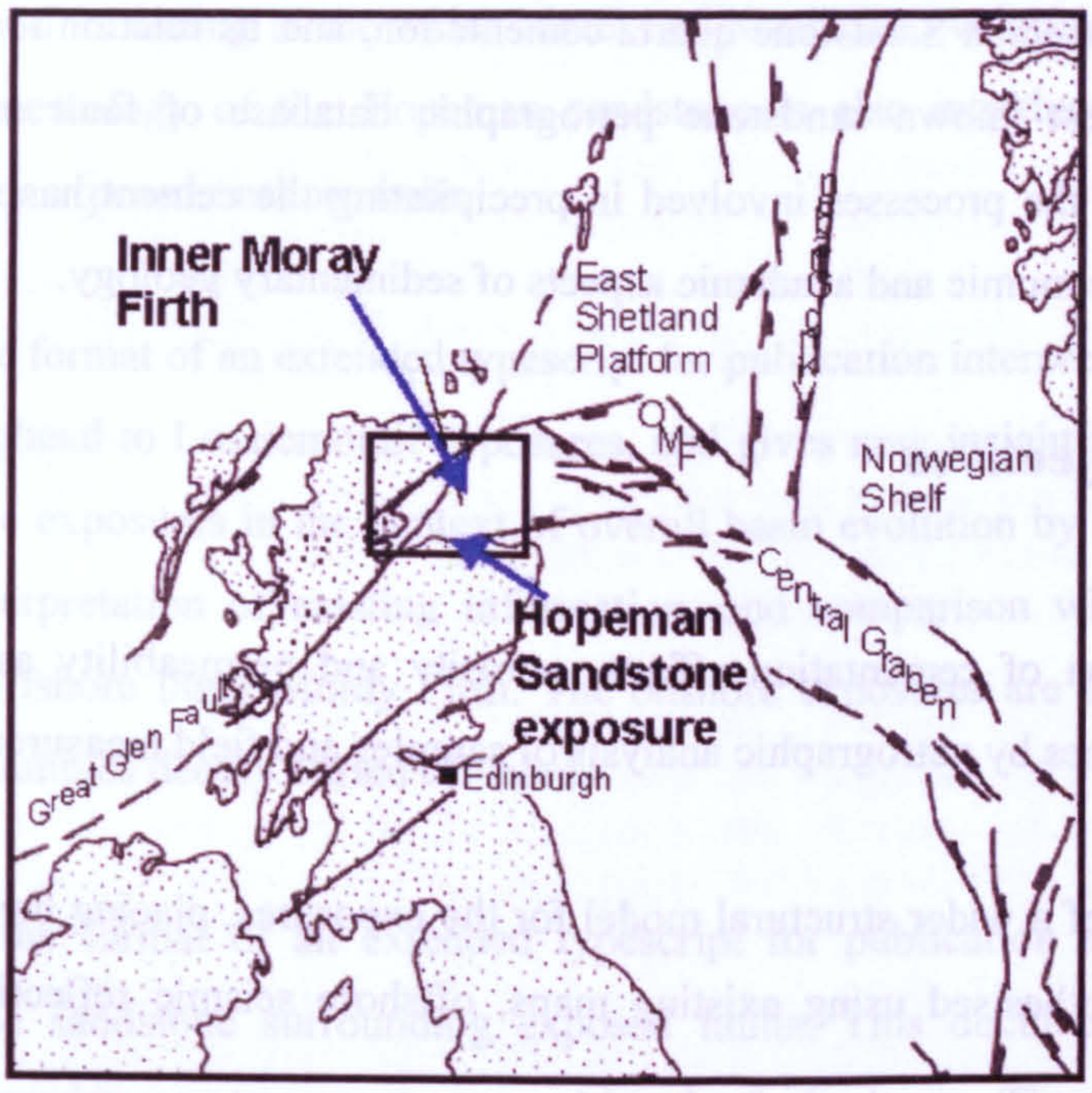


**Figure 1.2. Location map of the Inner Moray Firth Basin within the context of the North Sea Jurassic rift system. The Hopeman Sandstone is exposed on the southern Moray Firth coastline.**

Quartz cementation in the Hopeman Sandstone was first noted by Mackie in 1925 and unusual patchy silicification and localised cementation, in particular around joints and fractures, was first recorded by Peacock *et al*. (1968).

The extent of the faulted exposures of the Hopeman Sandstone allows a detailed 3-dimensional investigation of a structurally related case of diagenetic quartz cementation, providing excellent data for an investigation of cementation, fault seal development, porosity and permeability evolution and the processes of fluid flow and mass transfer. The sandstone is similar to offshore sands forming hydrocarbon reservoirs which also contain sand:sand fault contacts at both the seismic and sub-seismic scale. The onshore faults show localised and laterally varying quartz cement, and are accessible for intensive sampling. Investigations show that the cementation is unusual in two respects; firstly it is spatially related to fault planes and is asymmetric across those fault planes, and secondly the cement was precipitated

at shallow depth, and has not experienced the deep burial conditions typical of most extensively quartz cemented sandstones.

The thesis presented here concentrates upon deciphering the petrography and geochemistry of the unusual Hopeman Sandstone quartz cementation, and its relation to structural setting, creating the largest known sandstone petrographic database of fault associated cement. Understanding of the processes involved in precipitating the cement has implications for a number of both economic and academic aspects of sedimentary geology.

## 1.3 Key objectives

1 – Quantification of cementation effects, porosity and permeability associated with the exposed fault planes by petrographic analysis of samples and field measurements.

2- Development of a wider structural model for the exposures, placing the outcrops within a basin setting, synthesised using existing maps, offshore seismic reflection data and field observations

3- Understanding of fluid-rock interaction with respect to the quartz cement, using oxygen isotope and fluid inclusions methods. An understanding of the role and scale of fluid flow and mass transfer in the Inner Moray Firth and beyond.

4- Contribute to a broader understanding of the shallow burial diagenetic products and the resultant effect on porosity and permeability evolution in an oilfield sandstone analogue.

5- A greater knowledge of fault permeability development at shallow burial depth in sand:sand faults and the effects on surrounding sandstone.

## 1.4 Thesis contents

**Chapter 2** provides a background to the subject of diagenesis and in particular the historical issues regarding compaction, quartz cementation, fault seals and structurally controlled

diagenesis. This chapter also introduces and discusses fault development and field and laboratory insights into fault porosity and permeability evolution in clay free sandstones

**Chapter 3** reviews and discusses previous work on Inner Moray Firth structural development and stratigraphy, and its setting in the wider context of North Sea evolution. The geography, stratigraphy, sedimentology of the Hopeman sandstone is also introduced and discussed along with the other exposed onshore units.

**Chapter 4** is in the format of an extended typescript for publication interpreting the structural setting of the Burghead to Lossiemouth exposures, and gives new insight into the structural development of the exposures in the context of overall basin evolution by integrating recent data with a re-interpretation of existing information, and comparison with the history of structures in the offshore Inner Moray Firth. The onshore exposures are located on a horst block similar to examples deeply buried offshore.

**Chapter 5** is in the format of an extended typescript for publication and examines the petrography of the sandstone surrounding exposed faults. This documents a volumetric relationship of increasing quartz cement approaching the fault planes. The quartz cement is a shallow burial cement and paragenetically predates most other diagenetic phases, especially barite and late stage galena mineralisation.

**Chapter 6** is in the format of an extended typescript for publication and examines the fault related cement using fluid inclusion analysis and oxygen isotope data to deduce the origin and evolution of fluids from which the cement precipitated. Results of mass balance investigations show the volume of fluid necessary to import the volume of silica observed around the fault planes is on a basinal scale.

**Chapter 7** is a discussion chapter drawing on the previous chapters/papers to integrate stratigraphic, structural, petrographic, geochemical and basinal data from the thesis, presenting a model for quartz cementation in the Hopeman Sandstone. The discussion evaluates and critically analyses a number of hypotheses and explains the findings of this study in a wider scope. The relevance of this study both to the study of fluid flow and mass transfer in the upper crust, and to applications in petroleum geology is also addressed.

**Chapter 8** summarises the main conclusions from the thesis, their contribution to geological understanding, and examines the future direction and value of research in this area.

---

# References

**Corbett, P.W.M., Jensen, J.L. and Sorbie K.S., 1998.** A review of up-scaling and cross-scaling issues in core and log data interpretation and prediction. *In*: Core –Log Integration (eds: Harvey, P.K. and Lovell, M.A.), Geological Society Special Publication, 136, p.9-16.

**Fisher, Q.J., Knipe, R.J. and Worden, R.H., 2000.** Microstructures of deformed and non-deformed sandstones from the North Sea: implications for the origins of quartz cement in sandstones. *In*: Quartz Cementation in Sandstones (eds: Worden, R.H. and Morad, S.), Special Publication of the International Association of Sedimentologists, 29, p. 129-146.

**Fulljames, J.R., Zijerveld, L.J.J. and Franssen, R.C.M.W., 1997.** Fault seal processes: systematic analysis of fault seals over geological and production time scales. In Hydrocarbon Seals: Importance for Exploration and Production (eds. Moller-Pedersen, P. and Koestler, A.G.) Norwegian Petroleum Society Special Publication, 7, p. 51-59.

**Giles, M.R., Stevenson, S., Martin, S.V., Cannon, S.J.C., Hamilton, P.J., Marshall, J.D. and Samways, G.M., 1992.** The reservoir properties and diagenesis of the Brent Group; a regional perspective. In Geology of the Brent Group (eds. Morton, A.C., Haszeldine, R.S., Giles, M.R. and Brown, S.), Geological Society Special Publication, 61, p. 289-327.

**Giles, M.R., Indrelid, S.L., Beynon, G.V. and Amthor, J., 2000.** The origin of large-scale quartz cementation: evidence from large data sets and coupled heat-fluid mass transport modelling: *In*: Quartz Cementation in Sandstones (ed: Worden, R.H. and Morad, S.), Special Publication of the International Association of Sedimentologists, 29, p. 21-39.

**Glennie, K.W. and Buller, A.T., 1983.** The Permian Weissliegend of NW Europe: the partial deformation of aeolian sand dunes caused by the Zechstein transgression. Sedimentary Geology, 35, p. 43-81.

**Haszeldine, R.S., Samson, I.M. and Cornford, C., 1984.** Dating diagenesis in a petroleum basin: a new fluid inclusion method. Nature, 307, p.354-357.

**Kearey, P., Brooks, B.M. and Hill, I. 2001.** An introduction to geophysical exploration.(3rd edition), Blackwell Science.

**Lander, R.H. and Walderhaug, O., 1999.** Predicting porosity through simulating sandstone compaction and quartz cementation. American Association of Petroleum Geologists, 83, p. 433-449.

**Mackie, W., 1925.** The Principles that Regulate the Distribution of Particles of Heavy Minerals in Sedimentary Rocks, as illustrated by the Sandstones of the North-East of Scotland. Transactions of Edinburgh Geological Society, 11, p. 138-164.

**Peacock, J.D., Berridge, N.G., Harris, A.L. and May, F., 1968.** The Geology of the Elgin District. HMSO, Edinburgh.

**Warrington, G., Audley-Charles, M.G., Elliott, R.E., Evans, W.B., Ivimey-Cook, H.C., Kent, P.E., Robinson, P.L., Shotton, F.W. and Taylor, F.M., 1980.** A correlation of Triassic rocks in the British Isles. Geological Society of London, Special Report, 13,p. 1-78.

**Worden, R.H. and Morad, S., 2000.** Quartz cementation in oil field sandstones: a review of the key controversies. *In*: Quartz Cementation in Sandstones (ed: Worden, R.H. and Morad, S.), Special Publication of the International Association of Sedimentologists, 29, p. 1-20.

# Chapter 2.

This chapter introduces the subject of clastic diagenesis in sediments, and reviews our current understanding of the key processes and their implications for porosity and permeability evolution. An explanation of sandstone compaction, quartz cementation, secondary porosity and fault and fracture related cementation is presented. The second major focus of the chapter is faulting within clean sandstones, and how such faults interact with sub-surface fluids. The ways in which faults can act as traps and conduits to hydrocarbon, and other fluids, is discussed, and both laboratory and field studies of the temporal and spatial development of fault structures is discussed, with the aim of summarising present day knowledge on fault permeability. Many previous diagenetic studies suggest fault related fluid flow as a mechanism for cementation or dissolution, by examining solely the products of such a process. In contrast many structural geology studies have focussed on the internal characteristics of fault zones in order to understand their effect on fluids, without detailed consideration of any associated diagenetic products outwith the fault structure. In this chapter the aim is to bring together our understanding of the major controls on diagenesis with those factors controlling fault permeability development, to set a wider theoretical background for the ensuing papers, and to allow a more thorough reconciliation of the diagenetic data in this thesis, with available knowledge on structural evolution.

# Clastic Diagenesis and Fault Development

## 2.1 Introduction

The term clastic diagenesis is defined here as encompassing all of the physical and chemical processes which affect a body of sand from deposition through burial, until conditions of metamorphism prevail. This combination of physical and chemical mechanisms can destroy, fill, and create, porosity and permeability, dramatically reducing or enhancing the reservoir quality of oilfield sandstones (Fig. 2.1.). The understanding of diagenetic mechanisms and the consequent ability to develop predictive relationships of sub-surface phenomena therefore have important economic as well as academic implications. Faults in clean, clay free, sandstones can act as barriers or conduits to basinal fluids and can influence diagenetic products and phases. The porosity and permeability evolution of these faults is crucial in predicting how they may control fluid flow and consequently diagenesis.

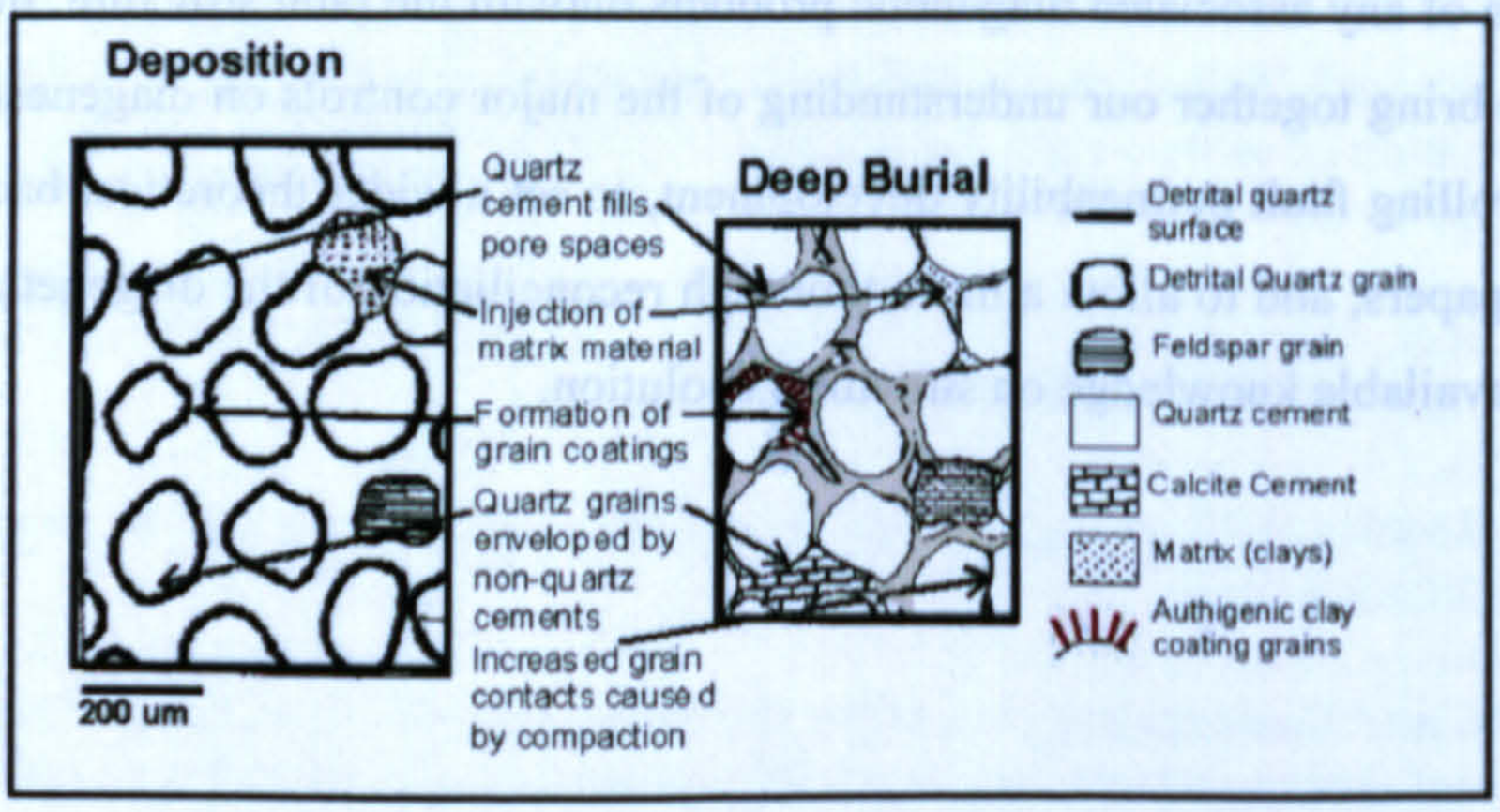


**Figure 2.1. Major diagenetic processes affecting a rock from deposition to deep burial. Compaction and cementation can be seen to destroy and infill pore space. Redrawn and modified from Lander aznd Walderhaug 1999.**

This chapter examines and summarises the current state of knowledge of diagenetic processes, focusing upon quartz cementation, a problem which is addressed in this thesis. It

also examines present understanding of fault permeability evolution through insights from structural studies.

## 2.2 Compaction

Compaction is one of the dominant mechanisms responsible for porosity loss during deep burial of sands (Houseknecht 1987, Lundegard 1992, Ehrenberg 1995). It can be divided into two processes, mechanical and chemical.

### 2.21 Mechanical compaction

Mechanical compaction occurs at depths of 0-2.5km, before chemical compaction, and involves the re-arrangement of non-ductile (brittle) grains through increased lithostatic stress associated with increasing burial depth. This grain re-arrangement results in a tighter packing configuration which reduces pore space. The volume of detrital grains is not reduced by mechanical compaction, however fracture and cleavage of grains may aid in the re-packing and volume reduction. The term Intergranular Volume (IGV) is used to describe the total volume between grains (Fig. 2.2.); it is a similar term to 'minus-cement porosity', but also includes any matrix material.

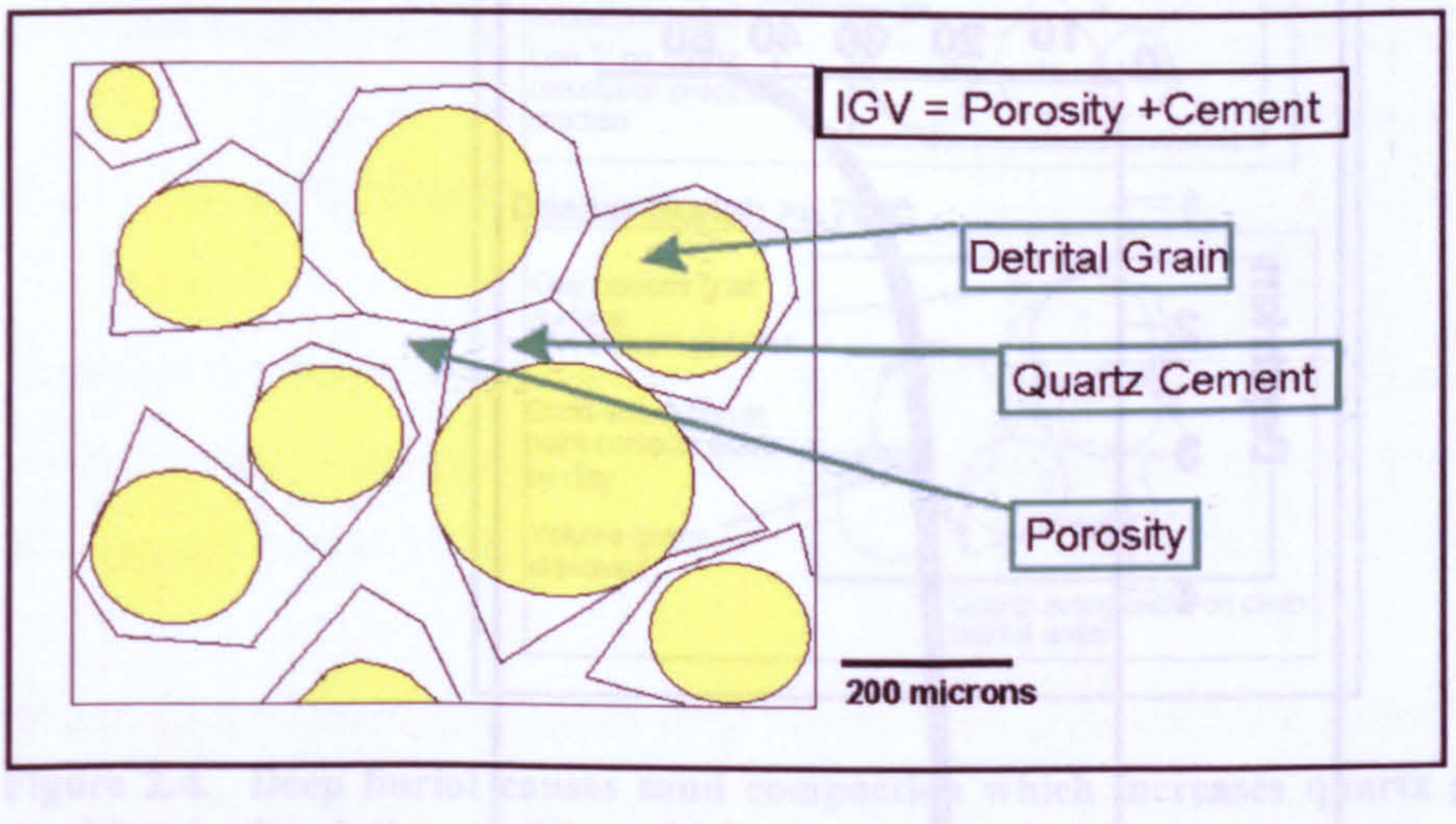


**Figure 2.2. Cartoon definition of the term Intergranular Volume (IGV). The term accounts for the volume of rock composed of present day pore space and cement. It is a measure of the compactional state of the rock, used to determine the importance of compactional versus cementational porosity loss. It is equivalent to minus-cement porosity where matrix is absent in a sediment.**

Published data concerning the depositional porosity of sands shows a common range between 35 and 49%, with a mean of 40% (Houseknecht 1987), based upon measurement of natural modern sands (Hamilton and Menard 1956, Beard and Weyl 1973, Pryor 1973) and laboratory packing experiments (Beard and Weyl 1973). The amount of porosity increases with increasing grade of sorting, and is strongly related to depositional environment. Dune sands were found by Pryor (1973) to have original porosity of 42 to 55%, mean 49%. The presence of a high volume of ductile lithic grains may involve total destruction of IGV due to deformation of the ductile fragments during mechanical compaction (Dickinson 1970, Rittenhouse 1971a).

In sands containing dominantly non-ductile grains, IGV can be reduced to 26% rock volume (Houseknecht 1987, 1989). Paxton *et al.* 2002 compiled a large thin section database of uncemented sandstones (Fig. 2.3) and showed that mechanical compaction reduces to about 26% whereby a stable framework is created which requires grain inter-penetration and chemical compaction to reduce IGV to less than 26%. This is in agreement with thin section estimates by Houseknecht (1987, 1989) and with the work of Graton and Fraser (1935) who found a value of 26% maximum intergranular volume, or porosity where cement is absent, through experiments packing perfectly spherical shapes.

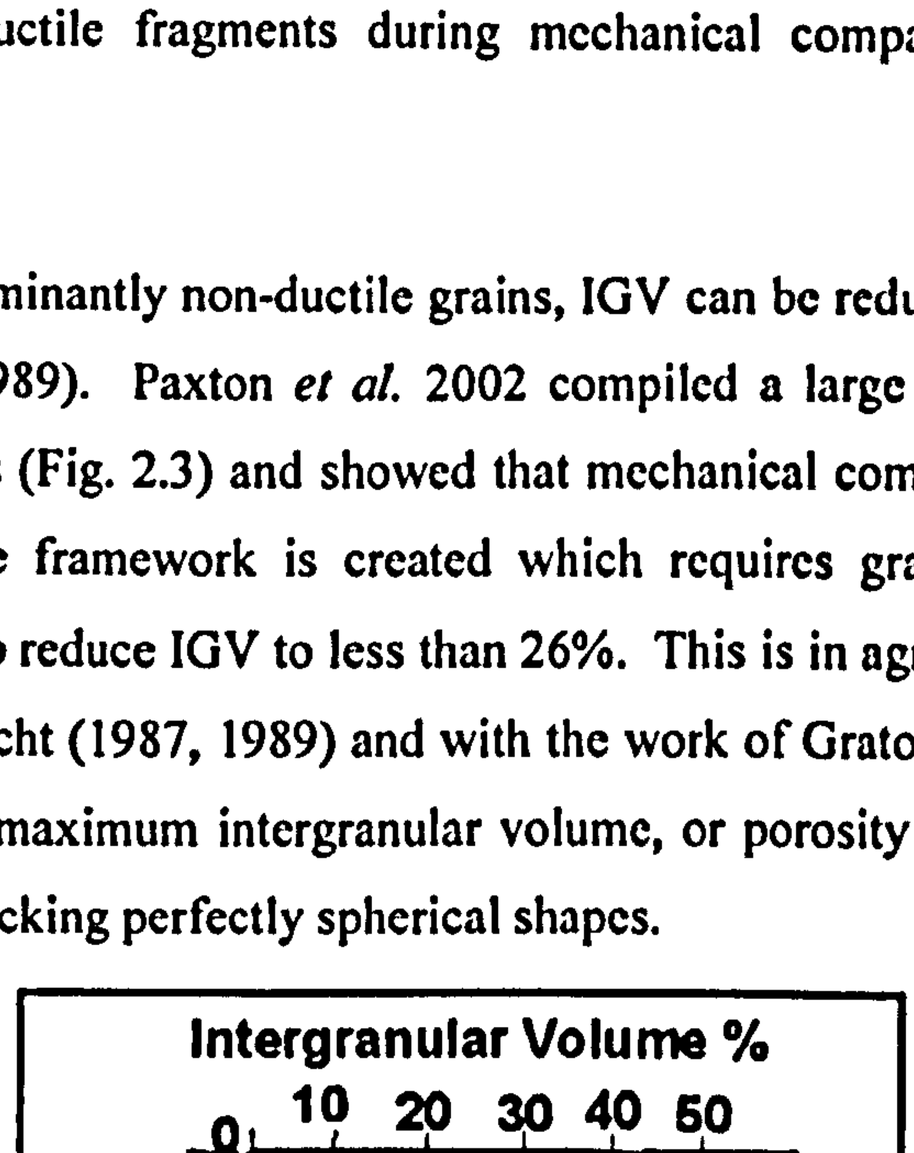


**Figure 2.3. Decrease in IGV with increasing burial depth, based upon a global thin section database of uncemented or poorly cemented quartzose sandstones, with no ductile grains. Redrawn from Paxton *et al.* (2002).**

## 2.22 Chemical compaction

At increasing lithostatic stress, typically at depths below mechanical compaction, which is around 2 km in sandstones, grain contacts begin to dissolve decreasing the volume of detrital framework grains. This leads to increased packing and further reduction in IGV. Extreme chemical compaction can lead to development of stylolites along which a large volume of detrital material is dissolved. Chemical compaction is implicitly related to precipitation of cements in sandstones by acting as a source of solute, which may precipitate locally (Fig. 2.4.), or be removed from the sand and precipitate in another unit. Dissolution and local re-precipitation of whole detrital grains may occur, with the volume occupied by the dissolved grain acting to increase porosity but having no effect on IGV. Ehrenberg (1995), in a review of quantitative petrographic methods and theory, pointed out that underestimation of IGV loss may occur where dissolution of grains is followed by collapse of the grain mold, reducing IGV, but difficult to detect.

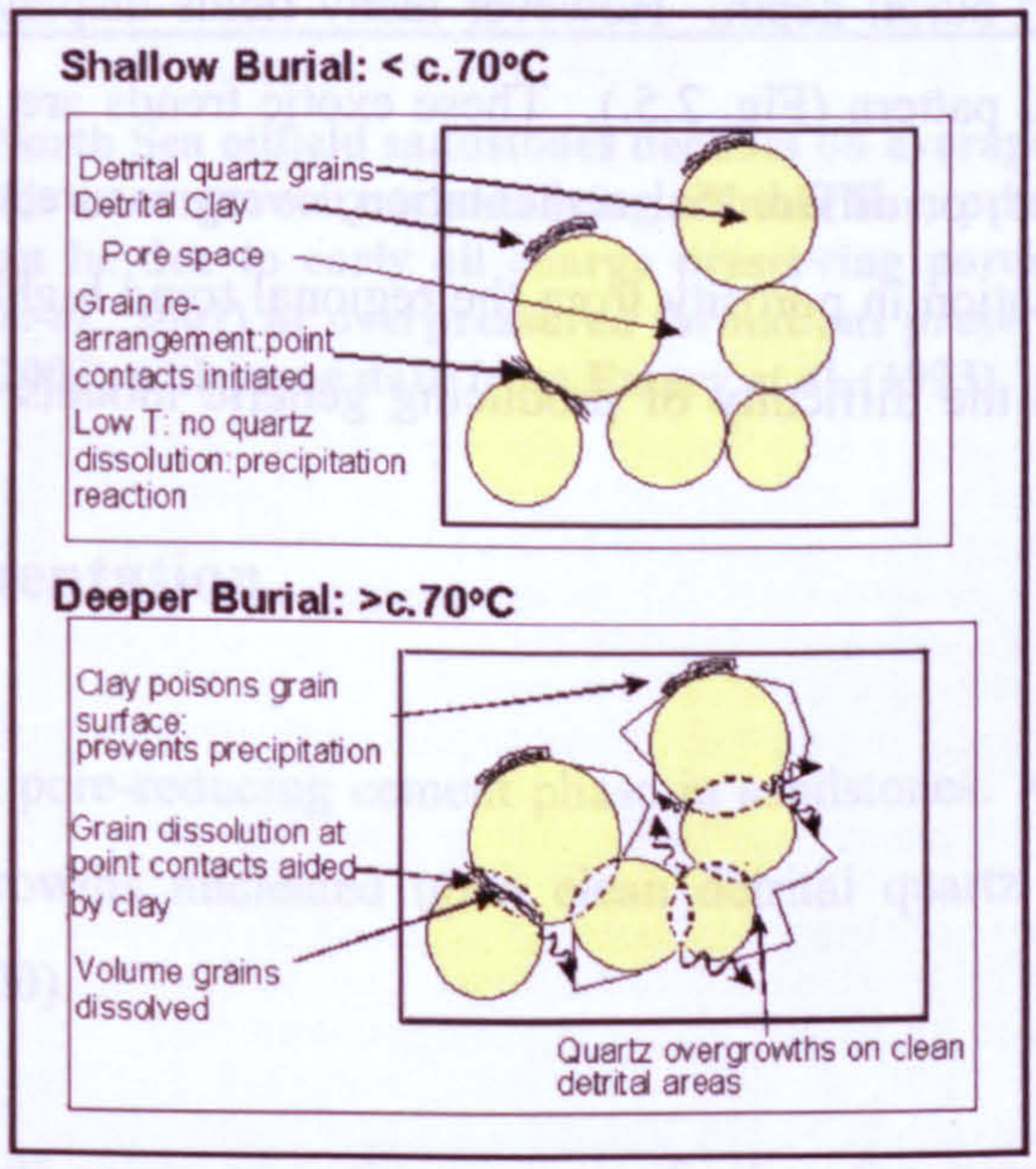


**Figure 2.4. Deep burial causes sand compaction which increases quartz grain:grain contact, resulting in dissolution of silica which may precipitate as quartz cement on adjacent suitable quartz grain surfaces.**

## 2.23 Effect on porosity and permeability

Porosity is reduced through compaction and cementation, and causes a reduction in the permeability of a sandstone. Collation of large databases of sandstone porosities and compositions at a range of burial depths has allowed the production of plots of IGV versus depth, revealing the quantitative effect of compaction on porosity and subsequently permeability. These 'compaction curves' can be used to predict the IGV of a sandstone at a specific burial depth. IGV plots do not account for cementation effects.

Paxton *et al.* (2002) published a compaction curve (Fig. 2.3.) for brittle, uncemented sands based on the examination of over 450 thin section samples. The curve allows the ideal IGV of a sandstone to be predicted if burial depth is known. Inversely the maximum burial depth of uncemented, and uplifted, sandstone can be estimated if the IGV is known.

The effects of cementation are accounted for in porosity-depth plots. A compilation of depth-porosity relationships from North Sea oilfields deeper than 2km shows a linear trend of c.8% porosity loss per km of burial depth. However many fields display porosity values which differ from the regional pattern (Fig. 2.5.). These exotic trends are a result of one or more processes of: - inhibited, or differential cementation; overpressure; and secondary porosity development. The variation in porosity from the regional trend highlights the complexity of diagenetic process and the difficulty of producing generic models, even within one basin system.

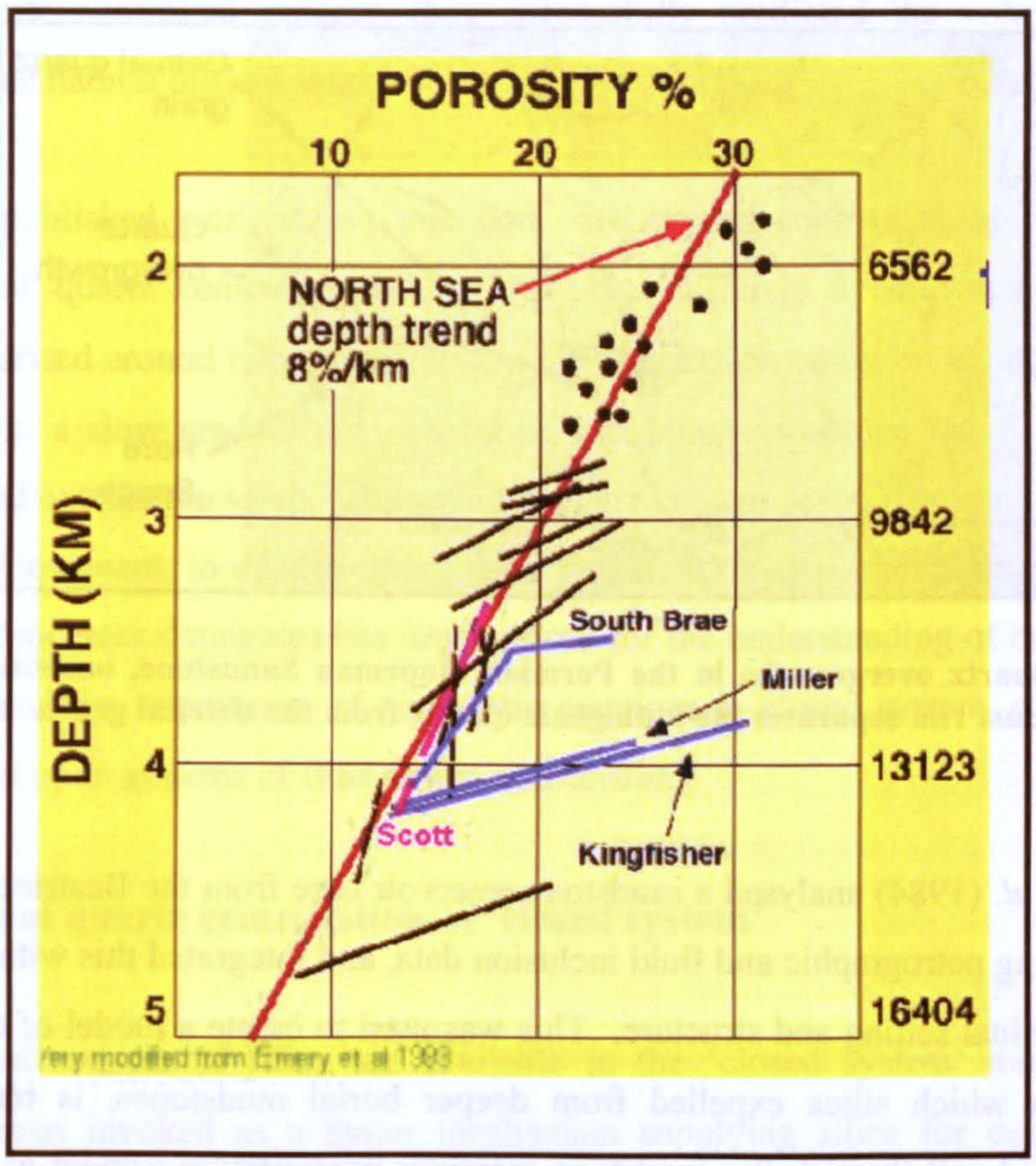


**Figure 2.5. Porosity in North Sea oilfield sandstones declines on average 8%/km with increasing burial depth. Many fields have porosity trends lying off this line, preserving higher porosities than predicted. This can be due to early oil charge preserving porosity (South Brae, Miller, Kingfisher) (Marchand *et al.*, 2001) or overpressured formations preserving secondary porosity. From Haszeldine et al. (2003) with some data from Emery et al. (1993).**

## 2.3 Quartz cementation

Quartz is the dominant pore-reducing cement phase in sandstones. Quartz cement typically forms syntaxial overgrowths nucleated upon clean detrital quartz grains (Fig. 2.6.) (e.g. Worden and Morad 2000).

Major disagreement still exists over the sources of silica for quartz cementation and the controls on its distribution, despite a great deal of published research using a variety of approaches, from petrography through to isotopic analysis and computer modelling. Numerous papers have been published, and some brief examples are presented to show differing methods of investigation and their differing conclusions on the origin of quartz cementation.

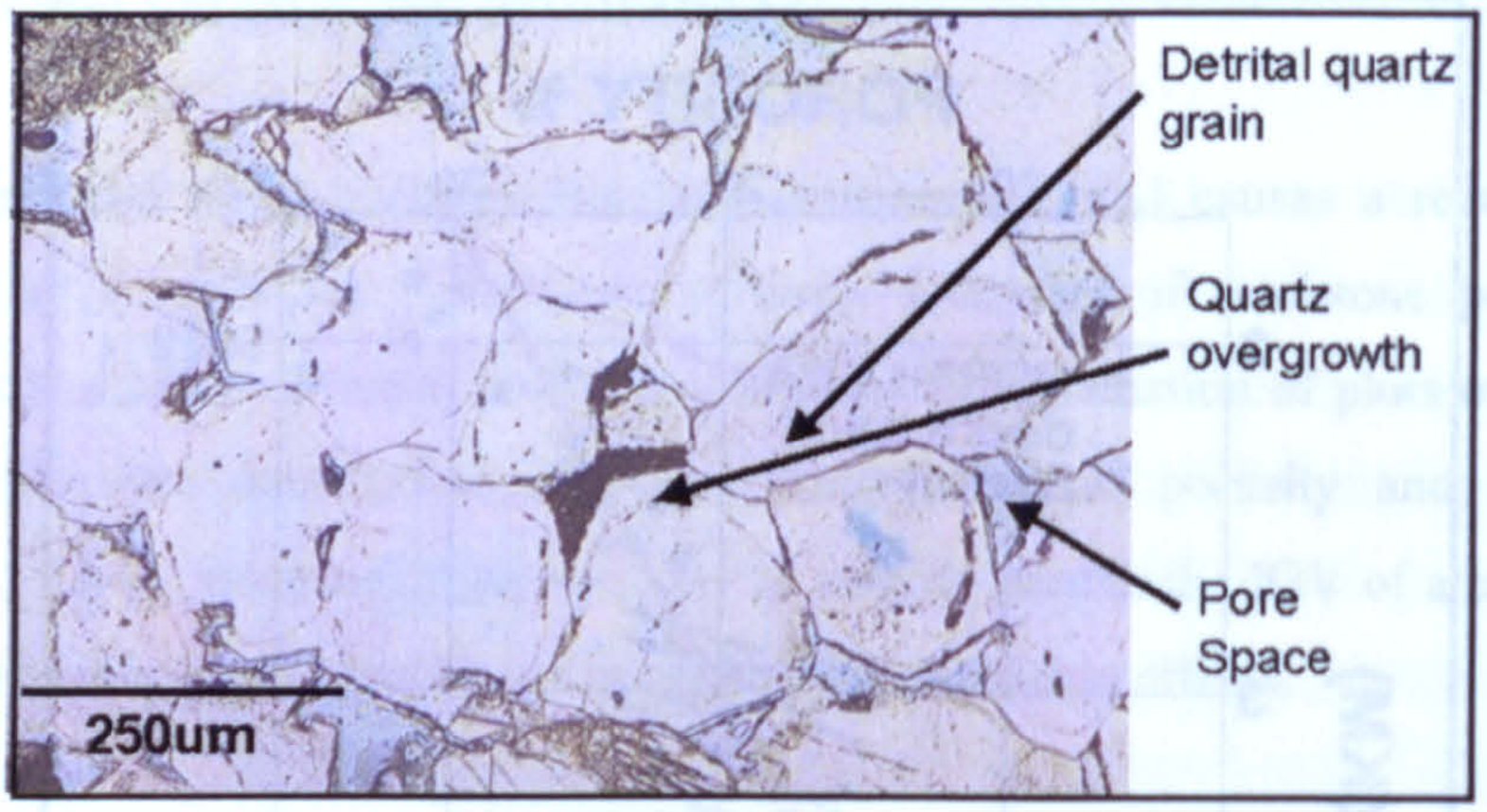


**Figure 2.6. Quartz overgrowths in the Permian Hopeman Sandstone, onshore Inner Moray Firth. A thin dust rim separates the authigenic quartz from the detrital grain. Blue dye marks pore space.**

Haszeldine *et al.* (1984) analysed a sandstone reservoir core from the Beatrice oilfield in the North Sea, using petrographic and fluid inclusion data, and integrated this with an analysis of the oilfield basinal setting and structure. This was used to create a model of convective cell fluid flow, in which silica expelled from deeper burial mudstones, is transported in a convective fluid cell through the sandstone reservoir precipitating cement at shallower and cooler depths in the most permeable horizons. In a similar petrographic approach Bjorlykke *et al.* (1992) analysed quartz cementation in the Brent Group oil reservoirs of the North Sea as part of an integrated diagenetic study. Through observation of thin sections they concluded that quartz cement was locally derived from detrital quartz dissolution and re-precipitation in an isochemical system controlled by burial depth. Lynch (1996) combined a petrographic study with oxygen isotope analysis of authigenic quartz from the Frio Formation, Gulf of Mexico, using the petrographic data to imply fluid flow and import of silica for cementation. Measurement of the oxygen isotope ratio of the cement was then used to suggest that ascending hot fluids transported silica. Petrography, isotope geochemistry and measurement of fluid inclusions within quartz cement were used by Hartmann *et al.* (2000) to conclude that authigenic quartz in the Permian Gharif Formation of Oman, grew in a local, closed system controlled by burial temperature. Lander and Walderhaug (1999) built on some of the principles of quartz cementation that have been derived from direct studies of sandstones to produce a computer model which simulates sandstone compaction and quartz cementation. Based upon the premise that quartz cementation is an internal, temperature and

precipitation rate controlled process, they successfully predicted the volumes of quartz cement for some natural oilfield sandstones.

A review of published work shows that both similar and contrasting approaches to the investigation of quartz cement genesis can lead to different conclusions. Opinions are frequently polarised around two arguments, one that quartz cementation is internally sourced and proceeds in a slow gradual manner during increasing sandstone burial; the other that silica is sourced outside the sandstone in which quartz cement precipitates, and is transported through fluid movement, in discrete more rapid cementation episodes. The extent to which each of these processes dominates has implications for the understanding of basin scale fluid flow patterns and the importance of diagenetic reactions in closed system, static porefluids and reactions in open systems of fluid and mass transfer.

## 2.31 Internal quartz cementation; a 'closed system'

Several internal sources of silica are available in the 'closed system' model. Pressure solution has been invoked as a major mechanism supplying silica for cementation (e.g. Bjorlykke *et al.*, 1992), and provides the simplest explanation. During deep burial (>2.5km) compaction point contacts between detrital quartz grains result in dissolution, in extreme cases forming stylolites. Silica diffuses along a concentration gradient through static pore fluids, from high silica activity at zones of dissolution, to low silica activity at sites of precipitation, leading to the growth of authigenic quartz on clean detrital quartz grain surfaces over a c.1m scale (Fig.2.4). Renard *et al.* (2000) conducted laboratory experiments growing quartz which indicated that the process is controlled by stress, temperature and grain size. Earlier work by Bjorkum (1996) pointed to temperature as the controlling factor in silica dissolution during diagenesis, and so more important than stress at grain contacts. In natural sandstones the presence, and in particular the textural distribution, of clay is an important factor in controlling pressure solution. Clay at point contacts between quartz grains is thought to trap a thin film of fluid which, during contact against an adjacent grain, assists the dissolution and diffusion of silica (Heald and Larese 1974). In contrast clay coating large areas of detrital grains can prevent the precipitation of quartz by reducing available detrital quartz sites for overgrowth precipitation (e.g. Fisher *et al.*, 2000). The rate of quartz cementation from pressure solution is likely to be controlled by kinetic factors. The rate-controlling step is either, rate of dissolution, diffusion through the pore water or rate of

precipitation. Whichever of these is the slowest will control the overall reaction speed. Studies of oilfield sand reservoirs show temperature is the key control on precipitation rate (e.g. Giles *et al.* 1992) and so in many cases temperature dictates rate of precipitation, and consequently, acts as the key control on the three-stage dissolution-diffusion-precipitation process. Geological observations of extensive authigenic quartz development at increased temperatures (>70°C) (e.g. Giles *et al.*, 1992, 2000) are in agreement with laboratory modelling of significantly enhanced quartz cement growth controlled by temperature (e.g. Bjorkum 1996, Renard *et al.,* 2000). Analysis of a large petrographic dataset of quartz cement volumes in sandstone reservoirs by Giles *et al.* (2000) from the North Sea, Oman, the Gulf Coast and Malaysia showed the onset of significant quartz cementation at burial depths equivalent to c.80°C (Fig. 2.7 and 2.8.). These data, from many different depositional facies, show that temperature is a greater control than facies and that the simplest predictive model for quartz cementation is temperature combined with an internal silica source. However the temperature control does not exclude the precipitation of authigenic quartz from hot fluids ascending to shallow depths in sedimentary basins.

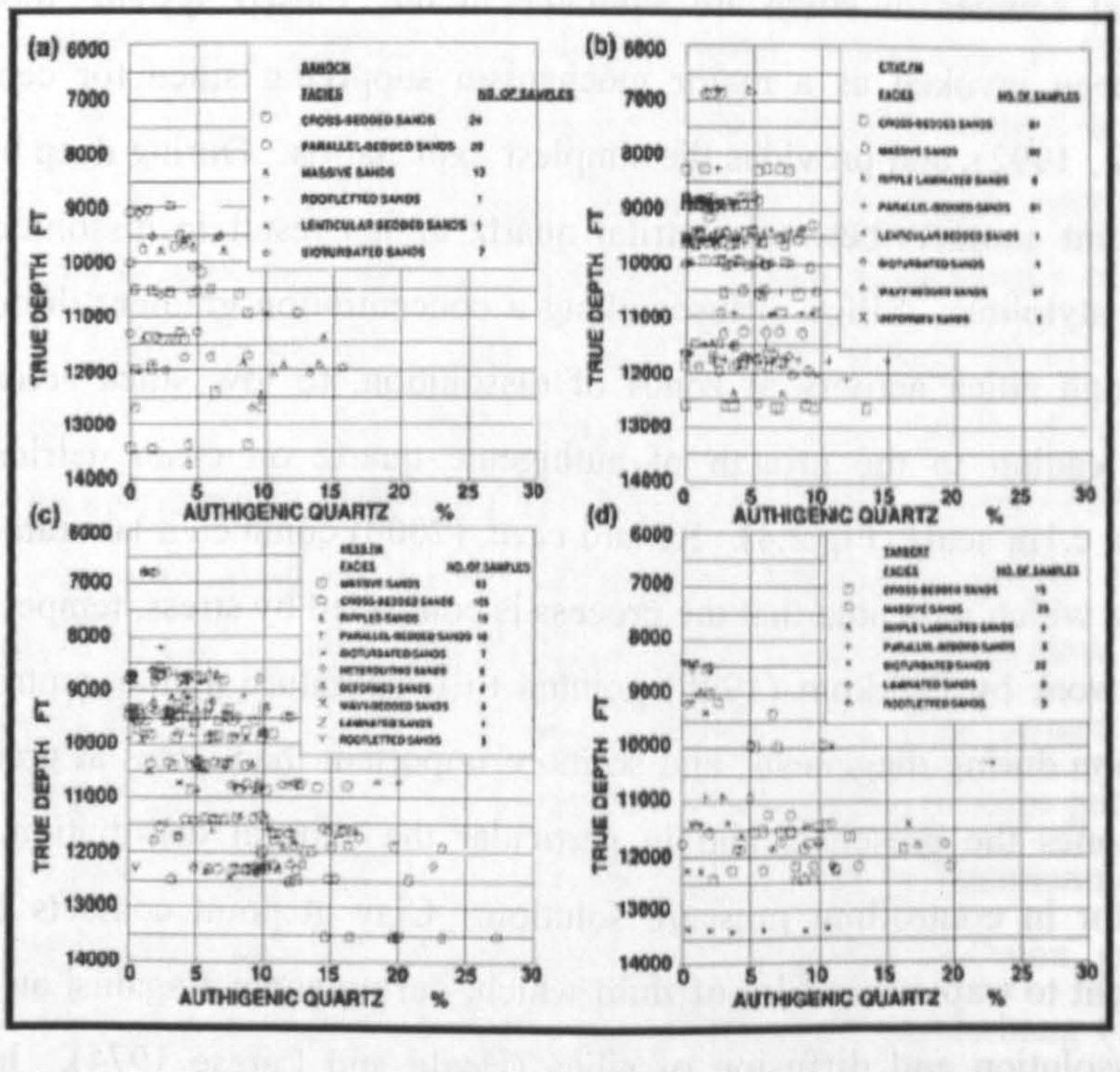


**Figure 2.7. Quartz cement volumes versus depth in four formations of the Brent Group, North Sea. Despite differences in facies a broad increase in maximum quartz cement occurs at c.9000ft in depth, equivalent to a temperature of 80°C +/- 10°C. Comparison with data from other basins (Fig. 2.8) provides evidence for a temperature control on the cementation process. From Giles *et al.*, 1992.**

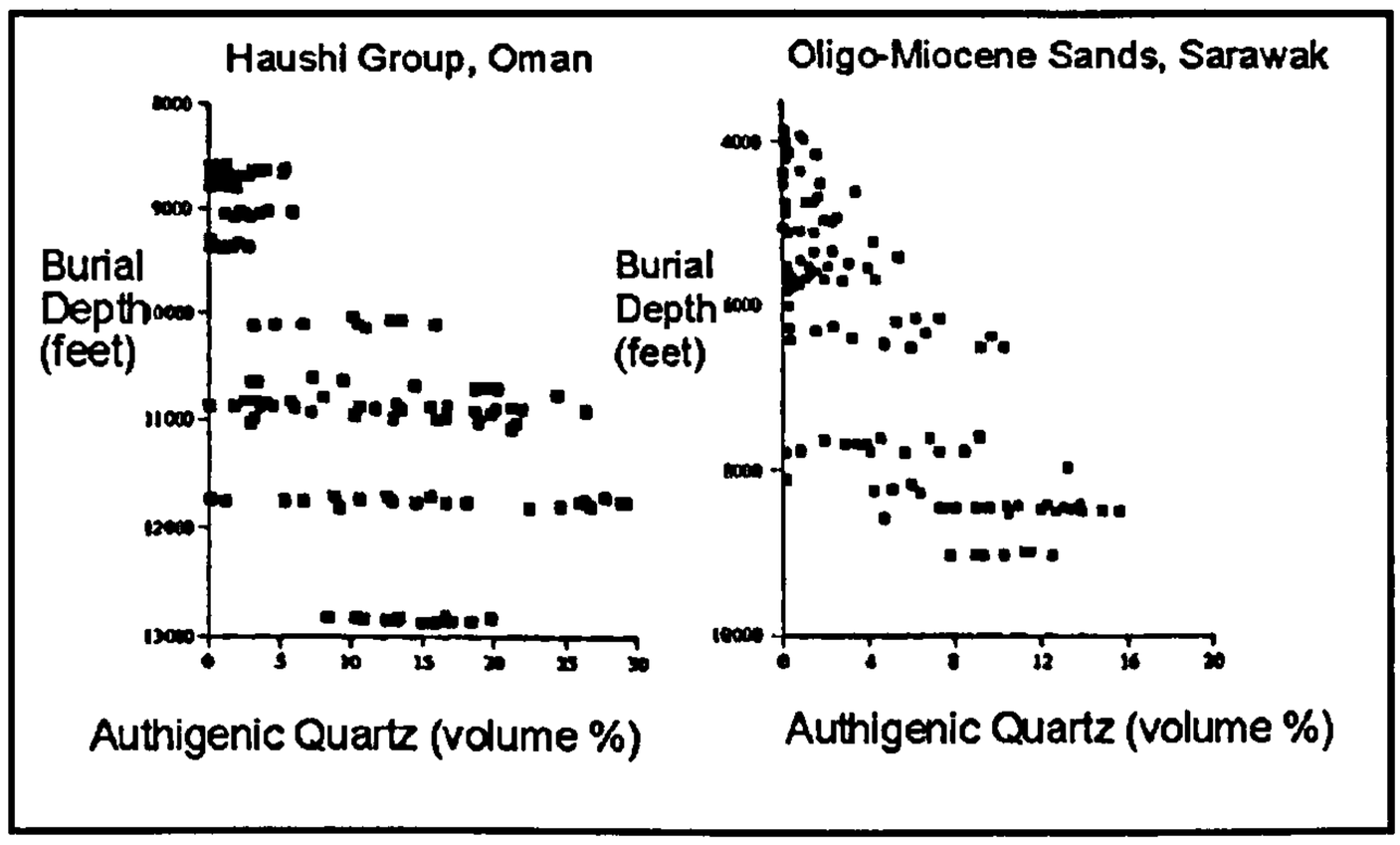


**Figure 2.8. A similar pattern of increasing quartz cement volume with depth is visible in two different basins. Significant cementation occurs at the same temperatures in both data sets, but at differing depths. The Sarawak basin has a higher geothermal gradient, allowing cementation to occur at shallower depths, and providing evidence for a strong temperature control on quartz cementation. Modified from Giles *et al.*, 2000.**

Aside from detrital quartz dissolution during chemical compaction, feldspar dissolution and burial transformations of clay have also been invoked as a local source of quartz cement. During burial, and increased temperature, feldspar can break down to form clay minerals such as kaolinite (1) and/or illite (2), releasing silica into solution.

$$2KAlSi_3O_8 + 2H+ + H_2O = Al_2Si_2O_5(OH)_4 + 4SiO_2 + 2K+ \qquad (1)$$

K-feldspar kaolinite quartz

$$2KAlSi_3O_8 + 2H+ = KAl_3Si_3O_{10}(OH)_2 + 6SiO_2 + 2K+ \qquad (2)$$

K-feldspar Illite quartz

At greater temperatures (~125°C) any K-feldspar remaining in the system can react with kaolinite to form illite and quartz. Albitisation of K-feldspar also occurs to produce quartz (Worden and Morad 2000) (3).

$$2KAlSi_3O_8 + 2.5Al_2Si_2O_5(OH)_4 + Na^+ = NaAlSi_3O_8 + 2KAl_3Si3O_{10}(OH)_2 +$$

K-feldspar kaolinite porefluid = albite illite

$$2SiO_2 + 2.5H_20 + H^+ \qquad (3)$$

quartz

Burial clay reactions involving the smectite to illite (and chlorite) reaction can provide silica in a clay-rich sand. At higher temperatures smectite reacts with $K^+$, producing illite and releasing silica which may be precipitated as quartz. Frequently this reaction occurs in mudrocks and so may be responsible for cementation around sand:mud contacts.

Another source of silica may be biogenic and volcanic silica incorporated on deposition. This form of silica is more unstable than quartz and thus may break down at lower temperatures and re-precipitate as authigenic quartz.

## 2.32 Imported silica and fluid flow: an 'open system'.

The import of silica into a sandstone requires an external source, a transport pathway and a mechanism to carry silica in solution. External, exotic, sources fall into two categories; shallow meteoric fluids containing silica in solution, and expulsion of hot fluids from deep basinal siliceous sediments.

Thiry and Marechal (2001) report silica precipitation from shallow groundwater in the Fontainebleau Sand of the Paris Basin, which has had a maximum burial depth of 100m. Fluid flux, and particularly movements in the groundwater table led to mass transfer of silica through the sand and the growth of discrete lenses of intensively cemented sand at very low temperature (<30°C) (Fig 2.9). An attempt to model the process required quartz precipitation rates to be 1000 times the typical value for deeply buried sands, and was favoured by high rates of meteoric water flush, although no mechanism was offered to explain the extremely high precipitation rates required.

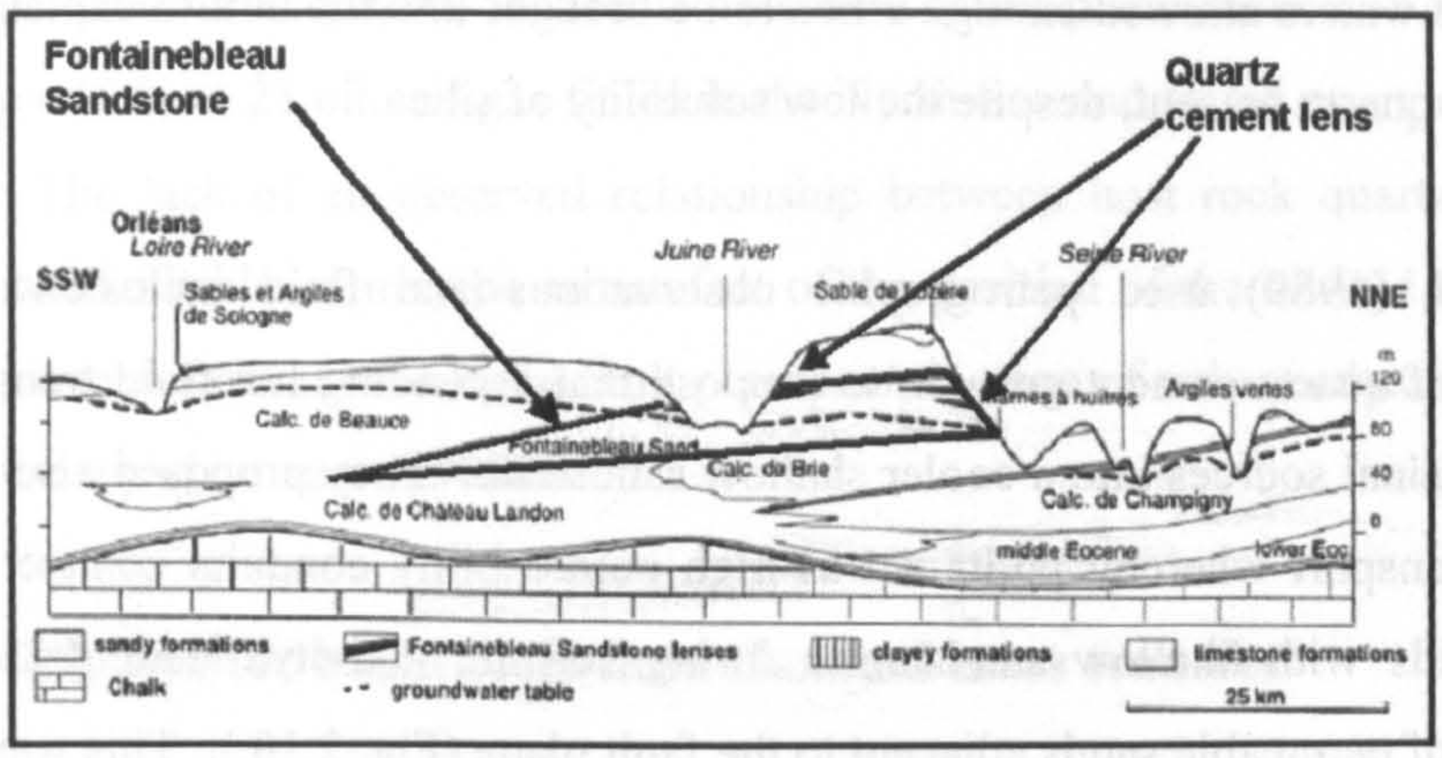


**Figure 2.9. Cartoon cross-section of the Fontainebleau Sandstone which crops out within the Paris Basin. Maximum burial of the Fontainebleau Sandstone is less than 100m, but lenses of significant shallow quartz cement have developed within the sandstone, possibly controlled by fluctuations in the groundwater table. Modified from Thiry and Marechal (2001).**

Macaulay (2003 pers. comm.) used oxygen and silicon isotope measurements and fluid inclusion analysis to show low temperature (<60°C), shallow burial, quartz cementation in the Lochaline Sandstone, Scotland. The silica was proposed to be sourced from dissolution of sponge spicules in an overlying chalk, which was transported down into the Lochaline sandstone through penetration of meteoric fluids, which then mixed with marine fluids contained in the sandstone pores. Meteoric fluid at 25°C can contain 13ppm silica, marine water only 6ppm, leading to precipitation of 7ppm quartz when meteoric fluids enter marine fluid saturated sandstone at low temperature (Bjorlykke 1994).

Deep basinal silica sources that are proposed are other sandstones or mudstones in the sedimentary succession. The processes described above (see 2.31) for releasing silica in closed hydrologic systems may take place within these units leading, in an open hydrological system, to a net export of silica from the sand or mud, and an import of silica into another sandstone (e.g. Gluyas and Coleman 1992) within the basin. Sources outside of the sedimentary succession have also been inferred (Burley *et al.*, 1989) implying mass transfer in a larger scale open system.

Transport of silica may occur through circulation of pore-fluids in the sediment column or fluid flow along discrete pathways, such as faults and fractures. Sullivan *et al.* (1997) proposed cross-formational fluid flow as the process which imported quartz into the lower Permian Rotliegendes of the southern North Sea. They suggested that convective circulation

of warm pore-waters allowed enough silica to be brought into the unit to explain the amount of authigenic quartz present, despite the low solubility of silica.

Burley *et al.* (1989) used petrographic observations and fluid inclusion data on the temperature of quartz cement growth, to propose that ascending hot fluid transported silica from deep basinal sources into a cooler shallow sandstone. They proposed a seismic valving method of transport whereby faults act as high permeability conduits connecting deep hot siliceous fluids with shallow sandstones during seismic activity, leading to preferential cementation of permeable sands adjacent to the fault plane (Fig. 2.10.). This warm fluid flow can explain high temperatures measured in fluid inclusions contained in quartz cements in units that have not been buried to great depths. The validity of the fluid inclusion method was questioned by Osborne and Haszeldine (1993), who plotted the temperature of inclusion homogenisation against present day burial depth, and found a positive correlation, leading them to argue that many inclusion temperatures are reset, and increased during subsequent burial. Therefore using temperatures measured in fluid inclusions deeply buried at present day, to estimate the temperature of cementation, may be erroneous.

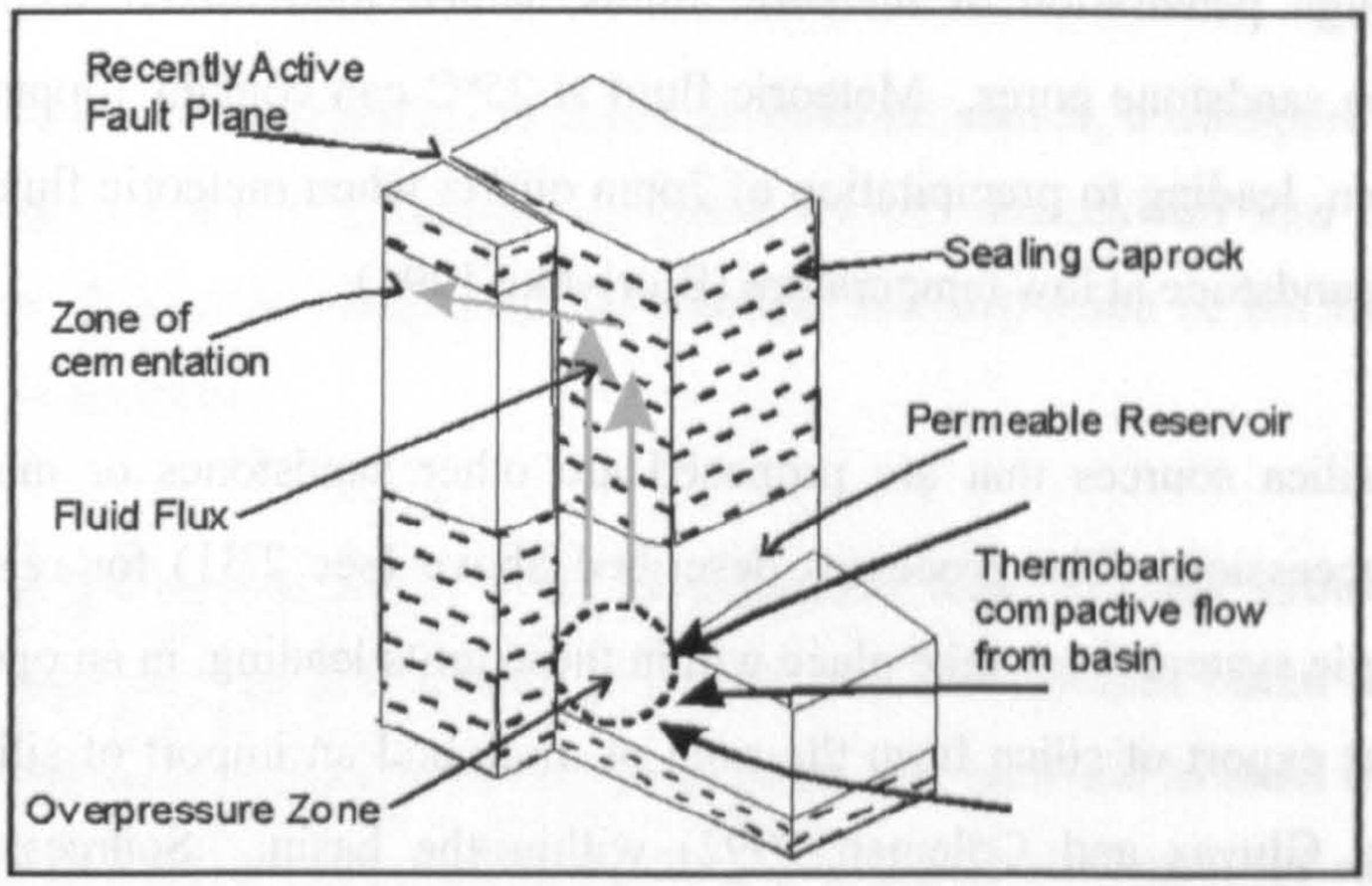


**Figure 2.10. Conceptual illustration of the seismic valving idea. Fault movement releases pockets of overpressure in deeply buried sandstones allowing hot solute transporting fluids to ascend into permeable reservoir sands precipitating diagenetic minerals. Redrawn and modified after Burley *et al.*, 1989.**

If faults and fractures act as transport pathways for hot fluids carrying silica which precipitates through cooling in shallower sands, then it may be expected that the surrounding sandstone would display increased quartz cement in comparison to the background sandstone

(Giles 1997). Fisher *et al.* (2000) looked at deformed (fault plane rocks and fractures) and undeformed rocks from 28 oil and gas fields in the North Sea and found no evidence for this relationship. The lack of an observed relationship between host rock quartz cement and quartz cemented fault planes may be an artefact of the position of the oilfield cores studied, which usually avoid close proximity to fault planes. Any zone of enhanced cement may still be undetected, dependent upon its scale.

## 2.33 Implications for basin scale fluid flux and mass transfer

One of the major arguments for a local silica source is the relative insolubility of silica at typical basinal temperatures. Quartz only has a solubility of 6ppm in marine water (25°C) and 13ppm in meteoric water. Although silica solubility increases exponentially with temperature, there is not a significant rise in absolute solubility until temperatures greater than 200°C. Therefore, even when carried in hot basinal fluids, it requires an extremely large fluid flux to transport the volume of silica required to account for the amounts of quartz cement typically observed in sandstones. Bjorlykke (1983) used silica solubility data to calculate that 100,000 volumes of water are required to produce 1 volume of quartz. Based on these figures, the precipitation of 20% volume quartz cement in a rock requires 2,000,000 pore volumes of fluid. For each pore volume the contribution to quartz cementation is therefore volumetrically small, requiring significant periods and/or rates of fluid import for externally derived silica to act as the major source for authigenic quartz precipitation. In a general consideration of fluid flow processes and diagenesis within sedimentary basins, Bjorlykke (1994) considers that such high volumes of fluid are likely to exceed the amounts available from compaction related fluid expulsion in most deeply buried basins.

The relatively successful quantitative models of quartz cementation in oilfield sandstones by Walderhaug (1996) and Lander and Walderhaug (1999) discount mass transfer and silica import primarily on the grounds of low silica solubility and the volumes of porefluid available in a basin. Such models therefore invoke local silica sources in a closed hydrologic system where growth of authigenic quartz is a three-stage process of dissolution-diffusion-precipitation. Silica diffuses through static porefluid along a chemical gradient of high silica activity at the site of dissolution to low silica activity at the site of precipitation over a scale of c.1m. This contrasts greatly in scale with the idea that silica is sourced tens-hundreds of metres from the site of precipitation, and transported in basinal fluids to the site of

precipitation. The low solubility of silica leads Bjorlykke (1994) to state that such fluid flow processes are only locally important in silicification of sandstones, and that local diffusion of silica through porefluids is the dominant mechanism.

Whilst this method appears to produce the greatest volume of quartz in deeply buried sandstones, the observations of low temperature shallow quartz precipitation by meteoric water flow, and the documentation of a shallow burial quartz cement precipitated from warm ascending fluids in this thesis, are evidence for the importance of fluid flux and mass transfer in sedimentary basins. The full importance of these processes for sandstone diagenesis and fault seal development remains to be quantified.

### 2.34 Quartz cementation summary

Specific case studies of authigenic quartz in sandstones demonstrate that silica may be sourced internally and externally. Principal internal sources are dissolution of detrital quartz grains, feldspar dissolution and clay reactions, with significant cementation occurring for burial temperatures of >70°C. External sources of silica proposed include the convection of hot fluids carrying silica from deeply buried sands and muds within a basin, and meteoric fluids penetrating into shallow burial sands. Identification of cases of internal and external quartz supply provides an insight into basin scale fluid flow and mass transfer of solutes. Internal quartz cement implies porefluid stasis and local diffusion, externally derived cements suggest hundred-kilometre scale lateral and vertical basinal fluid flow transporting material. The major controls of quartz cementation may be case specific (Haszeldine *et al.*, 2000); local sources may dominate in one basin, whilst in another silica may be brought into a sandstone from an exotic source. This makes any attempt to produce a general empirical model for quartz cementation in sandstones very difficult.

## 2.4 Secondary porosity

Diagenetic processes typically destroy reservoir quality by reducing porosity and permeability. By contrast, through dissolution of detrital grains as well as cements, secondary porosity can enhance the quality of a reservoir rock (Schmidt and MacDonald

1979) (Fig. 2.11.). There are a number of mechanisms ascribed to the dissolution of mineral species in deeply buried sediments.

At shallow burial meteoric fluids, often $CO_2$ rich, may penetrate basins and dissolve feldspar creating secondary pore space. This has been inferred in the Brent sandstones of the North Sea where early meteoric throughflow corroded feldspars and dissolved calcite cement, creating enhanced porosity (Giles *et al.*, 1992). At deeper burial, mixing of meteoric fluids with basinal brines or seawater can result in fluid which is undersaturated with respect to a mineral phase leading to dissolution of that phase (Plummer 1975).

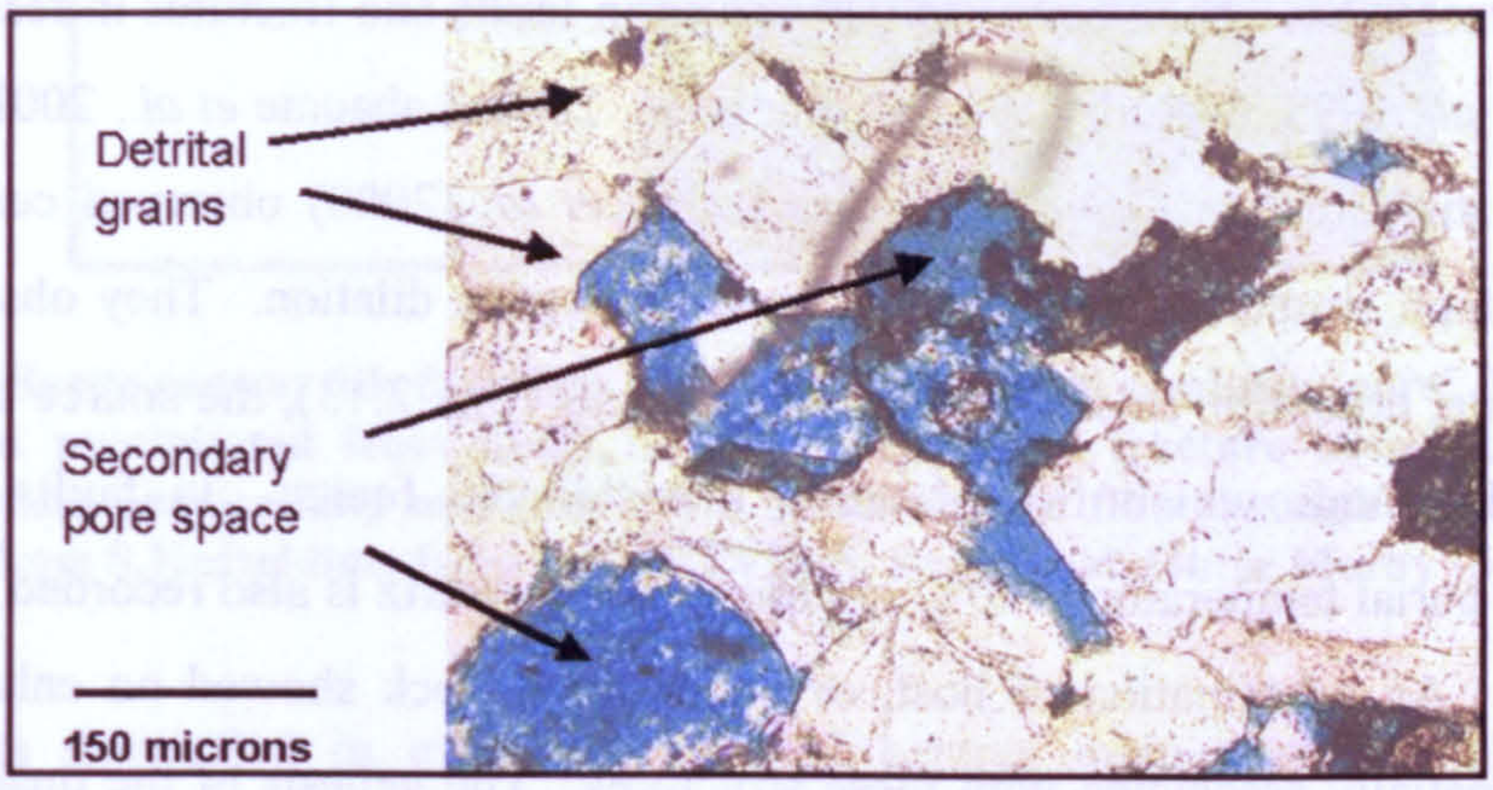


**Figure 2.11. Dissolution of Feldspar grains has resulted in secondary porosity development, enhancing bulk rock porosity. The effect on permeability is controlled by the connectivity of such pores. Thin section image, blue dye marks pore space. From the Fulmar Formation, North Sea.**

At greater burial depth, where meteoric fluids cannot penetrate, porewaters may act as solvents when they are enriched in organic acids, either from kerogen maturation (Surdam and Crossey 1984) or abiotic decarboxylation (Curtis 1978). Large scale fluid flow events, associated with seismic activity may instantaneously transport significant volumes of deep porefluid out of equilibrium, into shallower units causing dissolution (Burley *et al.*, 1989) Giles and De Boer (1989) proposed kinetically slow dis-equilibrium dissolution of feldspar over long time periods during burial.

Frequently secondary porosity may be destroyed through compaction during deeper burial, after which evidence of its creation may be difficult to detect. As discussed above mineral dissolution can provide solutes which form new cement phases (Fig. 2.6, 2.11).

## 2.5 Fault and fracture related cementation.

A particular aim of the arguments presented in this thesis is an elucidation of the relationship between fluids and faults and how this may be manifested in diagenetic phases within hydrocarbon basins. Examples taken from metallic mineralised basins often show quartz veins (e.g. Gleeson *et al.*, 2001) but the discussion here is restricted to the processes of hydrocarbon basins.

Diagenetic cements have been commonly observed in faults and fractures in reservoir sands. (e.g. Gaupp *et al.*, 1993, O'Reilly 1998, Fisher *et al.*, 2000, Labaume *et al.*, 2001) (Fig.2.12). In a detailed study of North Sea reservoirs Fisher *et al.* (2000) observed cements filling fractures and fault structures considered to have undergone dilation. They observed pyrite, barite, anhydrite, dolomite, calcite and siderite cements (Fig. 2.13), the source of which was proposed to be fluids which flowed along these dilated faults. In faults which have experienced a burial temperature >90°C microcrystalline quartz is also recorded within faults and fractures. An examination of host, or undeformed, rock showed no enhanced quartz cementation spatially associated with these structures. The genesis of the quartz cement is attributed to locally (<1m) sourced silica which preferentially cements the clean, fractured, high surface area:volume, cataclastic fault rocks (Fig. 2.14.). Such cementation can significantly add to the effectiveness of faults as seals to hydrocarbons and control the migration pathways of sub-surface fluids. In contrast to Fisher *et al.* (2000), Hippler (1993) documented a case of fault zone quartz cementation in the North Scapa fault, exposed onshore in the Orkney Islands, Northern Scotland. Detailed field and microstructural analysis showed that authigenic quartz and illite were precipitated within the cataclastic fault zone, attributed to have been sourced from exotic fluids flowing up the dilated fault zone during active, seismic scale, extensional movement. Further evidence of fault-related fluid flow was observed in traces of hydrocarbon within nearby fault surfaces.

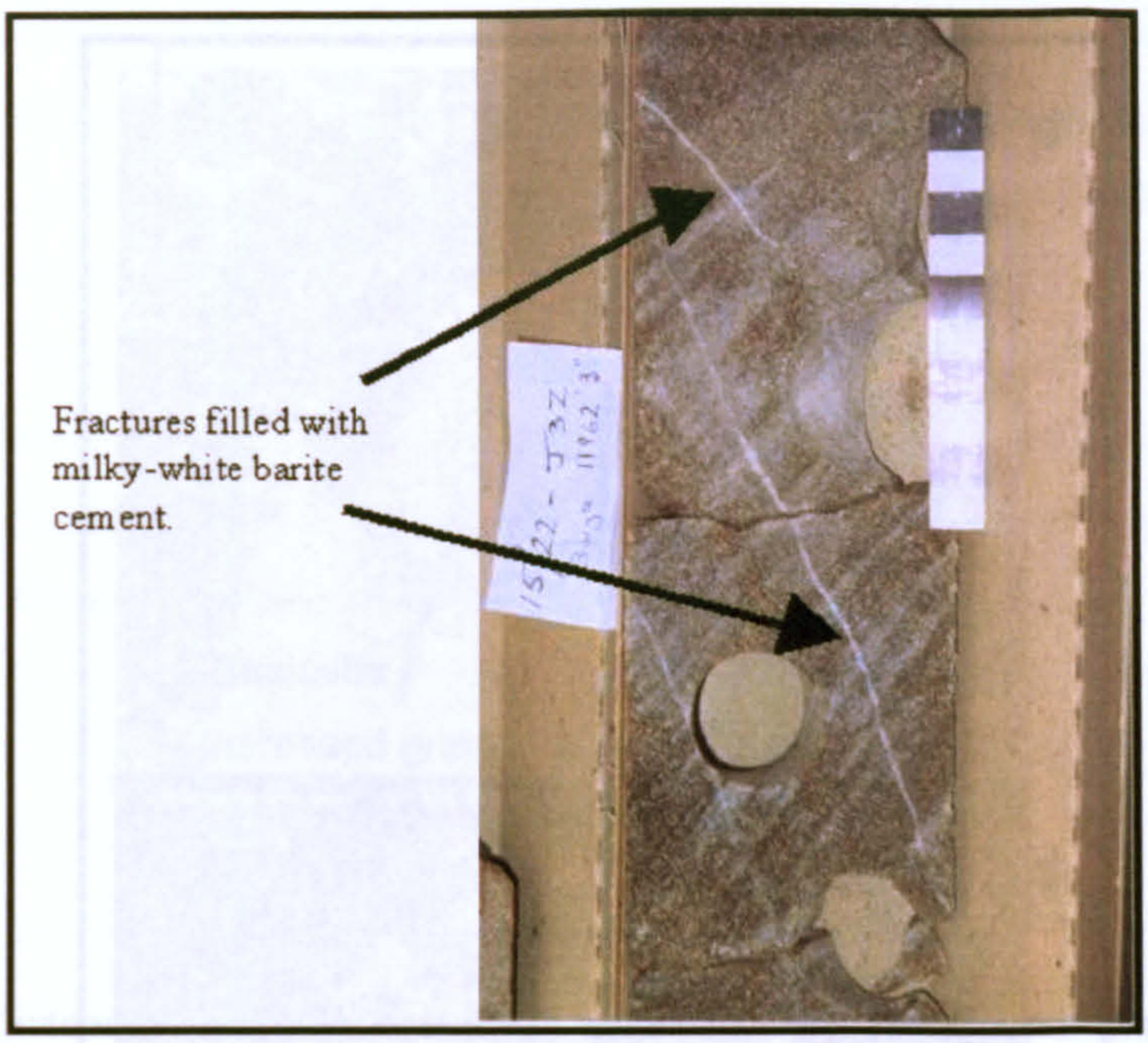


**Figure 2.12. Barite cement fills fractures in a North Sea oilfield sandstone core. The barite is an exotic cement precipitated from fluids flowing through the fracture network. The cement destroys fracture permeability and provides a baffle to fluid flow through this reservoir sand. Photograph from S.Haszeldine, from 11962ftTVDSS, Scott Field, Outer Moray Firth, North Sea.**

These results show that in most deep basinal centres there may be only local silica redistribution, with little fault/fracture transport of silica. However in some cases mass transfer and precipitation of quartz cement in faults and fractures does occur. Such a contrast suggests that local geological setting is an important factor in determining whether structurally related quartz cement can occur. Results presented in this thesis suggest that timing of faulting, versus availability of siliceous fluid, intra-basinal setting of the fault and relative permeability between host rock and fault plane, are all important aspects of whether this open system is switched on or off.

To fully understand the role of geological structures, and in particular faults, in the diagenesis of sandstones it is vital to further understand the relations between faults and fluid flow in sedimentary basins.

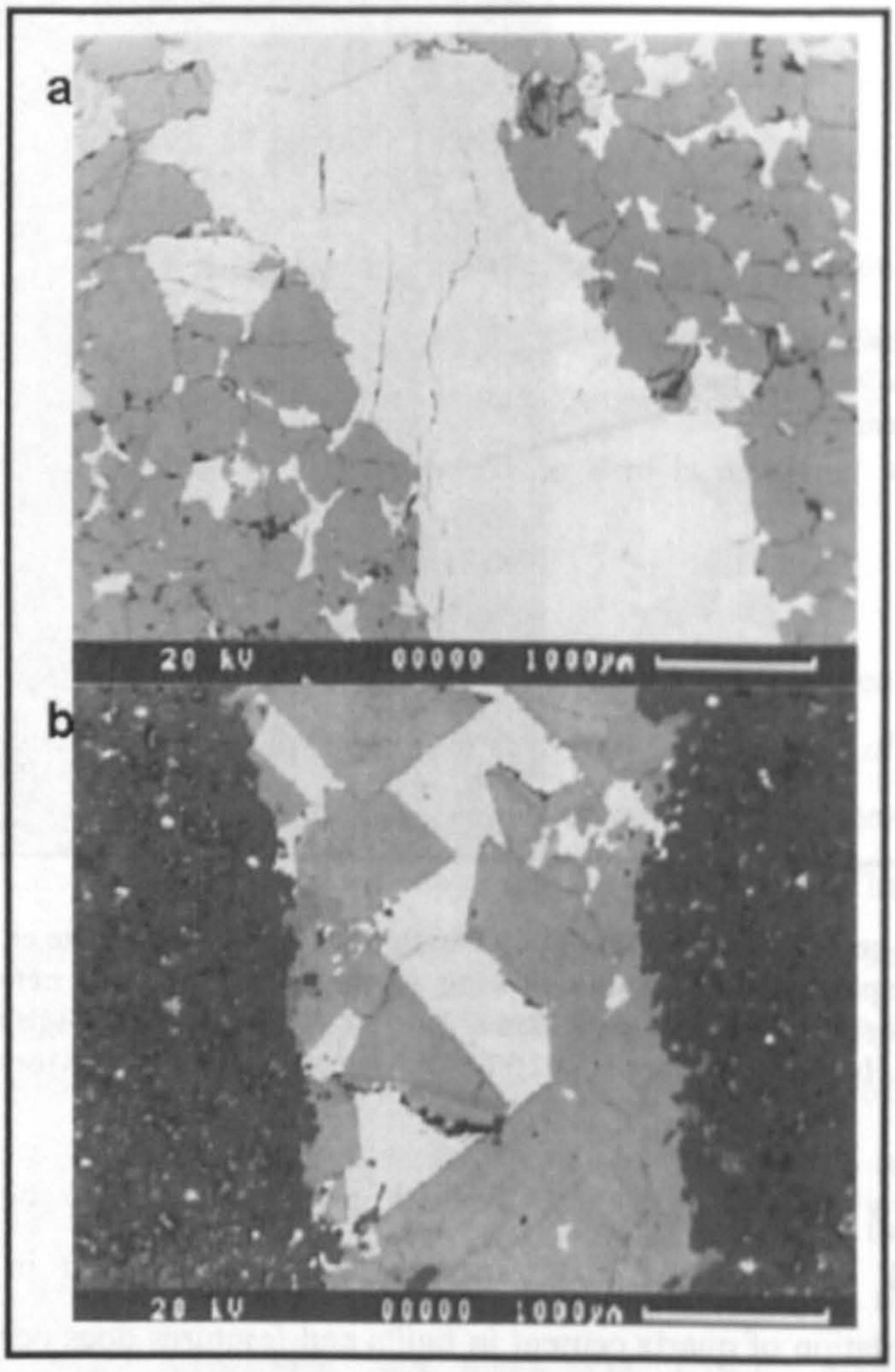


**Figure 2.13. a) Fracture filled with calcite cement, in a sandstone with a matrix cemented with calcite. b) Dolomite and anhydrite precipitated in a vein within a sandstone. Such cements are frequently produced through fluid flow and solute transport, forming permeability barriers. From Fisher and Knipe 1998.**

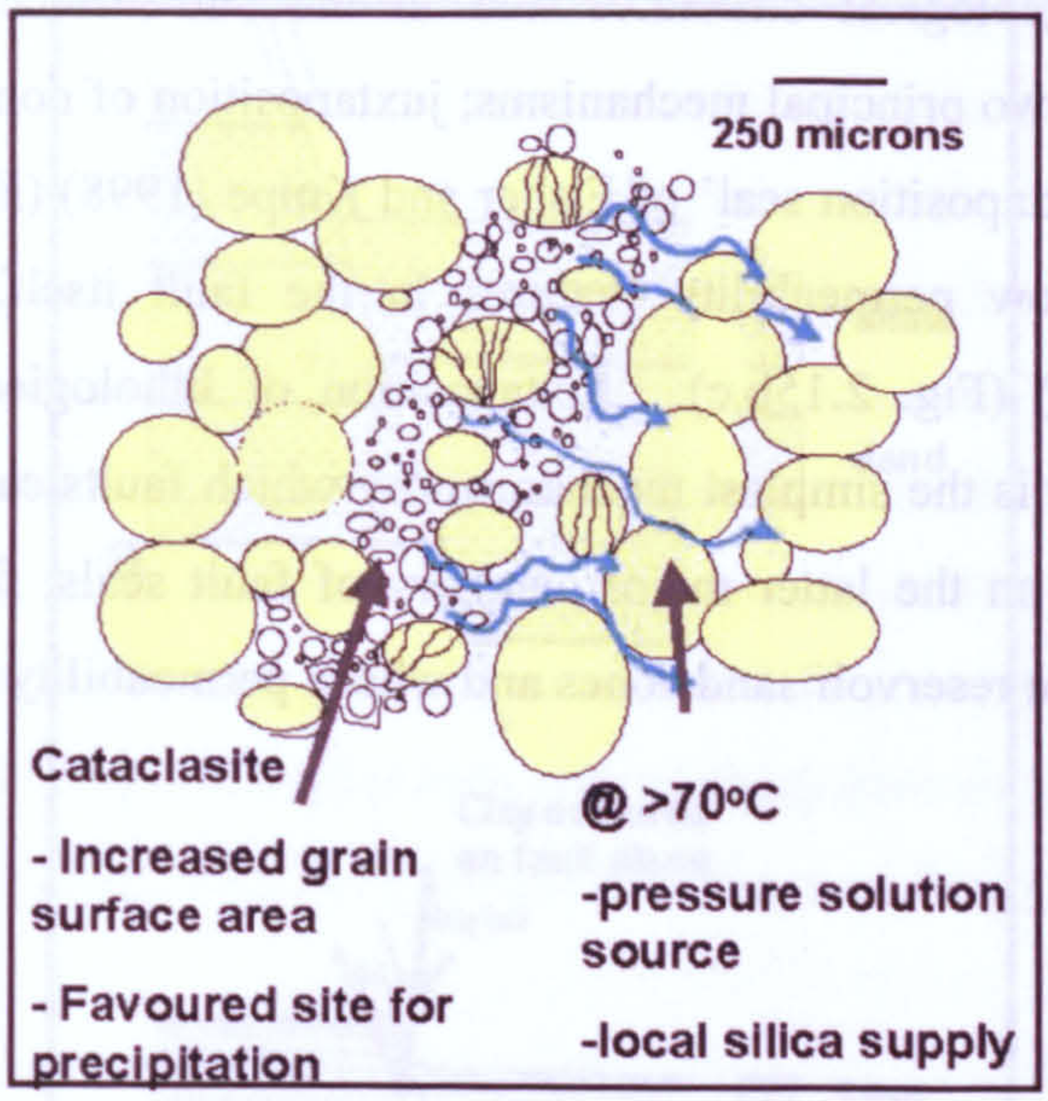


**Figure 2.14. Cartoon of the local system of quartz cementation in cataclastic faults within sandstones. Silica from metre-scale distances diffuses into the 'crush' zone which contains clean detrital quartz surfaces for precipitation . The effect has only been observed in sandstones buried to greater than c2.7km, equal to typical depths for the onset of significant cementation, in the North Sea. Further burial will typically result in significant development of overgrowths around the detrital grains.**

## 2.6 Fault-fluid interaction and diagenesis in sandstones

The above observations show that faults can act as conduits to basinal fluids, transporting fluid and precipitating cements, but faults can also act as low permeability seals and barriers to fluids, creating hydrocarbon traps. Research into the temporal development and characteristics of fault rock has been important in understanding when faults may act as seals, preventing fluid flow, and/or trapping hydrocarbons, and under what conditions they may act as conduits for fluids, leaking hydrocarbons or acting to control fluid flow pathways, mass transfer and diagenesis within sedimentary basins. The major drive behind research into fault permeability behaviour has been to predict how and when faults act to trap significant accumulations of hydrocarbons, however understanding the effects of fluid flow through permeable faults and the significance of the contribution of this process to enhancing seal development is also crucial. The present understanding of fault seal development within sandstones is presented here.

Faults are complex geological structures and in the sub-surface can create traps for hydrocarbons through two principal mechanisms; juxtaposition of non-reservoir units against reservoir units, the 'juxtaposition seal' of Fisher and Knipe (1998) (Fig. 2.15a), and through the development of low permeability features in the fault itself, a 'fault gouge' seal (Fulljames *et al.*,1997) (Fig. 2.15b,c). Juxtaposition of lithological units with differing permeability properties is the simplest mechanism by which faults can retard fluid flow, the focus in this thesis is on the latter major category of fault seals, fault gouge seal, which frequently occurs within reservoir sandstones and whose permeability is difficult to predict.

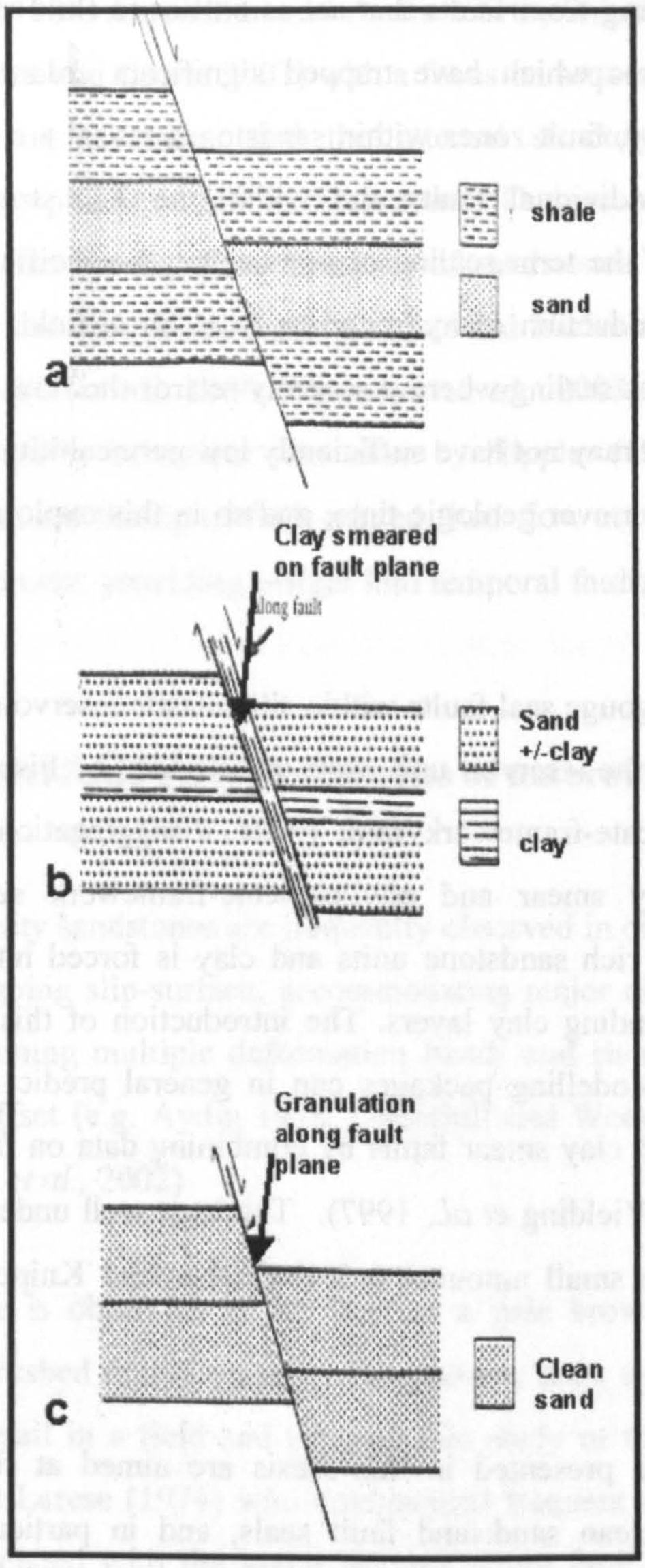


**Figure 2.15. Cartoon illustration of three fault seal scenarios. a) Juxtaposition of porous sandstone against low porosity mudstone. b) Clay smear seal, in which clay in the rock either side of the fault plane is smeared into, and along, the fault plane during movement creating a low permeability barrier. c) Cataclastic fault seal, produced through grain fragmentation and crushing, creating low permeability gouge in the fault plane. At burial depths greater than c.2.7km cataclastic fault planes may preferentially nucleate quartz cement in comparison to the host sandstone. Modified from Mair PhD (1997).**

As Fisher and Knipe (1998) point out in a review of faults in sandstone reservoirs, these intra-reservoir sand on sand faults are often simply termed sealing or non-sealing, where

sealing can mean anything from faults that act as baffles to fluid flow during production of oil, through to structures which have trapped significant columns of hydrocarbon over geologic time. In reality, fault zones within sandstones reveal a continuum of permeability values both between individual faults and within the 3-D structure of any one fault, highlighting that use of the term sealing or non-sealing is specific to the context of usage. For example, during production of hydrocarbon from an oilfield, a low permeability fault zone may be described as sealing where it severely retards the flow of hydrocarbon across it. However, the same fault may not have sufficiently low permeability to have trapped and held a column of hydrocarbon over geologic time, and so in this exploration context, the fault is described as non-sealing.

Low permeability fault gouge seal faults within siliciclastic reservoirs, with both hanging and foot walls composed of the reservoir unit, were sub-divided by Fisher and Knipe (1998) into clay smears, phyllosilicate-framework fault rocks, disaggregation zones, cataclasites and cemented faults. Clay smear and phyllosilicate-framework seals occur where faults propagate through clay rich sandstone units and clay is forced into, and smeared along, a fault plane from surrounding clay layers. The introduction of this clay into the fault zone reduces permeability. Modelling packages can in general predict with good accuracy the sealing potential of such clay smear faults by combining data on fault throw, clay type and number of clay layers (Yielding *et al.*, 1997). The least well understood faults are those in clean sandstones where small amounts (<5%) (Fisher and Knipe 1998), or zero, clay is present.

Some of the arguments presented in this thesis are aimed at further understanding the development of such clean sand:sand fault seals, and in particular the effect of exotic diagenetic cementation on the porosity and permeability of the faults and host rock surrounding them.

## 2.61 Fault seals in clean (<5% clay), porous sandstones

Work to unravel the permeability development of faults in clean, clay-free high porosity (>15%) sandstones has taken two major approaches. The first approach has been detailed field and micro-structural observations of natural deformation features (e.g. Aydin 1978,

Underhill and Woodcock 1987, Antonellini and Aydin 1994b, Shipton *et al.*, 2002, Rawling and Goodwin 2003, Shipton and Cowie 2003) with a focus on sequential development of the fault zone as displacement increases, and the internal structure and permeability of deformation bands and slip planes within the fault zone. The second approach has focused upon laboratory experiments involving compression of sandstones to produce deformation features comparable to those seen in nature (e.g. Scott and Nielsen 1991, Menendez 1995, Zhu and Wong 1996, Mair *et al.*, 2000, Ngwenya *et al.*, 2003). A third approach to unravelling fault –permeability behaviour was taken by Hippler (1993), and in this thesis, where diagenetic products and timing of fault related fluid flow are determined, and related to phases of fault development, providing insight into temporal fault behaviour and fault seal development.

## 2.62 Insights from field and geological studies of natural faults

Faults in clean high porosity sandstones are frequently observed in outcrop as complex zones consisting of a through-going slip-surface, accommodating major displacement, surrounded by a damage zone containing multiple deformation bands and short discrete slip surfaces, accommodating minor offset (e.g. Aydin 1978, Underhill and Woodcock 1987, Antonellini and Aydin 1995, Shipton *et al.*, 2002)

The main fault slip face is observed in the field as a pale brown-white striated surface composed of intensely crushed detrital grains. The damage zone surrounding the main slip face was described in detail in a field and petrographic study of the Simpson and St.Peter sandstones by Heald and Larese (1974) who documented frequent mm-displacement planar structures, spatially associated with the major through going fault slip face. The detailed spatial relationship of these structures to the main slip surface was dissected by Aydin (1978), Pittman (1981) and Jamison and Stearns (1982), through field studies of exposures in the south-west United States. These small-scale faults within the damage zone surrounding the main slip face have been described as microfaults, deformation bands (Aydin 1978) and granulation seams (Pittman 1981). The term deformation band has become commonplace to describe millimetre scale faults in high porosity sandstones and is used here.

Deformation bands within the Wingate Sandstone in Colorado were described in detail by Jamison and Stearns (1982) and in numerous subsequent field studies elsewhere (e.g. Underhill and Woodcock 1987, Antonellini and Aydin 1994a, Shipton and Cowie 2001) They are often the most commonly observed feature within fault zones in the field and are visible as pale buff-white colour millimetre thickness elongate bands parallel to the principle slip face (Fig 2.16). Deformation bands can occur as single isolated strands or as groups of anastamosing bands which have a cumulative displacement greater than isolated bands. Typically deformation bands occur as anastamosing complex groups adjacent to the main fault slip face, giving way to isolated, individual strands with increasing lateral distance from the slip face. Minor, laterally and vertically discontinuous slip planes are also seen within the damage zone, similar in appearance to deformation bands, but with increased displacement. In several exposed faults the width of the damage zone is proportional to displacement on the main slip face (e.g. Antonellini and Aydin 1995, Shipton and Cowie 2001).

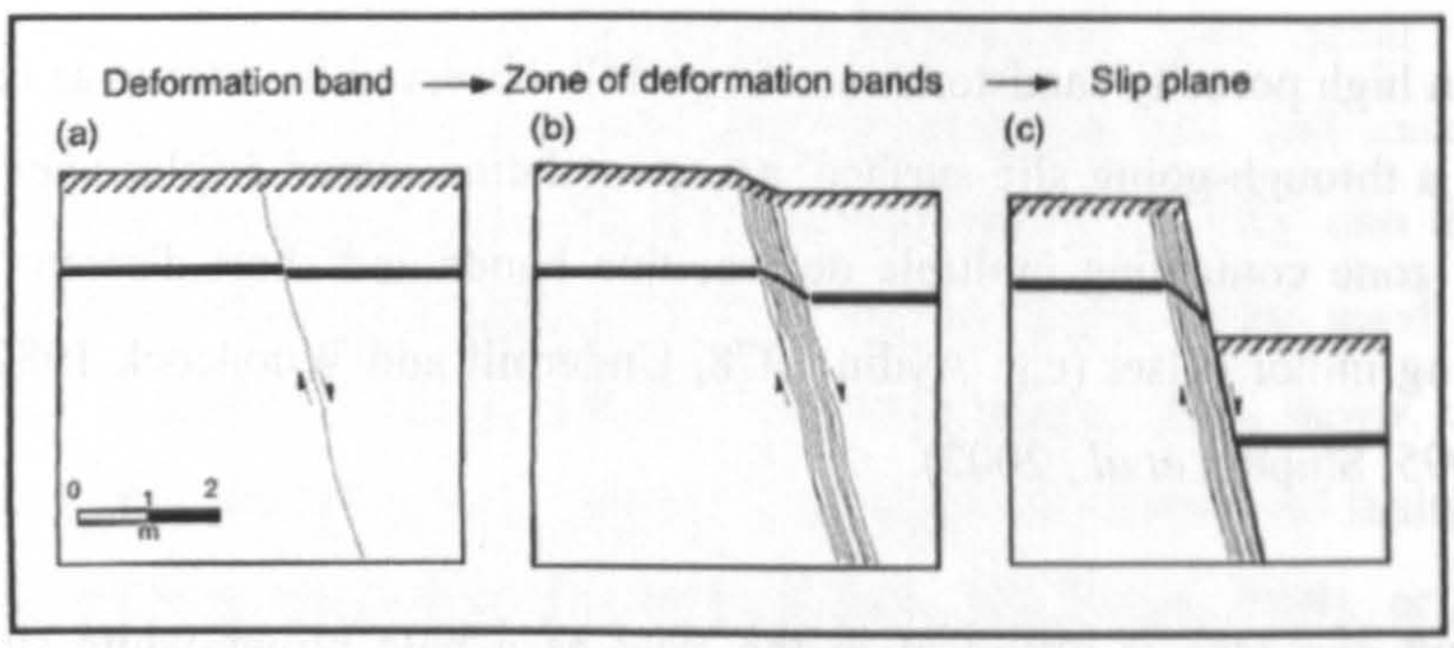


**Figure 2.16. Cartoon depicting the evolution of a typical normal cataclastic fault zone within clean sandstones, according to the Antonellini and Aydin (1994) model. Nucleation of a major slip surface evolves from a single millimetre slip deformation band (a) through to a cluster of deformation bands (b) and into a fault zone with a major through going slip face, which accommodates significant displacement (c). From Antonellini and Aydin (1994).**

Aydin (1978) and Aydin and Johnson (1978,1983) proposed that the development of deformation features in such sandstones follows a hierarchy from individual deformation bands with minor, mm-cm scale, slip to clusters of deformation bands with a cumulative displacement of tens of metres, through to individual slip surfaces with a throw greater than a few tens of metres, and surrounded by zones of deformation bands (Fig 2.16). An alternate model of development was proposed by Cowie and Shipton (1998) and Shipton and Cowie (2003), based upon observations of small scale (0-30m displacement) normal faults in the Navajo Sandstone in Utah, in which damage zones, composed of deformation bands, are

produced by periodic slip on a pre-existing main slip face. The damage zone is composed of deformation bands and discontinuous slip surfaces with minor throw (30-200cm). Periodic rupture of the main slip surface, in patches of a few hundred metres in size, causes propagation of the fault along strike and may cause failure of rock adjacent to the main fault plane, creating the damage zone. The maximum density of deformation features within the damage zone is constant and does not scale with throw. Once this maximum density of deformation bands within the damage zone has been reached a new through-going slip surface is created within the damage zone, which accumulates significant displacement and produces further deformation and damage at increasing distance from the main slip face, thus creating a wider overall damage zone and a hierarchy of slip surfaces around the master fault, with a greater number of slip surfaces developed where overall fault zone throw is greater.

Many field studies have quantified deformation band thickness as between 0.5-1mm in many different high porosity sandstones (e.g. Jamison and Stearns 1982, Aydin 1978, Underhill and Woodcock 1987). Internally the bands are composed of comminuted host rock grains, which show increasingly poor sorting and lower porosity with increased displacement. Jamison and Stearns (1982) observations of the Wingate Sandstone concluded that bands with displacement greater than 0.5mm formed anastamosing groups of deformation bands, which may have a cumulative displacement of metres (Aydin 1978) (Fig 2.16).

The fault zone as a whole therefore consists of a number of deformation features (deformation bands, clusters of deformation bands, slip surfaces) which can have different permeability than the surrounding host rock and thus can act as fluid seals. The effectiveness of the fault zone as a permeability barrier or fluid conduit is controlled by the microtextures and 3-D geometric properties of the component deformation features.

## 2.63 Microtextures and permeability of natural deformation features.

The microtextures of deformation features within clean, porous sandstones show a large, continuous range of grain size distributions. The development of grain size distribution is controlled by the displacement across the individual feature and the confining pressure at the time of deformation (effectively burial depth).

In a review of fault zone permeability, based on observations of oilfield cores from several basins around the world, Fisher and Knipe (1998) used detailed petrographic and image analysis techniques to unravel different microstructures seen in natural faults and divided the microstructures, into three categories. The least well developed, and most permeable, deformation textures were those first classified by Borradaille (1981) as disaggregation zones, formed during faulting at low burial depth and confining pressure (Fulljames *et al,* 1997) where particulate flow is the dominant mechanism, with little compaction and grain crushing (Fig 2.17b). The similarity between disaggregation zones and the host rock implies they are unlikely to significantly enhance or retard fluid flow in comparison to the host rock

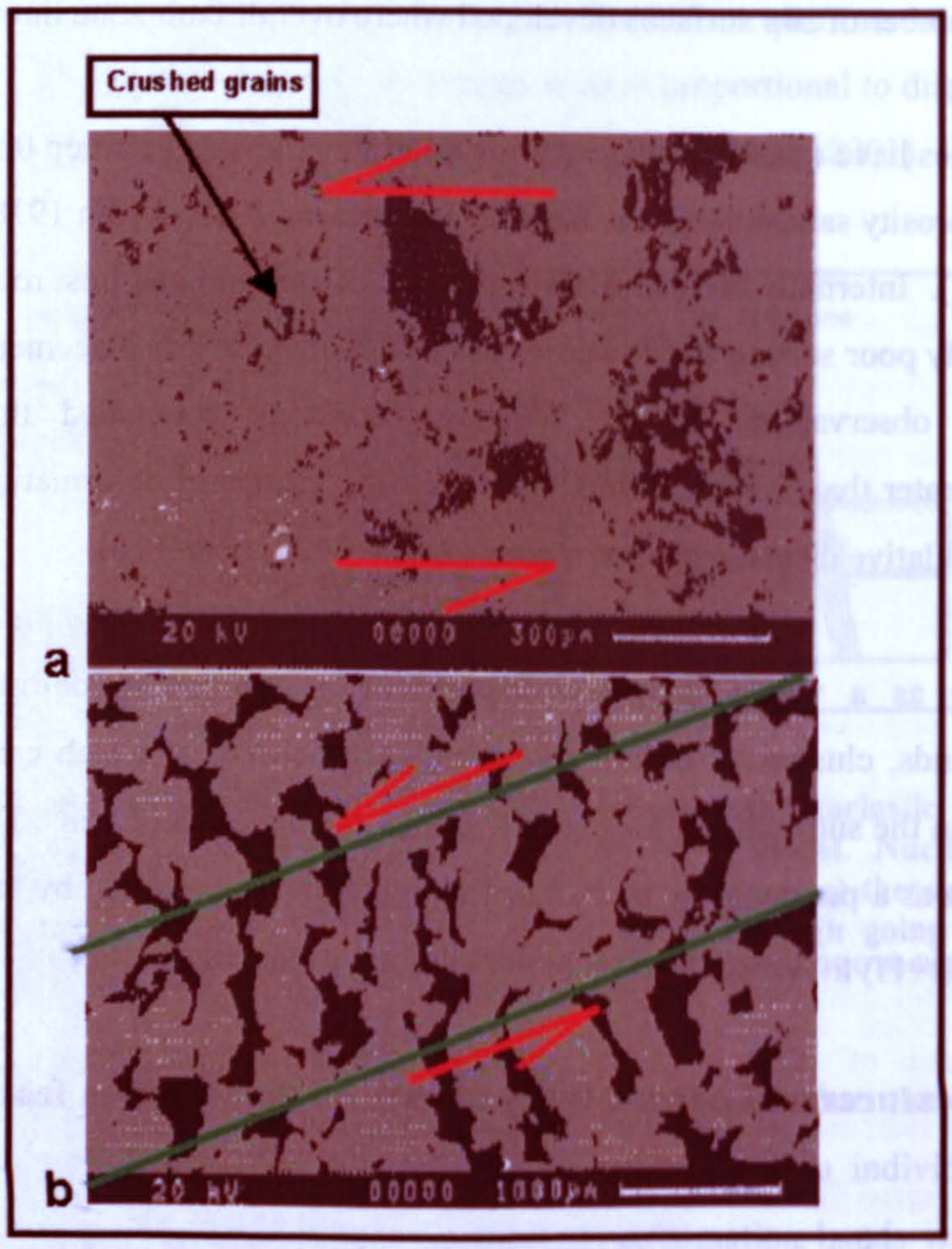


**Figure 2.17. a) SEM image of a cataclastic deformation band within a sandstone, showing grain size reduction produced as grains roll past each other at relatively high confining pressure. b) SEM image of a disaggregation zone, a millimetre scale fault formed at the low confining pressure of shallow burial. Grains roll past each other with less grain spalling and fracture than at greater burial depths. From Fisher and Knipe (1998).**

Fault rocks in which there has been some degree of grain fracturing are named clay-free cataclasites (Sibson 1977), and develop when faulting occurs at the greater confining pressures associated with increased sandstone burial depth. As displacement occurs detrital grains roll past each other leading to spalling of grain edges and fracturing, producing a broad grain size distribution between large detrital fragments surrounded by fine particles creating a poorly sorted, lower permeability, rock in comparison to the surrounding undeformed sandstone (Fig 2.17a). As described by Fisher and Knipe (1998) in micro-analysis of fault rocks from the North Sea and Australasia, cross-fault grain size distribution is relatively homogeneous with no discrete internal slip surfaces present. Cataclasites are the dominant texture observed in deformation bands in sandstones from both oilfields and outcrop analogues. The poor sorting produced in cataclasites also leads to enhanced compaction, despite the appearance of a dilational macrotexture, as fine grains and large grains pack together more efficiently (Fig 2.18a,b). This poor sorting leads to significantly reduced permeability in cataclastic deformation features in comparison to the host rock. Petrographic porosity measurement and field measurements using a portable mini-permeameter by Antonellini and Aydin (1994a) on clean, porous sandstones in Utah, show that porosity in a single deformation band falls by one order of magnitude in comparison to the host rock, and that permeability falls by an average of three orders of magnitude in a perpendicular direction across the cataclastic deformation band, although there is some along strike variation. The Antonellini and Aydin (1994a, 1995) data also shows that increasing development of cataclasis results in decreasing porosity and permeability. The main fault slip surfaces, which accommodated the most displacement, possess virtually zero porosity and permeability, in a perpendicular direction to the fault plane, which are up to seven orders of magnitude less than host rock. Crucially for understanding fluid flow through faults Antonellini and Aydin observed mineralisation between the two surfaces defining a slip plane, suggesting that fluid may be focused along slip surfaces, in a fault parallel direction. Shipton *et al.* (2002) combined detailed fault mapping with field mini-permeameter measurements of drill core from the sub-seismic sized Big Hole fault in the aeolian Navajo Sandstone, Utah, producing absolute permeability values for some deformation features. Four main elements of the fault system were identified; undeformed host rock, cataclastic deformation bands, slip surfaces and a (maximum) 30cm thick fault core, composed of amalgamated deformation bands, with slip surfaces on one or both sides, upon which the major displacement occurred. The undeformed host rock has permeabilities ranging from 5 to 3000mD, depending upon facies. Individual deformation bands have much reduced permeabilities, in comparison to the host

rock, of 0.9-1.3mD, and the fault core has a range of permeabliities down to <0.1mD. The fault core has a variable parted and closed texture between slip surfaces in the core samples, showing similarity with the observations of Antonellini and Aydin (1994a). Despite heterogeneity in the host rock permeability, the deformation features are clearly at least 1 order of magnitude lower in permeability. Shipton *et al.* (2002) also measured the bulk fault zone permeability perpendicular to the fault core, and found over a 5-10m transverse length across the fault zone, permeability is 30-40mD, with a thicker fault core creating lower bulk permeability.

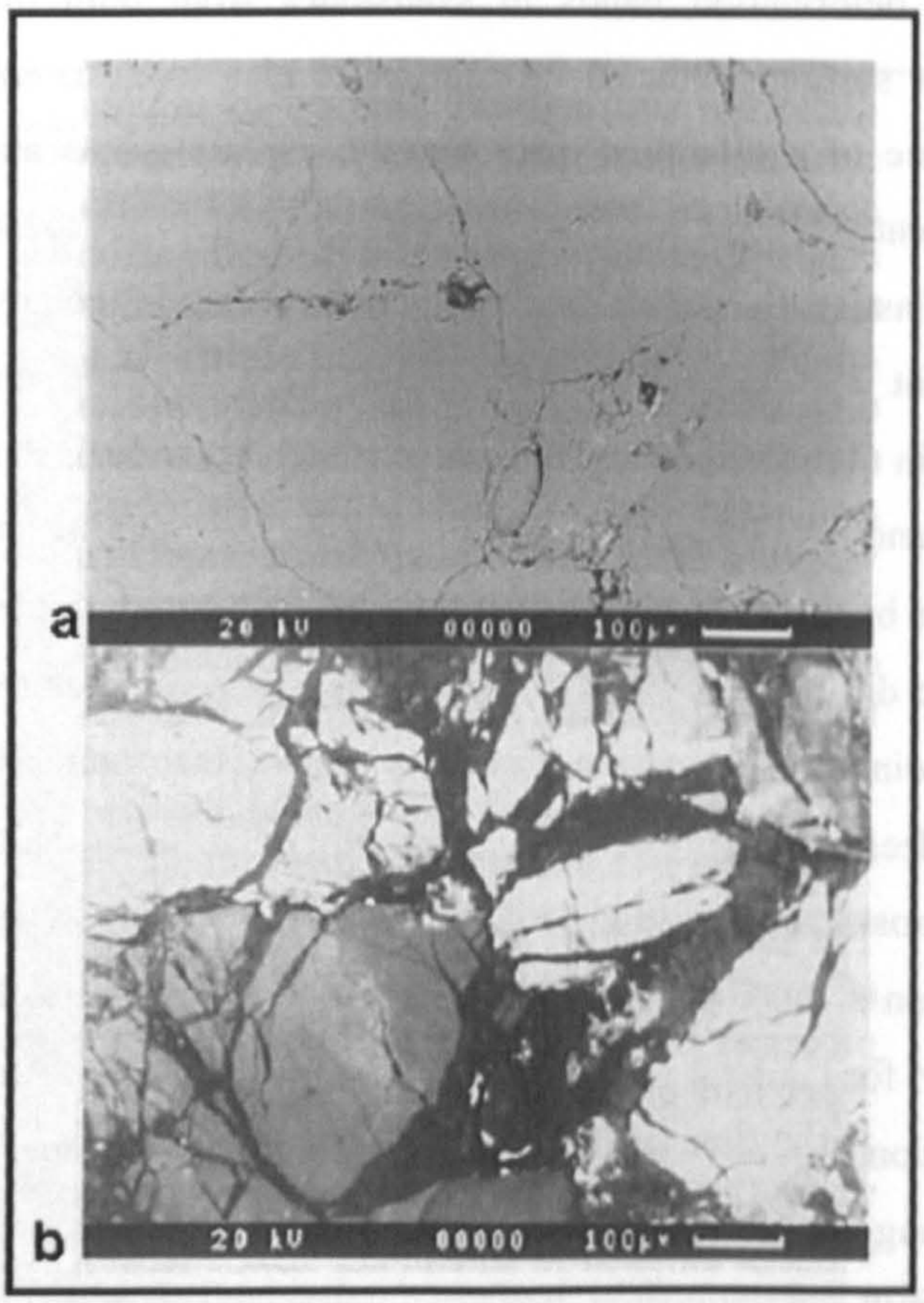


**Figure 2.18. a) SEM backscatter electron (BSE) image of a sandstone with a fault plane, in which only minor porosity is visible. b) SEM Cathodoluminesence (CL) image of (a) showing highly fractured grains cemented with quartz (black). Fresh fracture surfaces provide an ideal site for authigenic quartz nucleation. The overall texture is compactional, produced when fractured grains collapse into macroporosity. From Fisher and Knipe (1998).**

In the most highly developed cataclastic texture, observed exclusively in sandstones buried to depths greater than 2.8km (Fisher and Knipe 1998), extensively fractured grains and

fragments are present with a number of discrete slip surfaces within an individual deformation band. The slip surfaces contain the most extensively crushed grains, and result in a heterogeneous fault texture which contrasts with the broad cross-fault homogeneity of cataclasites developed at shallower burial depths. This concurs with field observations and measurements by Antonellini and Aydin (1994a) and Shipton *et al.* (2002) that these slip surfaces have the lowest permeability.

The ability of a fault to act as a trap or conduit for fluids is controlled not just by the permeability properties of the component deformation features, but also by the 3-D geometry of the fault zone. Within the fault zone deformation bands and slip surfaces enclose packages of relatively undeformed sandstone which can allow fluid flow across or along the fault, depending upon the along-strike and downdip geometry and continuity of the deformation features (Shipton *et al.*, 2002). Antonellini and Aydin (1995) report that deformation bands, both individuals and clusters, are the most continuous fault zone component in outcrop, frequently propagating and linking across the transfer zone between the discontinuous main slip surface segments. Despite displaying the lowest permeability microstructure, slip planes may be less effective barriers to perpendicular fluid flow than deformation bands, which also have a complex three-dimensional interconnectedness. According to these observations the most probable location for fluid flow is thus the stepover area between two major slip planes.

Observations of faults in outcrop has shown that they create complex and heterogeneous permeability structures. Major displacement occurs on slip planes, which are typically surrounded by deformation bands. The behaviour, with respect to fluid, of an individual fault is dependent on the microtextures of the components of the fault zone; deformation bands, slip planes and host rock, and the 3-D geometry of such features. Data suggests that faults with increasing throw will have wider damage zones and thus act as increasingly complex structures, and faults created at deeper burial depths will have lower permeabilities. Field permeability data shows that deformation bands in some faults have permeabilities 1 to 3 orders of magnitude less than host rocks, and slip surfaces have permeabilities an order of magnitude lower than deformation bands, although some slip surfaces may remain as open sub-vertical conduits.

## 2.64 Insights from laboratory produced faults.

Observation and description of faults in the field has led to a greater understanding of fault zone development, but essentially provides a snapshot in time of fault zone permeability, typically a significant period after the faults were active. This is useful for the prediction of fault-fluid behaviour in present day, tectonically inactive basins, but gives little information on the permeability evolution of individual deformation features through time. To understand more widely the full picture of structural control on basinal fluid flow regimes through time, especially during phases of significant basin development, it is crucial to be able to predict the evolution of permeability through fault zone development.

Although observations of natural faults has indicated that fault zone permeability develops through space and time, and has given many insights into such changes, a major approach to understanding the temporal evolution of fault permeability has been through laboratory experiments, in which blocks of natural sandstone are synthetically deformed under various states of confining pressure. The observation and measurement of porosity and permeability evolution is then possible during development of the fault zone through time.

The experimental procedure is similar for all such laboratory deformation of rocks (e.g. Zhu and Wong 1997, Mair *et al.*, 2000, Ngwenya *et al.*, 2003). Cylindrical cores of sandstone are cut and placed in a triaxial deformation rig, which applies maximum compressive stress along the length of the sample, and a cylindrical confining pressure (Fig 2.19). Confining pressure can be fixed, and equates to the pressure on a rock at a depth of burial in nature. To generate deformation, axial stress is increased through time on the sample with the aim of replicating natural stress fields during faulting.

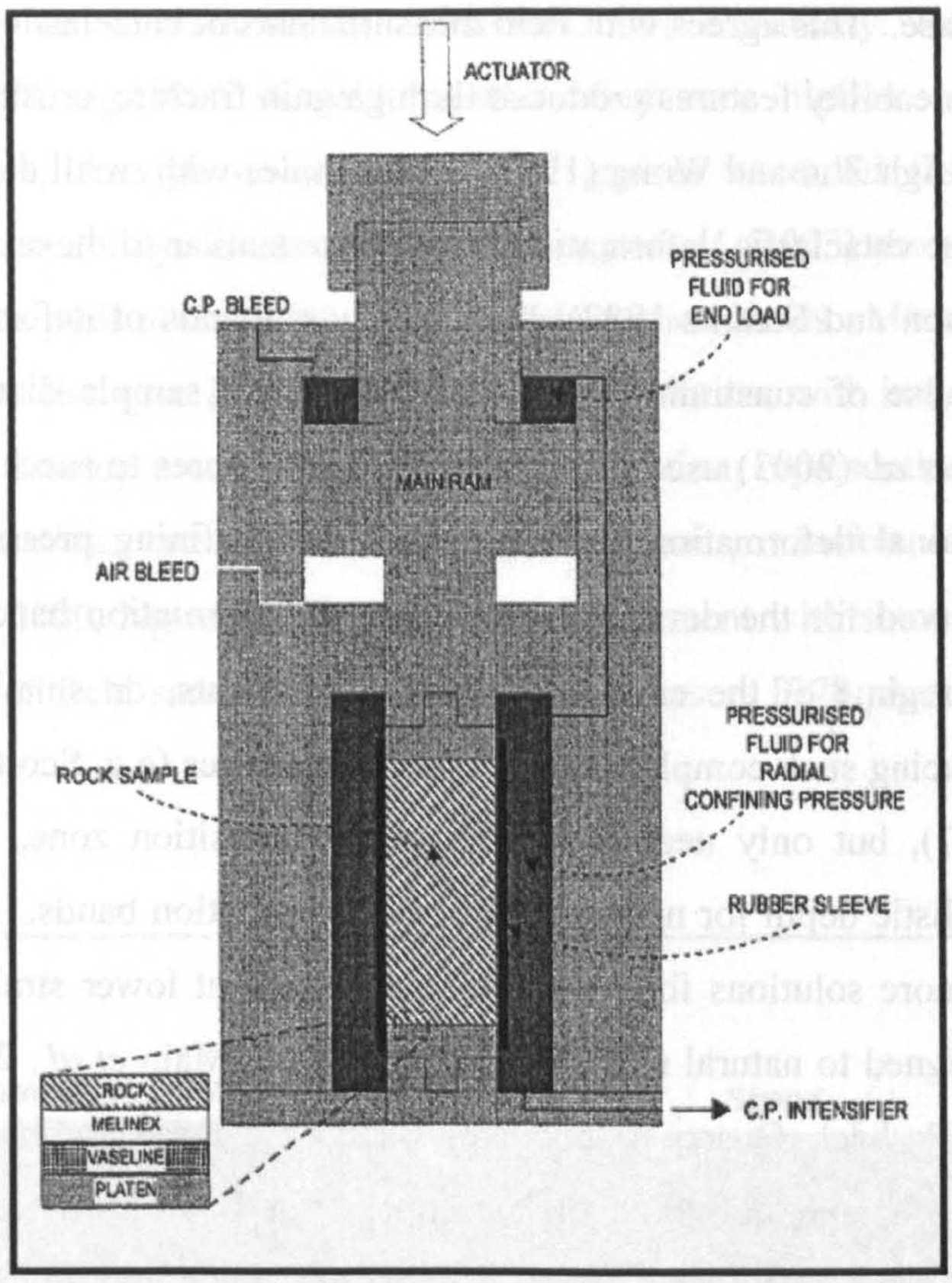


**Figure 2.19. Diagram of the 'big-rig' rock deformation instrument used to create micro-faults (deformation bands) in sandstones within the laboratory. Confining pressure can be varied to simulate differing burial depths, and fluid can also be introduced into the sample to assess geochemical reactions and permeability evolution during fault creation. The instrument can deal with cores of up to 10cm diameter, thought to be sufficient to allow replication of natural fault evolution. From Mair *et al.* (2000).**

Early experiments (e.g. Dunn *et al.,* 1973, Engelder 1974) used small cores (diameter <10cm) of porous sandstone placed under varying confining pressures which predominantly produced fractures and single, isolated shear features. Some grain crushing and generation of cataclastic gouge was observed, but overall these features did not display grain crushing on a scale comparable with natural faults observed in the field.

Zhu and Wong *et al.* (1997) and Wong *et al.* (1997) conducted deformation experiments, at differing confining pressures, on five sandstones with porosities from 15% to 35% and varying composition. Their results showed that during cataclastic deformation, porosity and permeability change together by a similar degree, but with increased deformation shear-enhanced compaction occurs through grain crushing and pore collapse, resulting in a rapid

permeability decrease. This agrees with field measurements of cataclastic deformation bands which are low permeability features produced through gain fracture, crushing and subsequent compaction. Although Zhu and Wong (1997) used samples with small diameters (<2cm) the microtextures of the cataclastic deformation bands were similar to those seen in nature (e.g. Aydin 1978, Jamison and Stearns 1982). However, compounds of deformation bands were not produced because of constraints imposed by the small sample diameter (Mair *et al.*, 2000). Ngwenya *et al.* (2003) used large, 10cm diameter, cores to successfully create more realistic 3-dimensional deformation band structures, at confining pressures similar to the burial depths observed for the development of natural deformation bands and fault zones, within the brittle regime of the crust. Previous experiments, on smaller diameter cores, succeeded in producing such complex 3-dimensional structures (e.g. Scott and Nielsen 1991, Wong *et al.*, 1997), but only near the brittle-ductile transition zone, which is likely to represent an unrealistic depth for natural cataclastic deformation bands. Larger samples are thought to allow more solutions for strain accommodation at lower strain rates, conditions which are more aligned to natural rocks (Mair *et al.*, 2000, Main *et al.*, 2001). Ngwenya *et al.* (2003) used Clashach Quarry (Hopeman) Sandstone cores, with relatively constant porosities of 12-18%, and deformed each sample at a fixed confining pressure, whilst increasing axial strain, creating deformation structures analogous to field examples (Fig 2.20). The log permeability of each sample evolved through three stages of deformation. Prior to rock failure, and the creation of visible deformation features, permeability showed a linear decrease as the rock compacted, followed by a transient permeability increase associated with a dynamic stress drop, indicating sample failure and thus faulting. Thirdly a 'quasi-static' permeability decrease occurred as elastic strain increased and new deformation bands were formed. The second, rock failure, stage of evolution in which permeability is increased beyond initial hydrostatic value, is interpreted to represent the 'suction pump' process of Rudnicki and Chen (1988) in which rapid, dilatant slip occurs, temporarily increasing the storage capacity of the sample. A similar process of seismic pumping of fluid during tectonic activity has been proposed to explain observations of fault-related mineralisation by Sibson *et al.* (1975). The largest increase in permeability during sandstone failure was observed for the lowest confining pressure, and so suggests that faulting at shallower depths is more likely to have enhanced permeability during phases of activity. Ngwenya *et al.* (2003) suggest that at higher confining pressures the 'suction-pump' mechanism is likely to be increasingly suppressed. The overall pre- through to post failure permeability evolution shows complex relations exist between porosity and permeability, and

increases in porosity do not ubiquitously lead to a rise in permeability. Both Ngwenya *et al.* (2003) and Zhu and Wong (1996) showed that whilst fault zone dilation and porosity increase occurred post-failure, through micro-cracking of grains, increased flow path tortuosity actually reduced permeability. Evidence from Ngwenya *et al.* (2003) shows that much of this dilation occurs in the pods of host rock between deformation bands. Microtextures produced in laboratory studies also give insight into fault zone evolution, with individual deformation bands observed to develop a constant grain size distribution, representing strain hardening, with further deformation, caused by increasing axial strain, manifest as new deformation bands (Mair *et al.,* 2000, Ngwenya *et al.,* 2003) in agreement with some models developed from observations of field samples (e.g. Aydin and Johnson 1978, Antonellini and Aydin 1994a).

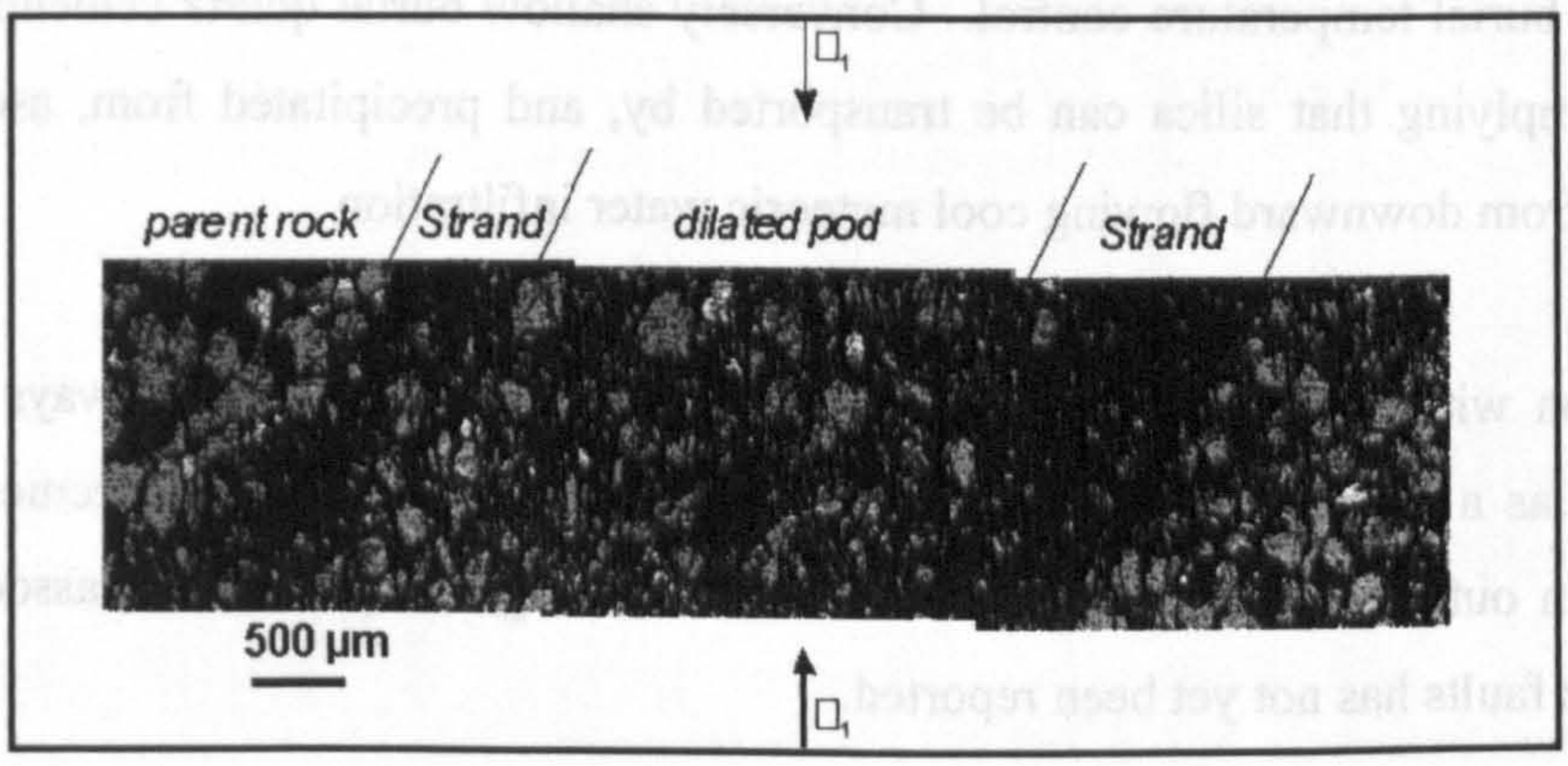


**Figure 2.20. Photographic cross-section of deformation bands produced during laboratory deformation of porous sandstone. Two strands, equating to deformation bands, can be seen enclosing a pod of dilated rock with frequent grain micro-fractures. The pod of dilated rock is present within clusters of anastamosing bands, agreeing closely with observation of natural structural features. At the edges of the section undeformed host rock can be seen representing typical sandstone between clusters of deformation within a fault zone. From Ngwenya *et al.* (2003).**

Laboratory experiments have recreated deformation features with 3-D geometries and microtextures in close agreement with field examples. Further, it has been shown that despite complex relations between porosity and permeability, for idealised displacement, shallow burial fault zones can display a transient enhanced permeability, and storativity, in relation to surrounding host rock during phases of movement.

## 2.7 Summary

The term diagenesis is used to cover the physical and chemical interactions which occur in a body of sediment following initial deposition and through to deep burial and the onset of metamorphism. Compaction is the dominant physical mechanism. Mechanical compaction can reduce pore volume to 26% rock volume, after which chemical compaction causes detrital grain dissolution and a further decrease in porosity (excluding cementation effects). Authigenic quartz is the major pore-filling cement in clastic sediments. Disagreement continues as to whether quartz is ubiquitously sourced internally, or whether external fluids can import silica. Typical reservoir sands display significant precipitation of quartz cement at temperatures of 70°C or above, attributed to a local supply of silica. Successful computer simulation of formation scale quartz cementation assumes an internal, pressure solution, source and burial temperature control. Conversely shallow burial quartz cements have been observed implying that silica can be transported by, and precipitated from, ascending hot fluids and from downward flowing cool meteoric water infiltration.

Cementation within structures shows that faults can act as transport pathways for basinal fluids, and as a mechanism of mass transfer and re-distribution. Quartz cement has been observed, in outcrop, associated with extensional faulting, but preferential association with sub-surface faults has not yet been reported.

Understanding of fault permeability evolution in clean, porous sandstones is crucial to unravelling fault related fluid flow and diagenesis, as well as in predicting faults which can trap hydrocarbons. Field studies have shown that such faults have a complex structure, with a main slip face, accommodating the majority of displacement, surrounded by a damage zone composed of isolated and clustered deformation bands, which are essentially small faults with millimetre to centimetre scale slip. The permeability of deformation bands and major slip planes is between 1 and 3 orders of magnitude less than the host rock, and so many of these faults act as hydrocarbon traps and fault seals in the subsurface. The measured permeability of natural fault zones provides a snapshot in time, typically a significant period after the structures were active. Mechanical laboratory deformation of sands, to produce artificial faults analogous to natural features, has been undertaken to unravel fault permeability evolution through time. Deformation bands formed at low confining pressure, equivalent to shallow burial, show a transient increase in permeability during active

movement, after which values fall in a quasi-static trend, suggesting that faults in sandstones at shallow burial may act as preferential flow pathways during displacement. With greater displacement the development of lower permeability slip faces may act as the lowest permeability fault zone feature, but are not developed in laboratory experiments.

Deep burial faults at temperatures >70°C are frequently quartz cemented on fresh surfaces produced during deformation. These form permeability barriers in sand:sand faults. The faults studied in this thesis are unusual, in that cemented textures have been produced at shallow burial by advected silica cement.

---

## References


**Antonellini, M.A. and Aydin, A., 1994a.** Effect of faulting on fluid flow in porous sandstones: petrophysical properties. American Association of Petroleum Geologists Bulletin, 78, p. 355-377

**Antonellini, M.A. and Aydin, A., 1995.** Effect of faulting on fluid flow in porous sandstones: Geometry and Spatial Distribution. American Association of Petroleum Geologists Bulletin, 79, p. 642-671.

**Aydin, A., 1978.** Small faults formed as deformation bands in sandstone. Pure and Applied Geophysics, 116, p913-930.

**Aydin, A. and Johnson, A.M., 1978.** Development of faults as zones of deformation bands and slip surfaces in sandstones. Pure and Applied Geophysics, 116, p. 931-942.

**Aydin, A. and Johnson, A.M., 1983.** Analysis of faulting in porous sandstones. Journal of Structural Geology, 5, p.19.

**Beard, D.C. and Weyl, P.K., 1973.** Influence of texture on porosity and permeability of unconsolidated sand: American Association of Petroleum Geologists Bulletin, 57, p. 349-369.

**Bjorlykke, K., Nedkvitne, T., Ramm, M. and Salgal, G.C., 1992.** Diagenetic processes in the Brent Group (Middle Jurassic) reservoirs of the North Sea: an overview. *In*: Geology of the Brent Group (ed. Morton, A.C., Haszeldine, R.S., Giles, M.R., and Brown, S.), Special Pulication of the Geological Society of London, 61, p.263-287.

**Bjorlykke, K., 1983.** Diagenetic reactions in sandstones. In: Sediment Diagenesis (ed. Parker, A. and Sellwood, B.W.), NATO ASI series, p.169-213.

**Bjorlykke, K., 1994.** Pore water flow and mass transfer of solids in solution in sedimentary basins. *In*: Quantitative Diagenesis: Recent Developments and Applications to Reservoir Geology (ed. Parker, A and Sellwood, B.W.), p.189-221. Kluwer.

**Bjorkum, P.A., 1996.** How important is pressure in causing dissolution of quartz in sandstones? Journal of Sedimentary Research A, 66 (6), p.147-154.

**Borradaile, G.J., 1981.** Particulate flow and the generation of cleavage. Tectonophysics, 72, p. 306-321.

**Burley, S.D., Mullis, J. and Matter, A., 1989.** Timing diagenesis in the Tartan Reservoir (UK, North Sea): constraints from combined cathodoluminescence microscopy and fluid inclusion studies. Marine and Petroleum Geology, 6, p.8-120.

**Cowie, P.A. and Shipton, Z.K., 1998.** Fault tip displacement gradients and process zone dimensions. Journal of Structural Geology, 20, 8, p.983-997.

**Curtis, C.D., 1978.** Possible links between sandstone diagenesis and depth related geochemical reactions occurring in enclosing mudstone. Journal of the Geological Society of London, 135, p. 107-117.

**Dickinson, W.R., 1970.** Interpreting detrital modes of greywacke and arkose. Journal of Sedimentary Petrology, 40, p. 695-707.

**Dunn, D.E., LaFountain, L.J. and Jackson, R.E., 1973.** Porosity dependence and mechanisms of brittle fracture in sandstones. Journal of Geophysical Research, 78, p. 2403-2417.

**Ehrenberg, S.N., 1995.** Measuring sandstone compaction from modal analyses of thin sections: how to do it and what the results mean. Journal of Sedimentary Research, 65A, 2, p.369-379.

**Engelder, J.T., 1974.** Cataclasis and the generation of fault gouge. Bulletin of the Geological Society of America, 85, p.1515-1522.

**Hippler, S.J., 1993.** Deformation microstructures and diagenesis in sandstone adjacent to an extensional fault: implications for the flow and entrapment of hydrocarbons. American Association of Petroleum Geologists Bulletin, 77, p. 625-637.

**Fisher, Q.J. and Knipe, R.J., 1998.** Fault sealing processes in siliciclastic sediments. In Faulting, Fault Sealing and Fluid Flow in Hydrocarbon Reservoirs (eds. Jones, G., Fisher, Q.J. and Knipe, R.J.). Geological Society Special Publication, 147, p.117-134.

**Fisher, Q.J., Knipe, R.J. and Worden, R.H., 2000.** Microstructures of deformed and non-deformed sandstones from the North Sea: implications for the origins of quartz cement in sandstones. *In*: Quartz Cementation in Sandstones (ed: Worden, R.H. and Morad, S.), Special Publication of the International Association of Sedimentologists, 29, p. 129-146.

**Fulljames, J.R., Zijerveld, L.J.J. and Franssen, R.C.M.W., 1997.** Fault seal processes: systematic analysis of fault seals over geological and production time scales. In Hydrocarbon Seals: Importance for Exploration and Production (eds. Moller-Pedersen, P. and Koestler, A.G.) Norwegian Petroleum Society Special Publication, 7, p. 51-59.

**Gaupp, R., Walzebuck, J., Matter, A., Platt, J., 1993.** Diagenesis and fluid evolution of deeply buried Permian (Rotliegende) gas reservoirs, northwest Germany. American Association of Petroleum Geologists, 77, n.7, p.1111-1128.

**Giles, M.R. and DeBoer, R.B., 1989.** Secondary porosity: Creation of enhanced porosities in the subsurface from dissolution of carbonate cements as a result of cooling formation water. Marine and Petroleum Geology, 6, p. 261-269.

**Giles, M.R., Stevenson, S., Martin, S.V., Cannon, S.J.C., Hamilton, P.J., Marshall, J.D. and Samways, G.M., 1992.** The reservoir properties and diagenesis of the Brent Group; a regional perspective. In Geology of the Brent Group (eds. Morton, A.C., Haszeldine, R.S., Giles, M.R. and Brown, S.) Geological Society Special Publication, 61, p. 289-327.

**Giles, M., 1997.** Diagenesis and its Impact on Rock Properties. A Quantitative Perspective. pp. 520. Kluwer, Amsterdam.

**Giles, M.R., Indrelid, S.L., Beynon, G.V. and Amthor, J., 2000.** The origin of large-scale quartz cementation: evidence from large data sets and coupled heat-fluid mass transport modelling: *In*: Quartz Cementation in Sandstones (ed: Worden, R.H. and Morad, S.), Special Publication of the International Association of Sedimentologists, 29, p. 21-39.

**Gleeson, S.A., Wilkinson, J.J., Stuart, F.M. and Banks, D.A., 2001.** The orgin and evolution of base metal mineralising brines and hydrothermal fluids, South Cornwall, UK. Geochimica et Cosmochimica, v65, 13, p.2867-2879.

**Gluyas, J.G. and Coleman, M.L., 1992.** Material flux and porosity changes during sediment diagenesis. Nature, 356, p.52-54.

**Graton, L.C. and Fraser, H.J., 1935.** Systematic packing of spheres - with particular relation to porosity and permeability. Journal of Geology, 43, p. 785-909.

**Hamilton, E.L. and Menard, H.W., 1956.** Density and porosity of seafloor surface sediments off San Diego, California. American Association of Petroleum Geologists, 40, p. 754-761.

**Hartmann, B.H., Juhasz-Bodnar, K, Ramseyer, K. and Matter, A., 2000.** Polyphased quartz cementation and its sources: a case study from the Upper Palaeozoic Haushi Group sandstones, Sultanate of Oman. *In*: Quartz Cementation in Sandstones (ed: Worden, R.H. and Morad, S.), Special Publication of the International Association of Sedimentologists, 29, p. 253-270.

**Haszeldine, R.S., Samson, I.M., Cornford, C., 1984.** Dating diagenesis in a petroleum basin: a new fluid inclusion method. Nature, 307, p.354-357.

**Haszeldine, R.S., Macaulay, C.I., Marchand, A., Wilkinson, M, Graham, C.M., Cavanagh, A., Fallick, A.E. and Couples, G.D., 2000.** Sandstone cementation and fluids in hydrocarbon basins. Journal of Geochemical Exploration, 69-70, p.195-200.

**Haszeldine, R.S., Cavanagh, A.J. and England G.L., 2003.** Effects of oil charge on illite dates an stopping quartz cement; calibration of basin models. Journal of Geochemical Exploration, 78-79, p.373-376.

**Heald, M.T. and Larese, R.E., 1974.** Influence of coatings on quartz cementation. Journal of Sedimentary Petrology, 44, p.1269-1274.

**Hippler, S.J., 1993.** Deformation microstructures and diagenesis in sandstone adjacent to an extensional fault: implications for the flow and entrapment of hydrocarbons. American Association of Petroleum Geologists Bulletin, 77, p. 625-637.

**Houseknecht, D.W., 1987.** Assessing the relative importance of compaction processes and cementation to reduction of porosity in sandstones. American Association of Petroleum Geologists Bulletin, 71, p. 633-642.

**Houseknecht, D.W., 1989**. Assessing the relative importance of compaction processes and cementation to reduction of porosity in sandstones: reply. American Association of Petroleum Geologists Bulletin, 73, p. 1274-1276.

**Jamison, W.R. and Stearns, D.W., 1982.** Tectonic deformation of the Wingate Sandstone, Colorado National Monument. American Association of Petroleum Geologists Bulletin, 66, p. 2584-2608.

**Lander, R.H. and Walderhaug, O., 1999.** Predicting porosity through simulating sandstone compaction and quartz cementation. American Association of Petroleum Geologists, 83, p. 433-449.

**Laubame, P., Sheppard, S.M.F., Moretti, I., 2001**. Fluid flow in cataclastic sandstones, Sub-Andean Zone, southern Bolivia. Tectonophysics, 340, n. 3-4, p.141-172.

**Lundegard, P.D., 1992.** Sandstone porosity loss- a "big picture" view of the importance of compaction. Journal of Sedimentary Petrology, 62, p. 250-260.

**Lynch, F.L., 1996.** Mineral/water interaction, fluid flow , and Frio Sandstone diagenesis: evidence from the rocks. American Association of Petroleum Geologists, 80, p.486-504.

**Macaulay, C., 2003.** Low temperature quartz cementation of the upper Cretaceous Lochaline Sandstone of Lochaline, Argyll, Scotland. pers comm. http://www.geos.ed.ac.uk/facilities/ionprobe/calumSi.

**Main, I.G., Mair, K., Kwon, O. Elphick, S.C. and Ngwenya, B.T., 2001.** Experimental constraints on the mechanical and hydraulic properties of deformation bands in porous sandstones: A review. *In* The Nature and Significance of Fault Zone Weakening (eds. Holdsworth, R.E et al.). Geological Society Special Publication 186, p.43-63.

**Mair, K., 1997.** Experimetal studies of fault zone development in a porous sandstone. PhD thesis, University of Edinburgh.

**Mair, K., Main, I.G. and Elphick, S.C., 2000.** Sequential development of deformation bands in the laboratory. Journal of Structural Geology, 22, p. 25-42.

**Marchand, A.M.E., Haszeldine, R.S., Macaulay, C.I., Swennen, R. and Fallick, A.E., 2000**. Quartz cementation inhibited by crestal oil charge: Miller deepwater sandstone, UK North Sea. Clay Minerals, 35, p.205-214.

**Menenedez, B., Zhu, W. and Wong, T-f, 1996.** Micromechanics of brittle faulting and cataclastic flow in Berea sandstone. Journal of Structural Geology, 18, p. 1-16

**Ngwenya, B.T., Kwon, O. Elphick, S.C. and Main, I.G., 2003.** Permeability evolution during progressive development of deformation bands in porous sandstones. Journal of Geophysical Research, 108, p.6-14.

**O'Reilly, C., Shannon, P.M., Feely, M., 1998.** A fluid inclusion study of cement and vein minerals from the Celtic Sea basins, offshore Ireland. Marine and Petroleum Geology, 15, n.6, p.519-533.

**Pryor, W.A., 1973.** Permeability-porosity patterns and variations in some Holocene sand bodies. American Association of Petroleum Geologists Bulletin, 57, p. 162-189.

**Osborne, M. and Haszeldine, R.S., 1993.** Evidence for resetting of fluid inclusion temperatures from quartz cements in oilfields. Marine and Petroleum Geology, 10, p.271-278.

**Paxton, S.T., Szabo, J.O., Ajdukiewicz, J.M. and Klimentidis, R.E., 2002.** Construction of an intergranular volume compaction curve for evaluating and predicting compaction and porosity loss in rigid-grain sandstone reservoirs. American Association of Petroleum Geologists, 86, p.2047-2067.

**Pittman, E.D., 1981.** Effect of fault related granulation on porosity and permeability of quartz sandstones, Simpson Group, Oklahoma. American Association of Petroleum Geologists Bulletin, 65, p. 2381-2387.

**Plummer, L.N., 1975.** Mixing of seawater with calcium carbonate ground water. Geological Society of America Memoir, 142, p. 219-236.

**Rawling, G.C. and Goodwin, L.B., 2003.** Cataclasis and particulate flow in faulted, poorly lithified sediments. Journal of Structural Geology, 25, 317-331.

**Renard, F., Brosse, E. and Gratier, J.P., 2000.** *In*: Quartz Cementation in Sandstones (ed: Worden, R.H. and Morad, S.), Special Publication of the International Association of Sedimentologists, 29, p. 67-78.

**Rittenhouse, G., 1971b.** Mechanical compaction of sands containing different percentages of ductile grains; a theoretical approach. American Association of Petroleum Geologists Bulletin, 55, p. 92-95.

**Rudnicki, J.W. and Chen, C-H., 1988.** Stabilization of rapid frictional slip on a weakening fault by dilatant hardening. Journal of Geophysical Research, 93, p. 4745-4757.

**Schmidt, V. and MacDonald, D.A., 1979.** The role of secondary porosity in the course of sandstone diagenesis. In Aspects of Diagenesis (ed. Scholle, P.A. and Schuger, P.R.), Society of Economic Palaeontologists and Mineralogists, Special Publication, 26, p. 175-207.

**Scott, T.E. and Nielsen, K.C., 1991.** The effects of porosity on the brittle-ductile transition. Journal of Geophysical Research, 96, p.405-414.

**Shipton, Z.K. and Cowie, P.A., 2001.** Analysis of three-dimensional damage zone development over a micron to km scale range in the high porosity Navajo Sandstone, Utah. Journal of Structural Geology, 23, 1825-1844.

**Shipton, Z.K., Evans, J.P., Robeson, K., Forster, C.B. and Snelgrove, S., 2002.** Structural heterogeneity and permeability in faulted aeolian sandstone: implications for subsurface modelling of faults. American Association of Petroleum Geologists Bulletin, 86, p. 6477-6490.

**Shipton, Z.K. and Cowie, P.A., 2003.** A conceptual model for the origin of fault damage zone structures in high-porosity sandstone. Journal of Structural Geology, 25, p.333-344.

**Sibson, R.H., Moore, J.M. and Rankin, A.H., 1975.** Seismic pumping; a hydrothermal fluid transport mechanism. Journal of the Geological Society of London, 131, p.653-659.

**Sibson, R.H., 1977.** Fault rocks and fault mechanisms. Journal of the Geological Society of London, 133, p.191-213.

**Sullivan, M.D., Macaulay, C.I., Fallick, A.E. and Haszeldine, R.S., 1997.** Imported quartz cement in aeolian sandstone grew from water of uniform composition but has complex zonation. Terra Nova, 9, p.237-241.

**Surdam, R.C. and Crossey, L.J., 1984.** Organic solvents, framework grain dissolution, and porosity enhancement. Society of Economic Palaeontologists and Mineralogists First annual midyear meeting, Published Abstract, 1, 1984.

**Thiry, M. and Marechal, B., 2001.** Development of tightly cemented sandstone lenses in uncemented sand: example of the Fontainebleau Sand (Oligocene) in the Paris Basin. Journal of Sedimentary Research, 71, 3, p. 473-483.

**Underhill, J.R. and Woodcock, N.H., 1987.** Faulting mechanisms in high porosity sandstones: New Red Sandstone, Arran, Scotland. In Deformation of Sediments and Sedimentary Rocks (eds. Jones, M.E. and Preston, R.M.F.). Geological Society Special Publication, 29, p. 91-105.

**Walderhaug, O., 1996.** Kinetic modelling of quartz cementation with porosity loss in deeply buried sandstone reservoirs. American Association of Petroleum Geologists, 80, p. 731-745.

**Walderhaug, O., Lander, R.H., Bjorkum, P.A., Oelkers, E.H., Bjorlykke, K. and Nadeau, P.H., 2000.** Modelling quartz cementation and porosity in reservoir sandstones: examples from the Norwegian continental shelf. *In*: Quartz Cementation in Sandstones (ed: Worden, R.H. and Morad, S.), Special Publication of the International Association of Sedimentologists, 29, p. 39-50.

**Wong, T-f., David, C. and Zhu, W., 1997.** The transition from bittle faulting to cataclastic flow in porous sandstones: Mechanical deformation. Journal of Geophysical Research, 102, p 3009-3025.

**Worden, R.H. and Morad, S., 2000.** Quartz cementation in oil field sandstones: a review of the key controversies. *In*: Quartz Cementation in Sandstones (ed: Worden, R.H. and Morad, S.), Special Publication of the International Association of Sedimentologists, 29, p. 1-20.

**Yielding, G. Freeman, B. and Needham, T.D., 1997.** Quantitative fault seal prediction. American Association of Petroleum Geologists, 81, p. 897-917.

**Zhu, W. and Wong, T-f., 1996.** Permeability reduction in a dilating rock: Network modelling of damage and tortuosity. Geophysical Research Letters, 23, p. 3099-3102.

**Zhu, W. and Wong, T-f., 1997.** The transition from brittle faulting to cataclastic flow: Permeability evolution. Journal of Geophysical Research, 102, p 3027-3041.

# Chapter 3.

This chapter introduces the geographical and geological background of the Hopeman Sandstone. The development of the North Sea basin is covered and the history of the Inner Moray Firth basin as part of this larger system is also introduced. The background to basin structure and sedimentology is presented allowing the Hopeman Sandstone exposures to be understood in a wide stratigraphic context. The local exposure setting of the Hopeman Sandstone on the southern Moray Firth coastline is also documented providing detail on the sequence of sediments exposed onshore and their structural relations. The chapter finishes with a discussion of the sedimentology of the Hopeman Sandstone and the preferred local correlation and naming of exposures within the Lossie Peninsula.

# The Hopeman Sandstone: Basinal setting, Sedimentology and Structure.

## 3.1 Introduction

The Hopeman Sandstone is part of a suite of Permo-Triassic sediments exposed on the southern shore of the Inner Moray Firth (IMF) basin, within the North Sea (Fig. 3.1). The sandstone crops out between Burghead to the west and Lossiemouth to the east, with Elgin to the south. Exposures are predominantly coastal cliffs and wave-cut platforms. Adjacent to the coast, and inland, are a number of small quarries in which the unit is visible. The focus of this project has been on coastal and quarry exposures in which structural features can be observed. The term 'Lossie Peninsula' is used throughout this thesis to describe the geographical area between Burghead and Lossiemouth in which the Hopeman Sandstone crops out (Figs 3.2 and 3.8).

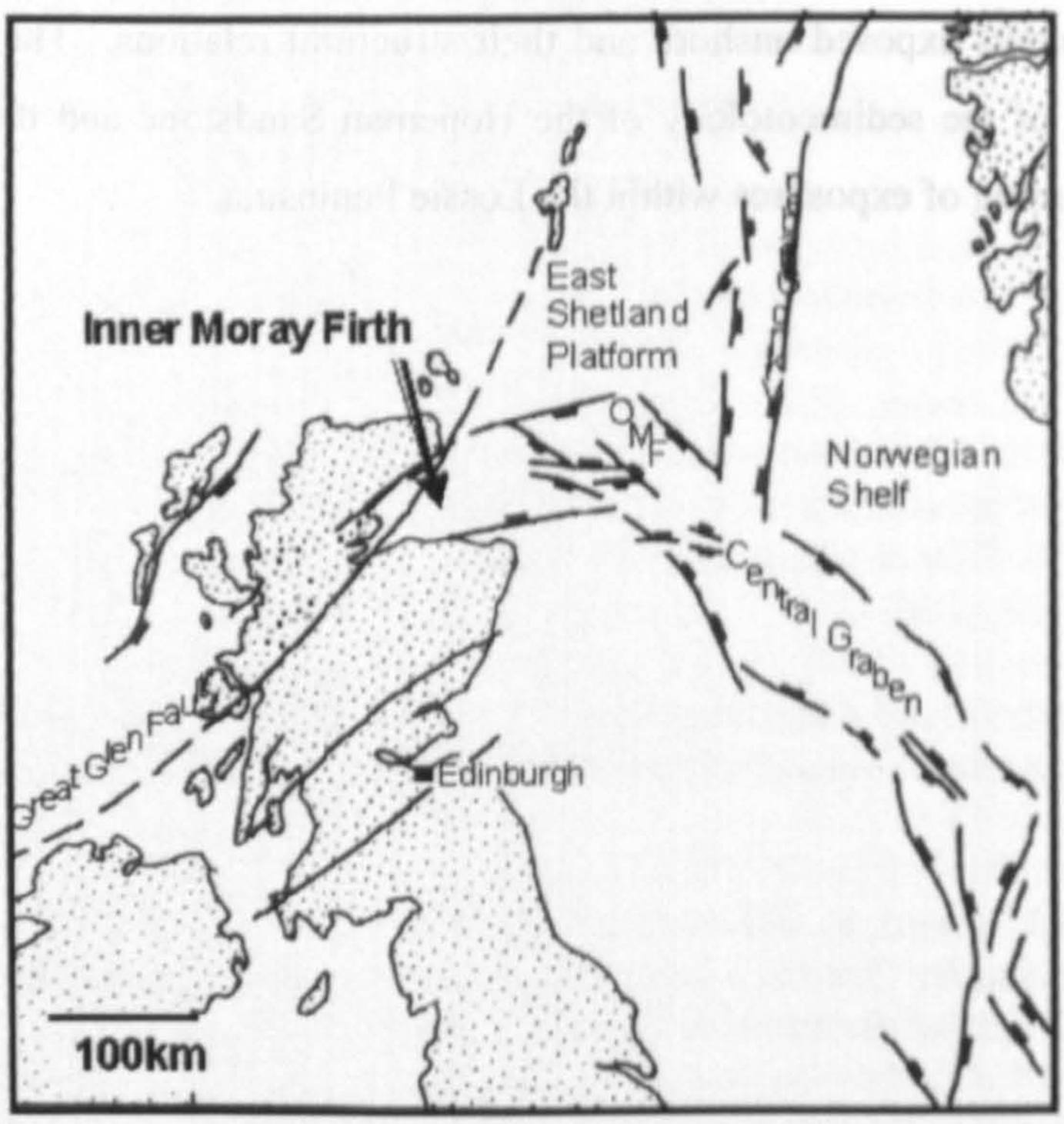


**Figure 3.1. Location map of the Inner Moray Firth Basin within the North Sea rift framework. The Inner Moray Firth forms the western arm of the principally Late Jurassic trilete rift system.**

## 3.2 Inner Moray Firth and North Sea basinal setting

The Inner Moray Firth rift basin is situated off the northeast of Scotland between the East Sutherland and Grampian coasts and represents the western arm of the trilete North Sea rift system (Thomson and Underhill, 1993) (Fig 3.2).

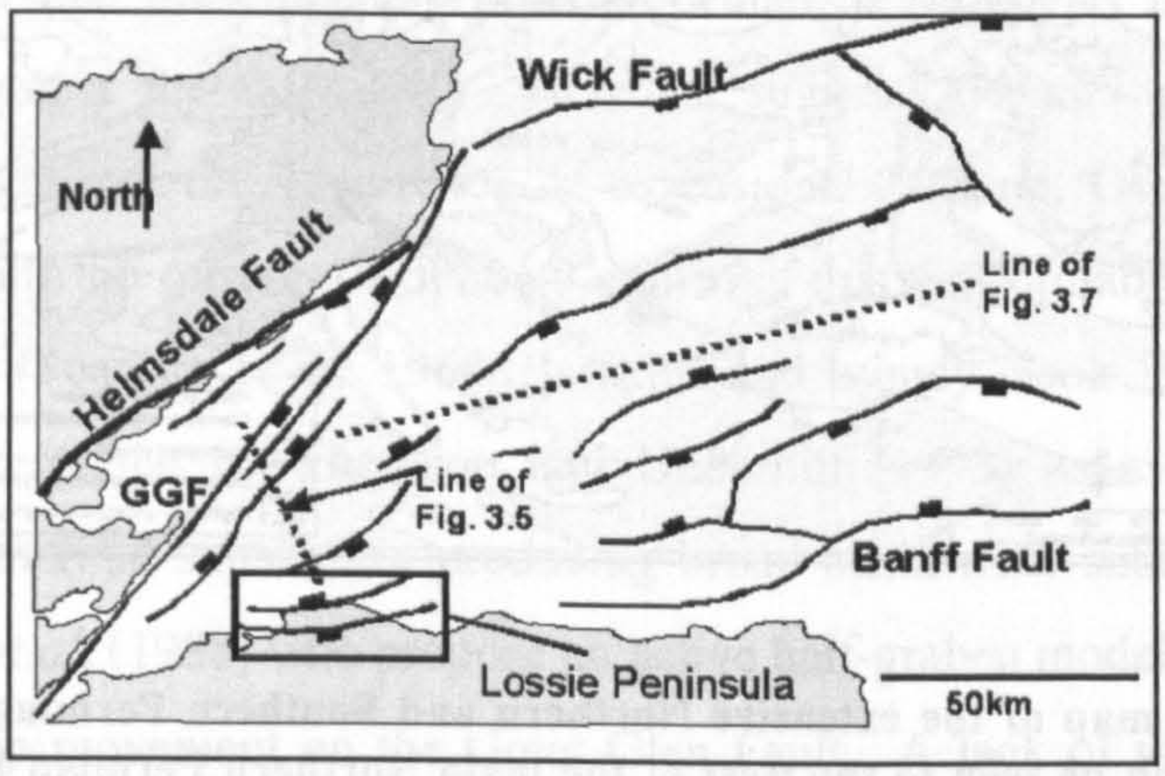


**Figure 3.2. Structural framework of the Inner Moray Firth Basin . The basin bounding faults, the Helmsdale, Wick and Banff faults are labelled along with the through-going Great Glen Fault (GGF). The Hopeman Sandstone crops out on the Lossie Peninsula, on the southern margin of the basin. The location of seismic cross-sections visible in figures 3.5 and 3.7 are marked.**

The major phase of North Sea development occurred during the Late Jurassic, but the basin was initiated during Devonian and Carboniferous rifting (Glennie and Underhill 1998) which in turn followed the coming together of the various tectonic slices which made up continental NW Europe by the end of the Caledonian Orogeny. The subsequent history of the basin has involved five major regional structural events, predominantly within an intra-plate setting (Glennie and Underhill 1998). The Moray Firth basins along with the similarly east-west trending Northern North Sea and Southern North Sea Permian basins (Fig. 3.3) were first developed during late Permian subsidence that may have been coeval with early subsidence around the later Central and Viking Grabens. Thermal subsidence continued until Middle Jurassic thermal doming, caused by a mantle plume, led to the onset of the main North Sea trilete rift system. The majority of present day petroleum traps were formed by subsequent Late Jurassic extension and fault block rotation caused by domal collapse centred on the Viking and Central Grabens. The late Cretaceous and Cenozoic were characterised by thermal subsidence and passive in-fill of sediments. A crucial phase of basin exhumation,

particularly in the western basins such as the Moray Firth, occurred in the Cenozoic, thought to be in response to the opening of the northeast Atlantic Ocean.


**Figure 3.3. Sketch map of the extensive Northern and Southern Permian sedimentary basins. The Moray Firth can be seen to the west of the main Northern Permian Basin. From Glennie (2003).**

## 3.3 Inner Moray Firth basin development

The present day basin is bounded by the Wick Fault to the north, the Helmsdale Fault to the west and the Banff Fault to the south. The eastern boundary of the basin with the Outer Moray Firth is marked by the Witch Ground and Buchan Graben (Roberts *et al.*, 1990) (Fig. 3.2.). The Great Glen Fault runs southwest to northeast along the western basin margin.

The basin overlies Devonian Old Red Sandstone of the older Orcadian Basin, which is taken to be the basement rock (sensu lato). Below the Devonian, offshore well 12/23-1 penetrated metamorphosed Caledonian crystalline basement (Roberts *et al.*, 1990). The major phases of Mesozoic basin development involved minor Permian extension and extensive Late Jurassic extension (Underhill 1991a), followed by regional inversion during the early Tertiary (Thomson and Underhill 1993).

The earliest Permian sediments appear to infill and drape a Devonian topography produced through 'Variscan' Permo-Carboniferous contractional thrusting and subsequent erosion. There is limited evidence from offshore seismic data of minor hanging wall thickening of early Permian sediment, suggestive of localised small scale extension of the pre-existing

thrust faults (Thomson and Underhill 1993). The majority of Early Permian sediment is likely to be passive infill over the Variscan unconformity.

Late Permian, Triassic and Early Jurassic sediments appear on offshore seismic data as a conformable package of broadly northerly thickening parallel layers, with no local thickness variation in relation to faults (Underhill 1991a). Glennie *et al.,* (2003) correlated borehole stratigraphy to show that the Upper Permian Hopeman Sandstone is interpreted to be of uniform thickness across the IMF (Fig 3.4) which suggests deposition during a thermal subsidence period, without the occurrence of extensional faulting. Observation from two BGS boreholes within the onshore sediments confirms this conformable Permian to Early Jurassic relationship (Peacock *et al*., 1968, Berridge and Ivimey-Cook 1967). The offshore observations are interpreted by Thomson and Underhill (1993) as evidence for a post-extension phase of thermal subsidence producing broad basin-wide subsidence. This is in contrast to Frostick *et al*. (1988) who propose an active half-graben model during the Triassic controlled by dip-slip movement on the Great Glen Fault. A lack of visible thickening of Triassic sediment over the Great Glen Fault (Underhill 1991a) and the presence of the Top Triassic Stotfield Chert as a palaeosol produced during a phase of tectonic quiescence (Naylor *et al*., 1989) cast doubt on the Frostick *et al*. interpretation. Roberts *et al.* (1989a) also contest that a model of an extensional half-graben and dip-slip movement on the GGF is unlikely, primarily based upon their observations of Triassic sediment distribution. Broad thermal subsidence is therefore the most likely mechanism for accommodation space creation during the late Permian to earliest Jurassic.

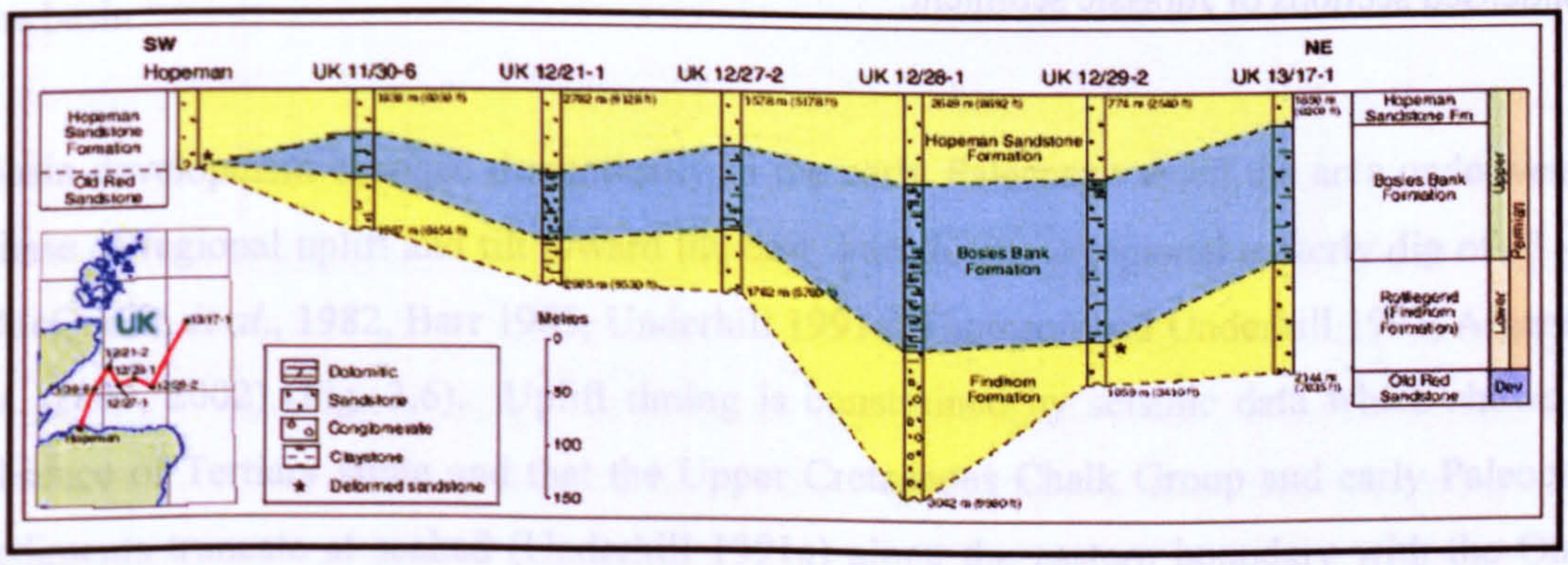


**Figure 3.4. Geological cross-section of the Permian of the Moray Firth. The Hopeman Sandstone is seen to extend across the basin at similar thickness, suggesting deposition in a passive setting. Offshore Permian sands and clays are observed, the absence of these units onshore of the southern Moray Firth may be attributed to its basin margin location. From Glennie *et al.* 2003.**

The Early and Mid Jurassic were characterised by relative uplift related to the emerging presence of North Sea doming (Underhill and Partington 1993). Underhill and Partington (1993) relate the doming to the development of a warm plume head in the Central North Sea, affecting a wide regional area. This uplift is expressed in the IMF as a series of mid-Cimmerian unconformities (Thomson and Underhill 1993) with regional onlapping of clastic-dominated sediments increasing to the east as overall stratigraphy thinned (Roberts *et al.*, 1990). The unconformities are characterised locally by onlap of mid-Jurassic sediments onto structural highs and condensed sequences, with deposition of Early and Mid-Jurassic within both the Inner and Outer Moray Firth.

The Late Jurassic represents the major phase of extensional basin development, post dating the deposition of the Hopeman Sandstone. Thick packages of argillaceous sediment, the Kimmeridge Clay Formation, were deposited throughout the basin and comprise at least 75% of the thickness of the Jurassic strata (Roberts *et al.*, 1990). The extension was controlled by dip-slip on the southwest-northeast trending Helmsdale fault to the west of the basin (Underhill 1991a,b), resulting in an overall wedge shaped basin geometry (Fig. 3.5). Seismic and onshore exposure data indicates dip-slip normal fault extension occurred basin-wide leading to the development of a number of smaller scale half-graben structures. These filled with syn-tectonic Late Jurassic sediment. At the end of the Late Jurassic this continuous syn-sedimentary activity gave way to isolated compactional fault movements with passive sediment in-fill of depocentres. Uplifted footwall sections throughout the basin show thin condensed sections of Jurassic sediment.

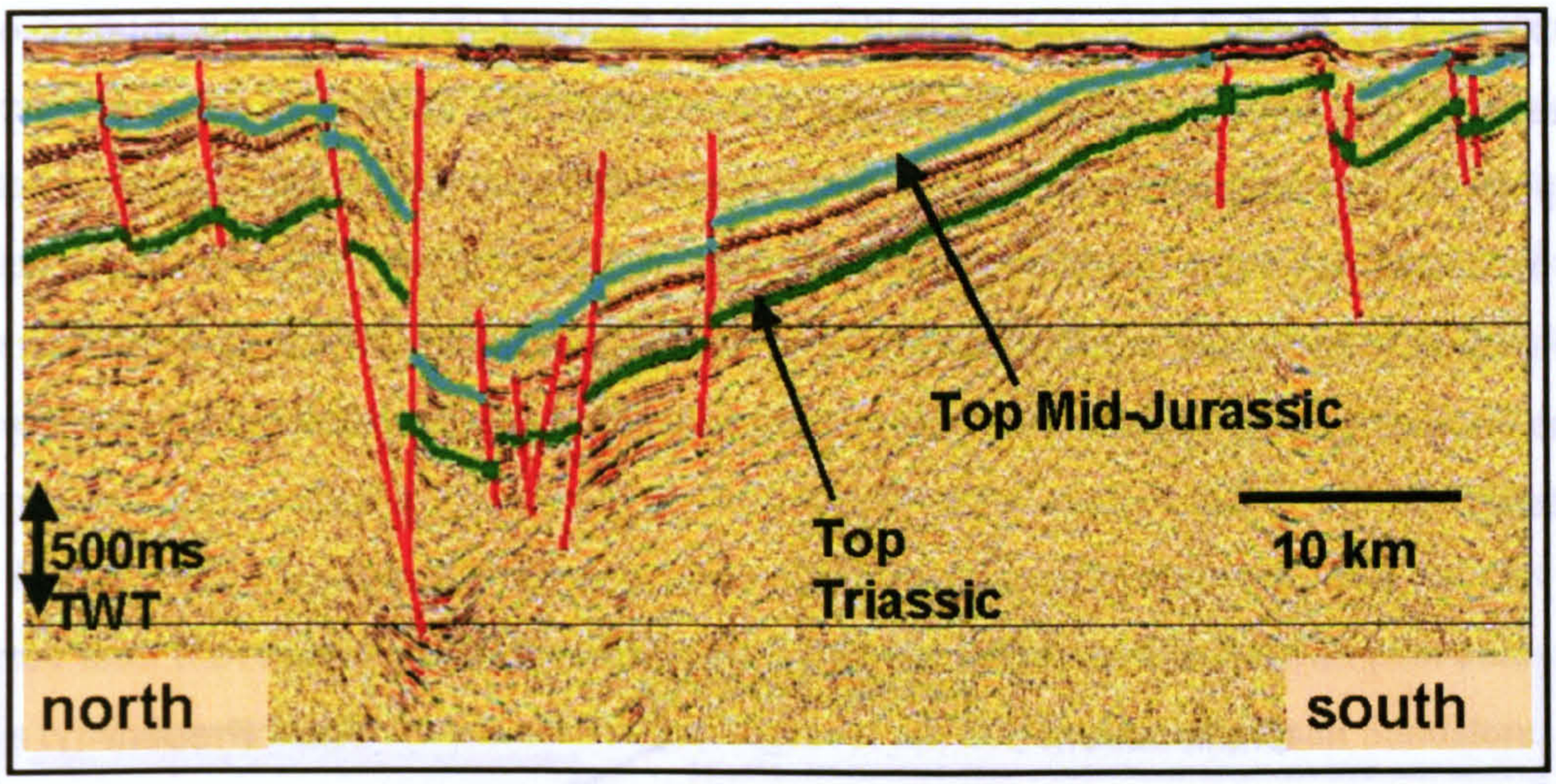


**Figure 3.5. Seismic reflection profile across the IMF basin from the Helmsdale coast (north) to the Lossie Peninsula (south). The first order half-graben structure with super-imposed sub-basins can be seen. The onshore Clashach and Burghead Faults can be correlated with offshore equivalents and form part of the same structural style of half-grabens and small horst blocks seen offshore. Line of section shown on figure 3.2.**

Following Late Jurassic rifting, the Cretaceous is characterised by a phase of thermal subsidence and passive in-fill of the Jurassic basin topography, with the depocentre shifting from the Jurassic half-graben to the northwest of the basin (Andrews *et al.,* 1990). Early Cretaceous sediments are predominantly sandstones and mudstones, the sands interpreted by Hancock (1984) as turbidites. Late Cretaceous sediments are principally chalk, cropping out on present day seafloor at the eastern edge of the IMF, therefore absent throughout most of the basin.

Basin development changed dramatically in the early Paleocene when the area underwent a phase of regional uplift and tilt toward the east, introducing a regional easterly dip of 2° - 3° (McQuillin *et al.*, 1982, Barr 1985, Underhill 1991a, Thomson and Underhill 1993, Argent *et al.,* 2000, 2002) (Fig. 3.6). Uplift timing is constrained by seismic data which shows an absence of Tertiary strata and that the Upper Cretaceous Chalk Group and early Paleocene sediments truncate at seabed (Underhill 1991a) along the eastern boundary with the Outer Moray Firth. The mechanism for such unprecedented regional tilting, not observed at the same magnitude elsewhere in the North Sea, has been explained by the opening of the northeast Atlantic (Glennie 1990), compressional effects of the Alpine Orogeny (Roberts

1989) and by Tertiary magmatism to the west of Scotland, leading to underplating of the crust with low density material (Brodie and White 1994). The latter explanation is offered to explain the continuing buoyancy of western basins within the British Isles, which if uplifted by northeast Atlantic rifting, may have been expected to have subsided over the subsequent 40 million years, as the basins and rift moved to their present day positions, c.1000km apart. The Alpine Orogeny appears a less likely mechanism than igneous underplating for the same reason.

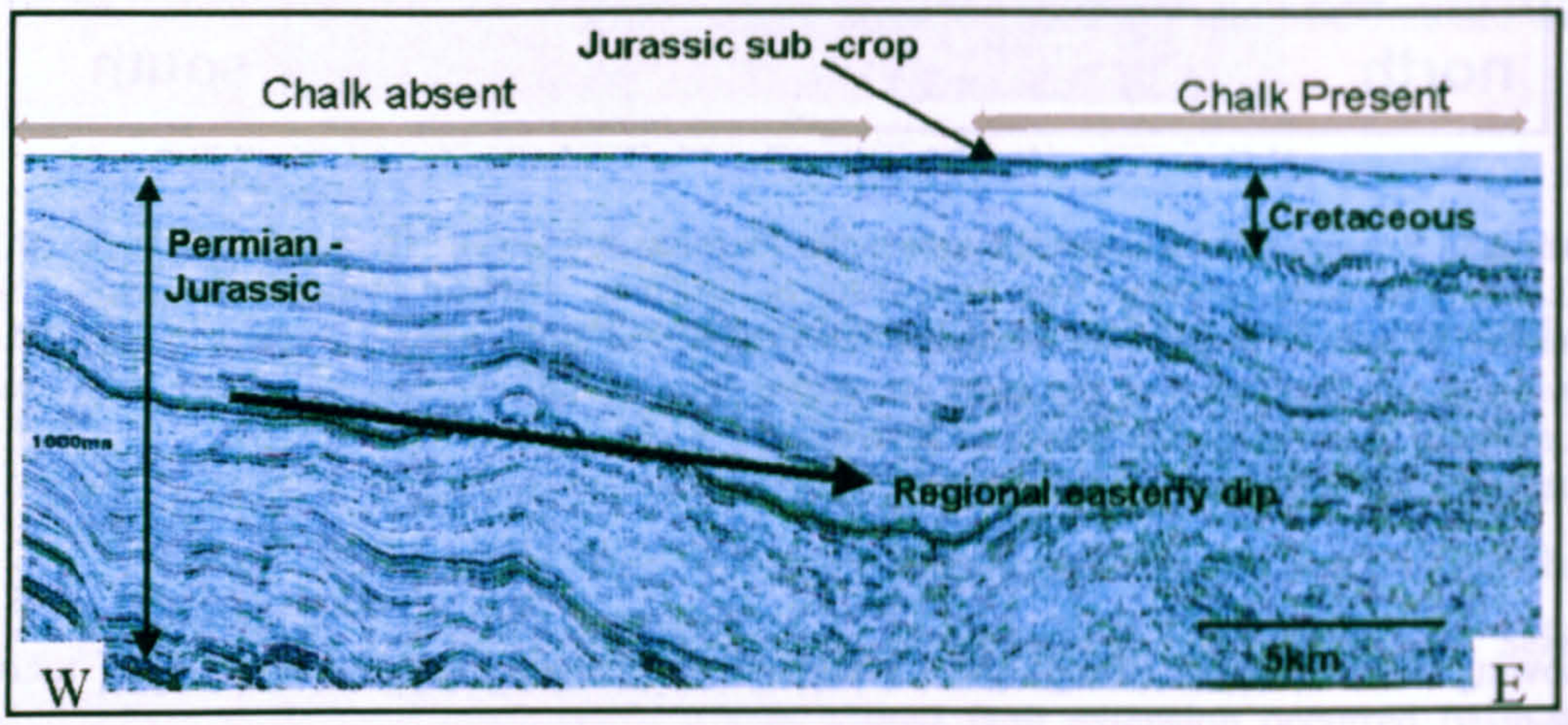


**Figure 3.6. Tertiary regional exhumation imparted a 2-3 easterly dip on the western IMF. The seismic section shows the prominence of the easterly dipping reflectors in the west of the basin where Cretaceous Chalk is absent allowing better seismic imaging. A similar degree of dip in the pre-Palaeocene sections further east provides evidence for the Early Tertiary age of exhumation and the present day regional dip. A section of Permian through to Late Jurassic reflectors can be seen. Modified from Argent *et al.*, 2002.**

Determination of the absolute amount of basin-wide uplift has been attempted using sonic velocity data (Roberts *et al.*, 1990), vitrinite reflectance, clay mineralogy (Hurst 1980), fission track (Argent *et al.*, 2002) and seismic data (Underhill 1991a). Roberts *et al.* (1990) suggest around 300m of uplift in the western extreme of the basin, McQuillin (1982) and Underhill (1991a) report c.1km of uplift in the same area. The fundamental difference in reported uplift values centres around the model of basin development. Roberts *et al.* (1990) suggest the western IMF is underlain by the thick, isostatically uncompensated crust, reported by Brodie and White (1994), and that the basin opened through strike-slip tectonics. As this does not require a phase of post-rift thermal subsidence, there was consequently no Upper Cretaceous-Tertiary sedimentation in the basin. It is now widely accepted, for the Inner

Moray Firth, that the basin developed through crustal extension over thinned lithosphere in the Late Jurassic (Underhill 1991a), and that consequently it is likely that a thicker Cretaceous sequence was deposited prior to regional uplift and erosion, indicating the basinal position on the northeast Atlantic rift shoulder was a more likely uplift mechanism than igneous underplating. However, this may depend on the scale of Tertiary underplating to the west of Scotland, which may have been sufficient to produce the observed uplift, but not to prevent some degree of later subsidence in the relatively distal eastern IMF basin. Within the Inner Moray Firth the regionally homogenous uplift led to the development of a number of localised fault movements, leading to the creation of uplifted horst blocks with post-Jurassic throws typically varying between 10-300m (Argent *et al.*, 2002). The Hopeman Sandstone on the Lossie Peninsula is interpreted as the onshore analogue of one of these blocks (Chapter 4). IMF stratigraphy is summarised in figure 3.7.

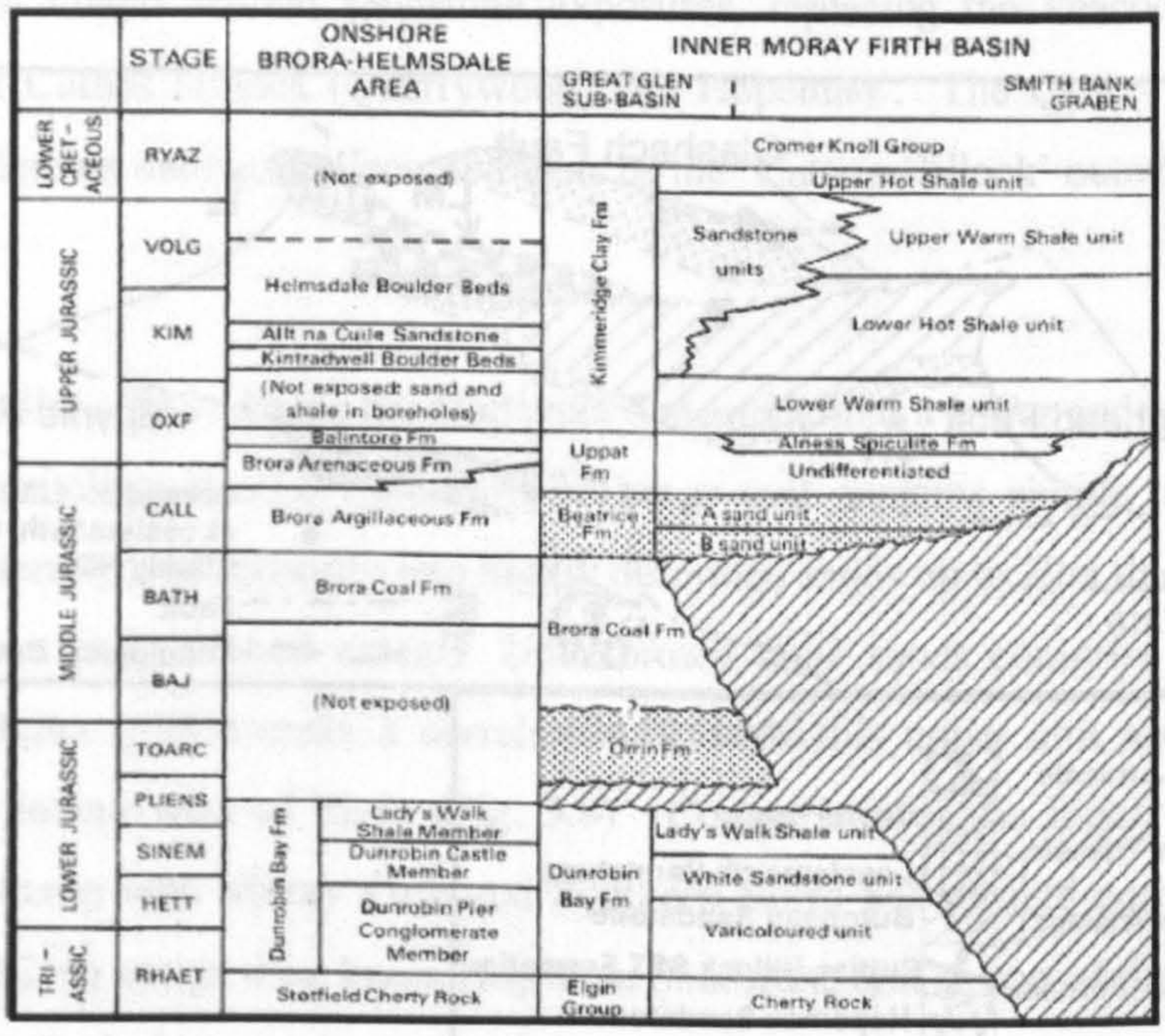


**Figure 3.7. Inner Moray Firth Triassic to Cretaceous offshore stratigraphy, with the onshore sequence at Helmsdale in the northwest of the basin for comparison. From Andrews *et al.* (1990).**

## 3.4 Lossie Peninsula exposure stratigraphy

A conformable Permo-Triassic sequence, of which the Hopeman Sandstone is part, is visible within the Lossie Peninsula coastal exposures (Fig 3.8). A second set of Permo-Triassic exposures occurs 6km inland on a topographical high northwest of Elgin. The specific age of each unit has been deduced through finds of various reptiles and track ways. Interest in these palaeontological features, and the corresponding attempt to date the local stratigraphy, has been ongoing since 1885 when Judd reported reptiles in the New Red Sandstone of the Elgin area. A Permo-Triassic age was tentatively assigned early in the 20th century (Watson and Hickling 1914) by comparison with reptile discoveries from Upper Permian and Mid-Triassic units elsewhere. Unusually well preserved fauna are found in Triassic Lossiemouth Sandstone Formation sediments, in comparison to other similar age units in the UK, which typically only display footprints.

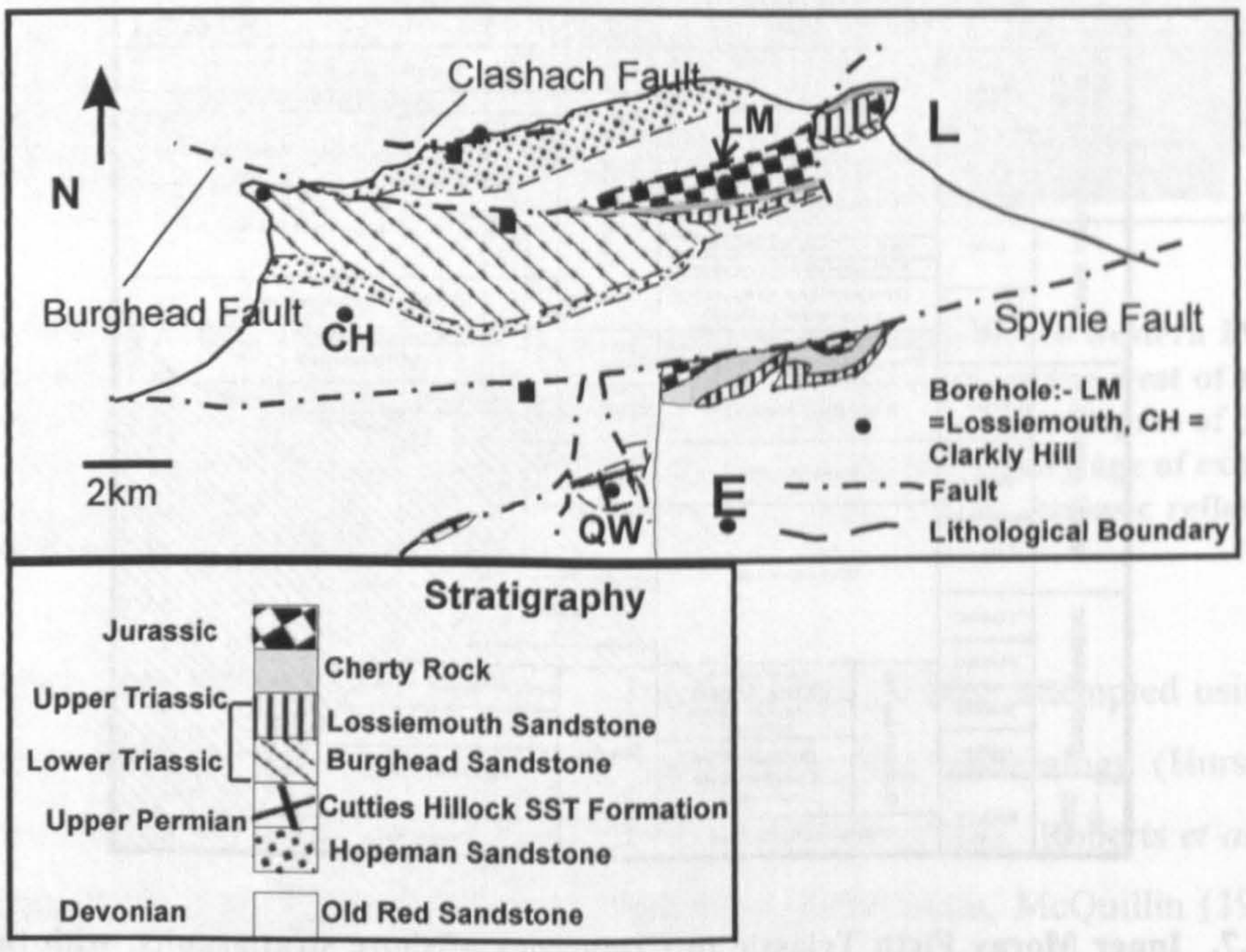


**Figure 3.8. Geological map of the Lossie Peninsula exposures and stratigraphic relationships. The two faults studied in the this thesis, Burghead and Clashach, are also show. Both are normal faults downthrowing to the south. L = Lossiemouth; QW = Quarry Wood; E = Elgin. Based upon BGS map, modified to include authors interpretation.**

## 3.41 Hopeman Sandstone Formation

The division, correlation and age of the Hopeman Sandstone Formation has been a matter of enduring debate. The first relatively recent classification was by Peacock *et al.* (1968) and was based upon previous work (Watson and Hickling 1914, Mackie 1925, Walker 1961). In this scheme the aeolian sandstone exposed along the coastline from east of Burghead to the Covesea Lighthouse and a similar sandstone exposed inland west of Elgin in the Quarry Wood location (Fig. 3.8) are grouped together. The sands are defined as the 'Sandstones of Cutties Hillock (Quarrywood) and Hopeman', and are assigned an Upper Permian to Lower Triassic age.

In 1980 Warrington *et al.* defined formal lithostratigraphical names for the Lossie Peninsula Permo-Triassic exposures, using the term 'Hopeman Sandstone Formation' to include both the coastal and inland aeolian sandstone exposures, replacing the Peacock (1968) name 'Sandstones of Cutties Hillock (Quarrywood) and Hopeman'. The Quarry Wood outcrops are more well known amongst palaeontologists as the 'Cutties Hillock' outcrops (Benton and Walker 1985).

Glennie and Buller (1983) divide the Hopeman Sandstone into a lower and upper unit on the basis of sedimentological observations. The lower unit contains simple transverse dunes which grade laterally and vertically into highly deformed sands up to 20m thick and hundreds of square metres in horizontal extent. Undeformed dune sands comprise the upper unit. Glennie and Buller (1983) make a correlation between this upper unit and the sandstone exposure 6km inland west of Elgin (Fig. 3.8). Comparison of the highly deformed sand observed in outcrop with Moray Firth and Southern North Sea oilfield cores leads Glennie and Buller (1983) to assign their lower Hopeman Sandstone unit as part of the 'Weissliegend' sandstones, late Early Permian in age, and the upper unit as Late Permian to Early Triassic. The age interpretation of the upper unit is based upon comparison of reptilian tracks found in the coastal exposures to reptilian remains in the exposures inland at Cutties Hillock.

In an alternative interpretation, focusing on palaeontological criteria, Benton and Walker (1985) argue that the sandstone exposed inland cannot be confidently correlated with the coastal Hopeman Sandstone. They point out that whilst the two exposures are lithologically similar, the coastal outcrops yield reptilian *dicynodont* footprints but no fauna. Subsequently

a single mould skull of *dicynodont* has been found adjacent to the coastal outcrops (Clark, 1999), but this still contrasts greatly with the inland Quarry Wood/ Cutties Hillock outcrops which yield multiple late Permian fauna. Benton and Walker's solution is to formally name the inland outcrops as the 'Cutties Hillock Sandstone Formation' until such time as a more accurate correlation can be established. The term Hopeman Sandstone Formation therefore refers specifically to the coastal exposures in their scheme. The find of the *dicynodont* skull in the coastal Hopeman Sandstone is used here to tie the inland and coastal exposures as time equivalent Upper Permian units (Fig 3.9). This is the simplest system based on available data, and matches field observations which highlight the difficulty of correlating the 'deformed beds' of the coastal outcrops, and therefore of further dividing the unit into an upper and lower. Williams (1973) split the deformed coastal sands into three separate vertical horizons, further highlighting the complexity of correlating the unit. Clemmensen (1987) concluded that the deformed sands occur randomly throughout the coastal exposures.

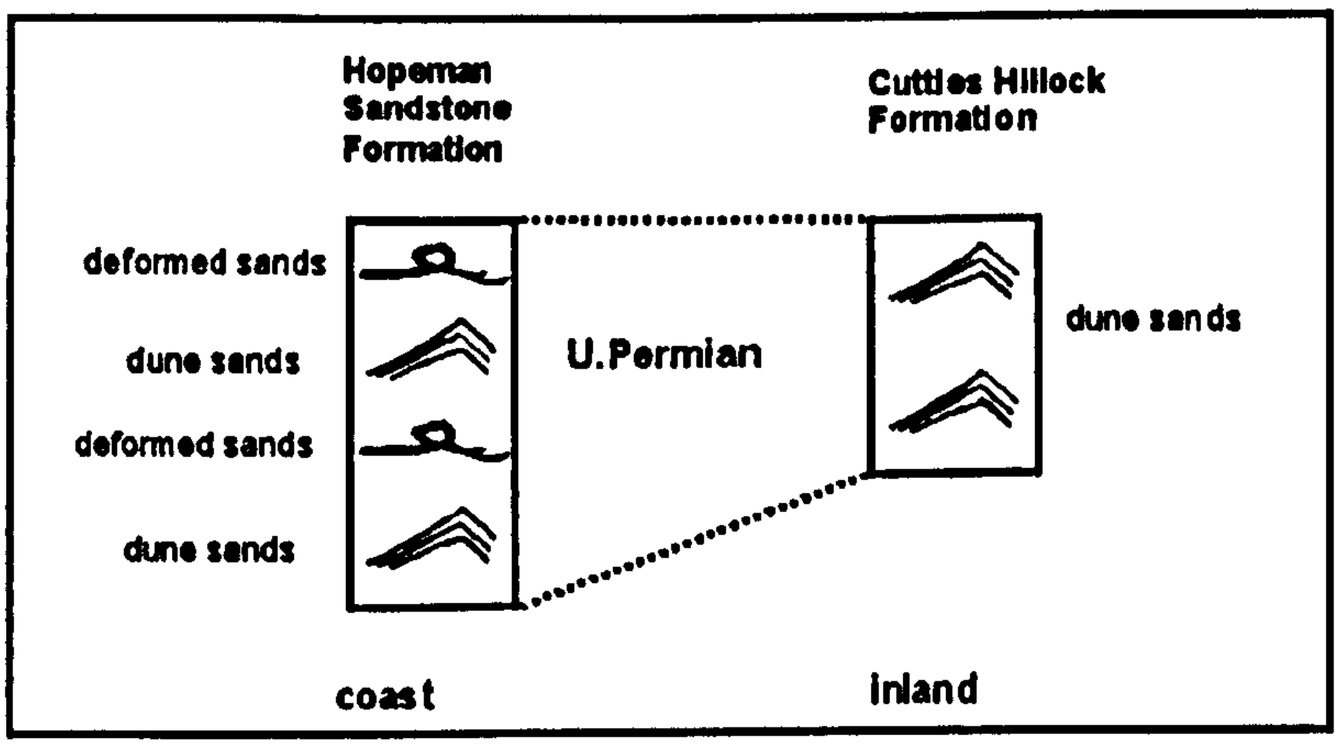


**Figure 3.9. Preferred onshore Upper Permian stratigraphy, with the coastal Hopeman Sandstone tentatively correlated with the inland Cutties Hillock Sandstone. Fossil trackways and fauna indicate the two formations are age equivalent, but the contorted sandstone beds appear restricted to the coastal sandstones. Based upon a division of Benton and Walker, 1985.**

The age of the inland Cutties Hillock Sandstone (definition of Benton and Walker 1985) was first suggested as Permian by Taylor (1894). In 1973 Walker compared fauna from Cutties Hillock with southern African examples and placed its age as close to the Permo-Triassic boundary. The most recent age assessment is that of Benton and Walker (1985) who place the Cutties Hillock Sandstone as lying at the 'extreme summit of the Permian'.

The age of the Hopeman Sandstone, as defined by Benton and Walker (1985), is Late Upper Permian based upon footprints attributed to *dicynodonts,* and reaffirmed by the skull find (Clark 1999). In particular the tracks are similar to footprints found around the Lower/Upper Permian boundary in the Penrith Sandstone (Hickling 1909, Watson 1909, Watson and Hickling 1914, Smith et al 1974) as well as in Dumfriesshire and Mansfield. Documentation in this thesis of significant fault related quartz cementation within the quarry suggests that preferential bone preservation in the quarry occurred because of early, shallow burial silicification, which did not typically occur elsewhere in the UK in similar age sandstone. The onshore Hopeman Sandstone, which is present throughout the offshore Inner Moray Firth (Fig 3.4), is also tentatively age-correlated with the Shearwater Salt Formation and the Turbot Anhydrite Formation in the Central North Sea by Glennie *et al.* (2003).

Crucially there is a good agreement for the coastal Hopeman Sandstone age between Peacock (1968), Glennie and Buller (1983) and Benton and Walker (1985) despite differences regarding the internal division and local correlation of the unit. For the purposes of this thesis an age of Upper Permian is assigned to the Hopeman Sandstone Formation and the upper section is considered to be laterally equivalent to the Cutties Hillock Sandstone..This is based upon a reconciliation of previous work and observations made here regarding the sedimentology of the unit. The classification of Upper Permian is sufficiently accurate for the purposes required.

## 3.42 Burghead Sandstone Formation

The Burghead Sandstone Formation (Warrington *et al.*, 1980), equivalent to the Burghead Beds of Peacock *et al.* (1968), consists of fluvial sandstones faulted against the Hopeman Sandstone in coastal exposures (Fig. 3.8). A British Geological Survey (BGS) borehole at Clarkly Hill, south of Burghead (Fig 3.8) encountered a package of Burghead Sandstone 78m in thickness conformably overlying the Hopeman Sandstone, with a bedding dip of between 3° and 5° north.

Toward the eastern side of the Lossie Peninsula the Burghead Sandstone thins and pinches out east of Lossiemouth. An age of Triassic was assigned by Peacock *et al.* (1968) based

upon stratigraphic observations and the assignment of a Permo-Triassic boundary age for the underlying Hopeman Sandstone.

## 3.43 Lossiemouth Sandstone Formation

The Lossiemouth Sandstone (Warrington *et al.*, 1980) crops out near Lossiemouth, Spynie and Findrassie (Peacock *et al.*, 1968) (Fig. 3.8). The unit is considered a lateral equivalent to the top of the Burghead Sandstone Formation (Peacock *et al.* 1968). Unusually well preserved fauna are found in the Formation, which, as for the Hopeman Sandstone, is unusual in comparison to other sandstones of similar age in the UK, which typically only display footprints, and may be due to the early silicification in the region which is documented in this thesis. On the basis of the reptilian fauna the Lossiemouth Sandstone is dated as Late Triassic (Carnian) (Benton, pers. comm., 2003). Thickness varies from 5m-30m.

## 3.44 Stotfield Chert (or Cherty Rock)

Conformably overlying the Burghead Sandstone Formation and the Lossiemouth Sandstone Formation, the Stotfield Chert is a 0.5-10m thick horizon. Mapping by Peacock *et al.* (1968) assigned a Top Triassic (Rhaetic) age to the Stotfield Chert, stratigraphically equivalent to marly limestone exposures which crop out near Golspie on the Sutherland coast (Judd 1873, Peacock *et al.*,1968). The Stotfield Chert is a strong reflector on seismic data immediately offshore the Lossie Peninsula, across the IMF basin, and is dated as Top Triassic.

## 3.45 Jurassic

The BGS borehole 3km southwest of Lossiemouth penetrates Lower Jurassic (Sinemurian) sediment (Berridge and Ivimey-Cook 1967) (Fig 3.8). A minimum thickness of 69m of sandstones, marls and muds was encountered, juxtaposed by the Burghead Fault against Old Red Sandstone to the north.

## 3.5 Hopeman Sandstone Formation sedimentology

The Hopeman Sandstone is a package of dune bedded sands of aeolian origin (Peacock 1968, Williams 1973, Glennie and Buller 1983, Clemmensen 1987), 60m thick (Berridge and Ivimey-Cook 1967) and dipping 3-5° north. The Formation can be divided into two main sedimentological units; dune bedded sands and deformed sands.

In outcrop the Hopeman Sandstone is a fine-medium grained, well-sorted clean sand. Colour varies between white, orange, buff and pink depending on location. Large scale (>10m) cross-bedding typical of aeolian dunes is visible in the coastal cliff and quarry exposures.

### 3.51 Dune Bedded sands

The large-scale cross bedding and uniform bedding angles lead Peacock (1966) and Glennie and Buller (1983) to interpret the Hopeman Sandstone as a series of laterally and vertically stacked transverse dunes. In a more detailed model Clemmensen (1987) interprets the formation as a series of complex star dunes comparable to the modern Rub' al Khali in Saudi Arabia and distinguishes two main types of aeolian unit. Type I is characterised by small – large (1m->10m) medium-high angle cross-bedded dune slip face and lee-side sands. Type II consists of large scale oppositely dipping cross-bedded deposits. Type II sands are deposited in the flanks of linear dune segments, consisting of grainfall and wind-ripple sands. The Clemmensen model correlates the coastal exposures into 9 genetic units based on the above criteria. These genetic units are part of a system of complex star dunes, between which smaller crescentic dunes, interdune flats, and infrequent ephemeral streams, occur. Observation of frequent, stacked, large scale and well laminated transverse dunes within coastal exposures of the Hopeman Sandstone seen during work for this thesis suggest the model of transverse dunes is the more correct, and as such is favoured here.

Rare fluvial deposits have been noted within the sandstone, containing small thicknesses of water-laid pebbles, clay clasts, small-scale cross-bedding and laminae of green silty-clay (Peacock *et al.*, 1968). These small river deposits are attributed to ephemeral streams running over the surface of dunes (Peacock 1966, Clemmensen 1987).

## 3.52 Contorted Sandstone unit

Deformation beds or contorted beds (Peacock 1966), constitute a significant proportion of the exposed Hopeman Sandstone. The original term 'Contorted Beds' is preferred here to avoid confusion with fault-related deformation features (deformation bands) discussed in this thesis. Composed of vertical beds, 'saucer' shapes, lobes, and minor soft sediment folds, contorted beds range in size from several metres to several hundred square metres, up to 15m vertically, and appear to occur throughout the exposed area, interspersed with undeformed dune sand between them. Peacock (1966) restricts their occurrence to within foreset beds; Glennie and Buller (1983) go further and divide the formation into an upper and lower unit, with the contorted beds confined to the lower unit. Clemmensen (1987) observes that these beds generally occur on dune foresets and adjacent to ephemeral streams (interdune areas) but does not report a vertical or lateral spatial variation within the exposures, only a decrease in occurrence away from present day shoreline.

Peacock (1966) proposes the origin of the contorted beds as liquefaction after heavy rainfall on dune flanks, leading to slumping. This is supported by the presence of the ephemeral streams which indicate there was periodic interaction between rainfall run-off and the dune surfaces. Glennie and Buller (1983) propose a marine inundation associated with the Zechstein marine transgression and a combination of deformation in shallow sub-aquatic and sub-aerial environments. During shallow water cover, 'saucer' shape contorted beds formed by the sinking of dune crust surfaces into underlying 'quicksand'. Other contorted beds developed through fluid escape which folded and deformed soft sediment and interacted with the dip slope of the dune to produce asymmetrical features. Contorted beds seen during fieldwork for this thesis are restricted to dune foresets, and given the association reported between foresets and ephemeral streams, it would seem most likely that interaction between rainfall and sediment causing slumping and contortion was the most likely deformation mechanism. Although production of contorted beds through the inundation of the Zechstein Sea cannot be ruled out, there is limited field evidence for a correlation between the contorted beds and any consistent lateral or vertical position within the exposed sandstone.

## 3.53 Mineralogical composition

Petrographic analysis of thin sections of Hopeman Sandstone was undertaken using optical and Scanning Electron Microscope (SEM) in both secondary electron (SE), cathodoluminescence (CL) and backscatter electron (BSE) modes. The rock is 95% quartz (predominantly monocrystalline), 3-5% feldspar (predominantly K-Fsp) and 0-2% rock fragments (Chapter 5). Detrital clay is absent except in rare local pebbly fluvial bands.

Diagenetic phases are quartz overgrowths, feldspar, and occasional carbonate cements, observed in the field. Locally barite and fluorite are significant and occur in fractures and mineralised reefs. Detrital K-feldspar frequently shows minor to extensive dissolution textures. Lead-zinc sulphide mineralisation is present around Burghead (Fig. 3.8), where Galena, Sphalerite and Chalcopyrite are developed. (Chapter 5). A patchy, clay free, grain coating iron oxide is present within dune foresets, giving an orange colour to the Hopeman Sandstone in outcrop.

## 3.6 Exposure structure

Two major normal east-west faults occur in the Lossie Peninsula with a number of associated smaller scale east-west structures on the coast. The first of these occurs north of Elgin downthrowing to the south and juxtaposing a Permian –Jurassic sequence against the Old Red Sandstone to the north, and named the Spynie Fault in this thesis.

The second fault crops out at Burghead (Fig. 3.8) and trends inland toward the east, mapped on the published geological map as cropping out again at Lossiemouth. Normal, dip-slip movement on the fault, to the south, downthrows Triassic (Burghead Sandstone, Lossiemouth Sandstone and Stotfield Chert) and Jurassic sediments against the Hopeman Sandstone and Old Red Sandstone to the north. Associated with this fault is a zone of deformation bands extending at least 13m from the main slip face into the footwall. These deformation bands are small scale faults with mm-cm slip (Edwards *et al.*, 1993, Ogilvie, 2001), the frequency of which decreases with increasing distance from the main slip face. The fault forms a major focus of the thesis and is termed here the 'Burghead Fault', based on the excellent exposure at its outcrop in this location, and to avoid confusion with earlier work (Underhill 1991a)

which uses the term 'Lossie Fault' for an adjacent, offshore fault shown here to be a separate structure (Chapter 4).

Along the coastline a minor east-west fault, with downthrow to the south, is exposed in Clashach Cove and again at Clashach Quarry (Fig. 3.8.). Hopeman Sandstone forms both the footwall and hanging wall. The name 'Clashach Fault' is defined here, as again a large part of this thesis focusses on this structure.

The east-west trending faults are proposed as Late Jurassic in age, based upon observed cross-cutting relationships and an integration of the onshore structures with seismic data from offshore in Chapter 4 of this thesis. A subordinate set of north-south faults are mapped on the Peninsula, predominantly in close proximity to Elgin (Fig 3.8), on which minor normal throw has occurred, and defined as post-Liassic in age by Peacock *et al.* (1968). These may be transfer or relay structures of similar age to the east-west normal faults.

## 3.7 Summary

The North Sea trilete rift system was initiated following Devonian-Carboniferous rifting. Permian thermal subsidence saw the development of two major Permian basins, Northern and Southern. Mid Jurassic thermal doming led to Late Jurassic extensional rifting creating the trilete extensional rift basin architecture seen at depth today. The IMF forms the extreme western arm of this rift system. Post-rift thermal subsidence saw the deposition of thick Cretaceous and Tertiary sediment during thermal relaxation and passive subsidence.

In this wider North Sea context the Inner Moray Firth Basin developed from the Permian through to the Tertiary predominantly by Late Jurassic dip-slip extension hinged on the Helmsdale Fault and propagated through extensional faults within the basin. This extension saw the deposition of thick Upper Jurassic sediment sequences which form the majority of present basin-fill. During the Paleocene the basin experienced uplift and erosion of around 1km in the west, with localised differential fault movements related to the regional tectonic uplift event. The uplift and erosion is expressed at the present day by the 2-3° regional easterly dip and absence of Upper Cretaceous chalk and Tertiary sequences in the west of the basin.

Permian -Triassic sediments crop out on the southern shore of the Inner Moray Firth basin, unconformably overlying a basement of Devonian Old Red Sandstone. Lower Jurassic strata have been proven through onshore boreholes. At the base of this sequence is the Hopeman Sandstone, an Upper Permian aeolian sandstone exposed along c.8km of coastline. Major, seismic scale, to minor sub-seismic scale normal faults are visible within the Hopeman Sandstone. The Lossie Peninsula as a whole is unusually mineralised with quartz cement, localised around the faults, preserving unusual vertebrate faunas.

---

# References


**Andrews, I.J., Long, D., Richards, P.C., Thomson, A.R., Brown, S., Chesher, J.A. and McCormac, M., 1990.** The Geology of the Moray Firth. British Geological Survey, United Kingdom Offshore Report, HMSO, London.

**Argent, J.D., Stewart, S.A. and Underhill, J.R., 2000.** Controls on the Lower Cretaceous Punt Sandstone Member, a massive deep-water clastic deposystem, Inner Moray Firth, UK North Sea. Petroleum Geoscience, 6, p. 275-285.

**Argent, J.D., Stewart, S.A, Green, P.F. and Underhill, J.R., 2002.** Heterogeneous exhumation in the Inner Moray Firth, UK North Sea: constraints from new AFTA and seismic data. Journal of the Geological Society of London, 159, p. 715-729.

**Barr, D., 1985.** Palinspastic reconstruction of normal faults in the Inner Moray Firth: implications for extensional basin development. Earth and Planetary Science Letters, 75, p. 191-203.

**Benton, M.J., and Walker, A.D., 1985.** Palaeoecology, Taphonomy, and Dating of Permo-Triassic Reptiles from north-east Scotland. Palaeontology, 28,p. 207-234,

**Benton, M.J., 2003.** Personal Communication. On the age of the Lossiemouth Sandstone Formation.

**Berridge, N.G. and Ivimey-Cook, H.C., 1967.** The Geology of a Borehole at Lossiemouth, Morayshire. Bulletin of the Geological Survey of Great Britain, 27, p. 155-169.

**Brodie, J. and White, N., 1994.** Sedimentary basin inversion caused by igneous underplating: Northwest European continental shelf. Geology, 22, p. 147-150.

**Clark, N.D.L., 1999.** The Elgin Marvel: a scientific investigation into a fossil that isn't there! *In*: (Bennett, S (ed)) New Fossil Evidence: Moray and the North East. The Moray Society. 30-33.

**Clemmensen, L.B., 1987.** Complex star dunes and associated aeolian bedforms, Hopeman Sandstone (Permo-Triassic), Moray Firth Basin, Scotland. In: Desert Sediments: Ancient and Modern (ed. Frostick, L, and Reid, I.). Geological Society of London Special Publication, 35, p. 213-231.

**Edwards, H.E., Becker, A.D. and Howell, J.A., 1993.** Compartmentalization of an aeolian sandstone by structural heterogeneities: Permo-Triassic Hopeman Sandstone, Moray Firth, Scotland. In: Characterization of fluvial and aeolian reservoirs (ed. North, C.P.). Geological Society of London Special Publication, 73, p. 339-365.

**Frostick, L., Reid, I, Jarvis, J. and Eardley, H., 1988.** Triassic sediments of the Inner Moray Firth, Scotland: early rift deposits. Journal of the Geological Society of London, 145,p. 235-248.

**Glennie, K.W. and Buller, A.T., 1983.** The Permian Weissliegend of NW Europe: the partial deformation of aeolian sand dunes caused by the Zechstein transgression. Sedimentary Geology, 35, p. 43-81.

**Glennie, K.W. (ed.), 1990.** Permian. *In*: Introduction to the Petroleum Geology of the North Sea (ed. Glennie, K.W.) Blackwell, London, 402p.

**Glennie, K.W. and Underhill, J.R., 1998.** The development and evolution of structural styles in the North Sea. *In*: Introduction to the Petroleum Geology of the North Sea (4th ed.) (ed. Glennie, K.W.). Blackwell Science, Oxford.

**Glennie, K.W., Higham, J., and Stemmerik, L., 2003.** Permian. *In*: The Millenium Atlas: petroleum geology of the central and northern North Sea. (eds. Evans, D., Graham, C., Armour, A., and Bathurst, P.) The Geological Society of London, p. 91-103.

**Hancock, J.M., 1984.** Cretaceous. *In*: Introduction to the Petroleum Geology of the North Sea (1st ed.) (ed. Glennie, K.W.) Blackwell Science, Oxford.

**Hurst, A.R, 1980.** Occurrence of corroded authigenic kaolinite in a diagenetically modified sandstone clay. Clay Minerals, 28, 393-396.

**Judd, J.W., 1873.** The Secondary Rocks of Scotland. Quarterly Journal of the Geological Society, 29,p. 97-197.

**Judd, J.W., 1885.** The presence of the remains of Dicynodon in the Triassic sandstone of Elgin. Nature, 32, p.573.

**McQuillin, R., Donato, J.A. and Tulstrup, J., 1982.** Development of basins in the Inner Moray Firth and North Sea by crustal extension and dextral displacement of the Great Glen Fault. Earth and Planetary Science Letters, 60, p. 127-139.

**Mackie, W., 1925.** The Principles that Regulate the Distribution of Particles of Heavy Minerals in Sedimentary Rocks, as illustrated by the Sandstones of the North-East of Scotland. Transactions of Edinburgh Geological Society, 11, p. 138-164.

**Naylor, H., Turner, P., Vaughan, D.J. and Fallick, A.E., 1989.** The Chertty Rock, Elgin: A petrographic and isotopic study of a Permo-Triassic calrete. Geological Journal, 24, p. 205-221.

**Ogilvie, S.R. and Glover, P.W.J., 2001.** The petrophysical properties of deformation bands in relation to their microstructure. Earth and Planetary Science Letters, 193, no, 1-2, p. 129-142.

**Peacock, J.D., 1966.** Contorted beds in the Permo-Triassic aeolian sandstones of Morayshire. Bulletin of the Geological Survey of Great Britain, 24, 157-162.

**Peacock, J.D., Berridge, N.G., Harris, A.L. and May, F., 1968.** The Geology of the Elgin District. HMSO, Edinburgh.

**Roberts, D.G., 1989.** Basin inversion in and around the British Isles. *In*: Inversion Tectonics (eds., Cooper, M.A., and Williams, G.D.). Geological Scoiety of London Special Publication, 44, p.131-150.

**Roberts, A.M., Price, J.D. and Badley, M.E., 1989a**. Discussion on Triassic sediments of the Inner Moray Firth: early rift deposits (Frostick *et al.*1988). Journal of the Geological Society, London, 146, p.361-362.

**Roberts, A.M., Badley, M.E, Price, J.D. and Huck, I.W., 1990**. The structural evolution of a transtensional basin: Inner Moray Firth, NE Scotland. Journal of the Geological Society of London, 147, 87-103.

**Smith, D.B., Brunstrom, R.G.W., Manning, P.I., Simpson, S. and Shotton, F.W., 1974.** A correlation of the Permian rocks in the British Isles. Journal of the Geological Society of London, 130, p. 1-45.

**Taylor, W., 1894**. Note on Cutties Hillock reptiles. Natural Science,4, p. 472.

**Thomson, K. and Underhill, J.R., 1993**. Controls on the development and evolution of structural styles in the Inner Moray Firth Basin. *In*: Petroleum Geology of Northwest Europe: Proceedings of the 4th Conference (ed. Parker, J.R.),Geological Society London, p. 1167-1178.

**Underhill, J.R., 1991a**. Implications of Mesozoic-Recent basin development in the western Inner Moray Firth, UK. Marine and Petroleum Geology, 8, p. 359-369.

**Underhill, J.R., 1991b**. Controls on Late Jurassic seismic sequences, Inner Moray Firth, UK North Sea: a critical test of a key segment of Exxon's original global cycle chart. Basin Research, 3, p. 79-98.

**Underhill, J.R. and Partington, M.A., 1993**. Jurassic thermal doming and deflation in the North Sea: implications of the sequence stratigraphic evidence. *In*: Petroleum Geology of Northwest Europe: Proceedings of the 4th Conference (ed. Parker, J.R.), Geological Society London, p. 337-345.

**Walker, A.D., 1961**. Triassic reptiles from the Elgin area: *Stagonolepis, Dasygnathus* and their allies. Philosophical Transactions of the Royal Society, B, 244, p. 103-204.

**Walker, A.D., 1973**. The age of the Cutties Hillock Sandstone (Permo-Triassic) of the Elgin area. Scottish Journal of Geology, 9, p. 177-183.

**Warrington, G., Audley-Charles, M.G., Elliott, R.E., Evans, W.B., Ivimey-Cook, H.C., Kent, P.E., Robinson, P.L., Shotton, F.W. and Taylor, F.M., 1980**. A correlation of Triassic rocks in the British Isles. Geological Society of London, Special Report, 13,p. 1-78.

**Watson, D.M.S. and Hickling, G., 1914**. On the Triassic and Permian Rocks of Moray. Geological Magazine, 1, p. 399-402.

**Williams, D., 1973**. The sedimentology and petrology of the New Red Sandstone of the Elgin Basin, north-east Scotland, Unpubl. PhD thesis. University of Hull.

This page left blank

This page left blank

# Chapter 4.

This chapter is presented in the style of a manuscript for publication. The paper analyses the structural setting of the Lossie Peninsula within which the Hopeman Sandstone is exposed. Recent offshore seismic data is integrated with observations onshore to produce a new structural model for the Peninsula. Interpretation of seismic data from the wider Inner Moray Firth Basin is also presented, showing typical structural styles, and allowing comparison of the Lossie Peninsula structure with similar features offshore. This comparison is used to give insight into the genesis and history of the faults exposed onshore. This paper allows petrographic and geochemical data presented in chapters 5 and 6 to be interpreted in the context of the geological development of the Lossie Peninsula.

# A new structural model for the Lossie Peninsula, Inner Moray Firth.

Oliver F. Quinn, R. Stuart Haszeldine, J.R. Underhill and J.E. Dixon.

## Abstract

The Inner Moray Firth Basin, UK North Sea, forms the western arm of the trilete Late Jurassic North Sea rift system. Offshore seismic surveys have previously demonstrated that the basin was predominantly formed through ENE-WSW trending extensional Late Jurassic faults, which created a number of half-graben sub-basins and structurally high horst blocks. In response to Cenozoic regional uplift select Late Jurassic extensional faults were re-activated, causing increased displacement. Late Jurassic extension acted to deeply bury much of the pre-rift Permo-Triassic and Lower Jurassic sequences.

The Lossie Peninsula is defined here as the 13km E-W section of coast, on the southern margin of the Inner Moray Firth Basin, between Burghead in the west and Lossiemouth in the east. The Peninsula hosts exposures of Devonian to Jurassic sediment and several minor (<50m displacement) to major (>100m displacement) extensional cataclastic faults crop out. Observations and collation of geometric data onshore have been combined with the interpretation of extensive, recent, offshore seismic survey data to produce an integrated structural model of Lossie Peninsula development. The Top Triassic Stotfield Chert is exposed onshore and also forms a prominent seismic reflector which has been mapped both regionally and locally within the basin. Integration of seismic and field data has shown that the onshore Permo-Triassic sequence is structurally higher than the adjacent Permo-Triassic directly offshore.

The Lossie Peninsula is interpreted as a horst block, on the southern basin margin, bounded to the north by a fault in the 'blind zone' between the edge of onshore exposure and offshore seismic coverage. The horst block is bound to the south by the onshore Spynie Fault. This structure is named here the Hopeman Horst. The exposed Clashach and Burghead Faults, which trend ENE-WSW to E-W, form extensional intra-horst faults. The absence of post Jurassic sediment within the horst block means interpretation of fault history focuses upon observations of related structures offshore. An analogous horst block is seen 20km offshore, bounded to the SE by the regional Lossie Fault. This fault underwent 700-1000m of Late Jurassic extension and minor, 50-75m displacement during Cenozoic regional uplift. Comparison of the onshore faults within the Hopeman Horst with local and regional structural styles shows that the exposed faults are most likely Late Jurassic in age. Cenozoic re-activation cannot be ruled out, but is typically minor in offshore equivalents.

Extrapolation of regional stratigraphy combined with estimates of maximum Cenozoic basin exhumation indicate that the Hopeman Horst is likely to have remained a structural high following major Late Jurassic basin development, with a maximum burial of less than 1.5km.

## 4.1 Introduction

The Lossie peninsula lies on the southern margin of the Moray Firth, northeast Scotland (Fig. 4.1), and contains the only outcrops on the southern coast, of deepwater sediments from the Mesozoic of the Inner Moray Firth basin. The Peninsula forms a prominent, elongate, east-west trending feature, 13km long running between Burghead in the west and Lossiemouth in the east. Within the Lossie Peninsula a series of Permian to Jurassic sandstones are exposed which unconformably overlie the exposed Devonian Old Red Sandstone, which acts as the basement to the Inner Moray Firth basin (Fig. 4.2). The area was the focus of some of the earliest detailed British geological studies (e.g. Gordon 1859, Martin 1837, Huxley 1859, Wallace 1901, Watson and Hickling 1914) and has remained a focus of sedimentological studies (Peacock *et al.,* 1968, Glennie and Buller 1983, Clemmensen 1987, Frostick *et al.,* 1988, Naylor *et al.,* 1989) and palaeontological studies (e.g. Benton 1977, 1983b, Benton and Walker 1985, Clark 1999), including the discovery of the oldest dinosaur in Britain, *Saltopus* (Late Triassic (Carnian)) (M.Benton pers. comm. 2003), an unusually well preserved assemblage of Upper Permian reptilian footprints, and a *dicynodont* skull mould (Clark 1999). The peninsula sediments also host galena and fluorite mineralisation (Peacock *et al.,* 1968, Naylor et *al.* 1989)

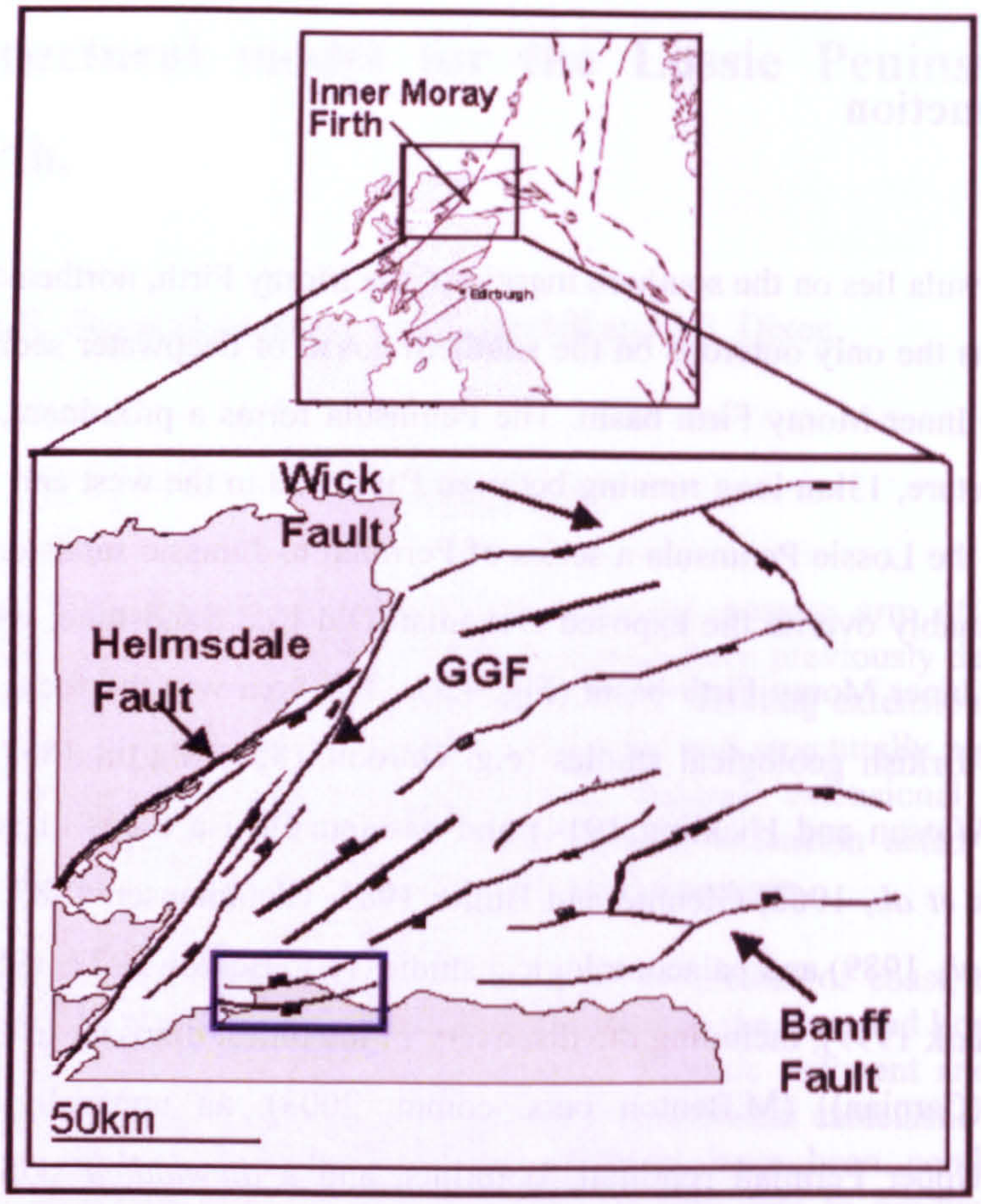


**Figure 4.1. Location of the Inner Moray Firth Basin on the extreme western arm of the trilete North Sea rift system (inset). Major structural features within the basin are shown. The basin is bounded by the Helmsdale Fault to the northwest, the Wick Fault to the north and the Banff Fault to the south. The Lossie Peninsula is located within the boxed area on the southern basin margin. GGF = Great Glen Fault. Some data from Underhill 1991a, some from this study.**

Previous sedimentological work has focussed upon the Upper Permian aeolian Hopeman Sandstone which crops out in coastal cliffs and adjacent quarries along most of the Peninsula length (Fig. 4.2), and which acts as a sedimentological, and age, analogue for many Southern North Sea Rotliegend gas fields (Glennie and Buller 1983). The excellent coastal and quarry exposure of the Upper Permian Hopeman Sandstone means the peninsula is also a popular location for academic and industry fieldtrips. Major to minor, seismic (>50m) to sub-seismic (<50m) scale faults are exposed within the Lossie Peninsula, but have received less attention than the sedimentology, and palaeontology, of the rock exposures. Previous structural work has focussed on a seismic scale fault, and the surrounding damage zone, exposed near Burghead (Fig. 4.2). Edwards *et al.* (1993) used the fault as an analogue to predict the effects of structural compartmentalisation of hydrocarbon reservoirs, and Ogilvie *et al.* (2001) used

samples of the fault plane to characterise permeability effects of faults in sandstone, within the laboratory. The scope of these papers does not cover the presence of the faults, or the exposure locally onshore of equivalents to deeply buried offshore IMF Permo-Triassic sediments. In contrast, numerous studies of the offshore Inner Moray Firth basin have been undertaken, driven by the discovery of the only commercial oil discovery to date, the Beatrice Field in 1976 (Linsley *et al.*, 1991), using extensive seismic reflection surveys and oil exploration well data (e.g. Haszeldine *et al.*, 1984, Roberts *et al.*, 1988, Underhill 1991, Thomson and Underhill 1993, Argent *et al.*, 2000, 2002). Detailed characterisation of the controls on the development of offshore sediments (e.g. Roberts *et al.* 1989a, Underhill 1991, Glennie and Buller 1983, Glennie *et al.*, 2003), and accurately characterised patterns of tectonic development and history (e.g. Underhill 1991, Thomson and Underhill 1993, Argent *et al.* 2002), have resulted in a good understanding of the offshore basin evolution. However, despite this characterisation of the basin, the discovery of commercial hydrocarbon fields has been poor (only one to date), in comparison to the rest of the North Sea system, and the reasons for this have remained unclear. However, a recent structural model by Argent *et al.* (2002) aims to classify faults within the basin into different categories, which have different possibilities of acting as hydrocarbon traps, based upon the timing of fault development and re-activation history. Faults that were re-activated during basin inversion are proposed to be more likely to have leaked hydrocarbons from former traps. By contrast, faults which did not reactivate provide secure seals.

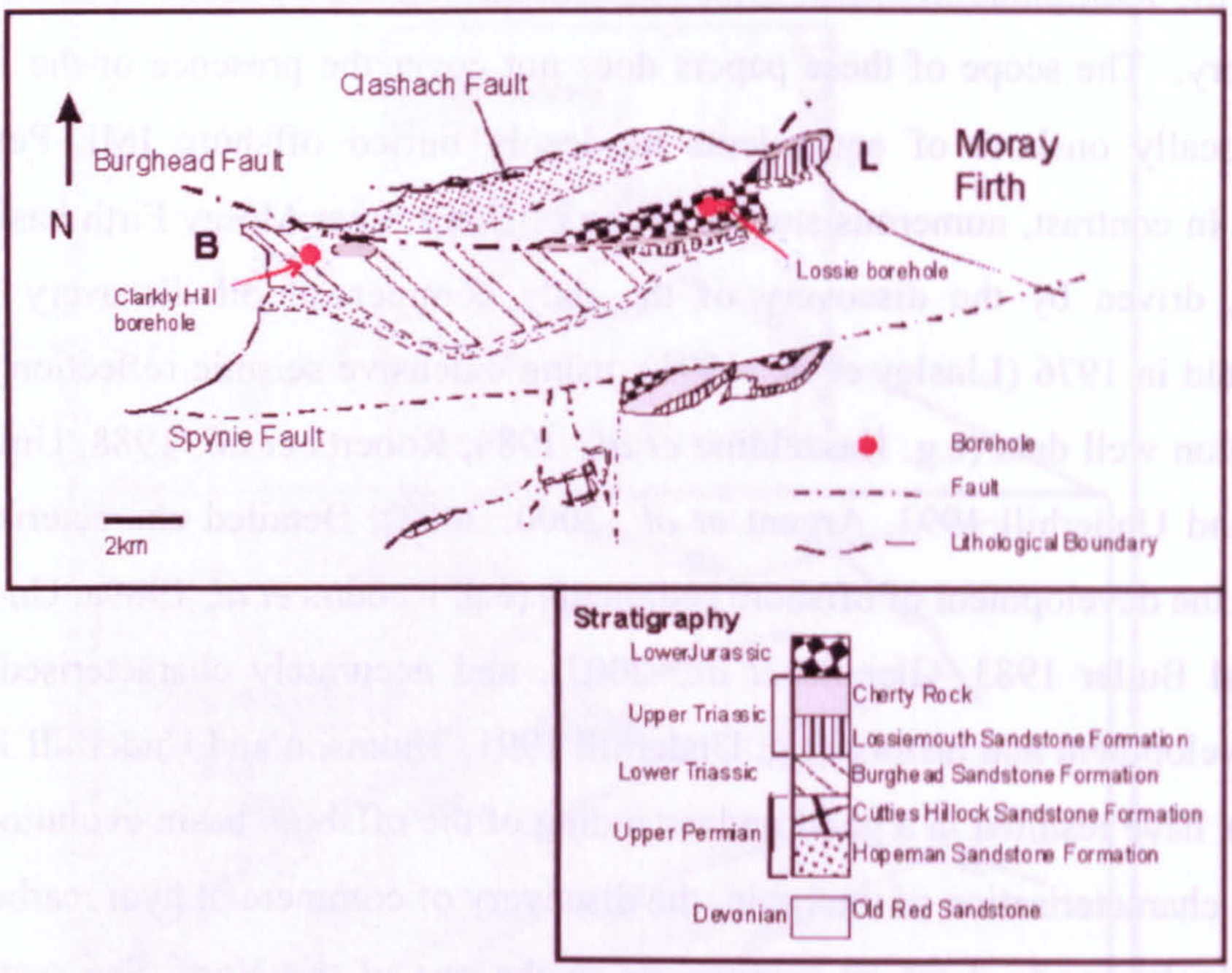


**Figure 4.2. Geological map of the onshore Lossie Peninsula. The outcrop locations of the Top Triassic Cherty Rock can be seen along with the onshore outcrop of several fault structures. Onshore British Geological Survey boreholes are also shown. Adapted and re-drawn from BGS Sheet 95 (Peacock *et al.*, 1967).**

Recently acquired high quality offshore seismic reflection data, and borehole information, allows for the first time an integration of the known onshore geology of the Lossie Peninsula with offshore data from the Inner Moray Firth Basin (Fig. 4.3). Utilising these two sources of data the present paper reconciles offshore sub-surface structural interpretations with observations onshore to produce a structural framework for the Peninsula, and seeks to understand this in the context of regional structural styles in the western Inner Moray Firth, and within the recent model for basin-wide structural styles by Argent *et al.* (2002). Consideration of the onshore fault history at seismic scale, and at sub-seismic scale, within a wider basin framework provides a basis for understanding the relevance, and origin, of localised diagenetic features recorded around the exposed faults (Quinn *et al.*, [in prep], Chapter 5 and Chapter 6). This has implications for the prediction of similar diagenetic processes offshore and consequently for the presence of diagenetic fault seals in the wider basin. Locally, the structural model provides a basis for understanding the development of the Lossie Peninsula, and the unusual exposure on the southern basin margin, of sediments which are deeply buried offshore.

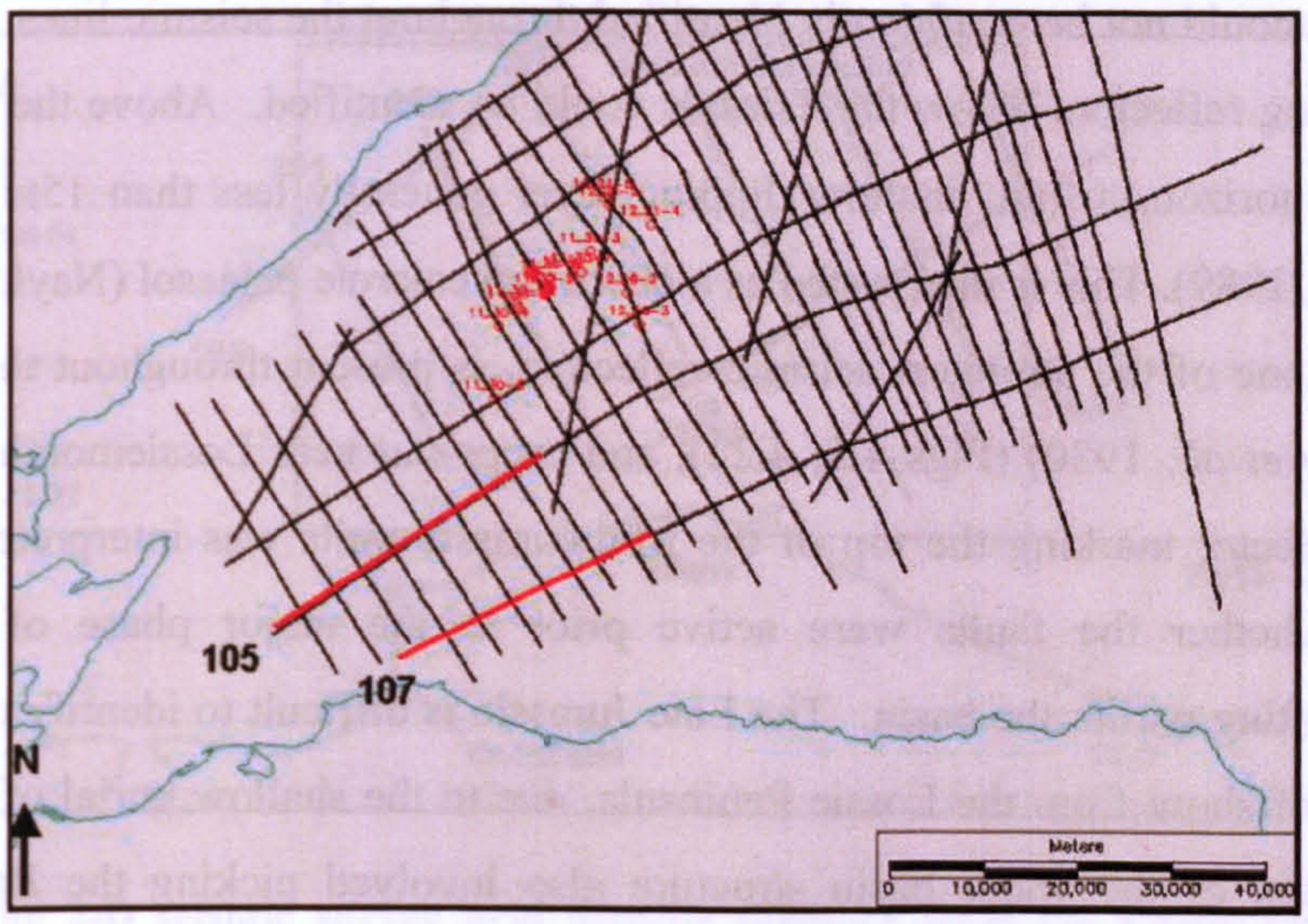


**Figure 4.3. The grid of available Inner Moray Firth 2-D seismic data for this study. Boreholes drilled in and around the Beatrice Field are also shown. Two of these wells, 11/30-1 and 11/30-2 were used to depth convert the seismic data. The area covered by seismic lines 105 and 107 in Figs. 4.19 and 4.20 is also shown.**

## 4.2 Database and methodology

### 4.21 Offshore seismic data

A recent (1997) seismic reflection survey was undertaken by Fugro. Over 2500km of 2-D lines were shot throughout the Inner Moray Firth Basin (Fig. 4.3) with a horizontal spacing of typically 1-2km between lines, but rising to a maximum of 4km immediately adjacent to the Lossie Peninsula (Fig. 4.4). The seismic data was interpreted using Schlumberger Geoquest software. The absence of Upper Cretaceous chalk in the Inner Moray Firth, which is the cause of many sub-Cretaceous North Sea imaging problems (Argent *et al.*, 2000), ensures the data quality is, in general excellent, allowing sub-Jurassic horizons to be picked with confidence. The two major aims of offshore seismic interpretation were to understand the structure of the western region of the Inner Moray Firth offshore from the Lossie Peninsula, and to interpret in detail an area of 20km x 15km immediately offshore from the Peninsula (Fig 4.4) for input into an integrated onshore and offshore structural model. A strategy of identifying stratigraphic seismic reflection horizons which could be equated to units onshore was taken, to assist in marrying the sources of data onshore and offshore.

Permian units could not be confidently identified throughout the seismic lines, but occasional shallow dipping reflectors below the Triassic could be identified. Above the Permian is the Top Triassic horizon, a thin, shallow dipping layer generally less than 15m thick onshore (Naylor et al., 1989). This is interpreted as a chertified calcrete palaesol (Naylor *et al.*, 1989), it appears as one of the strongest seismic reflectors, is present throughout the Inner Moray Firth (Linsley *et al.*, 1980) (Figs 4.5, 4.22), and crops out near Lossiemouth, onshore. The sandstone reflector marking the top of the Mid-Jurassic units was interpreted as an aid to identifying whether the faults were active prior to the major phase of Late Jurassic extensional rifting within the basin. The Late Jurassic is difficult to identify on seismic data immediately offshore from the Lossie Peninsula, due to the shallow burial of the sediments. Characterisation of the wider basin structure also involved picking the Base Cretaceous unconformity, which is absent in the western and southern parts of the basin, and in the area directly offshore from the Peninsula. The structure of the offshore basin was characterised by mapping the position and orientation of fault structures, which were picked on individual seismic lines and mapped in plan view by operator interpretation, within the seismic interpretation software (Fig. 4.24). An absence of available boreholes in close proximity to the geographic study area precludes the use of an ideal, more proximal, well for the depth conversion. All seismic data was interpreted in two-way time, and depth converted to calculate actual stratigraphic positions and absolute depths. Seismic velocity data was taken from wells 11/30-1 and 11/30-2, in the Beatrice Field. The Beatrice data comes from deeply buried Lower-Mid Jurassic sediments, at >2000m, meaning the seismic velocity value was interpreted as probably greater than the maximum velocity within the more shallowly buried basin margin sediments. Two extremes for seismic velocity have been used to calculate the depth to particular horizons for structural calculations, 2000m/s and 3000m/s, as well as the mean Lower –Mid Jurassic Beatrice Field velocity value, 3600m/s

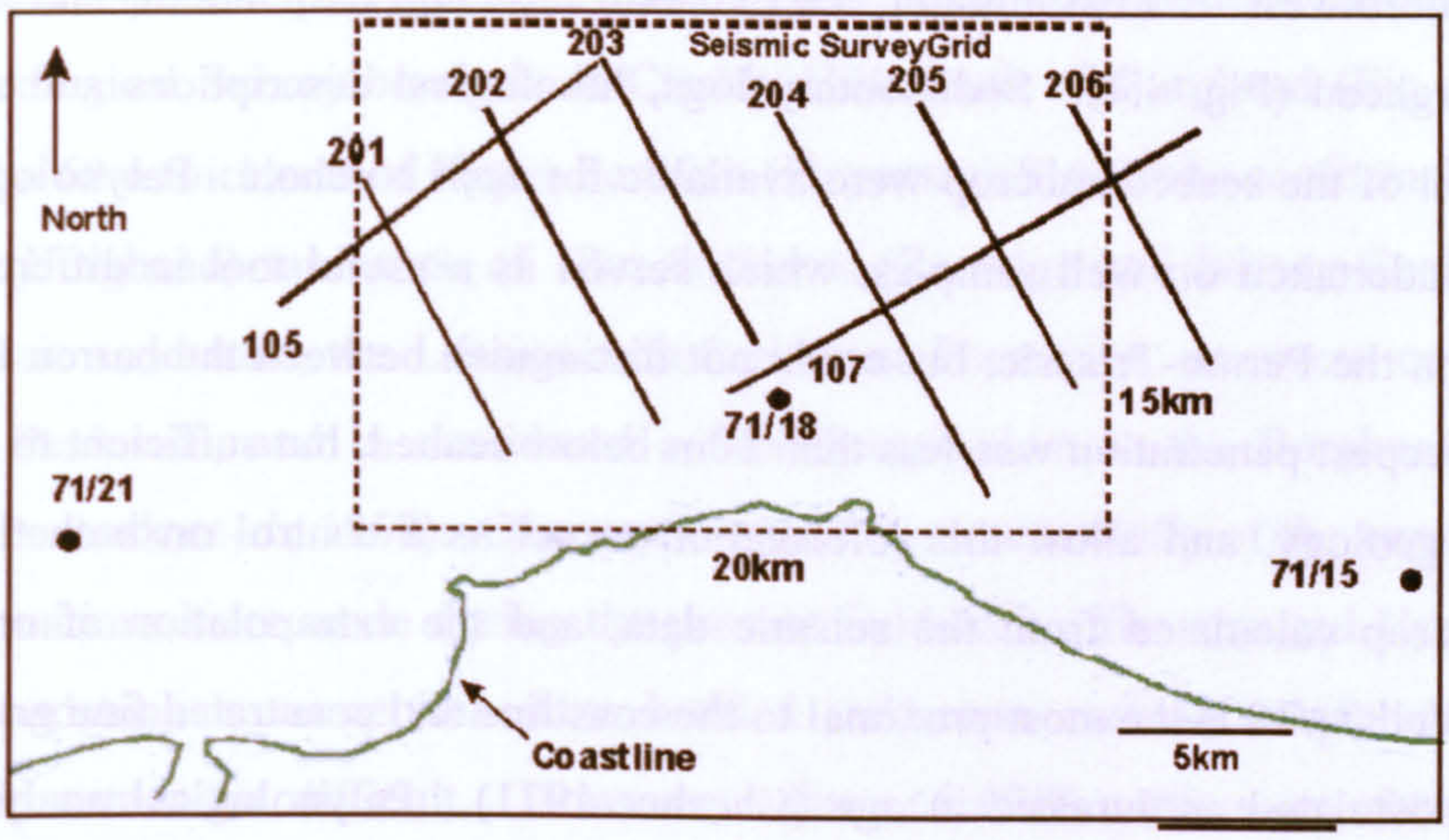


**Figure 4.4. The 2-D seismic survey grid directly offshore from the Lossie Peninsula. Grid spacing is 4km between dip lines. The offshore shallow British Geological Survey boreholes are also shown. Dashed box outlines the local area interpreted in detail to aid characterisation of the Peninsula structural setting.**

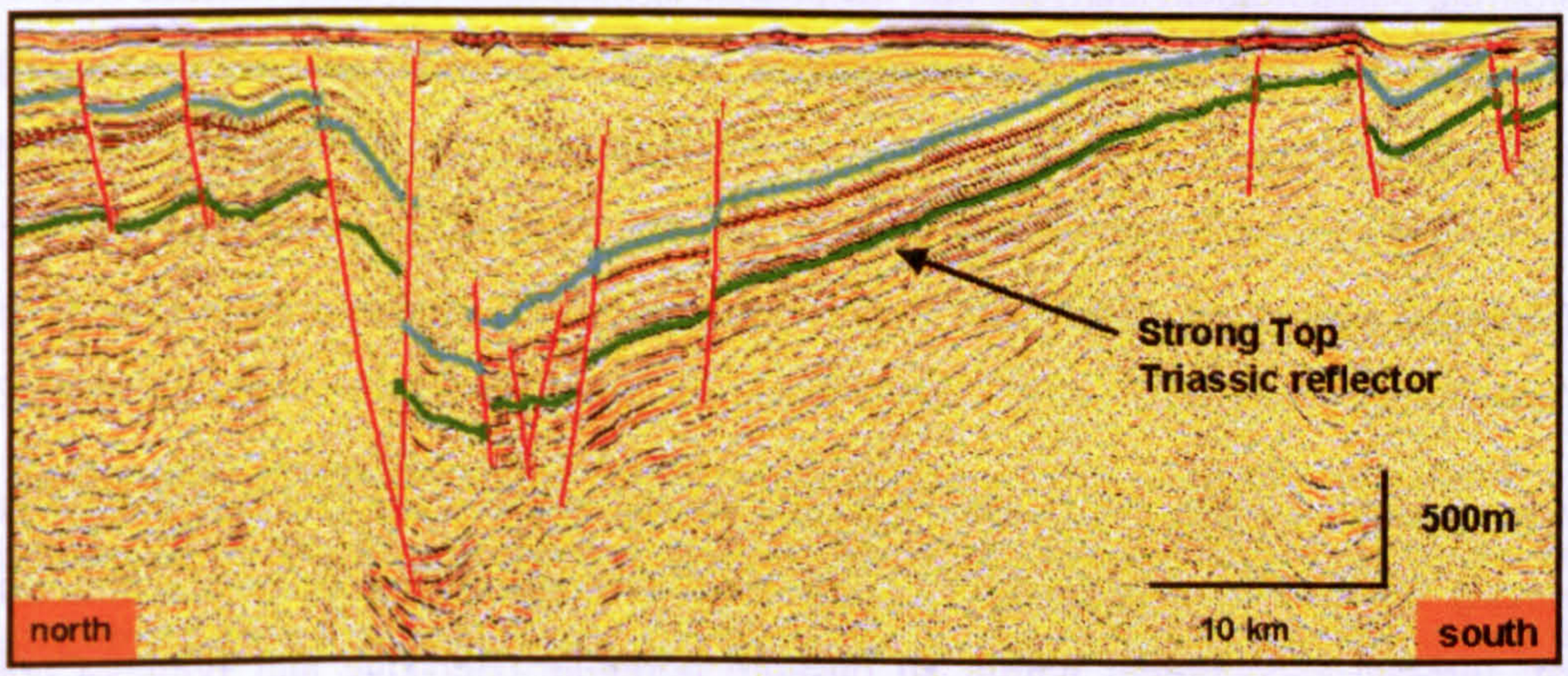


**Figure 4.5. The Top Triassic reflector (green) can be seen to be present from the southern basin margin to the northern boundary of the basin. The consistency of the Top Triassic horizon on seismic data throughout the basin makes it a key surface for interpretation of the Inner Moray Firth. Seismic line 202. Dark green = Top Triassic, Light blue = Top Mid-Jurassic.**

## 4.22 Offshore shallow borehole data

The basin margin position of the Lossie Peninsula has precluded any local (<50km distant) deep exploration hydrocarbon boreholes. However, a number of shallow British Geological Survey boreholes were drilled in the early 1970's within the Inner Moray Firth, and three boreholes which penetrate bedrock lie in close proximity to the Peninsula. Well 71/18 lies

3km north-northwest of Lossiemouth, 71/15 14km east of Lossiemouth, and 71/21 10km west of Burghead (Fig. 4.4). Sedimentary logs, lithological descriptions and stratigraphic classification of the seabed subcrop were available for each borehole. Palynological studies were also undertaken on well samples, which served as a useful tool in differentiating the Jurassic from the Permo-Triassic, but could not distinguish between the barren Permian and Triassic. Deepest penetration was less than 50m below seabed, but sufficient to characterise the seabed geology, and allow this information to act as a control on both the predicted seabed subcrop calculated from the seismic data, and the extrapolation of onshore units offshore. Well 71/18 is the most proximal to the coastline and penetrated fine grained, white, sandstone postulated as Jurassic in age (Chesher 1971). Palynological analysis reported miospores and microplankton and inferred a likely Lower to Mid Jurassic age for the sandstone, which was encountered under 10m of drift, and down to a maximum penetration of 18m below seabed. Well 71/21, west of Burghead, encountered grey Permo-Triassic sandstone on the seabed under 13m of clay drift (Chesher 1971). The sample was found to be barren during palynological analysis, and the precise age could not be determined. Permo-Triassic white - buff sandstone was also encountered in well 71/15 14km east of Lossiemouth (Fig. 4.4) (Chesher 1971).

## 4.23 Onshore exposure data

The onshore exposures within the Lossie Peninsula consist of Devonian Old Red Sandstone unconformably overlain by a package of conformable Permian to Top Triassic sediments, with Early Jurassic encountered within an onshore borehole (Berridge and Ivimey-Cook 1967) (Chapter 3, Fig. 3.8). Data concerning the thickness and geometry of the units which crop out on the Peninsula has been gathered and calculated from pre-existing geological maps (BGS sheet 95), geological survey memoirs (Peacock *et al.*, 1968), and onshore borehole data (Berridge and Ivimey-Cook 1967). Fieldwork was undertaken to collect further geometric data from the well exposed coastal Permian and Triassic sediments in order to more accurately characterise the dip and strike of the exposed units, and to examine and identify the geometry of the Top Triassic Stotfield Chert (or Cherty Rock), which acts as the strongest seismic reflector offshore.

A conformable relationship between the Permian and Triassic Formations was established in a British Geological Survey borehole at Clarkly Hill, south of Burghead (Fig. 3.8), which encountered a 60m thickness of Upper Permian (Hopeman) Sandstone conformably overlain by Triassic (Burghead) sandstone of 78m thickness (Berridge and Ivimey-Cook, 1967). A second Triassic sandstone, the Lossiemouth Sandstone Formation, crops out on the eastern side of the Peninsula, and is considered a lateral equivalent to the Burghead Sandstone Formation (Peacock *et al.*, 1968). Observations of true structural dip of the exposed Permo-Triassic Formations were made during the present fieldwork. The exposed Upper Permian Hopeman Sandstone is an aeolian dune bedded sandstone, making measurement of true structural dip somewhat difficult. However, values of 4°-8° north were obtained during fieldwork, and these are reasonably consistent with the overlying Triassic. The Burghead Sandstone Formation (Triassic) is a visibly bedded fluvial sandstone with dips ranging consistently throughout the exposures from 2° to 7°, with a mean of 4°, in agreement with the geological map which reports bedding dips of between 5° and 7°, generally toward north, within coastal Triassic sandstones. The Top Triassic Stotfield Chert caps the exposed sequence within the Peninsula, ranging in thickness from 0.5 to 15m (Peacock *et al.*, 1968, Naylor et al., 1989), and dipping offshore (north) between 3° and 8°, although internal bedding surfaces are difficult to identify. Proven total Permo-Triassic thickness is 138m in the Clarkly Hill borehole (Berridge and Ivimey-Cook 1967). A second British Geological Survey borehole, 3km southwest of Lossiemouth (Fig. 4.2), penetrates Lower Jurassic (Sinemurian) sediments with a minimum thickness of 69m of sandstones, marls and muds, juxtaposed by the Burghead Fault against Devonian Old Red Sandstone to the north. No structural data is available for the Lower Jurassic. The Devonian basement crops out on the coast toward the east of the Peninsula, and bedding surface dips vary between 2° and 9° around north, which is comparable to the overlying Permo-Triassic Formations.

Structural data concerning fault orientation was collected from two key coastal localities, at Burghead, where a seismic scale fault (throw >50m) is exposed, and at Clashach where a sub-seismic scale fault (throw <50m) is accessible (Fig. 4.2). The fault exposed at Burghead is named here the 'Burghead Fault', based on the excellent exposure at its outcrop in this location, and to avoid confusion with earlier work (Underhill 1991a) which links this onshore fault to the offshore Lossie Fault. The Lossie Fault and the onshore fault are interpreted to be separate structures in this paper. The Burghead Fault crops out on the foreshore at Burghead and trends inland toward the east at 090°, cropping out again at Lossiemouth (Fig. 4.2) on the

east of the Peninsula. Normal, dip-slip movement on the fault to the south, downthrows Triassic (Burghead Sandstone Formation, Lossiemouth Sandstone Formation and Stotfield Chert) and Lower Jurassic sediments against the Upper Permian Hopeman Sandstone and Devonian Old Red Sandstone to the north. A major splay fault of the main Burghead Fault crops out on the adjacent foreshore trending 080°. Along the coastline a minor normal fault, with downthrow to the south, is exposed in Clashach Cove and again at Clashach Quarry (Fig. 4.2), trending 075°-090°, and with Upper Permian Hopeman Sandstone forming both the footwall and hanging wall. The name 'Clashach Fault' is proposed here, based upon the geographical location of the exposures, and to simplify fault description in this paper. A subordinate set of north-south post-Liassic (Peacock *et al.*, 1968) faults are mapped on the Peninsula, predominantly in close proximity to Elgin, and south of Lossiemouth (Fig. 4.2), on which minor normal throw has occurred, and which are ubiquitously cross-cut by the major east-west and ENE-WSW trending structures.

A second regional fault, comparable in orientation to the coastal Burghead and Clashach faults, runs east-west from south of Lossiemouth through to the geographical edge of the Peninsula in the west (Fig. 4.2). This fault is named here the 'Spynie Fault', after the nearby geographic area. The fault has been inferred on the geological map based upon observed stratigraphic relations and outcrop, but does not crop out onshore (Peacock *et al.*, 1968). Devonian sediments are downthrown to the south against Devonian, and along strike north of Elgin the series of Permian to Triassic sediments observed at the coast are downthrown and juxtaposed against the Devonian Old Red Sandstone to the north. The presence of the Lower Jurassic was inferred by Peacock *et al.* (1968) based upon stratigraphic thickness of the underlying sediments, but is not seen at outcrop within the locality.

## 4.3 Seismic interpretation results

Interpretation of offshore Inner Moray Firth seismic data has been undertaken on both a regional and local scale. Local interpretation around the Lossie Peninsula has allowed the onshore and offshore geology to be tied together, and the regional analysis has allowed this model to be understood within the context of known basin structural styles.

## 4.31 Regional seismic interpretation

Regional mapping of the Top Triassic reflector shows a general thickening, and increasing depth of burial, of the Permo-Triassic sediment moving from the southern section of the basin toward the north (Fig. 4.22). On the southern margin of the Moray Firth, adjacent to the coastline, the Top Triassic is at the relatively shallow burial depth of a few hundred metres. Burial depth increases to greater than 3km moving north toward the Great Glen Fault, and the basin bounding Helmsdale Fault, creating an overall half-graben basin structure (Fig. 4.9). The Top Mid-Jurassic horizon follows a parallel trend to the Top Triassic, with a broad deepening and minor to moderate thickening moving north from the southern basin margin.

A series of ENE-WSW and NE-SW trending normal fault structures are present throughout the basin (Fig. 4.6). These faults typically penetrate horizons from the Top Triassic through to the Late Jurassic, and selectively cut the overlying Cretaceous, where present (Fig. 4.7). Where seismic data quality is sufficient the majority of faults can be seen to root into the Devonian basement, cutting the entire Permo-Triassic sequence. The faults can be correlated and mapped between each seismic line, and typically form a series of linked segments, tens of kilometres in length. The Permo-Triassic and Mid-Jurassic sediments display a consistent thickness across individual faults within the series of extensional faults in the basin. Combined with the observation of general Permian to Mid-Jurassic thickening northward within the basin, this indicates that sediment deposition occurred as a passive in-fill over a pre-existing topography, prior to the development of the ENE-WSW and NE-SW normal fault series. Regionally Late Jurassic sediments thicken across these faults, into the hanging wall, demonstrating significant Late Jurassic extensional movement, and the creation of sediment accommodation space (Fig. 4.7). These observations are in agreement with previous studies of the Inner Moray Firth which propose basin development primarily through extensional rifting during this Late Jurassic period, hinged on the Helmsdale Fault to the north (Underhill 1991a, Thomson and Underhill 1993). The Late Jurassic faulting created a series of horst blocks and associated half-graben sub-basins within the larger scale basin, and locally controlled the thickness of Late Jurassic sediment, and the burial depth of the underlying pre-rift Permo-Triassic and Mid-Jurassic sediments (Fig. 4.7-4.12).

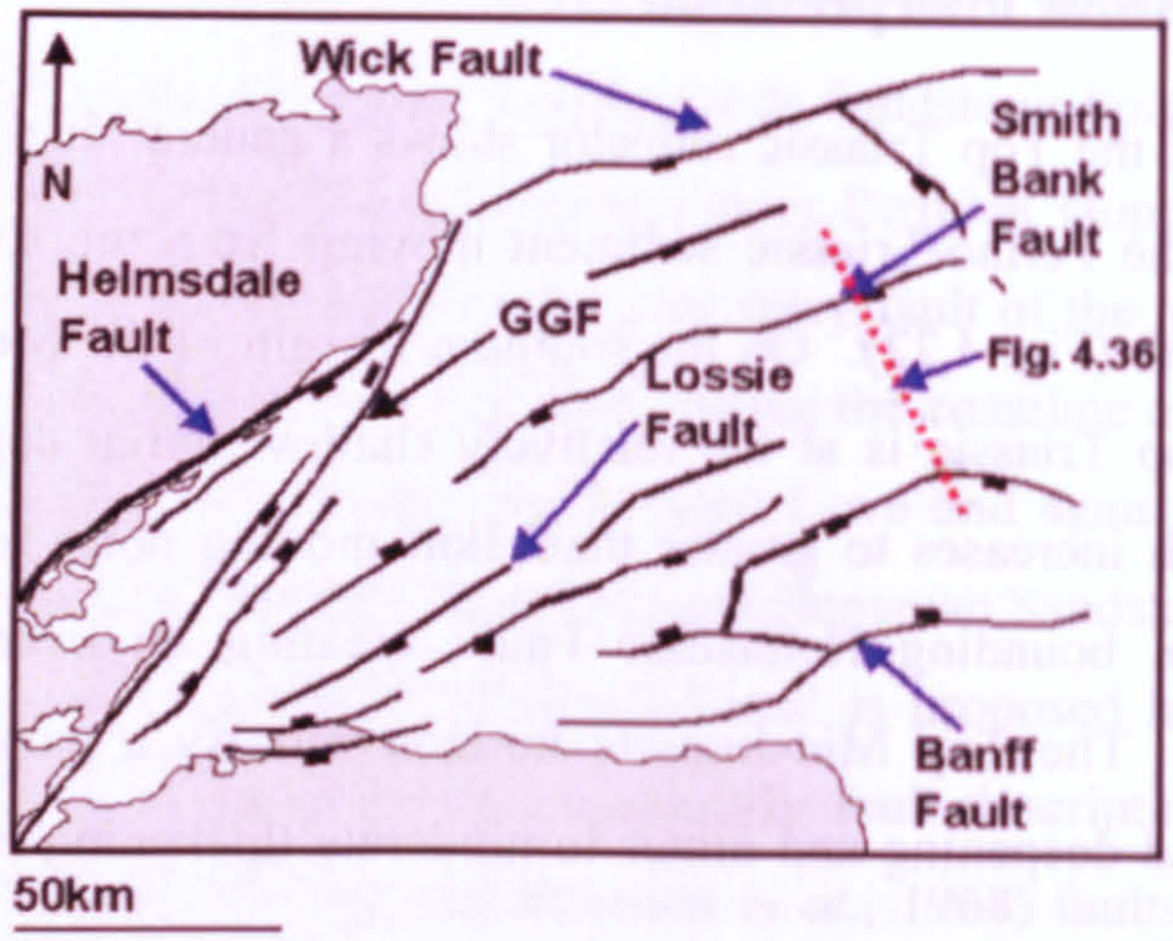


**Figure 4.6. Major basin faults within the Inner Moray Firth basin. ENE-WSW extensional Jurassic faults dominate, with the exception of the NE-SW transtensional Great Glen Fault. Major basin bounding faults, the Helmsdale, Wick and Banff faults are shown. Also shown is the regional extent of the Lossie Faults, which lies directly offshore from the Lossie Peninsula. Line of section seen in figure 4.36 is marked by dashed (red) line. Some data from Underhill 1991.**

The Base Cretaceous reflector crops out on the seabed to the east of the region directly offshore from the Lossie Peninsula. This subcrop is a product of a 2-3° regional easterly dip within the Inner Moray Firth, produced by westerly increasing Cenozoic basin exhumation (Argent *et al.,* 2000, 2002) (Fig. 4.13). Mapping of the Base Cretaceous seismic horizon, where present, shows that it onlaps onto Jurassic sediment and in-fills topographic lows, suggesting it was deposited following the end of the extensional fault activity, possibly during thermal subsidence. Selective Late Jurassic age extensional faults penetrate through the Cretaceous and offset the Base Cretaceous seismic reflector, representing further extensional displacement (Fig. 4.7). Where observed in the western region of the Inner Moray Firth this displacement is minor compared to the amount of Late Jurassic extension. Observation of re-activated Late Jurassic faults, throughout the wider basin, leads Argent *et al.* (2002) to conclude that this displacement occurred regionally in response to basinwide Cenozoic uplift.

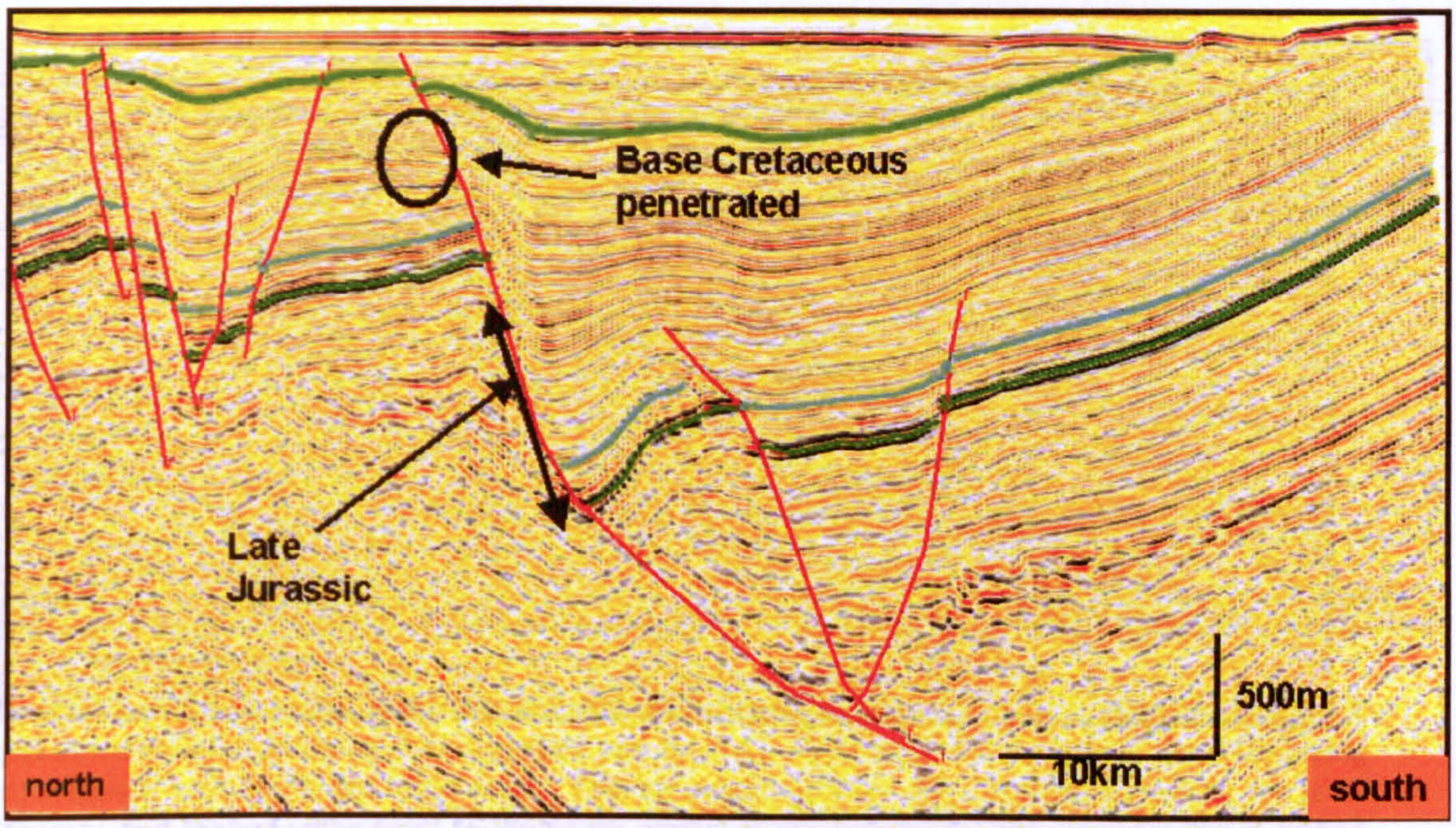


**Figure 4.7. An extensional ENE-WSW basin fault which cuts the Top Triassic, Jurassic and Base Cretaceous, propagating to present day seabed. The fault can be seen to root into the basement. Dark green = Top Triassic, Light blue = Top Mid-Jurassic, Bright green = Base Cretaceous. Lossie Fault, seismic line 209.**

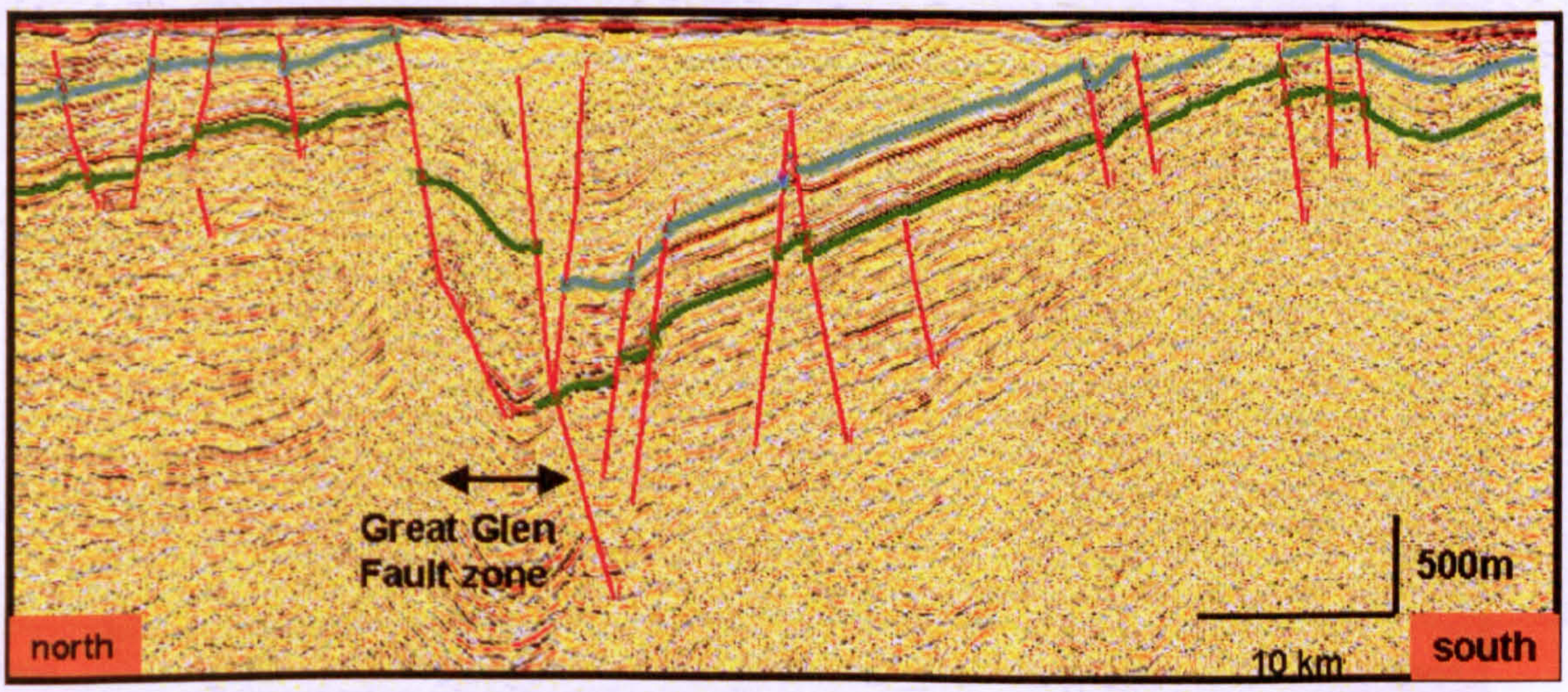


**Figure 4.8. Basin profile along seismic line 201, the most westerly of the available seismic data. The consistent increase in burial depth of the Top Triassic and Top Mid-Jurassic can be seen. Overall the basin sediments are at shallow depths compared to further east (e.g. Fig. 4.11.). The Great Glen Fault forms a prominent strike-slip fault through the basin, but was not responsible for major Late Jurassic extension through which the half-graben structure developed. Isopach maps of the Late Jurassic (Underhill 1991a) demonstrate that sediment accommodation space was controlled by the Helmsdale Fault onshore to the west of this section, and displacement subsequently occurred on the Great Glen Fault. Colour picks as for Figure 4.7.**

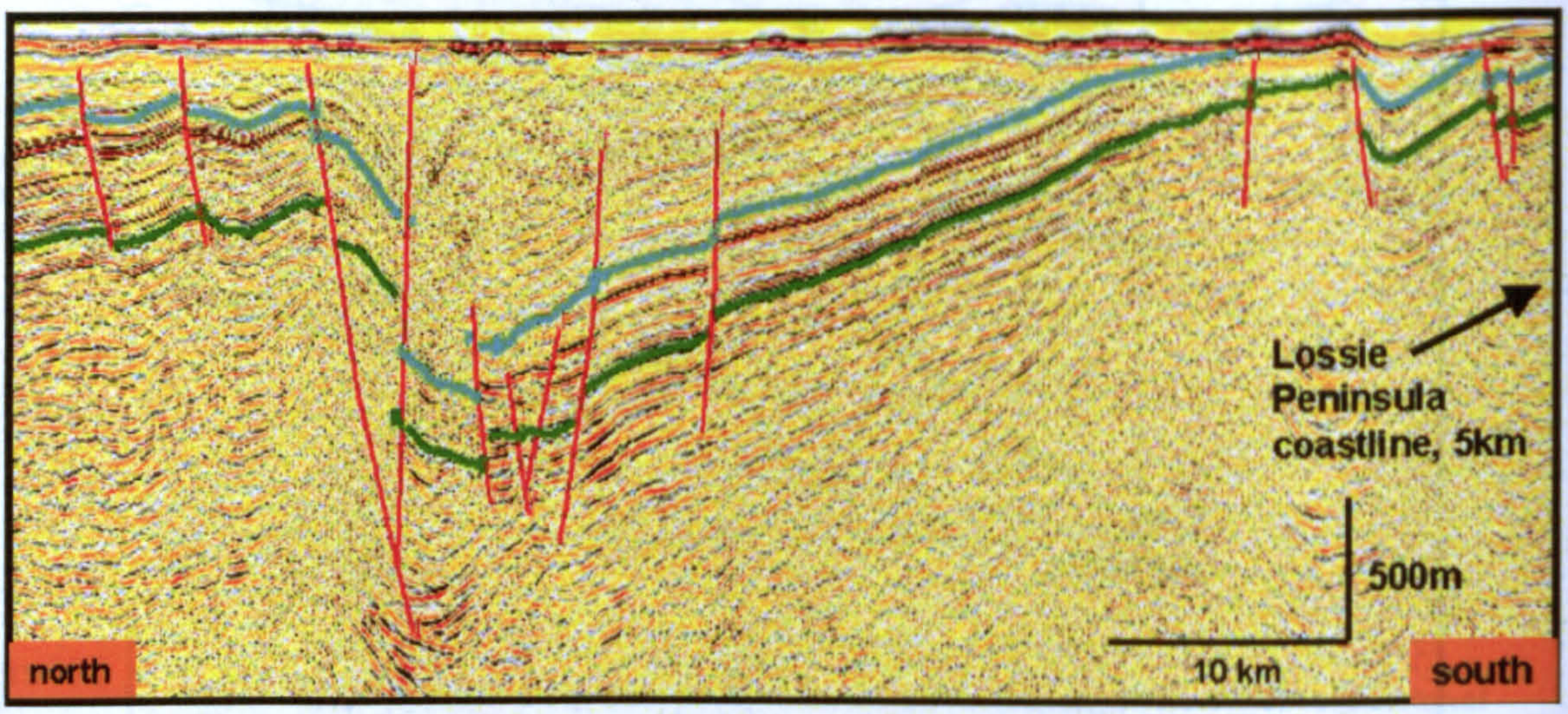


**Figure 4.9. Basin profile along seismic line 202, which runs north directly offshore from the Lossie Peninsula. Increasing burial depth of the Top Triassic and Top Mid-Jurassic from relatively shallow burial on the southern section of the basin can be seen within the overall half-graben basin structure. The Top Triassic to Top Mid-Jurassic thickens moving into the Helmsdale Fault onshore to the west of this section, but shows no variation over intra-basin faults. Colour picks as for Figure 4.7.**

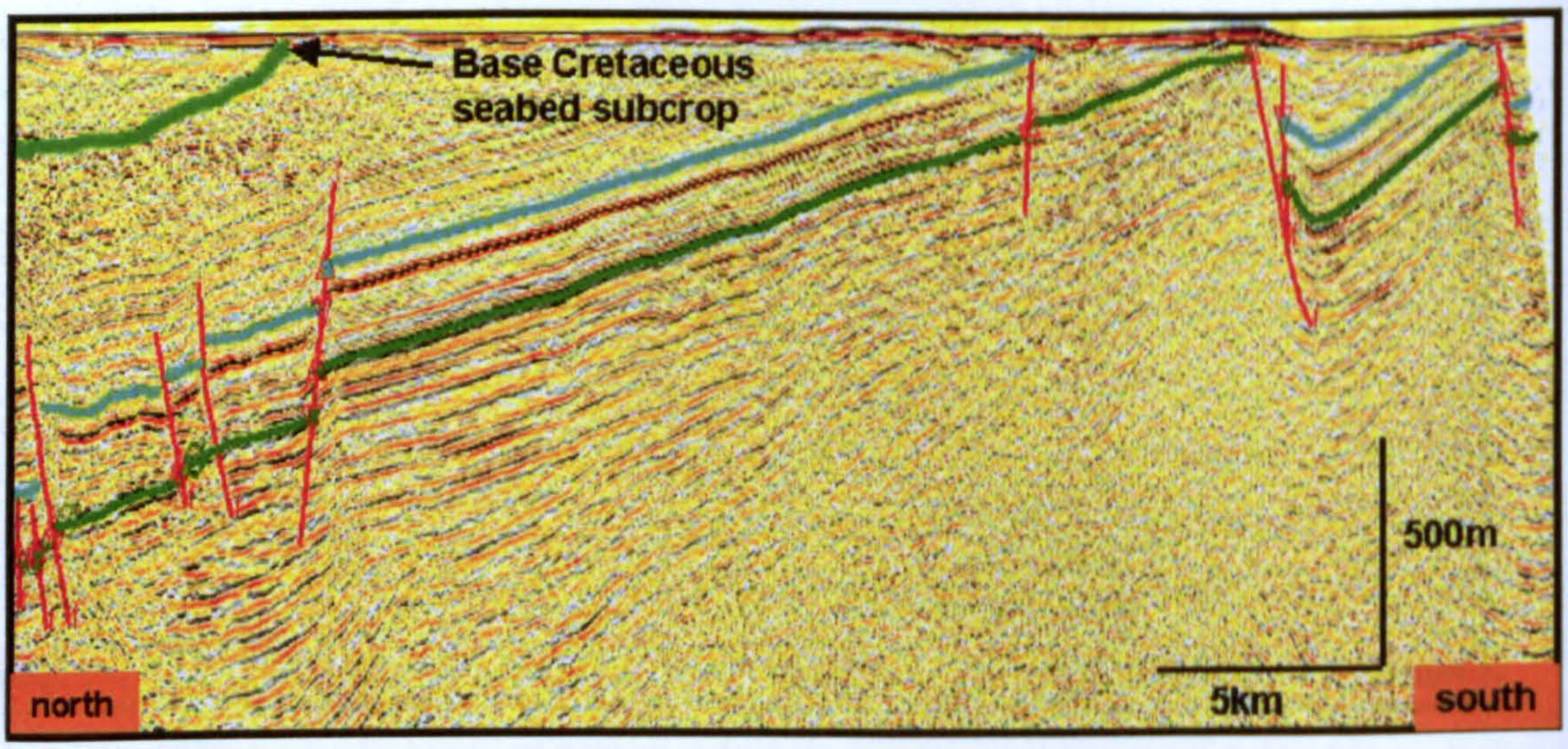


**Figure 4.10. Seismic line 203 running north from the Lossie Peninsula. As for seismic line 201 and 202 the increasing northerly burial depth of Top Triassic and Top Mid-Jurassic can be seen. The increased total burial depth on line 203 has resulted in preservation of the Base Cretaceous in the deepest part of the basin on this line. Colour picks as for Figure 4.7.**

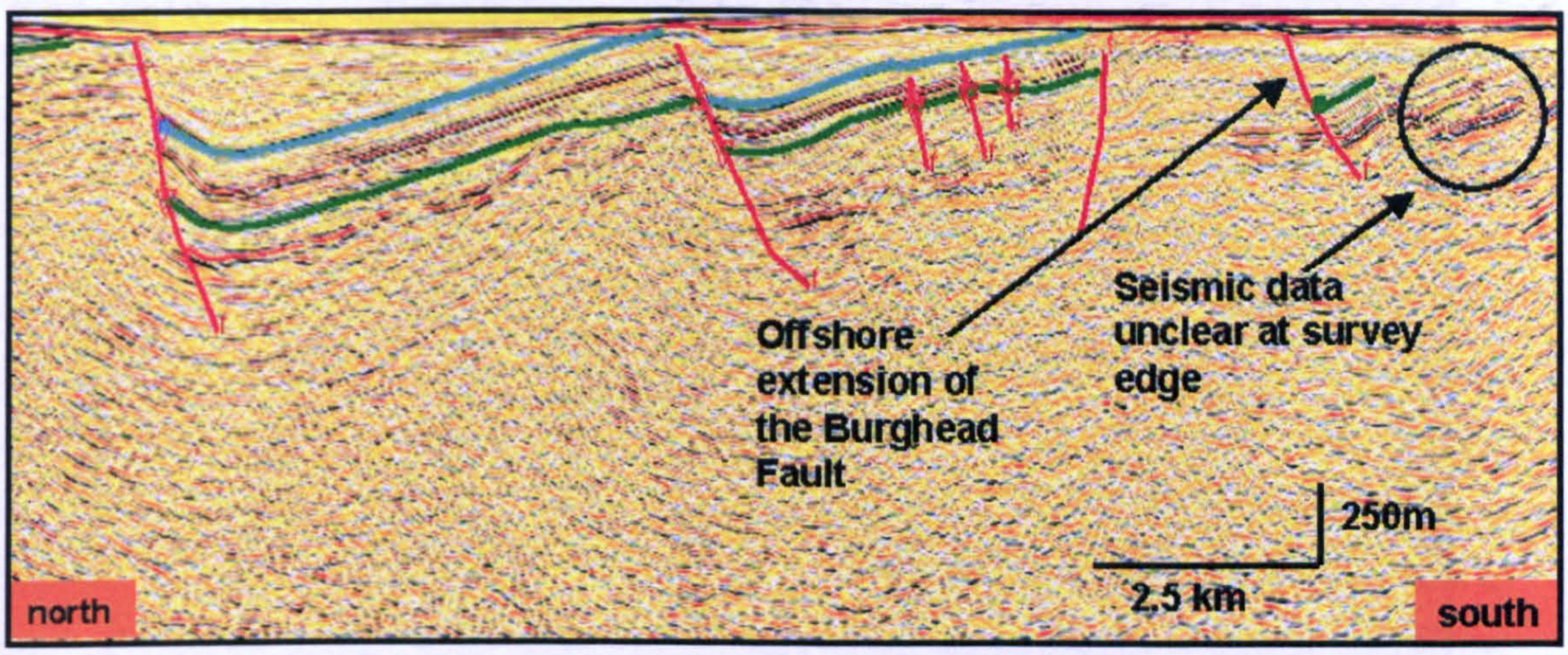


**Figure 4.11. Regional view of seismic line 204, which runs to the west of the Lossie Peninsula. A series of extensional faults and half-graben can be seen, along with the northerly downthrowing fault which is parallel to the blind zone. This structure uplifted the TopTriassic above the level of present day seabed. The fault to the south of this downthrows the Top Triassic and is linked to the Burghead Fault onshore. Seismic data quality at the southern edge of the survey is poor, but suggests minor extensional faulting may be present. The regional Lossie Fault can also be seen. Colour picks as for Figure 4.7.**

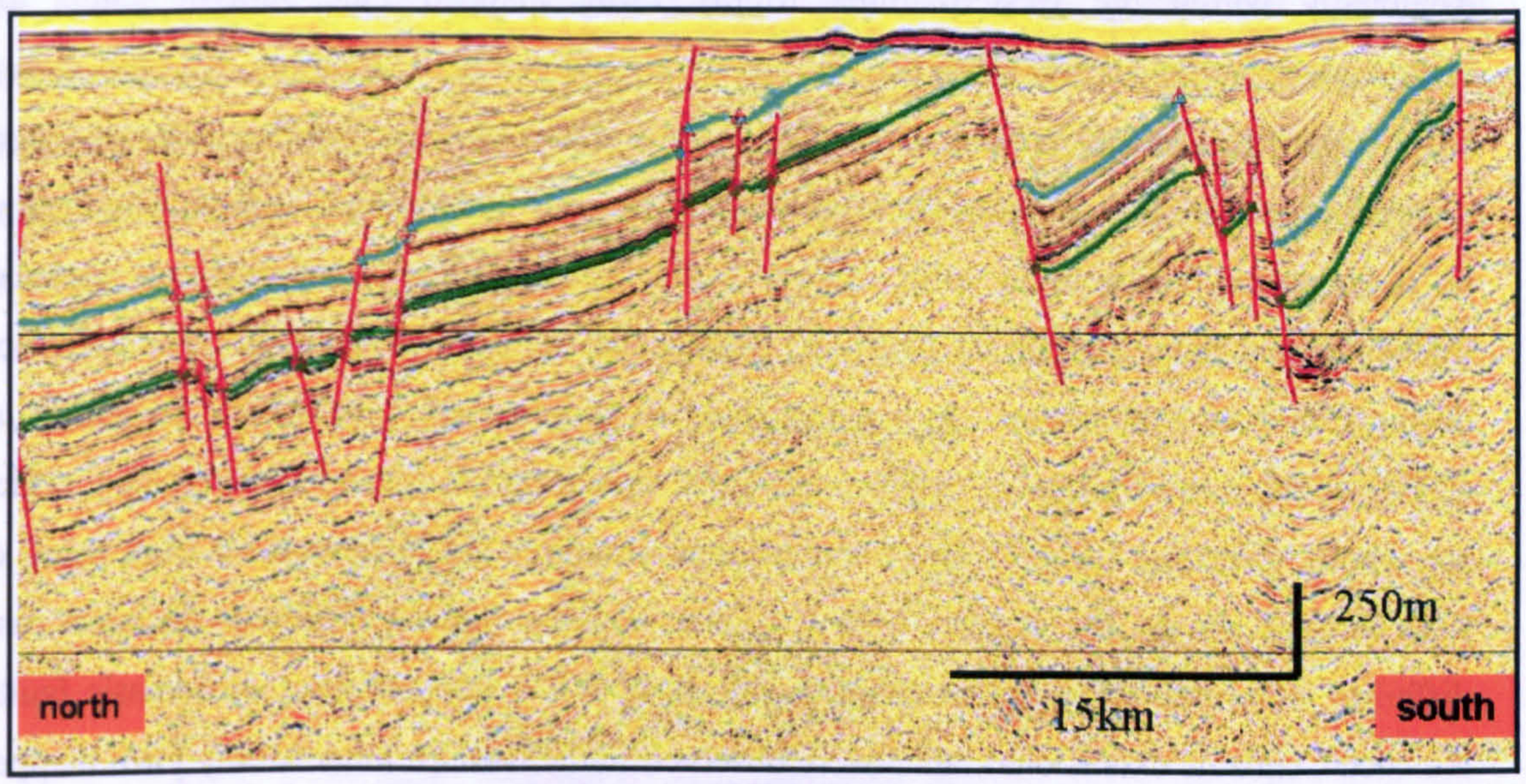


**Figure 4.12. Seismic line 205 to the east of the Lossie Peninsula. Several extensional faults can be seen displacing the Top Mid-Jurassic and Top Triassic. The northerly downthrowing fault on line 204 cannot be mapped directly onto line 205 without major lateral offset, suggesting the fault terminates between mapped lines.**


**Figure 4.13. Subcrop map of the Base Cretaceous. Absent from the area surrounding the Lossie Peninsula, the Cretaceous is preserved in the deeper basin to the north and east.**

Regionally within the western Inner Moray Firth, mapped Late Jurassic faults are characterised by their ENE-WSW to SW-NE trend, and can be divided into two sub-groups based upon periods of activity. Group 1 show Late Jurassic hanging wall sediment thickening, and do not penetrate the overlying Cretaceous and younger sediment, indicating no re-activation during basin uplift. Group 2 display Late Jurassic hanging wall sediment thickening and also penetrate the overlying Cretaceous, indicating re-activation and extension during Cenozoic exhumation. In a wider study of Moray Firth development Argent *et al.* (2002) define a third group of extensional faults, in addition to those identified here, which are wholly Cenozoic in age. These extensional structures are differentiated from those of Late Jurassic age by the absence of any control on Late Jurassic sediment thickness, and differing fault orientations to the characteristic ENE-WSW trend of the Late Jurassic faults. No such Cenozoic extensional faults were observed in the western Inner Moray Firth mapped in this study. The overall relatively shallow burial of the western basin, and the absence of significant post Jurassic sediments removes the possibility of observing such structures at present day. In the work of Argent *et al.* (2002) the Cenozoic extensional faults appear more frequent in the eastern, deeper, areas of the basin suggesting that they may not have been present in the western Inner Moray Firth.

## 4.32 Local seismic interpretation

Five survey lines running dip parallel (IMF97/201-205), and two strike lines (IMF97/107-108), running perpendicular to the coastline were selected for their relevant geographic position (Fig. 4.4), and used for the detailed characterisation of the local 20km x 15km structure offshore from the Peninsula. As for the regional survey the Top Triassic and Top Mid-Jurassic horizons were mapped in detail, but the position in the western apex of the basin means the Base Cretaceous was not present (Fig. 4.13). The Top Triassic is at a relatively shallow burial depth of less than 500m on the southern basin margin, and forms a low angle surface dipping toward the north. Mapping of the surface shows lateral continuity in an east-west direction proving the absence of the subordinate north-south trending normal faults which are occasionally present further offshore and, to a lesser extent, onshore.

Seismic lines 201-203 lie north of the main east-west Peninsula coastline, ending 5km offshore and leaving a 5km zone between the edge of the marine survey and the exposure on the Lossie Peninsula coastline, defined here as the blind zone. Across this blind zone interpretation is based upon a reconciliation of the nearest onshore data and offshore seismic lines (Fig. 4.13). On all three survey lines the depth of the Top Triassic is 370-480m below seabed at the edge of the survey, and deepens along a dip of 3-7° with increasing distance from the coastline (Figs. 4.15-4.20).

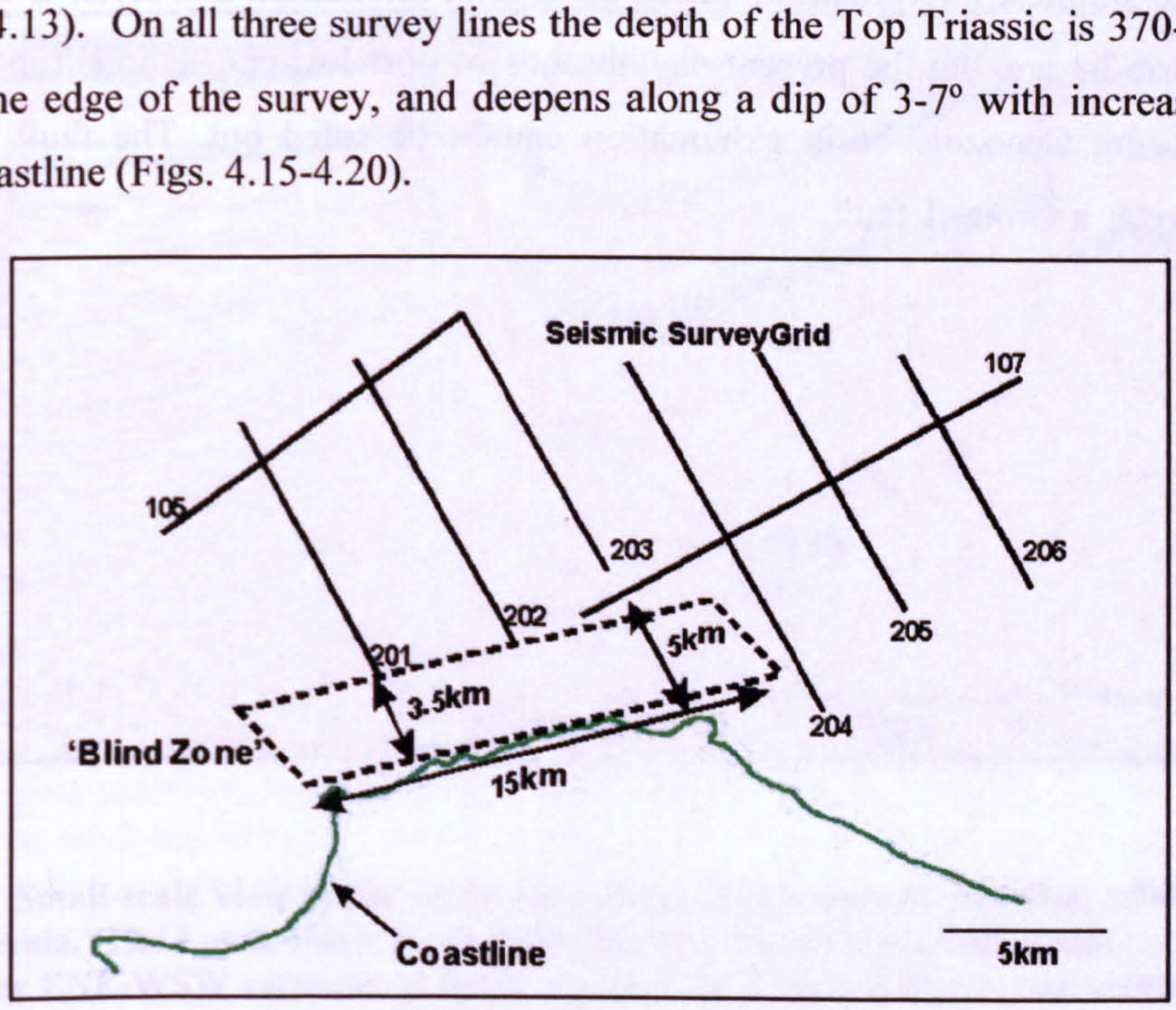


**Figure 4.14. The area of the 'blind zone' between offshore seismic reflection coverage and onshore exposures, across which these two datasets are integrated.**

Fault history interpretation and classification in the region directly offshore from the Lossie Peninsula is complicated by the present day shallow sediment burial depth, and the absence of post-Jurassic sediment, and upper sections of the Late Jurassic. However the history of some faults can be reconstructed where the same fault is present in the deeper basin, where post-Jurassic sequences are intact. A number of normal faults striking ENE to WSW have been mapped, following the characteristic trend of the series of Late Jurassic extensional faults seen on seismic data throughout the western Moray Firth.

On survey line 202 (Fig. 4.16) an ENE-WSW trending extensional fault is present 6km offshore, along with a subsidiary minor fault, and can be mapped on lines 203 (Fig. 4.17) and 204 (Fig. 4.18) to the east, but is absent from survey line 201 (Fig. 4.15) to the west, suggesting it terminates between survey lines 201 and 202. The fault is interpreted to be c.10km in lateral extent. Adjacent to the Lossie Peninsula this normal fault downthrows to the southeast, cutting the Top Triassic and Top Mid-Jurassic horizons, which do not display any thickness variation across the fault. A thin, <170m, sequence of Late Jurassic sediment is also present in the hanging wall and crops out on the seabed. The overall sediment burial depth is shallow, <500m, making observation of the geometry of the Late Jurassic sediment difficult. The simplest interpretation, based upon fault orientation and style, is that the fault is Late Jurassic in age, but the present day absence of post-Jurassic sediment means any re-activation during Cenozoic basin exhumation cannot be ruled out. The fault is therefore classified here as a Group 1 fault.

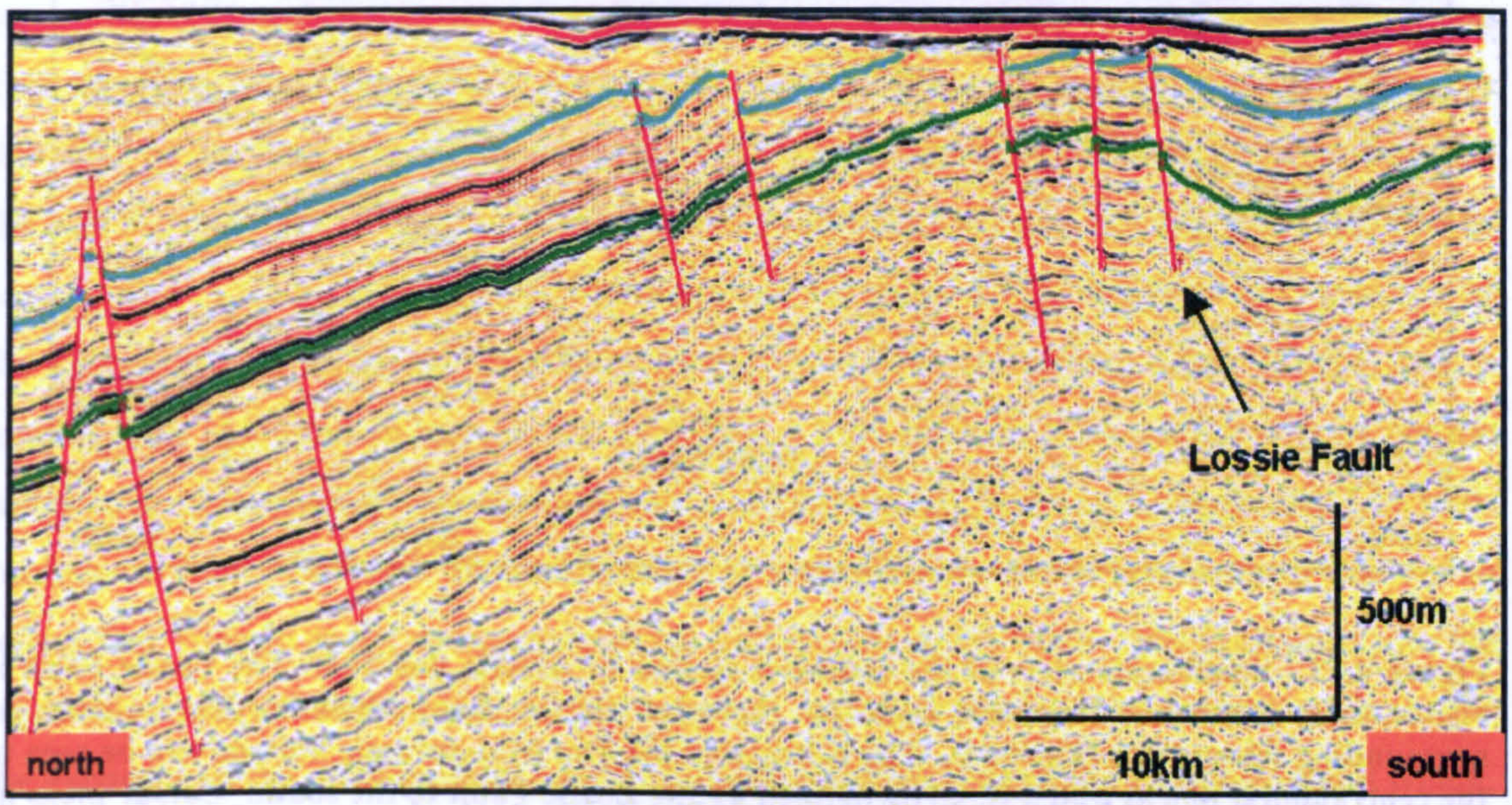


**Figure 4.15. A small-scale view of seismic line 201 showing minor extensional faults. The most southerly fault appears to show the typical hanging wall buttressing seen on the Lossie Fault further offshore, although data quality is not as high as on the edge of the survey line. Colour picks as for Figure 4.7.**

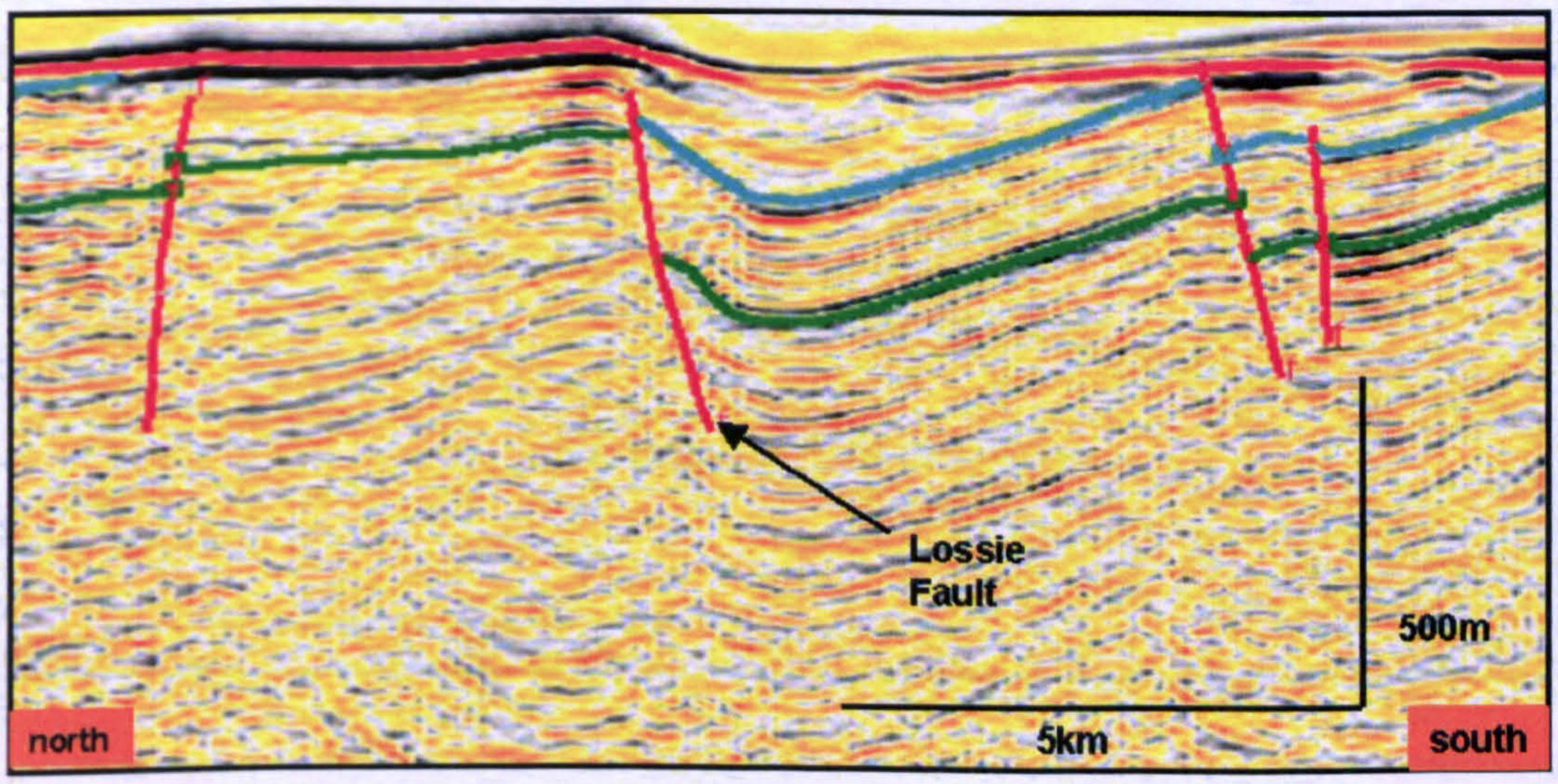


**Figure 4.16 Small-scale view of the southern section of seismic line 202 5km offshore from the Lossie Peninsula. The Lossie Fault can be identified by the characteristic folding of hanging wall strata. Other ENE-WSW extensional faults mapped on Figure 4.24 are also visible. The 'blind zone' runs from the southern edge of this seismic line to the Peninsula coastline. Colour picks as for Figure 4.7.**

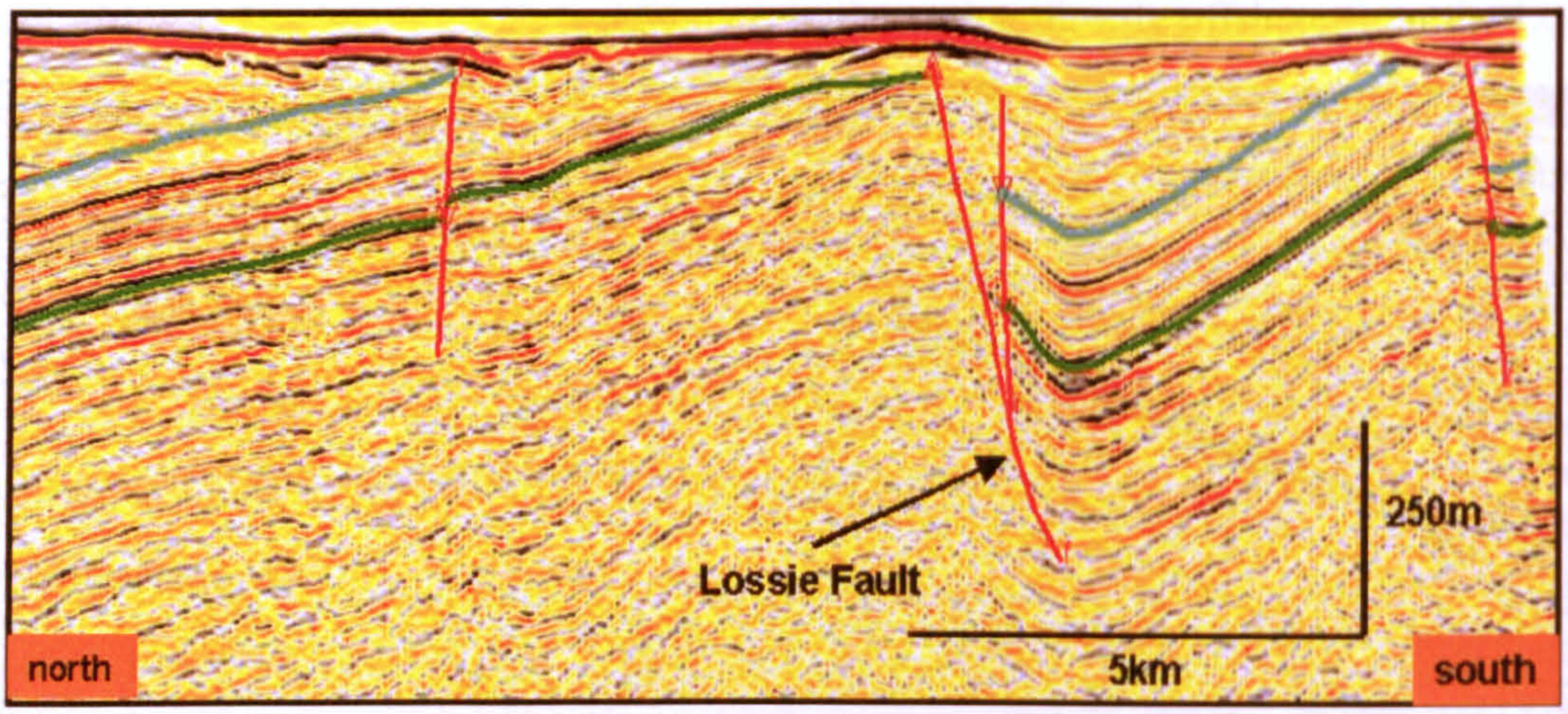


**Figure 4.17. Small-scale view of the southern section of seismic line 203. The Lossie Fault is visible, and another extensional fault on the edge of the line, which is also present on surrounding seismic lins (Fig.4.24). The subcrop of the Top Mid-Jurassic horizon can be seen in the central horst block, which is partly defined by the Lossie Fault to the south. Colour picks as for Figure 4.7.**

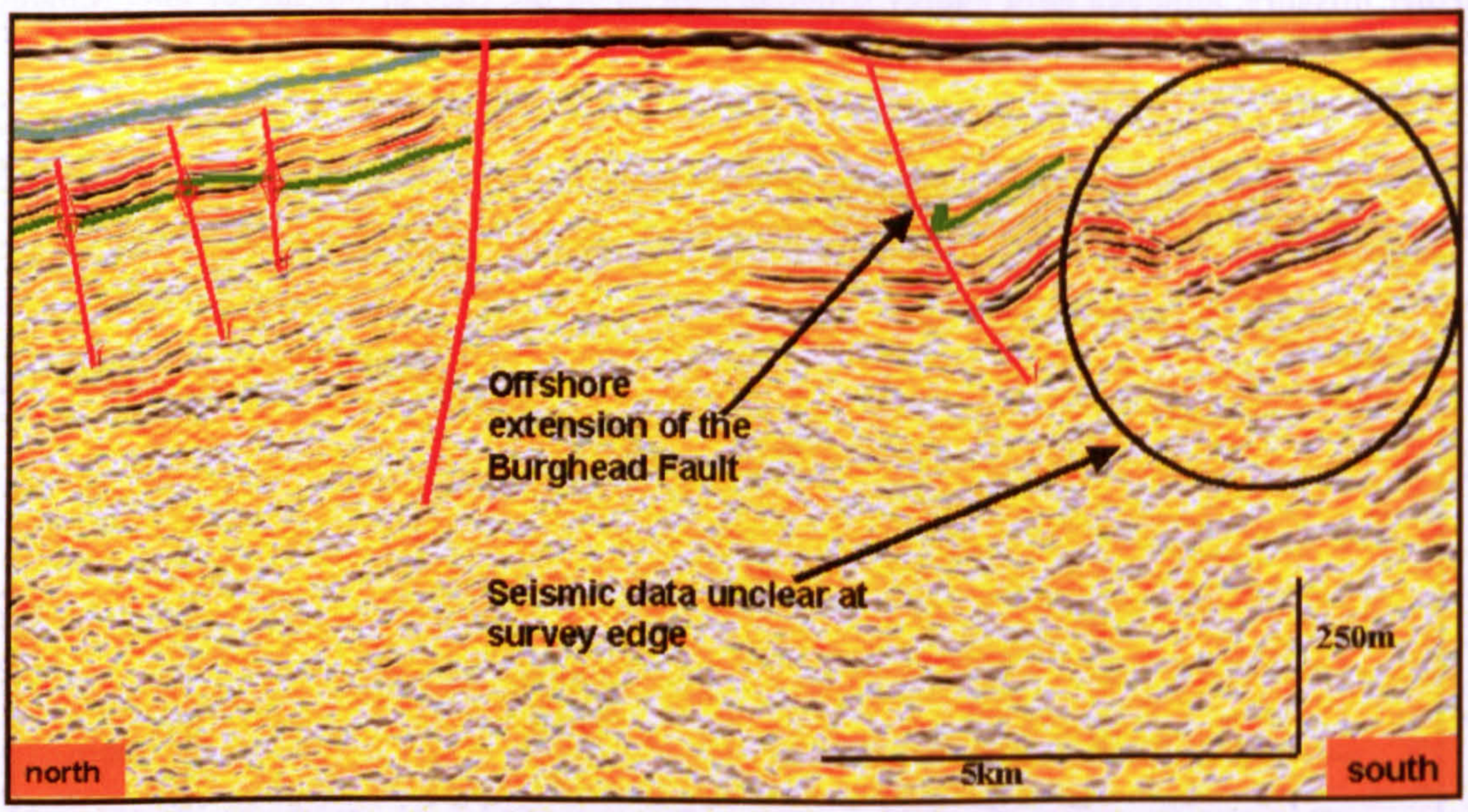


**Figure 4.18 The southern edge of seismic line 204. The most southerly fault propagates to the seabed and downthrows the Top Triassic to the south. To the north of this fault and extensional structure which downthrows to the north can be seen. In the footwall of this fault the Top Triassic has been uplifted above the level of present day seabed. This fault lies parallel to the 'blind zone' further west. Colour picks as in Figure 4.7.**

Seismic survey line 204 runs parallel to the eastern coastline of the Lossie Peninsula, through the blind zone between survey lines 201-203 and the coastline, to the west (Figs. 4.4, 4.14).

Along strike from the blind zone the Top Triassic is cut by a normal fault, identified on survey line 204. This sub-vertical fault downthrows to the north, and the regionally strong Top Triassic reflector is absent to the south. The Top Triassic is at shallow depth (200m) to the north of the fault (Fig. 4.18), suggesting that following the relative uplift of the footwall the Jurassic and Top Triassic horizon in the footwall have been eroded, and that Devonian to Late Triassic subcrop at the seabed at the present day (Fig. 4.35). No seismic expression of the Devonian and Permian strata can be detected. Two kilometres south of this fault a normal fault is present on survey line 204 (Fig. 4.18). Seismic data quality is poor for the southern section of the survey line, making identification of the Top Triassic and Top Mid-Jurassic difficult. However the fault appears to cut a reflector which is tentatively inferred to be the Top Triassic as the strongest reflector locally, and in the basin. The fault roots into the basement and appears to propagate to the seabed. Along with the seismic data, evidence for the existence of the offshore fault comes from the trend onshore of the Burghead Fault which, if extrapolated offshore, coincides with the position of the fault mapped from seismic data on survey line 204 (Fig. 4.23). The two seismic strike lines running NE-SW immediately offshore, 105 (Fig. 4.19) and 107 (Fig. 4.20), reveal the presence of two minor NNW-SSE normal faults which downthrow broadly towards the north-east. These are comparable to the minor north-south faults observed onshore, and have only a minor effect on sediment geometry.

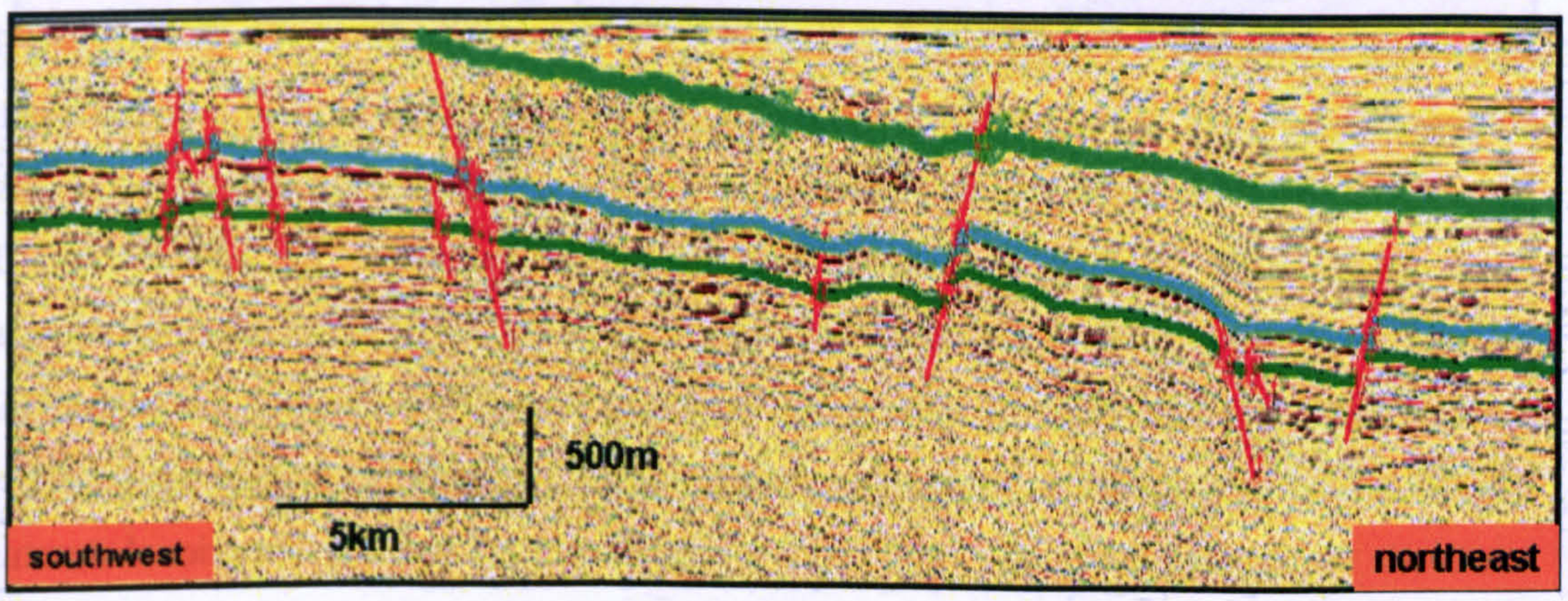


**Figure 4.19. A regional view of seismic strike line 105. The regional dip toward the east can be seen, increasing the depth of the Top Triassic and Top Mid-Jurassic. The Base Cretaceous can be seen to intersect the seabed toward the west. Fault history can be interpreted more easily where the Base Cretaceous is present. A series of faults can be seen which are minor north-south extensional faults, or represent ENE-WSW extensional faults cutting the seismic line at a shallower angle. Only one fault can be observed to cut the Base Cretaceous horizon, showing minor re-activation during basin uplift. Colour picks as for Figure 4.7.**

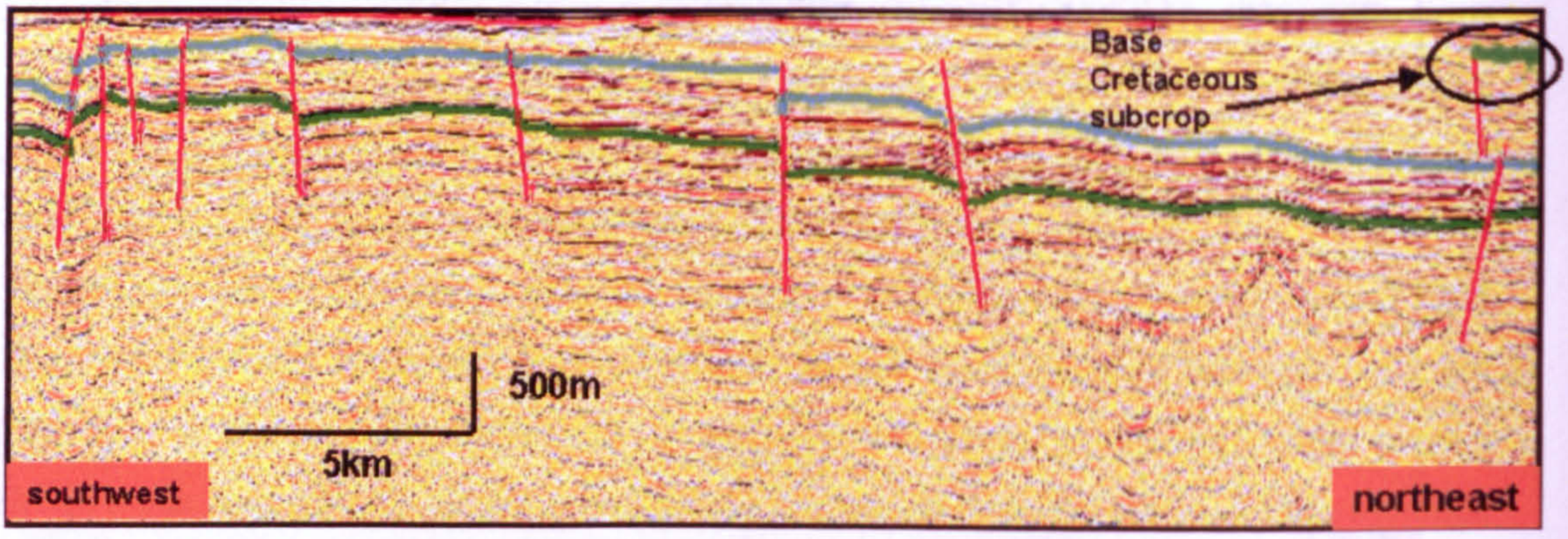


**Figure 4.20 Seismic line 107 showing the increasing burial of the Top Triassic and Top Mid-Jurassic toward the east. The Base Cretaceous crops out on the seabed on the eastern edge of this image. A series of minor north-south faults, and ENE-WSW faults cutting the survey line at shallow angle, can be seen. Colour picks as for Figure 4.7.**

Locally the largest scale structural feature is the Lossie Fault which defines the south-eastern boundary of a horst block, present 10km offshore from the Lossie Peninsula. The Lossie Fault is a regional feature which can be traced from survey lines 201-204 (Figs. 4.15-4.18) in the west of the basin for >60km, trending in a ENE-WSW direction. This normal, extensional fault cuts through Triassic to Cretaceous strata and downthrows to the southeast, with displacement increasing toward the ENE (Fig. 4.21). A characteristic feature of the Lossie Fault is buttressing of the hanging wall strata against the footwall block, causing significant bending of the hanging wall units, a process thought to be formed by the comparative strength of the indurated Devonian, basement, footwall block (Underhill 1991a) (Fig. 4.21). This buttressing allows the Lossie Fault to be traced from deeper in the basin onto seismic lines 201-203 directly offshore from the Peninsula. At >20km from the Peninsula coastline, where sediment burial depth is greater, Jurassic and Cretaceous units are preserved and the behaviour of the Lossie Fault can be more accurately interpreted than directly offshore from the Peninsula where much of the strata younger than Jurassic has been removed. Regionally, the Lossie Fault forms a significant Late Jurassic extensional structure, downthrowing the Top Triassic between 700-1000m, and also penetrating the overlying Base Cretaceous horizon, showing that the fault underwent two phases of activity, Late Jurassic extension and Cenozoic re-activation during basin exhumation (Fig. 4.21). The lack of any observable thickness variation of the Permian to Mid-Jurassic sediments moving through the hanging wall into the fault, demonstrates an initial Late Jurassic age and not re-activation of

an older structure. This is in agreement with regional observations of the series of extensional faults trending in the ENE-WSW/NE-SW direction. The Cretaceous sediment onlaps onto the Late Jurassic, demonstrating that although the Lossie Fault cuts through the Cretaceous it was not active during Cretaceous sediment deposition. These observations of the Lossie Fault, at greater distance offshore from the Peninsula, allow it to be classified here as a Group 2 fault, Late Jurassic in age, and re-activated during Cenozoic basin exhumation. If this fault behaviour is assumed to have occurred along the entire length of the Lossie fault then it can be used to define the history of the Fault in areas more adjacent to the Lossie Peninsula. The recent data available here also allows the position of the Lossie Fault to be re-interpreted, in contrast to Underhill (1991a), who mapped the Lossie Fault offshore as the equivalent of the onshore (Burghead) Fault, which crops out on the Peninsula (Fig. 4.23). Here it can be seen that the Lossie fault runs c.10km to the north of the southern Moray Firth coastline (Fig. 4.24), and that the onshore Burghead Fault is a distinct structure.

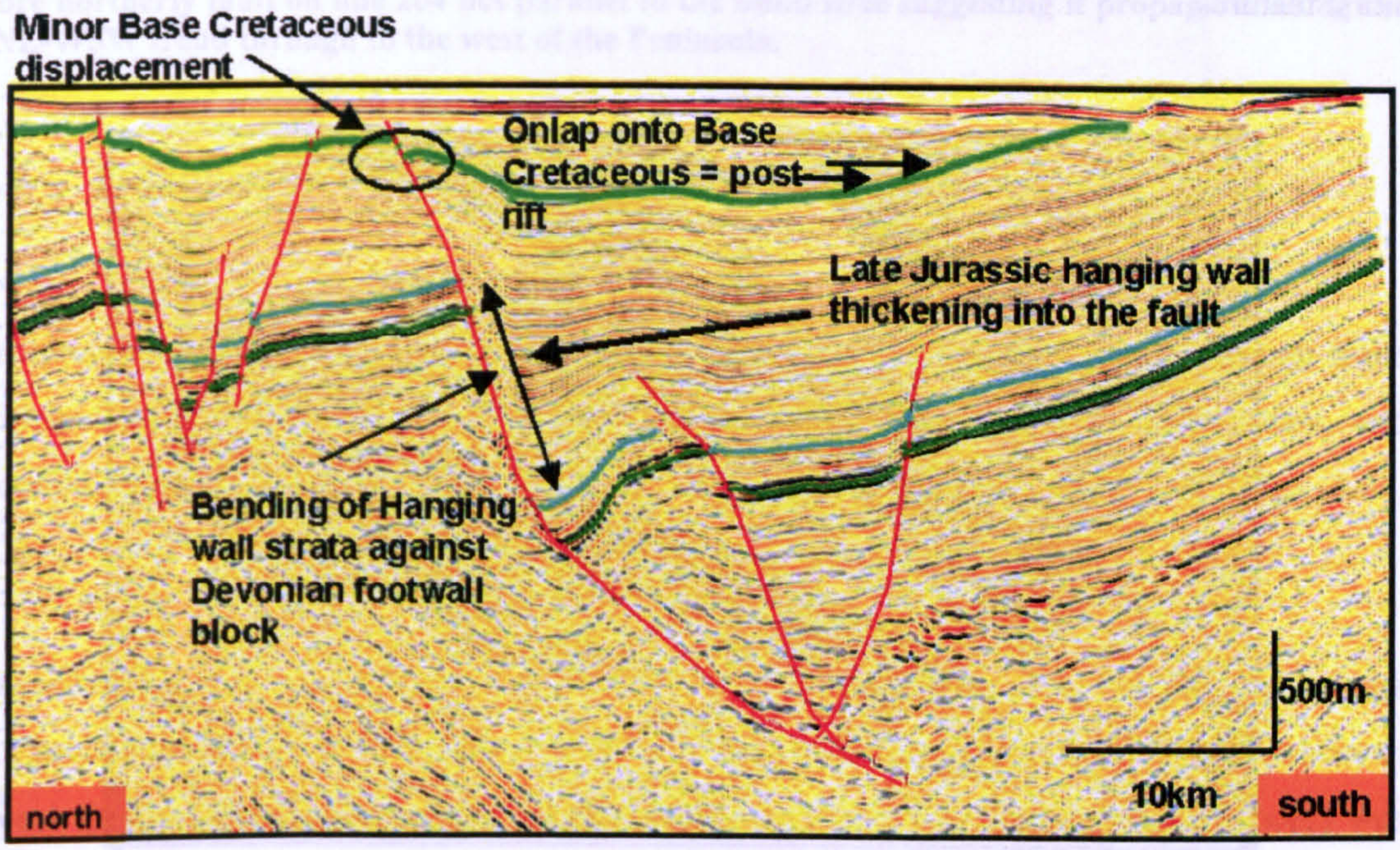


**Figure 4.21. The Lossie Fault on seismic line 209, 10km northeast of Lossiemouth. The thick (>750m) Late Jurassic hanging wall sediment shows the scale of Late Jurassic fault extension. Displacement of the Base Cretaceous reflector is relatively minor (75m) showing that although the fault re-activated during basin uplift, Late Jurassic extensional movement is predominantly responsible for the present day configuration. The folding of hanging wall strata is thought to be produced during fault movement by buttressing of soft sediment against the indurated footwall high. Colour picks as for Figure 4.7.**

The horst block defined to the southeast by the Lossie Fault runs 60km in length, and trends NE-SW (Figs. 4.22, 4.11) increasing in width from 2km in the southwest of the basin, to greater than 10km toward the northeast (Fig. 4.22). Downthrow to the south-east by the Lossie Fault creates a half-graben sub-basin on the southern basin margin, with the effect of increasing the burial depth of Permian to Mid-Jurassic sediments, relative to the 20km wide structural high further offshore (Fig. 4.11). The onshore Lossie Peninsula exposures of Permo-Triassic sediments are at a shallower depth than the regional trend of burial depth in the hanging wall of the Lossie Fault. A series of linked fault segments form the northern boundary to the horst block (Fig. 4.24), which locally increases in width moving along strike in an northeast trend, from the apex of the horst bounding faults on line 201, to 5km on line 203 (Figs. 4.6, 4.23).

The local 15km x 10km area offshore from the Lossie Peninsula is dominated by extensional faults which follow a ENE-WSW to NE-SW trend. These create half-graben sub-basins and horst features.

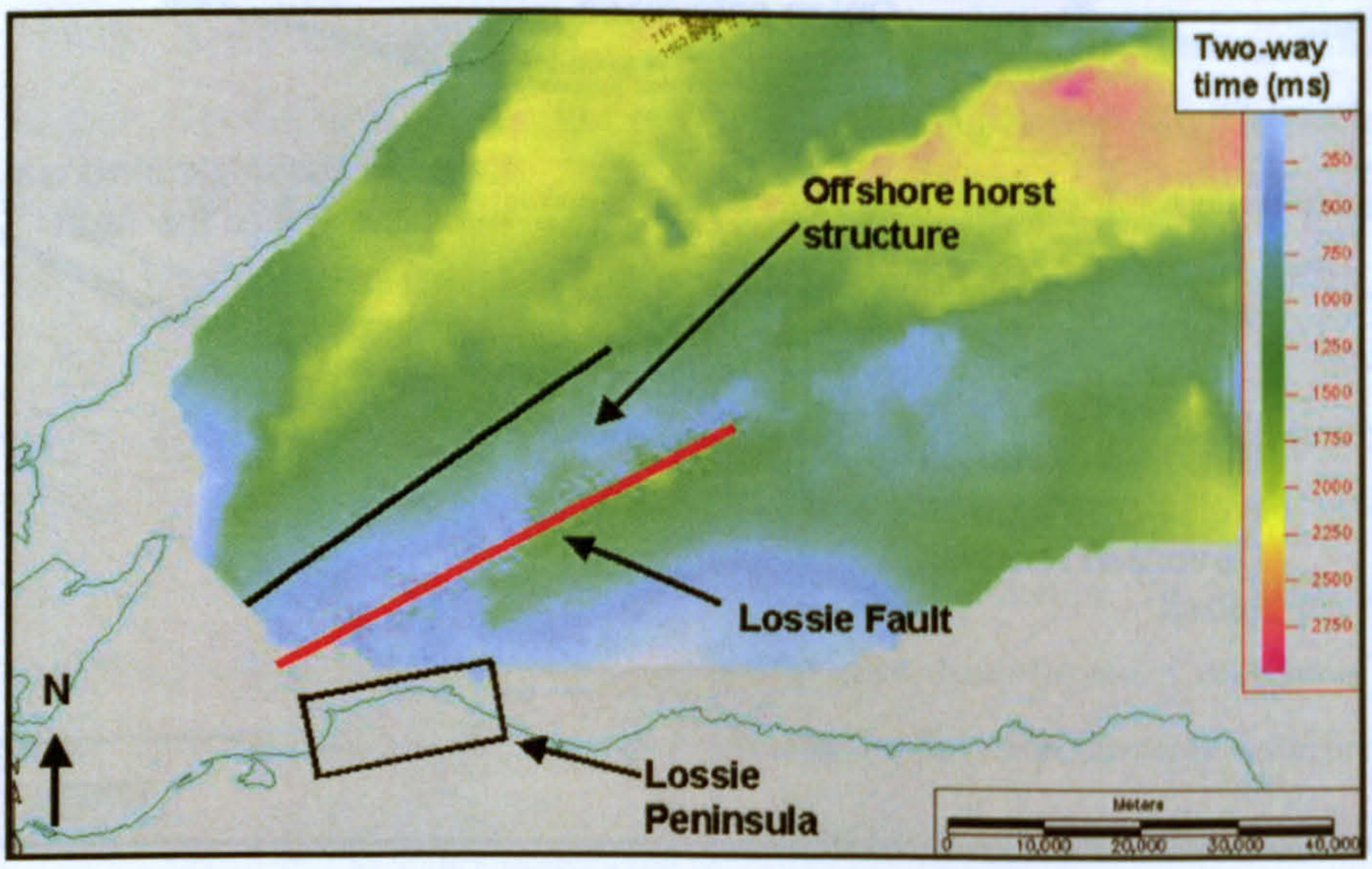


**Figure. 4.22. Top Triassic seismic horizon map for the Inner Moray Firth. The Lossie Fault and associated horst block are highlighted. Late Jurassic extensional ENE-WSW faulting locally controls the depth of the Top Triassic. On a basin scale the increasing burial depth of the Top Triassic to the north and north-west can be seen. Some data from Underhill *et al.*, 2003.**

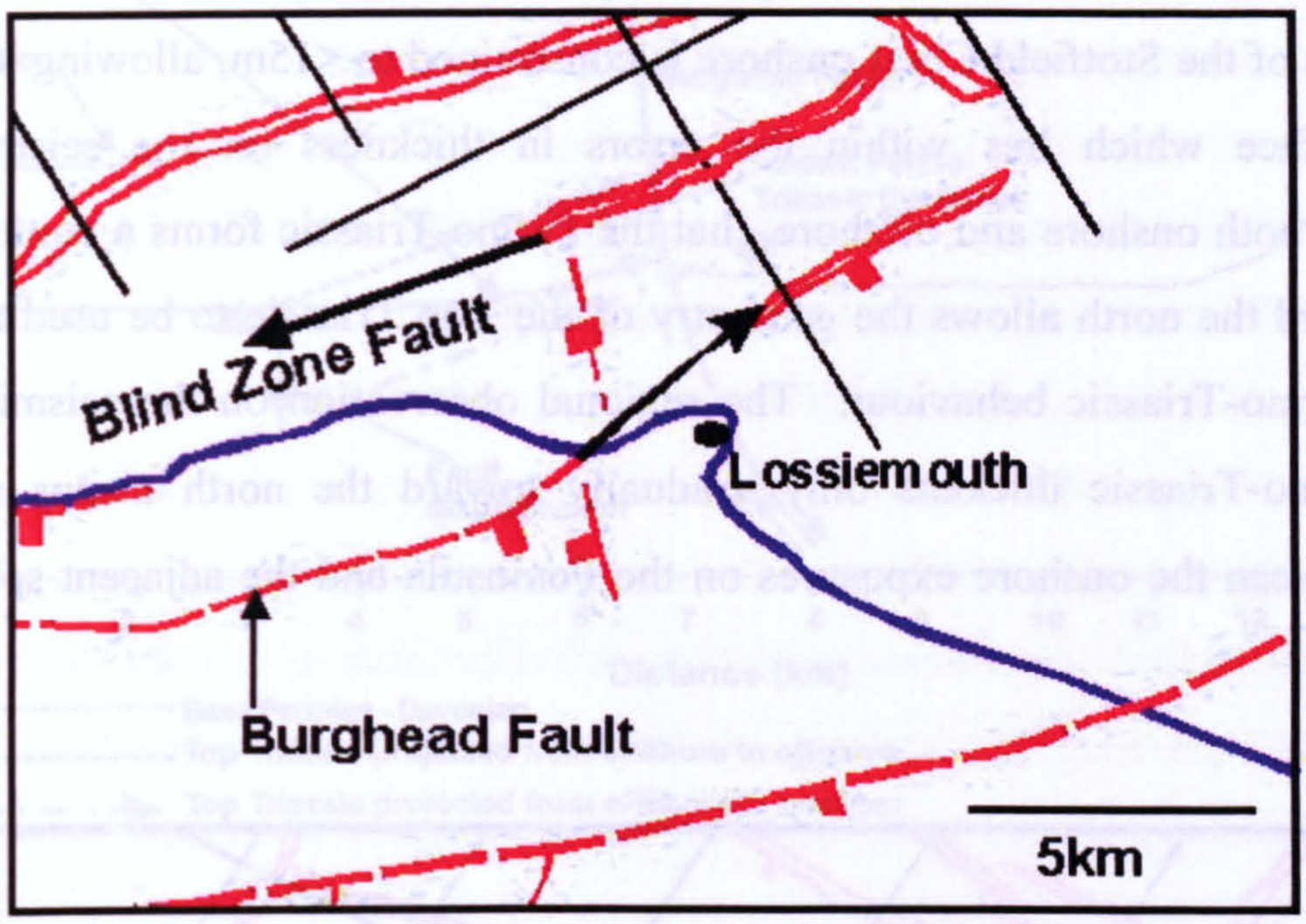


**Figure. 4.23. Extrapolating the Burghead Fault offshore from the well constrained coastal exposures at Lossiemouth allows it to be linked to the observed fault on seismic line 204. The more northerly fault on line 204 lies parallel to the blind zone suggesting it propagates along the ENE-WSW trend through to the west of the Peninsula.**

## 4.4 Integration of onshore and offshore data.

An integrated structural model for the Lossie Peninsula has been developed through three principal stages; interpretation of offshore seismic data, compilation of onshore data, and reconciliation of the two datasets across the offshore blind zone between them (Figs. 4.24, 4.25).

Integration of the two, onshore and offshore, datasets has been achieved chiefly through extrapolating offshore horizons identified on seismic data, through the blind zone, onshore to reveal their predicted outcrop location if they are unaffected by faulting. The process was reversed by projecting the exposed onshore strata offshore through the blind zone, allowing the difference between the two projections to be quantified (Fig. 4.25), and the creation of a structural model to tie the two observations together. Further, direct identification of the exposed Burghead Fault on seismic data offshore gives the model increased accuracy.

On both the onshore exposure data and offshore seismic survey the Top Triassic Stotfield Chert was selected as the key horizon, because it represents the most identifiable seismic

horizon offshore, and its location and geometry at outcrop, is well characterised onshore. The thickness of the Stotfield Chert onshore is constrained to <15m, allowing it to be used as a single surface which lies within the errors in thickness on the seismic data. The observations, both onshore and offshore, that the Permo-Triassic forms a conformable series dipping toward the north allows the geometry of the Top Triassic to be used as an accurate proxy for Permo-Triassic behaviour. The regional observation on the seismic survey data that the Permo-Triassic thickens only gradually toward the north means any thickness variation between the onshore exposures on the Peninsula and the adjacent seismic data are minor.

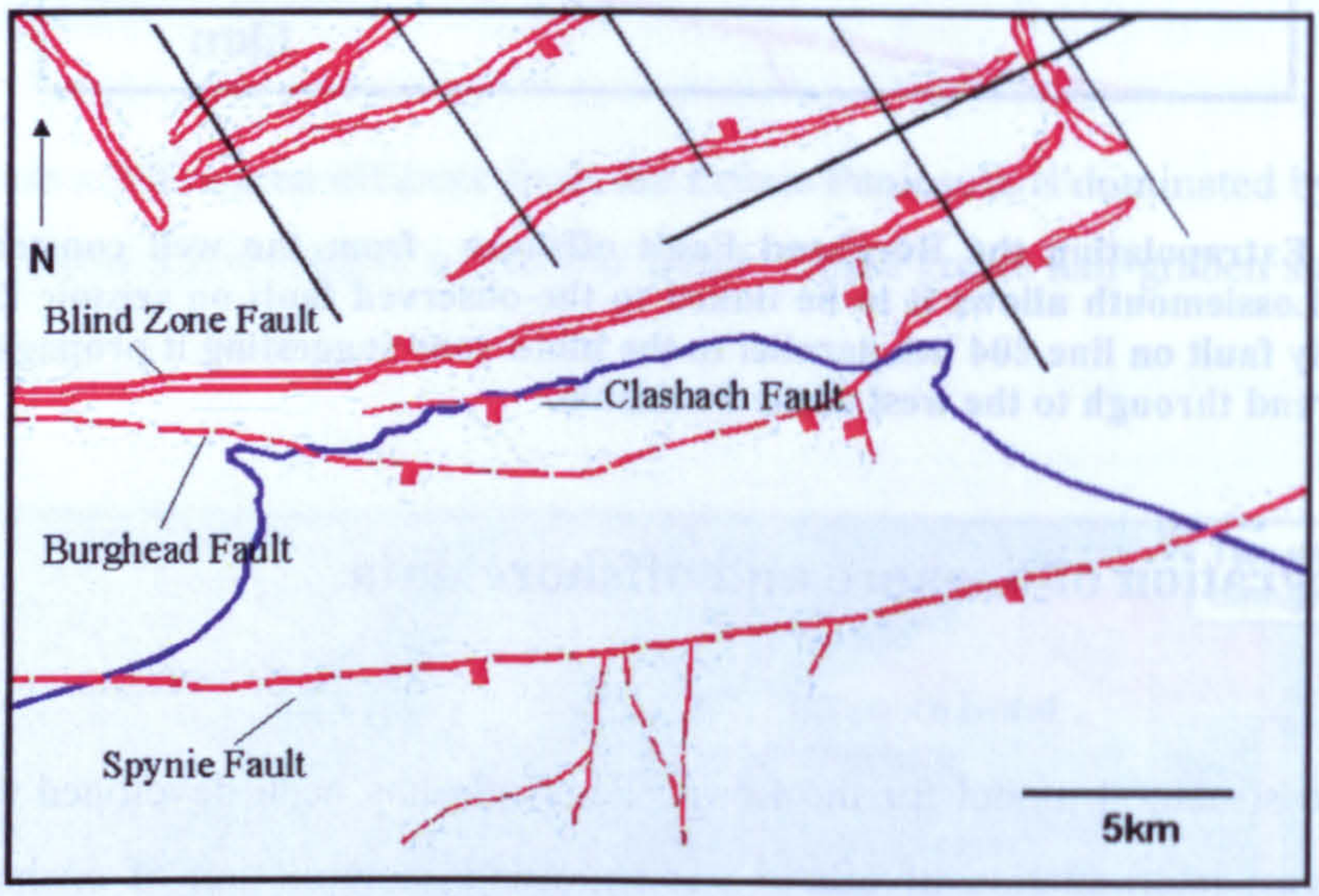


**Figure. 4.24. Final structural map of the onshore and offshore surrounding the Lossie Peninsula. The Burghead Fault can be seen to link offshore onto a fault mapped on seismic line 204. The blind zone fault propagates from seismic line 204 through to the west of the Peninsula. The blind zone fault is interpreted to continue further west of Burghead.**

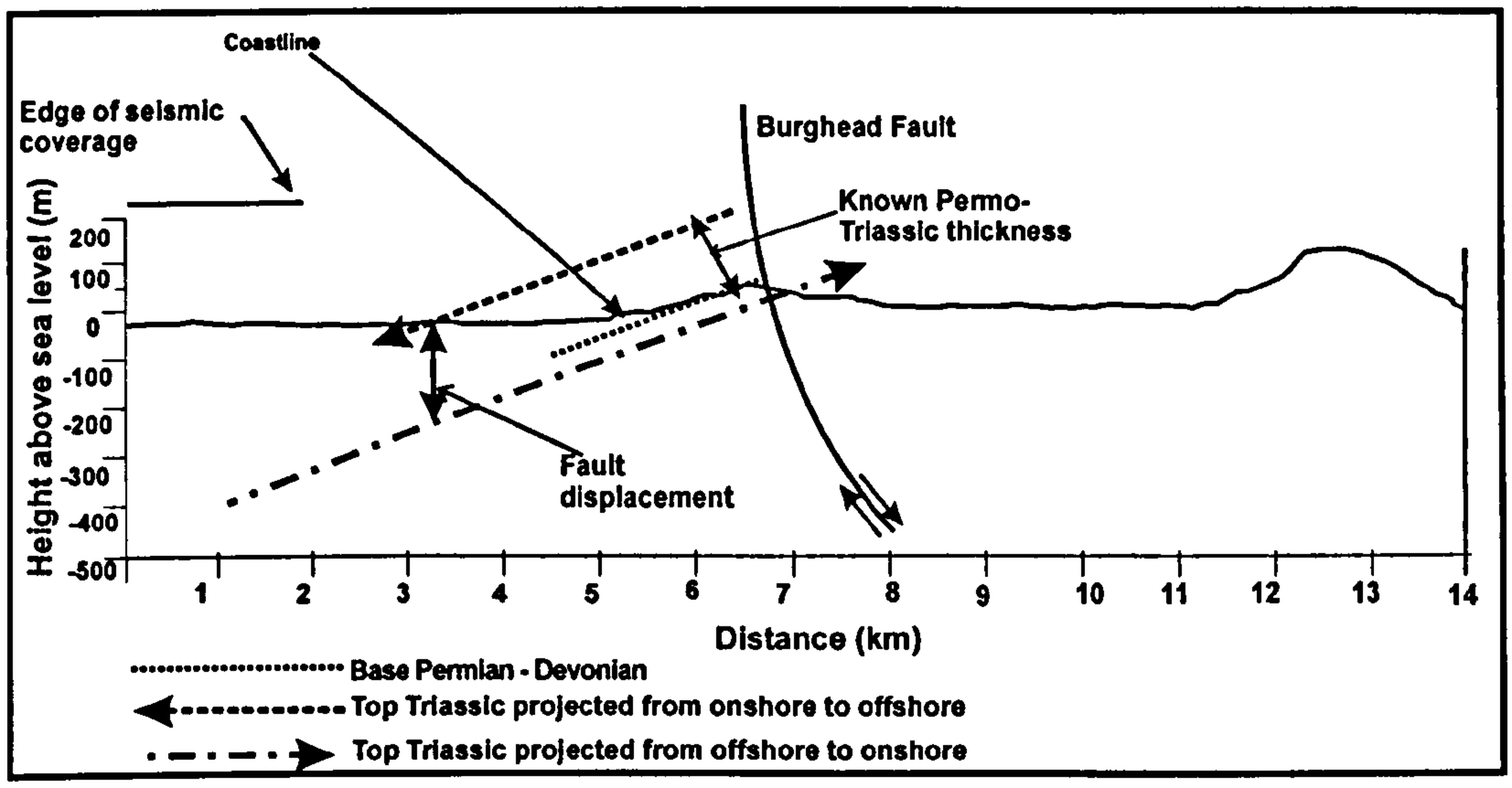


**Figure. 4.25. Cartoon cross-section NW-SE of the onshore to offshore profile. Themethodology for integrating the two datasets is shown. The onshore Top Triassic is calculated from the known Permian and Triassic thickness and the known base Permian-Devonian contact. The offshore Top Triassic horizon is extrapolated from the local seismic data. This allows the discrepancy between the two datasets to be measured, and the predicted subcrop/outcrop pattern to be predicted for each dataset.**

## 4.41 Linking offshore seismic with onshore faults

Seismic survey line 204 lies parallel to the eastern edge of the Lossie Peninsula allowing faults identified on the seismic data to be directly linked with those observed onshore (Section 4.4). The Burghead Fault trends offshore in a NE direction north of Lossiemouth, and may be expected to cross seismic line 204 if it has sufficient lateral extent. The onshore minor Clashach Fault is unlikely to propagate as far as seismic line 204, and the Spynie Fault trends south of the edge of the seismic data. Therefore the Burghead Fault is the most likely to be represented directly on seismic line 204. Two faults were identified on seismic line 204 parallel to the blind zone and coastline (Figs. 4.23, 4.24). The most northerly of these two faults downthrows to the north and is directly parallel to the blind zone to the west. The position, and direction of throw, of this fault makes it unlikely that this equates to the onshore Burghead Fault, which lies 3km further south and, although near vertical, downthrows to the south. It is likely that this fault seen on survey line 204 continues along trend through the blind zone, paralleling the onshore Burghead Fault. The second, more southerly, fault (Figs. 4.18, 4.23) downthrows to the south, and lies along trend from the Burghead Fault. It is therefore interpreted as the offshore extension of the onshore Burghead Fault. This offshore

fault is mapped on survey line 204, but is absent on line 205 indicating that the maximum offshore lateral extent of the Burghead Fault is c.10km to the east of Lossiemouth (Fig. 4.23). It has been shown here (section 4.32) that in contrast to previous interpretations the Burghead and Lossie Faults are different. No expression of the minor north-south extensional fault, which runs south from Lossiemouth onshore, can be detected on line 204, suggesting that this fault is not extensive along strike, and thus has only a small effect on the pattern of seabed subcrop immediately offshore. However the absence of the Top Triassic on seismic survey line 204 north of the proposed Burghead Fault makes this difficult to quantify (Fig. 4.18). The two minor NNW-SSE normal faults, identified on seismic survey lines 105 and 108 (Figs. 4.19, 4.20), are comparable to the minor north-south faults observed onshore. There is no evidence from the seismic data that these faults equate to the north-south fault seen onshore near Lossiemouth, although offshore these structures may be below the resolution of the seismic data.

## 4.42 Offshore Top Triassic projection onshore.

Projection of the Top Triassic from each seismic line was treated as an individual calculation, accounting for variation in burial depth and dip on each line (Fig. 4.25). The dip and burial depth of the Top Triassic were calculated at the southern end of each seismic line and projected to find the lateral distance at which the horizon would crop out onshore, accounting for water depth offshore and topography onshore. Figure 4.26 shows the predicted point of outcrop for the Top Triassic horizon from each of the survey lines 201-203. The values for seismic velocity (2.0, 3.0 km/s) that were used to convert the seismic data into true depths, show that variation in the projected position of Top Triassic outcrop is a maximum of 270m, showing seismic velocity is relatively unimportant (See Appendix A for methodology). For seismic line 204 the subcrop of the Top Triassic offshore can be seen directly. The predicted point of outcrop of the Top Triassic on survey line 201 is 4km south of the coastline, and south of the Burghead Fault. Along survey line 202 the projected point of outcrop is 2km south of the coastline, and on line 203, 1km offshore (Fig. 4.26). A line through the three projected outcrop points shows that the surface trace of the Top Triassic trends NE-SW and should intersect with the northerly downthrowing fault on survey line 204. This NE-SW projected Top Triassic trend is broadly coincident with the onshore boundary, and is produced by the regional easterly dip that was imprinted on the basin during Cenozoic uplift.

Comparison of the projected line of Top Triassic outcrop with the onshore geological map shows that on the map basement Devonian and overlying Permian sediments crop out to the north of the projected Top Triassic line (Fig. 4.25). This infers that the onshore Permo-Triassic sequence has been uplifted, in comparison to the equivalent offshore sequence covered by the seismic data, where the Top Triassic burial depth is always greater than 110m below seabed. The onshore Top Triassic is seen south of the Burghead Fault where it has been downthrown against the Permian and Devonian to the north, but again the projected onshore outcrop of the offshore Top Triassic is further south than this exposure (Figs 4.28, 4.29). These observations indicate that downthrow of the Top Triassic to the south by the Burghead Fault is less than the overall apparent uplift of the onshore Lossie Peninsula.

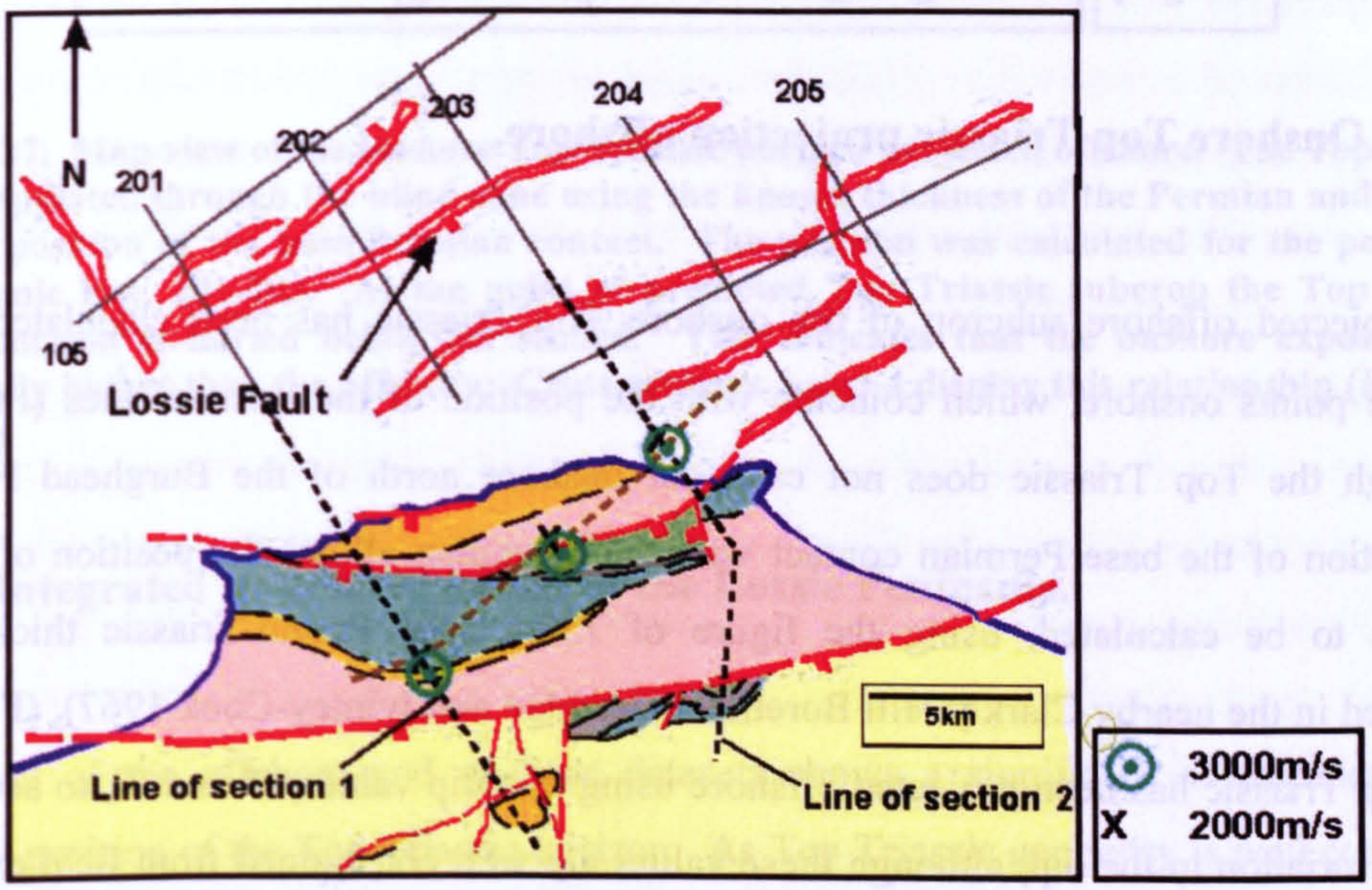


**Figure. 4.26a. Map view of the offshore Top Triassic horizon projected onshore. The Top Triassic was extrapolated through the blind zone from the edge of each seismic line, 201-203. The predicted Top Triassic outcrop lies to the south of exposed Devonian and Permian sediments indicating the onshore exposures are structurally higher than the offshore. Cross-sections 1 and 2 display this relationship (Figs 4.28 and 4.29).**

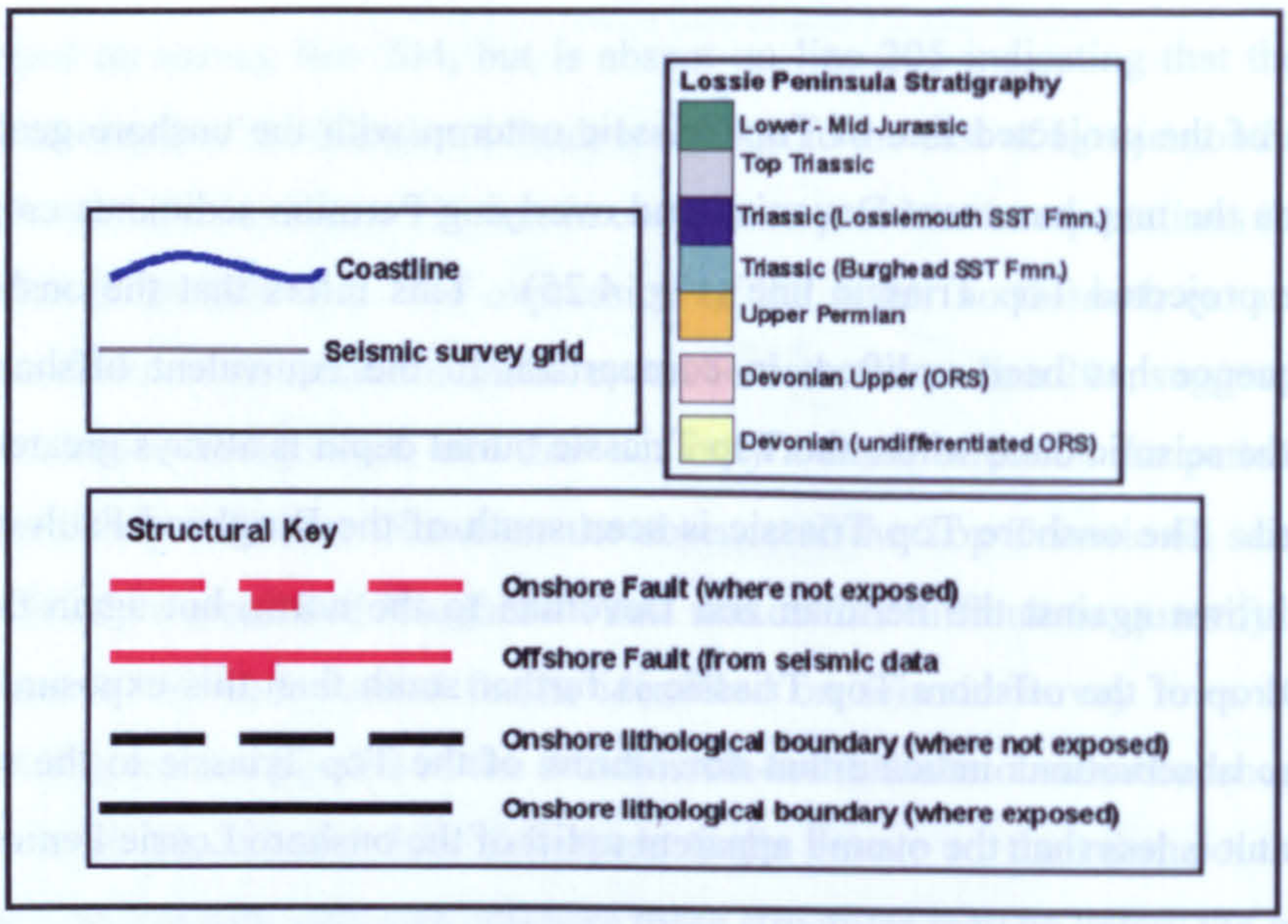


**Figure. 4.26b. Geographical and geological key for figure 4.26(a).**

## 4.43 Onshore Top Triassic projection offshore.

The projected offshore subcrop of the onshore Top Triassic has been calculated from 3 separate points onshore, which coincide with the position of the seismic lines (Fig. 4.27). Although the Top Triassic does not crop out onshore north of the Burghead Fault, the observation of the base Permian contact with the Devonian allows the position of the Top Triassic to be calculated, using the figure of 138m total Permo-Triassic thickness, as measured in the nearby Clarkly Hill Borehole (Berridge and Ivimey-Cook 1967), (Fig. 4.25). The Top Triassic has been projected offshore using two dip values, 5° and 7°, to account for natural variation in the dip, although these values are well constrained from field exposures. Further, the difference in Top Triassic subcrop position caused by using different dip values is <50m, showing that this does not cause a significant error. Figure 4.27 shows that, based upon onshore exposures and relations only, the Top Triassic is predicted to subcrop at between 2km and 3km offshore, which is in the blind zone between seismic coverage and the coastline. Connecting the projected points together shows a Top Triassic surface which traces NE-SW.

Comparison with seismic data projected into the blind zone shows that the actual Top Triassic horizon is at a depth of between 230m (seismic line 201) and 110m (seismic line 203) at the projected point of subcrop (Figs. 4.30, 4.31). This indicates that the onshore

sequence has been uplifted relative to the adjacent offshore strata, in agreement with the findings above (Section 4.42) of the projection of offshore data onshore.

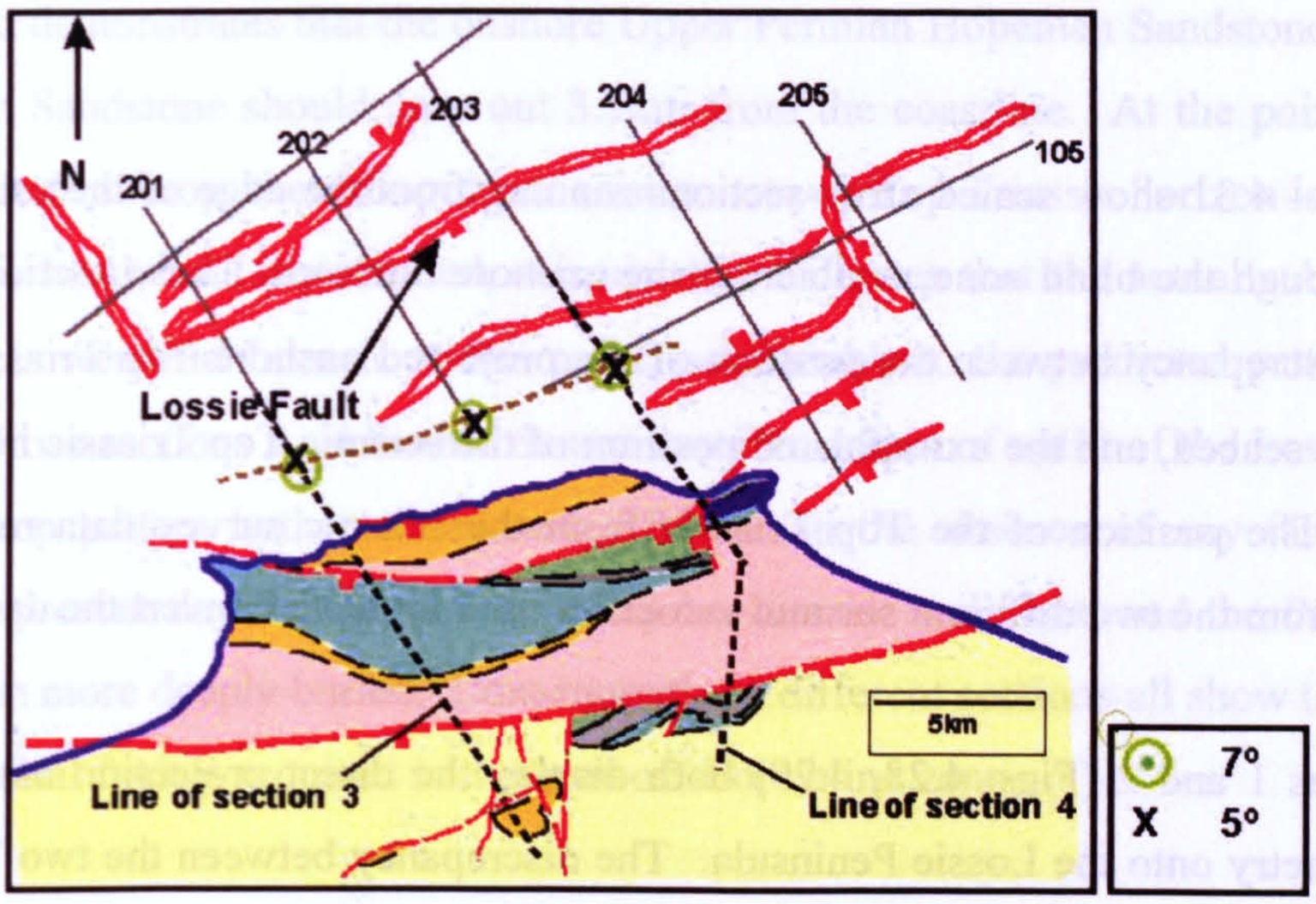


**Figure 4.27. Map view of the onshore Top Triassic horizon projected offshore. The Top Triassic was extrapolated through the blind zone using the known thickness of the Permian and Triassic and the position of the base Permian contact. The position was calculated for the position of each seismic line, 201-203. At the point of predicted Top Triassic subcrop the Top Triassic seismic horizon is buried below the seabed. This indicates that the onshore exposures are structurally higher than the offshore. Cross-sections 3 and 4 display this relationship (Figs. 4.30 and 4.31).**

## 4.44 Integrated structural model of the Lossie Peninsula.

Integration of the offshore and onshore datasets shows a significant discrepancy in the projected position of the Top Triassic horizon. As Top Triassic geometry is well constrained outwith the blind zone, through seismic coverage and onshore exposure, this implies that the position of the Permo-Triassic and Jurassic strata is affected by changes which occur in the blind zone.

The regional, and local, mapping of the offshore western Inner Moray Firth shows that the position of the Top Triassic and Top Mid-Jurassic horizons are chiefly affected by Late Jurassic extensional faulting, forming a series of horst blocks and half-graben sub-basins. Significant folding and transtensional faults are absent, with the exception of the Great Glen Fault in the northwest. The most likely explanation for the discrepancy between the structural positions of the onshore and offshore sequences is therefore the presence of an

extensional fault within the blind zone, which created relative uplift of the now onshore section of Permo-Triassic, and downthrow of the offshore sequence covered by the seismic survey.

Figures 4.28 – 4.31 show scaled cross-sections running from the edge of the seismic survey offshore, through the blind zone, and across the onshore outcrops. These sections show the calculated discrepancy between the position of the projected onshore Top Triassic, where it intersects the seabed, and the extrapolated position of the seismic Top Triassic horizon at the same point. The position of the Top Triassic from the seismic survey data represents the mean value from the two different seismic velocities used to depth convert the data.

Cross-sections 1 and 2 (Figs. 4.28, 4.29) both display the direct projection of the offshore seismic geometry onto the Lossie Peninsula. The discrepancy between the two Top Triassic positions seen on cross-section 1 is 230m, which equates to the mean displacement on the proposed extensional fault at that point. Cross-section 1 (Fig. 4.28), following the trend of seismic survey line 201, also shows the predicted onshore surface expression north of the Burghead Fault, when the offshore seismic Top Triassic horizon is extrapolated to the onshore, ignoring the blind zone displacement. This predicts that Lower-Mid Jurassic sediment would crop out onshore at present day. However, onshore exposure data shows that this is incorrect, and the Upper Permian presently forms the Peninsula coastline. Cross-section 1 also shows that the Burghead Fault increases the burial depth of the Top Triassic to the south, leading to the presence of Lower Jurassic within shallow onshore boreholes (Berridge and Ivimey-Cook 1967). Cross-section 2 (Fig. 4.29), following seismic survey line 203, demonstrates that if there were no offshore, blind zone, fault displacement the Top Upper Permian would crop out on the coastline near Lossiemouth. Onshore data shows that the actual Upper Permian crops out north of a small island offshore, and the Devonian is present onshore adjacent to line 203, again demonstrating the Peninsula wide effect of uplift.

Cross-sections 3 and 4 (Figs. 4.30 and 4.31) illustrate the predicted seabed subcrop pattern when the onshore Peninsula exposures are projected offshore, and there is no displacement within the blind zone. Cross-section 3 (Fig. 4.30) follows the same line as cross-section 1, along seismic survey line 201, and shows that the Upper Permian Hopeman Sandstone and Triassic Burghead Beds should subcrop on the seabed up to 2.5km from the coastline. At this point of predicted Top Triassic subcrop, the extrapolated seismic survey Top Triassic horizon

is 230m below seabed. This shows that the likely actual subcrop is Lower –Mid Jurassic at this point. Cross-section 4 (Fig. 4.31) follows the same line as cross-section 2, along seismic line 203, and demonstrates that the onshore Upper Permian Hopeman Sandstone and Triassic Lossiemouth Sandstone should crop out 3.5km from the coastline. At the point of the Top Triassic seabed subcrop, the extrapolated seismic survey Top Triassic horizon is 110m below seabed. This local, well constrained, seismic data indicates that the actual subcrop is more likely to be Lower-Mid Jurassic at this point, comparable to the predicted pattern on cross-section 3. Cross-sections 1 - 4 further demonstrate the effect of uplift of the Lossie Peninsula on the outcrop pattern both onshore and offshore. In the absence of any fault movement offshore the present day Peninsula would expose Jurassic sediment, and the Permo-Triassic would remain more deeply buried. Consequently, 4 different sections all show that a down to the north normal fault is required in the near-offshore blind zone.

The scale of this fault displacement in the blind zone has been determined by calculating the discrepancy between the projected positions of the onshore and offshore Top Triassic horizons at specific locations within the blind zone. Along the trend of seismic line 201 (cross-sections 1 and 3; Figs 4.28, 4.30), the displacement between the two Top Triassic horizons is a mean of 227m, implying that this is the amount of throw on the blind zone fault (Appendix B). In the blind zone adjacent to seismic line 202 the mean displacement is 154m. Adjacent to seismic line 203 (cross-sections 2 and 4; Figs. 4.29, 4.31), mean fault displacement is 110m. Values of fault displacement decrease from survey line 201 in the west to survey line 203 in the east. Fault displacements quoted are for the average depth values calculated from seismic data, using 2000m/s and 3000m/s for seismic velocity. These values, and the extreme high value of 3600m/s from the Beatrice Field, show that although fault throw values change the sense of displacement down to the north, and wider structural setting, remain the same (Appendix B).

Further evidence that the discrepancy between the onshore and offshore data is a product of an extensional fault within the blind zone, which created relative uplift to the south, comes from the observation on survey line 204 of the previously discussed extensional fault downthrowing to the north, which is directly adjacent to the blind zone (Fig 4.18). This fault on line 204 is interpreted to propagate to the west, through the blind zone, accounting for the required displacement of the Top Triassic horizon. The observed displacement of the fault on survey line 204 is a minimum of 100m, following the pattern of decreasing fault

displacement moving from west to east within the blind zone. The absence of the fault on survey line 205, 4km further east, indicates that either the fault terminates at some point between survey lines 204 and 205, or is below seismic resolution. Many extensional faults display a characteristic fault displacement- length profile, with maximum displacement occurring in the centre (Cowie 1998). The observation that displacement on the proposed blind zone fault increases toward the west, suggests that the mid-point of the fault is either at survey line 201, or further west, suggesting a minimum fault length of 28km.

Identification of the fault on survey line 204 also allows the location of the fault to be constrained within the blind zone more accurately (Fig 4.24). The fault has been mapped through the blind zone along a trend of ENE-WSW, following the local and regional orientation of the Late Jurassic extensional structures within the basin. Shallow British Geological Survey borehole 71/18 encountered probable Lower-Mid Jurassic sediment at subcrop 3km northwest of Lossiemouth (Chesher 1971). This suggests that the fault lies to the south of this point, because the Triassic- Jurassic boundary must subcrop on the seafloor between the coastline and the fault, meaning there is only a small section of Jurassic subcrop within the footwall, if any. The shallow depth of the Top Triassic on line 204 makes direct fault history interpretation difficult, but the similar orientation to the series of Late Jurassic faults strongly suggests that the fault is Late Jurassic in age. However the observation that the fault reaches present day seabed means the possibility that the fault was subsequently re-activated to produce increased displacement cannot be ruled out.

The Spynie Fault onshore is an extensional structure downthrowing to the south. Displacement across the fault has been calculated by extrapolating the Top Triassic horizon along the profile of cross-sections 1 and 3 (Figs. 4.26, 4.27), from the edge of seismic line 201, ignoring the coastal exposures, through to the position of the most southern outcrop of the Upper Permian in the hanging wall of the Spynie Fault (Fig 4.33). Based upon thickness relations the Top Triassic is predicted to have been c.50m above the Upper Permian. The predicted Top Triassic outcrop from the seismic data is structurally higher than this position showing that net fault displacement is downthrow to the south. Using the projected Top Triassic positions shows that total displacement is 120m on the Spynie Fault, a similar figure to the 120-230m calculated displacement for the northern blind zone fault. Displacement across the Spynie Fault measured from the mapped outcrop of the Upper Permian in the Burghead Fault hanging wall is 50m. The throw on the Burghead Fault has been calculated

using the proven values of 60m for Upper Permian thickness, and 78m for Triassic thickness from the nearby Clarkly Hill borehole (Berridge and Ivimey-Cook 1967). The observation of a minimum of 3m vertical Triassic hanging wall exposure, and 2m footwall exposure on the foreshore, constrains maximum normal displacement to 135m, and minimum normal displacement to 63m, in the west of the Peninsula. This figure is in agreement with the calculation of fault magnitude from extrapolation of the footwall Top Triassic across the fault.

Along the profile of cross-sections 2 and 4 (Figs. 4.26, 4.27) extrapolation of the offshore seismic Top Triassic horizon shows that the offset across the Spynie Fault is 520m (Fig. 4.34 4). From extrapolation of the mapped Top Triassic from the Burghead Fault hanging wall, displacement across the Spynie Fault is 450m. The throw of the Burghead Fault along this profile is estimated to be 275m, based upon the mapped Top Triassic horizon in the footwall and hanging wall. These values indicate that displacement for the onshore Burghead and Spynie Faults increases toward the east, following an opposite trend to the Blind Zone Fault.

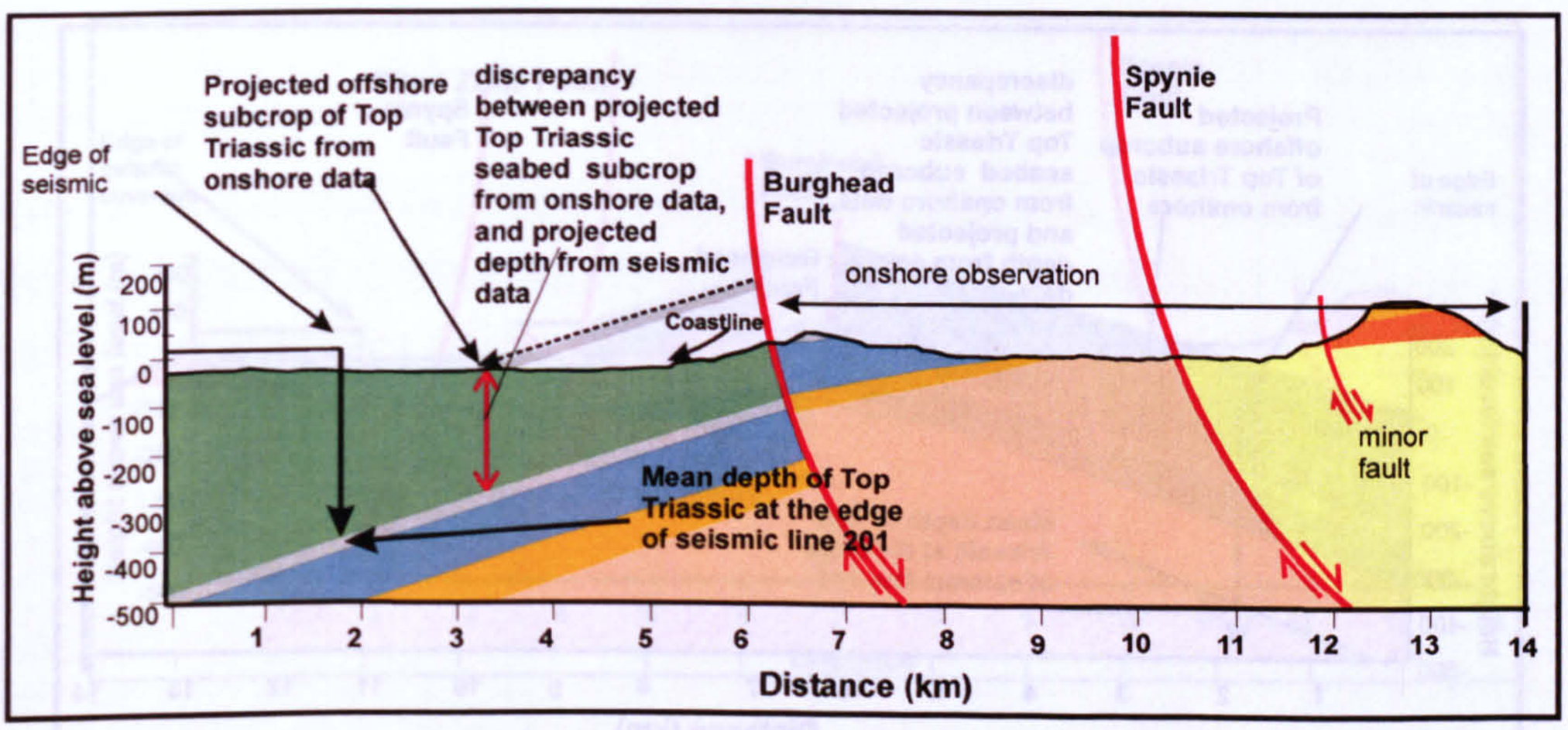


**Figure. 4.28. Cross-section along the profile of seismic line 201, showing the projection onshore of the offshore Top Triassic horizon. This reveals that the Lower-Mid Jurassic would be predicted to crop out onshore, north of the Burghead Fault. The observation of Upper Permian at outcrop on the coastline indicates that uplift occurs in the blind zone between the offshore seismic data and the coastline. Horizontal:vertical exaggeration 5:1. See Fig. 4.26 for section location.**

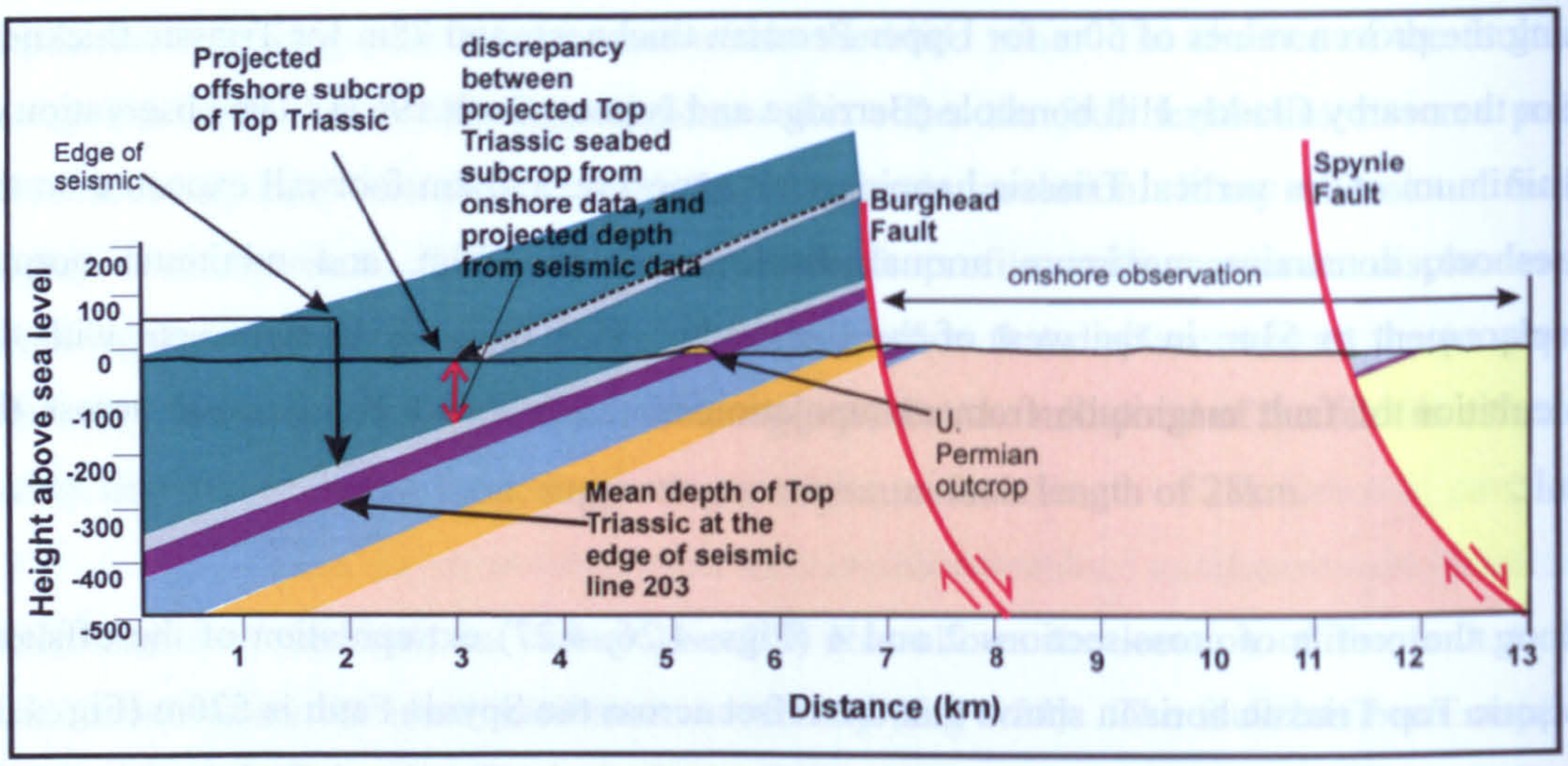


**Figure 4.29. Cross-section 2, along the profile of seismic line 203, showing the projection onshore of the offshore Top Triassic horizon. This shows that the Upper Permian would be predicted to outcrop onshore, north of the Burghead Fault. The observation of Devonian sandstone at outcrop on the coastline indicates that uplift has occurred between the edge of the seismic data and the shoreline. This uplift is less than along cross-section 1 where displacement in the blind zone appears to be greater. The Triassic thickens moving eastward into the basin. Scaled section, horizontal:vertical exaggeration is 5:1. See Fig. 4.26 for section location.**

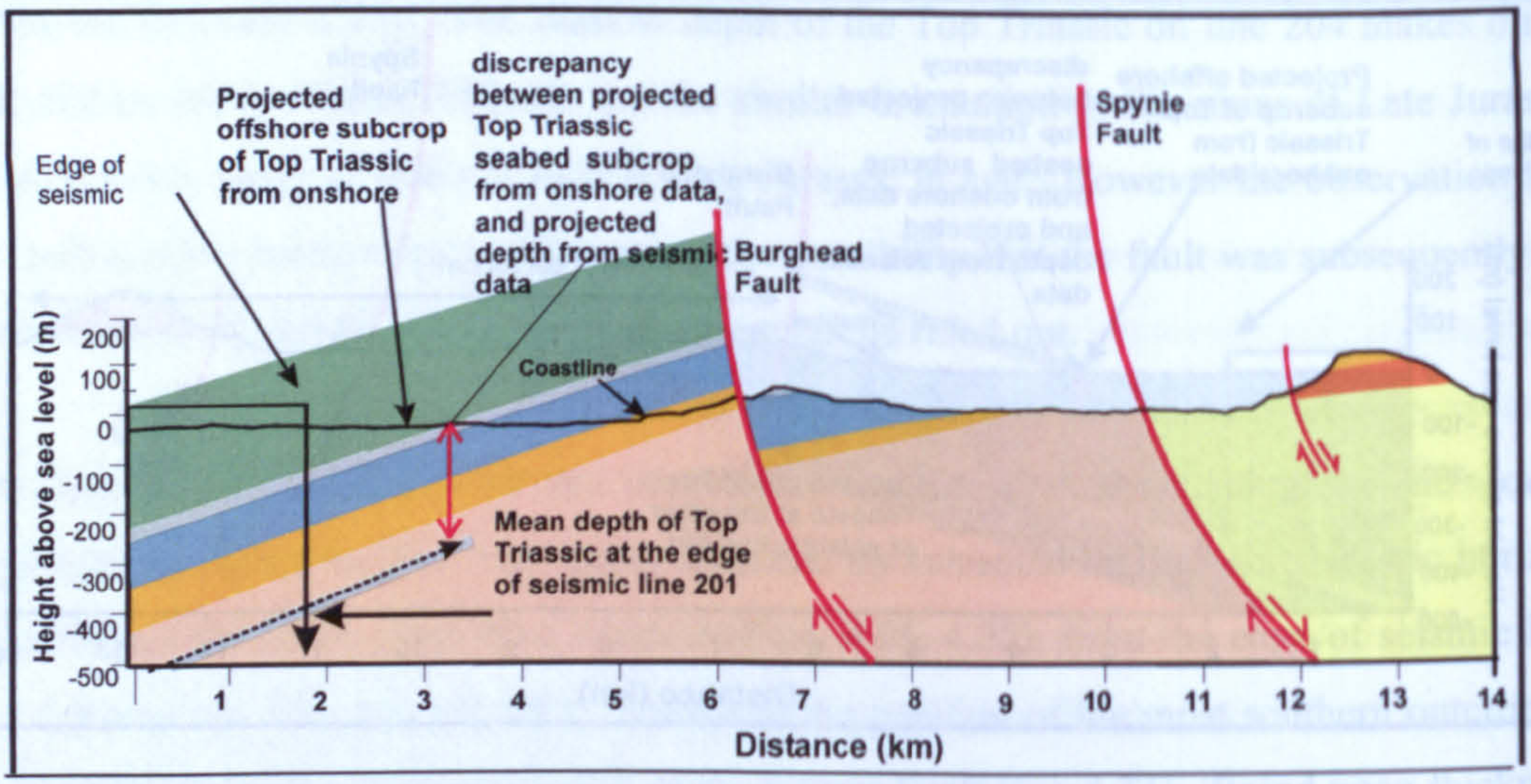


**Figure. 4.30. Cross-section 3, along the profile of seismic line 201, showing the projected subcrop offshore of the onshore Top Triassic horizon. The position of the onshore Top Triassic horizon is calculated from the known Permian and Triassic thickness and the location of the base Permian contact onshore, north of the Burghead Fault. Comparison with the extrapolated seismic Top Triassic horizon shows that at the point of onshore subcrop offshore the seismic horizon is 230m deeper. Scaled section, horizontal:vertical exaggeration is 5:1. See Fig. 4.27 for section location.**

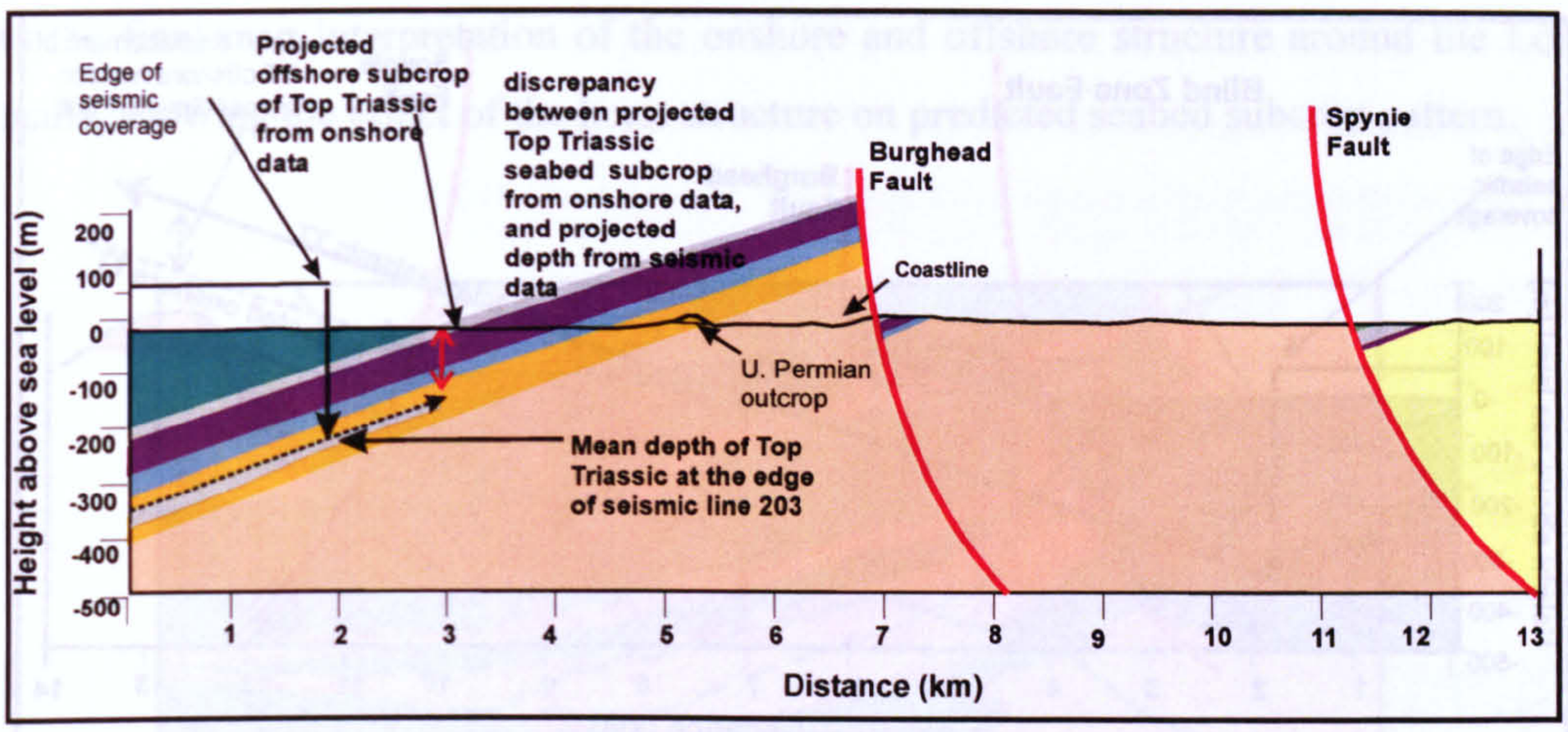


**Figure. 4.31. Cross-section 4, along the profile of seismic line 203, showing the subcrop offshore of the projected onshore Top Triassic horizon. The onshore Top Triassic horizon is calculated from known Permian and Triassic thicknesses and the mapped position of the base Permian within the Peninsula. This shows that at the point of seabed subcrop, local, well constrained seismic data indicates that the Top Triassic should be at a burial depth 120m greater. This offset is less than measured for cross-sections 1 and 4 further west, but still shows that the onshore exposures are structurally higher than the offshore continuation. Scaled section, vertical:horizontal 5:1. See Fig. 4.27 for section location.**

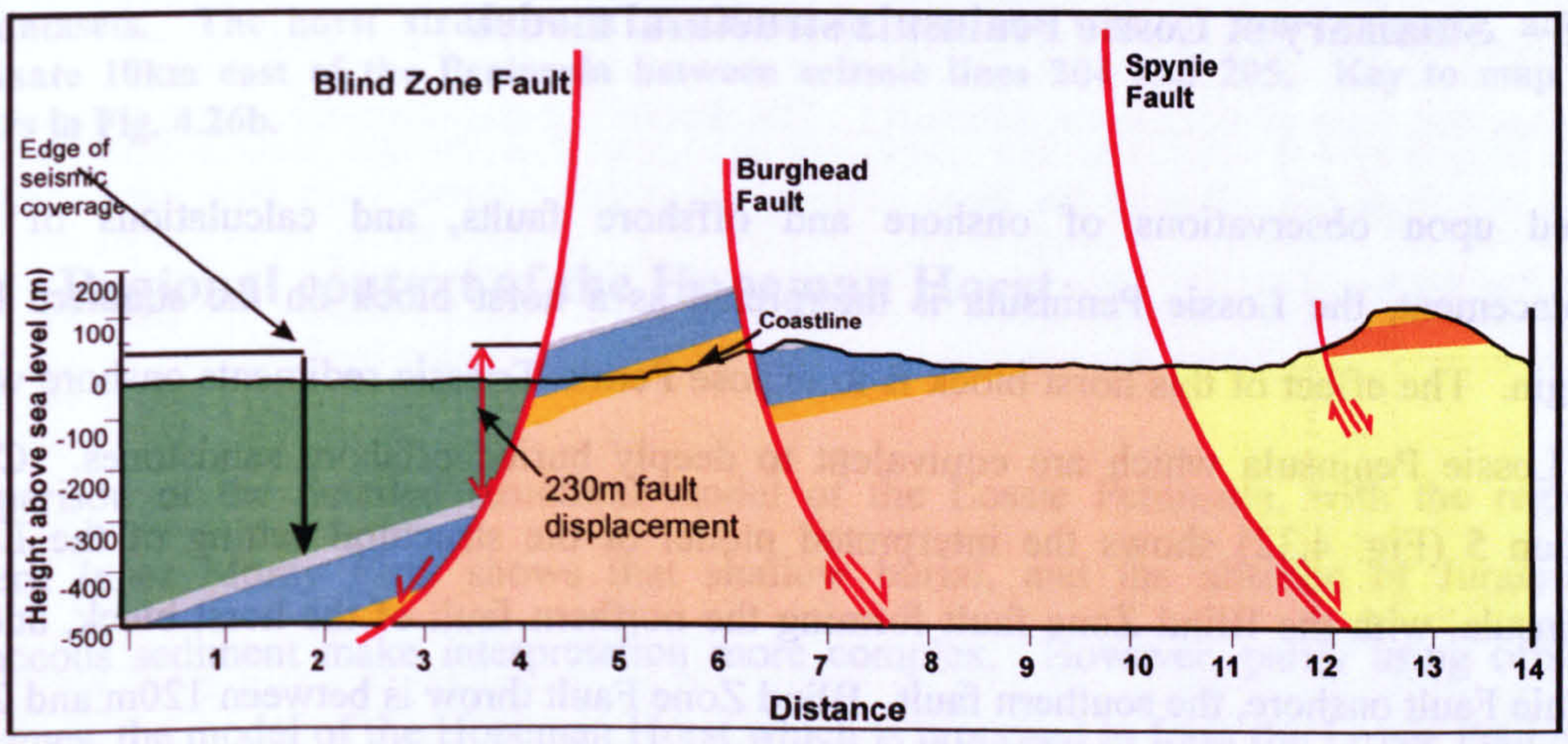


**Figure. 4.32.. Cross-section 5, along the profile of seismic line 201. The blind zone fault accounts for the calculated displacement between the onshore and offshore datasets. The fault downthrows to the north creating a structural horst block to the south. This horst is bound by the blind zone fault offshore and by the Spynie Fault onshore, creating a structural high 7km in width, and greater in length than the Lossie Peninsula. Scaled section, horizontal:vertical 5:1. See Fig. 4.34 for section location.**

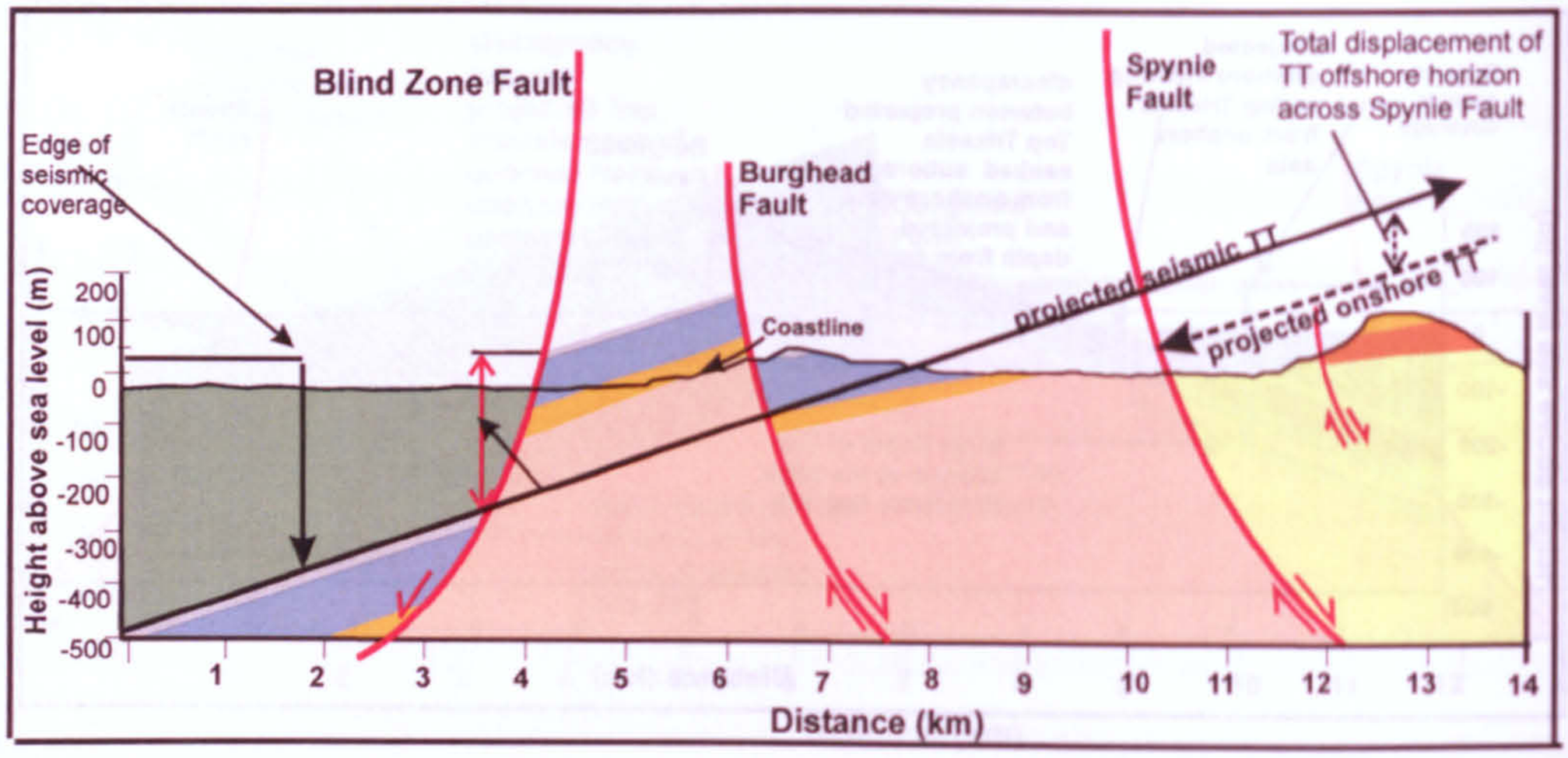


**Figure. 4.33. Cross-section 6, along the profile of seismic line 201. Extrapolation of the Top Triassic seismic horizon from offshore through to the hanging wall of the Spynie Fault, ignoring onshore relations. This shows the amount of displacement of the Top Triassic horizon by the horst-bounding Spynie Fault. The Spynie Fault has downthrown the Triassic by 120m. This is a similar value to the displacements recorded on the blind zone fault which marks the northern boundary of the Hopeman Horst. Scaled section, horizontal:vertical 5:1. Section location as cross-section 5, see Fig. 4.34.**

## 4.45 Summary of Lossie Peninsula structural model.

Based upon observations of onshore and offshore faults, and calculations of fault displacement, the Lossie Peninsula is interpreted as a horst block on the southern basin margin. The effect of this horst block is to expose Permo-Triassic sediments onshore within the Lossie Peninsula which are equivalent to deeply buried offshore sandstones. Cross-section 5 (Fig. 4.32) shows the interpreted model of the structural setting of the Lossie Peninsula, with the Blind Zone fault forming the northern fault of the horst block, and the Spynie Fault onshore, the southern fault. Blind Zone Fault throw is between 120m and 230m and maximum displacement on the Spynie Fault (restoring for effects of the Burghead Fault) is 450m. The Burghead Fault and minor Clashach Fault form intra-horst extensional faults. The Burghead Fault acts to downthrow the Permo-Triassic onshore by a maximum of 135m in the west of the Peninsula, increasing to 275m toward the east. The Clashach Fault throw is a maximum of 50m.

The horst block is named the Hopeman Horst in this paper, based upon the significant exposure of the Hopeman Sandstone on the coastline, within the structure. Figure 4.34

shows the final map interpretation of the onshore and offshore structure around the Lossie Peninsula, showing the effect of the horst structure on predicted seabed subcrop pattern.

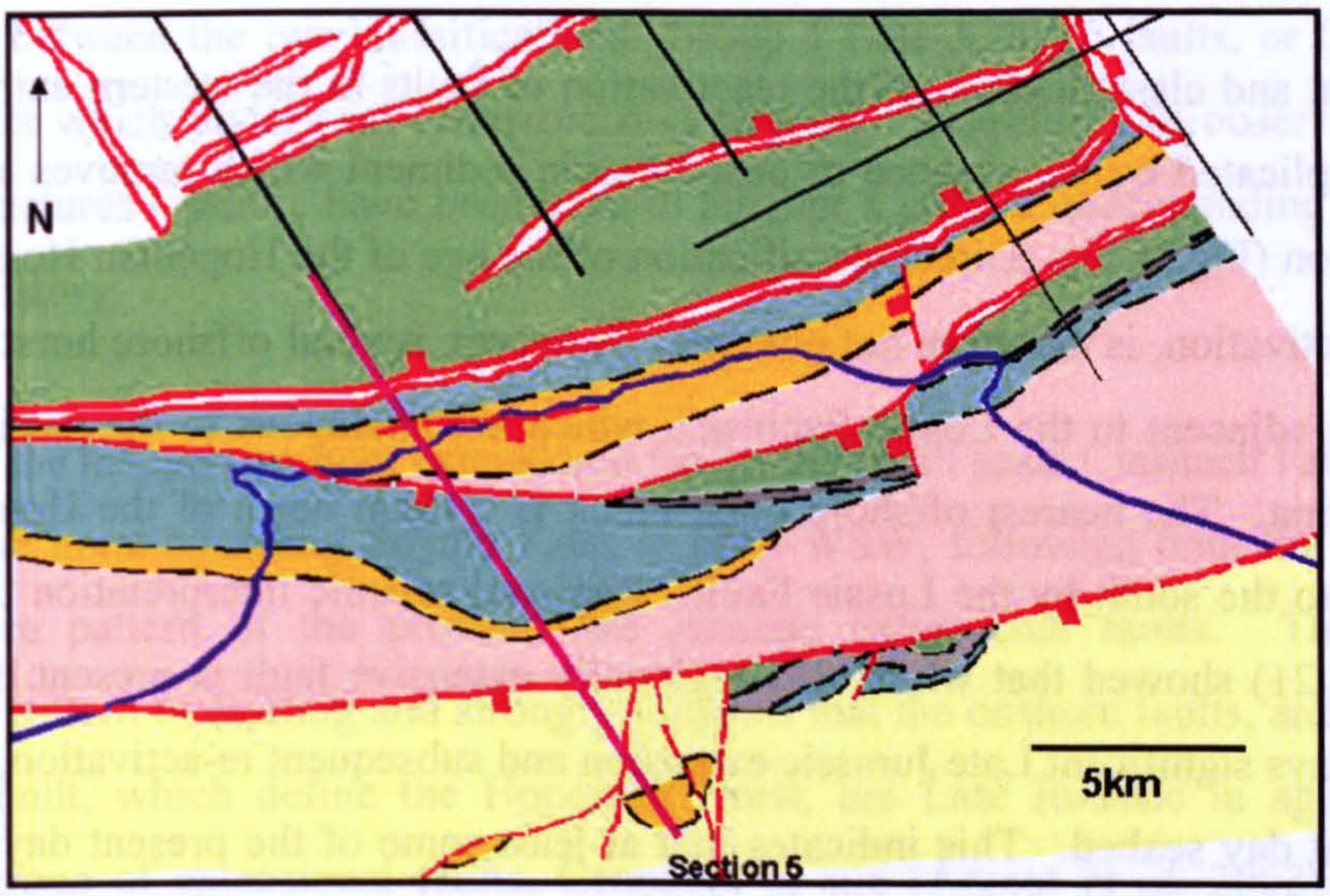


**Figure. 4.34. Geological map of the integrated onshore and offshore area of the Lossie Peninsula. The map reconciles onshore and offshore observations, and the integration of these two datasets. The horst structure is predicted to continue west of the Peninsula, and to terminate 10km east of the Peninsula between seismic lines 204 and 205. Key to map and colours in Fig. 4.26b.**

## 4.5 Regional context of the Hopeman Horst

Comparison of the detailed structural model of the Lossie Peninsula, with the regional western Inner Moray Firth shows that shallow burial, and the absence of Jurassic to Cretaceous sediment make interpretation more complex. However, partly using offshore analogues, the model of the Hopeman Horst which is proposed to form the Lossie Peninsula, can be still be examined within the wider structural context of the basin, and compared with the regional pattern of Late Jurassic extensional faults, as well as the basin horst and graben style.

### 4.51 Insight from analogous local structures

The regional western Inner Moray Firth basin is dominated by Late Jurassic faults which have either have remained inactive (Group 1) or have re-activated during subsequent

Cenozoic uplift (Group 2). A third category of extensional faults, initiated in the Cenozoic, were proposed by Argent *et al.* (2002) within the wider Inner Moray Firth basin, but were not identified within the western region of the Inner Moray Firth analysed in this study.

Identification, and classification, of the reactivation of faults in the western extremity of the basin is complicated by the absence of post-Jurassic sediment which removes any evidence of re-activation (Fig. 4.13). Direct classification of the age of the Hopeman Horst faults, and any fault reactivation, is therefore not possible. However, several offshore horst blocks exist in the region adjacent to the Lossie Peninsula which are analogous to the partially onshore Hopeman Horst. The nearest offshore horst block is c.10km north of the Hopeman Horst, and defined to the south by the Lossie Fault. Regional seismic interpretation of the Lossie Fault (Fig. 4.21) showed that where this regionally extensive fault is present deeper in the basin it displays significant Late Jurassic extension and subsequent re-activation, propagating to the present day seabed. This indicates that at least some of the present day scale of the associated horst was produced through Cenozoic age fault movement. In the majority of re-activated Late Jurassic faults this Cenozoic movement is expressed as minor extensional displacement, in comparison to the amount of Late Jurassic extension, but still acting to increase the scale of such horst structures. The amount of post-Jurassic re-activation can be measured from the offset of the Base Cretaceous reflector across each fault, and compared with the thickness of the Late Jurassic hanging wall sediment, to indicate the proportion of displacement caused by Late Jurassic extension and the proportion by Cenozoic re-activation (Fig. 4.21). For the Lossie Fault, 10 km northeast of the Lossie Peninsula, the Base Cretaceous displacement is <75m, compared to 700-1000m of Late Jurassic extension, demonstrating that fault re-activation had a small effect on total displacement, and thus the scale of the horst structure. The faults bounding the northern edge of the offshore horst block do not penetrate the Base Cretaceous showing that the re-activation is selective on an individual fault basis.

This demonstrates that Cenozoic re-activation of Late Jurassic faults did occur on one of the boundary faults of the nearest analogue structure within the local area of the Hopeman Horst. However that re-activation was selective and quantitatively small in comparison to the initial Late Jurassic extension.

## 4.52 Lossie Horst history

The absence of Late Jurassic sediment within the Hopeman Horst means it is not possible to differentiate between the two classifications: Group 1 Late Jurassic faults, or Group 2 Late Jurassic faults which underwent Cenozoic re-activation. Therefore the observations of the analogue structures offshore have been used to attempt a greater understanding of Hopeman Horst fault history.

The trend of the mapped onshore extensional faults, the small scale Clashach Fault, Burghead Fault, and the horst-bounding Spynie Fault is ENE-WSW, following both the regional and local offshore pattern of the proven Late Jurassic extensional faults. This is a well documented pattern of faulting and strongly suggests that the onshore faults, and the offshore blind zone fault, which define the Hopeman Horst, are Late Jurassic in age. A second significant group of extensional faults, Cenozoic in age (Argent *et al.* 2002) exist further offshore, but as well as not identified in the area analysed for this study, do not follow the characteristic ENE-WSW to NE-SW trend of the Late Jurassic faults. Offshore Late Jurassic faults that are analogous to the mapped onshore structures show no Upper Permian-Triassic or Lower-Mid Jurassic activity, indicating that the significant Late Jurassic extensional faults were not re-activated earlier faults. The offshore faults typically root into the Devonian basement, and the onshore Lossie Horst faults can also be seen to cut and juxtapose the Devonian basement.

The observed re-activation of the offshore Lossie Fault during Cenozoic uplift shows that fault re-activation, which is observed as more extreme in the deeper eastern areas of the basin (Argent *et al.*, 2002), also occurs in the shallow western areas (Fig. 4.21). However the amount of re-activation on the Lossie Fault is minor (<50-75m) compared with the amount of Late Jurassic extension (700-1000m) suggesting that on this regional scale fault (>60km) Cenozoic re-activation was not a significant factor in creating the present day horst structure. The lack of re-activation on the northern horst bounding faults further suggests re-activation was not necessary to create the significant horst block. Overall the typical range of Cenozoic offset on re-activated Late Jurassic faults, as measured by Argent *et al.* (2002), is 10-300m, significantly less than the maximum Late Jurassic displacement of up to 2.5km on the same faults. This basinwide data, combined with the local observations of the small scale of re-

activation on the Lossie Fault suggest that for the faults bounding the Lossie Horst, where relations cannot be deduced directly, that Late Jurassic extension alone could have been a valid mechanism for the creation of the present day horst structure.

The chosen model here is that the Hopeman Horst was created through Late Jurassic extension with no subsequent re-activation. Uplift to the present day position occurred as part of the process of Cenozoic basin-wide exhumation.

A simple burial curve has been devised for the Upper Permian Hopeman Sandstone within the Hopeman Horst, based upon known stratigraphic thickness offshore and the regional amount of uplift during Cenozoic exhumation (Fig. 4.35). Using the Upper Permian horizon means these values are a maximum for basinal sediment on the horst. This curve also takes into account constraints on burial depth from detailed petrographic observations on the state of compaction of the Hopeman Sandstone within the horst (Quinn *et al.*, in prep, Chapter 5).

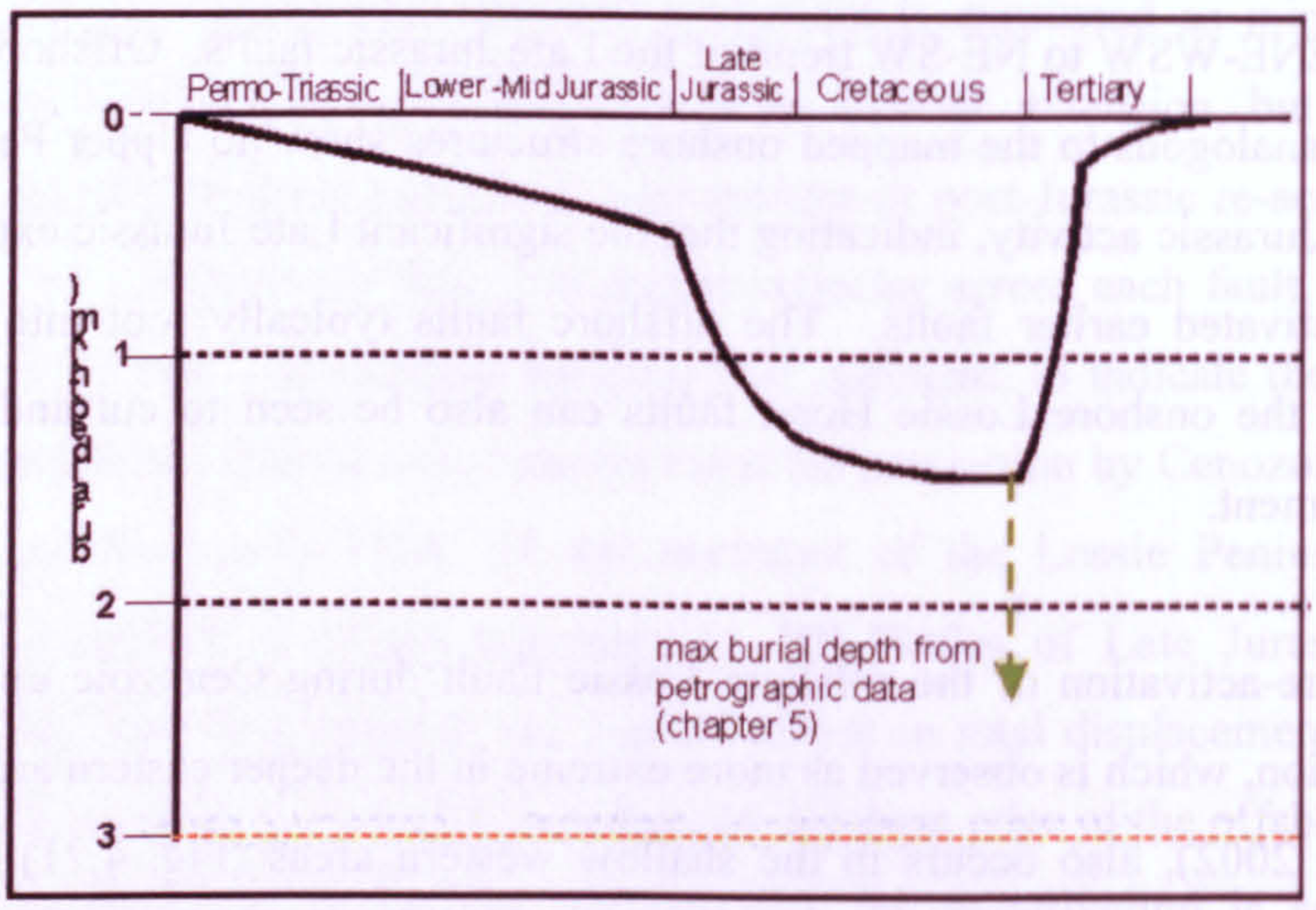


**Figure 4.35. A simple burial curve for the Upper Permian Hopeman Sandstone within the Hopeman Horst. The curve is based upon offshore thicknesses of Lower-Mid Jurassic sequences and estimates of basinwide burial associated with Late Jurassic extension. Uplift is constrained by published regional values. The maximum burial depth estimated from petrographic data is also shown (Quinn *et al.*, in prep., chapter 5)**

## 4.6 Discussion: Synthesis of onshore and offshore

### 4.61 Errors on stratigraphic projections

Consideration of the errors in the two datasets allows a level of confidence to be assigned to the model of the Hopeman Horst. Each of the two, onshore and offshore, datasets contains its own sources of potential inaccuracy in the projection of the Top Triassic horizon. Identification of the offshore seismic horizons is considered to be accurate based upon the high quality of the survey, tie-ins with the regional mapping of the surfaces, and the strength of the respective seismic reflectors. However the use of proxy values for seismic velocity, because of the lack of local deep wells, leads to uncertainty in the true depths, and dips, of the Top Triassic offshore. For the regional survey this was not particularly crucial because it was the general structural patterns of the basin which were analysed.

However, for the local offshore and onshore integration the absolute values of the Top Triassic are more important. To minimise this inaccuracy, the two synthetic values 2000 m/s and 3000 m/s were chosen to represent extremes below the Lower-Mid Jurassic interval velocity (3600m/s) in the nearest available well data (Beatrice Field). The difference in absolute depths caused by using 2000 m/s versus 3000m/s ranges from 50 to 95m (Appendices A and B), and dip values change by <3°. At shallower depths the difference between the two seismic velocities becomes less, so because this is a shallow burial case, the errors are small. Despite the possible range of true depths, cross-sections 1 – 4 (Figs. 4.28-4.31) show that because of the low values of stratigraphic dip, the subcrop/outcrop position is only altered by a maximum of 250m between the 2000m/s and 3000 m/s velocity values. As a proportion of the total length of the local offshore study area (15km north-south), this error equals <0.01%, and so is considered to be unimportant in the interpretation of the Lossie Peninsula as a horst block.

The difference in Top Triassic burial depths caused by using different seismic velocities does cause a change in the calculated Blind Zone Fault throw. As an example error using the two extreme synthetic velocity values, fault throw along cross-sections 1 and 3, for a 2000m/s seismic velocity, is 180m. For a seismic velocity of 3000m/s fault throw is 275m. Along the line of cross-sections 2 and 4, fault throw for 2000m/s is 87m, for 3000m/s 155m. Using the value of 3600m/s obtained from wells 11/30-1 and 11/30-2 produces an increased

fault throw at this position of 158m. These values demonstrate that if the true seismic velocity is closer to one of these extremes, the throw on the fault may be higher or lower than the mean values used in the paper, but that the down to the north sense of displacement along the fault does not change.

Inaccuracies on the projection of the onshore Top Triassic offshore, come from natural variation in thickness and dip values. The values of dip measured onshore were well constrained, from both the present fieldwork, and previous published mapped values. Dip values measured on the seismic data were also similar to those onshore. Using values of both 5° and 7° dip to project the Top Triassic offshore revealed a difference of 30m in seabed subcrop position, <0.01% of the of the length of the study area. Therefore uncertainty in dip value is not considered to introduce a significant error. Changes in thickness of the Permo-Triassic may move the projected position of seabed subcrop. However the observation throughout the basin that the Permian to Mid-Jurassic thickens gradually moving northward toward the Helmsdale Fault, 60km northwest, indicates that any thickness variation over the local scale of the blind zone is minimal.

### 4.62 Blind Zone Fault extent

The model of the Hopeman Horst assumes that one extensional fault accounts for the discrepancy between the onshore and offshore data. It is possible that two or more faults may cause this displacement. Comparison with the faults onshore reveals that the majority of displacement is taken up by individual faults relatively distant from each other. Minor faults, such as the Clashach Fault, may occur offshore but the limited displacement (<c.50m) means it would require 3 or 4 of these faults within the confined blind zone area to account for the calculated displacement. The observation on seismic line 204 of a single extensional fault downthrowing to the north further suggests the model of a single blind zone fault is the most likely.

### 4.63 Hopeman Horst fault age

Much insight into the timing of horst fault development has come from comparisons with local and regional structures offshore. The orientation of the two horst-bounding faults, and

Clashach and Burghead intra-horst faults, has been used to infer a Late Jurassic age. Within the offshore basin only one other significant series of faults, which are Cenozoic in age, have been proposed (Argent *et al.* 2002). This study found little evidence for such faults in the extreme western part of the basin studied, making it unlikely that the Hopeman Horst faults could belong to this series. The new extensional Cenozoic faults were produced during regional basin uplift toward the east. The occurrence in the eastern areas is speculated here to be due to the increased isostatic rebound resulting from deeper burial following tilting. The southern and western areas of the basin were structurally higher with 1-2km less overburden. It is proposed that this area was in isostatic equilibrium and so tectonically more stable, resulting only in re-activation of already existing faults.

Select Late Jurassic extensional faults were re-activated during the Cenozoic uplift. The simplest case model for the Hopeman Horst excludes any re-activation. Observations of the effects of such re-activation on analogous structures offshore in the basin shows it is typically minor compared to Late Jurassic extension. The most well-developed example of Cenozoic fault re-activation occurs on the Smith Bank Fault in the east of the Inner Moray Firth (Fig. 4.6). Total fault displacement is 2350m, formed by 750m of Cenozoic extension, and 1600m of Late Jurassic (Argent *et al.*, 2002, Underhill *et al.*, 2003) movement (Fig. 4.36). Cenozoic movement has therefore contributed 32% of present-day fault expression. The nearest offshore analogue to the Hopeman horst-bounding faults, the Lossie Fault, shows 50-75m Cenozoic extension as part of an overall extension of 700-1000m. Cenozoic extension is 7% of total fault displacement. Maximum calculated throw on the Blind Zone Fault, which bounds the Hopeman Horst to the north, is 230m. Using the scale relationship seen on the Lossie Fault of 7% of total fault length caused by re-activation, gives a hypothesised Cenozoic throw, if any, of 16m. If the scale of re-activation seen on the Smith Bank Fault occurred, this would lead to 69m of Cenozoic extension on the blind zone fault. This demonstrates that any re-activation would have caused only a minor difference to the present day scale of the Hopeman Horst.

The onshore Burghead Fault is interpreted as Late Jurassic in age, based upon its trend and position within the horst block. The observation of 69m of Lower Jurassic sediment south of the Burghead Fault shows that at least one phase of significant fault movement was post Triassic. The absence of local and regional variation of Permo-Triassic thickness variation across the Burghead Fault suggests it was not a pre-existing fault which was re-activated post

Lower Jurassic. The small scale Clashach Fault is only seen to cut the Permian in outcrop, but again the most probable age is Late Jurassic based on orientation and position within the Late Jurassic Hopeman Horst.

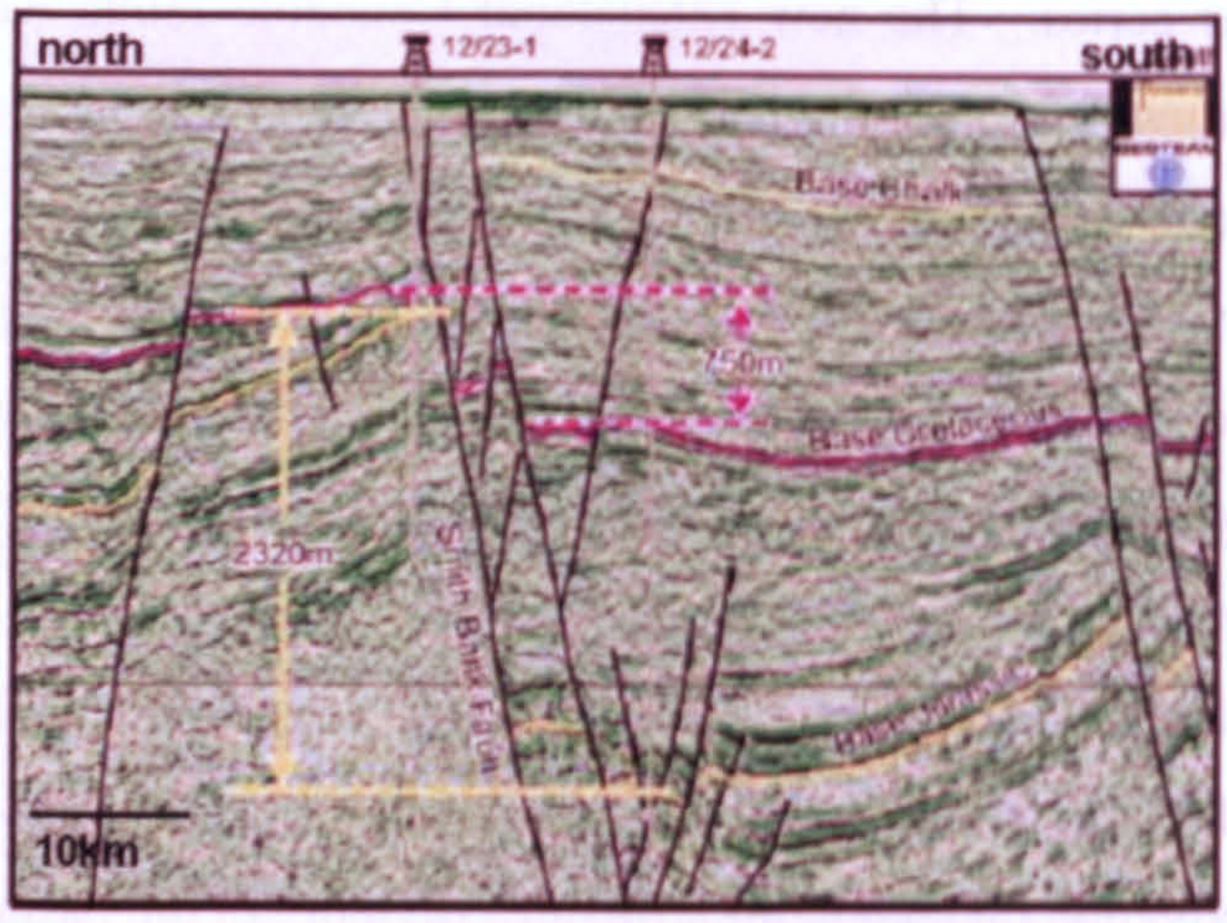


**Figure. 4.36. Cross-section across the Smith Bank Fault in the eastern Inner Moray Firth showing the best developed example of Cenozoic re-activation of a Late Jurassic extensional fault. Modified from Argent *et al.*, 2002.**

## 4.64 Hopeman Horst burial history

The Late Jurassic represents the major phase of Inner Moray Firth basin development, and deep sedimentary sequences offshore are dominated by thick (>3km) sections of Late Jurassic and younger sediment. The Permo-Triassic reaches a maximum thickness of >1km in the eastern extreme of the Inner Moray Firth (Glennie *et al.*, 2003), and thins toward the southern basin margin. Within the Hopeman Horst 200m of Permian to Lower Jurassic exists at present day, the Mid Jurassic having been removed. At the time of Late Jurassic basin extension sediment thickness within the area of the Horst was a minimum of 200m. However, assuming the presence of a Mid-Jurassic section comparable in thickness to the present day offshore, suggests Permian burial depth was 500m on the southern Moray Firth margin. The onset of extensional faulting led to the increased burial of much of the Permo-Triassic in the hanging walls of many faults. The combination of faults which led to the development of the Hopeman Horst is likely to have led to the preservation of shallow burial within the Horst block. Downthrow to the north by the blind zone fault assisted in producing the present day deeper burial of the Top Triassic on seismic data directly offshore. Thick

sequences of Late Jurassic, and younger, sediment in hanging walls are complimented by thinner sequences on footwalls where accommodation space was less. The structurally high Hopeman Horst is therefore unlikely to have ever been buried beneath a significant amount of Late Jurassic syn-faulting sediment. Further the position on the extreme southern basin margin is also likely to have precluded thick sequences of Late Jurassic sediment, and of younger Cretaceous sediment deposited during thermal subsidence following the Late Jurassic rifting. The Hopeman Horst is considered to have been a structural high which remained only shallowly buried throughout the extensional and post-extension phases of basin development.

## 4.7 Conclusions

- Western Inner Moray Firth basin development principally occurred through Late Jurassic extensional faulting, creating a broad half-graben basin hinged on the Helmsdale Fault to the northwest. A number of Late Jurassic half-graben features were created through movement on ENE-WSW to NE-SW oriented normal faults, which acted to deeply bury the pre-rift Permo-Triassic sediments. The presence of Late Jurassic horst blocks has created a number of structural high points, within which the Permo-Triassic sediments are at a relatively shallow burial depth.

- During the Cenozoic, uplift caused the extensional re-activation of selective Late Jurassic faults, producing increased amounts of displacement on individual structures. Such structures can be identified directly where the Base Cretaceous sediment is still in place at present day, and is cut by the fault plane. Regional tilt to the east has removed much of the post-Jurassic sediment in the west of the basin and produced seabed subcrop of the Base Cretaceous, making direct interpretation of fault history in the extreme south and west of the basin difficult.

- Faults can be divided into two categories in the western Inner Moray Firth. Group 1 are Late Jurassic normal extensional faults. Group 2 are Late Jurassic normal extensional faults that have been re-activated in the Cenozoic.

- The Lossie Peninsula contains the only exposures within the basin of Permo-Triassic sediment, which remains deeply buried offshore. The Top Triassic Stotfield Chert is

well exposed, and forms the most prominent and widespread seismic reflection horizon within the basin. Sub-seismic to seismic scale extensional ENE-WSW Late Jurassic faults are present within the Peninsula.

- Integration of seismic survey data surrounding the Lossie Peninsula, with the onshore exposure data, has shown that the onshore exposures are structurally higher than the more deeply buried Permo-Triassic offshore. This integration allows the Lossie Peninsula to be interpreted as a horst block. This horst is bound to the north by an inferred fault in the blind zone between seismic and onshore data with mean throws of 110-230m, and to the south by the Spynie Fault with a maximum 450m throw. The major Burghead, and minor Clashach, faults are intra-horst structures. The onshore Burghead Fault can be directly identified offshore on seismic line 204 to the east of the Peninsula and onshore maximum displacement varies between 135 and 275m. The Clashach Fault throws a maximum of 50m. The horst block is named here the Hopeman Horst. The new map is in figure 4.34 and in cross-section in figure 4.32.

- The absence of post-Jurassic sediment within the Hopeman Horst means that the interpretation of fault history focuses upon observations of analogue structures. The nearest offshore analogue horst block is bound by the Lossie Fault, which developed through 700-1000m of Late Jurassic extension and was re-activated in the Cenozoic with a further 50-75m extension. Combined with regional observations this demonstrates that Late Jurassic extension is a valid mechanism for production of the Hopeman Horst, and any Cenozoic re-activation was likely to have produced only minor extension.

- The area of the Hopeman Horst is likely to have been at <1km burial during Late Jurassic extension. The Horst remained as a structural high throughout subsequent basin development and was not deeply buried, a comparable structural history to analogous offshore horst structures.

# References


**Argent, J.D., Stewart, S.A. and Underhill, J.R., 2000.** Controls on the Lower Cretaceous Punt Sandstone Member, a massive deep-water clastic deposystem, Inner Moray Firth, UK North Sea. Petroleum Geoscience, 6, p. 275-285.

**Argent, J.D., Stewart, S.A, Green, P.F. and Underhill, J.R., 2002.** Heterogeneous exhumation in the Inner Moray Firth, UK North Sea: constraints from new AFTA and seismic data. Journal of the Geological Society of London, 159, p. 715-729.

**Benton, M.J., and Walker, A.D., 1985.** Palaeoecology, Taphonomy, and Dating of Permo-Triassic Reptiles from north-east Scotland. Palaeontology, 28,p. 207-234,

**Benton, M.J., 1977.** The Elgin Reptiles. The Moray Society, Elgin.

**Benton, M.J., 1983b.** The age of the rhynchosaur. New Scientist, 98, p.9-13.

**Benton, M.J., 2003.** Personal Communication. On the age of the Lossiemouth Sandstone Formation.

**Berridge, N.G. and Ivimey-Cook, H.C., 1967.** The Geology of a Borehole at Lossiemouth, Morayshire. Bulletin of the Geological Survey of Great Britain, 27, p. 155-169.

**Chesher, J.A. 1971.** British Geological Survey Inner Moray Firth borehole reports 71/15, 71/18, 71/21. BGS Library, Murchison House, Edinburgh.

**Clark, N.D.L., 1999.** The Elgin Marvel: a scientific investigation into a fossil that isn't there! *In*: (Bennett, S (ed)) New Fossil Evidence: Moray and the North East. The Moray Society. 30-33

**Cowie, P.A., 1998.** A healing-reloading feedback control on the growth rate of seismogenic faults. Journal of Structural Geology, 20, 8, p.1075-1087.

**Clemmensen, L.B., 1987.** Complex star dunes and associated aeolian bedforms, Hopeman Sandstone (Permo-Triassic), Moray Firth Basin, Scotland. In: Desert Sediments: Ancient and Modern (ed. Frostick, L, and Reid, I.). Geological Society of London Special Publication, 35, p. 213-231.

**Edwards, H.E., Becker, A.D. and Howell, J.A., 1993.** Compartmentalization of an aeolian sandstone by structural heterogeneities: Permo-Triassic Hopeman Sandstone, Moray Firth, Scotland. In: Characterization of fluvial and aeolian reservoirs (ed. North, C.P.). Geological Society of London Special Publication, 73, p. 339-365.

**Frostick, L., Reid, I, Jarvis, J. and Eardley, H., 1988.** Triassic sediments of the Inner Moray Firth, Scotland: early rift deposits. Journal of the Geological Society of London, 145,p. 235-248.

**Glennie, K.W. and Buller, A.T., 1983.** The Permian Weissliegend of NW Europe: the partial deformation of aeolian sand dunes caused by the Zechstein transgression. Sedimentary Geology, 35, p. 43-81.

**Glennie, K.W., Higham, J., and Stemmerik, L., 2003.** Permian. *In*: The Millenium Atlas: petroleum geology of the central and northern North Sea. (eds. Evans, D., Graham, C., Armour, A., and Bathurst, P.) The Geological Society of London, p. 91-103.

**Gordon, G., 1859.** On the geology of the lower or northern part of the province of Moray; its history, present state of inquiry, and points for future examination. Edinburgh New Philosophical Journal, 9, p.241-245.

**Haszeldine, R.S., Samson, I.M., Cornford, C., 1984.** Dating diagenesis in a petroleum basin: a new fluid inclusion method. Nature, 307, p.354-357.

**Huxley, T.H., 1859.** On the *Stagonolepis robertsoni*: and on the recently discovered footmarks in the sandstones of Cummingstone. Ibid. p.440-460.

**Linsley, P.N., Potter, H.C., McNab, G. et al., 1980.** The Beatrice field, Inner Moray Firth, UK North Sea. In: Giant oil and gas fields of the decade 1968-1978. American Association of Petroleum Geologists Memoir 30, p.117-129.

**Mackie, W., 1897.** The sands and sandstones of eastern Moray. Transactions of Edinburgh Philosophical society, 7, p.148-172.

**Martin, J.C, 1837.** On the Geology of Morayshire. Prize-essays and Transactions of the Highlands and Agricultural Society of Scotland, 5, p.417-440.

**Naylor, H., Turner, P., Vaughan, D.J. and Fallick, A.E., 1989.** The Cherty Rock, Elgin: A petrographic and isotopic study of a Permo-Triassic calcrete. Geological Journal, 24, p. 205-221.

**Ogilvie, S.R. and Glover, P.W.J., 2001.** The petrophysical properties of deformation bands in relation to their microstructure. Earth and Planetary Science Letters, 193, no, 1-2, p. 129-142.

**Peacock, J.D., Berridge, N.G., Harris, A.L. and May, F., 1968.** The Geology of the Elgin District. HMSO, Edinburgh.

**Quinn, O.F., Haszeldine, R.S., and Dixon, J.E., 2004.** Porosity and Permeability loss around faults through shallow burial quartz cementation in an aeolian sandstone. In preparation. Chapter 5.

**Quinn, O.F., Haszeldine, R.S. and Dixon, J.E., 2004.** Fault-related quartz cementation: Insights from isotope microanalyses and fluid inclusions. In preparation. Chapter 6

**Roberts, A.M., Price, J.D. and Badley, M.E., 1989a.** Discussion on Triassic sediments of the Inner Moray Firth: early rift deposits (Frostick *et al.*1988). Journal of the Geological Society, London, 146, p.361-362.

**Thomson, K. and Underhill, J.R., 1993**. Controls on the development and evolution of structural styles in the Inner Moray Firth Basin. *In*: Petroleum Geology of Northwest Europe: Proceedings of the 4th Conference (ed. Parker, J.R.),Geological Society London, p. 1167-1178.

**Underhill, J.R., 1991**. Implications of Mesozoic-Recent basin development in the western Inner Moray Firth, UK. Marine and Petroleum Geology, 8, p. 359-369.

**Underhill, J.R., Argent, J., Stewart, S., Green, P. and Quinn, O.F., 2003.** The role of Cenozoic normal fault activity in controlling petroleum prospectivity in the Inner Moray Firth basin, UK North Sea. 6th Petroleum Geology Conference: Northwest Europe and Global Perspectives, London, 2003.

**Wallace, T., 1901.** The Sandstones of the Moray Firth Area, and a short note on Northern Geology. Transactions of the Inverness Scientific Field Club, 6, p.119-139.

**Watson, D.M.S. and Hickling, G., 1914**. On the Triassic and Permian Rocks of Moray. Geological Magazine, 1, p. 399-402.

This page left blank

# Chapter 5.

This next paper presents results of the field and petrographic investigation into the fault-related quartz cementation in the Hopeman Sandstone, focussing upon the outcrop faults that form part of the structural setting documented in chapter 4. The thesis moves from the macro-scale regional setting towards the meso and micro scale relations between the sandstone and the structures, describing in detail the fault-related quartz cementation. Field observations are combined with detailed petrographic analysis of sandstone thin sections, permeability measurements and manipulation of point count data to unravel the extent of the unusual quartz cementation, and its effect on porosity and permeability evolution. The implications of the results for deeply buried equivalent sandstones, which may be hydrocarbon reservoirs, are discussed and use of the statistically significant petrographic dataset obtained here, for subsurface modelling is also covered. The previous structural paper presented in chapter 4 allows the scale of the outcrop relations to be considered within the overall local and basinal context. The detailed petrographic work in this chapter is built on in the next chapter through micro-scale geochemical analysis to unravel the sources and processes of cementation.

# Porosity and Permeability loss around sand:sand faults through shallow burial quartz cementation in an aeolian sandstone.

Oliver F. Quinn, R. Stuart Haszeldine and J.E. Dixon

## Abstract

Two extensional cataclastic faults crop out within the Upper Permian aeolian Hopeman Sandstone on the southern margin of the Inner Moray Firth Basin, UK North Sea. The Clashach Fault is a minor, sub-seismic scale structure (throw <50m) and the Burghead Fault is a larger scale feature (throw>100m).

Shallow burial (<1.25km) quartz cementation occurs asymmetrically across both fault planes. Authigenic quartz is localised in footwall sandstones. Hanging wall sandstones contain only minor amounts (<5%) of uniformly distributed quartz cement. The Clashach Fault footwall displays 2 differing cementation patterns. In the zone 0.5 to 13.8m from the fault plane, early carbonate cement, which has subsequently dissolved, occluded pore space and controlled quartz cement volume. The amount of quartz cement broadly increases with distance from the fault through this zone, as the volume of carbonate cement decreased. From 13.8 to 31.7m authigenic quartz volume decreases in a linear trend from a maximum of 26.5% at 13.8m, to 9% at 31.7m, and <5% at 42m. The larger scale Burghead Fault displays a simplistic pattern of decreasing quartz cement from a maximum of 29% at 0.5m from the fault plane to 24.5% at 13m distant, which is the edge of exposure. Values of quartz cement in the footwall of the Burghead Fault are predicted to fall along a linear trend to background levels of <5% over an 80m wide zone. Quartz cement cross-cuts facies and bedding surfaces.

Porosity and permeability are inversely related to quartz cement. In hanging wall sandstones mean porosity is 24.5%. In the Clashach Fault footwall zone from 0.5-13.8m porosity is inversely related to quartz cement volume within individual samples. In the zone from 13.8 to 31.7m porosity increases along a linear trend with increasing distance from the fault plane, from a minimum of 10% at 13.8m, to 18.6% at 31.7m. Footwall samples at 40-44m distant have porosities of 25%, comparable to hanging wall samples. Porosity through the Burghead Fault footwall broadly increases from a minimum of 2.3% at 0.5m from the fault plane to 6.1% at 13m distant. Permeability in uncemented hanging wall sands is 100-1000mD at Clashach Fault. Cemented footwall sandstone at both faults has a heterogeneous distribution of reduced permeability between 0.1-10mD. Both the extent of the cement zone, and decrease in porosity and permeability, scale positively with fault throw.

Footwall quartz cement is present at 3 exposures of the 2 faults along 5km of coastline suggesting the cementation is regionally extensive. Zones of early carbonate cement were present in 2 localities creating small, local, heterogeneous higher porosity zones. The Hopeman Sandstone acts as an analogue to hydrocarbon reservoir sandstones showing that fault-related quartz cementation can act to reduce porosity and permeability in fault-bound reservoirs at shallow burial. The subseismic Clashach Fault has a cementation zone 0.8 x fault displacement, the seismic scale Burghead Fault 0.5 x displacement.

## 5.1 Introduction

The potential of a sandstone to act as an economic hydrocarbon reservoir depends in part on the values and distribution of porosity and permeability. Numerous studies have successfully attempted to unravel, and quantify, the processes of burial diagenesis which modify porosity and permeability, with the ultimate aim of developing predictive models of reservoir quality (e.g. Haszeldine *et al.*, 1984, Giles *et al.*, 1992, Lander and Walderhaug 1999).

During sandstone burial, compaction and cementation act to destroy and occlude pore space and reduce permeability. Paxton *et al.* (2002) showed, from a global dataset, that in uncemented quartzose sandstones with rigid grains, mechanical compaction rapidly reduces porosity to about 28% during burial to 1500m, and slowly to a minimum of 26% between 1500 and 2500m. Porosity reduction below 26% is caused by the onset of chemical compaction, causing detrital grain dissolution and cementation. Further reduction of reservoir quality in quartzose sands is typically dictated by the precipitation of quartz cement, which occurs in significant quantity in many reservoirs at a burial temperature of >70°C, equivalent to a burial depth of 2.7km in the North Sea (e.g. Giles 1997, Bjorlykke *et al.*, 1992, Worden and Morad 2000). Lander and Walderhaug (1999) published a successful predictive computer model (EXEMPLAR™) of quartzose sandstone porosity evolution. This model integrated burial, compaction and quartz cementation to estimate porosity, and assumed quartz cementation is an internal, temperature controlled, process. Although the model is useful in predicting porosity in many clean sandstone reservoirs where quartz cement has been produced by closed system isochemical diagenesis, it cannot account for advection of externally derived diagenetic cements where simple kinetic rules need not apply.

To evaluate the hydrocarbon geology of individual reservoirs, the focus progressively moves to an increasingly mature and detailed stage. Consequently, reservoir models require increasingly detailed data, concerning porosity and permeability distribution. Such data may come from existing wells and/or generic models. However localised porosity and permeability anisotropic barriers, which may compartmentalise a reservoir, are difficult to account for. Intra-reservoir faults can be a major low permeability feature, and much recent work has quantified the permeability characteristics of seismic scale (>50m throw) to sub-

seismic scale (<50m throw) faults (e.g. Antonellini and Aydin 1994a,b, Shipton *et al.*, 2002). Such data can be input into reservoir models. Less well accounted for is the effect of any exotic cementation associated with such faults, which can act to reduce porosity and permeability in a heterogeneous manner, and is difficult to predict. Difficulties identifying such low porosity and permeability cementation features stem from the small scale of such features, perhaps less than 100m laterally around individual structures. Seismic reflection data is unable to detect such diagenetic features, and oil wells typically avoid low permeability fault zones. Accordingly, where such cementation is suspected to occur, little quantitative data exists for estimation of the effect on reservoir quality and input into both static and dynamic reservoir models.

On a larger scale, regional, basin-specific, porosity loss curves have been compiled for hydrocarbon basins using measured porosity data from existing wells, such as the North Sea, and combined with local subsurface data to produce profiles of depth-porosity for individual basins which demonstrate the effects of compaction and cementation. Processes which cause a deviation from this general trend, such as early hydrocarbon charge preserving porosity, or shallow burial cements, need to be characterised in order to predict their occurrence and quantify their importance. Shallow burial fault cementation events around faults may also affect this regional trend in specific structural and/or basin settings.

This paper examines an outcrop sandstone, which forms an analogue to hydrocarbon reservoirs at depth, and quantifies the effects on porosity and permeability of an unusual shallow burial quartz cement, which is spatially associated with normal fault structures. In contrast to most subsurface studies, the extent of 3-dimensional exposure around the fault planes has allowed an extensive, statistically significant, sample set to be obtained. Petrographic techniques and fieldwork have been used to unravel meso (field) scale cementation. Porosity and permeability patterns around cataclastic normal fault planes give insight into the scale and effects of such cementation. The paper also aims to serve as a benchmark database combining compaction, cementation, porosity and permeability measurements for a type-example fault associated cement. The case study can be utilised for input into hydrocarbon reservoir models of similar subsurface sandstones, which are thought to contain significant shallow and/or fault associated cements and which cannot be directly quantified.

## 5.2 Geological setting

The Inner Moray Firth (IMF) basin forms the western arm of the trilete North Sea rift system (Fig. 5.1 inset). The basin has a broad half-graben expression, 50km wide and 5km deep, developed principally through a number of Late Jurassic extensional faults hinged on the Helmsdale Fault to the west (Fig. 5.2). The western area of the basin underwent early Tertiary uplift, imparting a 2-3° regional eastward dip. Estimates of basin exhumation vary between 750m (Roberts *et al.* 1990) and 1km (Underhill 1991a). The Hopeman Sandstone Formation crops out along 8km of the southern basin margin, along the southern Moray Firth coastline (Fig. 5.1). The Formation is visible in wave-cut platforms, coastal cliffs 5-25m high, and in adjacent building stone quarries. Upper Permian in age (Benton and Walker 1985) and stratigraphically equivalent to the hydrocarbon bearing Weissliegend Sands of the Southern North Sea (Glennie and Buller 1983), the Formation is part of an exposed sequence of Permo-Triassic sandy sediments (Fig. 5.3). The Hopeman Sandstone unconformably overlies the lithologically similar Devonian Old Red Sandstone, which comprises the 'basement' of the IMF. The Hopeman is succeeded in a conformable sequence onshore by Triassic fluvial sands, a Top Triassic chert and Lower Jurassic sands and marls. The Top Triassic Stotfield Chert is a prominent seismic reflector within the offshore basin. The Hopeman Sandstone is composed of stacked transverse dune facies sands (Glennie and Buller 1983) interspersed with contorted sand beds, produced through soft-sediment liquefaction shortly after deposition (Peacock 1966, Clemmensen 1987). Two cataclasite faults are well exposed onshore, one on the coast and within the working Clashach Quarry (Fig. 5.3) and the other along the foreshore at Burghead (Fig. 5.3).

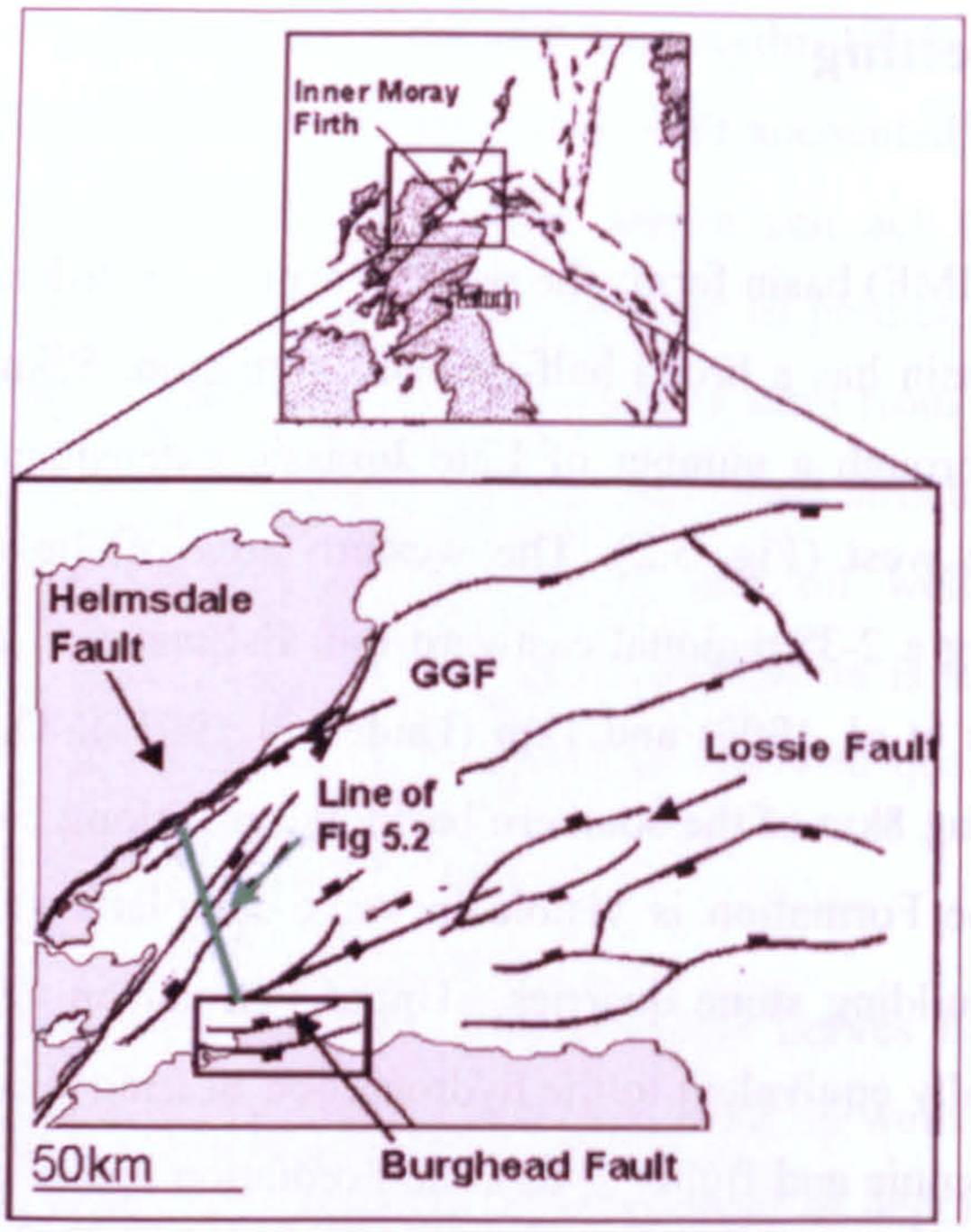


**Figure 5.1. Location of the Inner Moray Firth Basin on the extreme western arm of the trilete North Sea rift system (inset). Major structural features within this principally Late Jurassic extensional basin are visible along with the location of the onshore exposure of the Hopeman Sandstone on the southern basin margin. Boxed study area enlarged in Fig. 5.3. GGF = Great Glen Fault.**

The minor, sub-seismic scale Clashach fault is exposed along the length of the east-west face of Clashach Quarry (Plate 5.1) and in the adjacent Clashach Cove some 150m west (Plate 5.2). The fault trends 078-085°, with a mean dip in both localities of 75° south. Both the hangingwall and footwall consist of Hopeman Sandstone and in both outcrops around 10m of vertical exposure is visible. The proven onshore thickness of the Hopeman Sandstone is 60m (Berridge and Ivimey-Cook, 1967) restricting maximum throw to 50m. A poorly developed damage zone surrounds the main slip face composed of a number of rare, isolated deformation bands present up to 10m from the main fault. Poorly developed, the deformation bands display mm-scale slip and are separated by 1-4m of undeformed sand, the frequency of occurrence decreasing with increasing distance from the fault. The pervasively cemented and indurated footwall sands show near vertical jointing with regular 1-1.5m spacing.

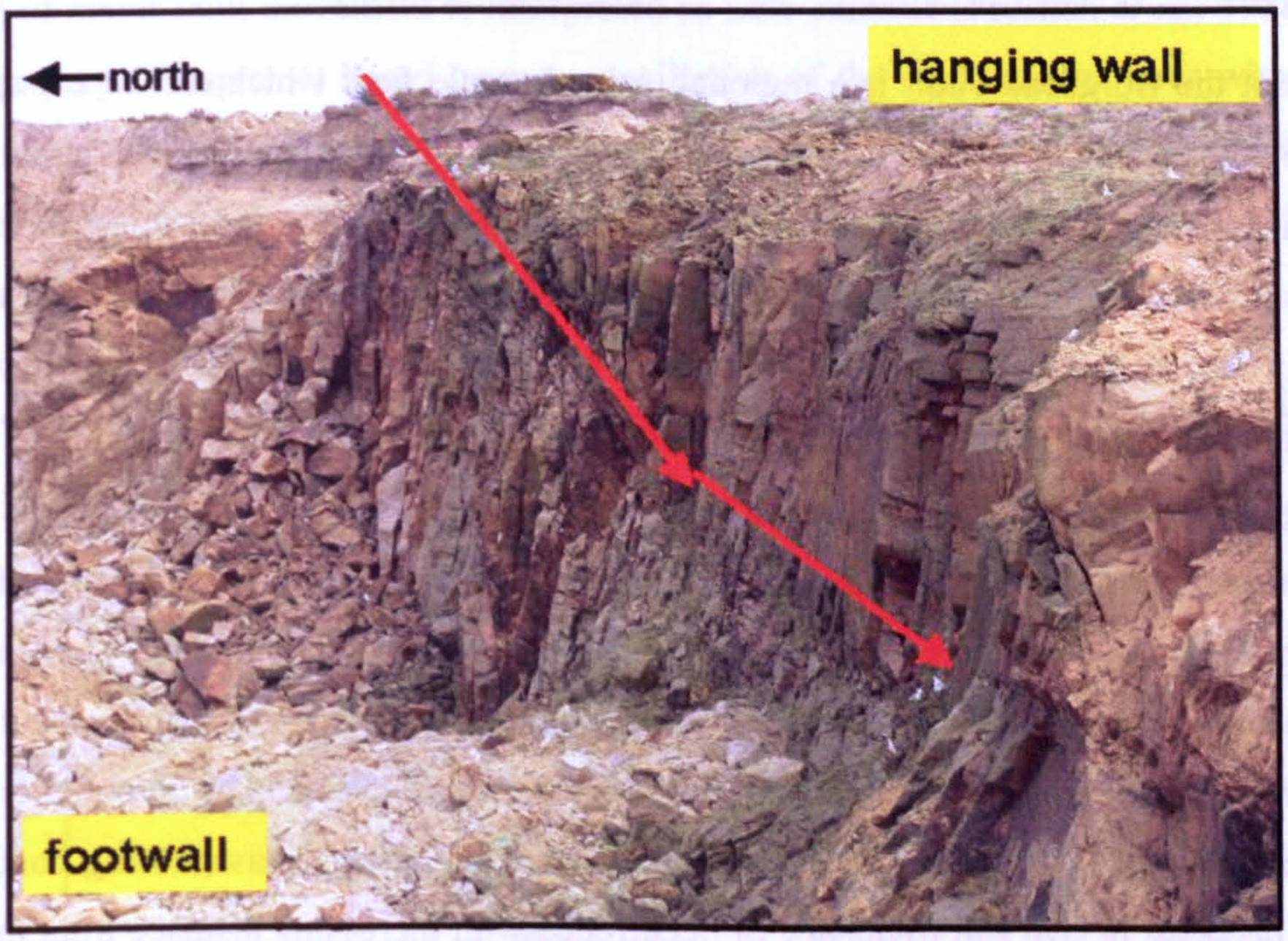


**Plate 5.1. Clashach Fault exposed in the Clashach Quarry, c.150m east of Clashach Cove (Plate 5.2.) (location on Fig. 5.3) where the Clashach Fault is also exposed. The main sub-seismic (<50m throw) fault slip face is highlighted. Only isolated single deformation bands surround the fault. Quarrying has removed most of the silicified footwall sandstone, prized as decorative building stone. Less well cemented hanging wall sands are unquarried as colour variations caused by the quartz cementation in the footwall, and the poorer state of lithification of the hanging wall make it less desirable. View looking east along quarry face for c.100m.**

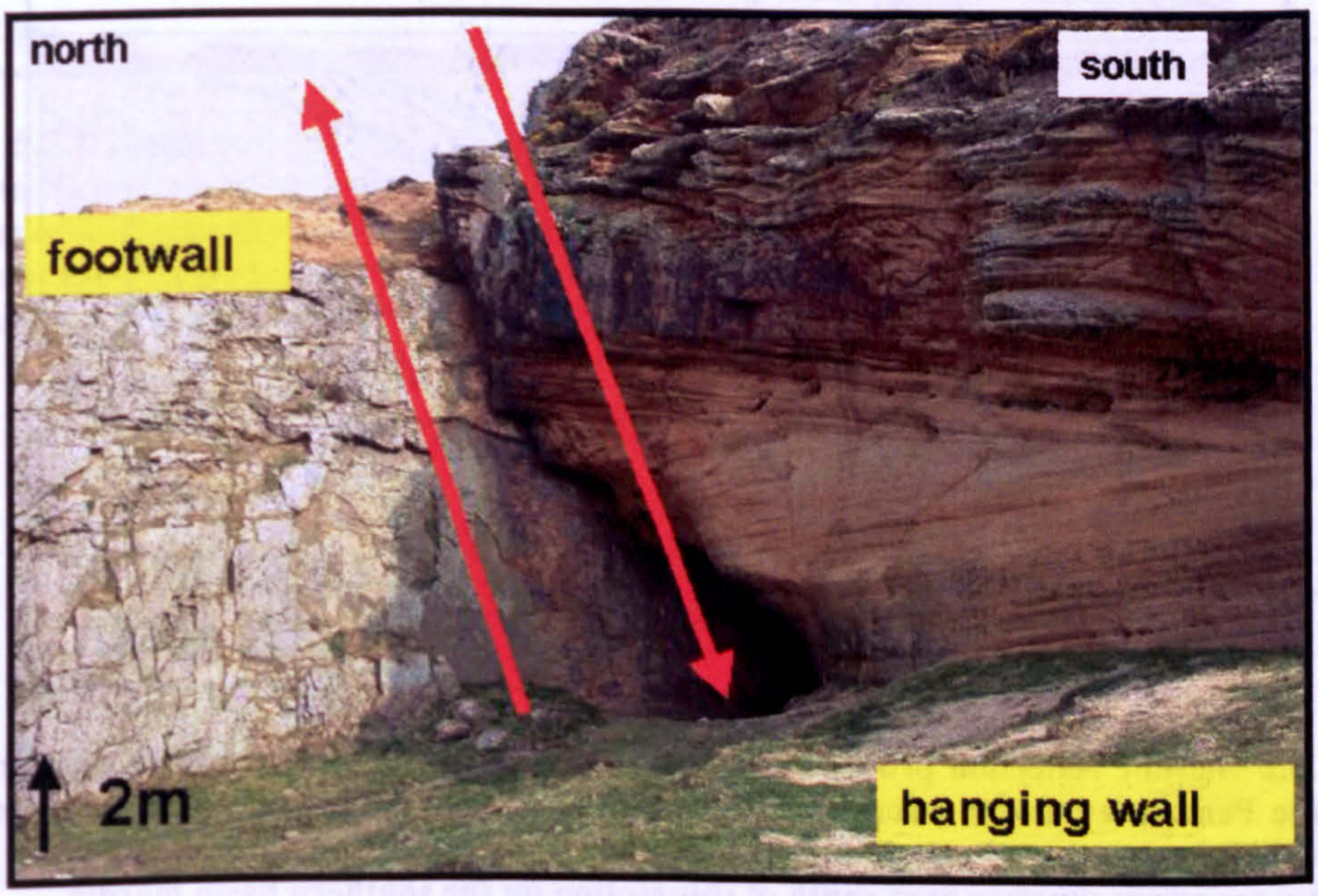


**Plate 5.2. Exposure of Clashach Fault in Clashach Cove, 150m west of Clashach Quarry (Plate 5.1) (location on Fig. 5.3). The grey low permeability fault slip face can be seen on the left, with the poorly cemented, orange coloured, hanging wall sands toward the right.**

In contrast the Burghead Fault is a regional, seismic scale fault which can be extrapolated offshore onto seismic reflection data (Quinn *et al.* in prep, Chapter 4). Upper Triassic fluvial sands in the hanging wall are downthrown to the south and juxtaposed against the aeolian Hopeman Sandstone in the footwall. The fault is exposed laterally for 30m at low tide and the main slip face strikes between 095-100° dipping between vertical and 80° south (Plate 5.3). The combined Permo-Triassic thickness in the nearby Clarkly Hill borehole is 138m (Berridge and Ivimey-Cook 1967) and a minimum of 3m of vertical exposure is visible on the foreshore, constraining maximum normal displacement to 135m. A major splay fault of the main Burghead Fault crops out on the adjacent foreshore trending 085°. The Burghead Fault consists of a main slip face which accommodated the majority of displacement, and a series of deformation bands which individually record mm scale slip. The deformation bands occur in clusters 25- 100cm in width, each composed of several anastamosing bands. The clusters decrease in size and frequency of occurrence with increasing distance from the main slip face. At distances greater than c.15m from the main slip face individual rare deformation bands occur. Exposure restricts observation of the maximum extent of deformation related structures.




**Figure 5.2 Seismic reflection profile across the IMF basin from the Helmsdale coast (north) to the Lossie Peninsula (south) where the Hopeman Sandstone is exposed. The first order Late Jurassic half-graben structure with super-imposed sub-basins can be seen. The onshore exposures are approximately 5km south of this section on the southern basin margin.**

Timing of major fault movement is interpreted as Late Jurassic (Frostick *et al.,* 1988, Quinn *et al.,* in prep., Chapter 4) based upon reconciliation of the onshore structures with seismic data directly offshore and basinwide styles of deformation. Quinn *et al.* (in prep. Chapter 4) interpret the onshore exposures as part of a horst block uplifted at the edge of the IMF basin. The Burghead and Clashach faults form extensional intra-horst faults.

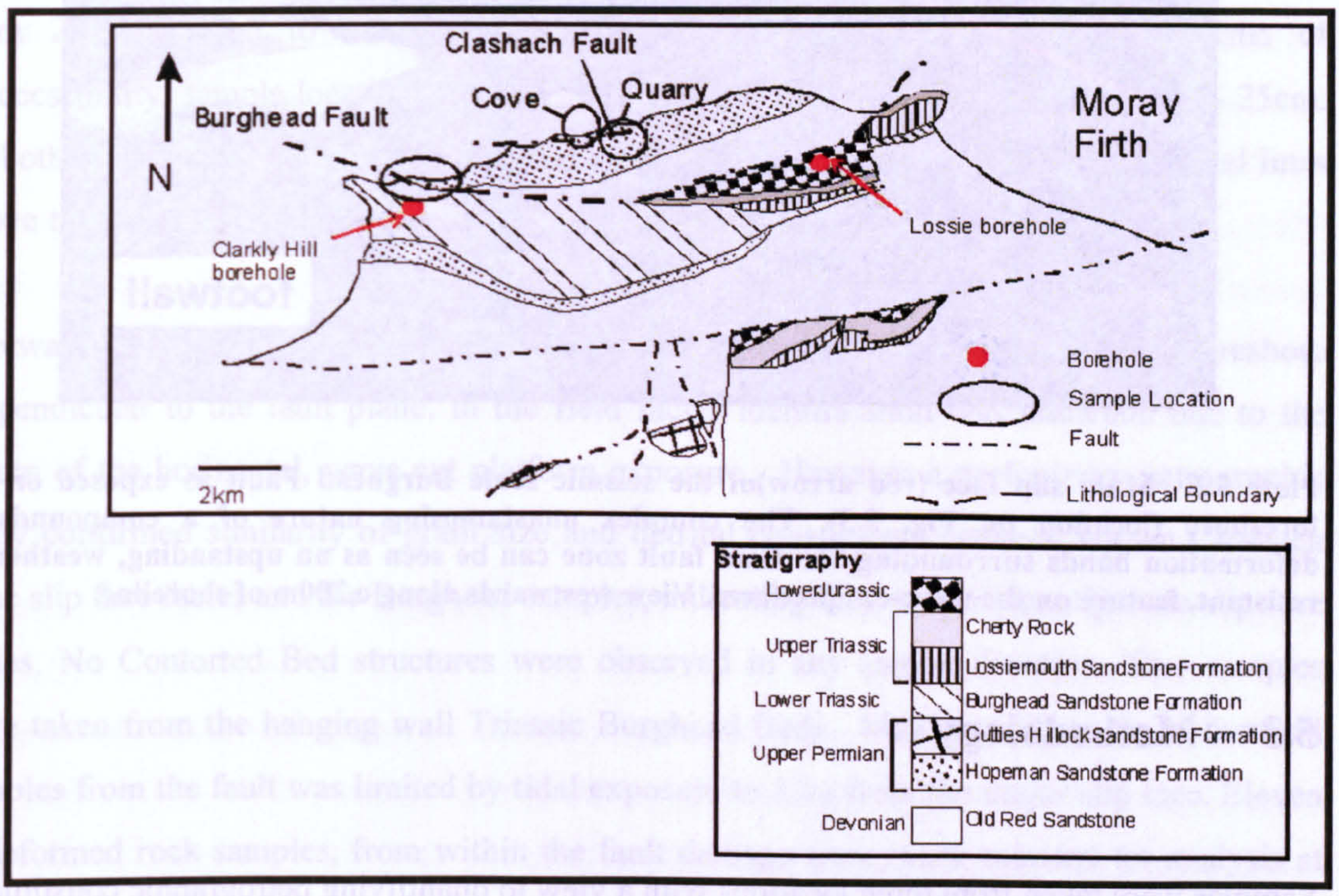


**Figure 5.3. Geological map of the onshore exposures and structures. Samples of Permian Hopeman Sandstone were taken in fault perpendicular traverses from the hanging wall through fault planes and into the footwall at two exposures of the sub-seismic Clashach Fault, and one traverse at the seismic scale Burghead Fault. The Permian Hopeman Sandstone lies at the base of the onshore sequence, directly overlying the Devonian basement.**

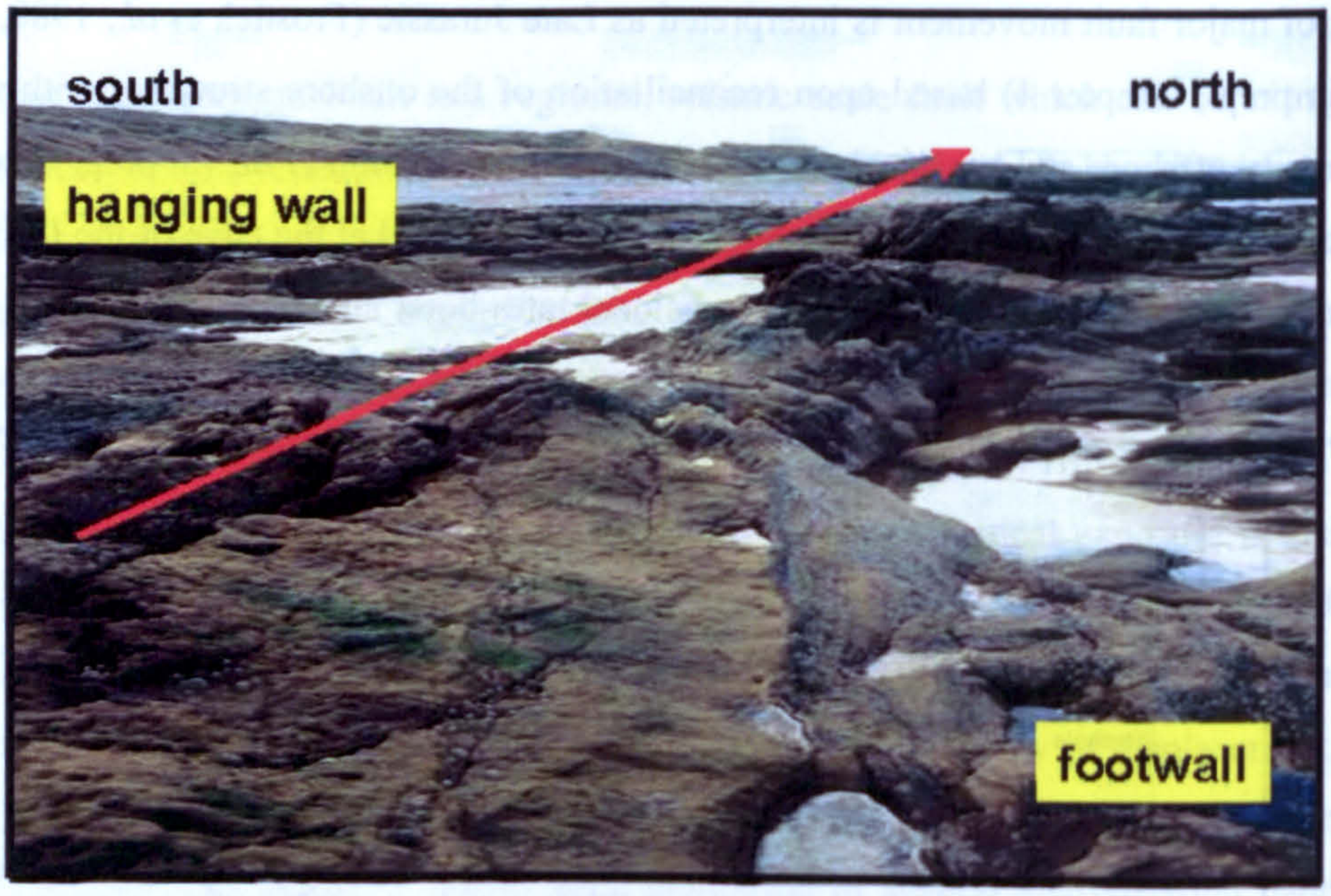


**Plate 5.3. Main slip face (red arrow)of the seismic scale Burghead Fault as exposed on the foreshore (location on Fig. 5.3). The complex anastamosing nature of a compounds of deformation bands surrounding the main fault zone can be seen as an upstanding, weathering resistant, feature on the wave-cut platform. View westwards along c.200m of shoreline.**

## 5.3 Methodology

Samples were taken from three locations with a view to quantifying petrographic constituents (Fig. 5.3). In Clashach Quarry 39 samples were taken in a traverse from the exposed fault plane through the footwall to maximum exposure at 32m distance, perpendicular to the main slip face. Dune slip and dune toe-set facies were sampled in both the hanging and footwalls to avoid bias associated with facies related diagenetic cements and significant variation in grain size. In both Clashach Quarry and Clashach Cove, facies identification was not problematic due to excellent exposure. A 1-inch water-cooled core drill was used to obtain sandstone plugs for thin section preparation. Sample location was marked and a 'TopCon' surveying instrument was used to document the position of each sample in three dimensions relative to the fault plane. Accuracy of surveyed points is better than 10cm in three-dimensions. The attitude and trace of the fault plane was also surveyed to enable accurate location of core plugs (Appendix C). The TopCon surveying method of location allows projection of a 2-D fault surface and the calculation of the true perpendicular distances of

samples from that plane, accounting for changing height of sample location more distant from the dipping fault plane surface.

Hanging wall exposure in the Clashach Quarry is restricted to a few metres vertically and horizontally. Two samples were taken from the hanging wall using the method outlined above. Eleven further hanging wall samples were taken from Clashach Cove over a distance from 2.2m through to 30m perpendicular to the fault plane. Due to problems of inaccessibility, sample location was measured using a tape measure to an error of +/- 25cm. At both the Clashach Quarry and Cove locations, sample traverses followed horizontal lines above the ground surface, and inevitably cross-cut different facies and bedding planes.

Footwall samples from the Burghead locality were taken in a traverse across the foreshore perpendicular to the fault plane. In the field facies identification was uncertain due to the nature of the horizontal, wave cut platform exposure. However a preliminary petrographic study confirmed similarity of grain size and detrital constituents between known Clashach dune slip face facies and the Burghead samples, indicating they are dominantly dune slip face facies. No Contorted Bed structures were observed in any sample location. Two samples were taken from the hanging wall Triassic Burghead Beds. Maximum distance of footwall samples from the fault was limited by tidal exposure to 13m from the major slip face. Eleven undeformed rock samples, from within the fault damage zone, were selected for analysis at specific intervals from the slip face with care to avoid sampling deformation bands. Deformation bands and the small pods of undeformed sandstone between individual bands within clusters were also specifically sampled, and their proximity to the major slip face recorded. Sample location was measured using a tape measure, with a measurement error of +/-25cm. Five samples were taken from both dune slip face and dune toe-set facies along the 8km of coastal outcrop and on cliff exposures adjacent to Clashach Quarry, within the footwall of the Clashach Fault, in order to obtain a typical background value of quartz cement.

Thin sections were made of each sample, impregnated with blue epoxy resin to highlight pore space. Each sample was then observed under optical microscope to identify detrital and diagenetic phases. The majority of grains with quartz overgrowth showed no 'dust rim' between grain and cement making quantification of authigenic quartz imprecise. Furthermore, because of the intense cementation, a significant number of samples contained

as little as 0-4% porosity causing further difficulty identifying individual quartz overgrowths. To identify authigenic quartz accurately a Phillips XL-30 Scanning Electron Microscope (SEM) fitted with a Cathodoluminescence (CL) detector was used to capture images of each section (Appendix D). Textures were also analysed using Secondary Electron (SE) and BackScatter Electron (BSE) imaging. Two to four images of each thin section were point counted for detrital constituents, quartz, feldspar and rock fragments. Diagenetic point count categories were: quartz cement, feldspar overgrowth, iron coating and pore-filling mineralisation, primary porosity and secondary porosity. The point count technique involved overlaying a transparent 450- point grid over each printed image adding to a total of 900 to 1800 counts per section. The higher number of counts per section was used to accurately determine the amount of quartz cement in samples in which total authigenic quartz volume was below 4%, and in those samples in which porosity is less than 4%. Calculated point count errors (Van der Plas and Tobi 1965) are typically between 2 and 3 % for sections counted with 900 to 1800points. For larger volumes counted this is a relatively small error, for smaller volume phases (e.g. authigenic K-feldspar) this is more significant and needs to be accounted for in any interpretation.

Porosity was determined using the point count method as above. Measurement using gas mercury or nitrogen gas porosimetry, was not undertaken because of the low porosity and lack of micropores, which meant point counting was the most reliable method (Van Der Plas and Tobi 1965).

Permeability was measured in the field using a gas-flow mini-permeameter on loan from Heriot-Watt, Institute of Petroleum Engineering, with a measurement accuracy of +/- 10% above 1mD permeability (e.g. Hurst and Goggin 1995). The permeameter injects Nitrogen gas (N2) at a fixed pressure into the face and measures the resistance to flow. For each individual measurement the probe tip was placed against the exposed sandstone, and held in place until a sufficient seal formed. Once a seal was developed, the resistance to gas flow was observed to decrease over 10-60 seconds, depending upon permeability, to a steady-state, proportional to rock permeability. (Appendix E) Measurement was undertaken following periods of dry weather to avoid the effects of relative permeability between the injected gas and water saturated sandstone pores. A permeability profile perpendicular to the Clashach Fault was taken, spanning from the footwall through the hanging wall was taken in the Clashach Cove location, with sample points every 0.5m where the exposures were accessible.

The Cove location was chosen to obtain permeability data because of the easier identification of facies and the consequent ability to constrain both inter and intra-facies variation in sands with little cement. Two permeability profiles of the uncemented hanging wall sands were obtained, one laterally across the exposure cutting two different facies, and ignoring variation in sedimentology, and one profile along a single foreset package of dune slip face facies, from base of exposure to dune crest. Both profiles together allow for natural depositional variability in the sandstone to be compared to the effect on permeability of the footwall cementation.

## 5.4 Field observations

### 5.41 Clashach Fault

Intensively cemented and indurated sandstone is visible at field scale in the footwall exposures of the Clashach Fault at both the Clashach Quarry [NJ162 701] and Clashach Cove [NJ159 702] localities. Exposure of the Hopeman Sandstone within Clashach Quarry is dominated by the footwall rock. Within the exposed footwall there are three field zones of differing hardness and colour variation, which are related to increasing distance from the fault. The first zone is 0-5m from the fault plane and the sandstone is very pink with minor 1-5cm patches of brown iron staining, variably siliceous and hard. Some grains can be removed from the surface with vigorous brushing. In the second zone, between 5-15m, the sandstone displays a less intense pink-white colour and is well indurated with small to large scale Liesegang bands. These are typically concentric rings of orange-brown colour, 0.2-1cm in width, coalescing to form metre scale textures. The third zone between 15 and 32m from the fault plane displays a lighter white to buff brown becoming more orange and similar to typical coastal exposures with increasing distance from the fault. Loose grains can occasionally be removed by brushing the surface. Moving through this 3rd field zone Liesegang bands are developed in a similar manner to zone 2, but become more common, and similar to the typically orange aeolian sand of nearby coastal exposures, with increasing distance from the fault. Within Clashach Quarry the hanging wall contains a zone 0-2m of wide of relatively well-cemented sand, similar to the 5-15m zone 2 in the footwall. This zone

rapidly deteriorates into poorly cemented, soft and loose, orange sandstone comparable with typical coastal exposures.

At Clashach Cove the footwall consists of a lower and upper section. The lower section from ground surface to 4m in height is intensely silicified and indurated with frequent sub-vertical joints. Colour variation is difficult to detect due to surface weathering but it appears to have a pink-grey-white colour and is texturally similar to the fault footwall field zones 1 and 2 in the Quarry. There is no immediately visible lateral variation in colour due to restricted exposure and sea-weathering. The upper section at Clashach Cove is orange coloured and less well indurated than the lower section, and displays significant nodular weathering typical of selective erosion of carbonate cement. The extensive hanging wall exposure within Clashach Cove is composed of orange colour, uncemented sand which erodes easily with loose sand grains. Large (>3m) liesegang bands occur in the visibly permeable hanging wall sands, and to a lesser extent in the upper zone of the footwall sandstone. The fault slip face consists of a grey silicified parallel layer on the footwall surface (Plate 5.4). Adjacent to this is a 0.3-0.5m fault 'core' zone with anastamosing deformation bands. Between the fault core and hanging wall is a 0.3-0.5m thick zone of iron mineralisation, with irridesence similar to Peacock Ore (Plate 5.4), although no copper is present.

At Clashach Quarry, the cemented footwall sands cross-cut both dune slip and toe-set facies, indicating that, at the field scale, the cement is not associated with any particular facies but cross-cuts facies. In the hanging wall both facies can also be seen, and both appear friable and similar in texture. Field investigations in the footwall exposures north of the Clashach Cove fault plane show that the Cove exposes several different facies variants of the Hopeman Sandstone. All are equally strongly cemented by quartz. This again indicates that quartz cement was not emplaced preferentially in one clean sub-facies with no grain coatings, but that silica cement affected all sub-facies.

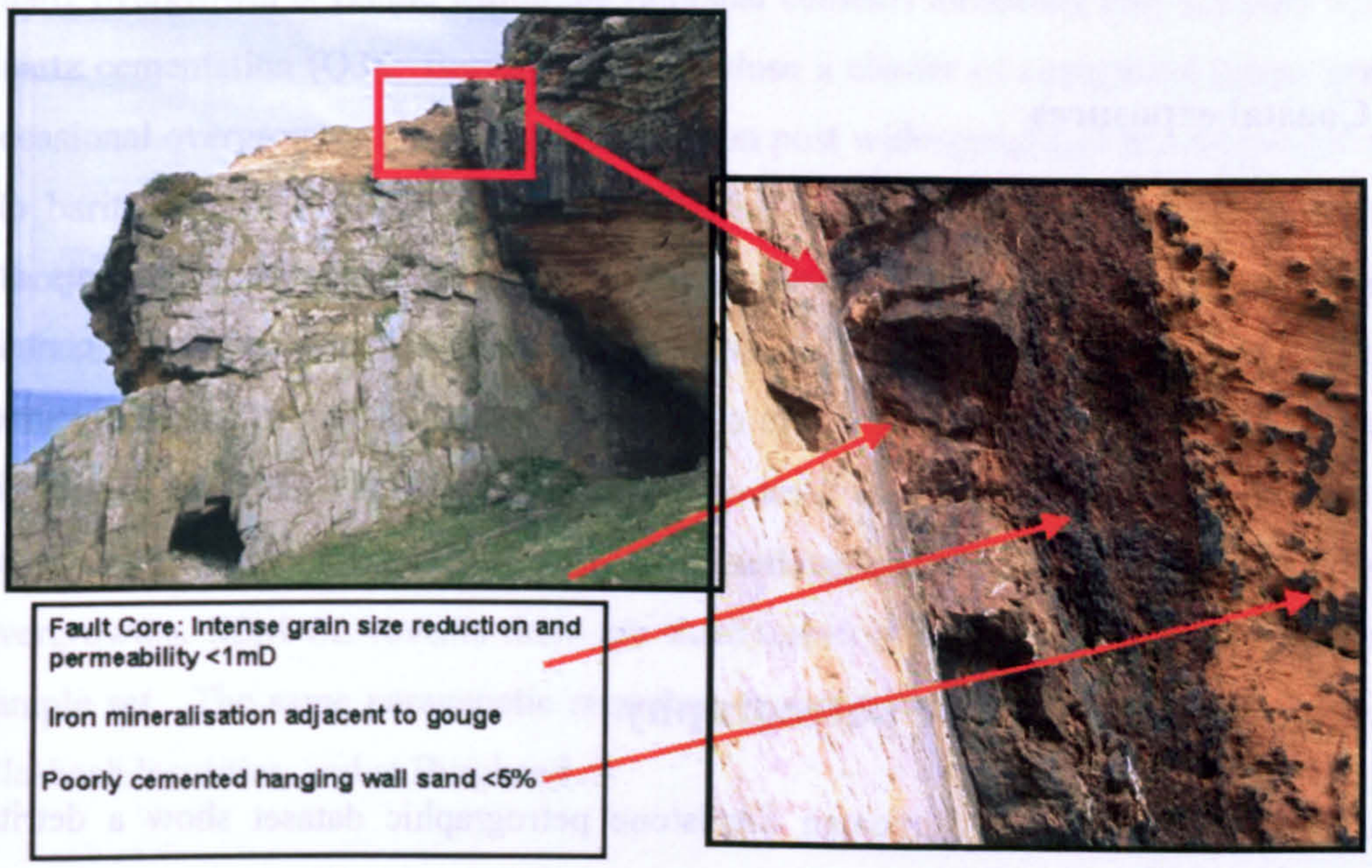


**Plate 5.4. Fault cross-section of the sub-seismic Clashach Fault showing the fault core and poorly cemented hanging wall sand.**

## 5.42 Burghead Fault

The footwall sandstone at Burghead [NJ121 692] is intensely cemented and extremely hard with a white-pinkish colour. On fresh surfaces the rock is comparable in hardness to a quartzite. The footwall exposure is limited by low tide to 13m of horizontal exposure perpendicular to the fault, which is homogeneously silicified and indurated, appearing harder than the equivalent sand in the footwall adjacent to the Clashach Fault. Frequent sub-vertical jointing is present adjacent to the fault on the wave-cut platform exposure. The hangingwall Triassic fluvial sands (Burghead Beds) are less well cemented and contain nodular carbonate cements. The Burghead Fault slip face and Splay Fault along the adjacent coast form upstanding weathering resistant features, which appears in the field to be related to silicified fault gouge material (Plate 5.3).

Lead –zinc mineralisation is visible in outcrop as small disseminated galena cubes present in occasional footwall locations of the Burghead Fault, however the distribution of hard silicified rock shows no particular spatial relationship with this mineralisation and silicification is pervasive in the footwall sandstone. No galena was documented within the fault plane structure.

### 5.43 Coastal exposures

Along the foreshore, outwith the intensely silicified footwall sandstone, exposures are homogeneous yellow-orange in colour and poorly indurated. Two coastal exposures contain 10-300m cemented reefs composed of c.1cm cubes of barite with 1-5cm of interstitial sand, forming a weathering resistant surface. West of Clashach fault [NJ147 699] and also within relatively unsilicified, sand metre scale patches of fluorite can be observed in cubic form.

## 5. 5 Hopeman Sandstone petrography

Point count data for the bulk Hopeman Sandstone petrographic dataset show a detrital composition of >95% quartz, 3-5% K-Feldspar (microcline), 0-2% Plagioclase, and 0-3% rock fragments (Appendix D). Rock fragments are predominantly chert and granite with infrequent muscovite flakes. Grain-coating clays and matrix are not observed except within rare small pebble beds. Under the scheme of McBride (1963) the sand is classified as a quartz arenite.

Diagenetic products consist of quartz cement, K-feldspar overgrowths, iron oxide and quartz, fluorite and barite within fractures and deformation bands (Fig. 5.4). Early quartz cement in fault proximal footwall sands occludes porosity and leads to the development of differing diagenetic histories between these sands and the hanging wall (Fig 5.4). Secondary porosity is poorly developed through partial to extensive dissolution of detrital feldspar grains with minor feldspar overgrowth preserved around remnant dissolved detrital grains. Two phases of iron oxide banding are present, and no clay was detected in either phase of iron. The first is a thin early eodiagenetic phase coating detrital grains. The frequency and occurrence of this phase is controlled by the presence of quartz overgrowths which when present 'seal' the early iron coating. Where overgrowths are absent the iron less frequently coats grains and is found in occasional pore space as well as forming Liesegang bands visible from thin section to outcrop. This second iron phase is also concentrated in minor fault planes and fractures. Euhedral authigenic quartz growth is constrained in the presence of feldspar overgrowth indicating that authigenic feldspar predates quartz. Fluorite in samples from coastal locations occurs as nodules preserving a grain floating texture with minus cement porosity >35%. No

quartz overgrowth is visible within the fluorspar cements indicating they pre-date widespread quartz cementation (Q3). Barite nodules enclose a cluster of compacted quartz grains with occasional overgrowths indicating precipitation post widespread quartz cement (Q2 and Q3). No barite was observed in the highly silicified sands in the footwalls of the two faults. Fluorite was observed in association with lead-zinc deposits around the Burghead Fault, and in fractures and some deformation bands indicating a second, mineralisation related, phase of fluorite cement.

Quartz cement is the most abundant diagenetic phase and forms well defined syntaxial overgrowths. SEM-CL reveals there are three zones of authigenic quartz within the whole sample set. The same paragenetic sequence occurs within the Hopeman Sandstone at both Clashach localities, and at Burghead.

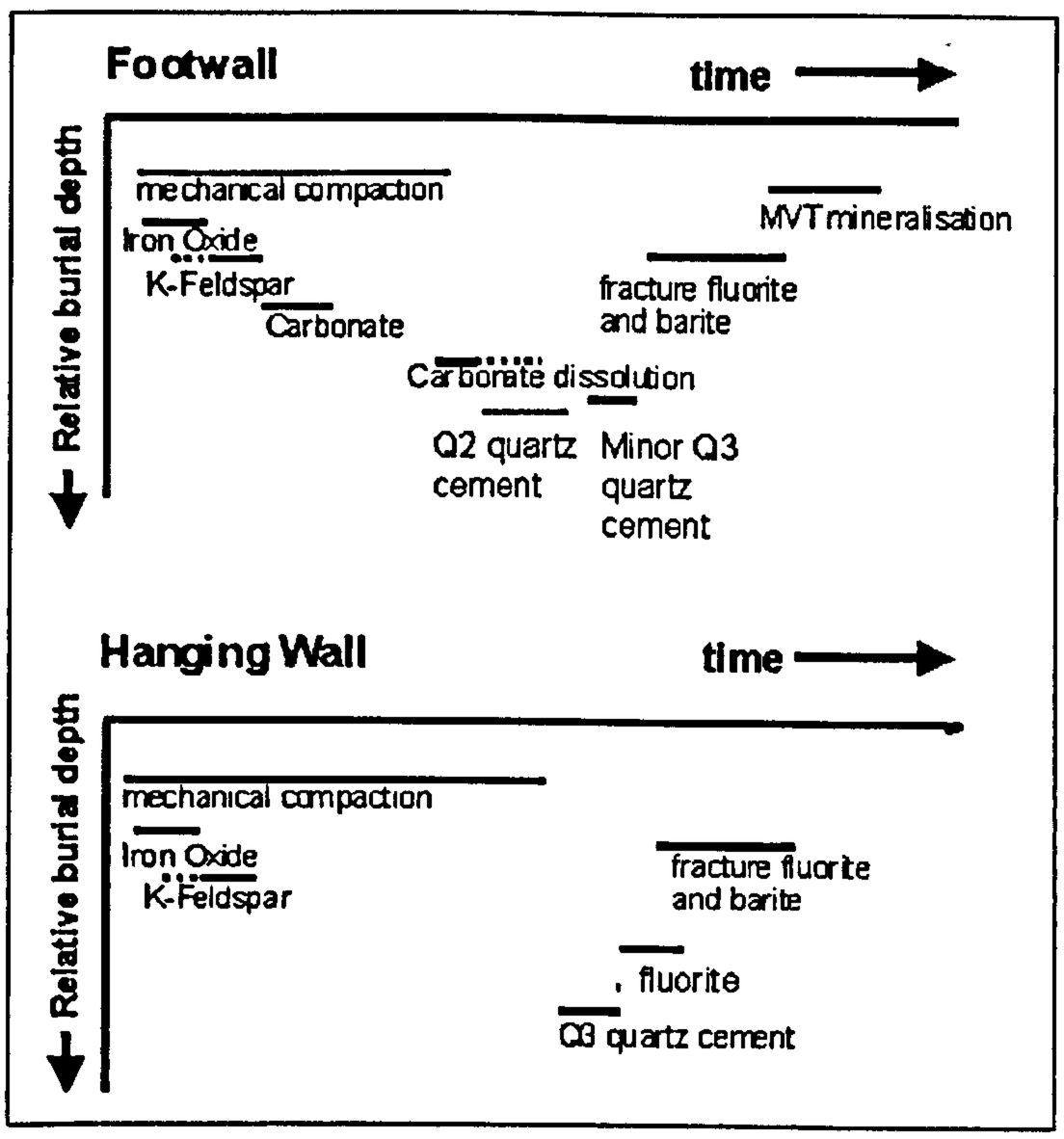


**Figure 5.4. Paragenetic sequence of the examined Hopeman Sandstone. The footwalls to normal faults follow a different diagenetic history that the hanging wall, with carbonate cementation, less mechanical compaction, dissolution and Q2 phase quartz cement occluding significant pore space during burial. The hanging wall, and sections of the footwall distal from the fault zones, do not experience localised carbonate or quartz cementation around exposed fault planes. Late stage Mississippi-Valley type lead-zinc mineralisation is concentrated in basinward footwalls, the early quartz cementation and low permeability fault structures act to prevent MVT mineralising fluids reaching the hanging wall directly adjacent to fault surfaces. Q1 is a detrital overgrowth and is not shown.**

**Q1:** The first phase is rare (<1%) and is only differentiated from detrital quartz grains by a dark and dull CL signature. The cement has a smooth, round surface texture indicative of transport and abrasion post-precipitation (Plate 5.5). This phase is interpreted as an inherited cement formed in the source rock environment, indicating a sedimentary source for the Hopeman Sandstone. A such it is not considered a diagenetic product in the typical sense.

**Q2:** The dominant cement phase consists of a brightly luminescent 'mottled' CL signature (Plate 5.5, 5.6, 5.7, 5.8) forming >90% of authigenic quartz overgrowths, which are up to 100μm in diameter. The characteristic bright luminescence of Q2 is unusual, most CL signatures of authigenic quartz are darker than the detrital grains (Hogg 1992), as for phase Q1. Petrographically the earliest phase of Q2 quartz overgrowth precipitated around the iron oxide that coats many detrital grains. Where no iron oxide coating exists the cement is infrequently optically recognised through the presence of a dust rim around the grain. Q2 and Q3 phases form homogeneous euhedral overgrowths in optical and SE modes. Q2 forms the major volumetric quartz cement at both Clashach and Burghead footwall localities, and is not seen in background samples distant from fault structures.

**Q3:** Identified by a light grey to black CL luminescence, which is more homogeneous than phase Q2 (Plate 5.9) under CL detection, Q3 post-dates the dominant cement of Q2 which has a brighter CL signature. Found throughout the hanging wall and 'background' sands where total cement volume is <4% phase Q3 is volumetrically minor and, where observed, can be occasionally similar in appearance to Q2. In these sands Q3 is precipitated around detrital grains as the only phase of quartz cement and forming small euhedral overgrowths. Around fault zones in footwall samples which contain significant volumes of Q2 cement, Q3 can occasionally to rarely be identified as the last phase of cement precipitated (Plate 5.9).

Following Q2 quartz cementation around Burghead Fault late stage mineralisation in-fills minor remaining porosity, and locally etches quartz overgrowths. The lead-zinc mineralisation consists of galena, sphalerite, chalcopyrite with associated fluorite. This fluorite is a later phase than seen in background coastal samples.

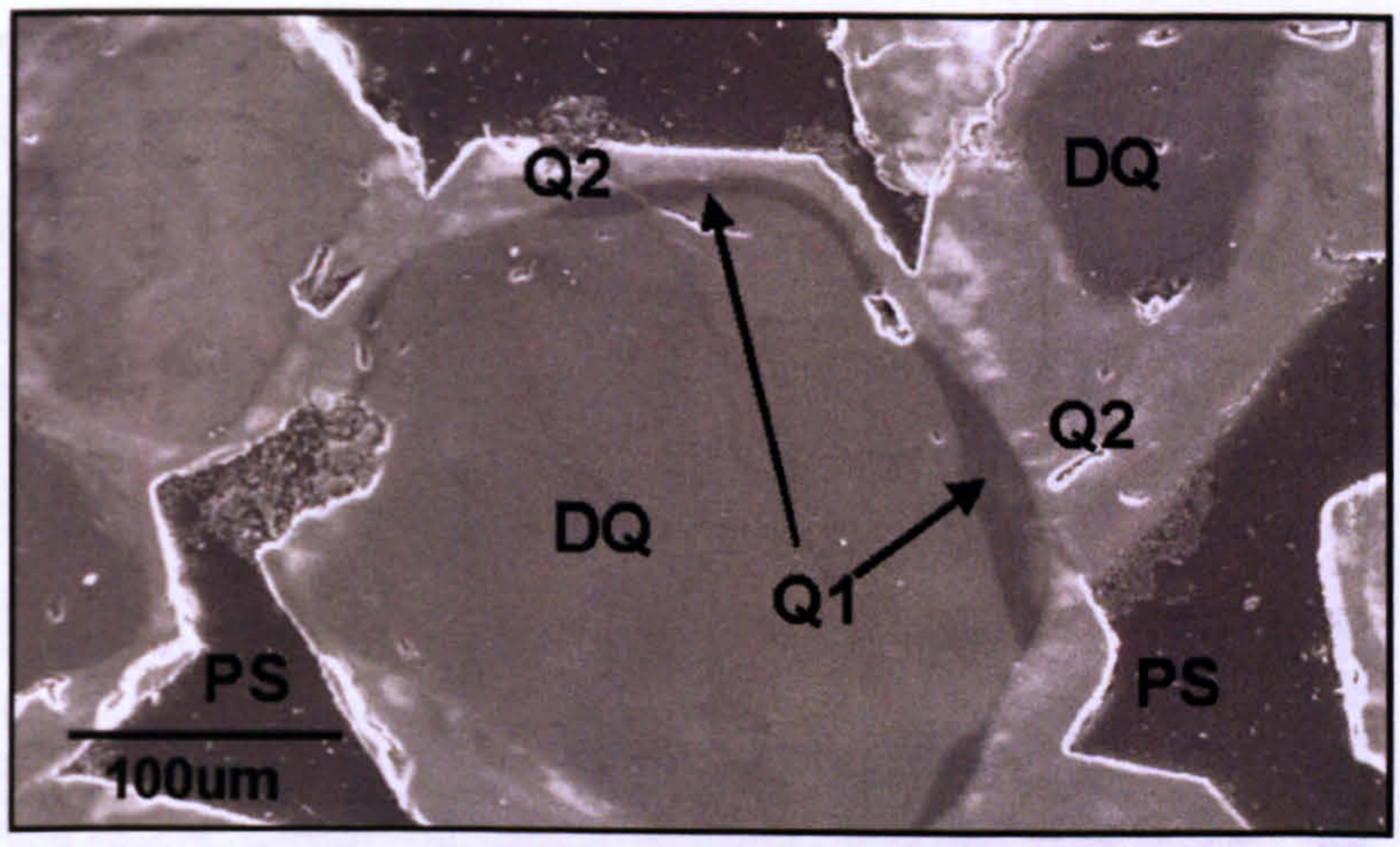


**Plate 5.5. SEM-CL image showing Q1 phase quartz cement, an inherited quartz overgrowth with a rounded texture produced during sediment transport. Phase Q2 surrounds phase Q1 and displays typical crystalline quartz overgrowth morphology and a characteristic bright heterogeneous CL texture. From Clashach Fault fault planes 21.5m *DQ=Detrital Quartz, PS= Pore Space.***

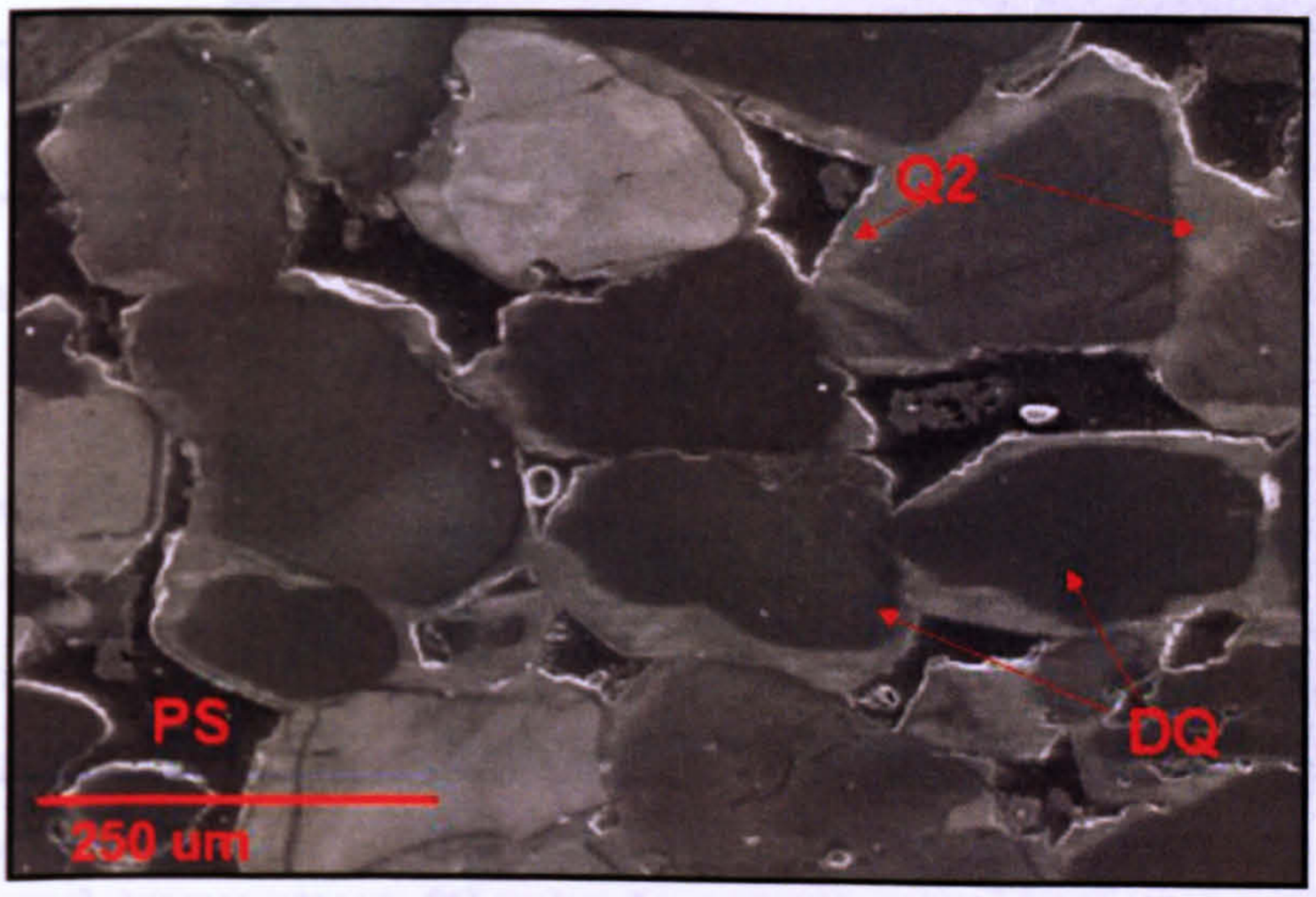


**Plate 5.6. SEM-CL image of Q2 quartz cement around several detrital quartz grains. The boundary between the detrital grains and the overgrowths is smooth, indicating that there was no, or minor, carbonate cement present prior to quartz cementation. Authigenic quartz has nucleated on smooth surfaces with no dissolution textures. Overgrowth edges do not display any etching or embayment associated with dissolution events, in contrast to Plate 5.10., where dissolution surfaces are common. From Clashach Fault footwall 19.5m from fault plane. *DQ=Detrital Quartz, PS= Pore Space.***

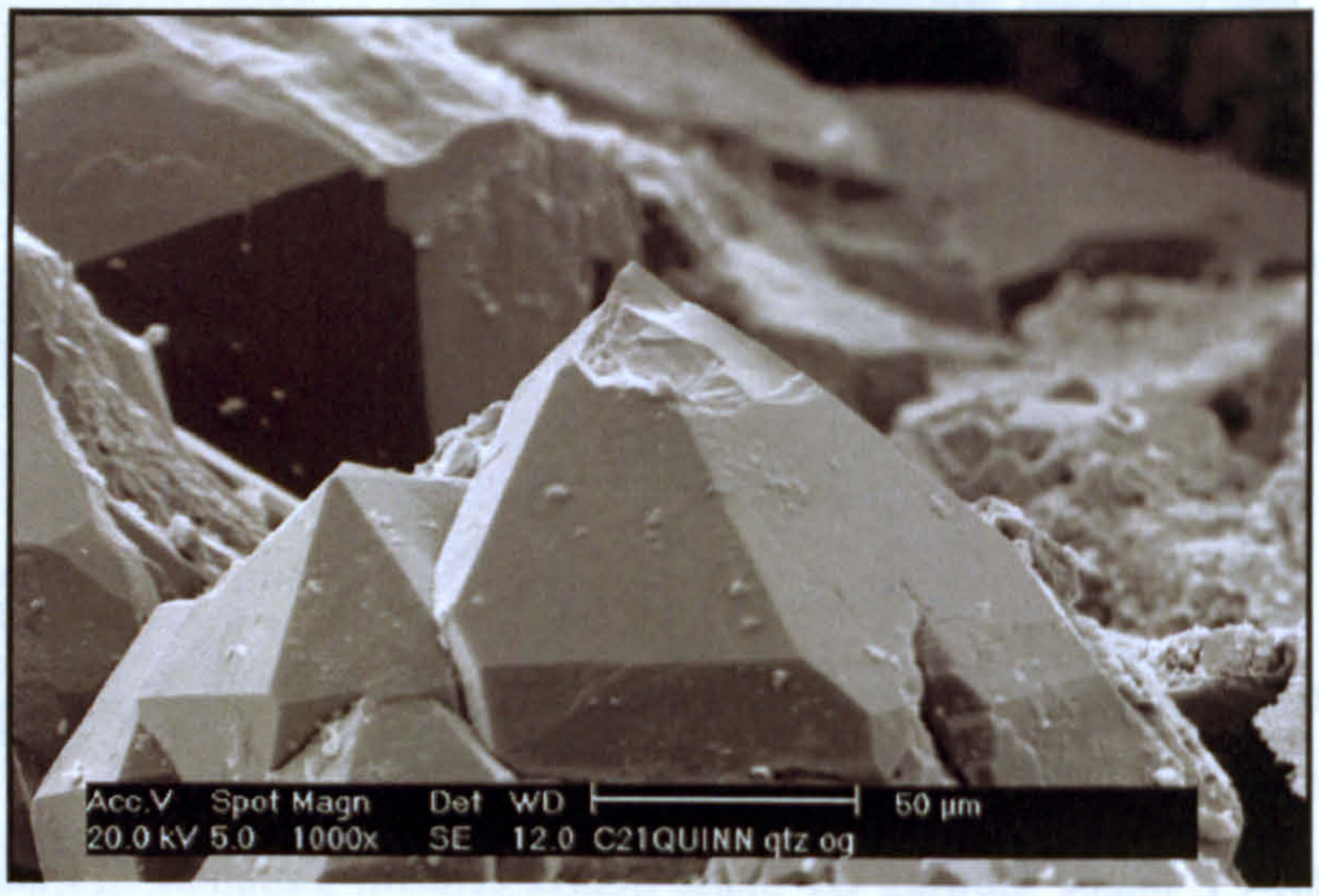


**Plate 5.7. SEM rock chip image of Q2 quartz overgrowths around a detrital quartz grain. Typical, well developed quartz crystalline morphology can be seen. Clashach Fault footwall sandstone 19.5m from the fault plane.**

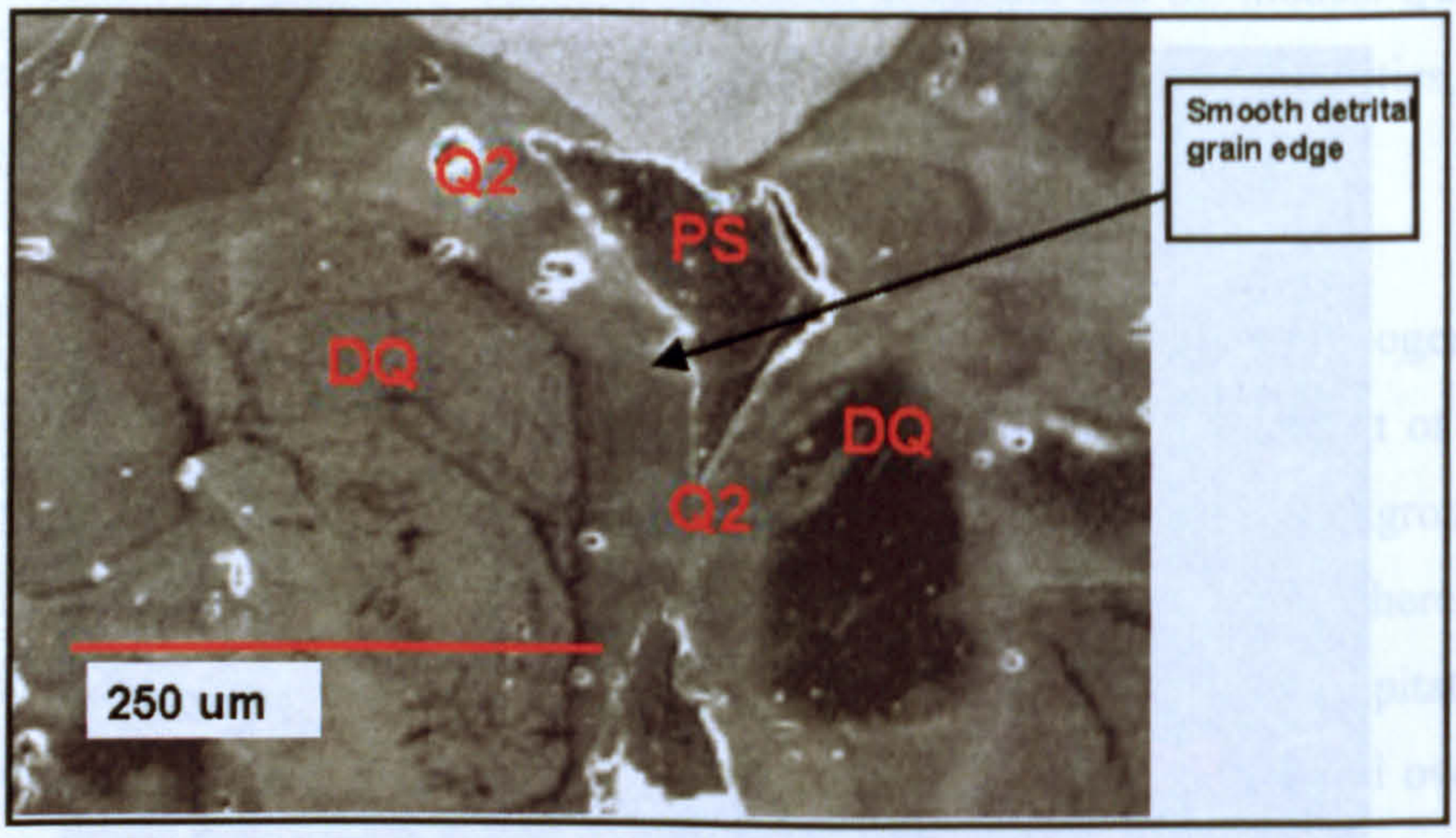


**Plate 5.8. SEM mixed SE and CL detectors showing Q2 quartz cement from the Hopeman Sandstone within the footwall of the Burghead Fault, displaying well developed overgrowth textures growing unconstrained into pore space. Q2 authigenic quartz displays characteristic bright, heterogeneous, luminescence and is nucleated on clean, smooth, detrital quartz grains with no evidence of etching or embayment which is seen in the footwall of Clashach Fault. From Burghead Fault footwall 5m from fault plane. *DQ=Detrital Quartz, PS= Pore Space.***

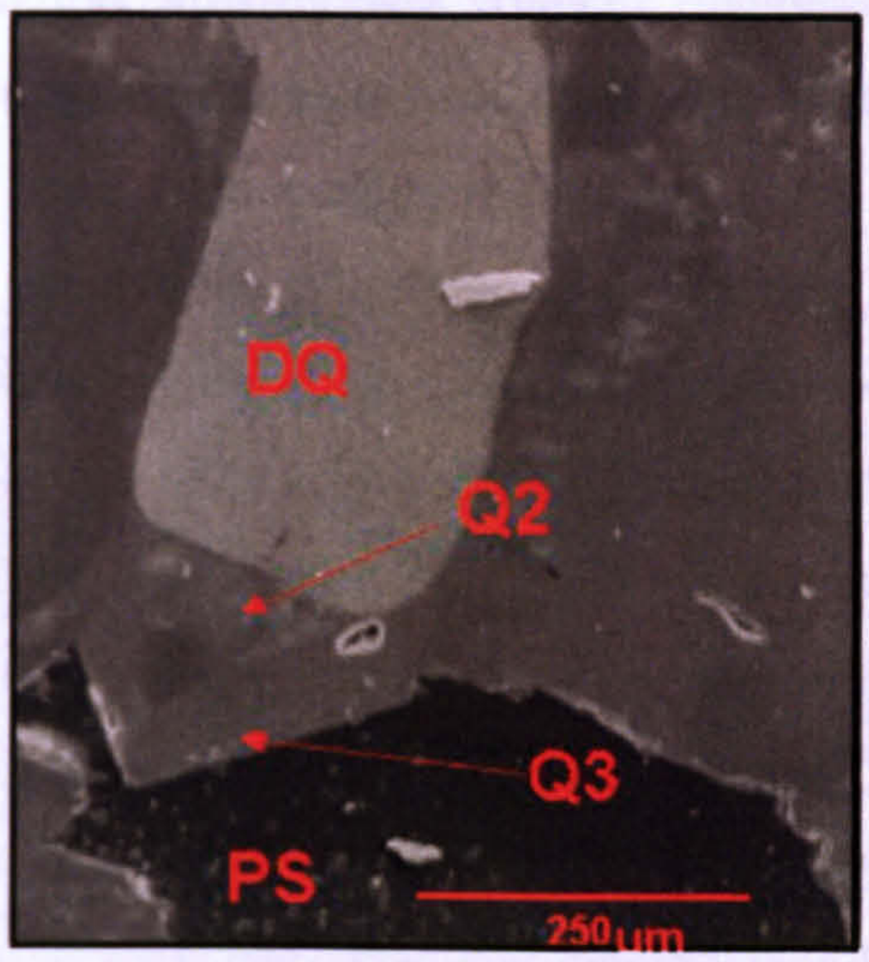


**Plate 5.9. SEM-CL image of Q3 cement showing homogeneous grey luminescence in comparison to the petrographically earlier heterogeneous Q2 cement. Q3 cement can be seen to postdate Q2 authigenic quartz in this sample from the edge of the Q2 cement zone in the Clashach Fault footwall. From Clashach Fault footwall 33m from fault plane. *DQ=Detrital Quartz, PS= Pore Space.***

## 5.6 Clashach Fault: cement, porosity and permeability data

### 5.61 Cementation

Point count data shows that the volume of Q2 phase quartz cement within the footwall varies systematically with distance from the main fault slip plane in two opposing trends, labelled zone 1 and zone 2. Within the footwall zone 1 runs from 0.5m through to 13.8m from the fault plane, and samples display a linear increase in quartz cement with increasing distance (Fig. 5.5)(Table 5.1) from the fault. Quartz cement rises along a linear trend from 4.2% at 0.5m from the fault plane a maximum of 26.5% at 13.8m. Samples within this zone display significant dissolution textures, with frequent etched and embayed detrital quartz grains (Plate 5.10) and large areas of porosity mimicking secondary pores. The extent of dissolution appears severe, and no traces of the pre-existing cement can be detected in thin section analysis, suggesting it has been completely removed. However, X-Ray Diffraction analysis of the sandstones reveals the presence of trace amounts of calcite cement, which are not seen outwith this fault-adjacent zone. The field observation of carbonate cement textures in the adjacent Clashach Cove fault exposure, further indicates that the now dissolved material was

likely a patchy carbonate cement. Quartz overgrowths are discontinuous around most individual grains, and appear to have been constrained during growth by the presence of this pre-existing cement (Plate 5.11), which has subsequently been removed. The position of overgrowths on the detrital grain are, in general, also constrained to patches of smooth grain surfaces which display no evidence of etching, indicating that the quartz cement pre-dated dissolution of the carbonate cement. Directly adjacent to the fault, in a zone restricted to <1m into the footwall, sandstones display evidence of authigenic quartz growing on previously etched detrital grains, suggesting quartz precipitation following dissolution of the carbonate cement (Plate 5.12.). Observation of quartz cement post-dating carbonate dissolution adjacent to the fault, and pre-dating dissolution with increasing distance into the footwall, suggests that carbonate dissolution was occurring as authigenic quartz began to precipitate near the fault, and that fault-related fluids may have removed carbonate gradually as they moved through the footwall sandstone. Zone 2 runs from 13.8m to 31.7m and is defined by a reversal in the trend of volume of authigenic quartz, which follows a linear trend, decreasing from a maximum of 26.5% at 13.8m to 9% at 31.7m (Fig. 5.5). Textural analysis shows that detrital grains in this zone have predominantly smooth grain boundary's upon which the quartz overgrowths have nucleated. Etched and embayed grains are absent. The authigenic quartz has grown in classical overgrowth morphologies into open pore space in a spatially unrestricted manner. This is in contrast to overgrowths in the fault adjacent zone whose growth appears to have been constrained by a pre-existing pore-filling cement. The absence of restrictions on the growth of authigenic quartz, and the presence of smooth detrital grain boundary's indicates that this zone did not contain carbonate cement, and that the early carbonate was restricted to 0.5-13.8m in footwall zone 1 adjacent to the fault plane. As quartz volume decreases, with increasing distance from the fault, the reduction in overall quartz cement volume is a product of smaller overgrowths, not a previous carbonate cement, or other authigenic quartz nucleation inhibiting material (Plate 5.13). Background samples from coastal exposures 40-44m contain only 4% mean authigenic quartz, and this is present as Q3 phase only. This indicates that the scale of the zone of increased cementation associated with the fault is around 32m into the footwall. Samples from the hanging wall, and from the nearby coastal exposures, contain smooth detrital grain boundary's, with no evidence of dissolution or grain coatings (Plate 5.14, 5.15), indicating that the carbonate cement was localised to 13.8m around the footwall fault plane, where it acted to control quartz cement volume and distribution. This may indicate a fluid flow and cementation phase around the

Clashach Fault prior to fluid flow associated with the Q2 phase quartz cementation. Such fluid flow event is not recorded around the exposed Burghead Fault.

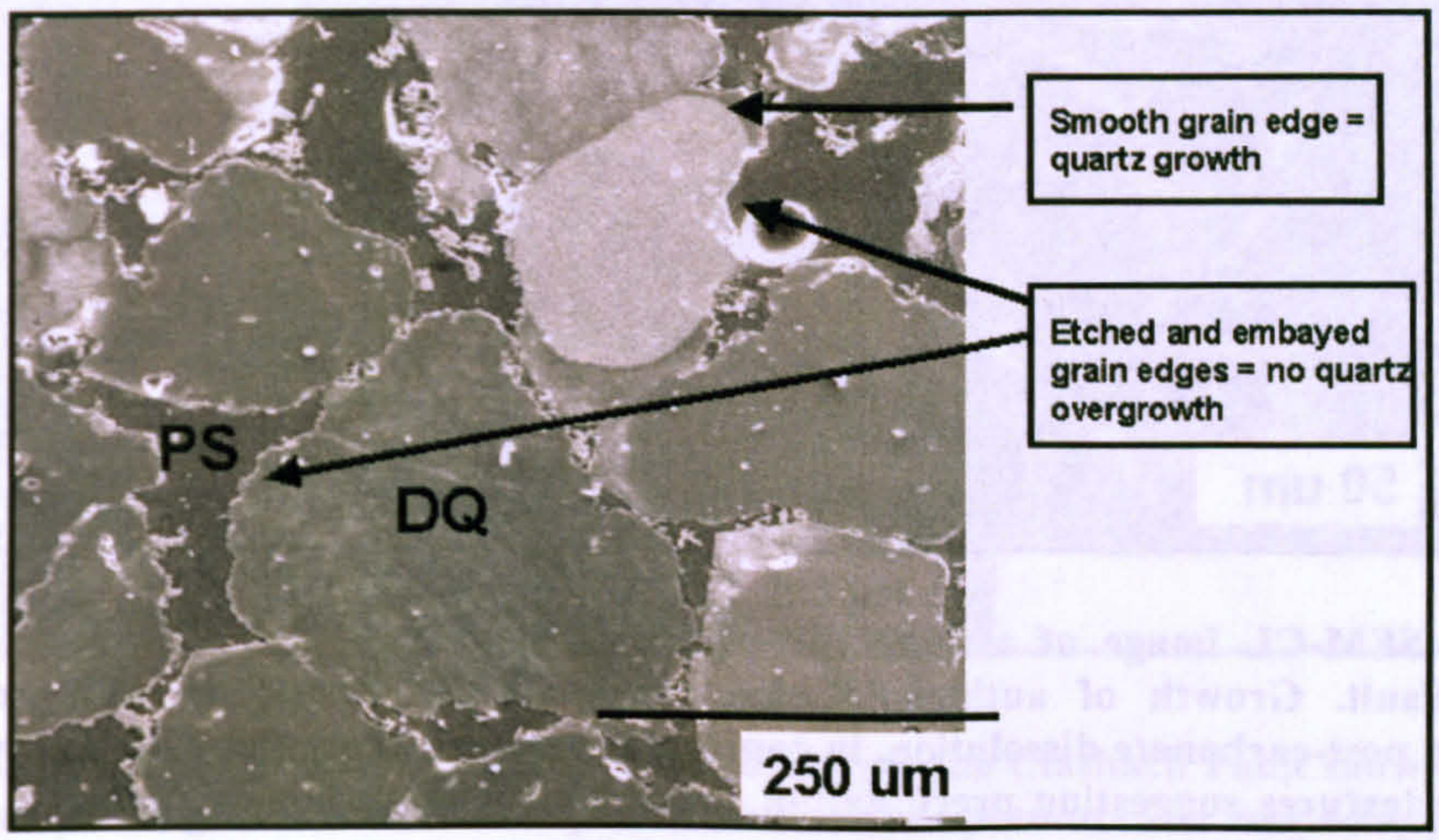


**Plate 5.10. SEM-CL image from within the 0.5-13m footwall zone of the Clashach Fault. Etched and embayed detrital quartz grains can be seen, most likely produced through the action of aggressive fluids which dissolved a previous carbonate cement. Quartz overgrowths are restricted to sections of detrital grains which have a smooth surface, suggesting the carbonate cement controlled the development of quartz cement. *DQ=Detrital Quartz, PS= Pore Space.***

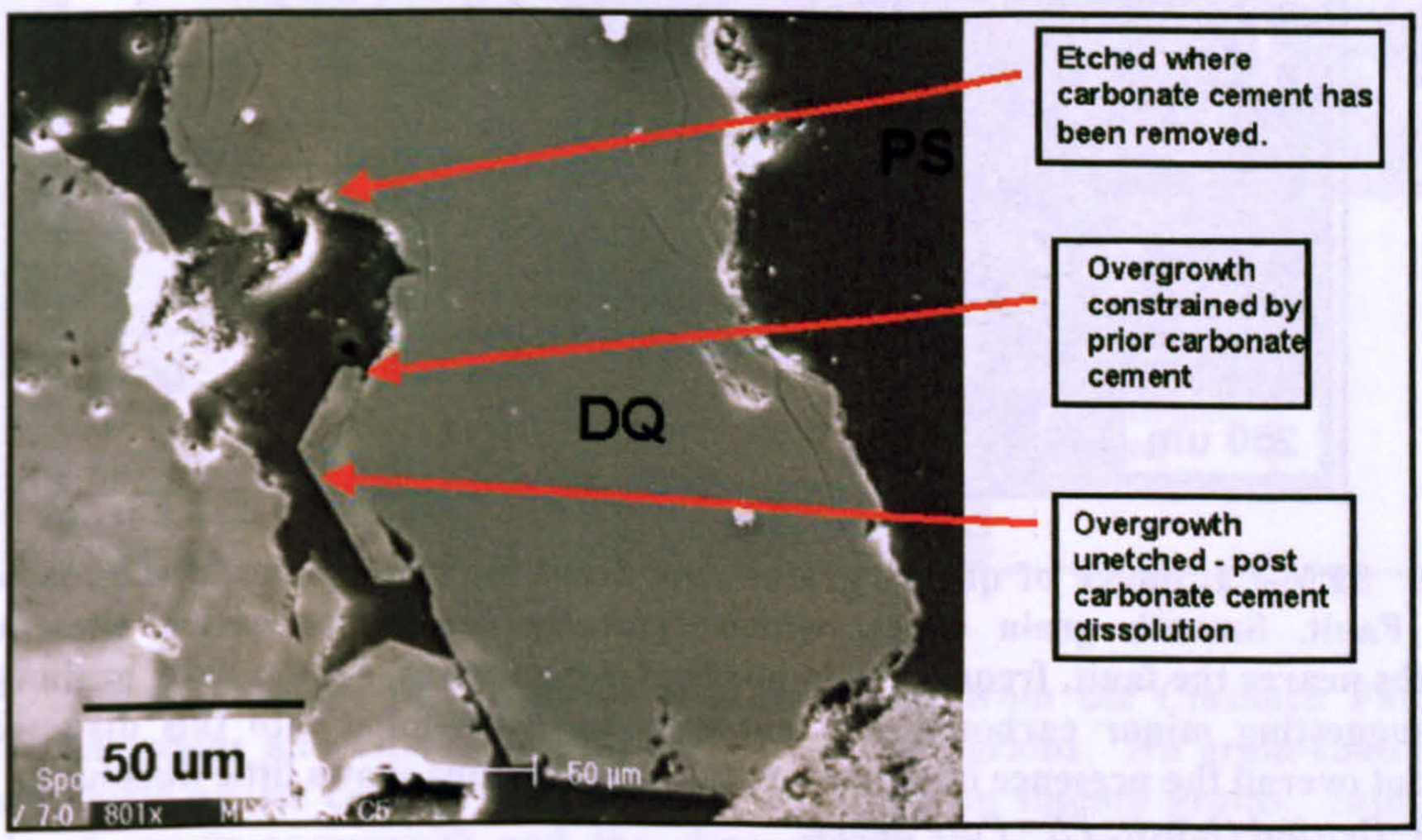


**Plate 5.11. SEM-CL image from 0.5-13m zone of the footwall of the Clashach Fault showing an etched and embayed quartz grain with minor quartz overgrowth on a smooth grain surface. Lateral growth of the overgrowth appears to have been constrained by pre-existing carbonate cement. From Clashach Fault footwall 4.2m from fault plane. *DQ=Detrital Quartz, PS= Pore Space.***

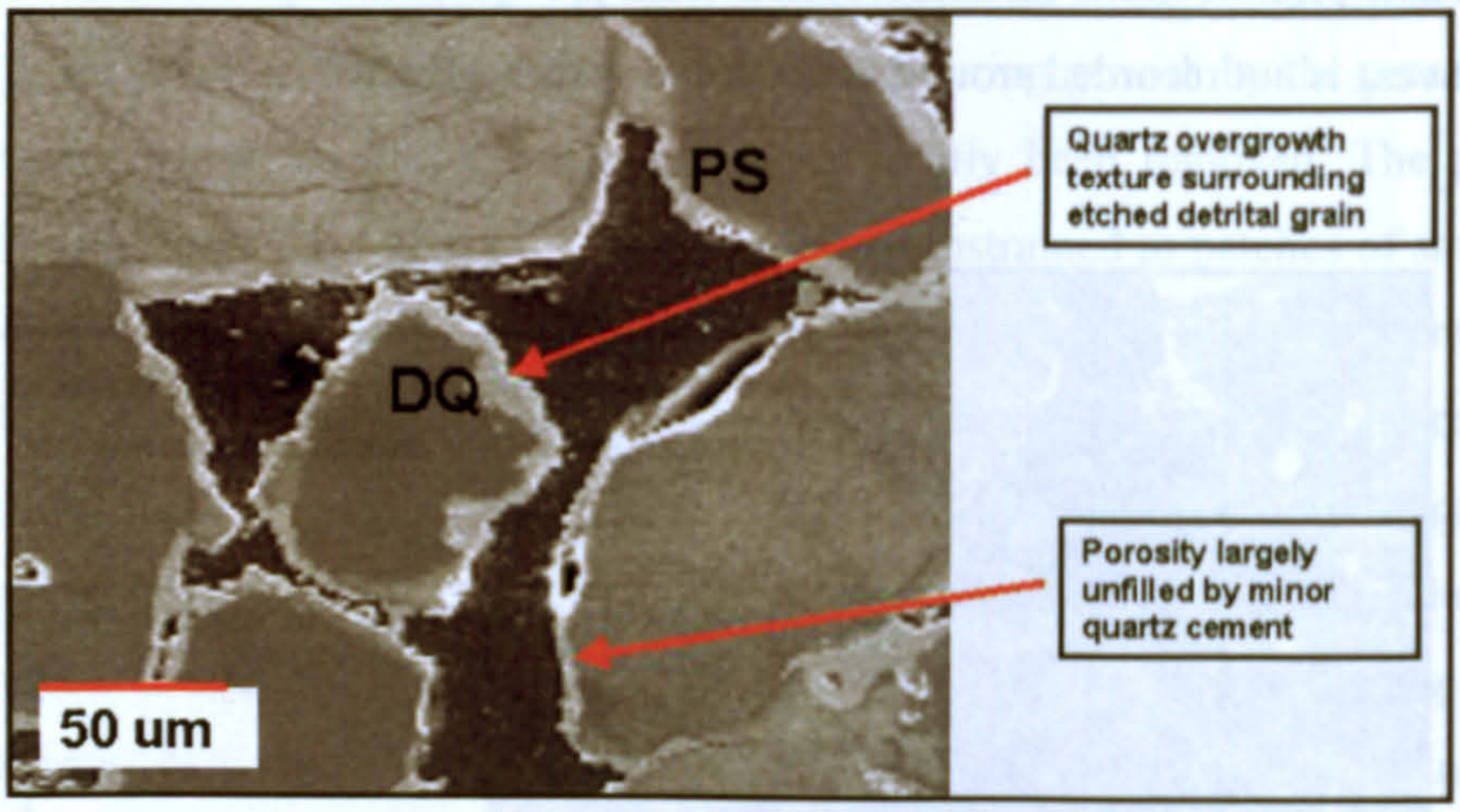


**Plate 5.12. SEM-CL image of a quartz overgrowth 20cm from the main fault slip face at Clashach Fault. Growth of authigenic quartz around the etched detrital grain suggests cementation post-carbonate dissolution, in contrast to samples at greater distance from the fault which have textures suggesting precipitation concurrent with carbonate removal. *DQ=Detrital Quartz, PS= Pore Space.***

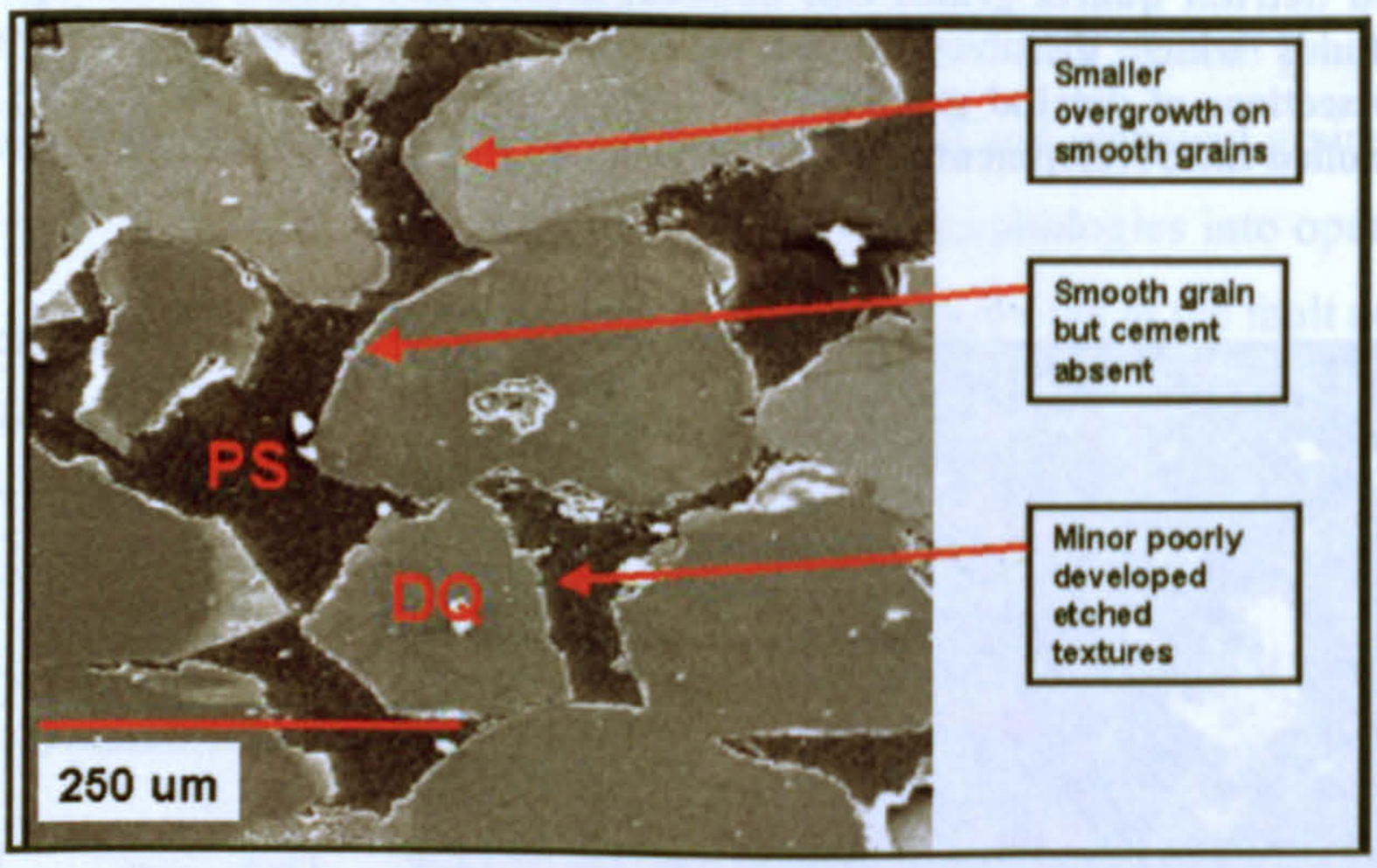


**Plate 5.13. SEM-CL image of quartz grains 29m from the fault plane in the footwall of the Clashach Fault. Smooth grain edges, which typically act as nucleation sites for quartz overgrowths nearer the fault, frequently do not host overgrowths. Minor, rare, grain etching can be seen, suggesting minor carbonate cement may have extended into this distance into the footwall, but overall the presence of clean detrital quartz grains shows little dissolution has taken place. *DQ=Detrital Quartz, PS= Pore Space.***

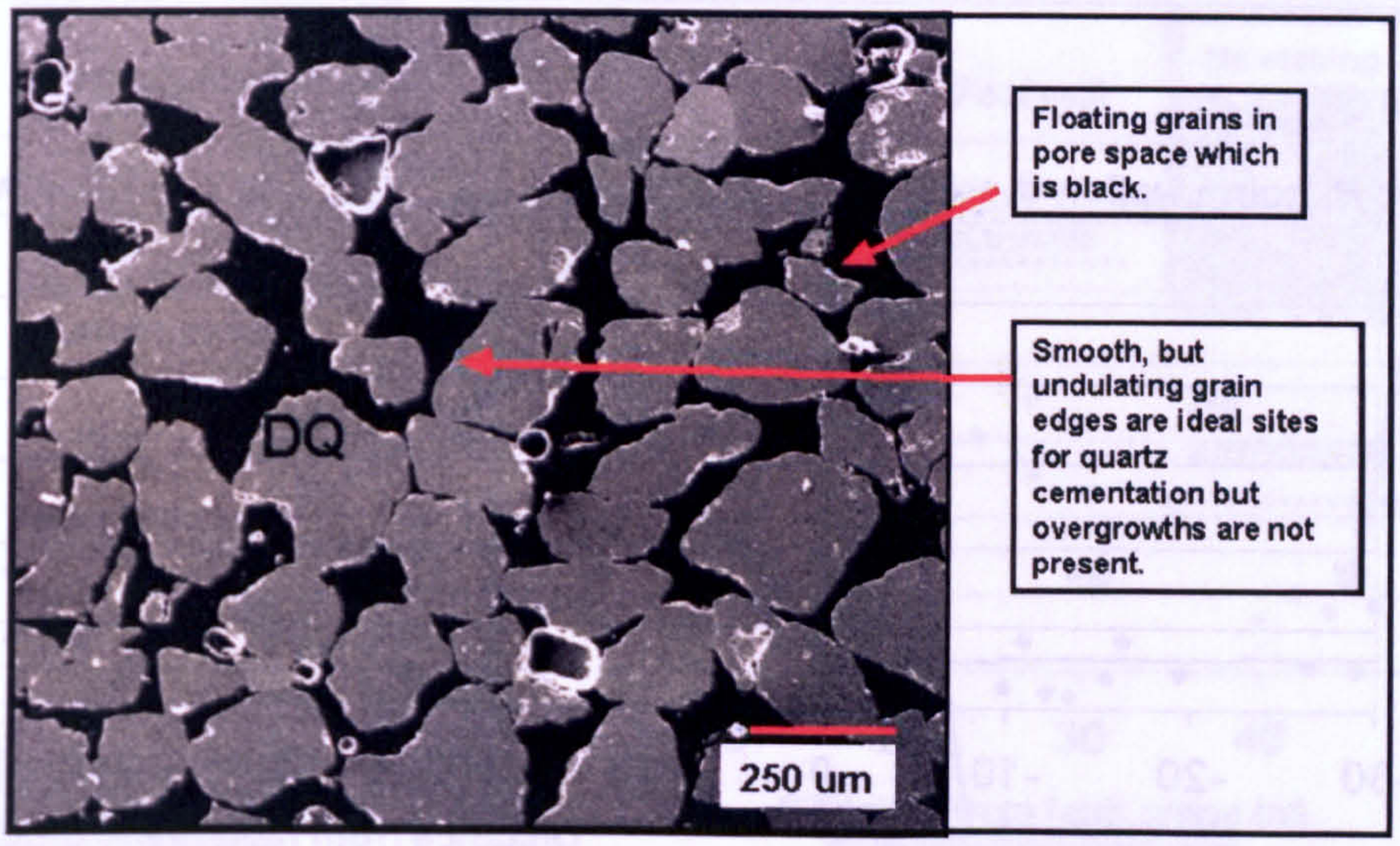


**Plate 5.14. SEM-SE image of hanging wall sandstone from the Clashach Fault showing rounded, clean detrital quartz grains with minor quartz cementation present. The lack of any dissolution textures suggests that no prior cements, which may have subsequently dissolved, were present in the hanging wall sands. From Clashach Fault hanging wall 4m from fault plane. *DQ=Detrital Quartz, PS= Pore Space.***

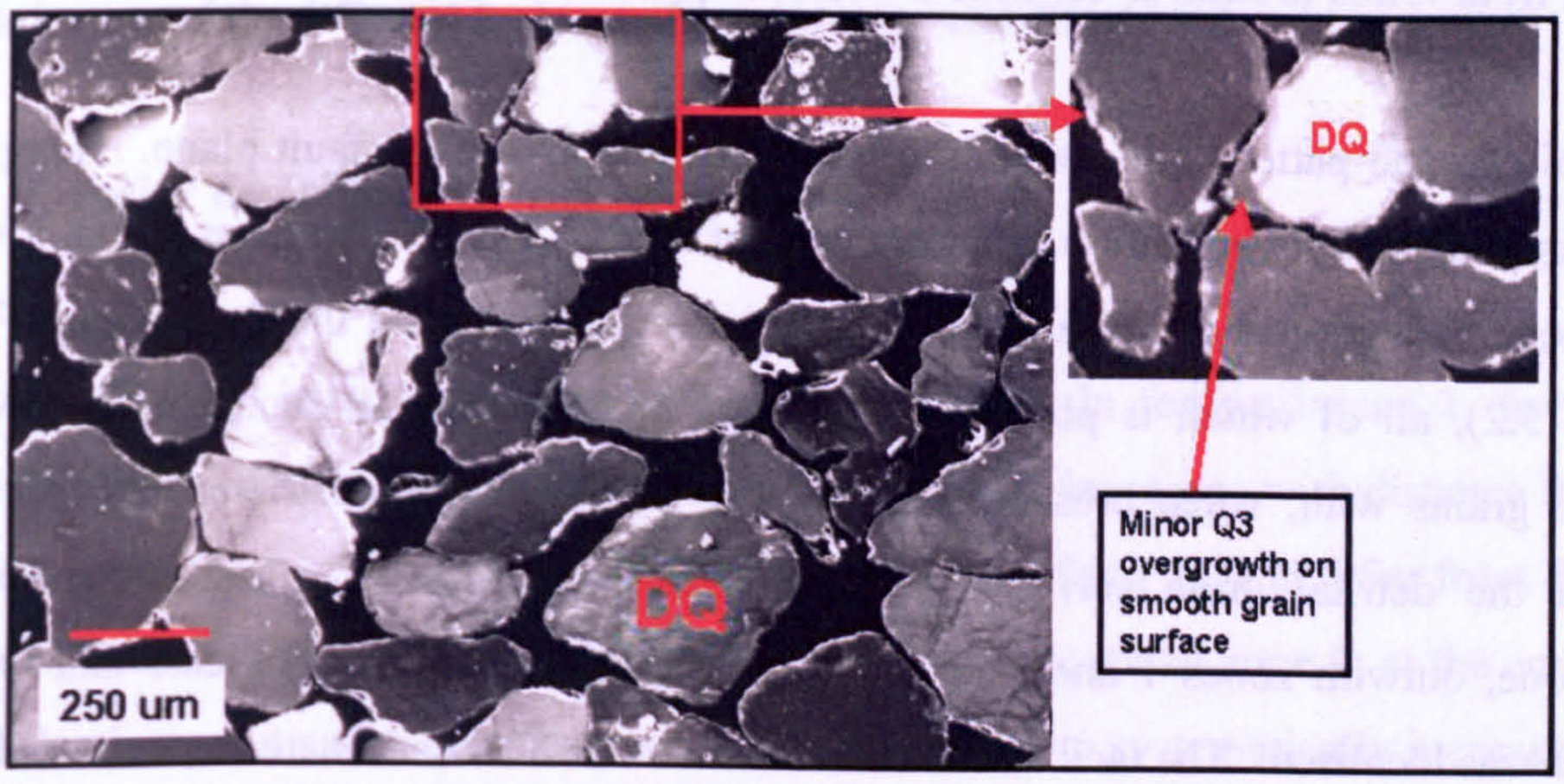


**Plate 5.15. SEM-CL image of a hanging wall sandstone from the Clashach Fault showing smooth detrital grains and minor Q3 overgrowths on rare grains. No grain-coating material which may inhibit quartz cement nucleation was detected. on smooth grains. Inset shows the small scale of quartz overgrowth and the characteristic homogeneous CL signature of Q3 cement. From 4m from the fault plane. *DQ=Detrital Quartz, PS= Pore Space.***

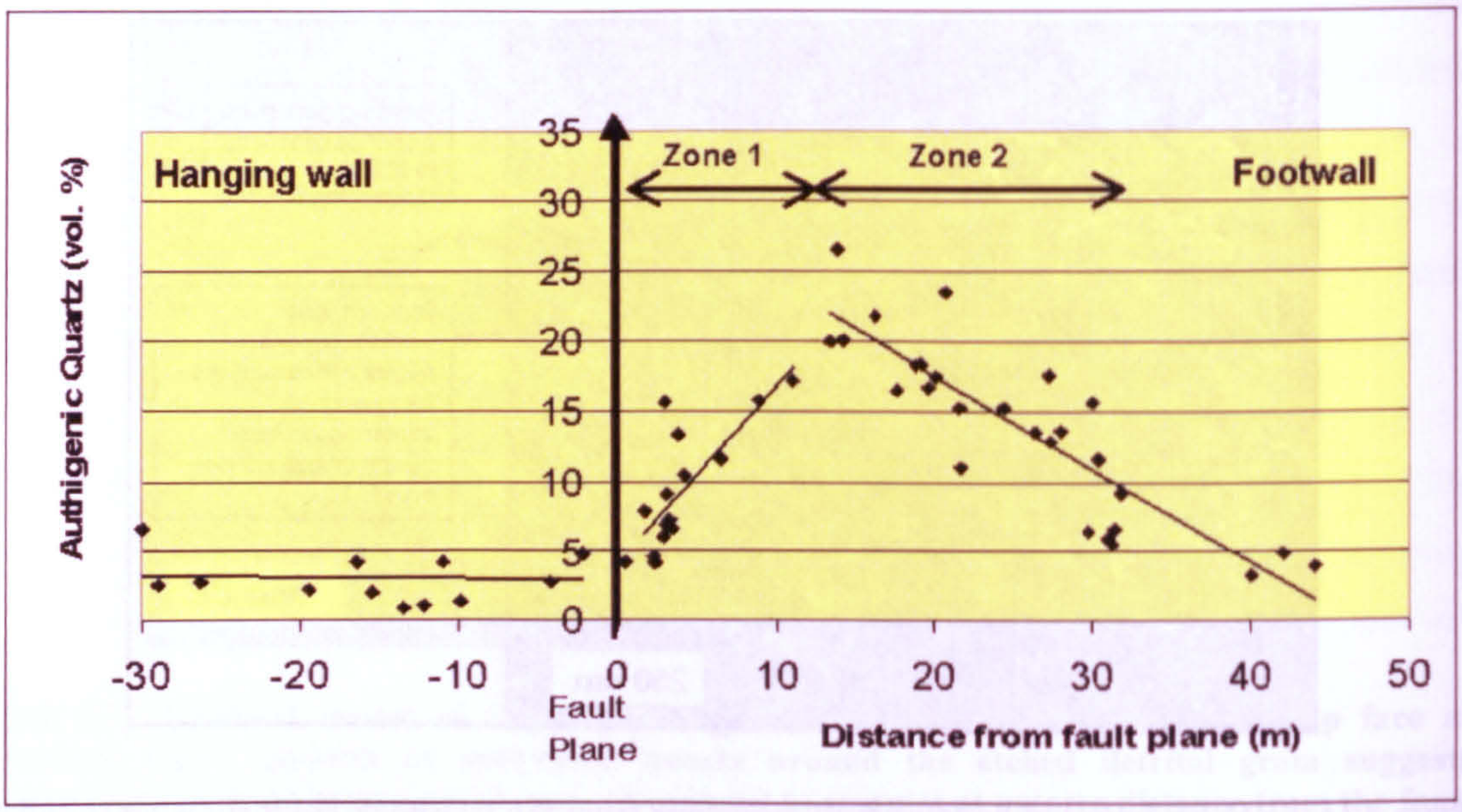


**Fig. 5.5. Quartz cement volume, measured from SEM-CL images by point counting. Sampling was in a south to north profile across the Clashach Fault in Clashach Quarry. Quartz cement follows an asymmetric trend across the fault plane. Hanging wall sands, and footwall sands at >40m distant, contain 3-4% authigenic quartz. The footwall displays two opposite trends, increasing quartz cement with distance from the fault from 0.5-13.8m, and decreasing quartz cement from 13.8m to 32m. $R^2$ for zone 1 = 0.57, zone 2 = 0.76.**

The volume and pattern of cementation is asymmetric across the fault plane. Hanging wall sands display a slight reduction in quartz cement from 4.8% at 2.3m from the fault slip face to a mean background of 3% at a distance greater than 2m from the fault plane (Fig. 5.5.) (Table 5.2), all of which is phase Q3. Textures of hanging wall samples display smooth detrital grains with, when present, overgrowths which grow unrestricted into pore space, around the detrital grain surfaces. Textures of hanging wall sandstone and footwall sandstone, outwith zones 1 and 2, 0.5-31.7m from the fault plane, indicate that Q2 quartz cement was localised. The lack of etched textures shows that carbonate cement was localised around the fault in patches within the footwall (Fig 5.6).

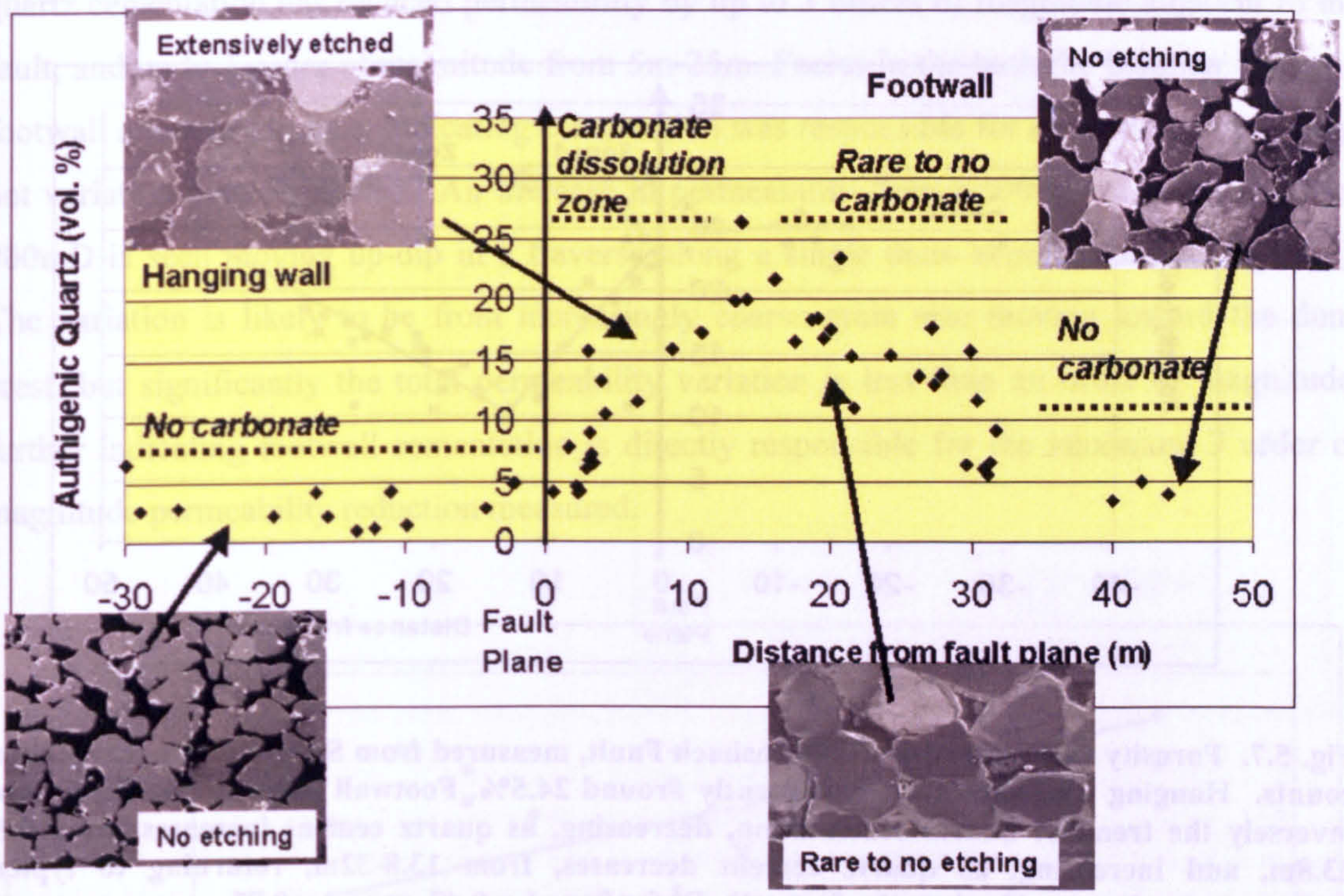


**Fig. 5.6. Quartz cement profile across Clashach Fault (Fig 5.5.) with representative petrographic SEM-CL images of the different textures of cementation and dissolution.**

## 5.62 Porosity distribution

Porosity displays an inverse relationship to quartz cement. In footwall zone 1, from 0.5m through to 13.8m from the fault plane, where quartz cement increases with distance from the fault plane, porosity decreases along a linear line of best fit from 24% at 0.5m from the fault plane to 9.9% at 13.8m (Fig. 5.7). This pattern reverses in footwall zone 2, at the equivalent 13.8m inflection point as the quartz cement trend, and porosity systematically increases along a linear line of best fit from 10% at 13.8m to 18.6% at 31.7m (Fig. 5.7). The coastal samples at 40-44m distant contain a mean porosity of 24%. The hanging wall porosity is consistently high, at 2.3m from the fault plane porosity is 23.3%, and at greater distances porosity is a mean value of 24.5%. These values are very similar to the background coastal samples from the footwall 40-44m from the fault.

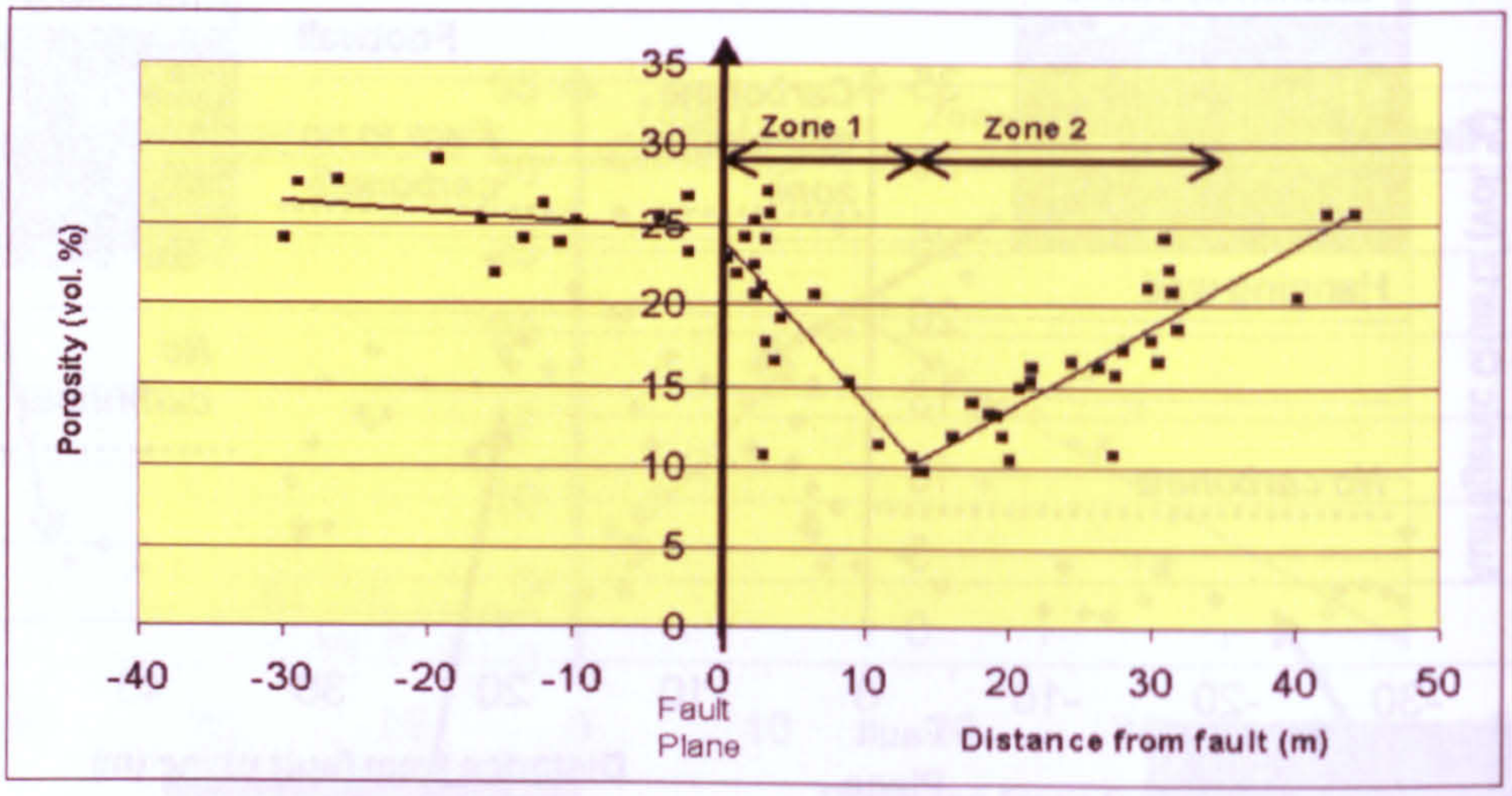


**Fig. 5.7. Porosity variation across the Clashach Fault, measured from SEM-CL images by point counts. Hanging wall values are consistently around 24.5%. Footwall porosity volume follows inversely the trend of quartz cementation, decreasing, as quartz cement increases, from 0.5-13.8m, and increasing, as quartz cement decreases, from 13.8-32m, returning to typical background values by 42m into the footwall. $R^2$ for zone 1 = 0.47, zone 2 = 0.77.**

## 5.63 Permeability distribution

Field measurements of permeability could not be made on identical samples as the point count data due to continued working within Clashach Quarry between field periods, which resulted in removal of quarry faces previously sampled for point count data. The non-destructive nature of the mini-permeameter technique allowed measurements to be taken in the Clashach Cove location, where complete traverses through the footwall and a significant distance into the hanging wall could be made. Footwall permeability in Clashach Cove was measured along the base of an individual cm thick dune slip face foreset in order to avoid measuring the effect on permeability of natural variation within facies. To quantify the natural intra-facies permeability variation, a lateral traverse through the hanging wall, cutting several dune slip facies foresets was measured.

Permeability, as for porosity, displays a trend of increasing value with increasing distance from the fault plane, rising from <1mD at 1m from the main fault slip face, to 10-100mD from 5m to 25m (Fig. 5.9). The background permeability values, at 45m into the footwall, and in the hanging wall all lie within the 100-1000mD range, meaning that the enhanced

quartz cementation has reduced permeability by up to 3 orders of magnitude adjacent to the fault, and up to 1 order of magnitude from 5m-25m. Facies in the both the hanging wall and footwall are dune slipface, indicating cementation was responsible for reducing permeability, not variation between facies. An increase in permeability from c.100mD to a maximum of 900mD is seen moving up-dip in a traverse along a single dune slipface foreset (Fig. 5.8). The variation is likely to be from increasingly coarse grain size moving toward the dune crest, but significantly the total permeability variation is less than an order of magnitude, further indicating footwall cementation is directly responsible for the maximum 3 order of magnitude permeability reduction measured.

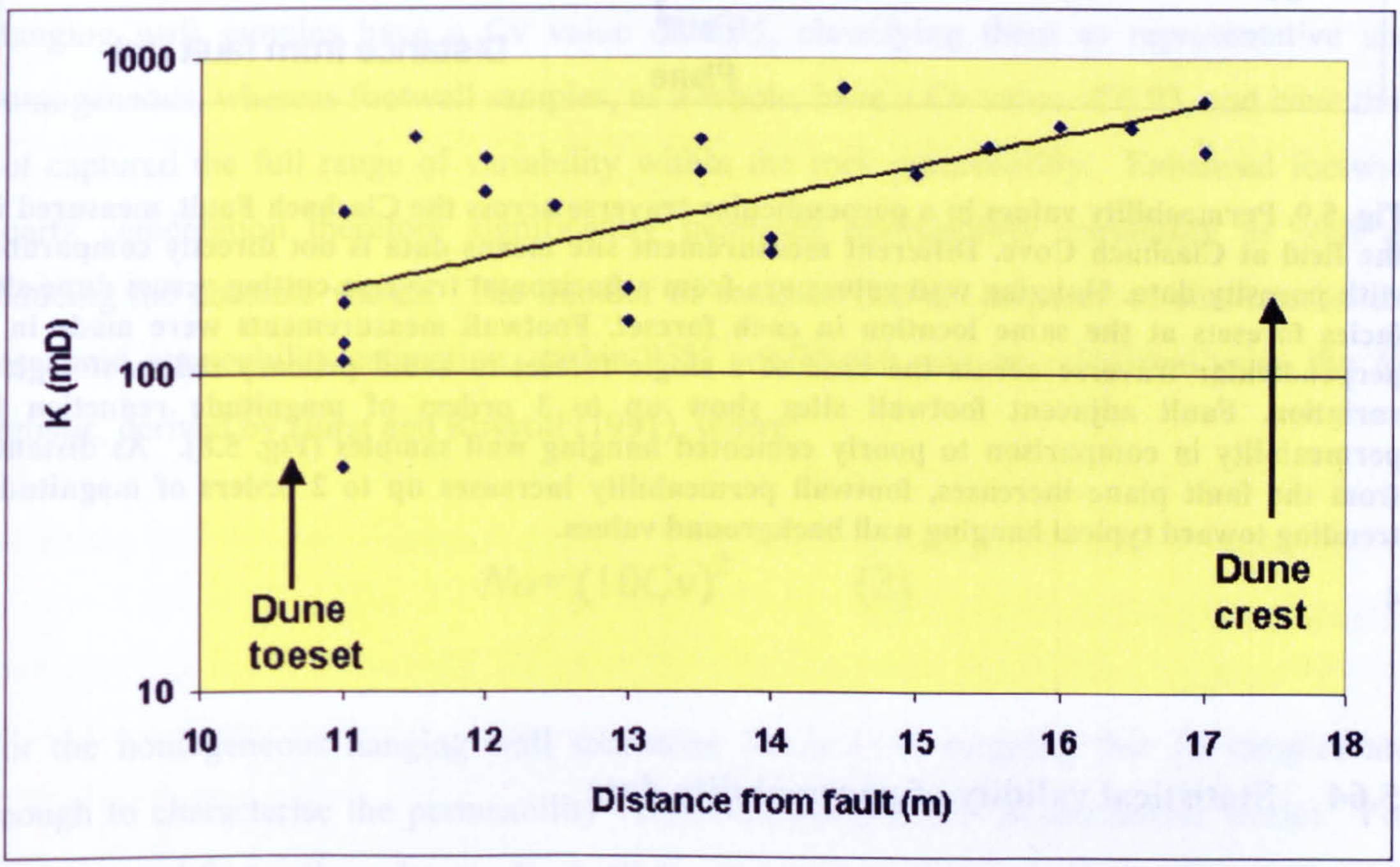


**Fig. 5.8. Permeability data from the poorly cemented hanging wall of the Clashach Fault. Measurements were made within dune-slip face facies, moving up-dip along a single dune-slip face foreset. The increase in permeability represents the natural increase moving up-dip through the dune foreset, where grain size becomes increasingly coarse. This range of facies permeability variation is within the same order of magnitude and is significantly less than the permeability reduction caused by footwall quartz cement. Trend line shown is the statistically fitted exponential trend.**

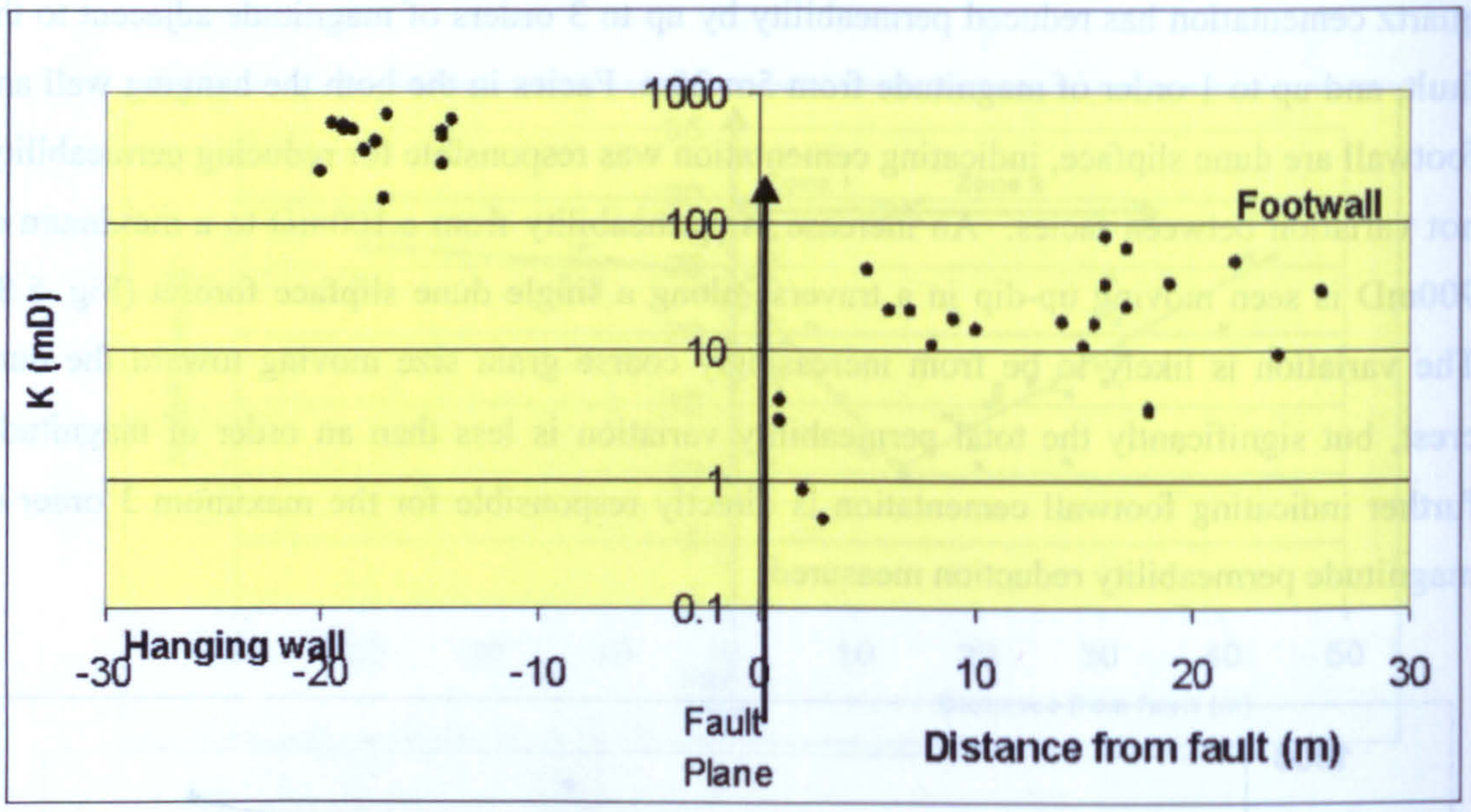


**Fig. 5.9. Permeability values in a perpendicular traverse across the Clashach Fault, measured in the field at Clashach Cove. Different measurement site means data is not directly comparable with porosity data. Hanging wall values are from a horizontal traverse cutting across dune-slip facies foresets at the same location in each foreset. Footwall measurements were made in a perpendicular traverse across the base of a single foreset to avoid primary sedimentological variation. Fault adjacent footwall sites show up to 3 orders of magnitude reduction in permeability in comparison to poorly cemented hanging wall samples (Fig. 5.8). As distance from the fault plane increases, footwall permeability increases up to 2 orders of magnitude, trending toward typical hanging wall background values.**

4

## 5.64 Statistical validity of permeability data

Field exposures have allowed frequent samples to be taken, which may not be available in analogous sub-surface settings, allowing detailed characterisation of the variation in permeability caused by differing volumes of cement and porosity. Analysis of the coefficient of variance (Cv) allows an understanding of how well the variation in permeability has been characterised. Accordingly a quantitative analysis of the number of samples required to accurately characterise a similar scale feature has been gained. The high number of samples has also allowed the inter-relations between cement volume, porosity and permeability to be quantified with greater accuracy than studies with sparse data available.

Statistical analysis of the permeability data using the coefficient of variation (Cv) allows classification of the hanging wall and footwall permeability as representative (Cv<0.5), heterogeneous and unrepresentative (0.5 <Cv<1), or very heterogeneous and unrepresentative (Cv>1), according to the scheme of Corbett and Jensen (1992) and Jensen *et al.* (1997) where Cv equals:

$$Cv = s.d./K_{ar} \qquad (1)$$

Where s.d. = standard deviation and $K_{ar}$ = arithmetic mean.

Hanging wall samples have a Cv value of 0.35, classifying them as representative and homogeneous, whereas footwall samples, as a whole, have a Cv value of 0.93, and have thus not captured the full range of variability within the rock permeability. Enhanced footwall quartz cementation therefore significantly increases permeability variability as well as reducing the absolute values. The number of samples that are required to characterise the measured permeability estimation, within 95% confidence, can be calculated using the *No* statistic, derived by Hurst and Rosvoll (1991), where:

$$No = (10Cv)^2 \qquad (2)$$

For the homogeneous hanging wall sandstone *No* is 11.9, meaning that 12 samples are enough to characterise the permeability variation measured (13 measurements made). For the cemented footwall sandstone, *No* is 87.1, compared to the 21 readings taken, indicating that more samples need to be taken to accurately characterise a sandstone with a similar level of heterogeneity.

## 5.7 Burghead Fault: cement, porosity and permeability data

### 5.71 Cementation

Quartz cement displays a simple pattern throughout the exposed Hopeman Sandstone footwall of the Burghead Fault. The small number of samples means values of cement quoted

here have been interpreted from a linear line of best fit. Quartz (Q2) cement volume increases from 24.5% at 13m distant to 29.2% at 0.5m from the main slip face (Fig 5.10) (Table 5.3). Quartz cement is ubiquitously Q2 phase and euhedral overgrowths are visible where there is some porosity. Where porosity is reduced to zero the morphology of the cement typically displays overgrowth textures with compromise growth boundary's dividing individual overgrowths. In several samples the cement displays the same CL signature as Q2 cement but appears to be a massive pore-filling macro-cement with boundary's and euhedral overgrowth structures difficult to identify, although this observation may be because of the lack of pore space. Such samples are more frequent in highly silicified sand adjacent to the fault. In comparison to observations within the footwall of the Clashach Fault, no detrital etching is seen, and quartz cement nucleates around smooth grain boundary's (Plate 5.16). Fractured grains, filled with authigenic quartz, were observed more frequently around the Burghead Fault near deformation bands and the main slip face, but not as regularly within the undeformed samples quantitatively analysed. Such fracture fill cement has the same CL signature (phase Q2) as the pore-filling overgrowth authigenic quartz indicating, texturally, that the cements are coeval, and suggesting that the Q2 phase of cement was emplaced during micro-fracture of the grains in response to the main phase(s) of faulting. Lead-zinc mineralisation observed in the footwall of the Burghead Fault can be seen to post-date the fault-related Q2 quartz overgrowths (Plate 5.17). Sample distance is restricted by the extent of footwall exposure from the fault.

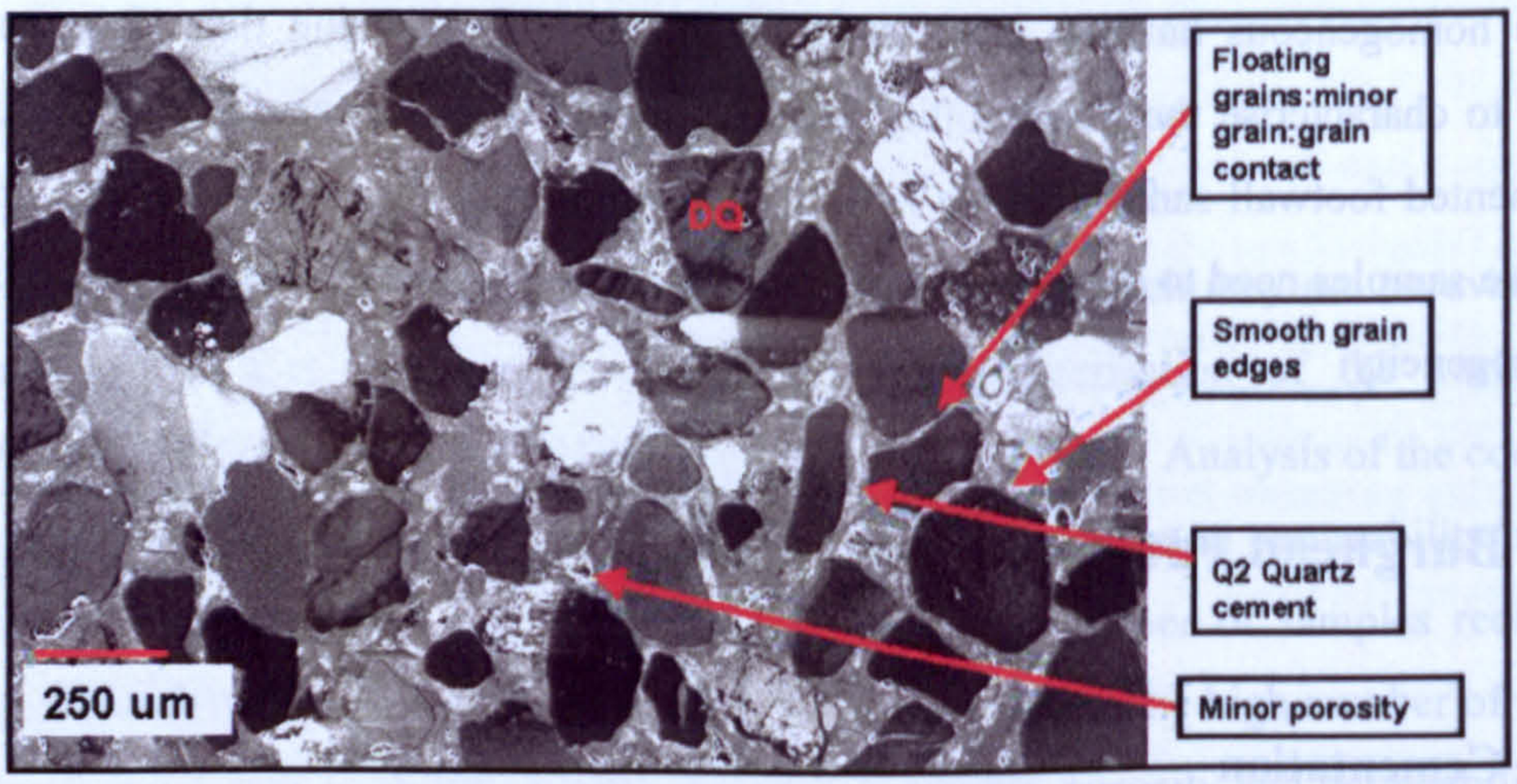


**Plate 5.16. SEM-CL image of Hopeman Sandstone in the Burghead Fault footwall. Early quartz cementation fills most of the pore space resulting in only minimal grain contact and some floating grains. Smooth grain edges indicate that there was no pre-exiting carbonate cement. From Burghead Fault footwall 8m into footwall. *DQ=Detrital Quartz.***

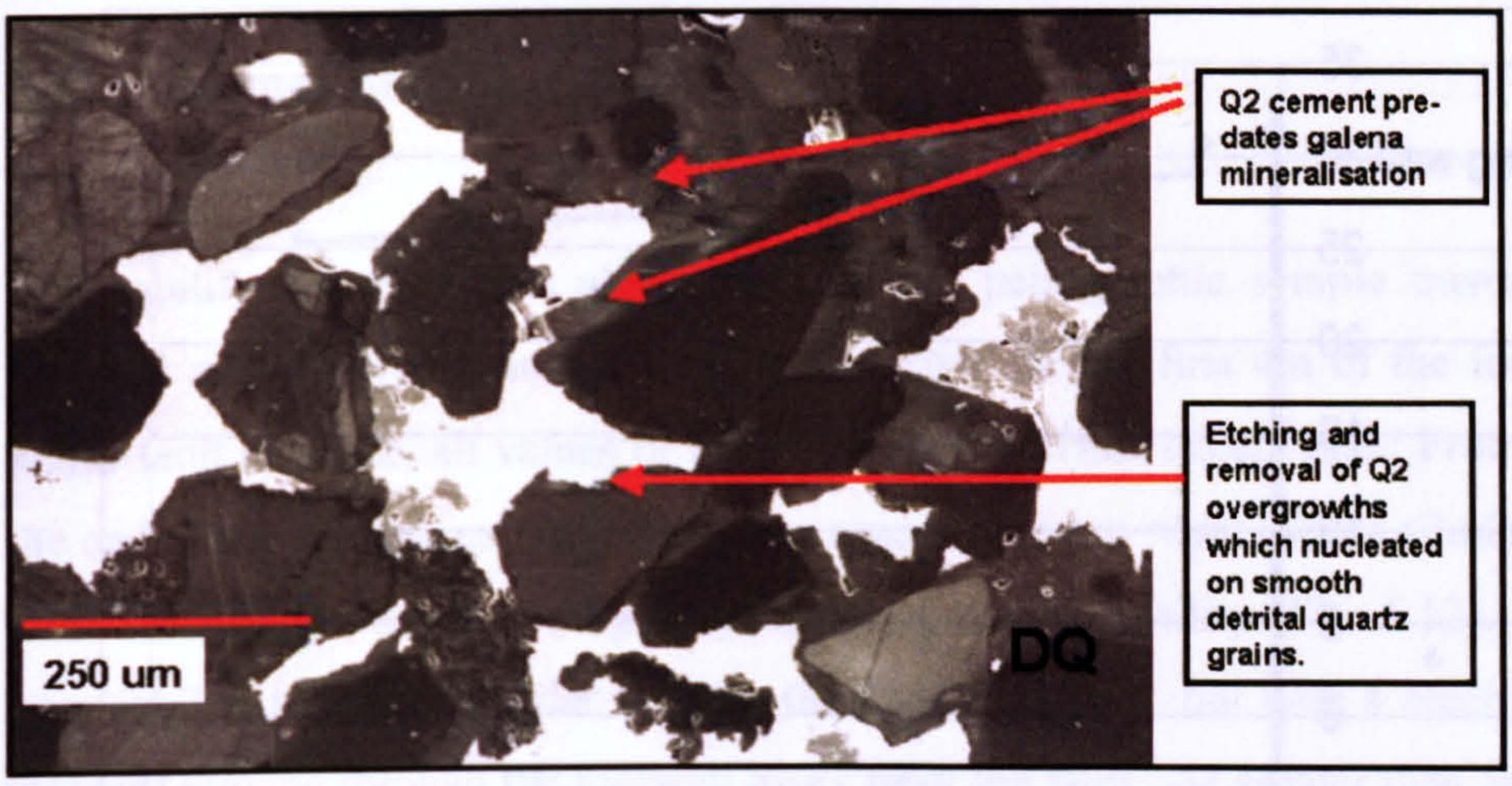


**Plate 5.17. SEM-CL image of Burghead Fault footwall sandstone containing galena mineralisation (bright white). The galena post-dates Q2 quartz precipitation and causes etching and removal of Q2 overgrowth and some rock fragment grains. From the Burghead Fault footwall 9.5m from fault plane. *DQ=Detrital Quartz.***

## 5.72 Porosity distribution

As at Clashach Fault, porosity follows an inverse trend to cement over the sample traverse distance. A linear line of best fit through the porosity data shows a decrease from 6.1% at 13m to 2.3% at 0.5m (Fig. 5.11). The trend of decreasing porosity approaching the main fault slip face is not as well defined as at the Clashach Fault, but correlates accurately with the volume of quartz cement within individual samples, showing cementation is the major control on porosity. Two samples of Triassic fluvial hanging wall sands display porosities of 14% and 18% at 2m and 5m respectively from the fault. Quartz cement is a minor cement in these sands and porosity is occluded by early nodular calcite cements.

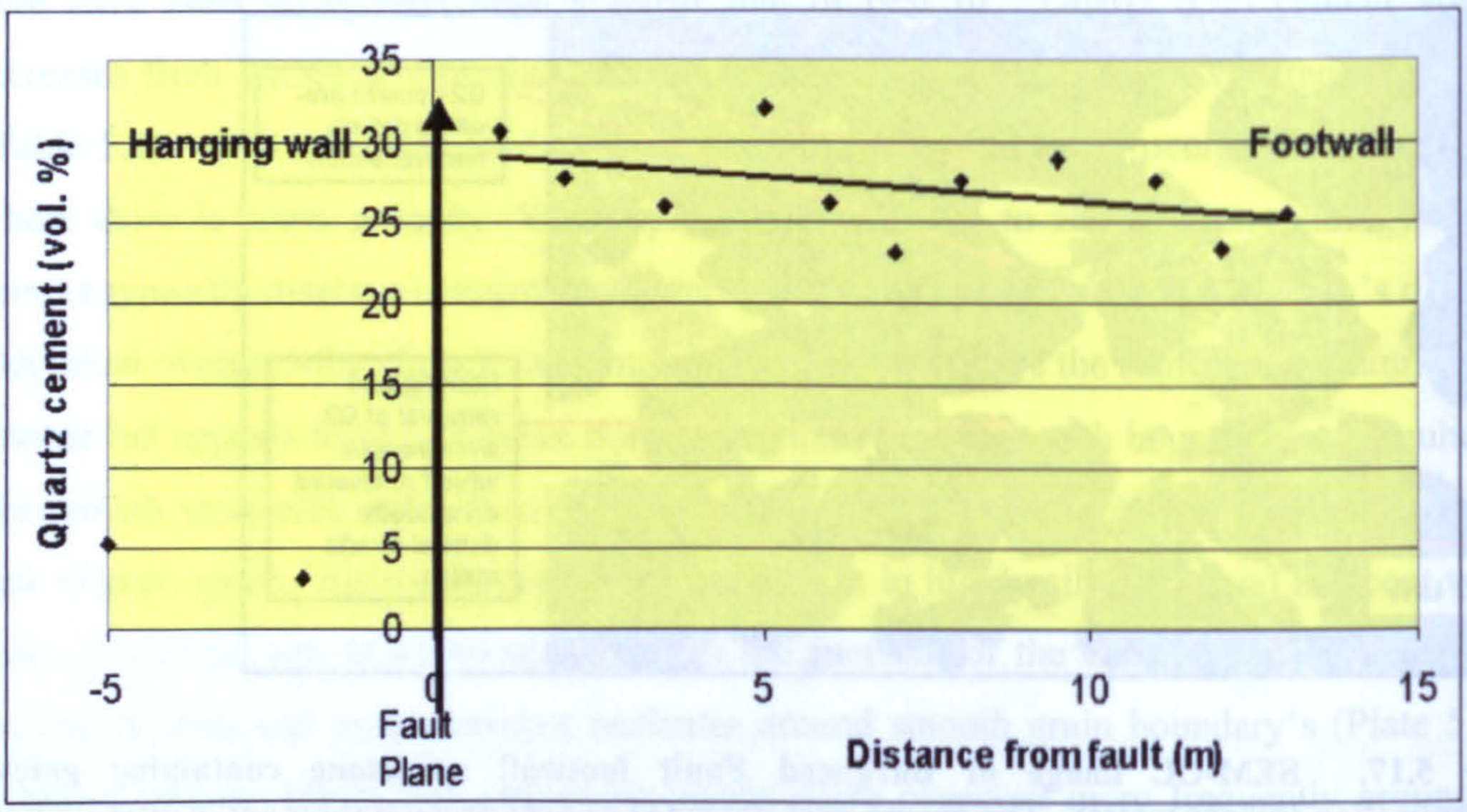


**Fig. 5.10. Quartz cement volume variation across the Burghead Fault. Footwall cement displays a broadly linear trend of decreasing cement with increasing distance from the main fault slip face. Hanging wall samples are from a different lithology, the fluvial Triassic Burghead Beds, but display significantly less quartz cement than the footwall Hopeman Sandstone, despite a difference in burial of less than a few hundred metres. All samples are within the fault damage zone but are from undeformed sandstone. Linear line of best fit with an $R^2$ value of 0.2174 for the smaller Burghead Fault data set.**

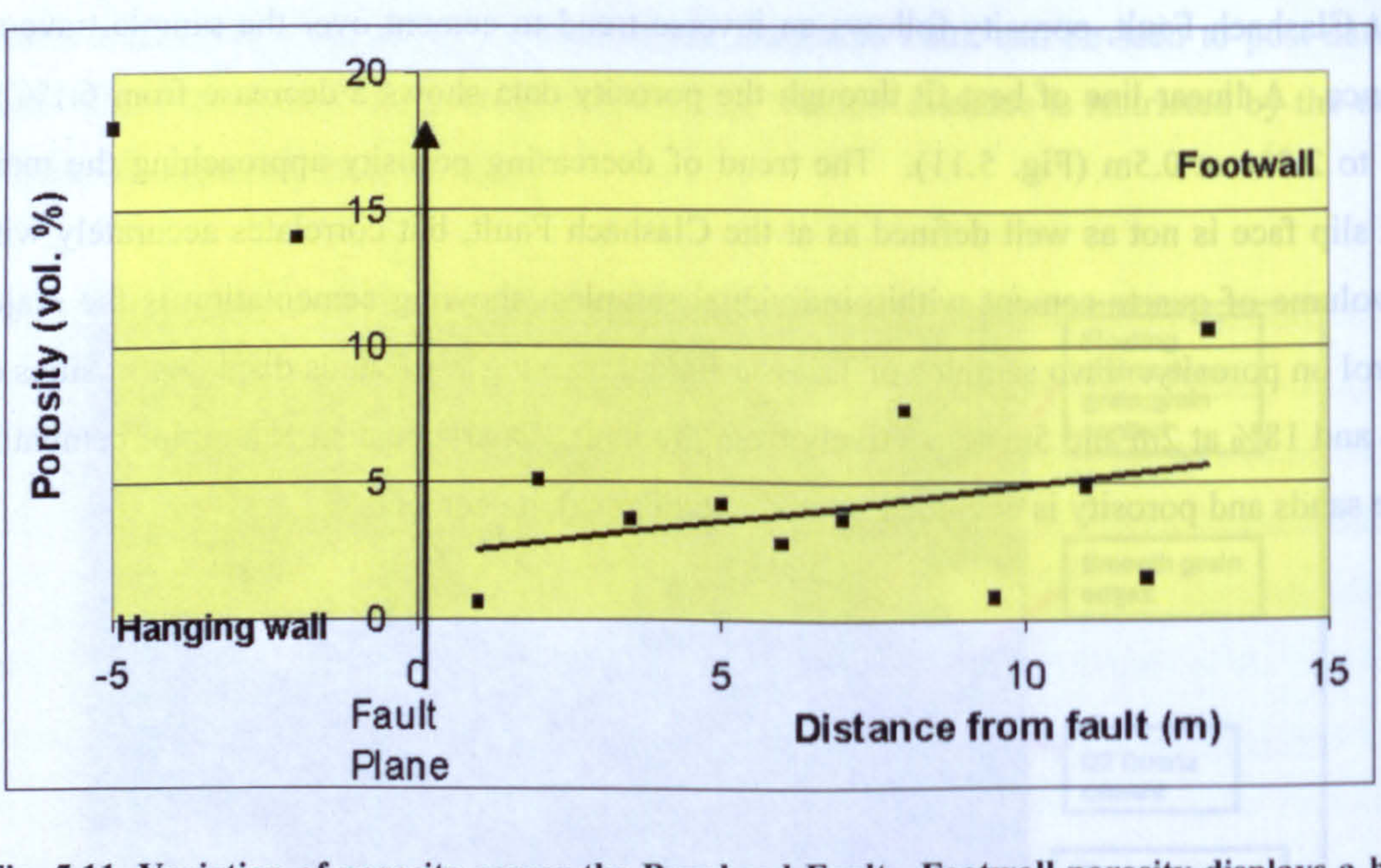


**Fig. 5.11. Variation of porosity across the Burghead Fault. Footwall porosity displays a broad increase with increasing distance from the main fault slip face. Individual samples with higher porosity have lower values of quartz cement. Overall each sample has low porosity in comparison to the background Hopeman Sandstone where average porosity >20%. Hanging wall samples are from the fluvial Triassic Burghead Beds, and contain minor quartz and carbonate cements compared to the footwall sandstone. Linear line of best fit with R2 = 0.1262 for the limited Burghead Fault dataset**

## 5.73 Permeability distribution

Permeability was measured along the identical petrographic sample traverse through the footwall and displays a similar trend to porosity. In the first 4m of the footwall from the major fault slip face, all values of permeability are <1mD except one. From 5m through to the end of the traverse at 13m, values are spread between <1mD up to <7mD, indicating, for most samples, an order of magnitude increase in permeability (Fig. 5.12). The pattern of permeability follows a similar trend to the Clashach Fault, but with a much reduced rate of increase moving through the footwall away from the fault. At greater than 5m from the fault plane at the Clashach Fault values fall into the 10-100mD bracket, an order of magnitude greater than measurements in the equivalent spatial position at Burghead, in agreement with the comparison of the trends of quartz cement volume at both faults. The resolution of the field permeameter is ~1mD so it may be assumed that the lowest values measured are a maximum permeability and that, particularly at the Burghead Fault the 0-5m portion of footwall rock may have permeability significantly less than 1mD.

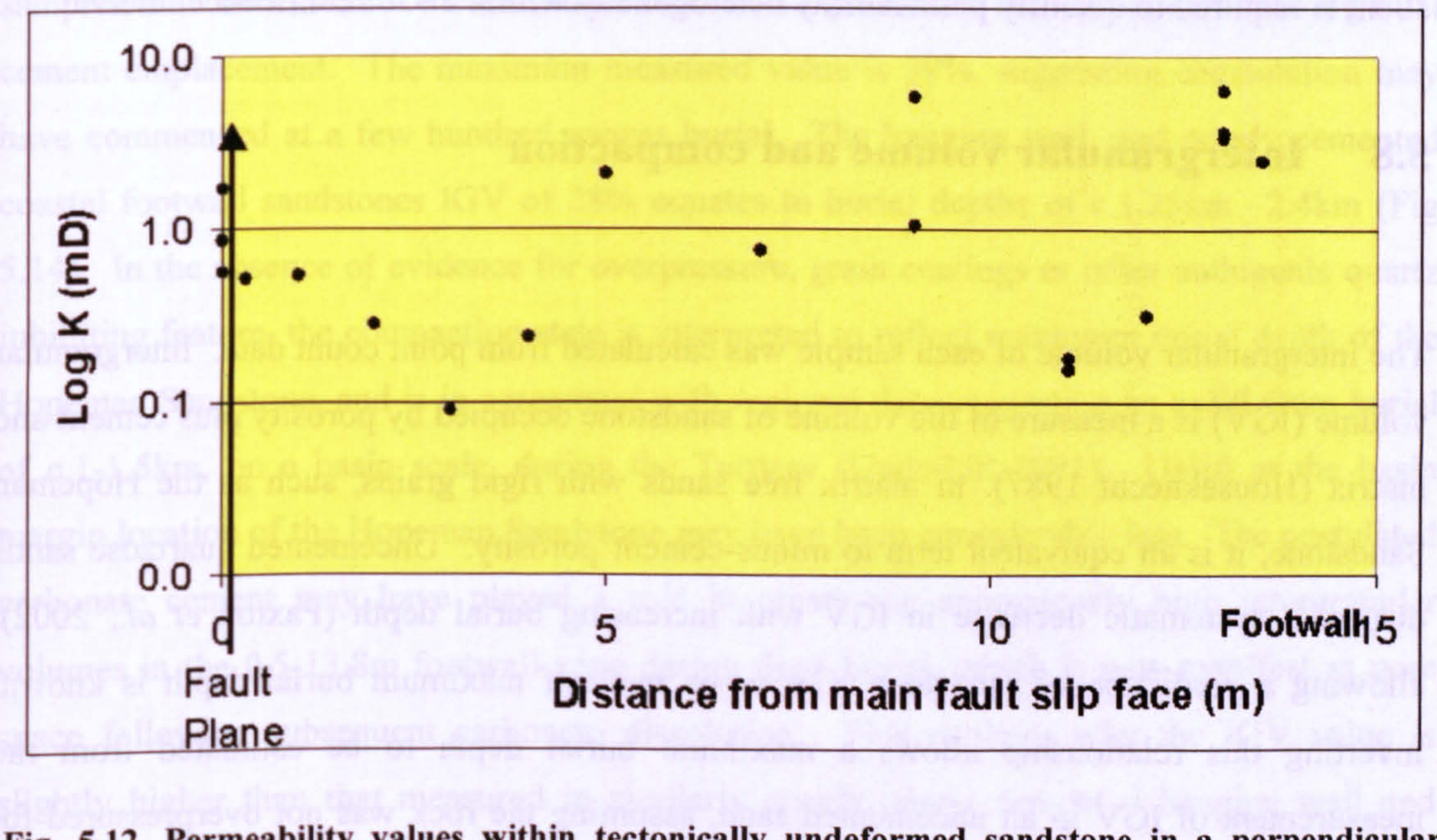


**Fig. 5.12. Permeability values within tectonically undeformed sandstone in a perpendicular traverse through the Burghead fault plane and into the footwall. Permeability is reduced up to 3 orders of magnitude compared to background Hopeman Sandstone, and shows a broad increase with increasing distance from the fault. Permeability values at greater than 5m from the main slip face are an order of magnitude less than the equivalent position in the footwall to the Clashach Fault (Fig 5.9), corresponding to the increased volumes of cement surrounding the Burghead Fault, suggesting a scale relationship between increasing throw and quartz cementation and decreasing porosity and permeability.**

## 5.74 Statistical validity of permeability data

Statistical manipulation of the Burghead Fault footwall permeability data using equation (1) reveals a Cv value of 1.17, classifying the sandstone as very heterogeneous with insufficient data to fully characterise permeability. In comparison to the Cv value of 0.35 for the uncemented sandstone at Clashach, this indicates that the authigenic quartz has introduced severe heterogeneity in comparison to uncemented sandstone. Absolute values of permeability in the Burghead Fault footwall are, in general, lower than those in the footwall of the Clashach Fault, with the spread in these lower values appearing to correspond to an increase in heterogeneity. Combined with the observation of higher total cement volumes around the Burghead Fault, in comparison to the Clashach Fault, a positive relationship between quartz cement volume and permeability variability is suggested. Using equation (2), calculated *No* for the Burghead Fault footwall is 137, indicating that a very high number of samples are required to characterise the permeability variation measured. As the permeability data were obtained over a 14m interval, the *No* value implies one sample per 10cm is required to quantify permeability heterogeneity within a 95% confidence interval.

## 5.8 Intergranular volume and compaction

The intergranular volume of each sample was calculated from point count data. Intergranular volume (IGV) is a measure of the volume of sandstone occupied by porosity plus cement and matrix (Houseknecht 1987). In matrix free sands with rigid grains, such as the Hopeman Sandstone, it is an equivalent term to minus-cement porosity. Uncemented quartzose sands display a systematic decrease in IGV with increasing burial depth (Paxton *et al.*, 2002), allowing a prediction of sandstone IGV to be made if maximum burial depth is known. Inverting this relationship allows a maximum burial depth to be estimated from the measurement of IGV in an uncemented sand, assuming the rock was not overpressured for significant periods of its deepest burial state. At the other extreme, in sandstones in which cement reduces porosity to almost zero, the IGV retains a close approximation to the burial depth at the time of final, or significant cementation, as compaction cannot continue once IGV is filled, and thus the depth of cementation can be estimated.

## 5.81 Clashach Fault

At the Clashach Fault intergranular volume generally decreases in a linear trend moving from the main fault slip face (Fig. 5.13). Within footwall zone 1, 0.5-13.8m distance from the fault, the sandstone displaying evidence of carbonate cement dissolution has a mean IGV of 30%. Mean IGV in the quartz cemented zone, 13.8 –31.7m, is 31% and shows a decrease with increasing distance from the fault plane, trending toward the typical values of IGV measured in poorly cemented background sandstones, which in the footwall sands at 40-45m from the fault plane is 28%. This value matches that measured in hanging wall samples, where mean authigenic quartz is 3%, and intergranular volume is 28%.

Zone 2, the 'cemented zone' (13.8 to 31m) mean IGV of 31%, is equivalent to a burial depth of between 500m and 1.25km on the intergranular volume-compaction curve of Paxton *et al.* 2002 (Fig. 5.14) at the time of significant, or final cementation. The rock burial depth at the onset of cementation may have been shallower, as the final IGV in extensively cemented samples is an indication of the maximum state of compaction in the sandstone following final cement emplacement. The maximum measured value is 39%, suggesting cementation may have commenced at a few hundred metres burial. The hanging wall, and poorly cemented coastal footwall sandstones IGV of 28% equates to burial depths of c.1.25km –2.4km (Fig 5.14). In the absence of evidence for overpressure, grain coatings or other authigenic quartz inhibiting feature, the compaction state is interpreted to reflect maximum burial depth of the Hopeman Sandstone, and is in agreement with regional data suggesting an uplift from burial of c.1-1.5km, on a basin scale, during the Tertiary (Underhill 1991). Uplift at the basin margin location of the Hopeman Sandstone may have been considerably less. The postulated carbonate cement may have played a role in preserving anomalously high intergranular volumes in the 0.5-13.8m footwall zone during deep burial, which is now manifest as pore space following subsequent carbonate dissolution. This explains why the IGV value is slightly higher than that measured in similarly poorly quartz cemented hanging wall and coastal sandstones. The lack of evidence of any carbonate cement in the significantly quartz cemented, 13.8-31.7m footwall zone 2, means it is likely that the values of IGV measured, do accurately represent the state of compaction of the sandstone at the time of quartz cementation.

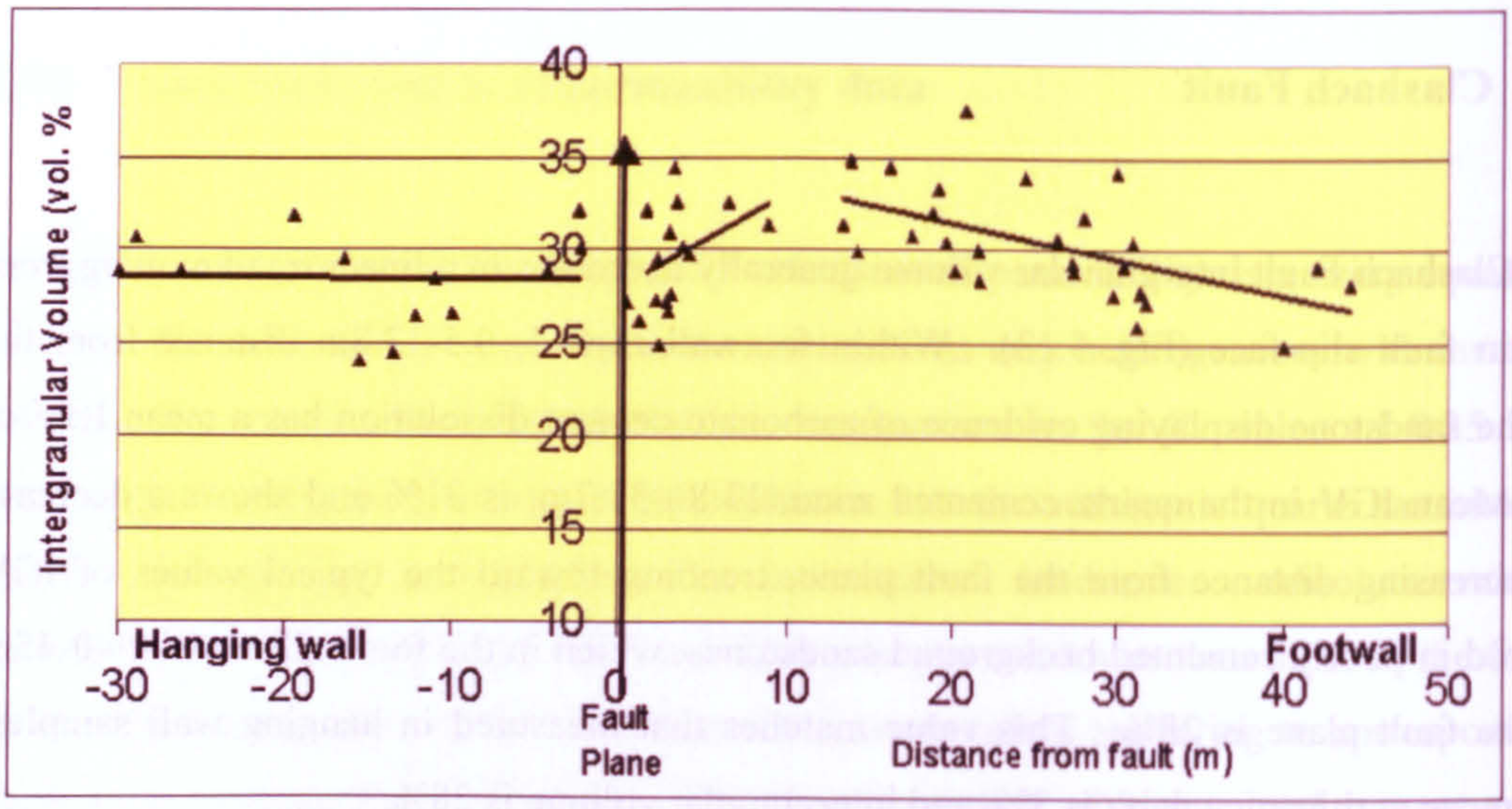


**Fig. 5.13. Intergranular volume variation across the Clashach Fault. Footwall IGV values are highest in samples with the greatest volume of quartz cementation, with a mean value of 31% in zone 2, 13.8-32m from the fault plane, through which IGV decreases in a linear pattern. The footwall zone 1 from 0.5-13.8m shows more scatter, but individual samples with a high amount of quartz cement, have high IGV. Hanging wall values, and footwall values beyond 40m, are a mean of 28 and 27% respectively. The high absolute values of IGV indicate that shallow cementation filled, and subsequently preserved, IGV prior to burial. Statistically fitted linear lines of best fit.**

As well as the absolute, shallow burial, value of IGV for the cemented footwall sand, the trend of decreasing IGV with increasing distance, and decreasing quartz cement, from the fault plane shows that Q2 phase quartz cement was emplaced during continued burial (Fig. 5.13). Increasing burial syn- and post-cementation caused continued compaction, a process increasingly arrested in footwall samples close to the fault containing higher volumes of cement. Burial depth-IGV error on the curve of Paxton *et al.* (2002) is +/-3%, however this range becomes increasingly crucial at depths below 1.5km, where only minor decreases in intergranular volume occur over significant ranges of burial. At the shallow depths observed for this case of cementation, the rate of change of IGV with depth is rapid allowing, with error bars, for a relatively accurate estimate of both absolute burial depth during significant cementation, and for the observation in incompletely cemented sands of subsequent burial (Fig.5.14)

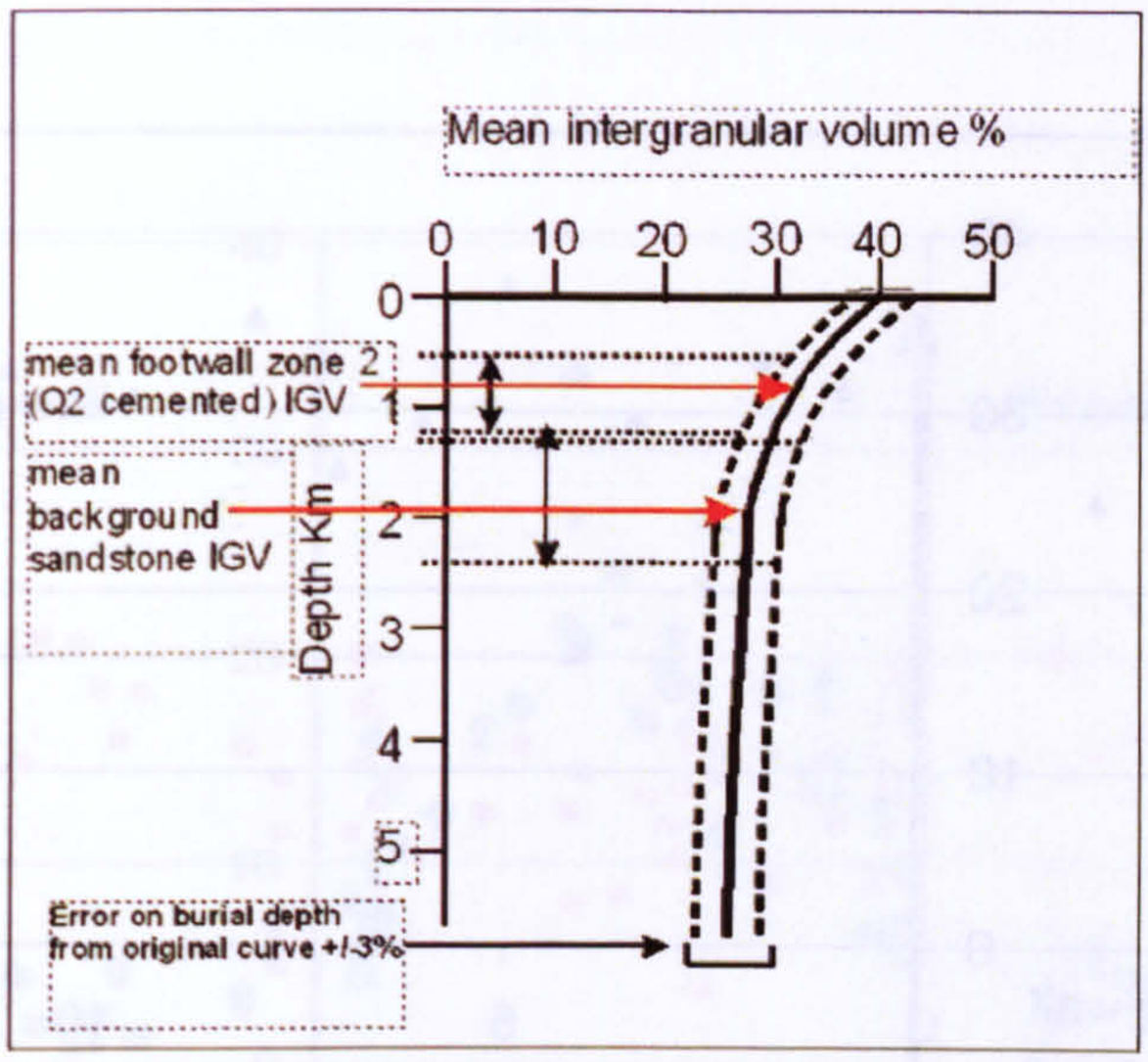


**Fig. 5.14. Intergranular volume decline with depth for uncemented quartzose sandstones, modified from Paxton et al. (2002). Mean present day intergranular volume in the 'cemented' footwall zone 2 equates to the compaction state of a sandstone buried to <1km, indicating that quartz cement emplaced at this depth preserved intergranular volume through further burial. Values for the 'cemented' zone 2 are a minimum, meaning cementation may have been at a shallower depth. The mean intergranular volume of the background Hopeman Sandstone equates to a burial depth of c.2km, and in the absence of significant cement preventing compaction, suggests this was a maximum burial depth, in agreement with regional stratigraphic and tectonic history. The range in burial depths is controlled by the +/-3% intergranular volume-depth error on the original plot of Paxton et al. (2002), but importantly shows the quartz cement was emplaced at a shallower depth than both maximum burial and the typical depth for extensive quartz cementation.**

## 5.82 Burghead Fault

IGV of exposed footwall sandstone adjacent to the main slip face of the Burghead Fault is a mean 32%, close to the mean figure for the most well cemented samples at Clashach Fault, 31% (13.8-31.7m) (Fig. 5.15). The lack of any observable systematic decrease in IGV with distance from the main slip face is a consequence of the short sampling traverse, compared to the long distance of cementation from the fault. Values are consistently high throughout the traverse, with minor decrease with increasing distance from the fault plane. The maximum value of 37% suggests cementation at a depth of c.300m, comparable to the maximum value observed at the Clashach Fault (39%). The lack of a significant trend of decreasing IGV with distance from the fault may be attributable to the increased size scale of the Burghead Fault, compared to the smaller Clashach Fault, and the increased amounts of quartz cement measured.

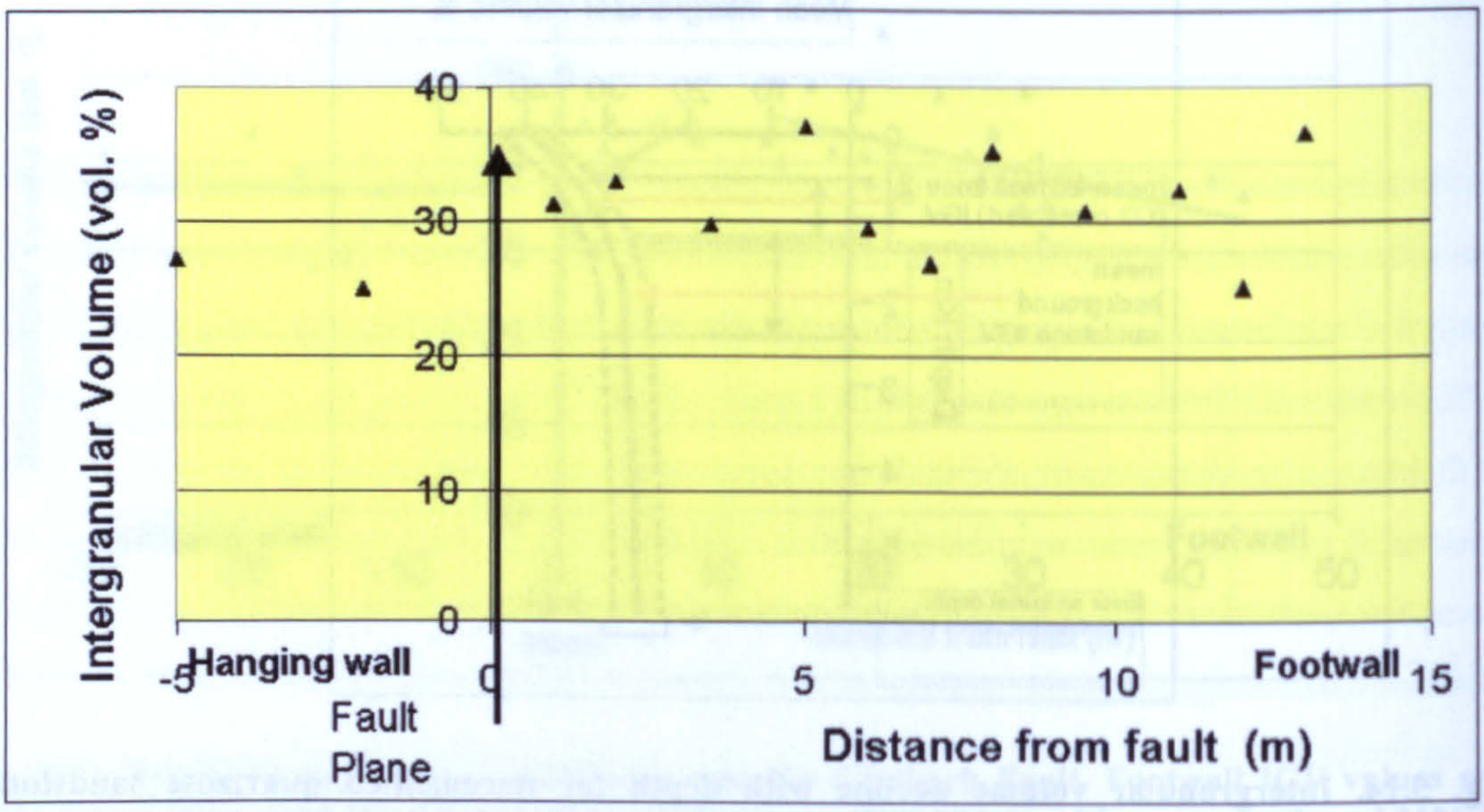


**Fig. 5.15. Intergranular volume pattern across the Burghead Fault. The footwall, Hopeman Sandstone displays a relatively consistent pattern of high values of intergranular volume, indicating cementation was emplaced at shallow burial depth, preventing mechanical compaction during further burial. Although, in comparison to the pattern at Clashach Fault (Fig. 5.13.), no trend of decreasing IGV with increasing distance from the fault can be identified. Comparison with background values for the Hopeman Sandstone of 27% IGV, indicates the cement was emplaced before maximum burial. The similarity of the IGV values between Clashach Fault and Burghead indicates that cementation was coeval at each fault.**

## 5.9 Compactional versus cementational porosity loss

Calculations of porosity loss using the method of Ehrenberg (1995) (Appendix D) reveal that with a depositional porosity of 40% compactional porosity loss (COPL) (terminology of Houseknecht 1987) is the dominant mechanism for pore space destruction in the Clashach Fault data set as a whole. The fourteen (from a sample set of 53) most highly cemented samples lose more porosity through cementation than compaction (Fig. 5.16). All contain greater than 15.2% quartz cement precipitated at shallow burial. All samples (except one) in which compaction dominates contain less than 15.2% cement providing further evidence for shallow cement precipitation occluding pore space prior to its destruction through burial compaction. Throughout zone 1, 0.5-13.8m from the fault plane, cementational porosity loss (CEPL) increases moving toward 13.8m, and then gradually decreases through zone 2 as quartz cement decreases.

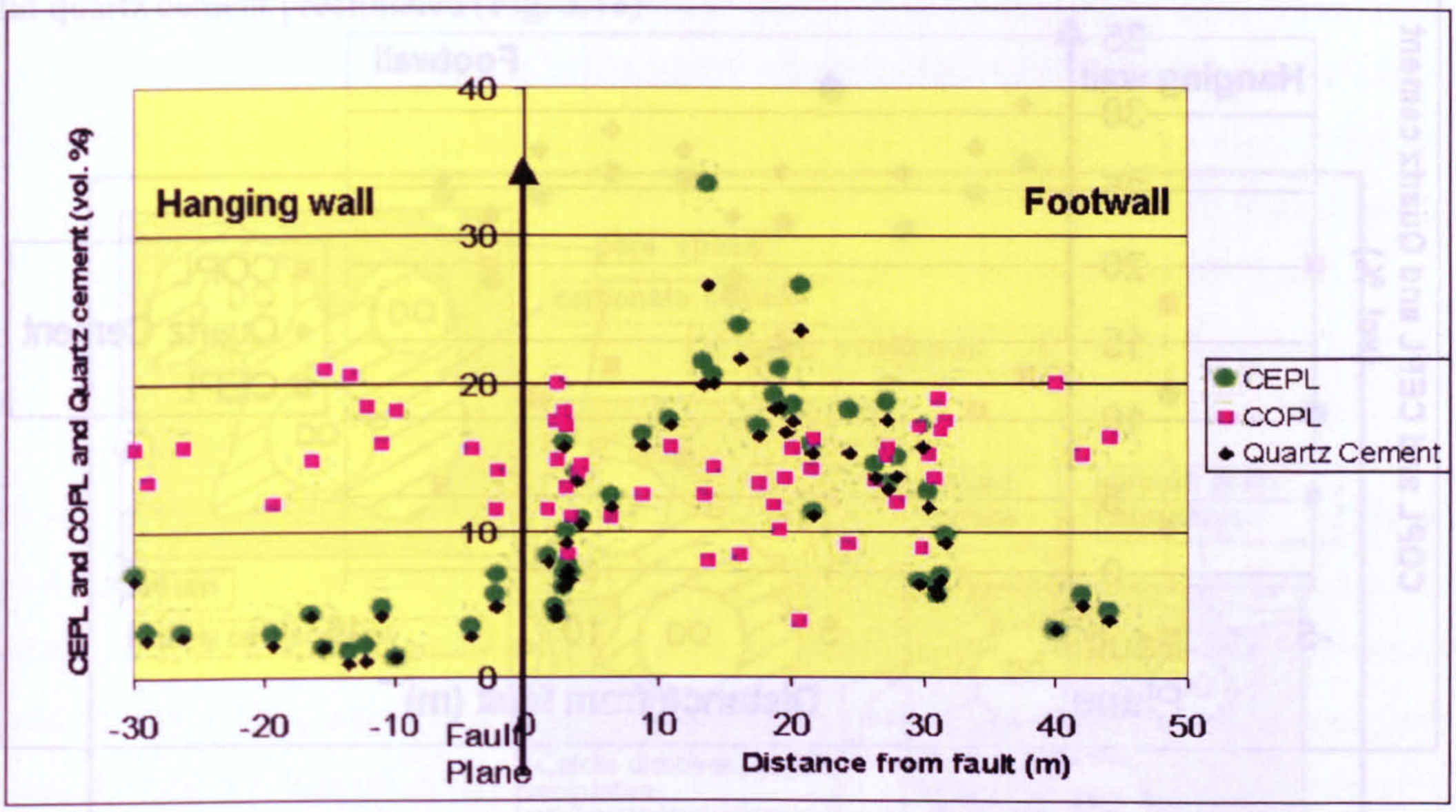


**Fig. 5.16. Compactional porosity loss (COPL) vs cementational porosity loss (CEPL) and quartz cement volume plotted together for the sandstone surrounding the Clashach Fault. Shallow cementation resulted in generally greater CEPL vs COPL for samples with greater than 15% quartz cement. Subsequent compaction in sandstones with less than 15% authigenic quartz resulted in the domination of compaction in porosity reduction, demonstrating significant shallow cementation must occur for CEPL to dominate. Overall the level of COPL is not altered by enhanced cementation, further porosity reduction is caused solely by higher values of quartz cement.**

In the footwall of the Burghead Fault CEPL dominates in all samples, except one (Fig. 5.17), with every sample containing greater than 22% authigenic quartz (Fig. 5.10). The overall higher volume of shallow cement in comparison to the Clashach Fault explains the increased prevalence of CEPL at Burghead. The dominance of cementation over compaction in removing porosity shows extensive cementation occurred during shallow burial, prior to and preventing, compaction during deeper burial. Evidence for deeper burial comes from both Clashach and Burghead faults where compaction is greater in less well cemented hanging wall and distal footwall samples. Assuming a similar relationship exists between cement volume and control on porosity loss between Burghead and Clashach shows that the zone of dominant cementational porosity loss at Burghead will extend until authigenic quartz volume is less than 15.2%. This is further discussed below.

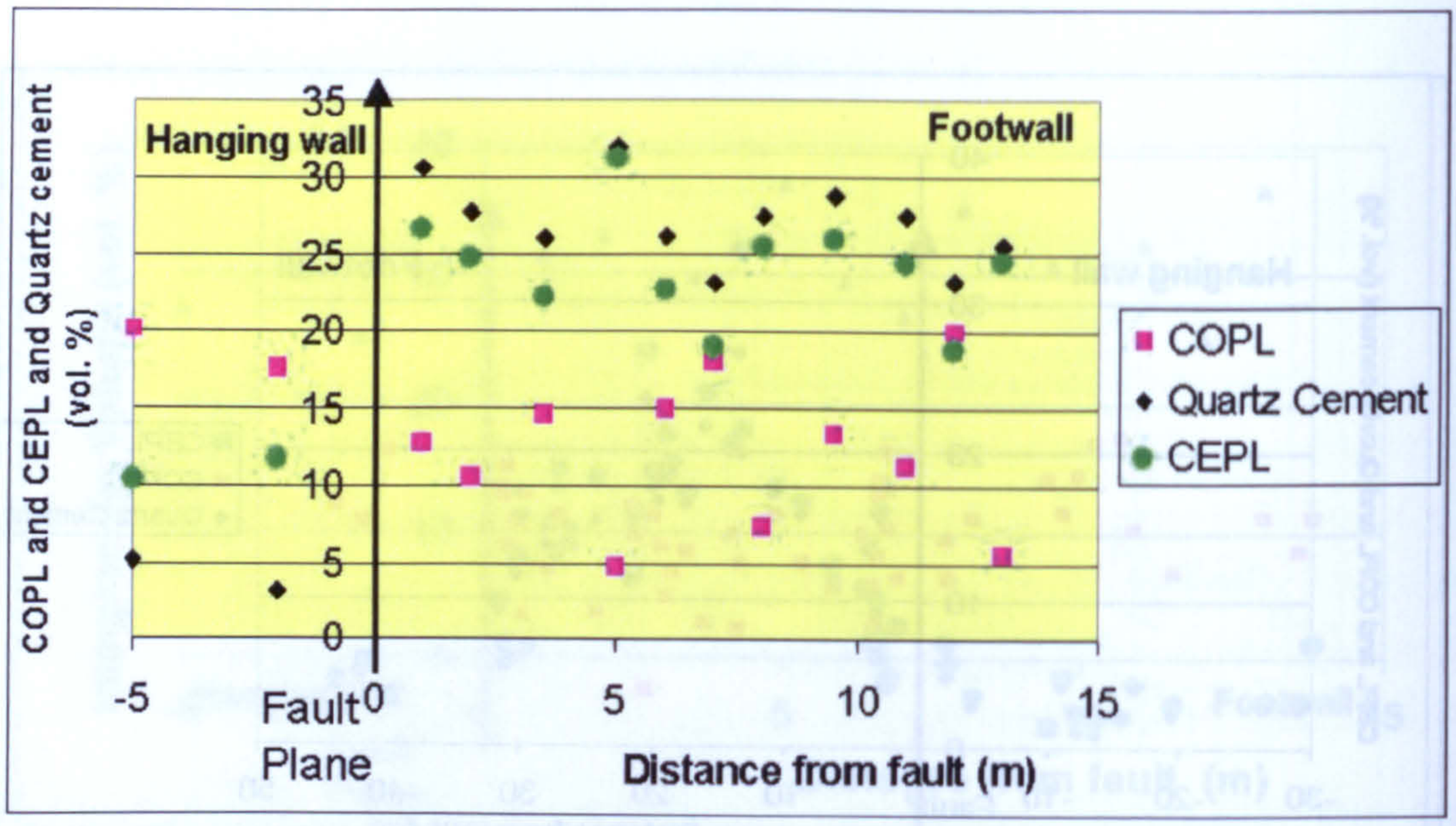


**Fig. 5.17. COPL vs CEPL and quartz cement volume are plotted together for the sandstone surrounding the Burghead Fault. The extreme shallow depth of cementation resulted in cementational porosity loss dominating in all footwall samples.**

## 5.10 Discussion

### 5.10.1 Dissolution of calcite cement by siliceous fluids

Textural observations of etched quartz grains, unusual overgrowth morphology, and X-Ray Diffraction detection of calcite traces throughout the dissolution zone, 0.5-13.8m into the footwall to the Clashach Fault, are evidence for the action of aggressive fluids dissolving carbonate cement and removing it from the system. The reverse solubility of carbonate cement compared to silica means as temperature decreases, quartz precipitates and carbonate dissolves, suggesting that an import of siliceous fluids along the Clashach fault plane removed an earlier patchy carbonate cement. The observation close to the fault (<1m) of Q2 quartz cement post-dating carbonate dissolution, in contrast to more distal samples in which Q2 authigenic quartz appears to have grown around the pore-filling cement, suggests that carbonate dissolution was earlier, closer to the fault plane but that the processes of carbonate dissolution and quartz precipitation were partially coeval, and genetically linked. The simplest explanation is that as siliceous fluids entered the sandstone through the fault zone, a

pre-existing patchy carbonate cement in the 0.5-13.8m footwall zone of the fault dissolved, and quartz cement precipitated (Fig. 5.18)

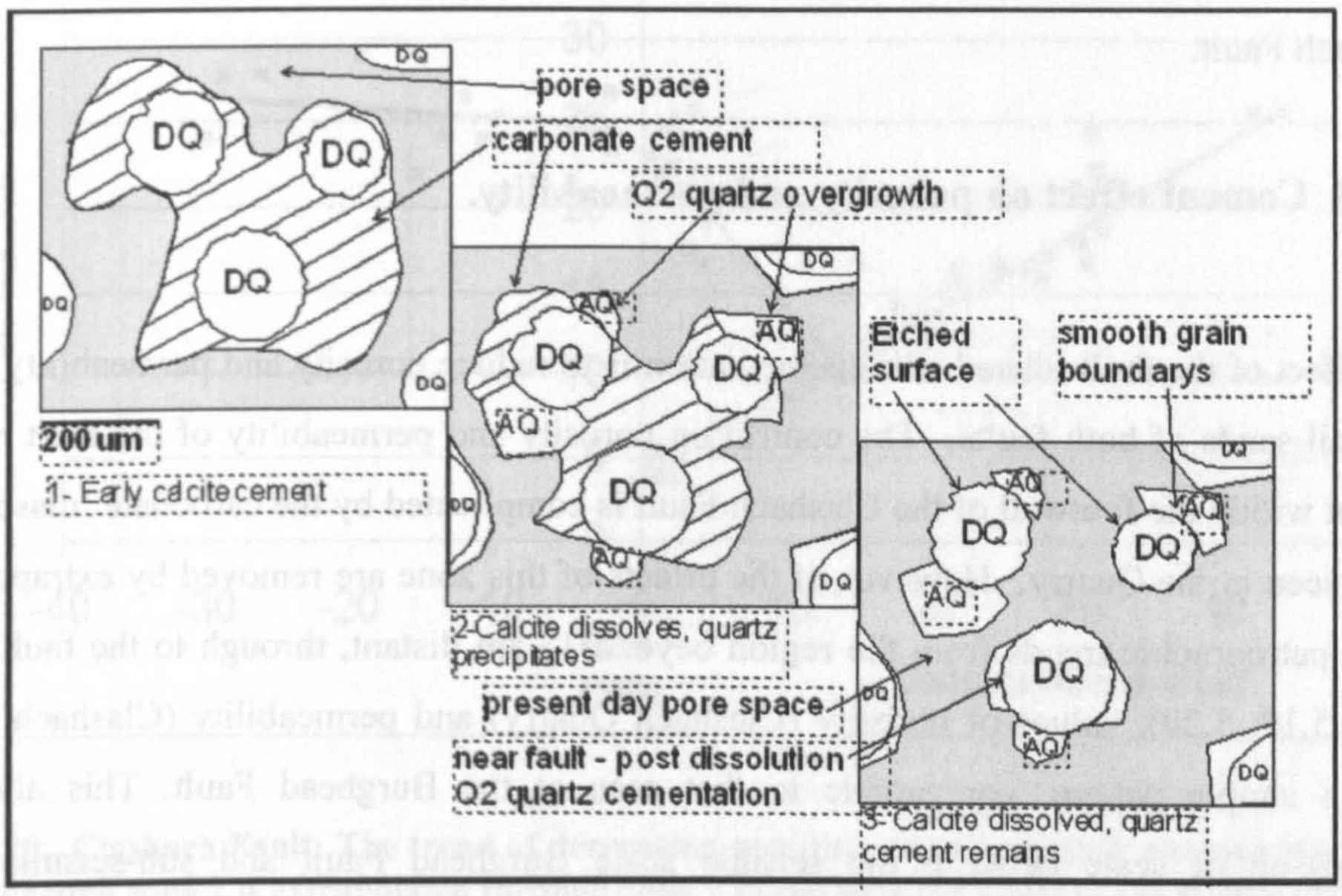


**Fig. 5.18. Cartoon of carbonate cement dissolution and Q2 cement precipitation in zone 1 of the Clashach Fault footwall. Early calcite cement begins to dissolve as siliceous fluid enters the system. Adjacent to the fault carbonate dissolution and the onset of Q2 precipitation overlap. Following complete carbonate dissolution etched and embayed quartz grains remain with quartz overgrowths.**

## 5.10.2 Extent of silica cementation.

The documentation of extensive quartz cementation along three fault perpendicular transects, at effectively random fault exposure locations, along c.5km of coastline suggests that the cementation is laterally very extensive on such a scale. At the Clashach Cove exposure, the presence of the cement along fault strike can be traced for >100m across the foreshore, to the edge of exposure. The vertical continuity is more difficult to constrain, and because of the lack of a relationship between facies and the presence or quantity of cement, is difficult to predict. However, for the Clashach Fault, with a throw between 8m and 50m, at least 8m of consistent vertical cementation can be observed in the quarry, equating to a minimum of c.20% of the total fault height, and a maximum of 100%. At the adjacent Clashach Cove c.3m of the 7m vertical footwall exposure is silica cemented, a minimum of c.40% of observed fault height. The absence of any such 'dissolution' zone, or carbonate cement, at

the Burghead Fault suggests that the carbonate was not obligatory along the entire fault plane. Inspection of extensive (km) coastal exposures of Hopeman Sandstone has yielded several other examples of carbonate cement. Thus minor calcite pods, typically 4m thick by 20m wide occur on some faults, but the strongest evidence for calcite cement comes from the Clashach Fault.

### 5.10.3 Cement effect on porosity and permeability.

The effect of the fault related silica cementation is to reduce porosity and permeability in the footwall sands of both faults. The control on porosity and permeability of the fault related cement within the footwall of the Clashach Fault is complicated by the carbonate 'dissolution zone' seen in the Quarry. However, if the effects of this zone are removed by extrapolation of the petrographic trends from the region beyond 13.8m distant, through to the fault plane (Figs. 5.19, 5.20), values of porosity (Clashach Quarry) and permeability (Clashach Cove) form a simple pattern, comparable to that seen at the Burghead Fault. This allows a comparison of scale between the seismic scale Burghead Fault and sub-seismic scale Clashach Fault.

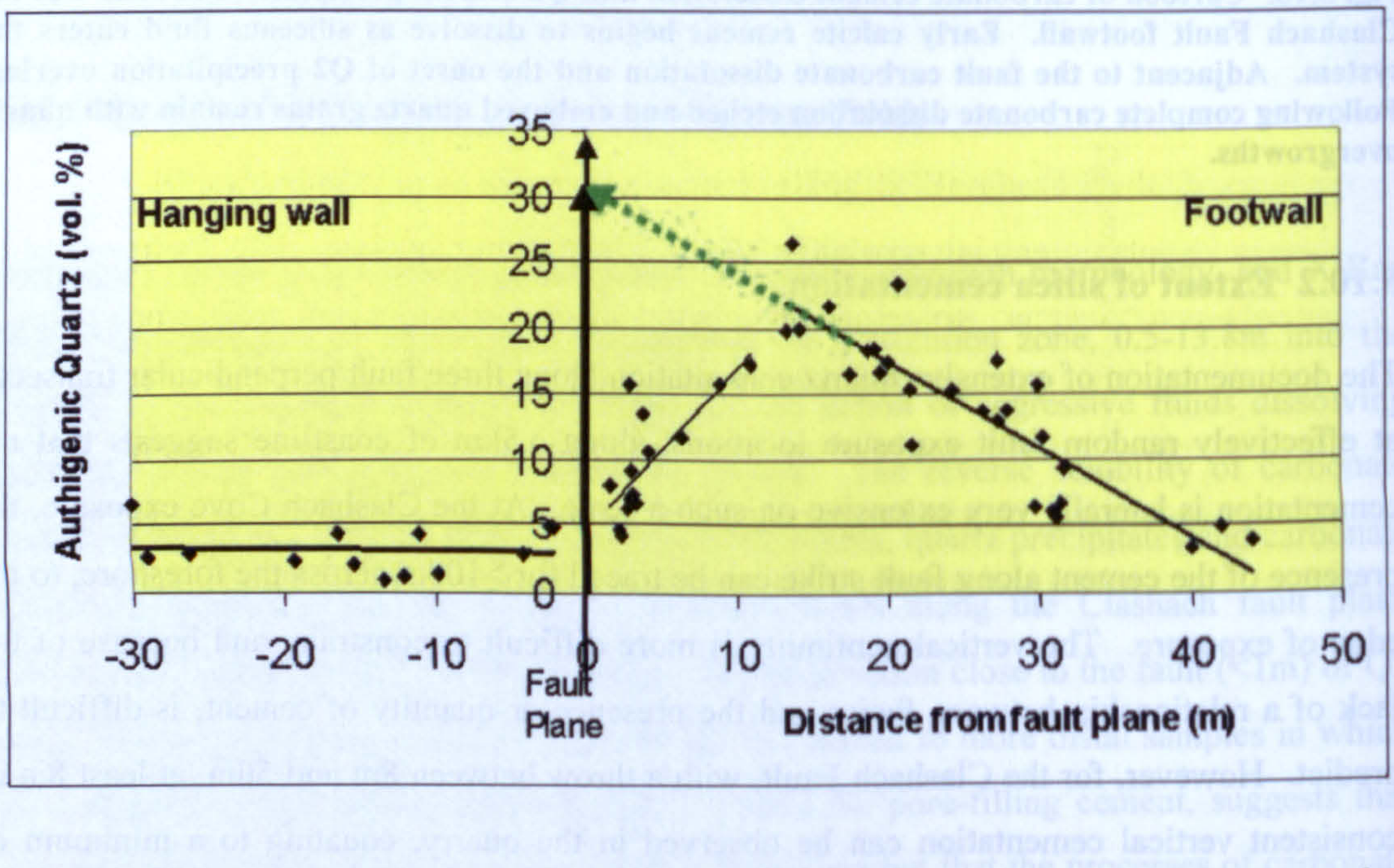


**Fig. 5.19. Clashach Fault: Extrapolation of the trend of increasing cement with decreasing distance toward the fault plane (Fig. 5.5). By removing the effects of the pre-existing carbonate cement the theoretical maximum quartz cement can be deduced. The projected value of authigenic quartz at 1m from the fault plane is 31% (+/-3%). This value is, within error, equivalent to the amount observed at 1m from the fault plane in the Burghead Fault (Fig. 5.10.).**

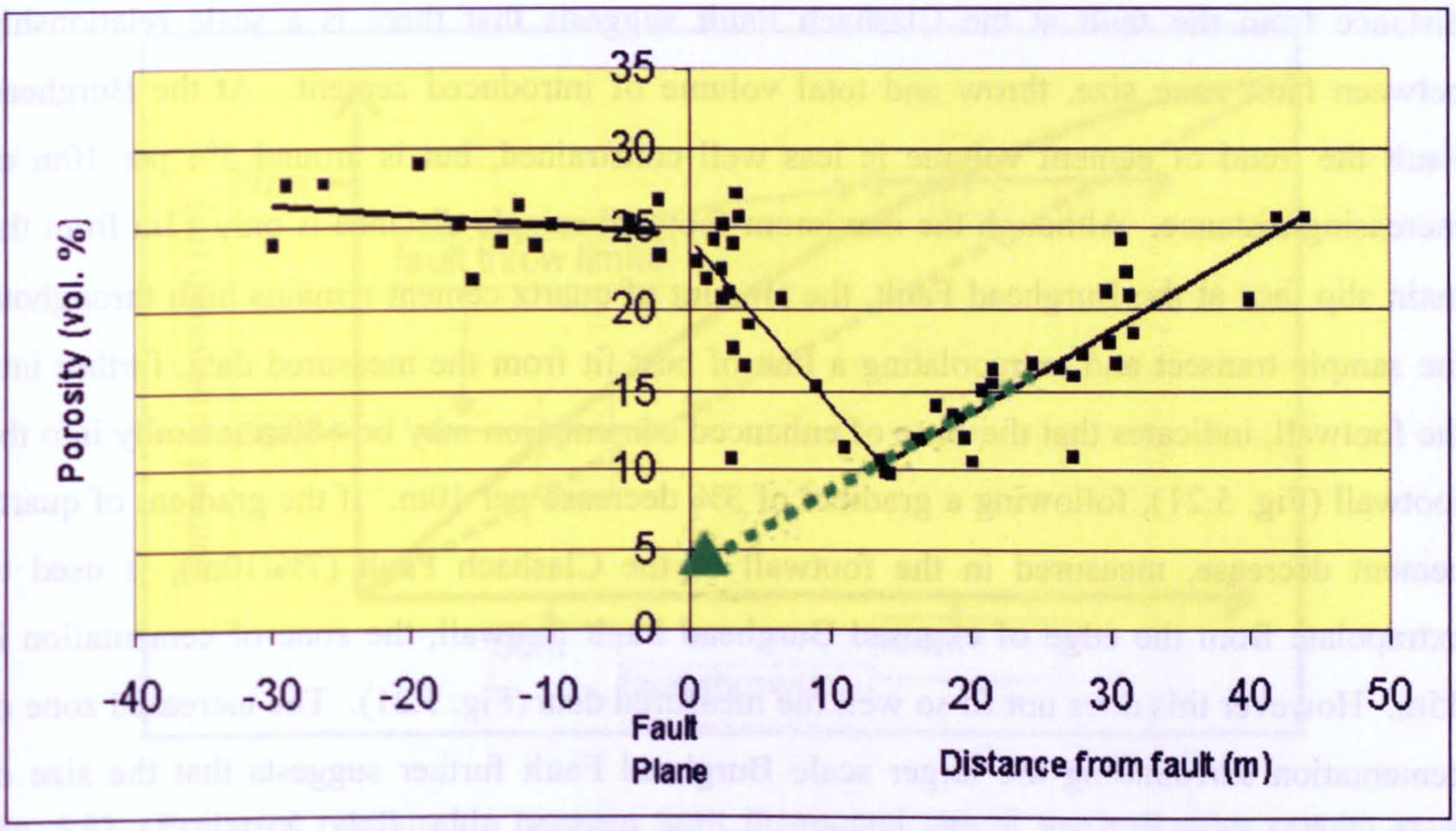


**Fig. 5.20. Clashach Fault: The trend of decreasing porosity with decreasing distance toward the fault through zone 2 is extrapolated through zone 1 to estimate the effect of Q2 quartz cement on porosity without a pre-existing carbonate cement. This shows that porosity would be reduced to values of <5% at 1m from the fault plane in the footwall, which is comparable to porosity values of 1-5% between 1 and 5m into the footwall of the Burghead Fault (Fig. 5.11).**

Removing the effects of the carbonate cement at the Clashach Fault (Fig. 5.19) reveals a predicted quartz cement volume of ~31% at the fault plane, comparable with the line of best fit value observed at Burghead of 29.5% cement at the fault plane. The similarity of the amount of cement adjacent to the fault planes suggests that this was the maximum available space in the sandstone which the quartz could fill at the time of cementation, so the absolute amount of cement, in any one sample immediately adjacent to fault planes, is a maximum controlled not by fault size but by available IGV. Extrapolation of porosity through zone 1 (Fig. 5.20) demonstrates that if the carbonate cement had not been present, porosity values in both the Clashach and Burghead footwalls would have been a similar value of <5% 1m from the fault plane, also correlating with localised permeability data from the footwall in Clashach Cove, where carbonate cement was absent.

For the Clashach Fault the well constrained trend of decreasing cement volume is 7% per 10m increase of distance from the fault, and the zone of enhanced cementation is restricted to

32m from the fault plane. Samples at 40-44m contain similar volumes of cement to background hanging wall sandstones. Crucially the rapid decrease in cement volume with distance from the fault at the Clashach Fault suggests that there is a scale relationship between fault zone size, throw and total volume of introduced cement. At the Burghead Fault the trend of cement volume is less well constrained, but is around 3% per 10m of increasing distance. Although the maximum footwall sample distance is only 13m from the main slip face at the Burghead Fault, the amount of quartz cement remains high throughout the sample transect and extrapolating a line of best fit from the measured data, further into the footwall, indicates that the zone of enhanced cementation may be >80m laterally into the footwall (Fig. 5.21), following a gradient of 3% decrease per 10m. If the gradient of quartz cement decrease, measured in the footwall of the Clashach Fault (7%/10m), is used to extrapolate from the edge of exposed Burghead Fault footwall, the zone of cementation is 45m. However this does not fit so well the measured data (Fig. 5.21). The increased zone of cementation surrounding the larger scale Burghead Fault further suggests that the size of quartz cement zone, and consequently area of porosity and permeability reduction, is controlled by the fault scale (Fig 5.22). This suggests a positive correlation between fault throw and the volume of fluids channelled through the fault zone.

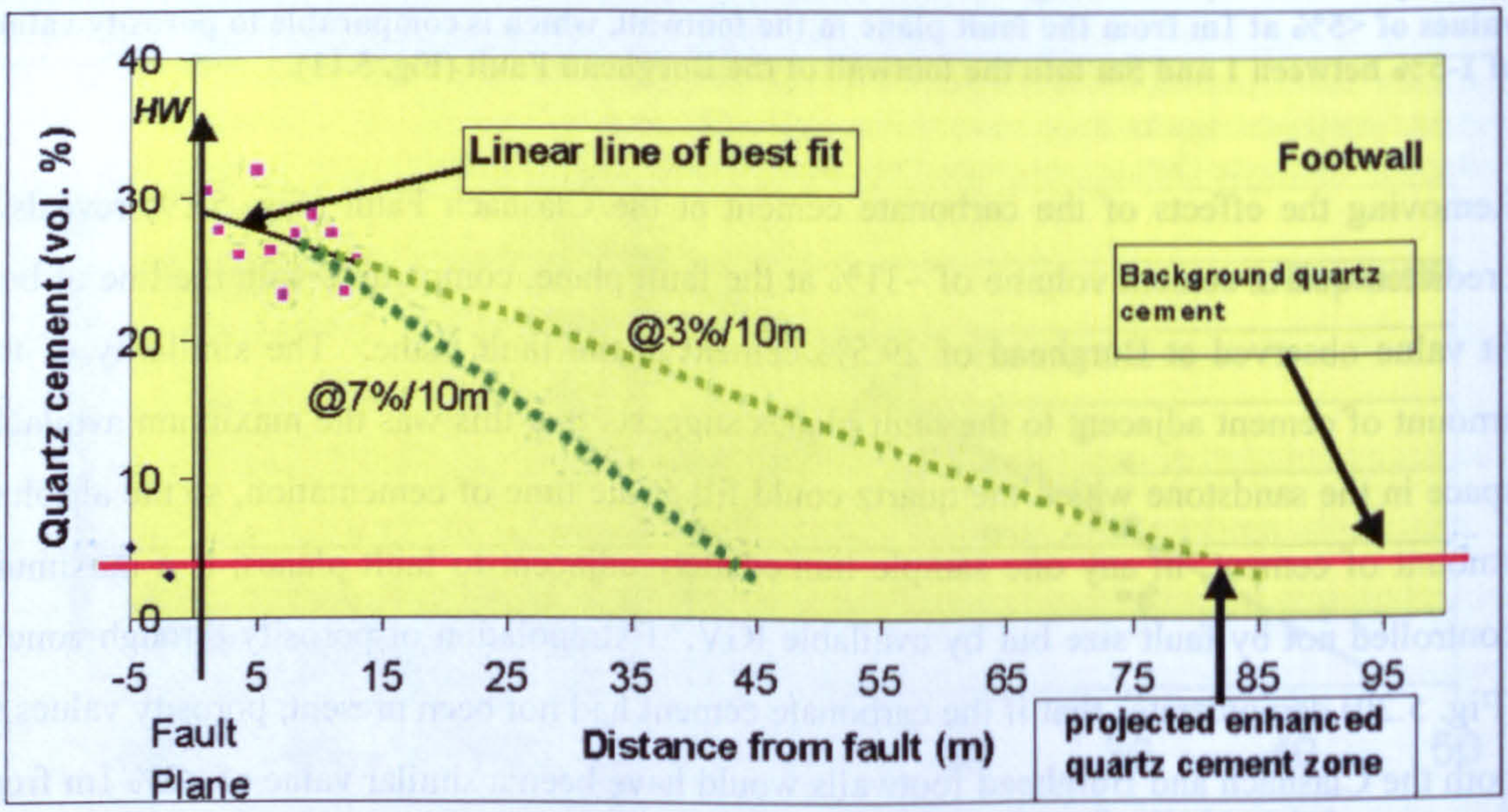


**Fig. 5.21. Extrapolation of the trend of decreasing quartz cement with increasing distance from the fault slip face of the Burghead Fault. Although the trend is less well constrained than for the Clashach Fault, the measured rate of decrease is 3% per 10m, leading to a c.80m zone of increased cementation around the fault. For comparison the more accurately constrained rate of cement decrease for the Clashach Fault is shown (7% per 10m), indicating that even at similar rate of decrease the zone of enhanced footwall cementation in the Burghead Fault is greater than**

**that at Clashach, indicating a positive scale relationship between fault displacement and extent of cement aureole.**

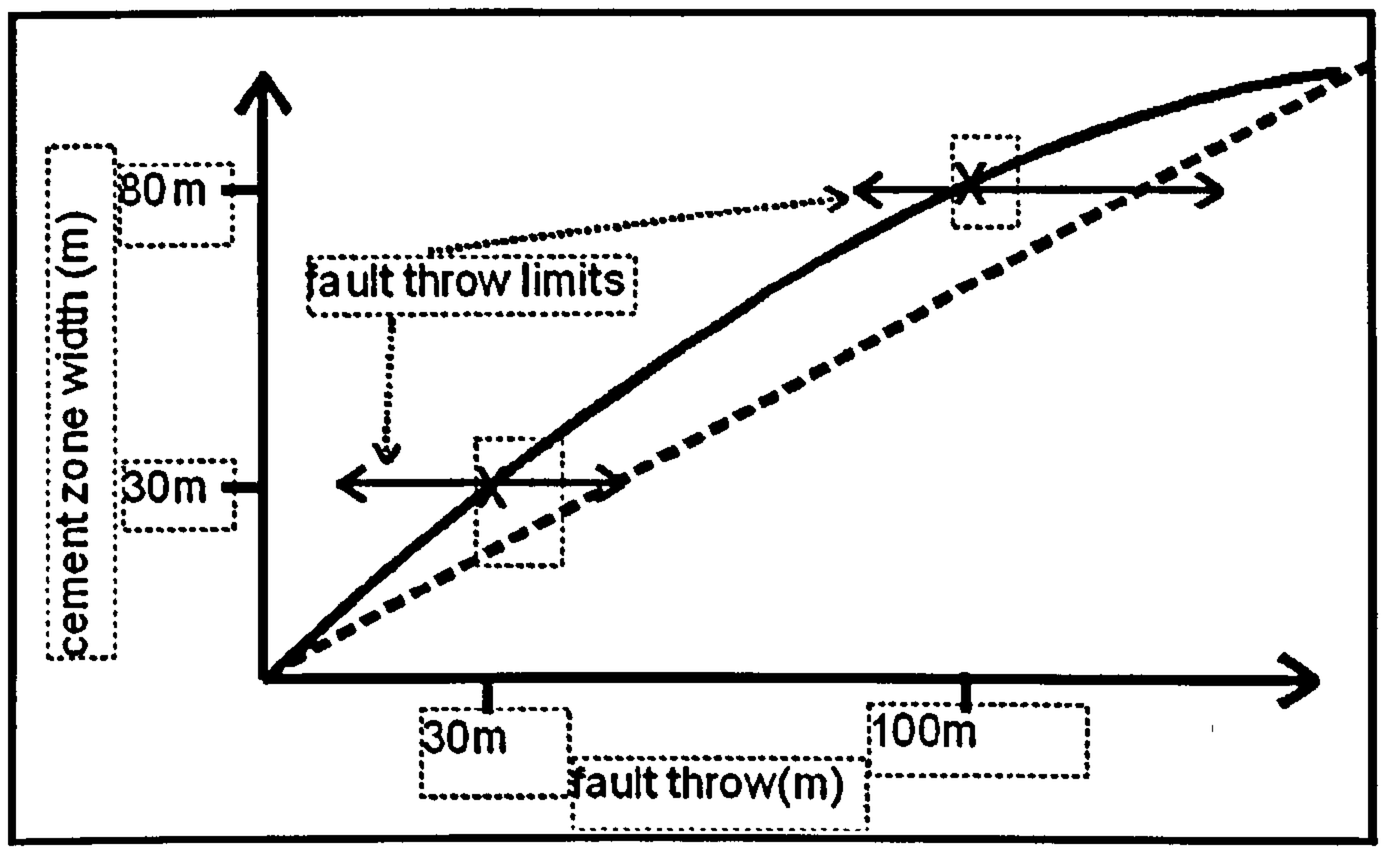


**Fig. 5.22. Projected relationship between fault throw and size of footwall silica cement zone. Only 2 data points are available, however assuming that a fault of zero throw has zero cement zone allows a curve to be tentatively fitted. This points to a maximum cement zone >100m for a fault throw of 100m. Both a linear (dashed line) and logarithmic (continuous line) relationship are within the bounds of fault throw. The zero throw: zero cement zone assumption only applies for cases of shallow burial exotic cementation. North Sea deformation bands buried to greater than c.90C, and with a throw <1cm, contain authigenic quartz cementation.**

### 5.10.4 Reservoir compartment and porosity effects.

Faults in the Hopeman Sandstone have been used to show the effect of structural compartmentalisation of a hydrocarbon reservoir (Edwards *et al.*, 1993). Porosity reduction by fault-associated cement in this reservoir analogue sandstone acts to reduce the potential size of such compartments. In order to use the data presented here to estimate the effect on a particular reservoir volume, individual fault scales and spatial frequency of faulting must be considered. As a simplified example, if the small scale Clashach Fault is situated 100m laterally from an uncemented fault (Fig. 5.23a) it creates a 100m fault bounded compartment. Assuming the footwall quartz cementation is continuous along Clashach fault strike (and ignoring carbonate cement effects of zone 1), the compartment has an ~30m cementation aureole around the minor fault, with a mean porosity of 15%, and a 70m section of unaffected sandstone with an average porosity of 24.5%. The fault related cement reduces total pore space in the compartment by 15%. If the two faults were 500m distant (Fig.5.23b), total

pore space reduction in the compartment would be only 2%. For a 100m compartment on the footwall side of the Burghead Fault, with a cement aureole of 80m with 15% mean porosity, and 20m of 24.5% porosity sandstone, overall pore space in the compartment would be reduced by 31%. This is compared to a 15% reduction if the fault throw had been an order of magnitude smaller (Fig. 5.23c). For a compartment with a 500m lateral dimension perpendicular to the fault, porosity reduction would be 6% (Fig. 5.23d). Thus prediction of fault scale and size of compartment are crucial in estimating the total porosity present, and for this dataset, correct estimation of fault scale can make up to 1 order of magnitude difference in the prediction of total compartment porosity, and potential hydrocarbon in place.

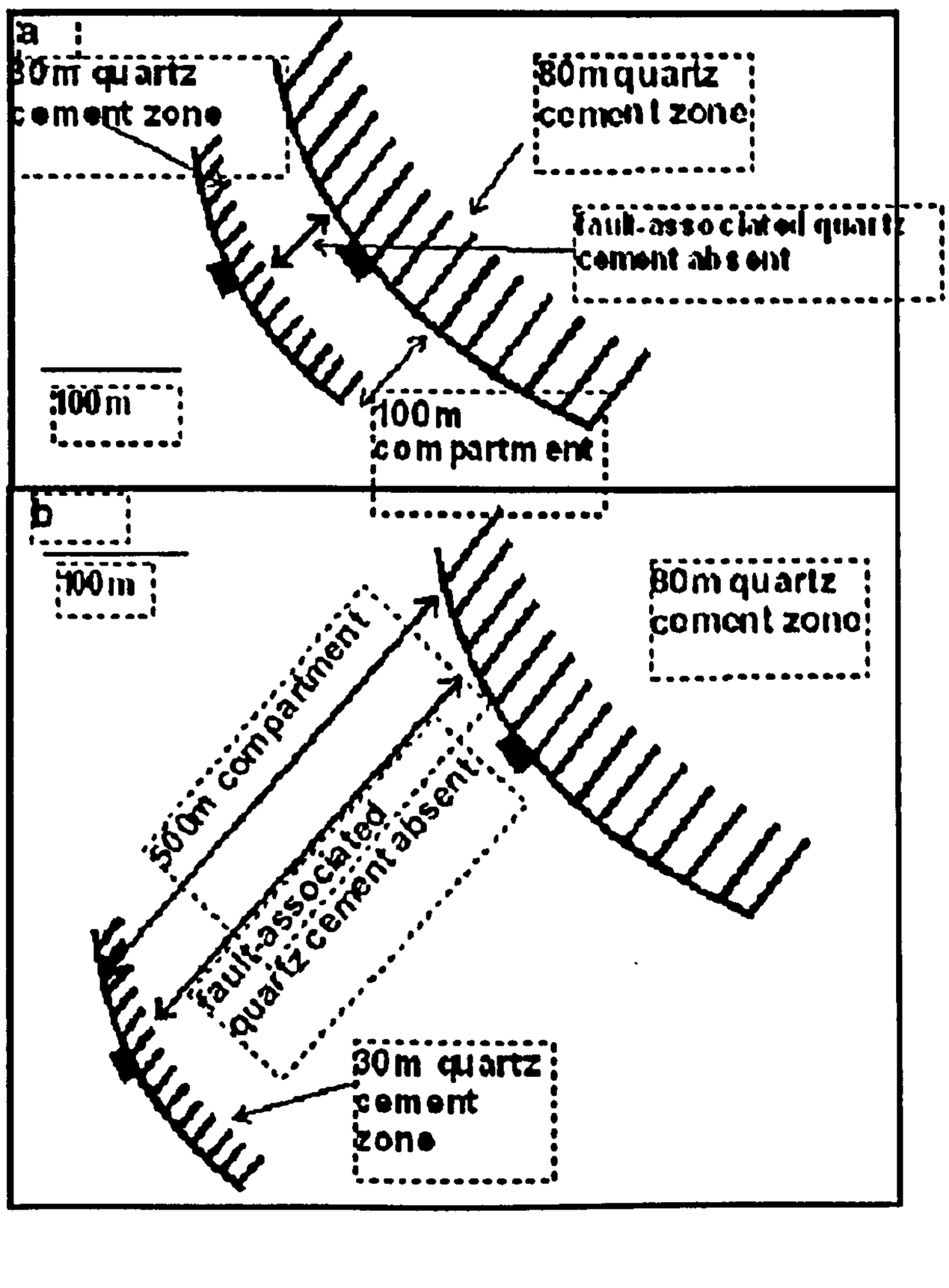


**FIg. 5.23 a) 100m compartment in the footwall of the Clashach Fault. Total porosity is reduced by the 30m quartz cement zone by 15%. b) 500m compartment in the footwall of the Clashach Fault. Total porosity is reduced by the 30m quartz cement zone by 2%.**

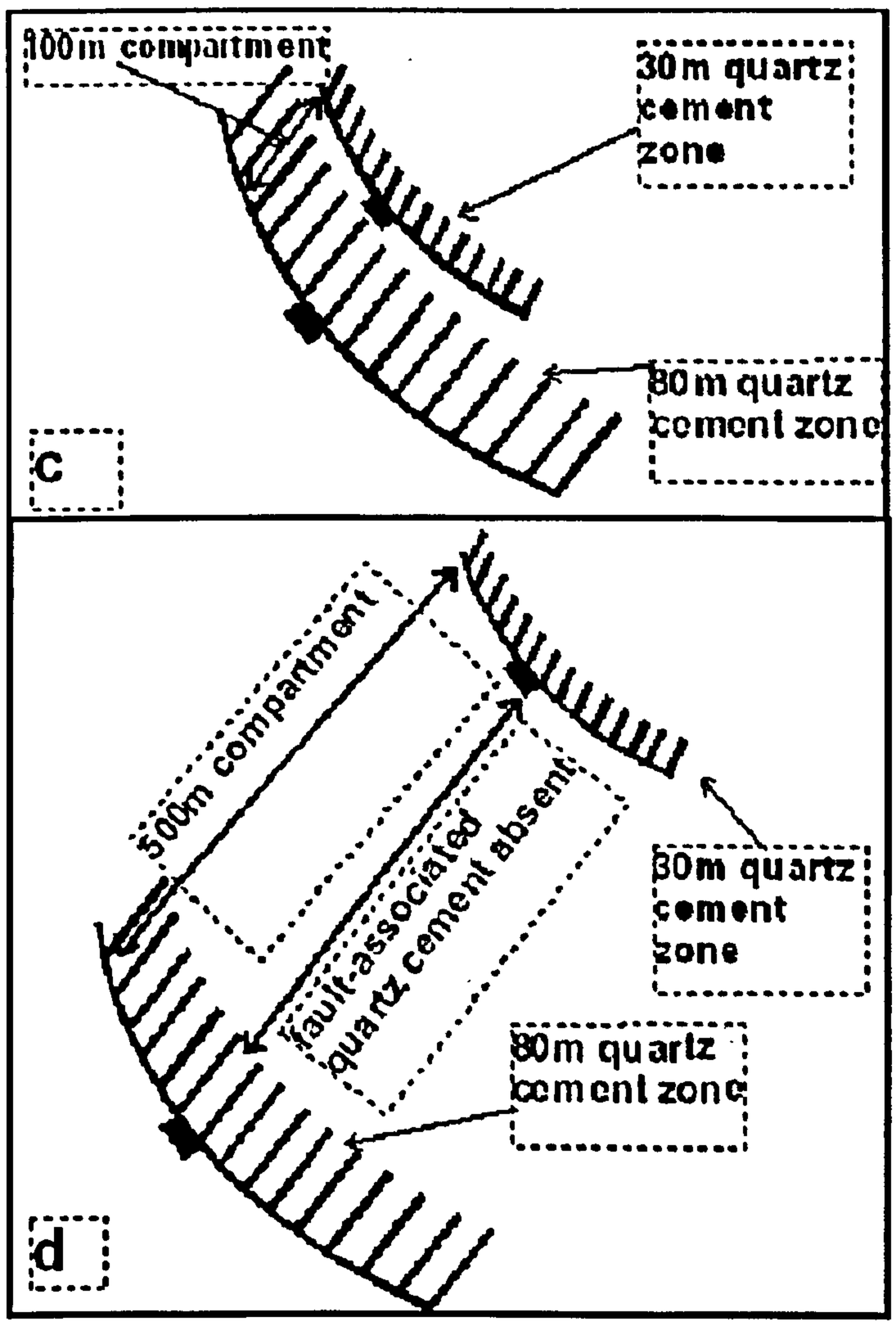


**Fig. 5.23. c) A 100m compartment in the footwall of the Burghead Fault. Total porosity loss caused by the quartz cement is 31% d) 500m compartment in the footwall of the Burghead Fault. Total porosity loss cause by the quartz cement is 6%.**

## 5.10.5 Permeability effects

Further to the control on the volume of porosity, the reduction in permeability around the faults acts to reinforce the compartmentalisation and may in some cases act as a fluid seal.In the most well cemented footwall zone adjacent to the fault slip planes, permeability is less than 1mD, a similar figure to deformation bands in the Hopeman Sandstone and other deformation bands measured globally (e.g. Antollenini and Aydin 1994a, Shipton *et al.*, 2002), which act as baffles and seals to fluid flow. Minor permeability variations, less than 1

order of magnitude, were measured within the uncemented hanging wall sands. The two faults, which show a scaling relationship between fault displacement and cement volume, also posses a positive scale relationship between displacement and absolute permeability reduction. The 13m footwall traverse at the Burghead Fault has a mean permeability of 2mD, a 13m section into the footwall at the Clashach Fault (at Clashach Cove) has a mean permeability of 8mD, showing that the absolute value of permeability is higher, but within an order of magnitude. This suggests that fault scale is not a crucial factor in the absolute permeability reduction adjacent to the fault, but with the predicted increase in the cemented zone (80m) at the Burghead Fault, is likely to extend the low permeability area. The observation of between 1 and 3 orders of magnitude permeability reduction in the cemented zones means that a significant permeability barrier of up to 30-50m is created, but only on the footwall side of the faults. If such asymmetry exists in a subsurface equivalent it leads to a focus of reservoir quality toward the hanging wall of the next fault in a horizontal direction. The effect of the cement on reservoir quality above indicates that production strategies need to be carefully considered on a case by case basis. As a general strategy, in reservoirs where fault-bound compartments are small (<c.100m), wells drilled perpendicular to faults, intersecting a number of compartments will be most efficient (Fig. 5.24a). Conversely, in hydrocarbon reservoirs with large (>100m) compartments, where the low permeability zone is proportionally small, wells drilled fault-parallel, with a bias away from the footwall (Fig. 5.24b) will be most effective.

## 5.11 Subsurface implications

The high level of sampling achieved in this case allows the dataset to be used in simulations of buried reservoirs where a similar fault-cementation relationship is expected. Detection and quantification of such structurally related features in the sub-surface is difficult due to the avoidance of faults during drilling and sampling of core. The critical parameter of permeability is also shown to be relatively homogeneous for the Hopeman Sandstone outwith the zone of enhanced footwall cementation ($C_v < 0.5$), and heterogeneous ($0.5 < C_v < 1$) to very heterogeneous ($C_v > 1$) within the immediate cemented footwall. The comparison of the effect of cementation on sandstone permeability heterogeneity in the footwall and hangingwall is valid, because both hangingwall and footwall data are from equivalent positions within dune slip face lamination facies. The *No* statistic shows that 12

measurements are required to characterise uncemented hanging wall permeability. This is a realistic number of data points if conventional oilfield core plugs at 30cm spacing are used to capture data for reservoir models. To characterise the permeability variation in the Clashach and Burghead Fault footwalls, 87 and 137 measurements respectively, would be required, representing an unfeasibly high number with conventional core analysis. If a core was taken through the footwall and into the fault plane this would be feasible using non-destructive, mini-permeameter techniques, but not through traditional core plug analysis. Realistically such fault zone core is rare. Where reservoir data, such as dynamic pressure partitioning, indicates there is a possibility of fault related cementation, it is usually unfeasible to obtain a sufficient number of permeability measurements to quantify the variation. In such cases the analogue data provided here may provide the best case input for a reservoir model.

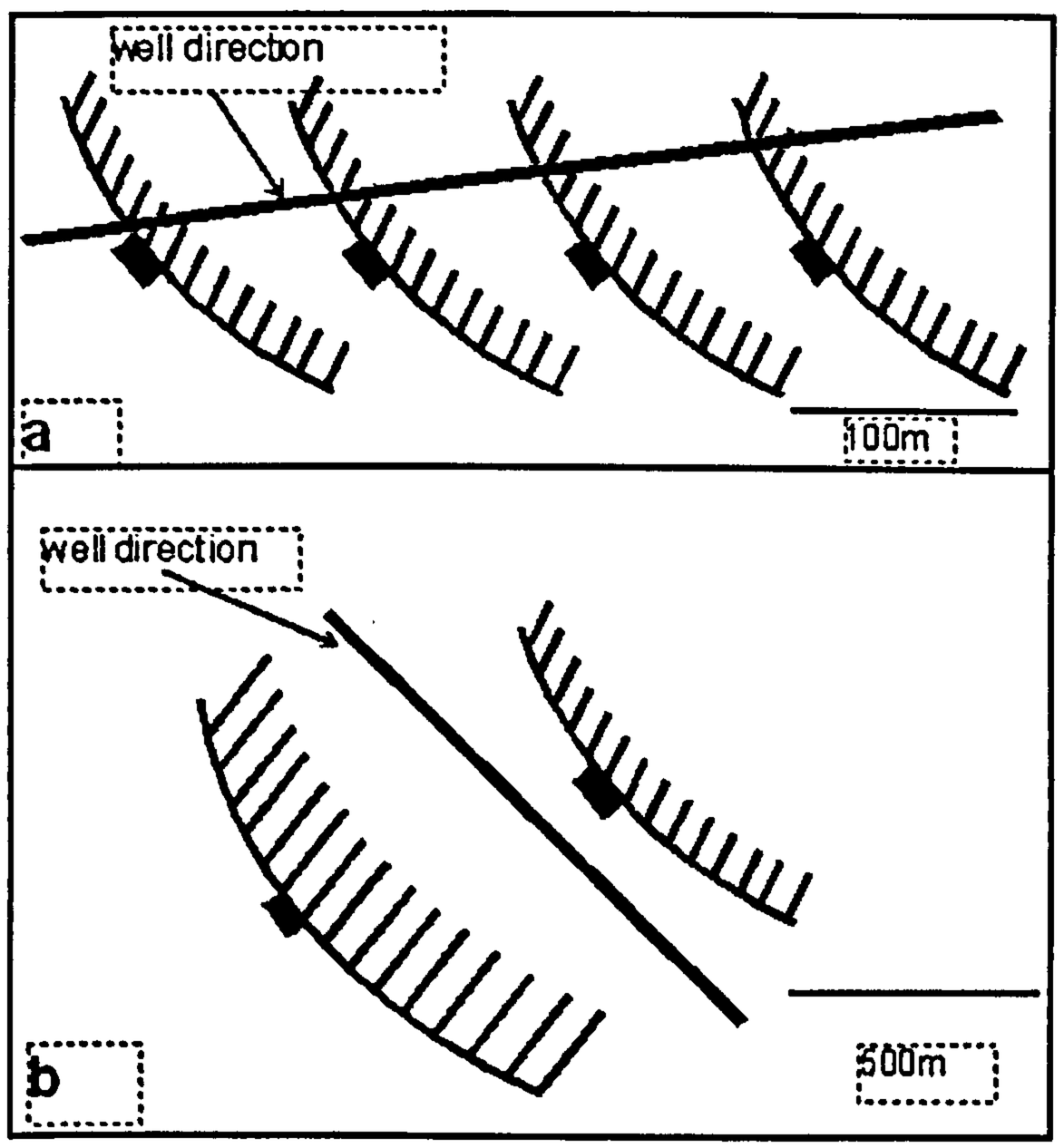


**Fig. 5.24. Alternate drilling strategies for compartmenalised reservoirs with quartz cemented footwalls.a) Where fault density is high, producing small compartments of c.100m lateral width, the most effective strategy is to drill fault perpendicular. b) For larger compartments, where footwall cement causes a smaller overall porosity loss, wells drilled fault parallel with a bias away from the footwall will be most efficient.**

This analogue is also valid where cases of extensive shallow cementation are suspected to have occurred and reservoir porosity and permeability data are required. The burial curve shows maximum burial of the Hopeman Sandstone is less than 2.4km, below the depth at which quartz cement is generally predicted to occur in significant quantity. Normally, in uncemented cases, the compaction curve of Paxton *et al.* (2002) predicts that porosity should be 27% (+/3%) (Fig. 5.14). The effect of the 32m cement zone at the Clashach Fault, is to produce a mean porosity of 15%. Thus porosity is a maximum c.12% below predicted for the maximum burial depth of the Hopeman Sandstone. At the Burghead Fault the observed 13m cement zone reduces porosity from a predicted maximum value of 27% (+/-3%) to a mean value of 5%, a reduction of 22%.

## 5.12 Conclusions

- Shallow burial (<1km) quartz cementation occurs asymmetrically across two normal fault planes in the exposed aeolian Hopeman Sandstone. Authigenic quartz preferentially occurs in the footwall of both faults, and decreases in volume, along a linear trend, to values comparable to those measured in adjacent hanging wall sandstones. Authigenic quartz distribution is primarily controlled by fault location and cross-cuts sedimentary facies. Within the footwall of the sub-seismic scale Clashach Fault, cement volume decreases from a maximum value of 26.5% to near background values of 4.0% at 44m distant from the main fault slip plane. The footwall of the seismic scale Burghead Fault contains a maximum of 31% quartz cement, broadly decreasing to 26% at 13m, and predicted to decrease to 4.0% background levels at c.80m from the fault plane.

- Porosity is reduced from background values of 24.5% to a predicted minimum of 2.0% in the footwall of the subseismic scale Clashach Fault, and from a maximum of 11% at 13m to a minimum of 0.6% in the footwall of the seismic scale Burghead Fault. In the dataset as a whole porosity is inversely related to quartz cement volume.

- Permeability in uncemented hanging wall sandstone is 100-1000mD and homogeneous at Clashach Fault. Cemented footwall sandstone at Clashach and

Burghead has permeabilities reduced to 0.1-10mD and is heterogeneous. Both faults could form fluid seals in producing oilfields.

- The three-dimensional extent of the footwall quartz cement is uncertain. The observation of extensive quartz cement at three exposures of two faults along c.5km of coastline suggests the cement is regionally extensive if not ubiquitous. Zones of early carbonate cement, now dissolved adjacent to the fault, are present at two 20m x 3m exposures of the Clashach Fault, creating small, local, heterogeneous higher porosity zones.

- Using the Hopeman Sandstone as a subsurface hydrocarbon reservoir analogue allows the utilisation of extensive datasets presented here in reservoir models where similar localised and/or shallow burial diagenetic cements are present. Simple calculations show reservoir degradation and compartmentalisation by faults can be enhanced by fault-associated cements. The data presented here suggests the zones of enhanced footwall cementation scale positively with fault throw in associated reservoir compartments. Consequently drilling strategies should focus on fault-strike parallel paths in large (>100m) compartments, and fault perpendicular paths in small (<100m) compartments, accounting for the asymmetry, and scale of the zone of reduced porosity and permeability.

- In the subseismic scale Clashach Fault, the cementation zone ~0.8x fault displacement. In the seismic scale Burghead Fault the cementation zone ~0.5x fault displacement.

---

# References


**Antonellini, M.A. and Aydin, A., 1994a.** Effect of faulting on fluid flow in porous sandstones:petrophysical properties. American Association of Petroleum Geologists Bulletin, 78, p. 355-377

**Benton, M.J., and Walker, A.D., 1985.** Palaeoecology, Taphonomy, and Dating of Permo-Triassic Reptiles from north-east Scotland. Palaeontology, 28,p. 207-234,

**Berridge, N.G. and Ivimey-Cook, H.C., 1967.** The Geology of a Borehole at Lossiemouth, Morayshire. Bulletin of the Geological Survey of Great Britain, 27, p. 155-169.

**Aydin, A. and Johnson, A.M., 1983.** Analysis of faulting in porous sandstones. Journal of Structural Geology, 5, p.19.

**Bjorlykke, K., Nedkvitne, T., Ramm, M. and Saigal, G.C., 1992.** Diagenetic processes in the Brent Group (Middle Jurassic) reservoirs of the North Sea: an overview. *In*: Geology of the Brent Group (ed. Morton, A.C., Haszeldine, R.S., Giles, M.R., and Brown, S.), Special Pulication of the Geological Society of London, 61, p.263-287.

**Burley, S.D., Mullis, J. and Matter, A., 1989.** Timing diagenesis in the Tartan Reservoir (UK, North Sea): constraints from combined cathodoluminesence microscopy and fluid inclusion studies. Marine and Petroleum Geology, 6, p.8-120.

**Clemmensen, L.B., 1987.** Complex star dunes and associated aeolian bedforms, Hopeman Sandstone (Permo-Triassic), Moray Firth Basin, Scotland. In: Desert Sediments: Ancient and Modern (ed. Frostick, L, and Reid, I.). Geological Society of London Special Publication, 35, p. 213-231.

**Corbett, P.W.M. and Jensen, J.L., 1992.** Estimating the mean permeability-how many measurements do you need? First Break, 10, p.89-94.

**Edwards, H.E., Becker, A.D. and Howell, J.A., 1993.** Compartmentalization of an aeolian sandstone by structural heterogeneities: Permo-Triassic Hopeman Sandstone, Moray Firth, Scotland. In: Characterization of fluvial and aeolian reservoirs (ed. North, C.P.). Geological Society of London Special Publication, 73, p. 339-365.

**Ehrenberg, S.N., 1995.** Measuring sandstone compaction from modal analyses of thin sections: how to do it and what the results mean. Journal of Sedimentary Research, 65A, 2, p.369-379.

**Fisher, Q.J., Knipe, R.J. and Worden, R.H., 2000.** Microstructures of deformed and non-deformed sandstones from the North Sea: implications for the origins of quartz cement in sandstones. *In*: Quartz Cementation in Sandstones (ed: Worden, R.H. and Morad, S.), Special Publication of the International Association of Sedimentologists, 29, p. 129-146.

**Frostick, L., Reid, I, Jarvis, J. and Eardley, H., 1988.** Triassic sediments of the Inner Moray Firth, Scotland: early rift deposits. Journal of the Geological Society of London, 145,p. 235-248.

**Giles, M.R., Stevenson, S., Martin, S.V., Cannon, S.J.C., Hamilton, P.J., Marshall, J.D. and Samways, G.M., 1992.** The reservoir properties and diagenesis of the Brent Group; a regional perspective. *In:* Geology of the Brent Group (eds. Morton, A.C., Haszeldine, R.S., Giles, M.R. and Brown, S.) Geological Society Special Publication, 61, p. 289-327.

**Giles, M., 1997.** Diagenesis and its Impact on Rock Properties. A Quantitative Perspective. pp. 520. Kluwer, Amsterdam.

**Giles, M.R., Indrelid, S.L., Beynon, G.V. and Amthor, J., 2000.** The origin of large-scale quartz cementation: evidence from large data sets and coupled heat-fluid mass transport modelling: *In*: Quartz Cementation in Sandstones (ed: Worden, R.H. and Morad, S.), Special Publication of the International Association of Sedimentologists, 29, p. 21-39.

**Glennie, K.W. and Buller, A.T., 1983.** The Permian Weissliegend of NW Europe: the partial deformation of aeolian sand dunes caused by the Zechstein transgression. Sedimentary Geology, 35, p. 43-81.

**Haszeldine, R.S., Samson, I.M., Cornford, C., 1984.** Dating diagenesis in a petroleum basin: a new fluid inclusion method. Nature, 307, p.354-357.

**Houseknecht, D.W., 1987.** Assessing the relative importance of compaction processes and cementation to reduction of porosity in sandstones. American Association of Petroleum Geologists Bulletin, 71, p. 633-642.

**Hurst, A. and Rosvoll, K.J., 1991.** Permeability variations in sandstones and their relations to sedimentary structures: In: Reservoir Characterisation II (ed: Lake, L.W., Carroll Jr, H.B., Wesson, T.C.) San Diego California, Academic Press, p.315-338.

**Hurst, A. and Goggin, D., 1995.** Probe permeametry – An overview and bibliography. American Association of Petroleum Geologists Bulletin, 79, 463-473.

**Hogg, A.J.C., Sellier, E. and Jourdan, A.J., 1992.** Cathodoluminescence of quartz cements in Brent Group sandstones, Alwyn South, UK North Sea. *In*: Geology of the Brent Group (eds. Morton, A.C., Haszeldine, R.S., Giles, M.R. and Brown, S.) Geological Society Special Publication, 61, p. 289-327.

**Jensen, J.L., Lake, J.W., Corbett, P.W.M. and Goggin, D.J., 1997.** Statistics for petroleum engineers and geoscientists. Engelwood Cliffs, NJ, Prentice Hall p.390.

**Lander, R.H. and Walderhaug, O., 1999.** Predicting porosity through simulating sandstone compaction and quartz cementation. American Association of Petroleum Geologists, 83, p. 433-449.

**Macaulay, C., 2003.** Low temperature quartz cementation of the upper Cretaceous Lochaline Sandstone of Lochaline, Argyll, Scotland. pers comm. www.geos.ed.ac.uk/facilities/ionprobe/calumSi

**Mair, K., 1997.** Experimental studies of fault zone development of a porous sandstone. Unpublished PhD thesis, University of Edinburgh.

**Marchand, A.M.E., Haszeldine, R.S., Macaulay, C.I., Swennen, R. and Fallick, A.E., 2000.** Quartz cementation inhibited by crestal oil charge: Miller deep water sandstone, UK North Sea. Clay Minerals, 35, p.201-210.

**McBride, E.F., 1963.** A classification of common sandstones. Journal of Sedimentary Petrology, 33, p.664-669.

**McQuillin, R., Donato, J.A. and Tulstrup, J., 1982.** Development of basins in the Inner Moray Firth and North Sea by crustal extension and dextral displacement of the Great Glen Fault. Earth and Planetary Science Letters, 60, p. 127-139.

**Ogilvie, S.R. and Glover, P.W.J., 2001.** The petrophysical properties of deformation bands in relation to their microstructure. Earth and Planetary Science Letters, 193, no, 1-2, p. 129-142.

**Paxton, S.T., Szabo, J.O., Ajdukiewicz, J.M. and Klimentidis, R.E., 2002.** Construction of an intergranular volume compaction curve for evaluating and predicting compaction and porosity loss in rigid-grain sandstone reservoirs. American Association of Petroleum Geologists, 86, p.2047-2067.

**Peacock, J.D., 1966.** Contorted beds in the Permo-Triassic aeolian sandstones of Morayshire. Bulletin of the Geological Survey of Great Britain, 24, 157-162.

**Peacock, J.D., Berridge, N.G., Harris, A.L. and May, F., 1968.** The Geology of the Elgin District. HMSO, Edinburgh.

**Quinn, O.F., Haszeldine, R.S., Underhill, J.R. and Dixon, J.E., 2004.** A new structural model for the Lossie Peninsula, Inner Moray Firth. In preparation. Chapter 4.

**Quinn, O.F., Haszeldine, R.S. and Dixon, J.E., 2004.** Fault-related quartz cementation: Insights from isotope microanalyses and fluid inclusions. In preparation. Chapter 6.

**Roberts, A.M., Price, J.D. and Badley, M.E., 1989a.** Discussion on Triassic sediments of the Inner Moray Firth: early rift deposits (Frostick *et al.*1988). Journal of the Geological Society, London, 146, p.361-362.

**Roberts, A.M., Badley, M.E, Price, J.D. and Huck, I.W., 1990.** The structural evolution of a transtensional basin: Inner Moray Firth, NE Scotland. Journal of the Geological Society of London, 147, 87-103.

**Shipton, Z.K., Evans, J.P., Robeson, K., Forster, C.B. and Snelgrove, S., 2002.** Structural heterogeneity and permeability in faulted aeolian sandstone: implications for subsurface modelling of faults. American Association of Petroleum Geologists Bulletin, 86, p. 6477-6490.

**Thomson, K. and Underhill, J.R., 1993**. Controls on the development and evolution of structural styles in the Inner Moray Firth Basin. *In*: Petroleum Geology of Northwest Europe: Proceedings of the 4th Conference (ed. Parker, J.R.),Geological Society London, p. 1167-1178.

**Underhill, J.R., 1991a**. Implications of Mesozoic-Recent basin development in the western Inner Moray Firth, UK. Marine and Petroleum Geology, 8, p. 359-369.

**Van der Plas, L. and Tobi, A.C., 1965.** A chart for judging the reliability of point counting results. American Journal of Science, 263, n.1, p.87-90.

**Worden, R.H. and Morad, S., 2000.** Quartz cementation in oil field sandstones: a review of the key controversies. *In*: Quartz Cementation in Sandstones (ed: Worden, R.H. and Morad, S.), Special Publication of the International Association of Sedimentologists, 29, p. 1-20.

This page left blank

# Chapter 6.

This next paper focuses on geochemical analysis of authigenic quartz in the Hopeman Sandstone, using fluid inclusion and stable isotope methods. The investigation moves from the field scale patterns of cementation documented in chapter 5, to detailed microanalysis. The paper focuses on deducing the origin of the different phases of authigenic quartz presented in detail in the petrographic study in chapter 5. Fluid inclusion and in-situ oxygen isotope measurements are combined to elucidate the sources of porefluid from which the different phases of quartz precipitated. This allows fresh insights into the role of closed system, static pore fluid, diagenesis versus open system diagenesis with fluid flow conditions prevailing. Building upon chapters 4 and 5, the interaction of fluids with faults is unravelled, providing new information on fault permeability development and its effects. This geochemical data is used to produce a model of diagenetic and fluid evolution in the Hopeman Sandstone.

# Fault-related quartz cementation: Insights from isotope microanalyses and fluid inclusions.

Oliver F. Quinn, R. Stuart Haszeldine and J.E. Dixon

## Abstract

Quartz cementation is localised around 2 exposed Late Jurassic extensional fault planes, the small scale (<50m) Clashach Fault and the larger scale (>100m) Burghead Fault, in the Hopeman Sandstone, within the Inner Moray Firth Basin. Maximum burial of the Sandstone was between 1.25km and 2.4km, which is shallower than the typical burial depth observed for the development of significant quartz cement in sandstones (2.5km/70°C). Two zones of quartz cement have previously been identified using Cathodoluminescence (CL) (Quinn *et al.*, Chapter 5). Q2 authigenic quartz is found solely in footwall locations adjacent to the Clashach and Burghead fault slip planes. The volume of Q2 cement decreases by >20% with increasing distance from the fault planes. In sandstone distant from any structural features a consistent, volumetrically minor, phase of quartz cement is present (Q3).

Two distinct fluid inclusion assemblages are present in samples containing Q2 overgrowths from the 2 footwalls. Two-phase, liquid and vapour, inclusions are present in microfractures which are healed with quartz cement, and occur exclusively within detrital grains. Microfractures are interpreted as being formed by local tectonic activity on the extensional fault planes and healed by rapid cementation during, or immediately after, faulting. Homogenisation temperatures (Th) range from 151°C to 181°C for samples from both faults, with a mean Th of 166°C. Single phase, aqueous, inclusions are present in Q2 phase quartz overgrowths within the footwalls, representing trapping temperatures of <60°C. The microfracture quartz cements and Q2 overgrowths display the same characteristic CL signature. No fluid inclusions were observed in Q3 cements.

Oxygen isotopes of Q2 and Q3 overgrowths were measured in-situ by using Secondary Ion Mass Spectrometry (SIMS). At Clashach Fault $\delta^{18}O$ values show an increase from +17.9‰ 4.2m from fault, to a maximum of +20.8‰ at 30.4m, the edge of the Q2 cement zone. Q2 overgrowth $\delta^{18}O$ values from the Burghead Fault footwall rise from +17.5‰ at 0.1m from the fault slip face, to consistent values of between +19.1‰ to +19.5‰ up to 14m distant. Hanging wall Q3 cements from the Clashach Fault have a mean $\delta^{18}O$ value of +23.1‰, and range from +21.1‰ to +24.8‰. An isotopic profile across a single quartz cemented deformation band shows $\delta^{18}O$ is a minimum mean of +20.7‰.

Fluid inclusion and oxygen isotope data indicate that Q2 quartz cement precipitated from a hot, $\delta^{18}O$ enriched, siliceous basinal fluid near the fault planes, which mixed with an isotopically lighter Jurassic meteoric porefluid, recorded as a mixing line in Q2 cement $\delta^{18}O$ values through the Clashach Fault footwall. The mixing line exists over a longer section of the Burghead Fault footwall, corresponding to the increased scale of Q2 cementation. Hanging wall Q3 cements precipitated from slightly evolved Jurassic meteoric porefluids close to, or at, the maximum burial temperature of c.84°C (2.4km at 35°C/km). Deformation band $\delta^{18}O$ values suggest internal quartz precipitation at <500m burial, and temperatures significantly <60°C, pre-dating the import of Q2 precipitating fluids and Q3 burial related cementation. Q2 cement records a period of open hydrologic conditions which punctuated progressive closed system burial diagenesis in the Hopeman Sandstone

## 6.1 Introduction

Quartz cement is a common and volumetrically abundant diagenetic mineral in deeply buried sandstones, and acts as a major culprit of porosity loss in many hydrocarbon-bearing sandstones. Despite a wealth of studies the fundamental question remains largely unresolved. This is whether quartz cement is entirely internally derived in a closed diagenetic system, or if basin scale fluid flow and mass transfer can import silica for quartz cementation. Numerous approaches to solving this problem have been taken including petrographic analysis of oilfield sandstones (e.g. Haszeldine *et al.,* 1984, Bjorlykke *et al.,* 1992, Lynch 1996, Hartmann *et al.,* 2000), fluid inclusion measurement (e.g. Haszeldine *et al.,* 1984, Walderhaug 1994, Marchand *et al.,* 2000), computer modelling (e.g. Lander and Walderhaug 1999), laboratory simulations of quartz growth (e.g. Bjorkum 1996, Renard *et al.,* 2000), isotopic investigations (e.g. Land 1984, Hervig *et al.,* 1995, Graham *et al.,* 1996, Marchand *et al..,* 2002), and studies of outcrop analogues to hydrocarbon bearing sandstones (e.g Hippler 1993, Thiry and Marechal 2001). Even with all this data the conclusions remain divided between advocates for an internal silica source, and those for an external source.

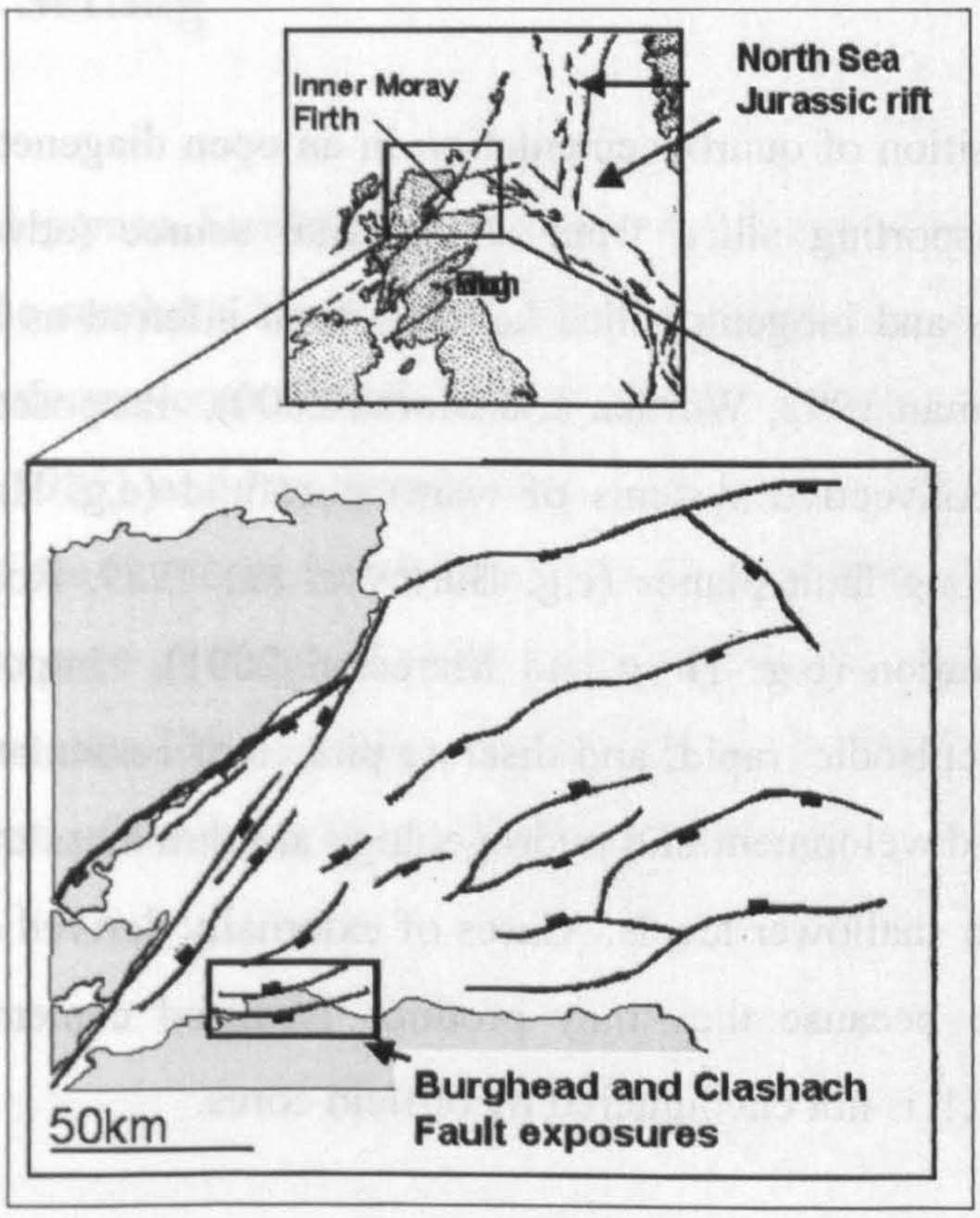


**Fig. 6.1 Location of the Inner Moray Firth on the extreme western arm of the trilete North Sea rift system (inset). Major structural features are shown along with the location of the onshore exposures of the Hopeman Sandstone on the southern basin margin (Fig. 6.2). Some details from Underhill 1991.**

Proposed internal sources of silica within a sandstone include pressure solution between detrital quartz grains, dissolution of feldspar grains, and diagenetic clay reactions (e.g. Bjorlykke *et al.*, 1992). Internal quartz cementation is considered to be a three stage dissolution-diffusion-precipitation process occurring over a c.1m scale, within static porefluids (Worden *et al.*, 1998). Macro-scale occurrence of cement is ubiquitous throughout a given sandstone buried to a sufficient temperature. Intra-sand meso- and micro-scale quartz overgrowth location is controlled by grain size and the presence of precipitation inhibiting grain coatings, particularly clays, such as chlorite (e.g. Heald and Laresse 1974, Fisher *et al.*, 2000), as well as distance from local silica sources. Compilations of data for some North Sea oilfields (Giles *et al.*, 1992) show a gradual increase in quartz cement volume from when burial depth reaches a temperature of 70°C (2.7km North Sea). Recent successful attempts to predict reservoir-scale porosity in deeply buried sandstone oil reservoirs, have used computer models of quartz cementation and compaction. These assume that silica for cementation is supplied internally in a temperature controlled gradual, burial process, from pressure solution between detrital quartz grains, and that the cementation process is controlled by the rate of precipitation (Lander and Walderhaug 1999).

In contrast, the proposition of quartz cementation in an open diagenetic system involves the import of fluids transporting silica from an external source (advection). Surrounding mudstones, sandstones and biogenic silica have all been inferred as likely external sources (e.g. Gluyas and Coleman 1992, Worden and Morad 2000). Proposed mechanisms of silica transport have been convective systems of warm porefluid (e.g. Haszeldine *et al.*, 1984, Lynch 1996), flow along fault planes (e.g. Burley *et al.*, 1989, Rossi 2002) and shallow meteoric water penetration (e.g. Thiry and Marechal 2001). Import of silica for quartz cementation suggests episodic, rapid, and discrete phases of cementation. The implications for sedimentary basin development and hydrogeology are that mass transfer can occur when deep hot fluids flow to shallower levels. Cases of externally derived quartz cementation are less well documented because they may produce localised cementation adjacent to the transport pathway which is not encountered by oilfield cores.

An unusual shallow-burial quartz cementation which is spatially associated around fault planes, and described in detail by Quinn *et al.* (in prep., Chapter 5), is investigated here to determine the likely sources of silica for cementation and the nature of the porefluid from

which the diagenetic quartz precipitated. Analysis of fluid inclusions in authigenic quartz gives insight into the temperature of authigenic quartz precipitation and to the nature of the fluid from which the cement precipitated. This data can be integrated with the analysis of cement oxygen isotopic ratios to constrain the source of the cementing fluid. Porefluids from different sources have different isotopic ratios: Jurassic meteoric fluids are depleted in $^{18}O$ with a characteristic value $\delta^{18}O$ of -7‰. By contrast typical present day North Sea deep basin fluids may have $\delta^{18}O$ values > +1‰ (e.g. Smalley and Warren 1994, Girard *et al.*, 2001). Ion microprobe analysis provides a high spatial resolution method of analysing oxygen isotope ratios within in-situ authigenic quartz. It also allows variation of isotope values within individual overgrowths to be measured.

A statistically significant number of in-situ isotopic analyses have been combined with fluid inclusion temperatures to reconstruct the evolution of quartz cementation and palaeo-fluids within the exposed aeolian Hopeman Sandstone within the Inner Moray Firth basin.

## 6.2 Geological Setting

The Upper Permian Hopeman Sandstone Formation crops out along 8km of the southern basin margin, along the southern Moray Firth coastline (Figs. 6.1, 6.2). The Formation is visible in wave-cut platforms, coastal cliffs and in adjacent quarries. Upper Permian in age, (Benton and Walker 1985) and stratigraphically equivalent to the hydrocarbon bearing Weissliegend Sands of the Southern North Sea (Glennie and Buller 1983), the Formation is part of an exposed sequence of Permo-Triassic sandy sediments. The Hopeman Sandstone unconformably overlies the lithologically similar Devonian Old Red Sandstone, which comprises the 'basement' of the Inner Moray Firth basin (Fig. 6.2).

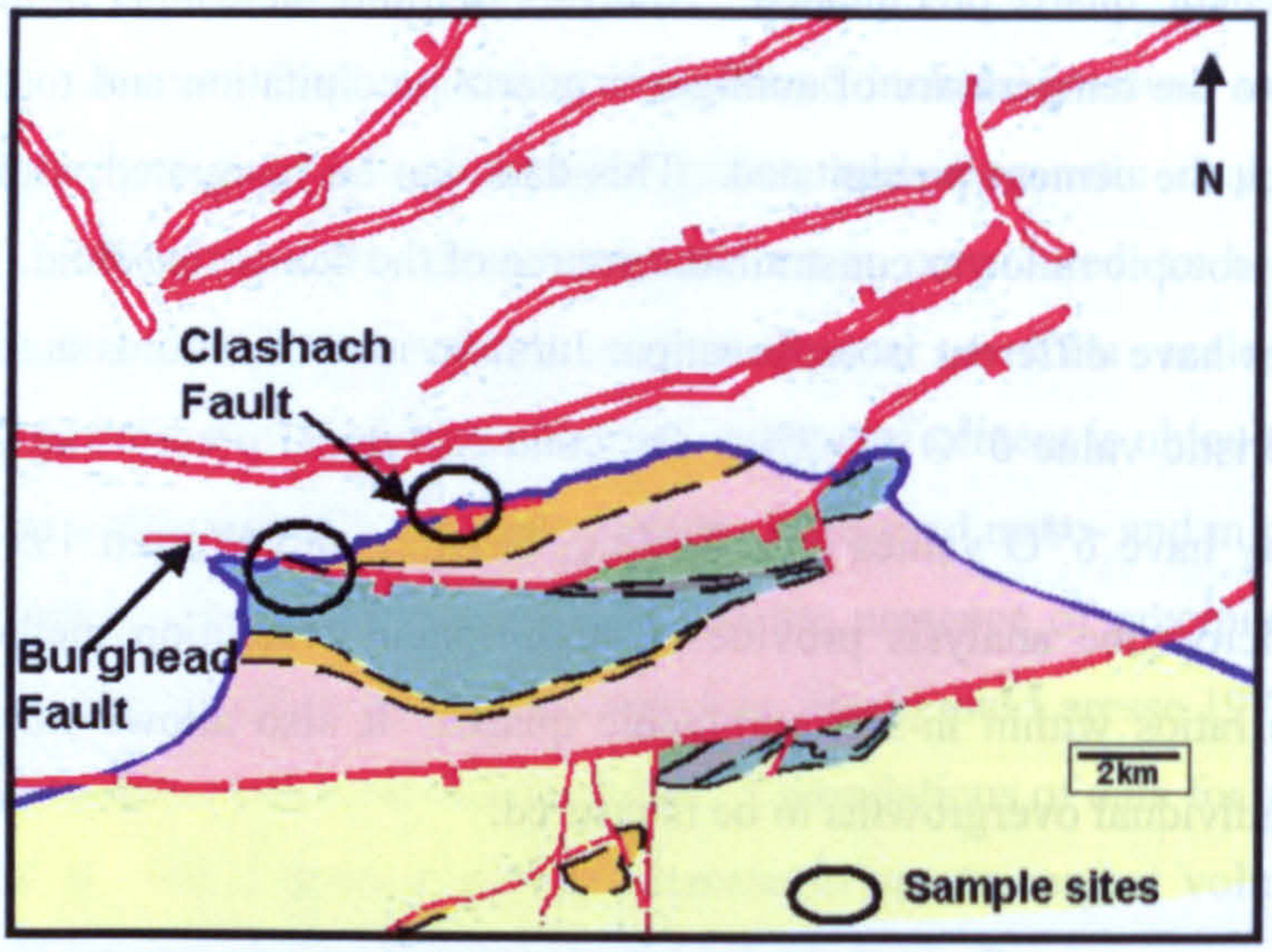


**Fig.6.2..Geological and structural map of the onshore and offshore Lossie Peninsula. The Burghead and Clashach exposed faults, from around which samples for isotopic and fluid inclusion analysis were taken can be seen.**

The Inner Moray Firth (IMF) basin forms the western arm of the trilete North Sea rift system, and has a broad half-graben expression, 50km wide and 5km deep, developed principally through a number of Late Jurassic extensional faults (Fig. 6.1). The western area of the basin underwent early Tertiary uplift and erosion, imparting a 2-3° regional eastward dip. Estimates of basin exhumation vary between 750m (Roberts *et al.,* 1990) and 1km (Underhill 1991). The Hopeman Sandstone is succeeded in a conformable sequence onshore by Triassic fluvial sands (Burghead Beds, Lossie Sandstone Formation), a Top Triassic chert and Lower Jurassic sands and marls. The Hopeman Sandstone is composed of stacked transverse dune facies sands (Glennie and Buller 1983), interspersed with contorted sand beds, produced through soft-sediment liquefaction shortly after deposition (Peacock 1966, Clemmensen 1987). Two normal cataclasite faults are well exposed onshore, one on the coast and within the working Clashach Quarry, and the other along the foreshore at Burghead (Fig. 6.2).

The minor, sub-seismic scale (displacement <50m) Clashach fault is exposed along the length of the east-west face of Clashach Quarry and in the adjacent Clashach Cove some 150m west. The fault trends 078-085°, with a mean dip in both localities of 75° south. Both the hangingwall and footwall consist of Hopeman Sandstone and in both outcrops around 10m of vertical exposure is visible. The proven onshore thickness of the Hopeman Sandstone is 60m (Berridge and Ivimey-Cook, 1967) restricting maximum throw to 50m. A

poorly developed fault damage zone surrounds the main slip face, composed of a number of rare, isolated millimetre-scale faults (deformation bands) present up to 10m from the main slip face. The deformation bands are separated by 1-4m of undeformed sandstone, the frequency of band occurrence decreasing with increasing distance from the fault. Pervasively quartz cemented and indurated footwall sands show near vertical jointing with regular 1-1.5m spacing.

In contrast the Burghead Fault is a regional, seismic scale (throw >50m) fault which can be extrapolated offshore onto seismic reflection data (Quinn *et al.*, in prep, Chapter 4). Upper Triassic fluvial sands (Burghead Beds) in the hanging wall are downthrown to the south and juxtaposed against the aeolian Hopeman Sandstone in the footwall. The fault is exposed laterally for 30m at low tide and the main slip face strikes between 095-100°, dipping between vertical and 80° south, with a maximum normal displacement of 135m at the position of fault exposure. The Burghead Fault consists of a main slip face, which accommodated the majority of displacement, and a series of deformation bands which individually record mm scale slip. The deformation bands occur in clusters 25- 100cm in width, each composed of several anastamosing bands. The clusters decrease in both size and frequency of occurrence with increasing distance from the main slip face. At distances greater than c.10m from the main slip face individual rare deformation bands occur. Exposure restricts observation of the maximum extent of deformation related structures, but the fault zone can be observed to be developed on a larger scale than the Clashach Fault zone.

The Lossie Peninsula, within which the Hopeman Sandstone and Burghead and Clashach faults crop out, has been interpreted as a horst block of Late Jurassic age, forming a regional structural high on the basin margin (Quinn *et al.*, in prep, Chapter 4). In this model, which is based upon basinwide styles of deformation and reconciliation of the onshore structures with seismic data directly offshore, the two faults exposed onshore are intra-horst extensional faults. A Late Jurassic age is assigned to the major phase of movement on the Burghead and Clashach faults, although minor re-activation during the Cenozoic cannot be ruled out. Extrapolation of regional stratigraphy, basin uplift history, and petrographic data suggests the maximum burial depth for the Hopeman Sandstone was 1.25-2.4km, following Late Jurassic basin extension.

## 6.3 Quartz cementation in the Hopeman Sandstone

A detailed diagenetic study, and the effect of fault-associated quartz cementation on porosity and permeability evolution of the Hopeman Sandstone was given in Quinn *et al.* (in prep., Chapter 5). The main features of fault-associated authigenic quartz are summarised here.

### 6.31 Authigenic quartz petrography

SEM-CL petrography reveals three phases of authigenic quartz in the Hopeman Sandstone; Q1 an inherited authigenic overgrowth, Q2 occurs in samples adjacent to fault planes, and Q3 is found in the background sands at distance from structural features. Q1 is not considered diagenetic quartz in the true sense, and is identified by a dark CL signature and rounded overgrowth edges. Q2 has a characteristic bright, heterogeneous, CL signature (Fig. 6.3) and is only found in association with the two exposed fault planes. Q2 phase cement forms overgrowths which are up to 100μm in diameter. Q3 is found to post-date phase Q2 in some samples, and forms a volumetrically minor cement in the exposed hanging wall, and background, Hopeman Sandstone. Quartz cemented microfractures occur within detrital quartz grains surrounding both faults. SEM-CL examination of these grains reveals that many healed microfractures have CL signatures which are in continuity with the CL signature of surrounding quartz overgrowths (Fig. 6.4). Within individual sections many of these microfractures follow a common orientation, and at Clashach occur closer to the fault plane, but are absent with increasing distance through the footwall.

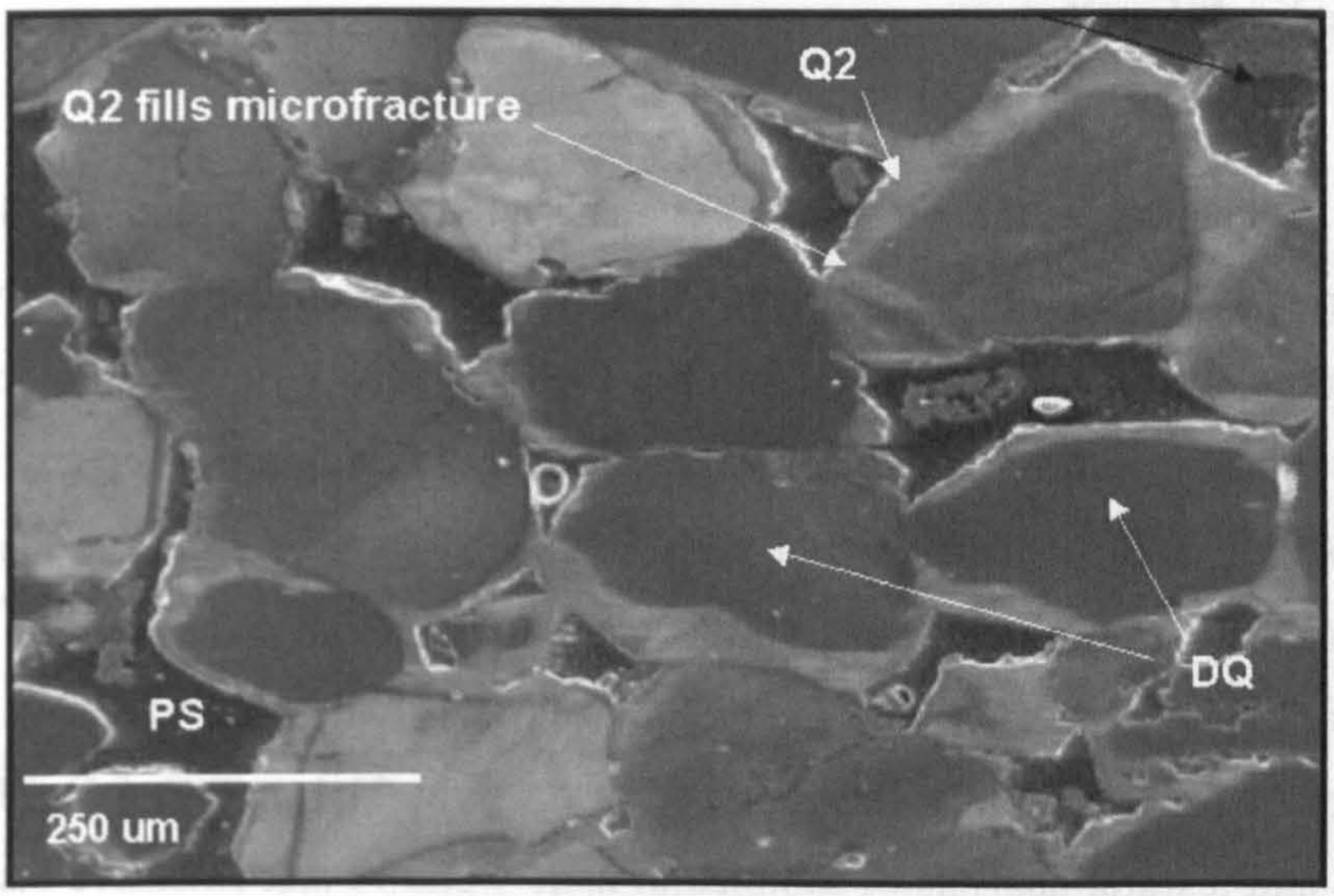


**Fig. 6.3.. SEM-CL image of Q2 quartz cement around several detrital quartz grains. The characteristic bright CL signature allows differentiation of cement from pore space and detrital quartz. A fracture filled with quartz cement which is in CL continuity with the overgrowth cement. Sample from Hopeman Sandstone 4.2m from the fault plane, in the Clashach Fault footwall. DQ = detrital quartz, PS = pore space, Q2 = Q2 quartz cement.**

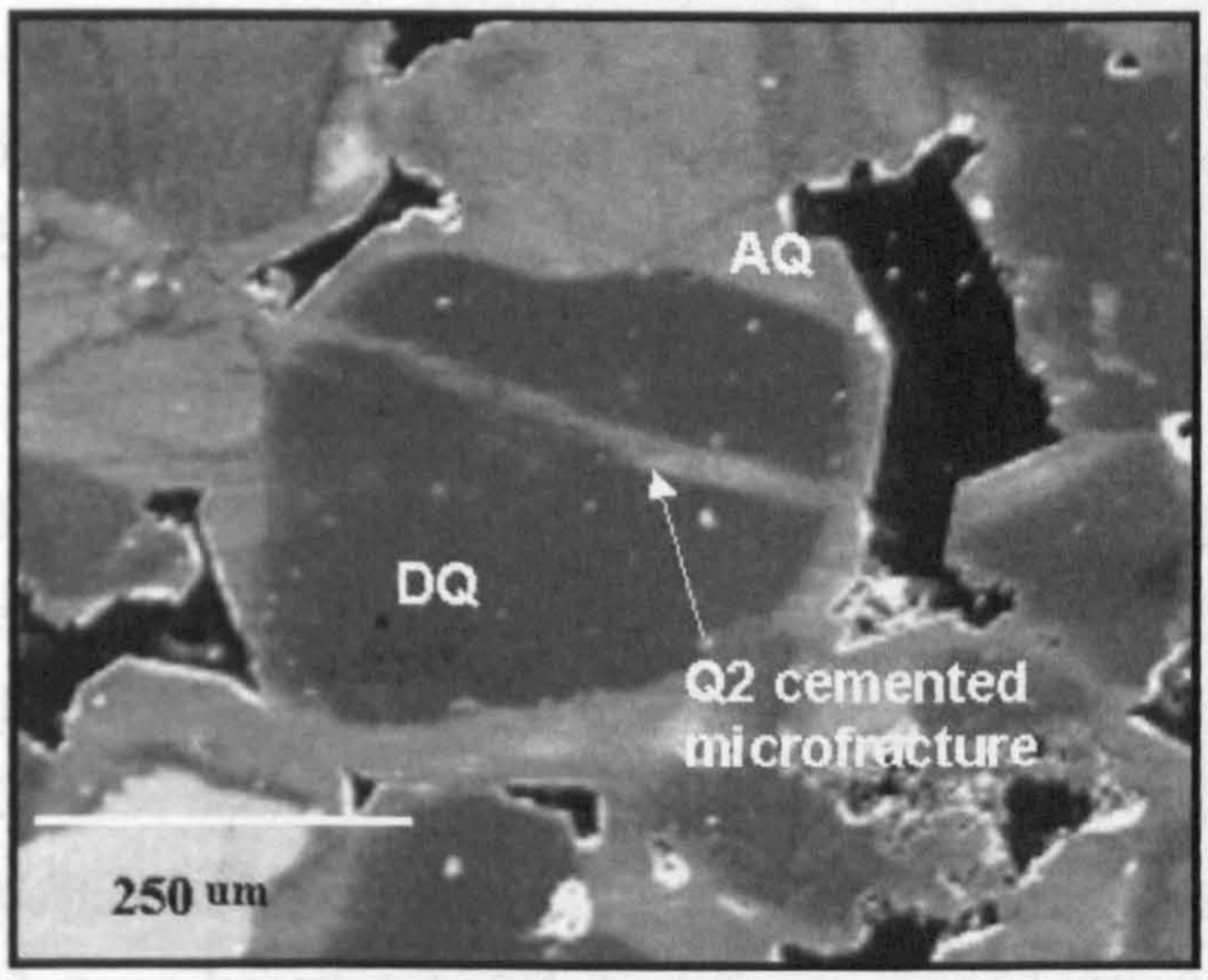


**Fig. 6.4.. SEM-CL images of Clashach footwall samples showing the location of ion microprobe analysis pits. A) Analysis of a detrital quartz grain. B) Four craters from ion microprobe analysis in Q2 quartz overgrowth, clearly distinguishable from the dark CL signature of the detrital grain. C) Analyses in both detrital grains and a large quartz overgrowth.**

## 6.32 Clashach Fault

Point count data shows that the volume of Q2 phase quartz cement within the Clashach Fault footwall varies systematically with distance from the main fault slip plane in two opposing trends, labelled zone 1 and zone 2. Within the footwall zone 1 runs from 0.5m through to 13.8m from the fault plane, and samples display an increase in quartz cement with increasing distance from the fault. Quartz cement rises from 4.2% at 0.5m from the fault plane to a maximum of 26.5% at 13.8m. Zone 2 runs from 13.8m to 31.7m and is defined by a reversal in the pattern of Q2 cement volume, which follows a linear trend decreasing from a maximum of 26.5% at 13.8m to a minimum of 5.6% at 31.1m (Fig. 6.5). Field, X-Ray Diffraction, and textural analysis of samples in zone 1 shows that extensive dissolution of a pre-existing carbonate cement occurred following precipitation of Q2 quartz cement. This carbonate cement reduced the available pore space, and nucleation sites, available for authigenic quartz growth in this zone. Moving through the fault plane the pattern of quartz cement is asymmetrical. Hopeman Sandstone hanging wall sands display a slight reduction in quartz cement from 4.8% at 2.3m from the fault slip face to a mean background of 3% at a distance greater than 2m from the fault plane (Fig. 6.5). Hanging wall quartz cement is consistently Q3 phase, with the exception of some Q2 cement which may be present in sandstone close to the fault plane (<1m). Textural analysis reveals no evidence for the extensive carbonate dissolution seen in the adjacent footwall sandstone, and grain-coating clays which may inhibit authigenic quartz nucleation are also absent.

The term deformation band is used to describe millimetre scale faults in high porosity sandstones (e.g. Aydin 1978). At the Clashach Fault quartz cemented micro-faults, or cataclastic deformation bands (Aydin 1978), are present in the footwall adjacent (<2m) to the main fault slip face. Petrographic observations of a deformation band 0.25m from the main fault slip face indicate that the internal structure of the band is composed of large detrital quartz grains surrounded by a matrix of small (>5μm ) detrital quartz fragments, produced during deformation. The naturally low porosity, poorly sorted, deformation band is cemented with authigenic quartz further reducing porosity to <1%. The complex texture precludes recognition of a characteristic SEM-CL signature, and classification of the cement as Q2, Q3 or another unknown phase is not possible.

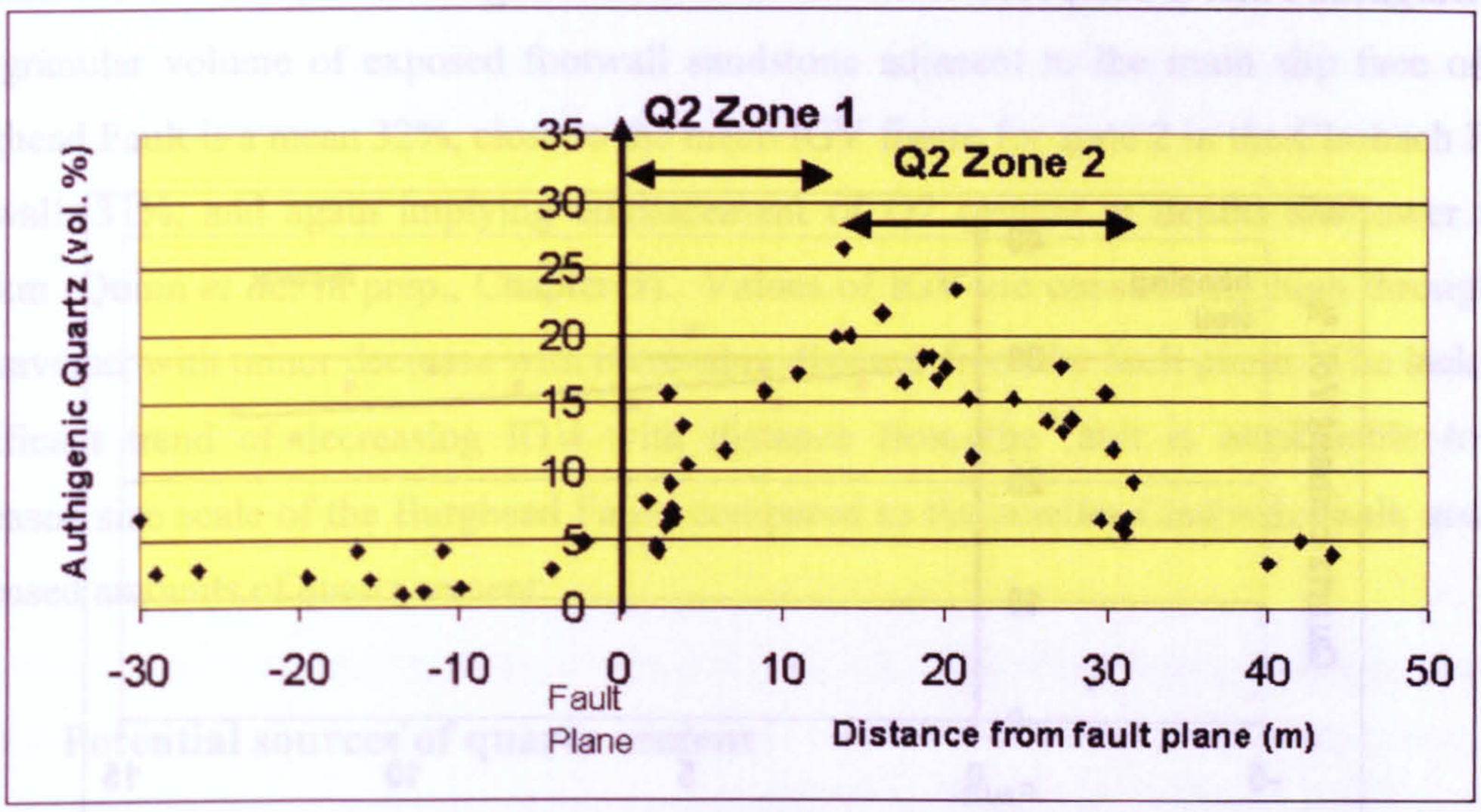


**Fig 6.5. At the Clashach Fault quartz cement volume follows an asymmetric trend across the fault plane. Hanging wall sands, and footwall sands at greater than 40m distant contain 3-4% authigenic quartz. The footwall displays two opposite trends, increasing quartz cement with increasing distance from the fault from 1-1m, and decreasing quartz cement 13m to 31m.**

## 6.33 Burghead Fault

Quartz cement displays a simple pattern throughout the exposed Hopeman Sandstone footwall of the Burghead Fault. Quartz (Q2) cement volume increases from 24.5% at 13m distant to 29.2% at 0.5m from the main slip face (Fig. 6.6). Quartz cement is ubiquitously Q2 phase and euhedral overgrowths are visible where there is some porosity. Where porosity is reduced to zero the morphology of the cement typically displays overgrowth textures with compromise growth boundaries between individual overgrowths. In several samples the cement displays the same CL signature as Q2 cement but appears to be a massive pore-filling macro-cement. All samples are from within the fault 'damage zone', but are undeformed sandstone between observable clusters of deformation bands.

In comparison to observations within the footwall of the Clashach Fault, no textural evidence of any carbonate cement dissolution is seen, and quartz cement can be seen nucleating around smooth grain boundaries. Fractured grains, filled with authigenic quartz, were observed more frequently around the Burghead Fault than surrounding the Clashach Fault, and occur near the common clusters of deformation bands and main fault slip face. The hanging wall of

the Burghead Fault is composed of the fluvial Triassic Burghead Beds, and was not analysed here.

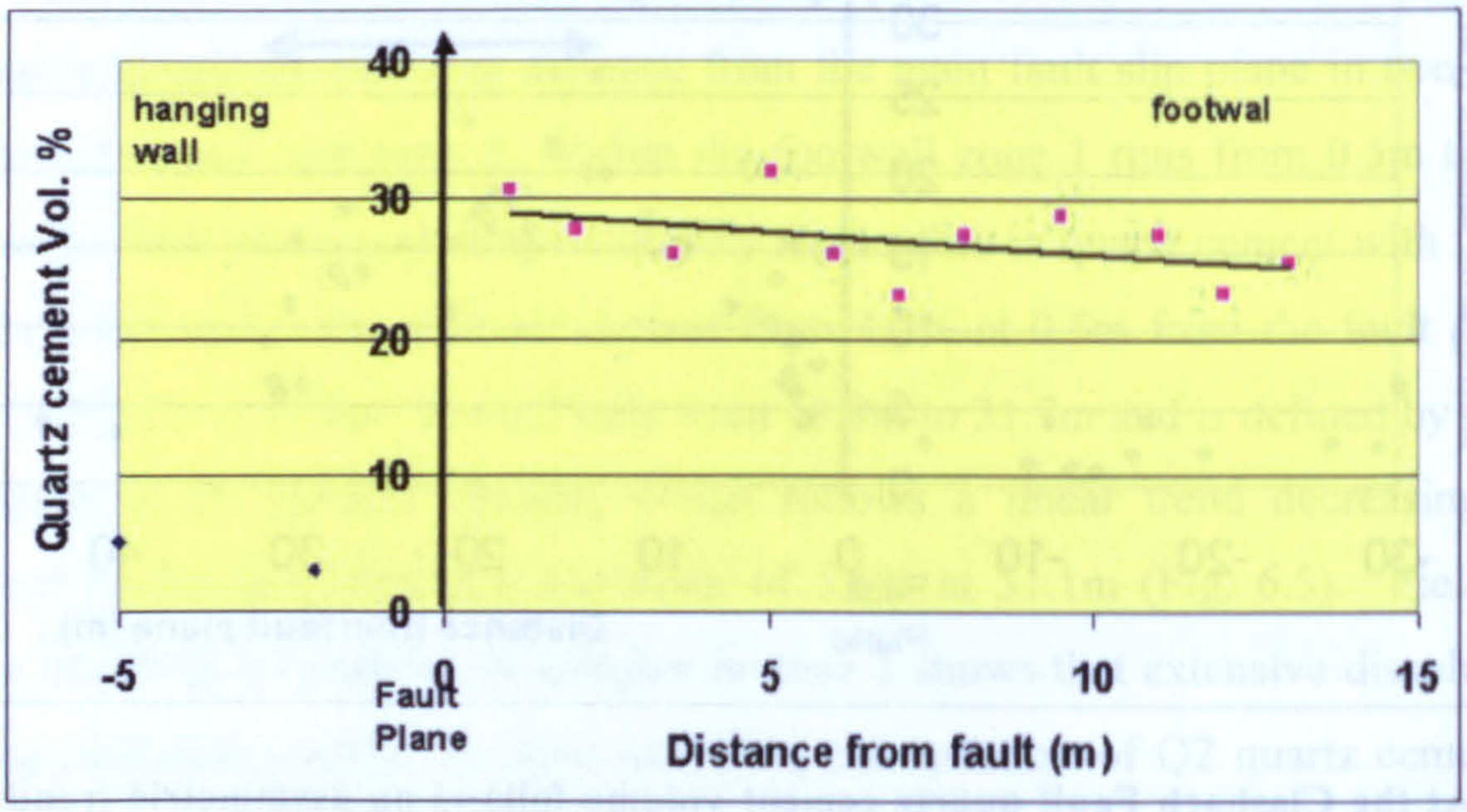


**Fig 6.6. Quartz cement volume variation across the Burghead Fault. The Hopeman Sandstone footwall Q2 cement displays a broadly linear trend of decreasing cement with increasing distance from the main fault slip face. Fault scale is larger than the Clashach Fault and corresponding quartz cement volume is larger. Hanging wall samples from the Triassic fluvial sand Burghead Beds display significantly less quartz cement than the footwall Hopeman Sandstone, despite a difference in burial of less than a few hundred metres, and similar detrital constituents. All samples are within the fault damage zone but are from undeformed sandstone.**

## 6.34 Textural constraints on cement emplacement

Mean intergranular volume (IGV) (pore space and cement) (Paxton *et al.*, 2002) in footwall samples of the Clashach Fault from the quartz cement zone 2, 13.8 –31.7m, is 31%. Calculation of the IGV of each sample shows that the major phase of Q2 quartz cement around the Clashach Fault acts to preserve a high volume. Using well constrained compaction-porosity loss plots (Quinn *et al.*, in prep., Chapter 5), this shows cement emplacement was at a shallow burial depth of between 500m and 1.25km, prior to compaction and porosity loss associated with deeper burial. The textural data also constrains maximum burial depth of the exposed Hopeman Sandstone to 1.25-2.4km (Quinn *et al.*, in prep., Chapter 5). Structural analysis and offshore seismic data suggest maximum burial was likely 1.5km (Quinn *et al.*, in prep., Chapter 5). Moving through the footwall of the Clashach Fault from the fault plane shows that IGV decreases gradually indicating that cementation occurred through at least some continuing burial compaction, and that much of the authigenic quartz was emplaced prior to maximum burial.

Intergranular volume of exposed footwall sandstone adjacent to the main slip face of the Burghead Fault is a mean 32%, close to the mean IGV figure for zone 2 in the Clashach Fault footwall, 31%, and again implying emplacement of Q2 cement at depths shallower than 1.25km (Quinn *et al.*, in prep., Chapter 5). Values of IGV are consistently high throughout the traverse, with minor decrease with increasing distance from the fault plane. The lack of a significant trend of decreasing IGV with distance from the fault is attributable to the increased size scale of the Burghead Fault, compared to the smaller Clashach Fault, and the increased amounts of quartz cement.

## 6.35 Potential sources of quartz cement

The Hopeman Sandstone has a simple detrital mineralogy (Qtz >95%, K-Feldspar 3-5%, Plagioclase 0-2%, rock fragments 0-3%). Internal sources of silica for cementation of the Hopeman Sandstone are therefore limited to pressure solution between silica grains and/or dissolution of detrital K-feldspar grains. Textural data shows that the IGV is high in the extensively cemented sandstone adjacent to the fault, and that contact between detrital quartz grains is minimal. In the most extreme samples, grains are floating in quartz cement and there is virtually no grain:grain contact. These observations combined with the inferred shallow, low temperature, maximum burial indicate that any detrital quartz dissolution through pressure solution was minimal, and insufficient to account for the local volumes of silica observed adjacent to the fault planes. K-feldspar grains can be seen to display varying levels of dissolution which must have resulted in release of silica into the porefluid. The small amount of K-feldspar in the whole system (3-5%) shows any dissolved silica produced would be volumetrically minor, and unable to act as the source for Q2 quartz cement.

External sources for the silica may be an influx of silica saturated meteoric waters (e.g. Blatt 1979), which have been inferred to cause minor quartz cementation during shallow burial in some oilfield sandstones (Giles *et al,* 1992). Localised, extensive silicification from infiltration of meteoric fluids has been documented in the Fontainebleau Sandstone, related to water table fluctuations (Thiry and Marechal 2001). External silica may also be provided by advection of deep, warm, basinal fluids carrying silica released from mudstone burial reactions (e.g. Sullivan and McBride 1991). Cooling of hot siliceous fluids in shallow

sandstones which have multiple sites for quartz precipitation, may lead to silicification. Silica precipitation from such meteoric or basinal fluids may be predicted to be controlled by the fluid transport pathways, such as around the water table in the Fontainebleau Sandstone, or around faults which acted as fluid conduits (e.g. Burley *et al.*, 1989).

Given the absence of a significant internal source at the calculated depth of Q2 quartz cementation, the silica was likely to have been sourced externally, from shallow meteoric waters, or from ascending hot basinal fluids.

## 6.4 Analytical Methods

### 6.41 Fluid inclusion microthermometry

#### 6.41.1 Sample selection and preparation

Fifty-seven petrographic samples were taken for a larger diagenetic study of quartz cementation around faults in the Hopeman Sandstone (Quinn *et al.*, in prep., Chapter 5). Based upon the observed decrease in cement volume with increasing distance from the fault planes, ten samples were chosen from this data-set for fluid inclusion analysis. Samples were chosen to identify the conditions under which fault-associated cementation occurred, and to measure any systematic change in fluid inclusions with distance from the fault. Six samples were taken from a profile through the footwall of the Clashach Fault, at distances of 3.2, 6.5, 16.2, 18.7, 21.5 and 29.7m. Four samples were also obtained from the footwall of the Burghead Fault in a perpendicular profile to the fault, at 2, 4.5, 10 and 14m. Care was taken during collection and preparation to avoid heating the samples to greater than 30°C. Thick sections of 100μm were made at the University of Edinburgh and double polished with a water cooled system to prevent overheating and damage of inclusions.

#### 6.41.2 Analytical equipment and procedure.

Each thick section was observed using a Leitz Metallux optical microscope to identify fluid inclusion assemblages for thermometric analysis (FIA's). A fluid inclusion assemblage (FIA) is the most finely discriminated petrographically distinct group of inclusions (Goldstein and Reynolds 1992), and two sets of FIA's of interest were noted in the samples. Several grains on each section which showed well defined FIA's were selected and the

sections were cut into small chips using a water-cooled microdrill. To avoid the effects of any heating associated with the microdrill the chips were cut with a wide diameter which encompassed multiple (tens's) grains, with the grain and overgrowth of interest at the centre.

Microthermometry was carried out using equivalent Linkam TH600 heating-freezing stages at the University of Leoben, Austria and the University of Edinburgh and a Leitz Metallux microscope with magnifications of 10X, 20X, 40X and 60X. For two-phase liquid-vapour inclusions homogenisation temperature (Th) is close to the minimum trapping temperature of the inclusion, and so close to the temperature of quartz cementation (e.g. Roedder 1979). Th was obtained by step-heating the sample at 0.1°C intervals until the vapour bubble of an individual inclusion was observed to disappear. As soon as the bubble disappeared the temperature was dropped, if the bubble re-appeared within less than 3°C, the sample was not considered to have fully homogenised, and was heated one step higher. This method of cycling ensures accurate determination of homogenisation temperatures. For chips in which multiple inclusions were present, the small increment of step temperature increase allowed most inclusions to be homogenised in ascending temperature order, avoiding overheating and stretching of cooler inclusions. A pressure correction can be applied to Th measurements to give a more accurate estimate of trapping temperature, however this correction is not needed when methane is present within a fluid, as homogenisation temperatures are similar to minimum trapping temperature (Hanor 1980). The samples analysed here are from a known hydrocarbon-bearing basin, which suggests, along with evidence to indicate that diagenetic quartz precipitated from deep basinal fluids, that methane is likely to be present and no pressure correction is required.

Freezing 2-phase aqueous inclusions and observing the temperature of first ice melting (Te) and of final ice melting (Tm) gives information on the salinity of the fluid present. The small size of the inclusions (typically < 5-7μm) and the collapse of some vapour bubbles on freezing, meant that Te and Tm could not be observed for the 2-phase FIA's present. Thus any 2-phase freezing temperatures are a poor constraint on fluid chemistry.

A number of single-phase all liquid inclusions were documented within diagenetic quartz. Chips containing single-phase inclusions were placed in a fridge (+3°C) for 3 weeks to attempt nucleation of a vapour bubble and distinguish whether the inclusions were significantly metastable 2-phase inclusions or true low temperature (<50-60°C) single-phase

(Goldstein and Reynolds 1992). No bubble nucleation was observed, and a number of chips were subsequently held at –10°C on the Linkam freezing stage for 12 hours, but again, no vapour bubble nucleation was observed. Selected single-phase aqueous inclusions were analysed using a Raman spectrometer at the University of Leoben, Austria. The Raman technique projects a laser beam into the inclusion of interest which interacts with the vibrational modes of molecules of dissolved species, causing Raman scattering of the laser. The spectrum detected corresponds to the energies of molecular vibrational modes in different species which may be present in the sample, allowing identification of the likely composition (Burke 2001).

## 6.42 SIMS oxygen isotope microanalysis

### 6.42.1 Sample selection and preparation

Fourteen thin section samples were selected from the pre-existing petrographic dataset from the onshore Hopeman Sandstone (Quinn *et al.*, in prep., Chapter 5), with the aim of characterising the nature, and any variation, of quartz cement isotopic ratio both adjacent to and at increasing distance from the fault planes. Four Clashach Fault footwall samples were taken, at 2.9, 4.2, 11 and 30.4m from the fault plane, and 2 hanging wall samples at 2.2 and 30m. Each thin section sample was cut into a 1-inch round and coated with a thin (0.02μm) coat of gold, to assist with the prevention of charge build-up. The advantage of the ion probe over conventional $^{18}O/^{16}O$ techniques is that individual overgrowths, and zones within those overgrowths, can be targeted. Authigenic quartz typically displays a different cathodoluminescence (CL) signature to detrital quartz allowing the overgrowth to be identified accurately. Prior to SIMS analysis SEM-CL and secondary electron (SE) maps of each section were produced assisting with the location of particular overgrowths when the sample was viewed in the reflected light optical viewing system of the ion probe. Following SIMS analysis each section was then viewed again by SEM-CL to identify the exact location of each microanalysis (Fig. 6.7). This crucially allows isotope measurements of the detrital grains and overgrowths to be identified, and analyses which overlapped both detrital grain and authigenic quartz to be differentiated, and rejected if necessary.

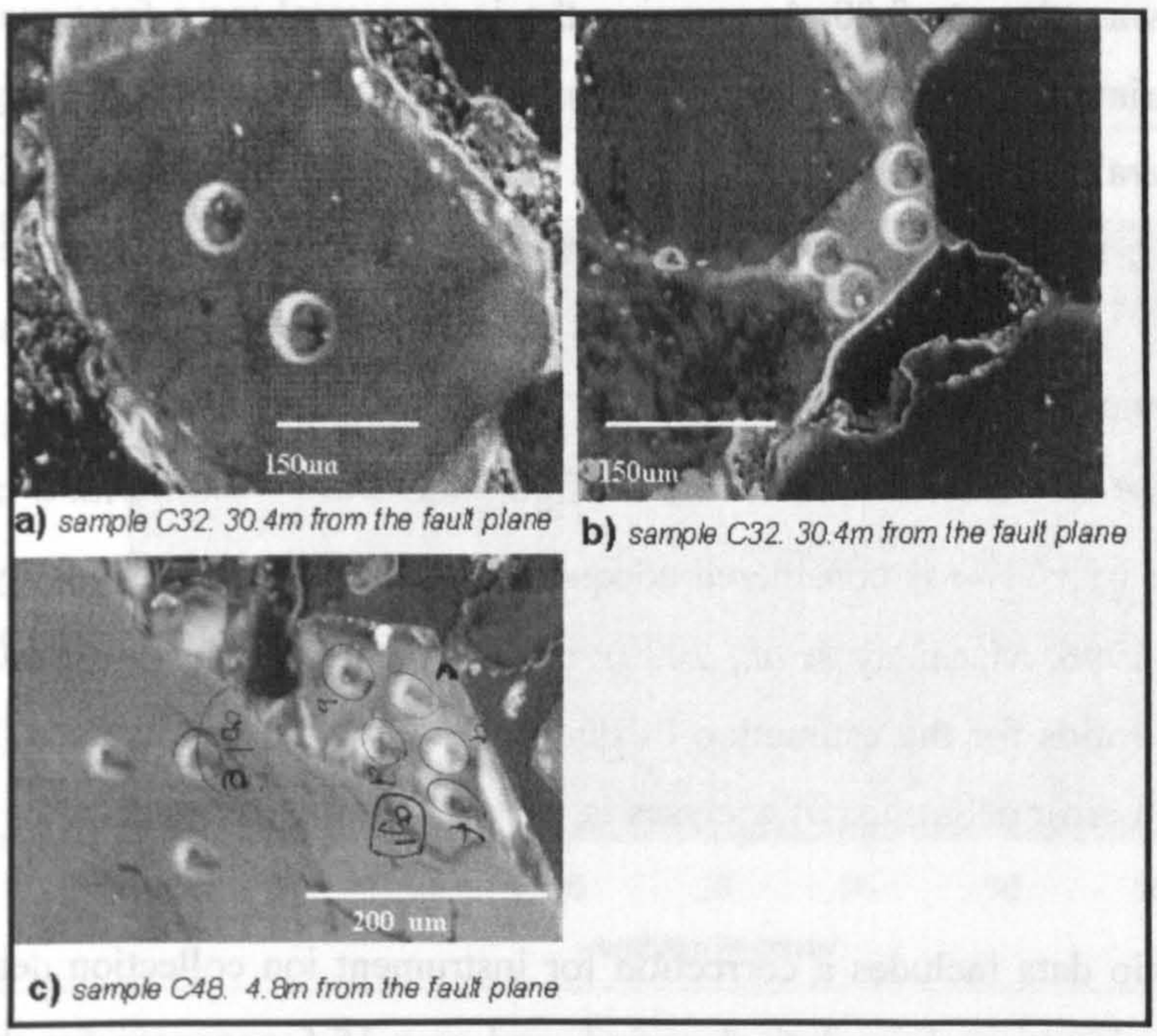


a) *sample C32. 30.4m from the fault plane*

b) *sample C32. 30.4m from the fault plane*

c) *sample C48. 4.8m from the fault plane*

**Fig. 6.7.. SEM-CL images of Clashach footwall samples showing the location of ion microprobe analysis pits. A) Analysis of a detrital quartz grain. B) Four craters from ion microprobe analysis in Q2 quartz overgrowth, clearly distinguishable from the dark CL signature of the detrital grain. C) Analyses in both detrital grains and a large quartz overgrowth.**

### 6.42.2 Analytical and instrumental conditions

The oxygen isotope ratios of detrital quartz and in-situ diagenetic quartz overgrowths were measured by secondary ion mass spectrometry (SIMS) at the University of Edinburgh in two periods, 16/6/03 to 28/6/03, and 17/7/03 to 18/7/03 (Appendix F). Analyses were undertaken using a Cameca ims-4f ion microprobe equipped with a Charles Evans and Associates control system. All analyses were made with a focused primary beam of 133Cs+ ions accelerated onto the standard gold coated thin sections. Primary beam currents were maintained between 4-5nA for both analytical sessions (June and July), and beam width was 20-25μm, producing circular to oval ablation craters (Fig. 6.7) approximately equal to the beam size. The impact of the beam on the sample produced high-energy negative secondary ions ($^{18}O$- and $^{16}O$-) which were accelerated and focused into a mass spectrometer, where ions with energies of 350 +/- 20eV were magnetically separated and counted on a Balzers SEV217 electron multiplier. A high-energy Cameca electron flood gun was used to counter the effects of any positive charge build-up on the sample surface, either from the incoming Cs+ beam or from the ejection of negative ions. The secondary electron gun voltage was adjusted until the

sample current was close to 0.00uA, meaning the instrumental mass fractionation (IMF) is insensitive to variations in sample charging (Schaeur and Williams 1990, Hervig *et al.* 1992), resulting in generally stable secondary currents. Eighty cycles of counting $^{18}O^-$ (8secs) and $^{16}O^-$ (1sec), using magnetic peak switching, were measured in each analysis leading to total count times for $^{18}O^-$ of 640 s and for $^{16}O^-$ of 80 s, for each analysis undertaken. Each individual analysis of quartz took 13-15mins. The mean internal precision on individual analyses using the SIMS technique in this configuration was +/-1‰, with a range of 0.76-1.6‰. An error of +/-1‰ is considered adequate for oilfield reservoir quality applications (Graham *et al.,* 1996, Macaulay *et al.,* 2000), and results in a range of +/-5°C when using oxygen isotopic ratios for the estimation of quartz precipitation temperature (Hervig *et al.,* 1995). The mean error on groups of analyses is, naturally, smaller.

Raw isotopic ratio data includes a correction for instrument ion collection deadtime, which was calibrated prior to each analytical period, and was 15.6 nanosecs for these analyses. Instrumental mass fractionation (IMF) of samples has been observed to occur over individual analytical sessions, and is thought to be caused by progressive ageing of the electron multiplier (Eiler *et al.,* 1995b). Typically this drift in mass fractionation leads to a depletion in the heavy isotopes relative to true composition. Analyses of the unknown samples were interspersed with repeated analysis of standard quartz grains to constrain the pattern of IMF drift within each daily analytical session. The pattern of IMF drift is generally linear with time and can be modelled by least squares regression of the values obtained from analyses of the standard samples (Fig. 6.8), allowing a correction to be applied to the data. Data quoted as 'corrected' accounts for the effects of IMF. Figure 6.9 shows the daily-drift corrected oxygen isotopic ratio of the measured standard grain. This indicates that there was no significant long-term drift between daily sessions, either throughout the first 2 week analytical period (June), or the second, 2 day analytical period (July). Two grains of the international standard Bogala Quartz and 1 grain of the international standard NBS-28 were used during the two analytical periods. Bogala Quartz ($\delta^{18}O_{SMOW}$ = 12.3‰ +/-0.3‰) was shown to be homogeneous on the scale of ion microprobe analysis by Graham *et al.* (1996). NBS-28 is produced by, and was standardised to $\delta^{18}O_{SMOW}$ = 9.8‰ +/-0.1‰, by the U.S. National Institute of Standards and Technology (www.nist.gov). The length of the first analytical period (12 days), and the high number of unknown sample analyses made (n= 227) meant 2 grains of the Bogala Quartz standard, and 1 grain of NBS-28 quartz, were used.

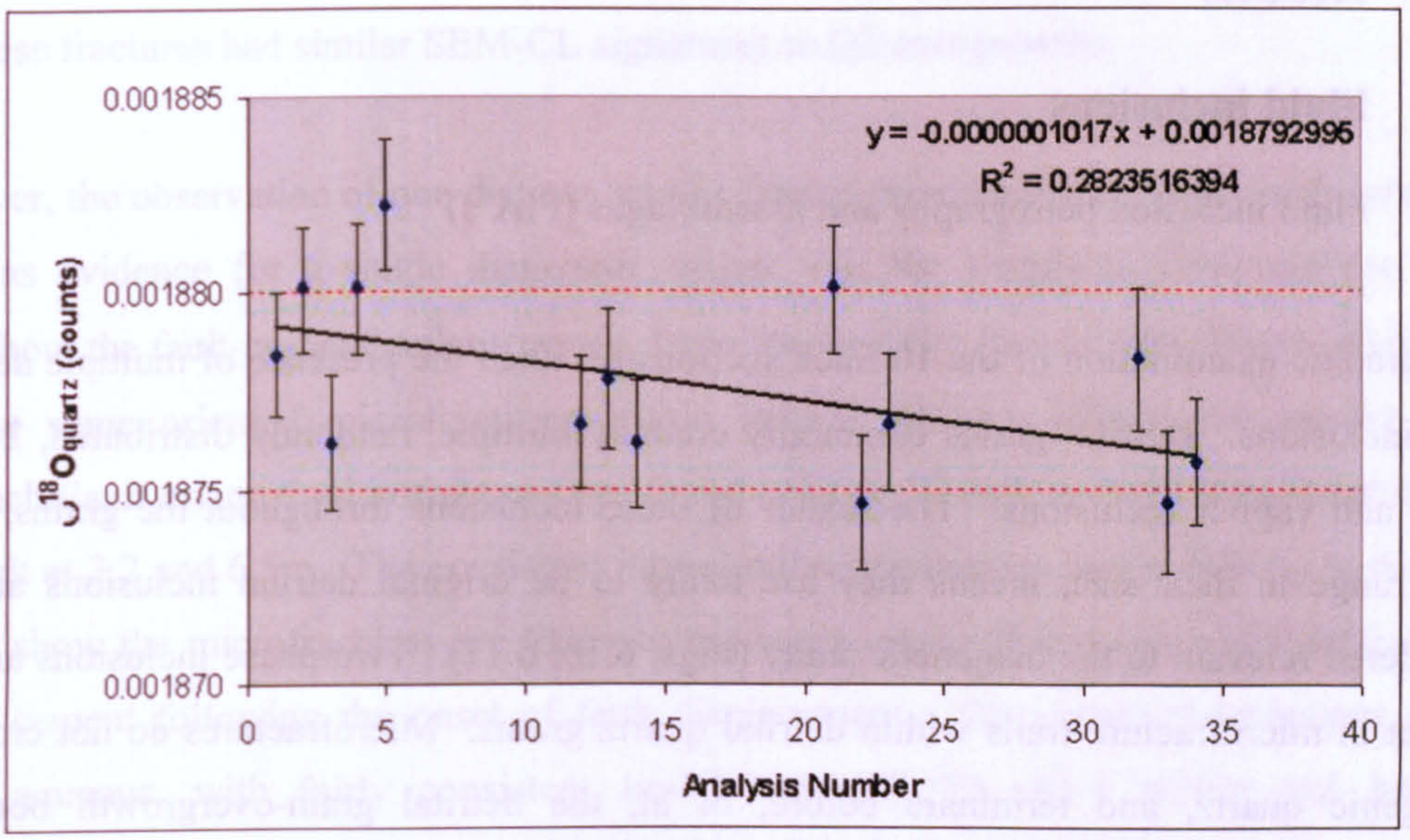


**Fig. 6.8..Total counts of $18O^-$ ions for each analysis of a homogeneous Bogala Quartz grain in one day. This demonstrates the effect of Instrumental Mass Fractionation throughout any single day of analysis. Interspersed between analyses of unknown samples, the regression of standard $18O^-$ values is used to correct IMF.**

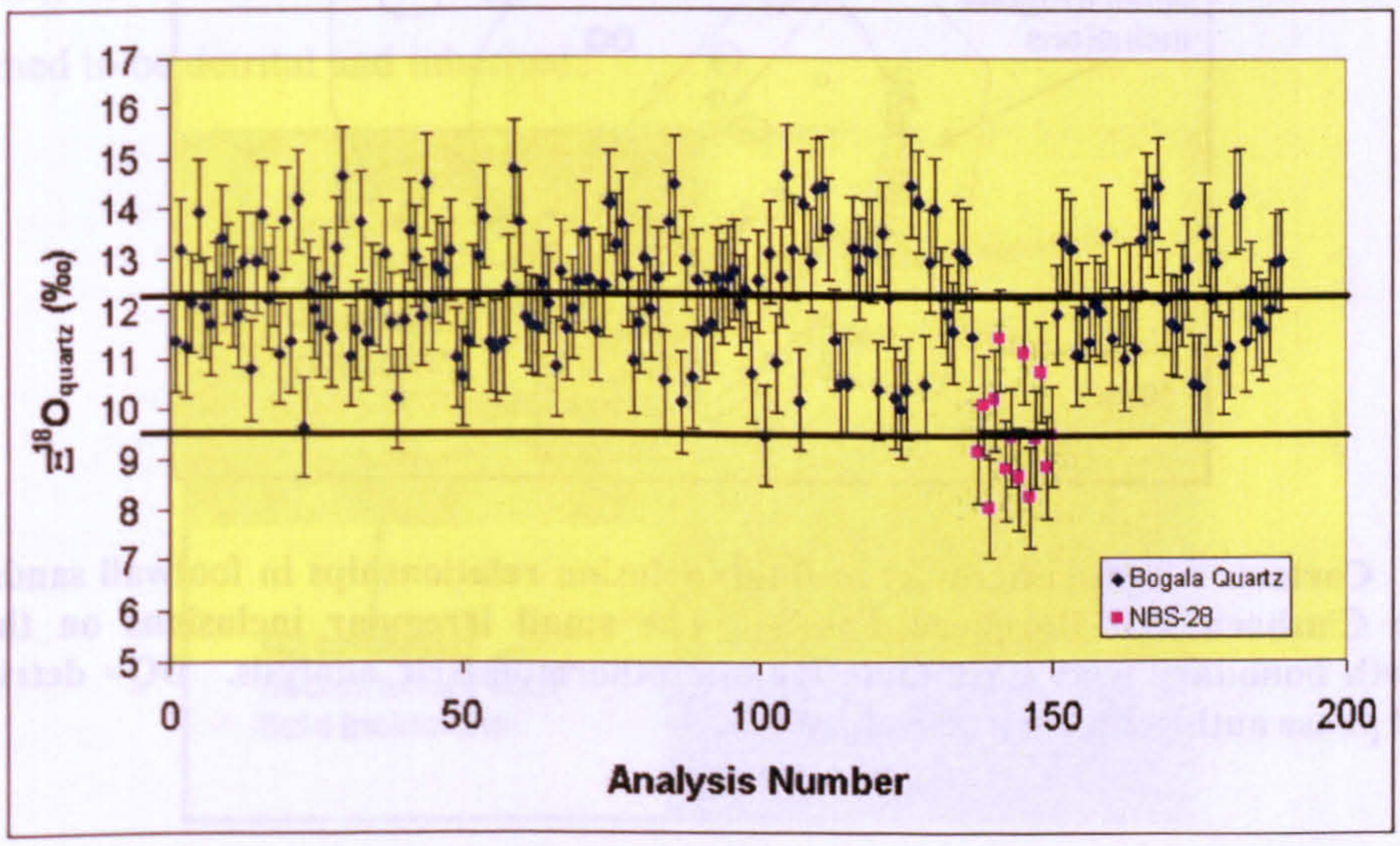


**Fig.6.9 $\delta^{18}O_{SMOW}$ for all standard analyses performed throughout the two analytical sessions. There was no long term drift throughout the two week and two day sessions. Standard material was Bogala Quartz with a mean measured $\delta^{18}O_{SMOW}$ of +12.3‰ (published $\delta^{18}O_{SMOW}$ = 12.3‰+/-0.3‰ ). In session 10 NBS-28 was used with mean measured $\delta^{18}O_{SMOW}$ +9.6‰ (published $\delta^{18}O_{SMOW}$ = + 9.8‰ +/-0.1‰). This can be seen as a systematically lower group of analyses. All analyses corrected for daily IMF.**

## 6.5 Results

### 6.51 Fluid inclusions

#### 6.51.1 Fluid inclusion petrography and assemblages (FIA's)

Petrographic examination of the 10 thick sections revealed the presence of multiple aqueous fluid inclusions. Detrital grains commonly contain multiple, randomly distributed, 2-phase liquid and vapour inclusions. The scatter of these inclusions throughout the grains, and a large range in their size, means they are likely to be original detrital inclusions and not considered relevant to the diagenetic study (Figs. 6.10, 6.11). Two-phase inclusions are also present in microfracture trails within detrital quartz grains. Microfractures do not cross-cut authigenic quartz, and terminate before, or at, the detrital grain-overgrowth boundary (pseduo-secondary) (Fig.6.11), indicating any trapped inclusions represent fluid conditions prior to, or at the onset of, quartz overgrowth precipitation.

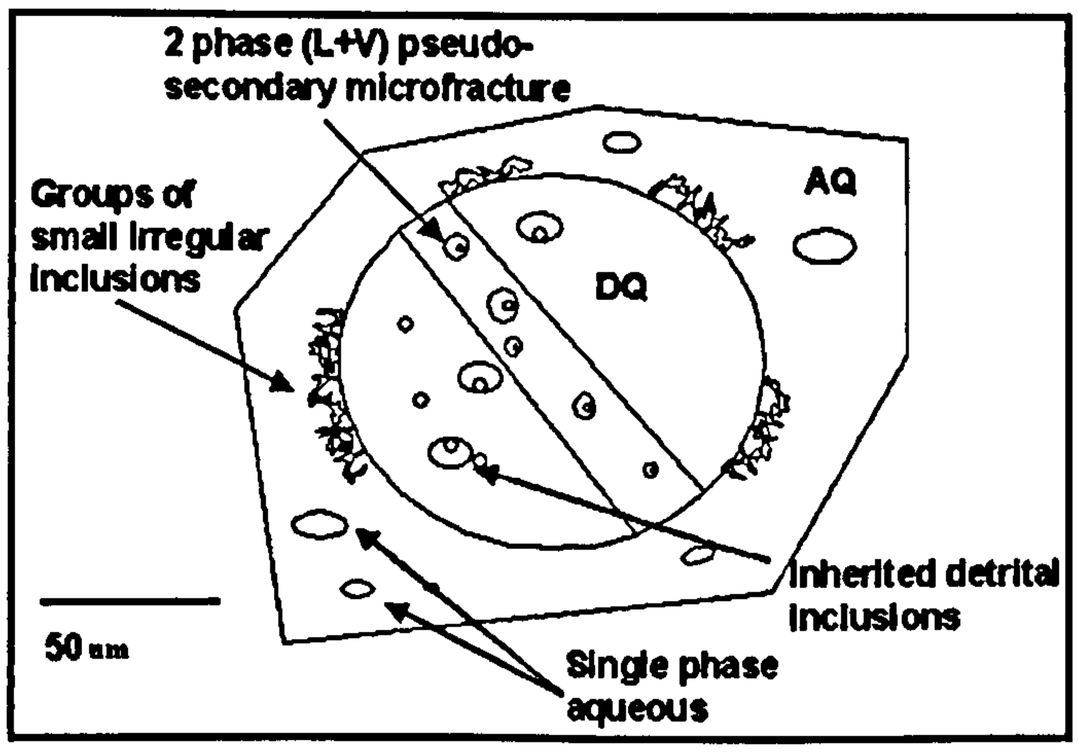


**Fig.6.10. Cartoon microstratigraphy of fluid inclusion relationships in footwall sandstone from both the Clashach and Burghead Faults. The small irregular inclusions on the detrital-overgrowth boundary were unsuitable for microthermometric analysis. DQ= detrital quartz, AQ = Q2 phase authigenic quartz overgrowth.**

Many of these trails appear randomly oriented, have similar SEM-CL signatures to the detrital grains, and are interpreted to be unrelated to the local diagenetic development. However, mapping of inclusions within multiple individual sections revealed one set of fluid inclusion bearing microfractures, with a consistent intra-section orientation. These sets of microfractures are proposed to represent larger-scale fault movement. The collected samples

were not oriented with respect to the fault plane during sampling, meaning absolute position with respect to the exposed faults cannot be calculated. Post thermometric analysis showed that these fractures had similar SEM-CL signatures to Q2 overgrowths.

However, the observation of one distinct set of oriented microfractures within each sample is taken as evidence for a single diagenetic origin. At the Burghead Fault sections from throughout the fault-perpendicular traverse, from the fault slip face to 14m distant, all display at least some oriented microfractures within detrital grains. Within the smaller scale Clashach Fault oriented microfractures are found only in the two footwall samples closest to the fault at 3.2 and 6.5m. The consistent intra-section orientations and proximity to the fault planes show the microfractures are likely to represent syn-fault features which healed with quartz cement following the onset of fault displacement. The observed inclusions are 2-phase aqueous, with fairly consistent liquid:vapour (L:V) ratios within and between individual thick sections. Combining microfracture orientation and inclusion consistency throughout the dataset, allows the measurements obtained to be interpreted confidently as a single FIA which samples a single diagenetic event (Goldstein and Reynolds 1992). To be certain that only inclusions within the correct FIA were measured, only oriented microfractures with at least 3 regular inclusions were considered for thermometric analysis. Single inclusions which occurred within, or in close proximity to, an apparent microfracture were assumed to be detrital and inherited.

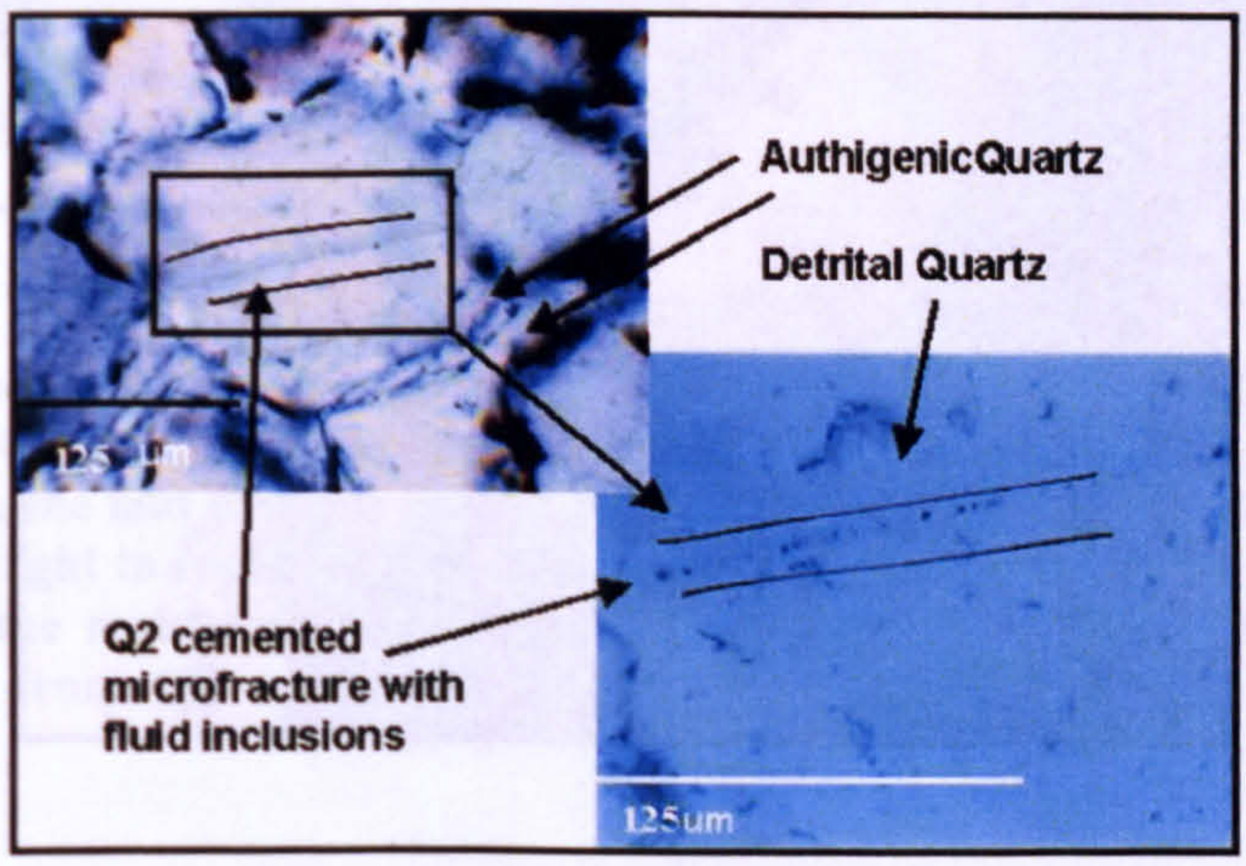


**Fig.6.11. A trail of small Pseudo-secondary fluid inclusions in a microfracture healed with quartz cement. The trail does not cross-cut the detrital grain-overgrowth boundary. From Burghead Fault footwall, 14m from the fault plane.**

Along the detrital grain-quartz overgrowth boundary numerous highly irregularly shaped, dark to light, inclusions are present. These are typically elongate along the grain-overgrowth boundary and can be up to 15μm in length (Figs. 6.10, 6.12). Small (<3μm) inclusions occur less frequently along the grain-overgrowth boundary and lie below the microscopic resolution available to determine their characteristics.

Single-phase aqueous inclusions are present within some of the larger overgrowths, at varying distances between the detrital grain boundary and the edge of individual overgrowths (Figs. 6.10, 6.13). These inclusions vary in size from 3 to 15μm and have smooth internal surfaces and are rounded to elongate. Typically they occur as isolated single inclusions within the authigenic quartz, with some overgrowths containing 2 inclusions at varying distances apart. These single-phase inclusions occur in samples from both the Burghead and Clashach fault localities, and at least 2 inclusions were present in each section examined. These inclusions are defined as a single FIA based upon their similar internal characteristics, relatively consistent position within quartz overgrowths, and occurrence throughout the sample set.

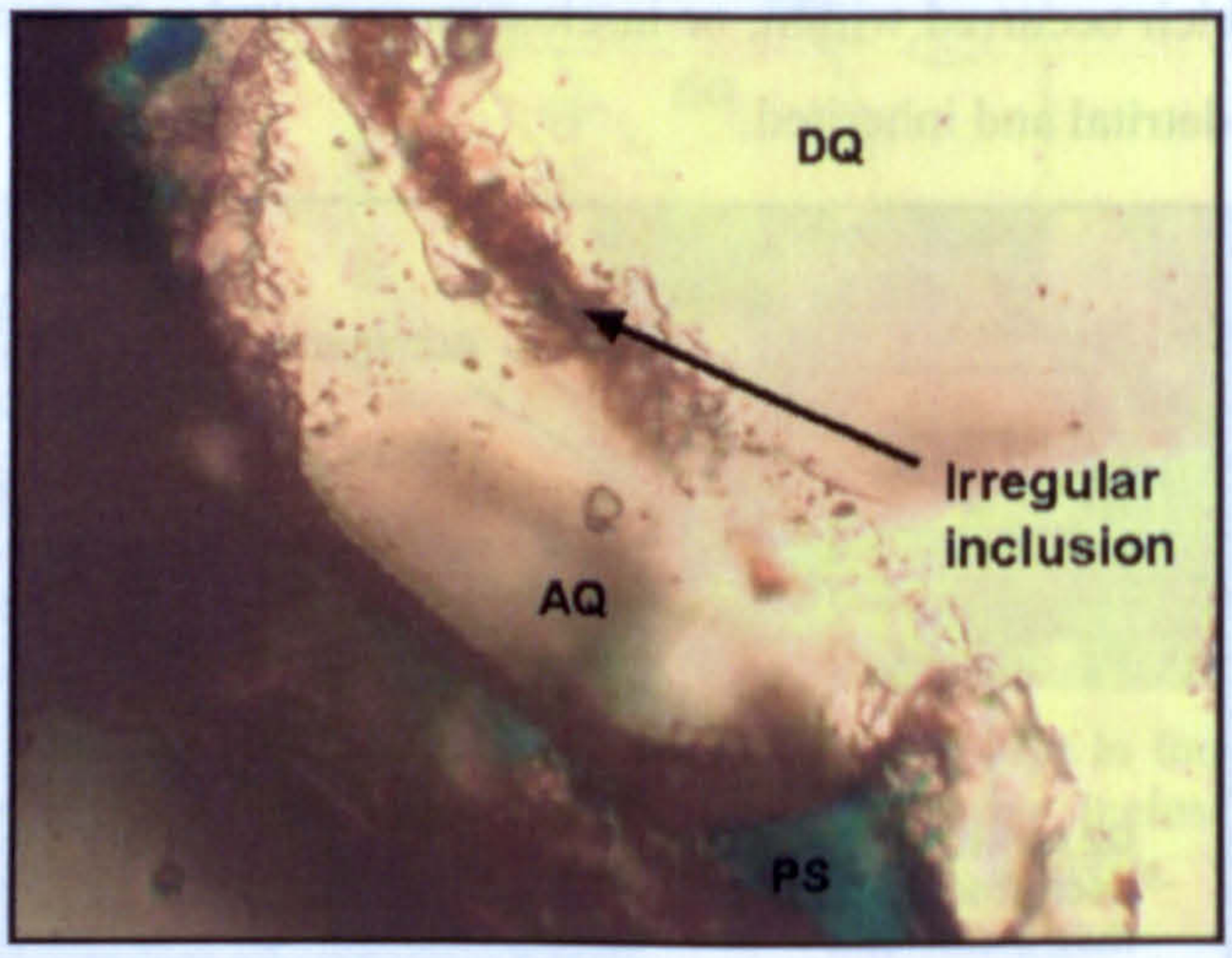


**Fig. 6.12. Image of a complex, irregular, fluid inclusion within Q2 quartz cement positioned close to the detrital grain boundary. A thin layer of iron oxide can be seen coating the detrital grain but not affecting overgrowth nucleation. From Clashach Fault footwall, sample C5 at 6.5m from the main fault slip plane.**

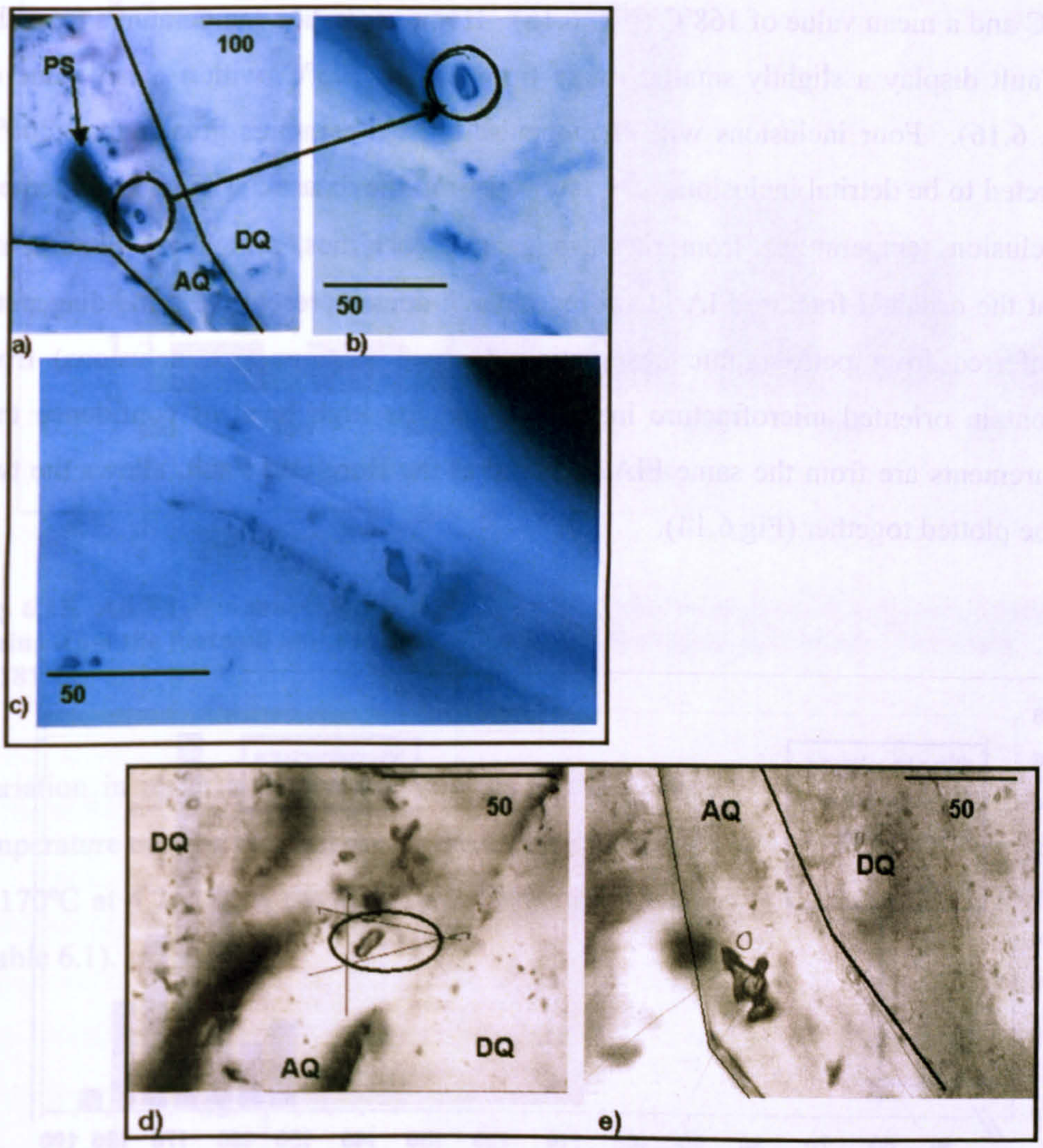


**Fig. 6.13. One phase all-liquid fluid inclusions within Q2 quartz cement inclusions. Images a) and b) are from C16, 16.2m from the main slip face of the Clashach Fault. show a single phase inclusion trapped in the mid to outer section of overgrowth. A dark spot can be seen on the left of the inclusion, thought to represent the 3-Dshape of the inclusion wall. c) Isolated single phase liquid inclusion in the middle of a Q2 overgrowth, sample C16. d) and e) show single phase aqueous inclusions from Q2 overgrowths in samples A19 and A24 in the footwall of the Burghead Fault.**

### 6.51.2 Fluid inclusion thermometric analyses

Forty-eight oriented microfracture 2-phase aqueous inclusions were measured, 23 from Clashach Fault footwall samples and 25 from the Burghead Fault footwall. The total dataset displays a range of homogenisation temperatures from 151 to 181°C, with the majority (35)

between 160 and 175°C (Fig. 6.14) (Table 6.1). The mean homogenisation temperature is 166°C. The inclusions measured from the Clashach Fault footwall samples have a range of 153 to 181°C and a mean value of 168°C (Fig. 6.15). Homogenisation temperatures from the Burghead Fault display a slightly smaller range from 151 to 175°C, with a mean value of 165°C (Fig. 6.16). Four inclusions with homogenisation temperatures greater than 200°C were interpreted to be detrital inclusions and removed from the dataset. The good agreement between inclusion temperatures from the two sample localities, which are 6km apart, suggests that the oriented fracture FIA identified in each does represent the same diagenetic event, as inferred from petrographic observation. Only 2 sections (23 inclusions) from Clashach contain oriented microfracture inclusions, but the high level of confidence that these measurements are from the same FIA as found at the Burghead Fault, allows the two datasets to be plotted together (Fig 6.14).

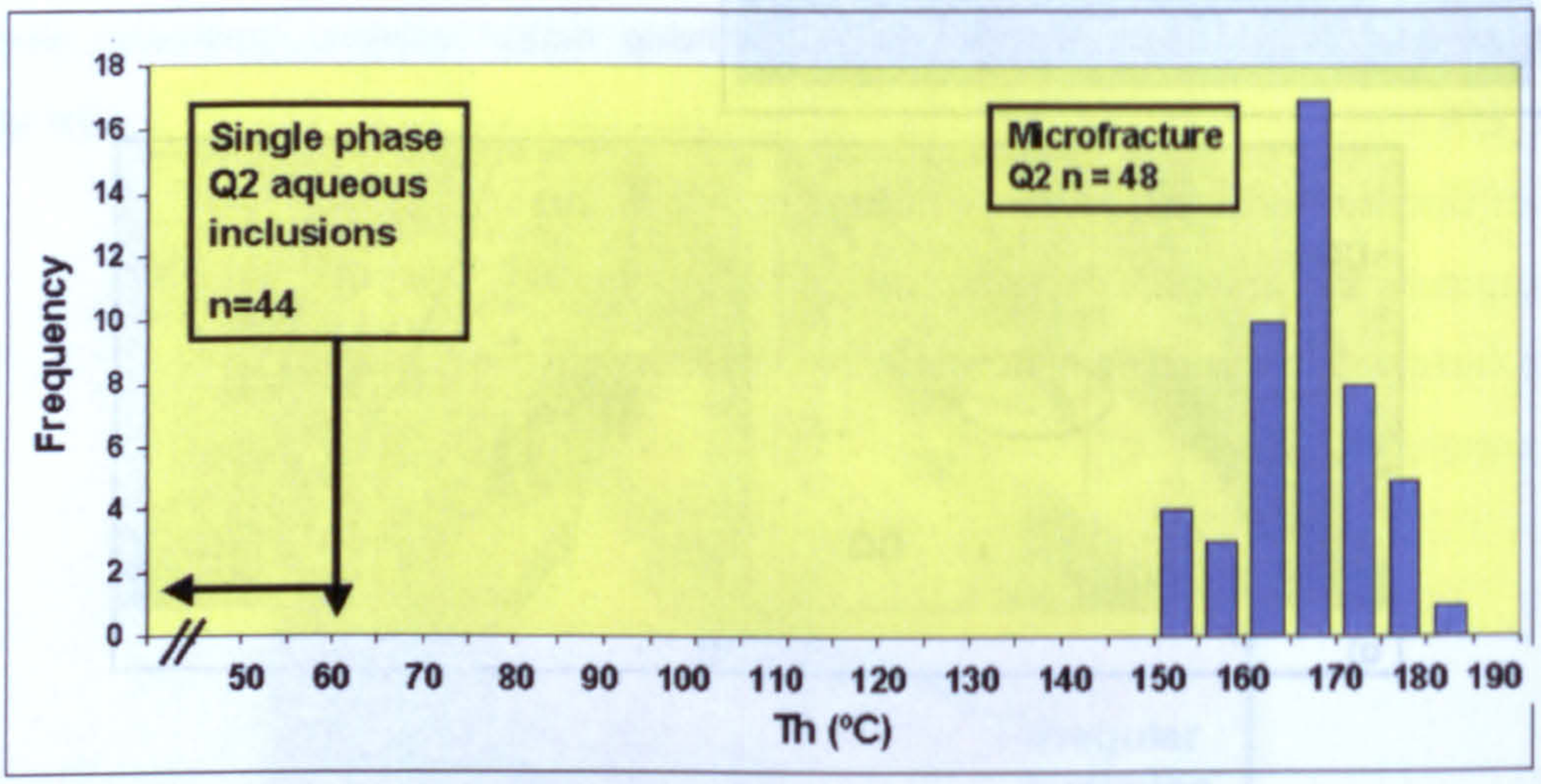


**Fig. 6.14. Histogram plot of all Th data from authigenic, Q2, fluid inclusions in Clashach and Burghead fault footwall Hopeman Sandstone. Hot temperatures ranging between 150 to 185°C are from oriented microfractures in detrital grains. Single phase aqueous inclusions in Q2 overgrowths indicate cool homogenisation temperatures below c.60°C.**

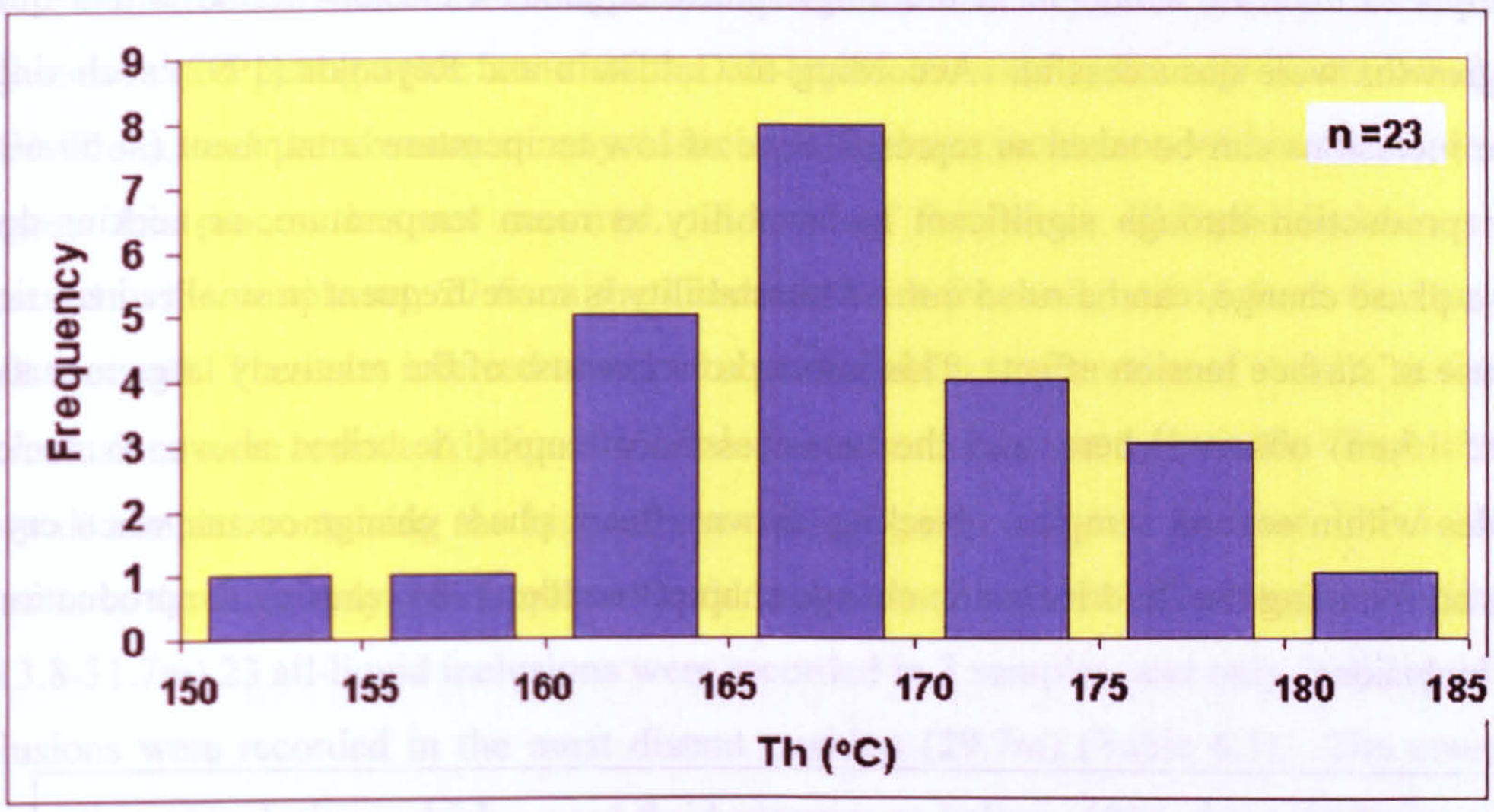


**Fig. 6.15. All Th data measured from Q2 cement which cements oriented microcracks in detrital grains from the footwall immediately adjacent to Clashach Fault. Mean Th is 168°C, range is 153 to 181°C.**

Variation in mean inclusion Th between samples shows that there is a small decrease in temperature moving through the footwalls away from the main fault slip faces. Maximum Th is 170°C at 4.2m from the Burghead Fault, and minimum Th is 158°C at 14m (Fig. 6.17) (Table 6.1).

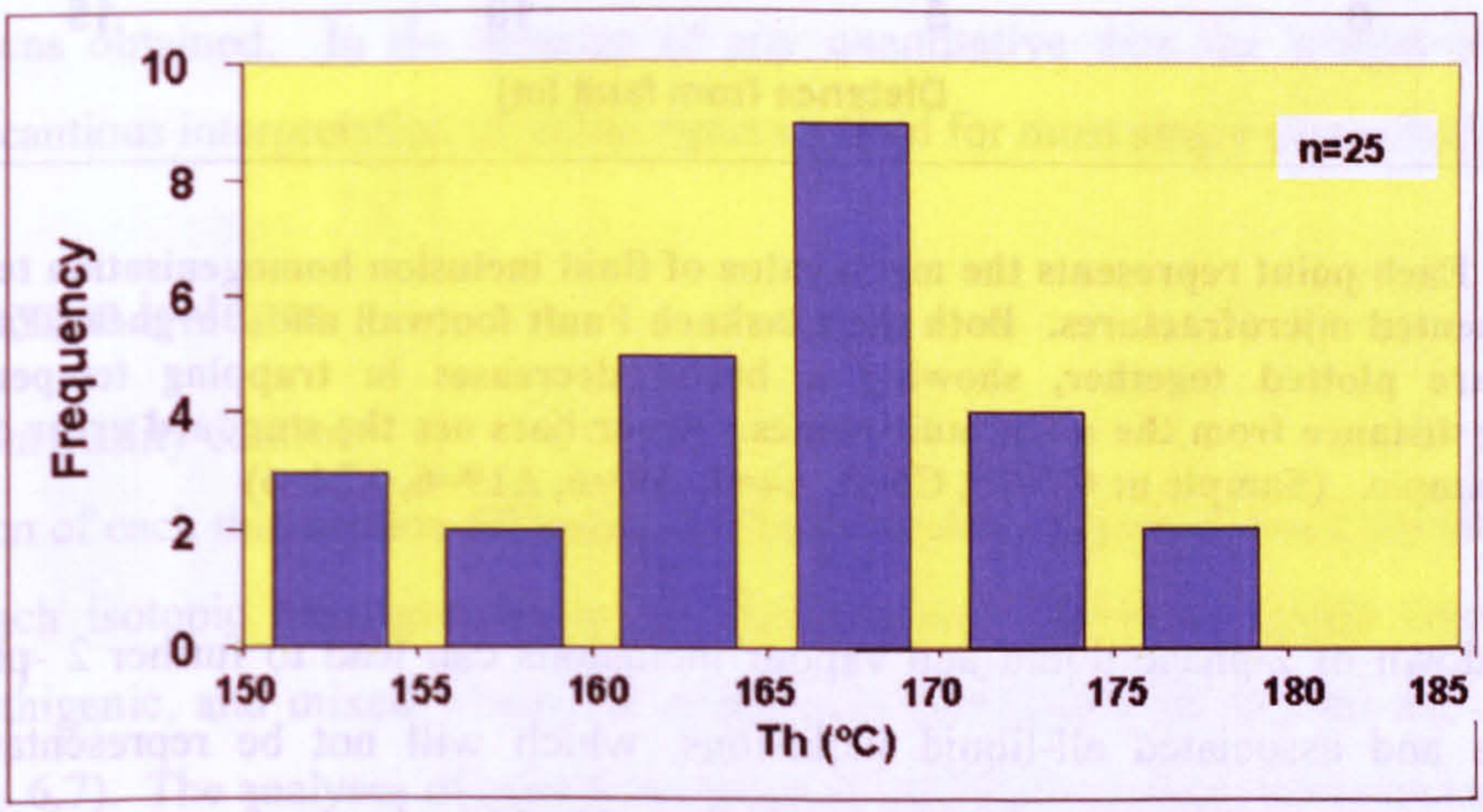


**Fig. 6.16. All Th data measured from Q2 cement which heals oriented microcracks in detrital grains from the footwall immediately adjacent to Burghead Fault. Mean Th is 165°C, range is 151 to 175°C.**

Attempts to nucleate a bubble in the single-phase aqueous inclusions found within quartz overgrowths were unsuccessful. According to Goldstein and Reynolds (1992) such single-phase inclusions can be taken as representative of low temperature entrapment (<~50-60°C) when production through significant metastability at room temperature, or necking-down after a phase change, can be ruled out. Metastability is more frequent in smaller inclusions, because of surface tension effects. This is ruled out because of the relatively large inclusions (up to 15μm) observed here, and the unsuccessful attempts, described above, to nucleate bubbles within several samples. Necking down after a phase change occurs when crystal walls surrounding the fluid inclusion change shape (Roedder 1984) causing the production of new inclusions.

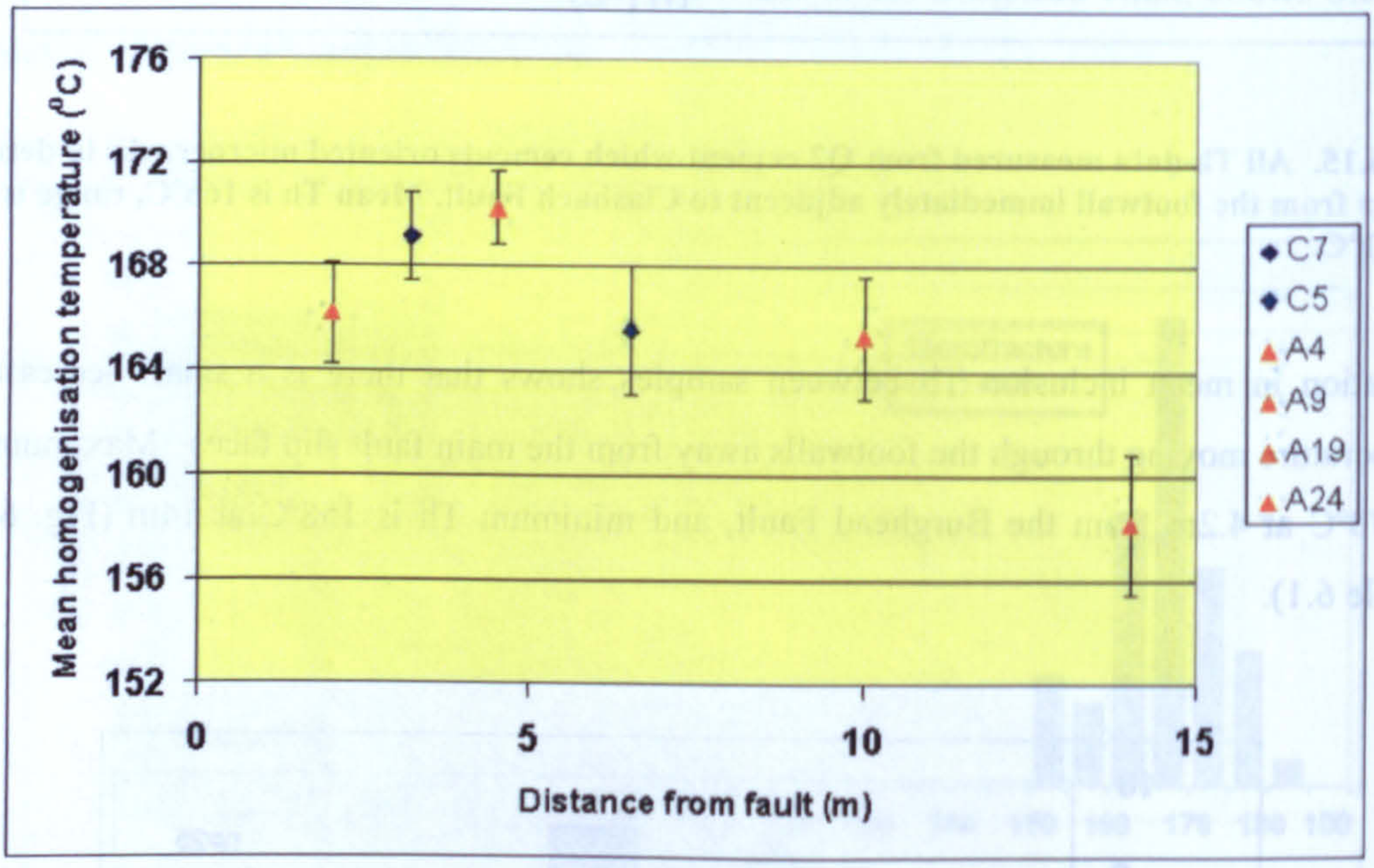


**Fig. 6.17. Each point represents the mean value of fluid inclusion homogenisation temperatures in Q2 cemented microfractures. Both the Clashach Fault footwall and Burghead Fault footwall samples are plotted together, showing a broad decreases in trapping temperature with increasing distance from the main fault planes. Error bars are the standard error on the mean for each sample. (Sample n: C7=15, C5=8, A4=7, A9 =6, A19=6, A24=6)**

Necking down of 2-phase liquid and vapour inclusions can lead to further 2 -phase (L+V) inclusions and associated all-liquid inclusions, which will not be representative of the trapping conditions of the original fluid inclusion. Necking down of a monophase inclusion has no effect on the density of the material and so does not affect the thermometric properties. The all-liquid inclusions recorded in the Hopeman Sandstone are typically isolated, or occur as a maximum of 2 inclusions in the same overgrowth, making it difficult

to rule-out the occurrence of necking down (Goldstein and Reynolds, 1992). However the well-constrained petrographic zone of the all-liquid inclusions, the significant number of observations, and the absence of any associated 2-phase inclusions within the same area, suggests this process has not occurred. A total of forty-three all-liquid inclusions were observed in the sample set, 27 from the Clashach Fault footwall, and 16 from the Burghead Fault footwall. These are inferred to record a precipitation temperature of <~60°C at the time the inclusions were sealed. All-liquid inclusions occur more commonly in the Clashach Fault footwall samples containing the highest amounts of quartz cement. In zone 1 (0.5-13.8m), adjacent to the fault, only 4 monophase liquid inclusions were seen in 2 samples. Within zone 2 (13.8-31.7m) 23 all-liquid inclusions were recorded in 3 samples, and only 2 all-liquid fluid inclusions were recorded in the most distant position (29.7m) (Table 6.1). The consistent observation of inclusions which record fluid entrapment below ~60°C, throughout the sample set, indicates that a decrease in the observed number of fluid inclusions may simply be a product of the decreasing amount of quartz cement which is present. All-liquid inclusion frequency within samples from the Burghead Fault does not display any significant increase or decrease with distance from the main fault slip face, although 7 inclusions were recorded in the most distant sample, 3 more than any other.

Analysis of single-phase aqueous inclusions with the Raman probe revealed a composition of saline water. The depth of the inclusions within the overgrowths, and their relatively small size produced low intensity spectras, and for several attempted measurements no discernible spectrum was obtained. In the absence of any quantitative data the weight of evidence suggests a cautious interpretation of saline aqueous fluid for most single-phase inclusions.

## 6.53 Oxygen isotopes

### 6.53.1 Data quality control

Examination of each thin section following ion microprobe analysis allowed the petrographic zone of each isotopic measurement to be characterised. Three categories were defined; detrital, authigenic, and mixed where the probe spot measured both detrital and authigenic quartz (Fig. 6.7). The analyses of mixed detrital and authigenic quartz cannot be used for any interpretation. SEM-CL and SE mapping of the sections prior to ion microprobe analysis resulted in a minor number of mixed detrital and authigenic measurements. A number of analyses were made on individual quartz overgrowths to constrain any internal variation.

Post ion probe SEM-CL observations allowed these to be placed in relative position from the detrital-overgrowth boundary to the edge of the overgrowth. The precision of the SIMS $\delta^{18}O$ technique was +/-1‰ for each individual analysis (Table 6.2). A number of microanalyses were made upon each section resulting in reduced errors of <1‰ for individual samples.

### 6.53.2 Detrital quartz

Forty-three analyses were made on 30 detrital grains (Fig. 6.18), with a $\delta^{18}O$ range of +5.2‰ to +14.3‰, and a mean $\delta^{18}O$ of +10.4‰ (Figs. 6.3, 6.18) (Table 6.2). Of the 43 analyses 22 were made on 16 grains from the Burghead Fault footwall samples with a $\delta^{18}O$ range of +5.2‰ to +13.1‰ (Table 6.2) and a mean value of 10.5‰ +/-0.4‰ (standard error [S.E.]). Repeat analyses were made on 3 grains, showing that maximum intra-grain variation is +11.4‰ to +13.1‰, suggesting some internal consistency within grains. Seventeen analyses were made on 12 grains within footwall samples from the Clashach Fault. The range of $\delta^{18}O$ is +6.9‰ to +14.3‰ with a mean value of +10.6‰ +/-0.5‰ (S.E.). A maximum intra-grain $^{18}O$ range of +9.7‰ to +12‰ was measured, based on a maximum of 3 repeat measurements in 3 grains from different samples (Table 6.2). Four analyses were made on 2 detrital grains from the hanging wall at Clashach Fault, with a $\delta^{18}O$ range of +6.4‰ to +12.5‰. The mean $\delta^{18}O$ is +9.4‰ +/-1.3‰ (S.E.)

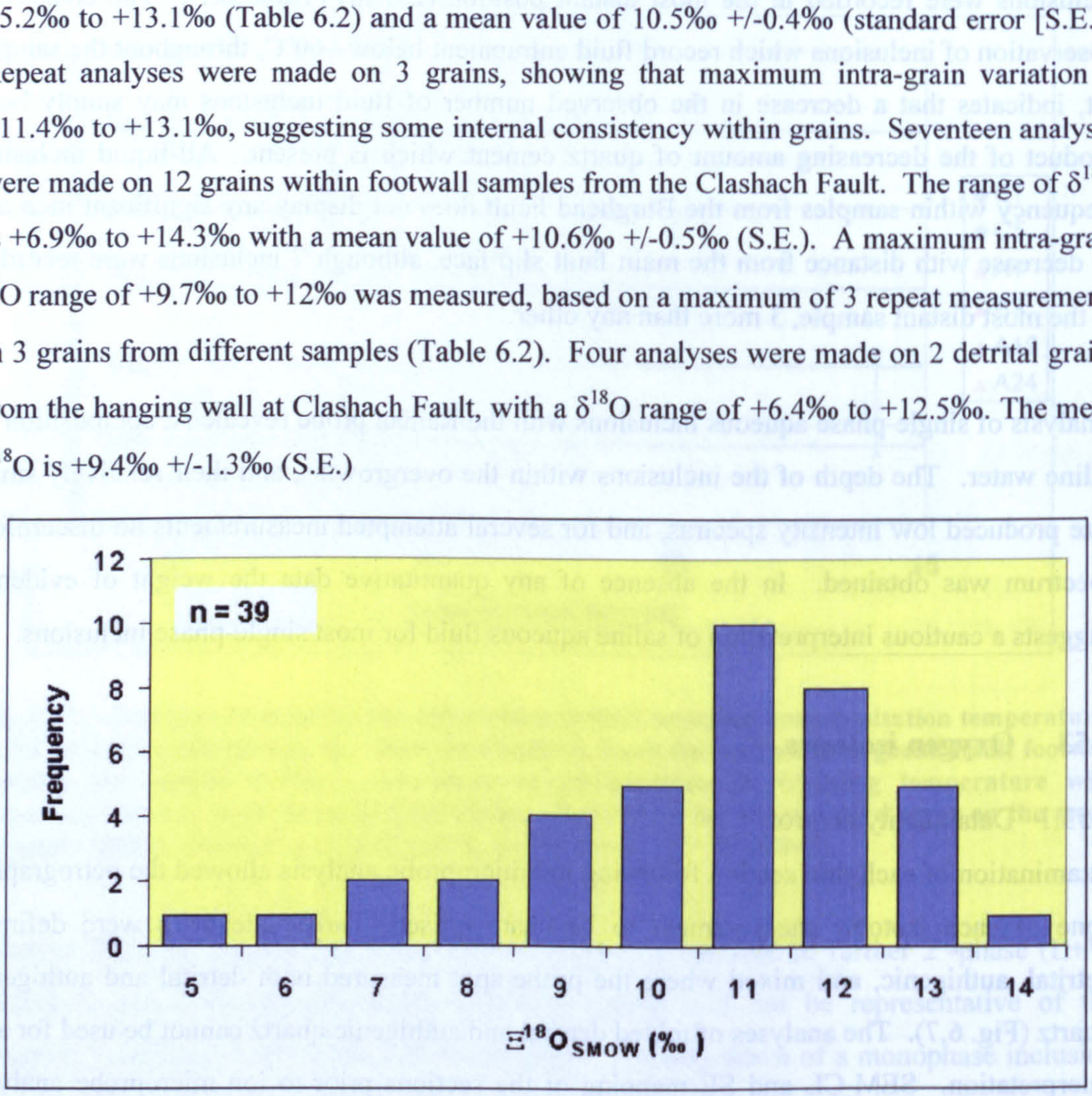


**Fig. 6.18. All $\delta^{18}O_{SMOW}$ anlayses made in detrital Hopeman Sandstone grains from both the Clashach and Burghead Fault footwalls. The $\delta^{18}O_{SMOW}$ mode is +1‰ and range is from +5.2‰ to +14.3‰**

The excellent consistency between the detrital $\delta^{18}O$ values of the Burghead and Clashach data confirms regional and petrographic evidence that the Hopeman Sandstone at both locations is mineralogically similar, with the same detrital grain source. Blatt (1987) reports average $\delta^{18}O$ values in sandstones of +11‰, +9‰ in igneous rocks, and +13‰ to +14‰ in metamorphic rocks. The mean $\delta^{18}O$ value of +10.5‰ found in the Hopeman Sandstone is in good agreement with this finding.

### 6.53.3 Authigenic quartz - Clashach Fault

A total of 74 analyses on 24 overgrowths, from 5 samples, were made of authigenic quartz from the footwall of the Clashach Fault, and 8 analyses from the hanging wall. Table 6.2 and the histogram in figure 6.19 shows the range of $\delta^{18}O$ in footwall samples is +14.2‰ to +29.3‰, with a mean value of +19.3‰ +/-0.28‰ (S.E.). The large range in the bulk footwall dataset can be explained by the systematic change in $\delta^{18}O$ values, which increase with increasing distance from the fault slip plane (Fig. 6.20). Mean sample $\delta^{18}O$ values increase from a minimum of +17.9‰ at 4.2m, to a maximum of +20.8‰ at 30.4m. Excluding the most distal sample at 30.4m, the maximum range within any one sample is 7.9‰, compared with a bulk dataset range of 15.1‰. All of the analyses were undertaken in samples dominated by Q2 phase quartz cement, suggesting that the measured variation in oxygen isotope value of any one sample is natural. Hanging wall and background samples from the Hopeman Sandstone away from structural features contain Q3 phase quartz cement, which has $\delta^{18}O$ values more positive (mean $\delta^{18}O$+23.1‰ +/-0.5‰) than observed in the footwall (Table 6.2). It is probable that analyses of the most distant sample from the fault at 30.4m, with a wide range of $\delta^{18}O$ from +16.6‰ to +29.3‰, include some Q3 cement which is observed to post date Q2 in minor quantities (Quinn *et al.*, in prep, Chapter 5).

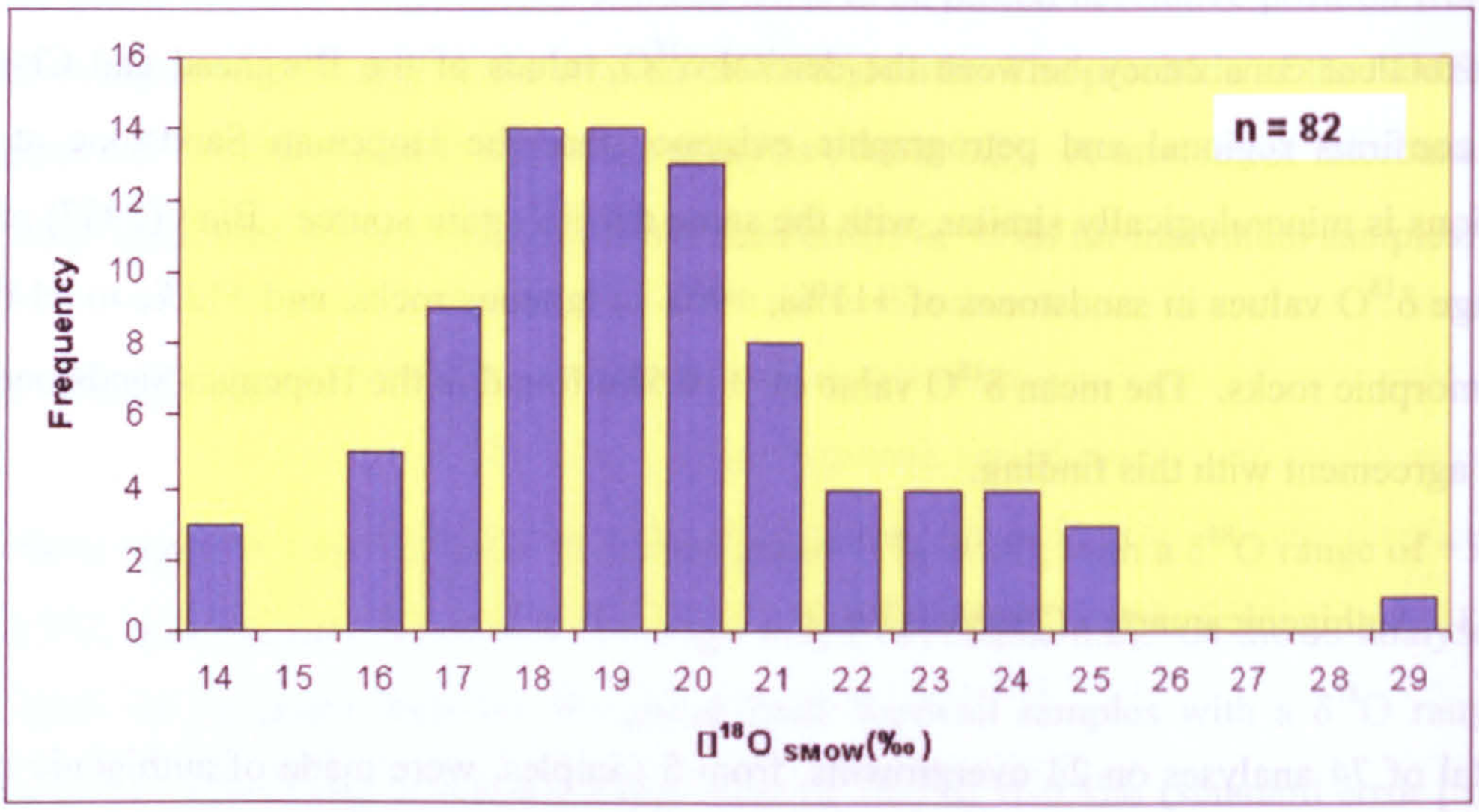


**Fig. 6.19. Histogram of $\delta^{18}O_{SMOW}$ data from Q2 overgrowth cement in footwall Hopeman Sandstone samples from Clashach Fault. Mode from the histogram distribution is between +18‰ and +19‰, and $\delta^{18}O_{SMOW}$ range is +14.2‰ to +29.3‰.**

Intra-overgrowth profiles of Q2 quartz cement were made within 7 overgrowths from 2 Clashach Fault footwall samples, at 4.2 and 13.8m. Figure 6.21 shows that the range in $\delta^{18}O$ values decreases moving through the overgrowth from +5.4‰ near the detrital grain boundary, to <1‰ nearer the overgrowth edge, although the number of data points also decreases. The positions of the analyses are plotted relative to the detrital grain in each overgrowth to capture general isotopic variation regardless of overgrowth scale. Using absolute positions for intra-overgrowth variation is not likely to produce more accurate profiles because cement in the same location in two equivalent overgrowths may not have precipitated at precisely the same time. The overall trend of intra-overgrowth isotope variation shows a slight enrichment in $\delta^{18}O$ values moving toward the overgrowth edge, mirroring the larger scale trend seen moving through the footwall to increasing distances from the fault.

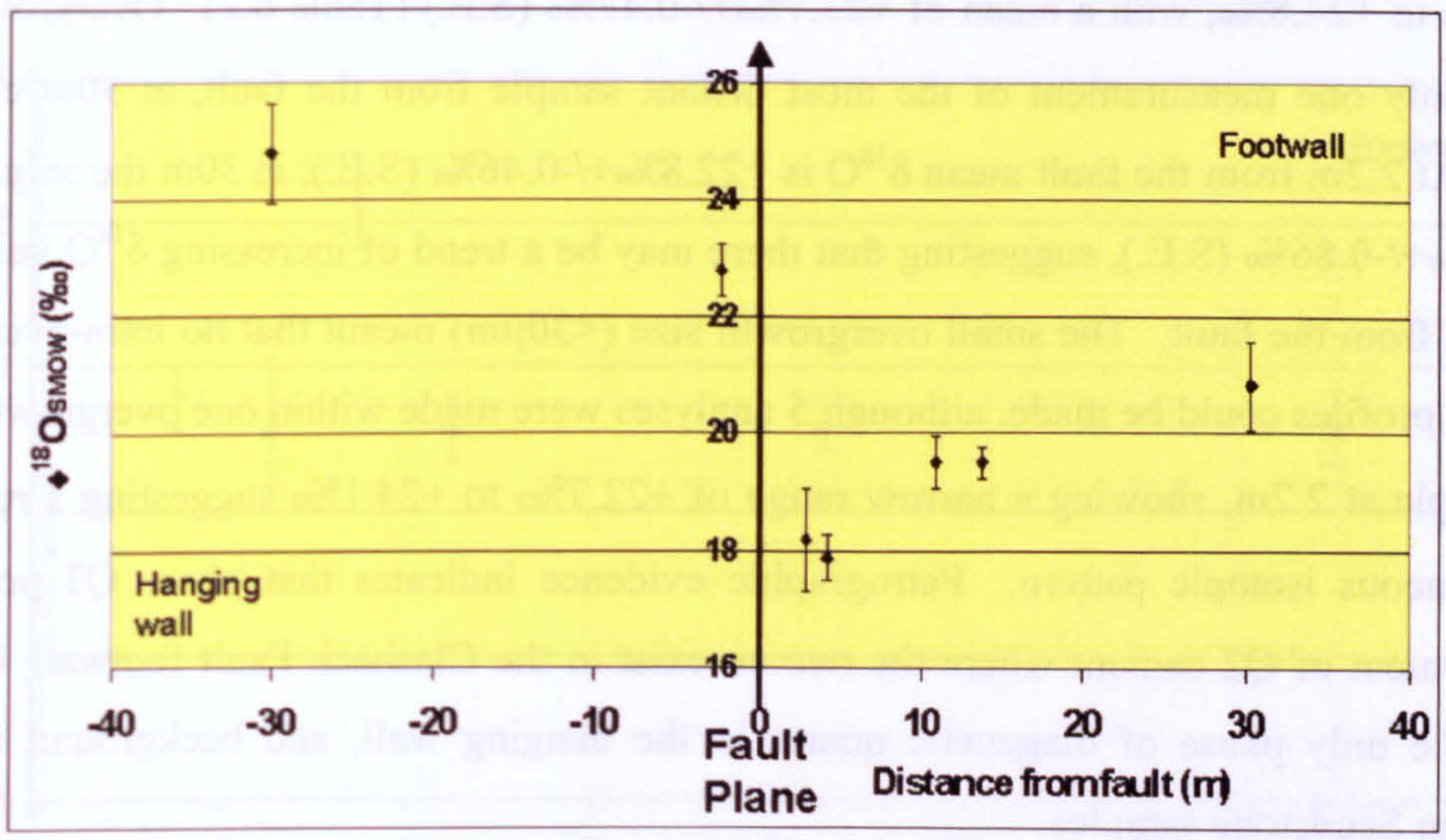


**Fig. 6.20. Mean $\delta^{18}O_{SMOW}$ values for samples around the Clashach Fault. Footwall $\delta^{18}O_{SMOW}$ ratios increase in a linear trend moving through the footwall from the fault plane, from a minimum of +17.5‰ at 4.5m to +20.8‰ at 30.4m. Hanging wall values are higher with a mean value of $\delta^{18}O$ +23.1‰. Error bars represent the standard error on the mean. (Sample n: -30m=1, -2.2m=7, 2.9m=9, 4.2m=16, 11m=19, 13.8m=12, 30.4m=18)**

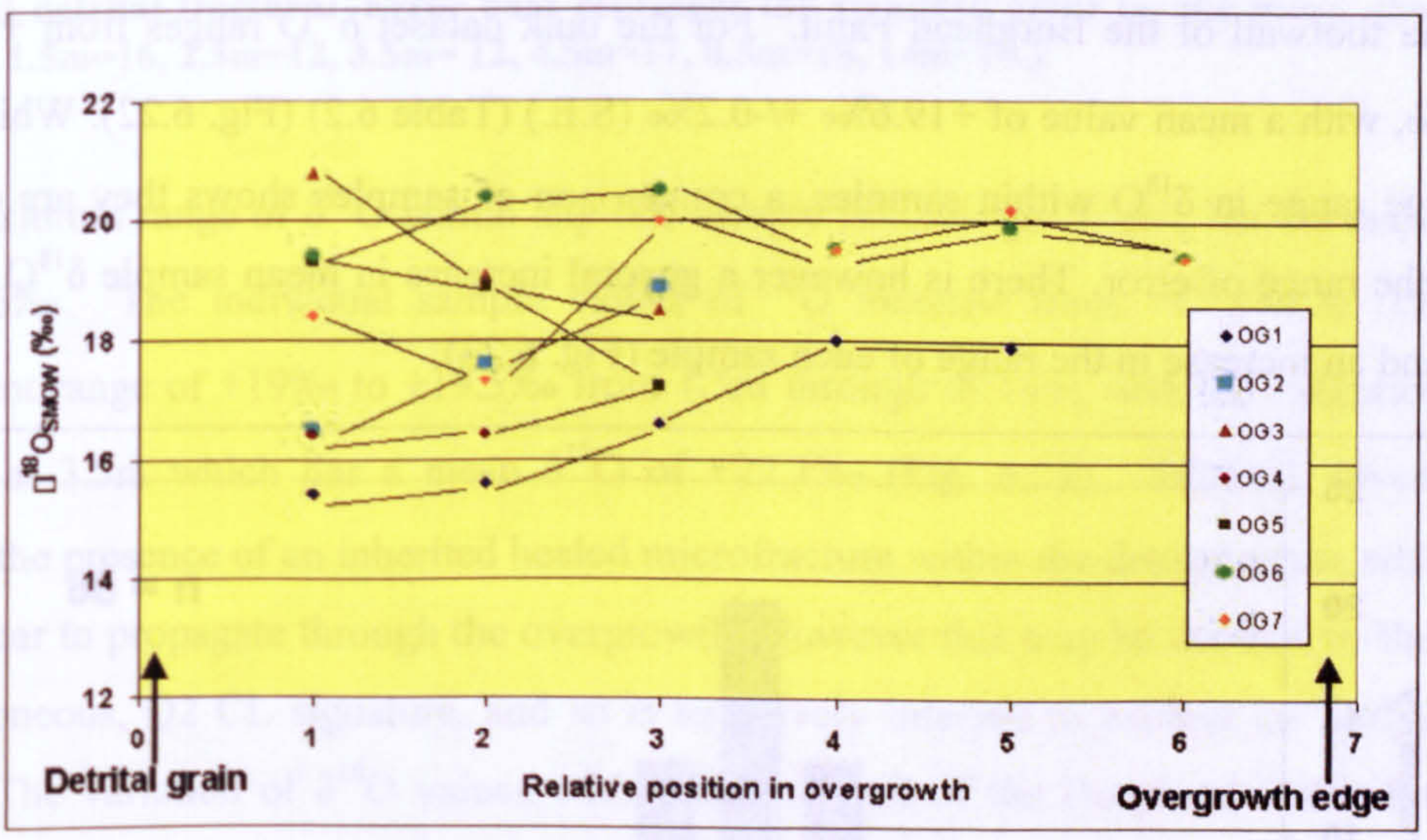


**Fig. 6.21. Profiles of $\delta^{18}O_{SMOW}$ through individual overgrowths from the Clashach Fault footwall Q2 cement. A decrease in the scatter and range of $\delta^{18}O_{SMOW}$ values and an overall increase in the mean may simply be a product of a decreasing number of measurements.**

The 8 hanging wall analyses of authigenic quartz were made on 3 Q3 overgrowths within 2 samples (Fig. 6.20). Q3 cement is volumetrically minor (<5%) (Quinn *et al.*, in prep., Chapter 5) compared to footwall Q2 cement, which reduces the number of accurate wholly authigenic quartz ion microprobe analyses that could be made. Values of $\delta^{18}O$ range from

+21.1‰ to +24.8‰, with a mean of +23.1‰+/-0.47‰ (S.E.) (Table 6.2). Overgrowth size meant only one measurement of the most distant sample from the fault, at 30m could be made. At 2.2m from the fault mean $\delta^{18}O$ is +22.8‰+/-0.46‰ (S.E.), at 30m the single value is 24.8‰+/-0.86‰ (S.E.), suggesting that there may be a trend of increasing $\delta^{18}O$ value with distance from the fault. The small overgrowth size (<30μm) meant that no intra-overgrowth analysis profiles could be made, although 5 analyses were made within one overgrowth, from the sample at 2.2m, showing a narrow range of +22.7‰ to +24.1‰ suggesting a relatively homogeneous isotopic pattern. Petrographic evidence indicates that phase Q3 post-dates emplacement of Q2 cement where the two co-exist in the Clashach Fault footwall, and that Q3 is the only phase of diagenetic quartz in the hanging wall, and background footwall Hopeman Sandstone samples.

### 6.53.4 Authigenic quartz – Burghead Fault

Eighty-six Q2 authigenic quartz analyses were made on 26 overgrowths, within 7 samples from the footwall of the Burghead Fault. For the bulk dataset $\delta^{18}O$ ranges from +15‰ to +24.3‰, with a mean value of +19.6‰ +/-0.2‰ (S.E.) (Table 6.2) (Fig. 6.22). Whilst there is a large range in $\delta^{18}O$ within samples, a comparison of samples shows they are constant within the range of error. There is however a general increase in mean sample $\delta^{18}O$ from 0-3.5m, and an increase in the range of each sample (Fig. 6.23).

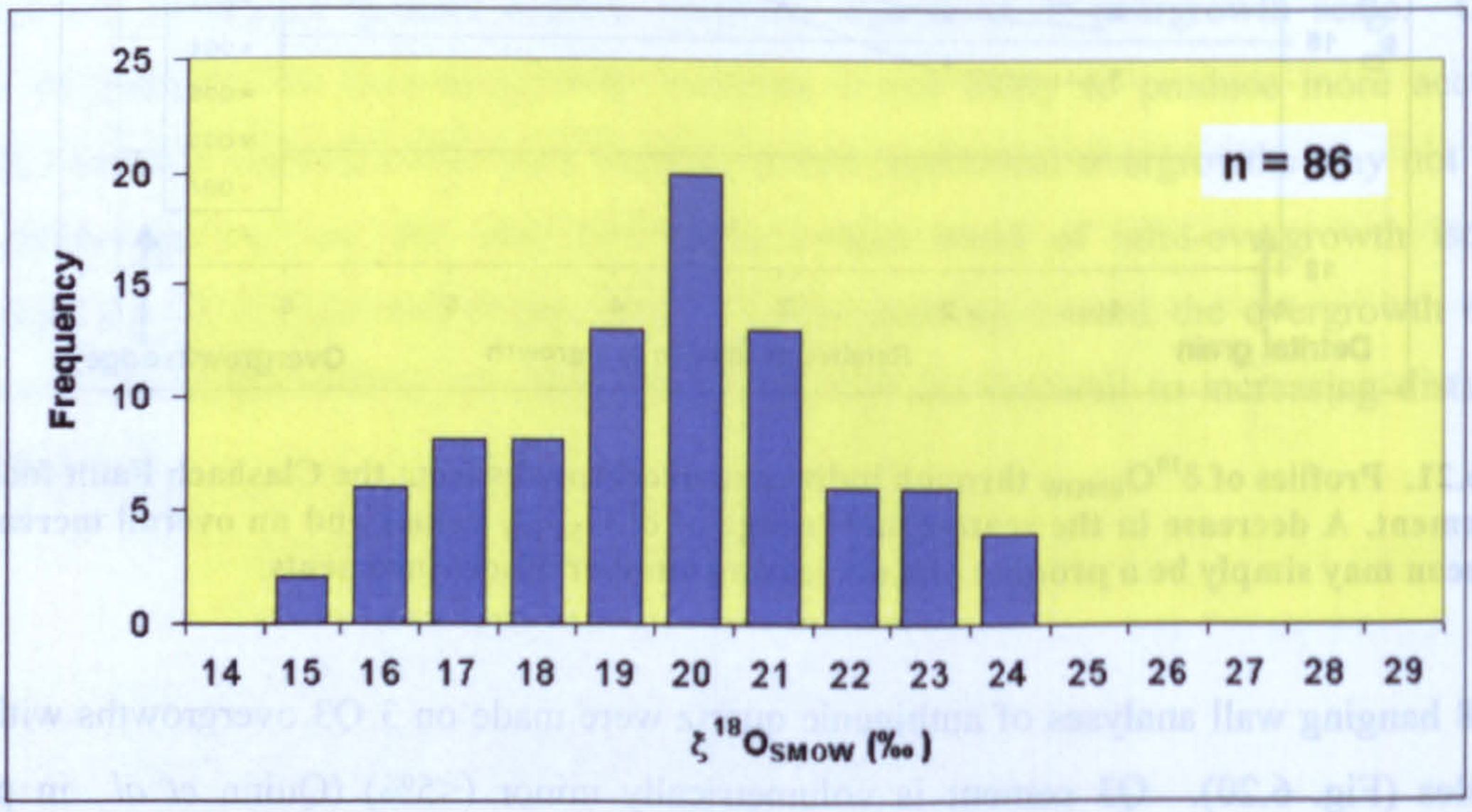


**Fig. 6.22. Histogram of $\delta^{18}O_{SMOW}$ data from Q2 overgrowth cement in footwall Hopeman Sandstone samples from the Burghead Fault. Mode from the histogram distribution is +20‰, and $\delta^{18}O_{SMOW}$ range is +15 ‰ to +24.3 ‰.**

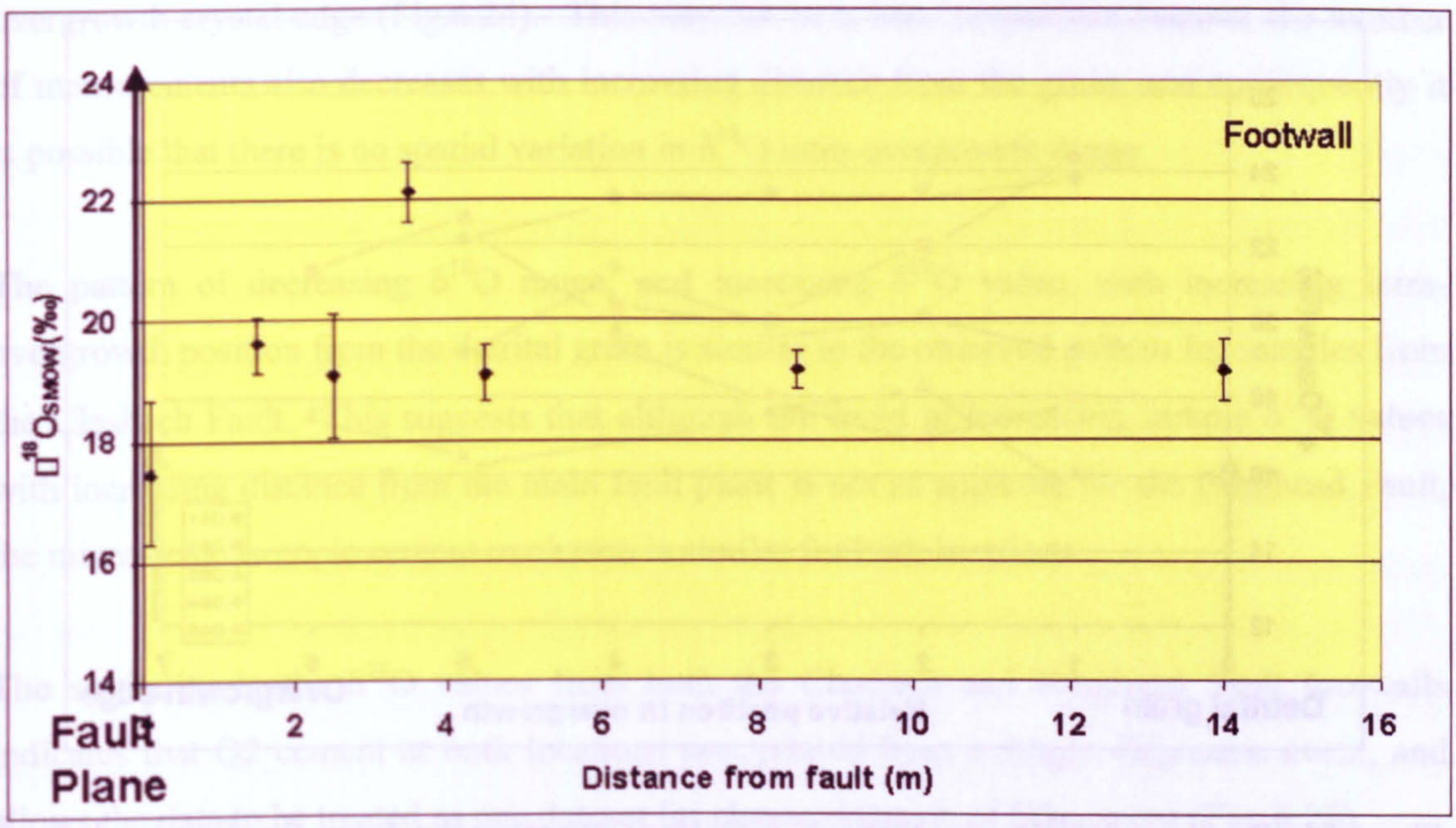


**Fig. 6.23. Mean $\delta^{18}O_{SMOW}$ values for samples around the Burghead Fault. Footwall $\delta^{18}O_{SMOW}$ ratios increase from 17.5‰ at 0.1m to a consistent +19.1‰ to +19.6‰ from 1.5 to 14m from the fault plane. At 3.5m sample mean is +22.1‰, which may be a product of some analyses of an inherited detrital fracture. Error bars represent the standard error on the mean. (Sample n: 0.1m=2, 1.5m=16, 2.5m=12, 3.5m= 12, 4.5m=17, 8.5m=18, 14m=10.)**

The maximum range of $\delta^{18}O$ within any one sample is 8.5‰ (at 2.5m), but the majority are below 6‰. The individual sample values of $^{18}O$ increase from +17.5‰ at 0.1m to a consistent range of +19‰ to +19.5‰ from 1.5m through to 14m, with the exception of the sample at 3.5m which has a mean $\delta^{18}O$ of +22.1‰ (Fig. 6.23). SEM-CL investigation reveals the presence of an inherited healed microfracture within the detrital grain, which does not appear to propagate through the overgrowth. However this may be masked by the bright, heterogeneous, Q2 CL signature, and so is tentatively inferred to explain the outlying data point. The variation of $\delta^{18}O$ values within the footwall of the Burghead Fault shows less variation than those from the Clashach Fault footwall. The only distinct increase in $\delta^{18}O$ value occurs from 0.1m to 1.5m. This absence of a well-defined trend is likely a consequence of the increased scale of the fault at Burghead compared to Clashach. Q2 cement volume shows only a minor decrease moving from the main fault slip face through the footwall (Fig. 6.5), suggesting that the zone of Q2 cementation is much larger than that surrounding Clashach Fault and may extend 80m into the footwall (Fig. 6.25). Any trend of increasing $\delta^{18}O$ value may not be picked up from the limited footwall exposure.

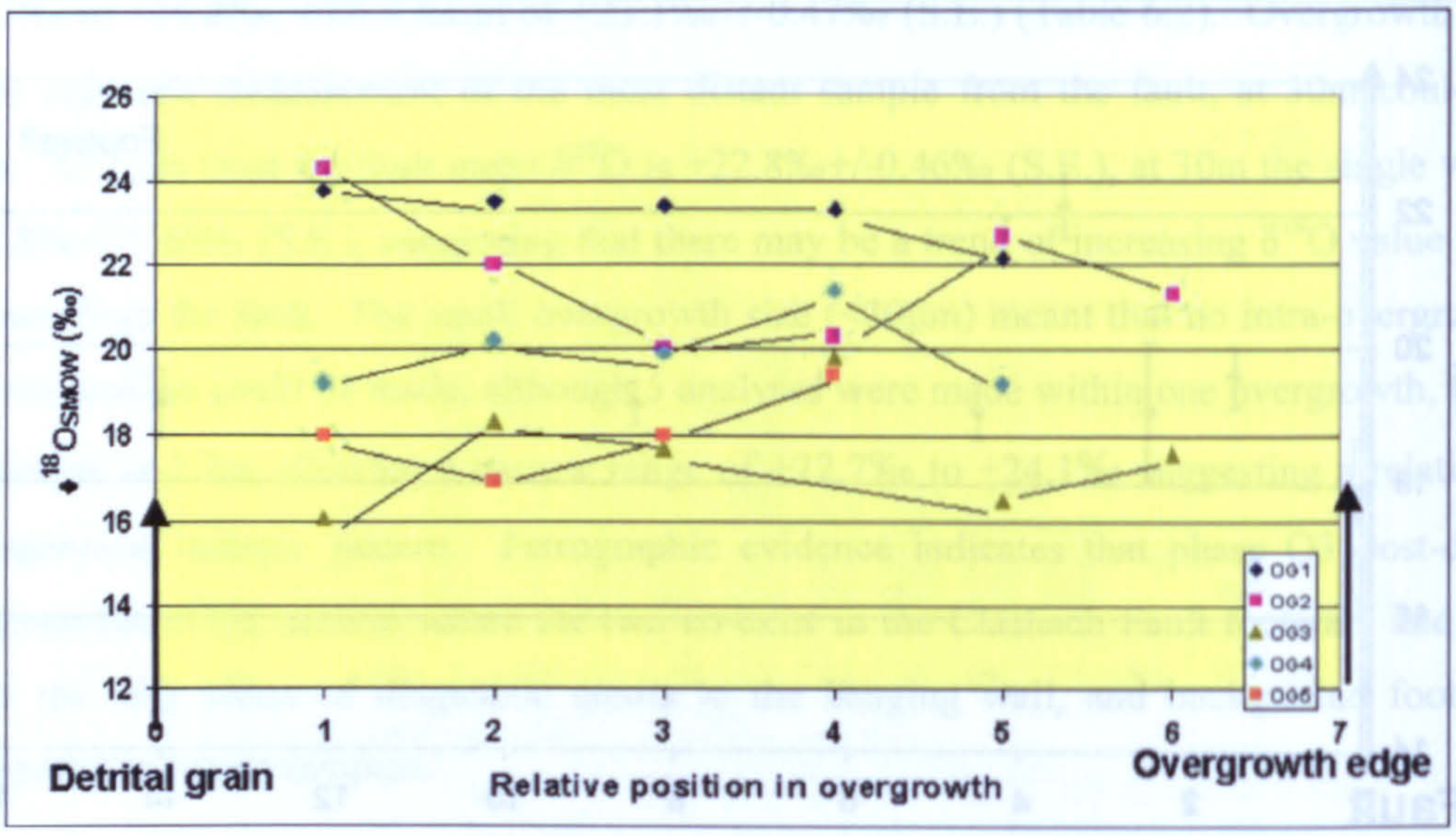


**Fig. 6.24. Profiles of $\delta^{18}O_{SMOW}$ through individual overgrowths from the Burghead Fault footwall Q2 cement. A decrease in the scatter and range of $\delta^{18}O_{SMOW}$ values and an overall increase in the mean may simply be a product of a decreasing number of measurements.**

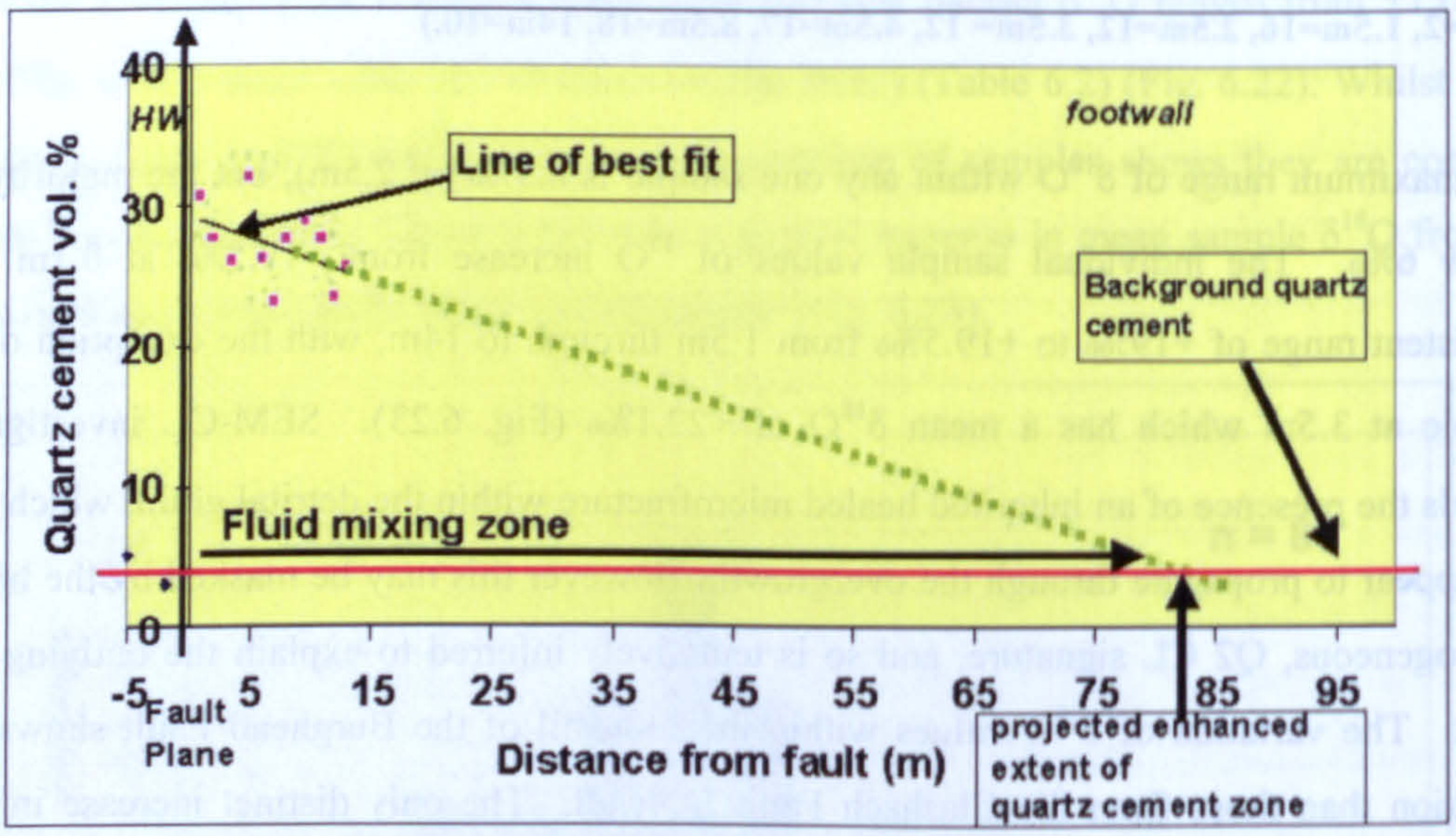


**Fig. 6.25. Extrapolation of the trend of decreasing quartz cement with increasing distance from the fault slip face of the Burghead Fault, through to measured background values. Despite the large uncertainty in the extrapolation this suggests the zone of Q2 cementation within the footwall of the Burghead Fault is greater than that seen around the smaller-scale Clashach Fault.**

Intra-overgrowth profiles were made from 5 overgrowths within 4 samples, at 3.5, 4.5, 8.5 and 14m from the fault plane. The total range of $\delta^{18}O$ is 8.2‰ in the position adjacent to the detrital grain boundary, and decreases to 3.9‰ between the analyses closest to the

overgrowth crystal edge (Fig.6.24). This may not be a true comparison because the number of measurements also decreases with increasing distance from the grain, and consequently it is possible that there is no spatial variation in $\delta^{18}O$ intra-overgrowth range.

The pattern of decreasing $\delta^{18}O$ range, and increasing $\delta^{18}O$ value, with increasing intra-overgrowth position from the detrital grain is similar to the observed pattern for samples from the Clashach Fault. This suggests that although the trend of increasing sample $\delta^{18}O$ values with increasing distance from the main fault plane is not as apparent for the Burghead Fault, the micro-scale isotopic cement evolution is similar for both locations.

The similarity in the $\delta^{18}O$ values from both the Clashach and Burghead Fault footwalls indicates that Q2 cement at both locations precipitated from a single diagenetic event, and allows the data to be treated as one dataset for characterisation of Q2 cement (Fig. 6.26).

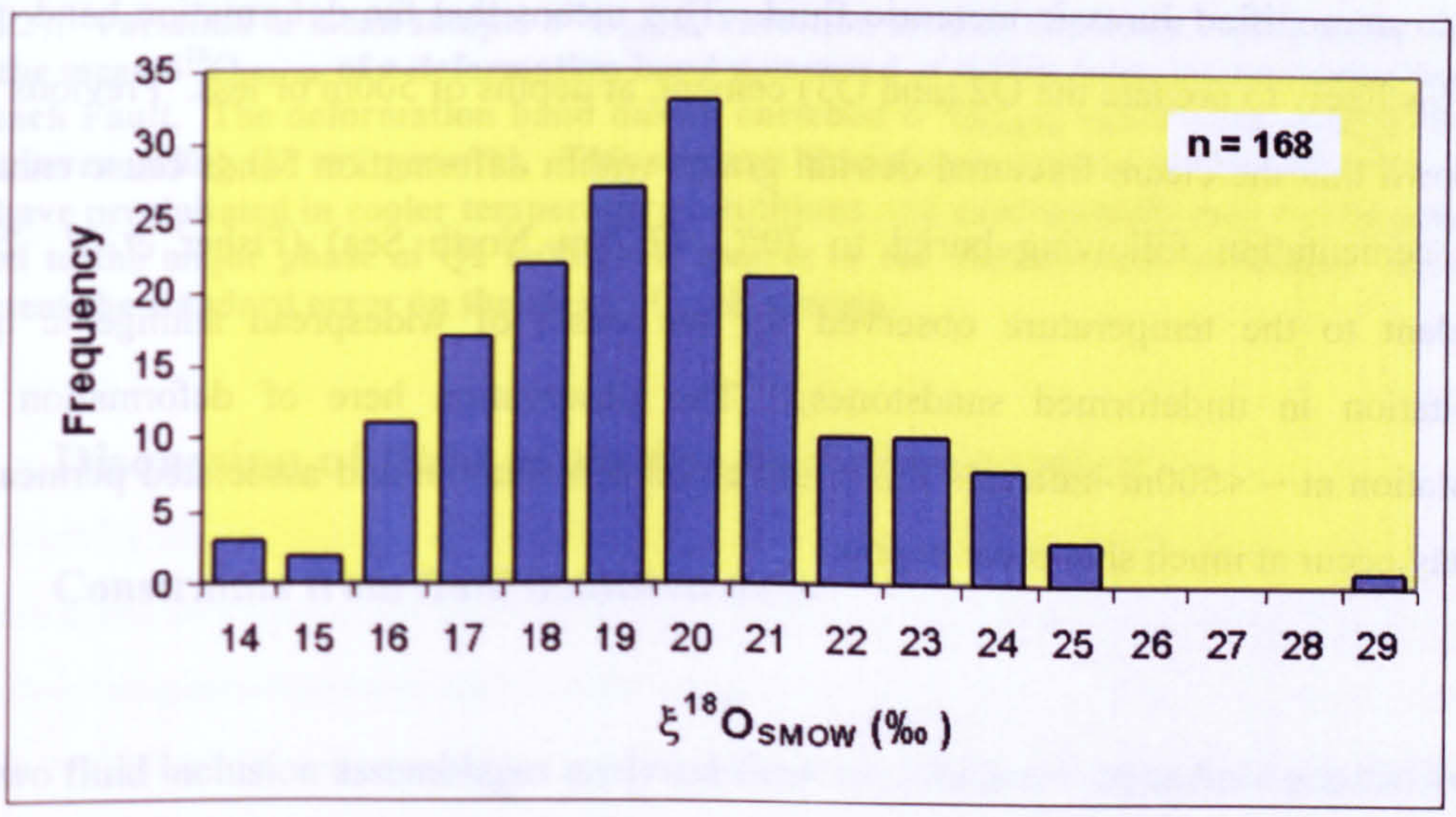


**Fig. 6.26. Histogram of all Q2 footwall cement $\delta^{18}O_{SMOW}$ values from both the Clashach and Burghead Faults. The data forms a unimodal bell curve distribution which is weighted toward lower $\delta^{18}O_{SMOW}$ values.**

### 6.53.5 Clashach Fault deformation band

A profile across a single deformation band, situated 0.25m from the main slip face of the Clashach Fault was analysed. Four spots were analysed with the ion microprobe in a profile across the band, avoiding large visible detrital fragments. The consistent presence of detrital fragments less than the spot size (20-25μm) meant that each analysis incorporated varying unknown amounts of detrital material as well as quartz cement. Areas with the least visible

detrital quartz fragments were chosen to maximize the amount of authigenic quartz analysed. Values of $\delta^{18}O$ range from +18.3‰ to +23.1‰, with a mean $\delta^{18}O$ of +20.7‰ +/-0.9‰ (S.E.) (Table 6.2). The observation that these values include at least some detrital material means they represent minimum $\delta^{18}O$ values of quartz cement, because detrital values are well characterised with a mean $\delta^{18}O$ of +10.5‰. This detrital value is below any probable authigenic quartz $\delta^{18}O$ value and will act to reduce any measured $\delta^{18}O$ below true authigenic cement value. Comparison of deformation band $\delta^{18}O$ analyses with pure Q2 and Q3 authigenic quartz shows that these values are most similar to Clashach Fault Q3 hanging wall quartz cement and footwall Q2 overgrowths at 30.8m from the fault plane (Fig. 6.27). The $\delta^{18}O$ deformation band values are also higher than all Q2 samples (except at 3.5m) from the Burghead Fault footwall. The conditions of deformation band cementation were likely to be closer to those during precipitation of Q3 quartz cement within the sandstone, from meteoric fluids slightly modified during burial. However the $\delta^{18}O$ signature of the deformation band is closer to unmodified Jurassic meteoric fluid. This means that the deformation band quartz cement is likely to predate the Q2 (and Q3) cement, at depths of 500m or less. Previous work has shown that the clean, fractured detrital grains within deformation bands cause enhanced quartz cementation following burial to 70°C, (2.7km North Sea) (Fisher *et al.*, 2000), equivalent to the temperature observed for the onset of widespread authigenic quartz precipitation in undeformed sandstones. The observation here of deformation band cementation at ~ <500m indicates this preferential cementation and associated permeability loss may occur at much shallower depths.

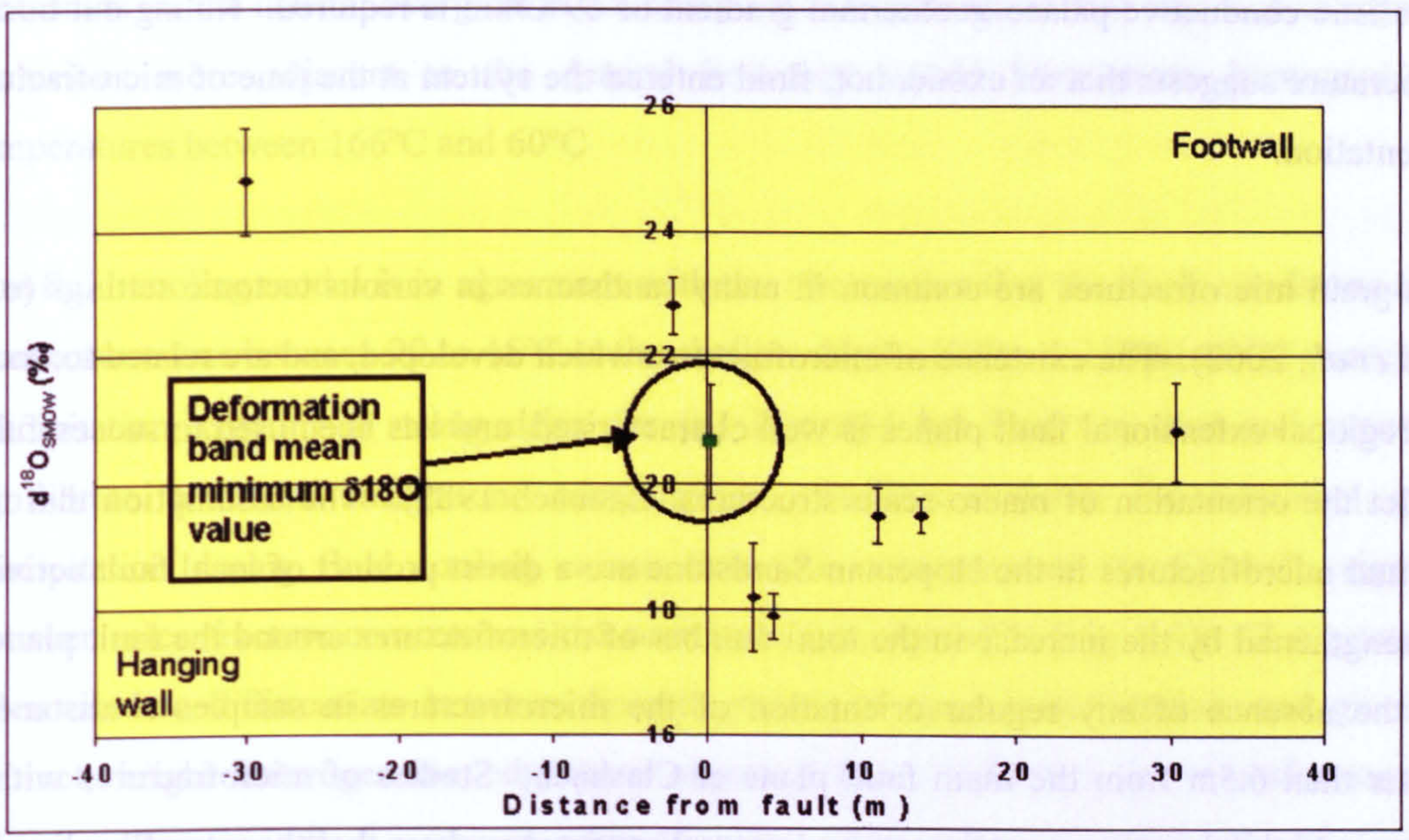


**Fig. 6.27. Variation in mean sample $\delta^{18}O_{SMOW}$ variation around Clashach Fault, as for Fig. 6.20, with the mean $\delta^{18}O_{SMOW}$ of a deformation band measured at 0.25m from the main slip face of the Clashach Fault. The deformation band has an enriched $\delta^{18}O_{SMOW}$ value lying outside the trend of the surrounding Q2 overgrowths. This suggests that quartz cement in the deformation band may have precipitated in cooler temperature conditions and consequently may not be genetically related to the major phase of Q2 authigenic quartz in the undeformed sandstone. Error bars represent the standard error on the mean of each sample.**

## 6.6 Discussion of fluid evolution and cementation

### 6.61 Constraints from fluid inclusion data

The two fluid inclusion assemblages analysed show two distinct temperature populations; hot detrital grain microfracture healing, and cooler overgrowth cementation. The 166°C mean minimum trapping temperature of the microfracture inclusions indicates the presence of hot fluids in the system during healing of the microfracture by precipitation of quartz cement. The maximum burial depth of the onshore Hopeman Sandstone, as constrained by Quinn *et al.* (Chapter 5) is 2.4km and may have been considerably less at 1.5km. The maximum palaeo-temperature reached by the sandstone was therefore considerably less than either the mean or lowermost individual value of microfracture inclusion homogenisation temperature. Assuming a geothermal gradient of 35°C/km equates to a maximum burial temperature of 84°C, which is 82°C less than the mean microfracture Th, and 67°C less than the lowest measured Th value of 151°C. For temperatures of 166°C to be recorded at 2.4km an

unrealistic conductive palaeo-geothermal gradient of 69°C/km is required. Ruling out burial temperature suggests that an exotic, hot, fluid entered the system at the time of microfracture cementation.

Intra-grain microfractures are common in many sandstones in various tectonic settings (e.g. Reed *et al.*, 2002). The existence of microfractures which developed, and are related to, local and regional extensional fault planes is well characterised, and has been used to successfully predict the orientation of macro-scale structures (Laubach 1989). The assumption that the oriented microfractures in the Hopeman Sandstone are a direct product of local fault activity is strengthened by the increase in the total number of microfractures around the fault planes, and the absence of any regular orientation of the microfractures in samples at distances greater than 6.5m from the main fault plane at Clashach. Studies of microfractures within quartz in both laboratory experiments and natural sandstones show that the rate of healing by authigenic quartz can be geologically instantaneous, occurring synkinematically (Reed and Laubach 2000), as well as at shallow burial depths (Laubach 1989). Rapid healing of the oriented microfractures surrounding the main faults indicates that the inclusion Th represents a minimum value, which is close to the true temperature of fault related imported hot fluids, and that microfracture cementation was geologically instantaneous syn or post fault activity.

Single-phase, low temperature inclusions examined within Q2 quartz overgrowths point to the existence of different porefluid temperature conditions from those of the microfracture healing, during the latter overgrowth precipitation. The probable entrapment temperature of the overgrowth inclusions is <60°C, which is more than 100°C below the mean microfracture homogenisation temperature (166°C). Single-phase overgrowths were observed less frequently adjacent to the fault at Clashach, and increase in occurrence moving through the footwall away from the fault. This observation suggests that a higher proportion of overgrowth volume precipitated at higher temperatures nearer the fault, but that there was some precipitation at cooler temperatures. The position of these inclusions in mid-outer overgrowth positions shows that they are likely to record the fluid conditions during the latter stages of cementation. The intra-overgrowth inclusion distribution combined with the pattern of single-phase inclusion frequency throughout the footwall sample profile suggests cooling of an imported fluid spatially away from the fault, and also through time. The two inclusion clusters may be defined as representative of end-member fluids. The absence of any intermediate temperature inclusions may be explained by the lack of any measurable

inclusions on the detrital-overgrowth boundary. It is hypothesised that any such overgrowth inclusions more adjacent to the detrital boundary would have mean homogenisation temperatures between 166°C and 60°C

The fluid-cooling model is in agreement with the observation that the likely sandstone burial temperature was between 20 to 45°C at the shallow depths (500m-1.25km) of Q2 overgrowth precipitation, creating a strong drive for the imported hot fluids to cool and eventually equilibrate with the background temperature. Further evidence for continual quartz precipitation during fluid cooling comes from the continuity of the SEM-CL signature between microfracture cements and the surrounding overgrowths (Fig. 6.4). CL-signature is often used to differentiate between discrete phases of quartz cementation, and given the distinct, bright heterogeneous signature observed here, indicates the microfracture and overgrowth cementation represent a single event. The same general trend of increasing frequency of single-phase inclusions with increasing distance from the fault plane, is seen in samples from the Burghead Fault footwall, indicating that the same fluid temperature evolution occurred. The proposal that Q2 cementation occurred on a larger scale in the footwall of the Burghead Fault implies that an increased volume of siliceous fluid was imported and that lateral fluid cooling occurred over a longer section of the footwall, producing a lower temperature gradient which is more difficult to detect.

Raman probe detection of salinity in the single-phase Q2 overgrowth inclusions demonstrates that the fluid was probably sourced from an evolved saline basinal brine. Any meteoric fluids, and any porewater at such shallow burial depths, would show a comparatively low salinity to basinal fluid suggesting advection of silica is a more likely source than downward meteoric flow.

## 6.62 Constraints from $\delta^{18}O$ data .

### 6.62.1 Clashach Fault

The pattern of increasingly enriched values of Q2 $\delta^{18}O$ with increasing distance from the Clashach Fault (Fig. 6.20) can be explained by integration with petrographic observations and fluid inclusion temperature data. As shown above the fluid inclusion Th data records the evolution of cementation from a hot fluid of mean Th 166°C to a cooler fluid with Th<60°C.

The proposed model of a discrete episode of Q2 quartz cementation and a lateral and temporal cooling of fluid in the system is further supported by the isotopic data.

The measured $^{18}O/^{16}O$ ratio of quartz cement is a product of the temperature of precipitation, and the $^{18}O/^{16}O$ composition of the fluid from which the cement grew. Figure 6.28 displays a plot of quartz oxygen $\delta^{18}O$ value as a function of temperature and porefluid $\delta^{18}O$, based on the fractionation curves of Matsuhisa *et al.* 1979.

The most depleted $\delta^{18}O$ values adjacent to the fault, at 2.9 and 4.2m, have Q2 $\delta^{18}O$ values of +18.2‰ and +17.9‰ respectively (Fig. 6.20). Calculation of $\delta^{18}O$ of potential source fluids shows that cements with such depleted $\delta^{18}O$ values must have precipitated at a temperature greater than 70°C for the fluid $\delta^{18}O$ value to fall within the known compositions of reasonable surface or basinal fluids. If precipitation occurred at temperatures <70°C fluid $\delta^{18}O$ would be more depleted than –7‰, which is less than any meteoric or basin fluid. Precipitation at the other temperature end member, near the recorded mean Th of 166°C within the microcrack authigenic quartz, requires precipitation from a fluid with $\delta^{18}O$ +3‰ to +4‰, which is comparable to typical evolved North Sea basinal fluids (e.g. Girard *et al.*, 2001, Marchand *et al.*, 2002), and realistic as a source fluid given the recorded hot temperatures, and setting within a structurally high horst block at the basin margin.

Combining the evidence for shallow burial Q2 cementation, and the absence of an internal silica source at this depth, implies that silica for Q2 cementation was imported through advection. The depleted $\delta^{18}O$ values in hot authigenic quartz show that cementation from siliceous meteoric fluids can be ruled out adjacent to the fault.

The observation of increasing $\delta^{18}O$ values moving through the footwall shows a systematic change in Q2 cementation conditions from the fault to the footwall boundary of Q2 occurrence. No change in isotope trend is seen between petrographic zones 1 and 2 reaffirming the SEM-CL observation that the cement is the same Q2 phase. The most enriched $\delta^{18}O$ footwall value is +20.8‰ at 30.4m from the fault, where Q2 volume approaches background values of 5%. Single-phase inclusions are more frequently observed in Q2 cement with increasing distance from the fault, suggesting cooler precipitation conditions. Assuming precipitation at 60°C this represents growth from a fluid of –7‰, equivalent to Jurassic meteoric water. If precipitation of the +20.8‰ Q2 cement was from

temperatures near 166°C this would represent growth from a +6‰ basinal fluid. This is beyond typical +$\delta^{18}O$ values for enriched basinal fluids, and is +2‰ to +3‰ heavier than the calculated maximum fluid $\delta^{18}O$ value adjacent to the fault. If precipitation occurred from simple cooling of a +3‰ basinal fluid, $\delta^{18}O$ quartz would be >+27‰, much higher than measured values (Fig. 6.28). Precipitation at the extreme distant edge of the footwall Q2 zone is therefore interpreted as growth from a dominantly Jurassic meteoric fluid, at around 60°C and slightly elevated above burial temperature.

Q2 cementation records isotopic signals of two different fluids close to the fault and at the extreme edge of occurrence. The trend of increasing $\delta^{18}O$ values between the fault plane and the most distant Q2 cement is interpreted as representing mixing of an $\delta^{18}O$ enriched hot basinal fluid, which was introduced at the main fault slip face, with cool, $\delta^{18}O$ depleted Jurassic meteoric porefluid present within the Hopeman Sandstone. The measured $\delta^{18}O$ Q2 values represent growth from a fluid at decreasing temperature as well as increasingly meteoric, along a mixing line (Fig. 6.28).

Q3 cement in the hanging wall of Clashach Fault has a mean $\delta^{18}O$ of +23.1‰. The small size of overgrowths precluded fluid inclusion analysis, but precipitation following Q2 cementation implies growth at, or close to, the maximum proposed burial temperature of c.84°C. A cement with a $\delta^{18}O$ value of +23.1‰, precipitating at 80°C, has a source fluid $\delta^{18}O$ of -1‰. At 60°C $\delta^{18}O$ of the fluid is -6‰. Both these possible values can be representative of buried and slightly modified Jurassic meteoric porefluid. The precipitation of Q3 cement from a slightly modified Jurassic meteoric fluid supports the model that Q2 cement precipitated from mixing of a hot siliceous basinal fluid and a cool pre-existing Jurassic meteoric porefluid. This Jurassic porefluid was subsequently modified by subsequent burial, or locally, from any remaining $\delta^{18}O$ enriched imported fluid. Prior to Q2 and Q3 cementation an influx of Jurassic meteoric fluid into the Hopeman Sandstone is reasonable given the stratigraphic position of the formation, c.100m below the Lower Jurassic.

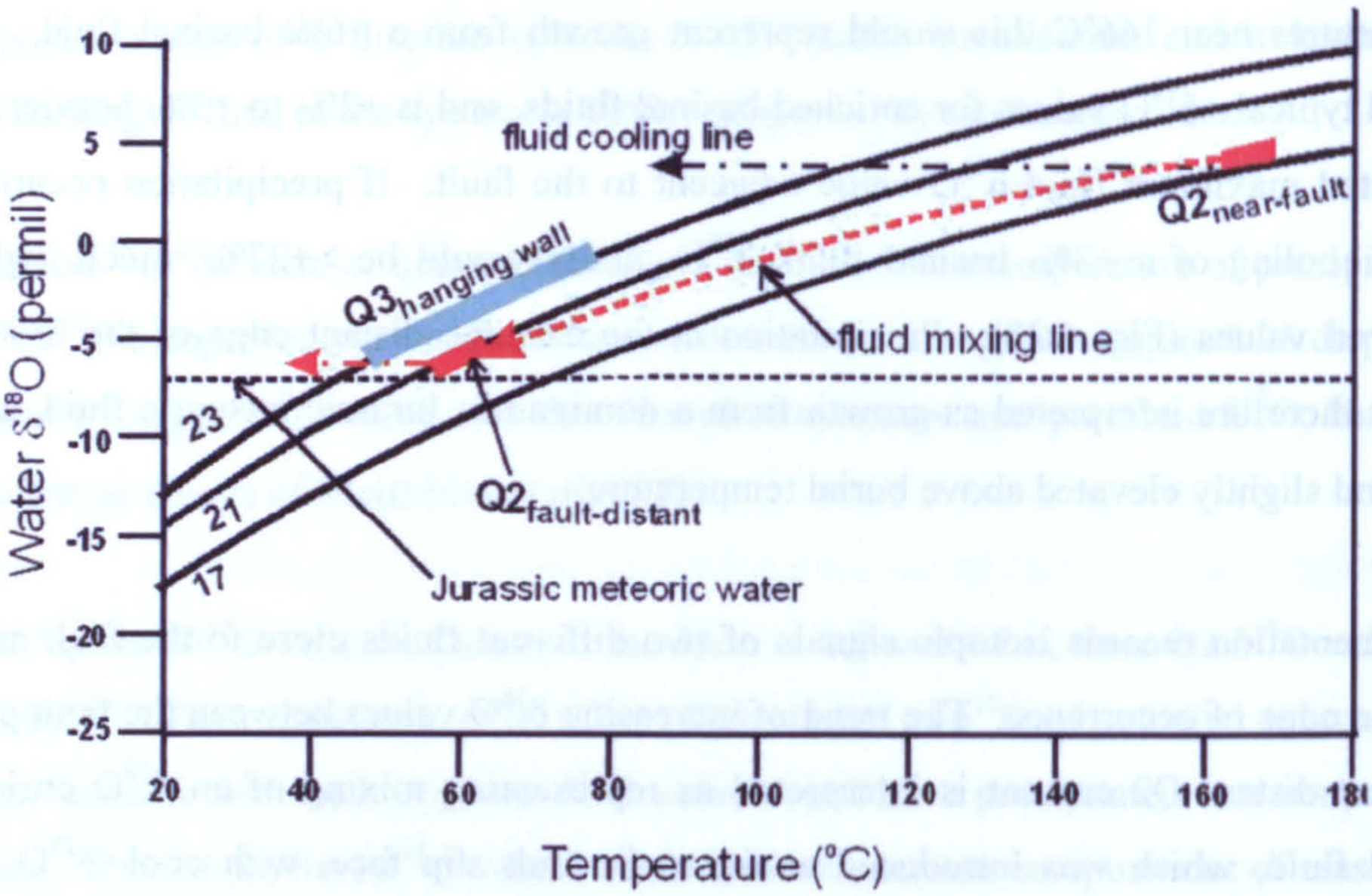


**Fig. 6.28. Oxygen isotope fractionation curves for 17‰, 21‰ and 23‰. The isotopic mixing line observed in Q2 cements shows how the oxygen isotope values change moving away from the fault plane of the Clashach Fault. Oxygen isotope fractionation curves from Matsuhisa et al.,1979.**

The presence of some low Th, single-phase fluid inclusions in samples in close proximity to the fault suggests that at least some Q2 cement precipitated in this position at low (<60°C) temperature. The position of the inclusions in the mid to outer overgrowth suggests that fluid cooling occurred through time close to the fault as well as with increasing distance into the footwall. Examination of intra-overgrowth $\delta^{18}O$ values from Clashach footwall samples show a broad $\delta^{18}O$ enrichment moving through the overgrowth from detrital grain boundary to crystal edge (Fig. 6.21). This micro-scale trend represents the product of fluid cooling during continued overgrowth precipitation. The range in $\delta^{18}O$ values is much greater in cement closer to the detrital grain boundary, and decreases with increasing distance through individual overgrowths. This may record initially faster cooling producing more heterogeneous $\delta^{18}O$ values, on the spatial scale of the ion microprobe, close to the grain boundary. As the rate of cooling slowed Q2 cement records more homogeneous $\delta^{18}O$ values toward overgrowth boundaries.

### 6.62.2 Burghead Fault

The lack of a significant trend in $\delta^{18}O$ values from the limited section of exposed Burghead Fault footwall is proposed to be a product of the increased lateral extent of the footwall Q2

cement zone. Hot basinal fluid adjacent to the fault is recorded by Q2 $\delta^{18}O$ +17.5‰ at 0.1m from the main slip face. Mixing of this fluid with a background cool meteoric fluid is proposed to have caused the observed values of +19‰ to +19.5‰ through to 14m. The increased volume of Q2 cement, over a projected 80m footwall zone, implies that a larger volume of hot siliceous basinal fluid entered the Hopeman Sandstone at the Burghead Fault, leading to mixing over a longer footwall transect. The entire extent of the Q2 fault-related cement zone is seen in the footwall of the Clashach Fault, allowing the complete mixing line from hot basinal fluid to cool meteoric fluid to be detected. For the Burghead Fault only a section of this mixing line adjacent to the fault has been analysed. Extrapolation following the trend seen at the Clashach Fault suggests Q2 $\delta^{18}O$ rises over a lower gradient, to a similar maximum value of +20.8permil at 80m.

The positive relationship between fault scale, cement volume and fluid mixing zone shows that the amount of imported hot fluid is related to fault size. The observation that isotopes do not quickly rise to meteoric fluid values in close proximity to the Burghead Fault indicates that a higher volume of fluid entered the sandstone than at Clashach Fault, and mixed laterally over a distance greater than 14m. The presence of single-phase inclusions in Q2 cement surrounding the Burghead Fault shows that fluid cooled through time close to the fault. As at Clashach Fault the observation that single-phase inclusions become increasingly common moving further away from the fault suggests a combined process of temporal cooling of the basinal fluid and lateral mixing with Jurassic meteoric fluid.

## 6.63 Sources of silica

Evidence of Q2 cement precipitation from enriched $\delta^{18}O$ basinal fluids suggests the source of silica was deeply buried sediment within the basin. Recorded healed microfracture mean inclusion temperatures of 166°C indicate a fluid sourced from between 4 to 5km burial under a geothermal gradient of 35-40°C/km. The positive $\delta^{18}O$ signature of the fluid indicates isotopic enrichment from water interaction with clay mineral recrystallisation reactions which can also supply silica (Wilkinson *et al.*, 1992). Seismic data (Quinn *et al.*, (in prep.), Chapter 4) shows that during the Late Jurassic basin extension the Permo-Triassic and Lower-Mid Jurassic were buried to >5km offshore within the Inner Moray Firth Basin. Deep burial, and heating to >160°C, of these sandstones and mudstones is likely to have caused widespread recrystallisation of smectite to illite in mudstones and clay-rich sandstones, generating

enriched, +ve $\delta^{18}O$ fluids (Wilkinson *et al.*, 1992, Aplin *et al.* 1993). This burial depth is also equal to that required to generate a fluid temperature similar to the end member high recorded by inclusion data.

## 6.64 Deformation band cement

The measured deformation band $\delta^{18}O$ values of +18.3‰ to +23.1‰, with a mean $\delta^{18}O$ of +20.7‰+/-0.9‰ (S.E.) have been interpreted as shallow burial deformation band cementation prior to Q2 cement emplacement and Q3 precipitation. The $\delta^{18}O$ values were observed to include some low $\delta^{18}O$ detrital material meaning they are a minimum. The mean deformation band $\delta^{18}O$ of +20.7‰ implies precipitation from a Jurassic meteoric fluid at 60°C. However as this is a minimum it is probable that the true cement $\delta^{18}O$ is greater than +20.7‰ and that precipitation was from pure Jurassic meteoric fluids at cooler temperatures (Fig. 6.29). The maximum recorded $\delta^{18}O$ of +23.1‰ represents cement growth at 45°C from meteoric fluid, suggesting a higher proportion of cement was encountered in this analysis. This is in contrast with proposed models of enhanced internal deformation band cementation (e.g. Fisher *et al.*, 2000). These models propose that quartz cementation of deformation bands is insignificant until burial temperatures of >70°C are reached, which is equivalent to conditions inferred for the onset of closed system sandstone quartz cementation. The interpretation in this paper suggests that silica dissolved in static pore fluids during fault activity can re-precipitate geologically rapidly at burial temperatures below 60°C, and possibly as low as 20°C at <500m burial.

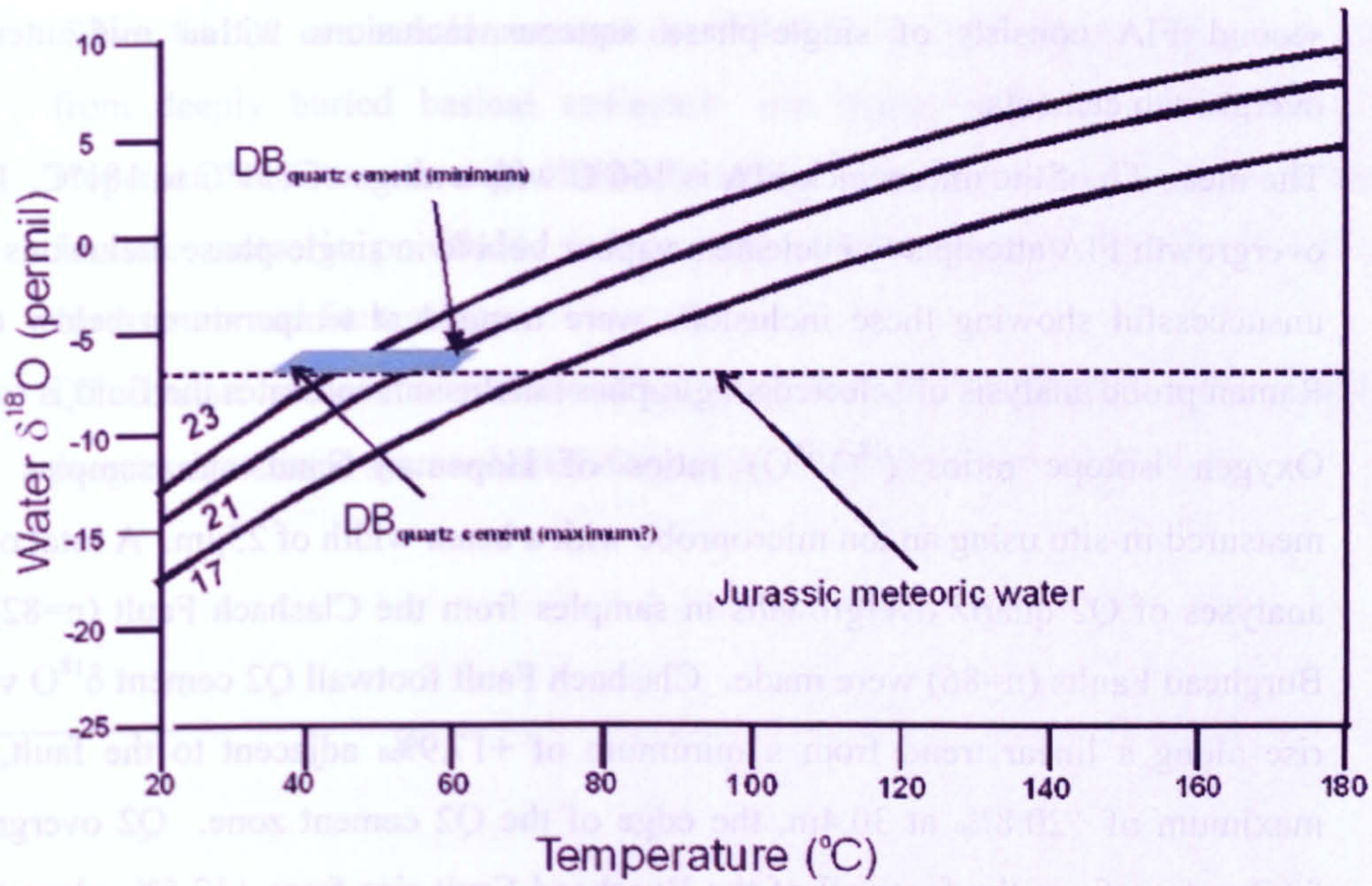


**Fig. 6.29. Oxygen isotope fractionation curves for 17‰, 21‰ and 23‰. The Clashach Fault deformation band mean and potential maximum d18O values are shown. Analyses incorporate some detrital material and represent a minimum Deformation band cement precpitated from unmodified Jurassic pore fluids at low temperature during shallow burial. Based on Matsuhisa et al., 1979.**

Integrating the $\delta^{18}O$ isotopic data from the deformation band and Q3 burial cement shows that Jurassic meteoric porefluid in the Hopeman Sandstone evolved from unmodified pore fluid ($\delta^{18}O$ -7‰) at shallow depth, through to a slightly modified fluid with a mean $\delta^{18}O$ signature of –5‰ to 0‰ during burial. The $\delta^{18}O$ data from the Q2 cement represents an incursion of hot temperature fluid from the fault planes into the Jurassic meteoric porefluid. Diagenetic events prior to, and following, the exotic fluid import, follow a closed static pore fluid system. Open system diagenesis was a temporary event which punctuated progressive fluid evolution and cementation.

## 6.7 Conclusions

- Two distinct fluid inclusion assemblages (FIA's) have been identified within Q2 phase quartz cementation from the Hopeman Sandstone footwalls of the Clashach and Burghead Faults. The first FIA consists of 2-phase liquid and vapour inclusions within fault-related detrital microcracks healed with Q2 phase quartz cement. The

second FIA consists of single-phase aqueous inclusions within mid-outer Q2 overgrowth cements.

- The mean Th of the microcrack FIA is 166°C with a range of 151°C to 181°C. In the overgrowth FIA attempts to nucleate a vapour bubble in single-phase inclusions were unsuccessful showing these inclusions were trapped at temperatures below 60°C. Raman probe analysis of selected single-phase inclusions indicates the fluid is saline.
- Oxygen isotope ratios ($^{18}O/^{16}O$) ratios of Hopeman Sandstone samples were measured in-situ using an ion microprobe with a beam width of 25μm. A total of 168 analyses of Q2 quartz overgrowths in samples from the Clashach Fault (n=82) and Burghead Faults (n=86) were made. Clashach Fault footwall Q2 cement $\delta^{18}O$ values rise along a linear trend from a minimum of +17.9‰ adjacent to the fault, to a maximum of +20.8‰ at 30.4m, the edge of the Q2 cement zone. Q2 overgrowth $\delta^{18}O$ values from the footwall of the Burghead Fault rise from +17.5‰ close to the main fault slip face, to consistent values of between +19.1‰ to +19.5‰ up to 14m distant.
- Hanging wall Q3 cements from the Clashach Fault have a mean $\delta^{18}O$ value of +23.1‰. An isotopic profile across a single deformation band shows $\delta^{18}O$ is a minimum mean of +20.7‰.
- Fluid inclusion and oxygen isotope data indicate that Q2 quartz cement precipitated from a hot, $\delta^{18}O$ enriched, basinal fluid near the fault planes, which mixed with an isotopically lighter Jurassic meteoric porefluid, producing a mixing line of Q2 cement $\delta^{18}O$ values through the Clashach Fault footwall. The presence of the same mixing line is inferred to exist over a longer section of the Burghead Fault footwall corresponding to the increased scale of Q2 cementation.
- Hanging wall and background Q3 cements precipitated from slightly evolved Jurassic meteoric porefluids close to, or at, the maximum burial temperature of 84°C (2.4km at 35°C/km).
- Deformation band $\delta^{18}O$ values suggest internal quartz precipitation at shallow burial depths, <500m, and temperatures significantly <60°C. Deformation band quartz cement pre-dates the import of Q2 fluids and Q3 burial related cementation. This deformation band quartz cementation occurred at a shallower depth than that observed in previous studies, which propose the onset of significant deformation band cementation at a burial depth equivalent to >70°C.

- Silica for Q2 cementation around the Clashach and Burghead Faults was sourced from deeply buried basinal sediments and transported into the shallow burial Hopeman Sandstone through fluid advection. Cooling and mixing with background Jurassic meteoric porefluids led to cementation spatially associated with Late Jurassic normal fault planes.
- Q2 cement records a period of open hydrologic conditions which punctuated progressive closed system burial diagenesis in the Hopeman Sandstone.

---

# References


**Aplin, A.C., Warren, E.A., Grant, S.M., Robinson, A.G., 1993.** Mechanisms of quartz cementation in North Sea reservoir sands: constraints from fluid compositions. *In:* Diagenesis and Basin Development (ed. Horbury, A.D. and Robinson, A.G.), American Association of Petroleum Geologists studies in geology, 36, p.7-22.

**Aydin, A., 1978.** Small faults formed as deformation bands in sandstone. Pure and Applied Geophysics, 116, p913-930.

**Benton, M.J., and Walker, A.D., 1985.** Palaeoecology, Taphonomy, and Dating of Permo-Triassic Reptiles from north-east Scotland. Palaeontology, 28,p. 207-234,

**Berridge, N.G. and Ivimey-Cook, H.C., 1967.** The Geology of a Borehole at Lossiemouth, Morayshire. Bulletin of the Geological Survey of Great Britain, 27, p. 155-169.

**Bjorkum, P.A., 1996.** How important is pressure in causing dissolution of quartz in sandstones? Journal of Sedimentary Research A, 66 (6), p.147-154.

**Bjorlykke, K., Nedkvitne, T., Ramm, M. and Saigal, G.C., 1992.** Diagenetic processes in the Brent Group (Middle Jurassic) reservoirs of the North Sea: an overview. *In*: Geology of the Brent Group (ed. Morton, A.C., Haszeldine, R.S., Giles, M.R., and Brown, S.), Special Publication of the Geological Society of London, 61, p.263-287.

**Blatt, H., 1979.** Diagenetic processes in sandstones. Special Publication of the SEPM, Tulsa, Oklahoma, 26, 141-157.

**Blatt, H., 1987.** Oxygen isotopes and the origin of quartz. Journal of Sedimentary Petrology, 57, p.373-377.

**Burke, E.A.J., 2001.** Raman microspectrometry of fluid inclusions. Lithos, 55, p. 139-158.

**Burley, S.D., Mullis, J. and Matter, A., 1989.** Timing diagenesis in the Tartan Reservoir (UK, North Sea): constraints from combined cathodoluminescence microscopy and fluid inclusion studies. Marine and Petroleum Geology, 6, p.8-120.

**Clemmensen, L.B., 1987.** Complex star dunes and associated aeolian bedforms, Hopeman Sandstone (Permo-Triassic), Moray Firth Basin, Scotland. In: Desert Sediments: Ancient and Modern (ed. Frostick, L, and Reid, I.). Geological Society of London Special Publication, 35, p. 213-231.

**Eiler, J.M., Valley, J.W., Graham, C.M. and Baumgartner, L.P., 1995a.** Ion microprobe evidence for the mechanisms of stable isotope retrogession in high grade metamorphic rocks. Contrib. Mineralogy and Petrology, 118, p.365-378.

**Fisher, Q.J., Knipe, R.J. and Worden, R.H., 2000.** Microstructures of deformed and non-deformed sandstones from the North Sea: implications for the origins of quartz cement in

sandstones. *In*: Quartz Cementation in Sandstones (ed: Worden, R.H. and Morad, S.), Special Publication of the International Association of Sedimentologists, 29, p. 129-146.

**Giles, M.R., Stevenson, S., Martin, S.V., Cannon, S.J.C., Hamilton, P.J., Marshall, J.D. and Samways, G.M., 1992.** The reservoir properties and diagenesis of the Brent Group; a regional perspective. In Geology of the Brent Group (eds. Morton, A.C., Haszeldine, R.S., Giles, M.R. and Brown, S.) Geological Society Special Publication, 61, p. 289-327.

**Girard, J.-P., Munz, I.A., Johansen, H., Hill, S. and Canham, A., 2001.** Conditions and timing of quartz cementation in Brent reservoirs, Hild Field, North Sea: constraints from fluid inclusions and SIMS oxygen isotope microanalysis. Chemical Geology, 176, p.73-92.

**Glennie, K.W. and Buller, A.T., 1983.** The Permian Weissliegend of NW Europe: the partial deformation of aeolian sand dunes caused by the Zechstein transgression. Sedimentary Geology, 35, p. 43-81.

**Gluyas, J.G. and Coleman, M.L., 1992.** Material flux and porosity changes during sediment diagenesis. Nature, 356, p.52-54.

**Goldstein, R.H. and Reynolds, T.J., 1992.** Systematics of fluid inclusions in diagenetic minerals. SEPM short course 31 notes. SEPM, Tulsa, Oklahoma.

**Graham, C.M., Valley, J.W. and Winter, B.L., 1996.** Ion microprobe analysis of $^{18}O/^{16}O$ in authigenic and detrital quartz in the St.Peter Sandstone, Michigan Basin and Wisconsin Arch, USA: Contrasting diagenetic histories. Geochimica et Cosmochimica Acta, 60, p.5101-5116.

**Hanor, J.S., 1980.** Dissolved methane in sedimentary brines: potential effect on the PVT properties of fluid inclusions. Economic Geology, 75, p. 603-609.

**Hartmann, B.H., Juhasz-Bodnar, K, Ramseyer, K. and Matter, A., 2000.** Polyphased quartz cementation and its sources: a case study from the Upper Palaeozoic Haushi Group sandstones, Sultanate of Oman. *In*: Quartz Cementation in Sandstones (ed: Worden, R.H. and Morad, S.), Special Publication of the International Association of Sedimentologists, 29, p. 253-270.

**Haszeldine, R.S., Samson, I.M., Cornford, C., 1984.** Dating diagenesis in a petroleum basin: a new fluid inclusion method. Nature, 307, p.354-357.

**Heald, M.T. and Larese, R.E., 1974.** Influence of coatings on quartz cementation. Journal of Sedimentary Petrology, 44, p.1269-1274.

**Hervig, R.L., Williams, P., Thomas, R.M., Schaeur, S.N. and Steele, I.M., 1992.** Microanalysis of oxygen isotopes in insulators by secondary ion mass spectrometry. International Journal of Mass Spectrometry, 120, p.45-63.

**Hervig, R.L., Williams, P., Thomas, R.M., Schaeur, S.N. and Steele, I.M., 1995.** Oxygen isotope microanalysis of diagenetic quartz: possible low temperature occlusion of pores. Geochimica et Cosmochimica Acta, 59, p.2537-2543.

**Hippler, S.J., 1993.** Deformation microstructures and diagenesis in sandstone adjacent to an extensional fault: implications for the flow and entrapment of hydrocarbons. American Association of Petroleum Geologists Bulletin, 77, p. 625-637.

**Laubach, S,E., 1989.** Palaeostress directions from the preferred orientation of closed microfractures (fluid-inclusion planes) in sandstone, East Texas Basin, USA. Journal of Structural Geology, v.11, 5, p.603-611.

**Land, L. S., 1984.** Frio sandstone diagenesis, Texas Gulf Coast; a regional isotopic study. *In:* Clastic Diagenesis (ed. McDonald, D.A. and Surdam, R.C.), American Association of Petroleum Geologists Special Publication, 37, p.42-62.

**Lander, R.H. and Walderhaug, O., 1999.** Predicting porosity through simulating sandstone compaction and quartz cementation. American Association of Petroleum Geologists, 83, p. 433-449.

**Lynch, Leo F., 1996.** Mineral/Water interaction, fluid flow, and Frio Sandstone diagenesis: Evidence from the rocks. American Association of Petroleum Geologists, 80, p.486-504.

**Macaulay, C., 2003.** Low temperature quartz cementation of the upper Cretaceous Lochaline Sandstone of Lochaline, Argyll, Scotland. pers comm. www.geos.ed.ac.uk/facilities/ionprobe/calumSi

**Macaulay, C.I., Fallick, A.E., Haszeldine, R.S., Graham, C.M., 2000.** Methods of laser-based stable isotope measurement applied to diagenetic cements and hydrocarbon reservoir quality. Clay Minerals, 35, 313-322.

**Marchand, A.M.E., Haszeldine, R.S., Macaulay, C.I., Swennen, R. and Fallick, A.E., 2000.** Quartz cementation inhibited by crestal oil charge: Miller deepwater sandstone, UK North Sea. Clay Minerals, 35, 205-214.

**Marchand, A.M.E., Macaluay, C.I., Haszeldine, R.S. & Fallick, A.E. , 2002.** Pore water evolution in oilfield sandstones: constraints from oxygen isotope microanalysis of quartz cement. Chemical Geology, 191, 285-304

.

**Matsuhisa, Y., Goldmsith, J.R., and Clayton, R.N., 1979.** Oxygen isotopic fractionation in the system quartz-albite-anorthite-water. Geochimica et Cosmochimica Acta, 43, p.1131-1140

**Paxton, S.T., Szabo, J.O., Ajdukiewicz, J.M. and Klimentidis, R.E., 2002.** Construction of an intergranular volume compaction curve for evaluating and predicting compaction and porosity loss in rigid-grain sandstone reservoirs. American Association of Petroleum Geologists, 86, p.2047-2067.

**Peacock, J.D., 1966.** Contorted beds in the Permo-Triassic acolian sandstones of Morayshire. Bulletin of the Geological Survey of Great Britain, 24, 157-162.

**Quinn, O.F., Haszeldine, R.S., Underhill, J.R. and Dixon, J.E., 2004.** A new structural model for the Lossie Peninsula, Inner Moray Firth. In preparation. Chapter 4.

**Quinn, O.F., Haszeldine, R.S., and Dixon, J.E., 2004.** Porosity and Permeability loss around faults through shallow burial quartz cementation in an aeolian sandstone. In preparation. Chapter 5.

**Reed, R.M., Laubach S.E, Clifts, S., Hooker, J.N. and Makowitz, A., 2002.** Macrofractures, microfractures, and fracture-cement relations in Permian sandstones from the Val Verde Basin, West Texas. Geological Society of America, south-central section. Annual Meeting, Abtract with Programs, 34, 3, p.11.

**Reed, R.M. and Laubach, S.E., 2002.** Crack-seal texture in quartz-lined opening mode fractures formed in quartz-rich sandstone; an example of interrelated structure and diagenesis. Geological Society of America, Annual Meeting, Abstracts with Programs, 32, 7, p.229.

**Renard, F., Brosse, E. and Gratier, J.P., 2000.** *In*: Quartz Cementation in Sandstones (ed: Worden, R.H. and Morad, S.), Special Publication of the International Association of Sedimentologists, 29, p. 67-78.

**Roberts, A.M., Badley, M.E, Price, J.D. and Huck, I.W., 1990.** The structural evolution of a transtensional basin: Inner Moray Firth, NE Scotland. Journal of the Geological Society of London, 147, 87-103.

**Roedder, E., 1979.** Fluid inclusion evidence on the environment of sedimentary diagenesis. *In*: Aspects of Diagenesis (ed. Scholle, P.A. and Schlunger, P.R.) Special Publication of the Society of Economic Palaeontologists and Mineralogists, 26, p. 89-107.

**Roedder, E., 1984.** Fluid Inclusions. Mineralogical Society of America, Reviews in Mineralogy, 12, 644p.

**Rossi, C., Goldstein, R.H., Ceriani, A. and Marfil, R., 2002.** Fluid inclusions record thermal and fluid evolution in reservoir sandstones, Khatatba Formation, Western Desert, Egypt: A case for fluid injection. American Association of Petroleum Geologists, 86, p.1773-1799.

**Schaeur, S.N. and Williams, P., 1990.** Elimination of cluster interferences in secondary ion mass spectrometry using extreme energy filtering. International Journal of Mass Spectrometry, 103, p.21-29.

**Smalley, P.C. and Warren, E.A., 1994.** The Miller Field. *In*: North Sea Formation Water Atlas (ed. Warren, E.A. and Smalley, P.C.). Geological Society London, Memoir15, p.52.

**Sullivan, K.B. and McBride, E.F., 1991.** Diagenesis of sandstones at shale contacts and diagenetic heterogeneity, Frio Formation, Texas. American Association of Petroleum Geologists Bulletin, 75, p.121-138.

**Thiry, M. and Marechal, B., 2001.** Development of tightly cemented sandstone lenses in uncemented sand: example of the Fontainebleau Sand (Oligocene) in the Paris Basin. Journal of Sedimentary Research, 71, 3, p. 473-483

**Underhill, J.R., 1991.** Implications of Mesozoic-Recent basin development in the western Inner Moray Firth, UK. Marine and Petroleum Geology, 8, p. 359-369.

**Walderhaug, O., 1994.** Temperatures of quartz cementation in Jurassic sandstones from the Norwegian continental shelf: evidence from fluid inclusions. Journal of Sedimentary Research, A, 64, p. 311-323.

**Wikinson, M., Crowley, S.F. and Marshall, J.D., 1992.** Model for the evolution of oxygen isotope ratios in the pore fluids of mudrocks during burial. Marine and Petroleum Geology, 9, p.98-105.

**Worden, R.H. and Morad, S., 2000.** Quartz cementation in oil field sandstones: a review of the key controversies. *In*: Quartz Cementation in Sandstones (ed: Worden, R.H. and Morad, S.), Special Publication of the International Association of Sedimentologists, 29, p. 1-20.

**Worden, R.H., Oxtoby, N.H. and Smalley, P.C., 1998.** Can oil emplacement prevent quartz cementation in sandstones? Petroleum Geoscience, 4, p.129-137.

# Chapter 7.

The previous chapters and papers presented different aspects of fault associated quartz cementation within the Hopeman Sandstone. This chapter brings together the results and discussion from these papers and uses this information to produce a holistic model of quartz cement precipitation in the Hopeman Sandstone. In particular, the evidence collected from stratigraphic, structural, petrographic and geochemical studies is synthesised to build upon the present understanding of the origin of silica, fluid flow regimes and the processes of quartz cementation in the Hopeman Sandstone. These insights are used to address the wider implications that this model of quartz cementation in the Hopeman Sandstone has for the four key subjects forming the thesis rationale; quartz cementation, porosity and permeability evolution, fault seals, and mass balance within basinal fluid flow regimes.

## 7.1 Summary of results

Chapter 2 investigated the current thinking on quartz cementation, revealing that opinion is traditionally divided as to whether the process is entirely internal, or if mass transfer of silica on a large scale occurs, leading to quartz precipitation from mobile basinal fluids (e.g. Haszeldine *et al.*, 2000, Worden and Morad 2000). Quartz cement in many North Sea sandstone oil reservoirs is interpreted to have formed from internal sources following burial to temperatures of >70°C (2.5km) (e.g. Giles *et al.*, 1992). Sandstones with a maximum burial depth of less than 2.5km typically contain only minor volumes of authigenic quartz.

Analysis of seismic data in chapter 4 showed that the Inner Moray Firth basin is a half-graben bound to the north-west by the Helmsdale Fault, which acted as the master fault for the major phase of basin development in the Late Jurassic, and created the present day half-graben basin style. Regional analysis of offshore seismic data showed that the IMF basin is dominated by Late Jurassic extensional faults, which locally form half-graben and horst block structures. Onshore the Lossie Peninsula is an uplifted horst block, named here the Hopeman Horst. The horst is bound offshore by the Blind Zone fault which downthrows to the north, and bound onshore to the south by the Spynie Fault which downthrows to the south. This 20km wide horst block runs laterally east-west for >20km and forms the geographical east-west Lossie Peninsula. The Hopeman Horst is analogous to Late Jurassic horst blocks mapped at depth offshore. The Clashach and Burghead Faults are Late Jurassic extensional features which form intra-horst faults within the Hopeman Horst. Interpretation of structural data shows that the Hopeman Horst is likely to have remained at shallow depth (<1.5-2.4km) throughout basin development. Within the basin this horst has been shown to represent a structural high on the southern basin margin, containing the most southerly exposures of Mesozoic sediment from the IMF. The Upper Permian Hopeman Sandstone crops out along the coastline and the Clashach and Burghead Faults are exposed in 3 localities.

Within the Hopeman Sandstone a volumetrically significant fault-related quartz cement (petrographic phase Q2) is present. This authigenic quartz differs from typical internally derived, burial-related quartz cement in several respects. Chapter 5 showed that maximum burial depth for the Hopeman Sandstone is 2.4km and may have been as shallow as 1.5km, much less than the typical depth observed for the onset of significant internal silica

cementation. Calculation of intergranular volume (IGV) in chapter 5 demonstrated that Q2 cement was precipitated at shallow burial depths of between 500m and 1.25km, prior to maximum burial of the sandstone, and below the 70°C temperature required to initiate internal quartz cementation. Petrographic observations indicate that, adjacent to the fault planes, there is no physical contact between many detrital quartz grains, ruling out pressure solution as an internal silica source. It was further shown that the volumetrically dominant Q2 phase of quartz cement is restricted to occur only in the footwalls of two normal faults, and that the volume of cement decreases with increasing distance from the fault. By contrast closed system, burial, cement distribution is typically homogeneous throughout a given sandstone and facies, being controlled on the micro-scale by the availability of precipitation sites. The Cathodoluminescence signature of normal, internally derived, quartz cement is dark, the Hopeman Sandstone fault-related authigenic quartz displays a brighter CL signal than detrital grains. The petrographic evidence presented in chapter 5 shows shallow cementation from an external silica source, focused around fault planes. These sites of shallow burial silica cementation preserve an unusual reptile vertebrate fauna.

Isotopic and fluid inclusion data in chapter 6 demonstrated the exotic nature of the fluid from which the Q2 cement precipitated. Fluid inclusion homogenisation temperatures revealed hot (mean 166°C) authigenic quartz precipitation in detrital grain microfractures, which were produced through extensional displacement on the Clashach and Burghead Faults. Cool (<60°C) Q2 overgrowth precipitation around detrital grains was recorded in single-phase fluid inclusions. SEM-CL petrographic evidence that microcrack and Q2 overgrowth cement are the same phase suggests that they precipitated from a single cooling fluid. The mean temperature of microcrack healing, 166°C, is >80°C above the maximum background burial temperature of the Hopeman Sandstone at the time of precipitation. This indicates that the cement precipitated from a hot fluid imported into the sandstone at shallow depth, which cooled during continued Q2 precipitation. Oxygen isotope analyses of in-situ Q2 overgrowths through the footwalls showed that there is a trend of increasing $\delta^{18}O$ values with increasing distance from the Clashach Fault. These values represent changing temperature and fluid conditions during continued Q2 precipitation. Close to the faults isotope values record precipitation from hot fluid, which increasingly mixed with Jurassic meteoric porefluid moving into the footwall. At Clashach Fault this cooling and mixing continued through to the edge of the Q2 cement aureole, where $\delta^{18}O$ signals record precipitation from a slightly heated and evolved Jurassic meteoric fluid. Structural analysis in chapter 4 showed

that the displacement and length of the Burghead Fault are an order of magnitude greater than the Clashach Fault. In chapter 5 it was shown that the lateral width of Q2 cement in the Burghead Fault footwall, perpendicular to the fault, is around 80m, which is 50m wider than at Clashach. This positive relationship between fault scale and size of cement zone is reflected in the isotope 'mixing line'. For the Burghead Fault this means that the trend of mixing and cooling fluids extends over a longer traverse, 80m wide, and at a shallower gradient.

## 7.2 A model of quartz cementation in the Hopeman Sandstone

The model presented and discussed below addresses three key aspects of Hopeman Sandstone Q2 quartz cementation:

- potential sources of silica and hot siliceous fluids,
- the scale of fluid flow and solute transport (mass balance),
- the local process of fluid mixing and quartz precipitation.

### 7.21 Sources of silica and hot fluids.

Externally derived silica in a sedimentary basin may be supplied by deep basinal clay reactions, from dissolution of thermally unstable grains in sandstones, or from a local silica rich source interacting with a hot fluid.

As discussed in chapter 6, clay reactions, feldspar dissolution, or pressure solution in the deep basin, may expel silica into more permeable sediments as burial proceeds. This silica can be carried from deep in the basin by advection of a hot fluid. Seismic survey data in chapter 4 showed that Permian to Mid Jurassic mudstones and sandstone were buried to a maximum depth of 5km, equivalent to 175°C (at 35°C/km). This temperature is high enough to cause mudstone reactions and release silica (Wilkinson *et al.*, 1992). During Late Jurassic extension maximum burial occurred south of the Helmsdale Fault, 30km north of the Lossie Peninsula, where the Permian to Mid Jurassic sediment reaches 3km thick. The Permo-Triassic is dominantly sandstone but Lower -Mid Jurassic mudstones could have acted as a

significant source, exporting silica into more permeable surrounding formations. Such fluid was also likely to have an enriched $\delta^{18}O$ composition, produced during clay reactions, and comparable to the calculated $\delta^{18}O$ oxygen isotopic composition of Q2 precipitating fluid. This process involves fluid flow, and silica sources, on a regional scale.

Shallow, cool, quartz cementation has sometimes been observed to be sourced from biogenic silica in other sandstones. Extensive shallow quartz cementation recorded in the Cretaceous Lochaline Sandstone of West Scotland, by Macaulay (Pers.Comm), was proposed to be sourced from dissolution of sponge spicules in overlying sediments. The quartz cement was focused in lateral bands 1m thick. The position of these bands was thought to be formed by fluctuations in the position of the water table. Dissolution of sponge spicules may occur at low temperatures of <60°C (Vagle *et al.*, 1994). However in the local area surrounding the Lossie Peninsula the Permo-Triassic sediments consists of aeolian and fluvial sands meaning there is no obvious immediate significant source of biogenic silica. Further, the spatial relationship of the cementation to fault planes suggests the faults acted as a key control on quartz precipitation, not vertical movements in the shallow water table. Sponge spicules further offshore in the Lower Jurassic may have provided a significant silica source, but there is no direct evidence of their contribution.

A local silica source could have been enhanced silica dissolution within the Clashach and Burghead Fault zones. Quartz cementation of deformation bands at deep burial (>2.7km) has been shown to occur through precipitation of silica sourced from detrital grain crushing and dissolution during fault movement. The process of cementation is inferred to follow the closed system model of dissolution-diffusion-precipitation, and is controlled by burial temperature (Fisher *et al.*, 2000). The observation that deformation bands preferentially precipitate quartz because of the increase in clean nucleation sites, suggests this system does not contribute silica to the undeformed rock cementation. The deformation band cements analysed in chapter 6 of this thesis have minimum δ18O values higher than typical Q2 cement in adjacent undeformed sandstones, indicating that authigenic quartz in deformation bands grew from cooler more meteoric rich fluids. The proposed evolution of Hopeman Sandstone porefluid shows that this cementation is likely to pre-date Q2 emplacement, and may be a separate phase. If Q2 silica was supplied from hot fluids dissolving silica in the main fault slip face and the surrounding deformation bands, it would be expected that cement would precipitate in these bands at the same time, if not before, the undeformed sandstone. It

is unlikely that silica transport by diffusion from the deformation features would occur because the clean internal quartz surfaces would act as preferable nucleation sites. This suggests the deformation features were unlikely to be the major source of Q2 silica.

From the above discussion regional scale fluid advection, transporting silica produced from deep basinal clay reactions, is proposed as the most likely source for Q2 cement silica. Dissolution of biogenic sponge spicules cannot be ruled out as a deep basinal silica source.

## 7.22 Scale of fluid flow process.

Many studies have ruled out silica supply from basinal fluid flow because of arguments concerning the low solubility of silica at typical basinal temperatures (e.g. Bjorlykke 1992, Fisher *et al.*, 2000). For many cases it is clear that the volume of fluid required to flow through a sandstone to produce the observed volume of authigenic quartz is at least one order of magnitude greater than the available fluid in the whole basin (e.g. Bjorlykke 1992). To test this, three scales of fluid flow were considered to have been possible for Q2 quartz precipitation in the Hopeman Sandstone;

- local horst-block scale fluid flow,
- Inner Moray Firth, pre-rift, Permian to Mid Jurassic sediments,
- expulsion from the Devonian basement

To discriminate between these 3 scenarios, a simple mass balance calculation was undertaken to determine how much siliceous fluid, expelled from a compacting volume of rock, is required to account for the volume of quartz cement calculated to be present along the entire 3-dimensional extent of the Clashach and Burghead Faults (Appendix G).

The Clashach Fault and Burghead Fault Q2 cementation zones contain a calculated mean Q2 quartz cement volume of 12.2% and 15% respectively. The calculation assumes the Clashach Fault is 4km long and that the Burghead Fault is 20km in length, and that the fault planes cut the entire c.150m of Permo-Triassic sandstones. It assumes that the Permo-Triassic sandstones are cemented along their entire contact with the 2 fault planes (length and height). In reality cement volume may be higher in the centre of the fault planes, and

decrease toward fault margins. The calculated volume of authigenic quartz does not account for any cementation around faults at deeper burial in the basin, or within the overlying Stotfield Chert which may have been silicified during the same process.

The calculation assumes that in the sediment acting to supply silica, 30% of pore volume is destroyed through burial compaction, and that this volume is expelled as a siliceous fluid. The temperature of expelled fluid is taken as 175°C, equivalent to 5km burial (at 35°C/km), and slightly higher than the mean recorded microcrack fluid inclusion Th (166°C) in the Hopeman Sandstone. Final recorded Q2 overgrowth precipitation temperatures were less than 60°C. Silica solubility decreases with temperature, from ~100ppm at 175°C to 30ppm at 60°C, indicating that 70ppm silica would precipitate for this temperature decrease. Compaction of 30% of rock volume would expel 300litres of fluid per $m^3$, which can precipitate $21g/m^3$ of silica for a temperature drop from 175°C to 60°C. The calculated volume of Q2 quartz around the Clashach and Burghead Faults is $9.7x10^{10}kg$. Using these conservative parameters to account for the volumes of cement around the Clashach and Burghead Faults, requires $2 x10^{12}m^3$ of source rock.

A volume of $10^{12}m^3$ can be represented by a number of scenarios. The Inner Moray Firth forms a half-graben basin in which Permian to Top Mid Jurassic sediments define, at present day, a wedge shape which thickens to the north. This wedge reaches a maximum thickness of 3km and extends >30km north-south (Figs. 7.1, 7.2). This Permian to Mid-Jurassic sequence trends for greater than 50km to the northeast, into the eastern Inner Moray Firth. Directly north of the Lossie Peninsula the present day Permian to Top Mid Jurassic reaches a burial depth of 3.5km adjacent to the Helmsdale Fault, and was buried to a minimum of 5km following Late Jurassic extension. This burial depth increases to the east. The volume of a wedge of 25km (NE-SW) x 30km (N-S) x 3km thick sediment is $1x10^{12}m^3$, comparable with the volume of rock required to expel a sufficient amount of fluid to account for the fault-related quartz cement.

The values of Permian to Top Mid-Jurassic sediment thickness represent a minimum, because they measure present day deeply buried, and compacted, volume. Assuming fluid was expelled as the rock was compacted from 40% porosity to a present day porosity of 10% means that 30% of original rock volume has been lost. This means the amount of porous rock required to produce the cement was actually 30% less than the volume of the present

day deeply buried Permian to Mid Jurassic, implying that it is a more than adequate source. The minimum volume of pre-compacted rock is $1.3x10^{12}m^3$, still within the same order of magnitude. This basic deduction of sediment volume assumes a homogeneous, porous, succession of sediment, and so may be considered a high-end case for fluid volume. This simple calculation shows that, assuming precipitation from simple, in-situ, cooling, the siliceous source fluid can reasonably be attributed to basinal sediments, without the need to incorporate Devonian basement sources. However in the following discussion of fluid flow processes, it is also shown that mechanisms of local fluid flow and precipitation may indicate that fluid flux on a scale larger than the sedimentary basin is required. Localised horst scale fluid flow can be ruled out. This basic calculation indicates within an order of magnitude that the cementation could have been the result of a basin-scale fluid flow process.

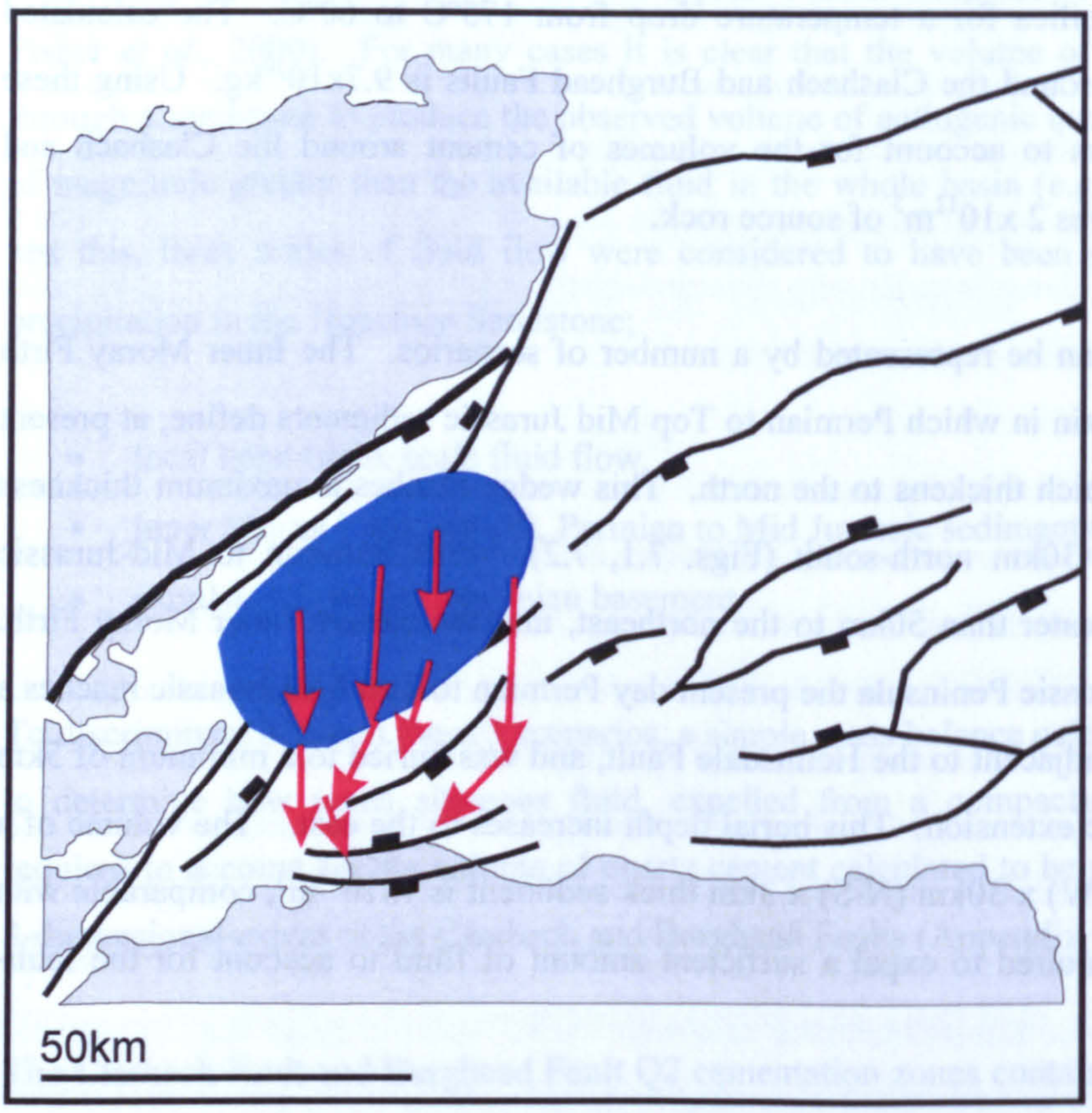


**Fig. 7.1. Cartoon of the required drainage area of the basin to provide the calculated amount of compactional fluid. Fluid travels up-dip toward the basin margin and is baffled by impermeable fault planes. The Hopeman Horst acts as a regional high on the southern basin margin and a focus for the fluid expulsion.**

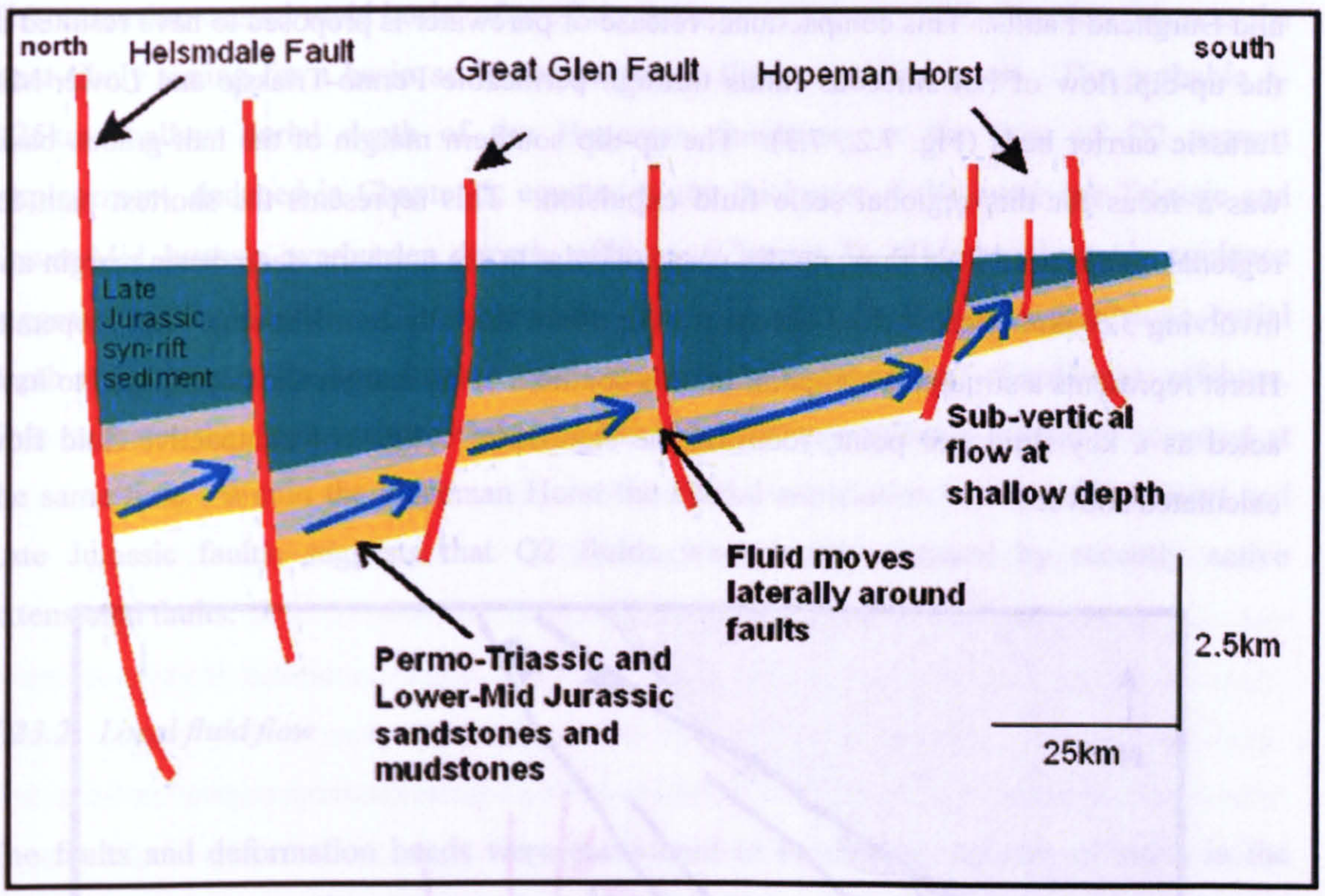


**Fig. 7.2. Cartoon cross-section of the Inner Moray Firth Basin at the end of the Late Jurassic. Pre-rift Permo-Triassic and Lower -Mid Jurassic sediment is deeply buried adjacent to the Helmsdale Fault underneath thick Late Jurassic syn-faulting sediments. Permo-Triassic and Lower to Mid Jurassic burial depth decreases moving south, up-dip. Late Jurassic sediment thins regionally onto the inactive basin margin in the south, and thicknes locally into Late Jurassic faults. Fluid released from sediment compaction flows up-dip through Permo-Triassic and Lower-Mid Jurassic carrier beds, moving laterally around lower permeability fault planes. Fluid ascends within the Hopeman horst where the Permo-Triassic is at shallow depth. Scales and fault extent exaggerated.**

## 7.23 Fluid flow process

### *7.23.1 Basin scale fluid flow*

Q2 cement precipitation from gradual lateral mixing of a hot basinal fluid with a cool background meteoric fluid indicates a focussed entry of a significant volume of basinal fluid into the Hopeman Sandstone. The spatial association of Q2 cement with the two fault planes, and the increasing strength of the hot fluid isotope signature closer to the faults indicates that, within the Hopeman Horst hot fluid ascended along, or parallel to, fault structures.

Compactional fluid flow from deep in the basin has been shown above to have the potential to supply sufficient silica to account for cementation along the entire lengths of the Clashach and Burghead Faults. This compactional release of porewater is proposed to have resulted in the up-dip flow of hot siliceous fluids through permeable Permo-Triassic and Lower-Mid Jurassic carrier beds (Fig. 7.2., 7.3). The up-dip southern margin of the half-graben basin was a focus for this regional scale fluid expulsion. This represents the shortest path for regional compactive fluid flow, up-dip perpendicular to the northern, deep, basin margin and involving 3.5-5km vertical fluid transport over 30km laterally (north-south). The Hopeman Horst represents a structural highpoint on this southern basin margin and is proposed to have acted as a key fluid exit point, focusing the significant volume of compactive fluid flow calculated above.

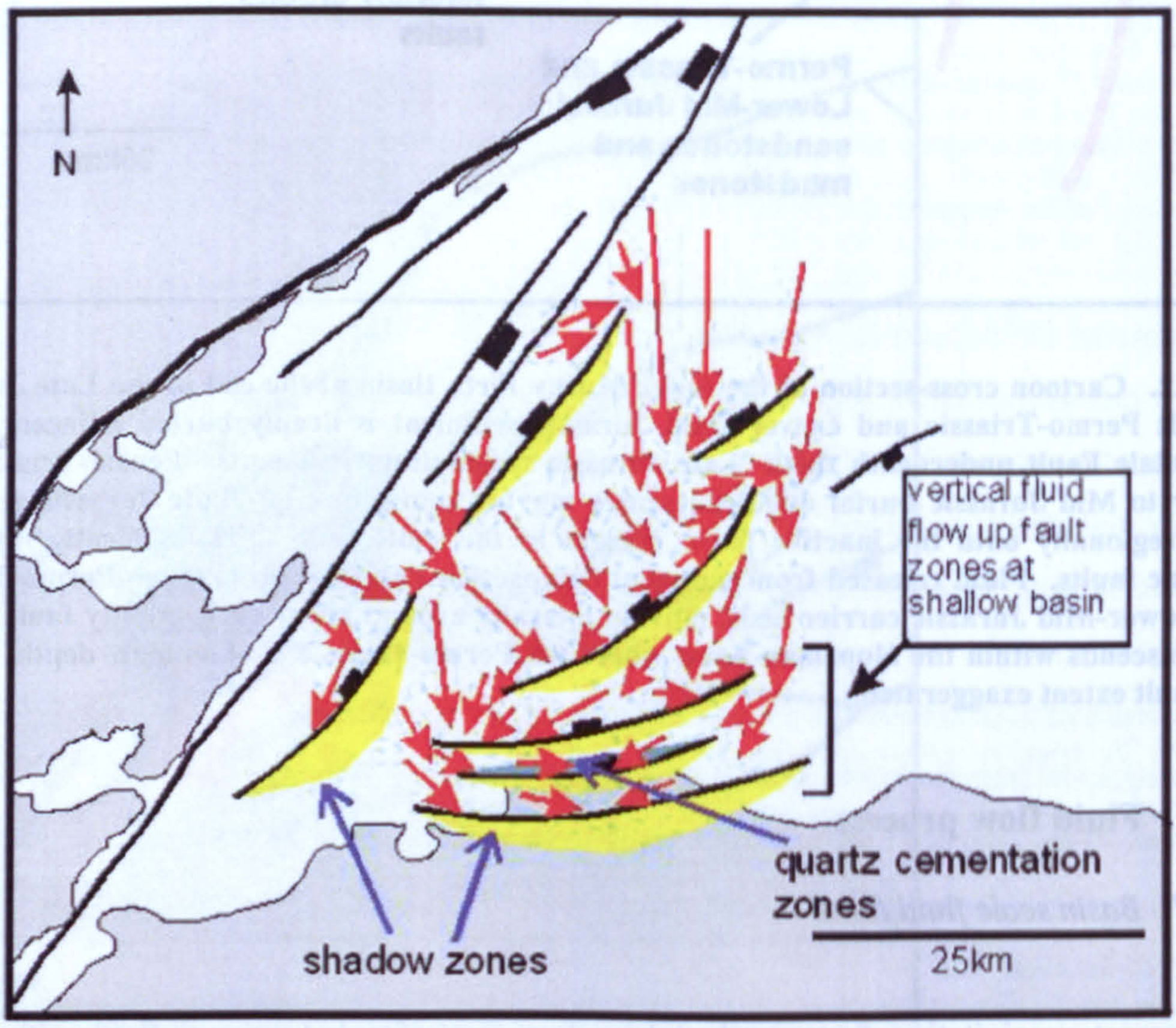


**Fig. 7.3. A projected fluid pathway for compactional, up-dip fluid flow. At deeper burial in the basin faults act as barriers to up-dip advecting fluids, causing the fluid to flow laterally around the structures. The thick Late Jurassic sequence prevents significant vertical flow and expulsion. On the southern basin margin faults within the shallow burial Hopeman Horst direct fluid sub-vertically and into the permeable Hopeman Sandstone. Advecting fluids are absent from 'shadow zones' on the basin margin side of faults. Quartz cementation, from cooling and mixing of hot advecting fluid with cool meteoric porefluid, is concentrated in the basinward footwalls of the Hopeman Sandstone, within the Hopeman Horst.**

The major phase of Inner Moray Firth development was during Late Jurassic basin extension. This extension caused rapid burial of pre-Late Jurassic sediment, indicating that this was the most likely timing for a basin scale compactional fluid expulsion event. The probable 1-1.25km shallow burial depth of the Hopeman Sandstone at the time of Q2 cement emplacement, deduced in Chapter 5, equates to the thickness of the overlying Triassic and Lower-Mid Jurassic overburden directly offshore (Chapter 4). This stratigraphic evidence suggests that the depth of Q2 cementation was equivalent to Hopeman Sandstone burial depth at the onset of the Late Jurassic, and coeval with the deep burial of sediments offshore. This indicates that burial-related fluid expulsion and Q2 precipitation probably occurred at the same time. Within the Hopeman Horst the spatial association between Q2 cement and Late Jurassic faults, suggests that Q2 fluids were locally focused by recently active extensional faults.

### *7.23.2 Local fluid flow*

The faults and deformation bands were considered to be unlikely sources of silica in the discussion concerning silica sources above, but the effect of these structures on basinal fluid flow patterns controlled local silicification. Faults can be considered to have acted either as conduits for fluid flow or as barriers to fluid.

The conduit model involves sub-vertical fluid flow along dilated fault slip faces and deformation bands during active Late Jurassic tectonic displacement. Short-lived dilation and transient increases in permeability are observed in laboratory experiments which create microfaults (e.g. Ngwenya *et al.*, 2003). In porous sandstones, deformation band permeability is observed to reduce to less than the surrounding undeformed sandstone, immediately following displacement. A short injection of fluid moving laterally from the fault into the permeable Hopeman Sandstone could lead to the observed spatial pattern of Q2 cement. This process of fluid injection could occur periodically, during fault displacement, and throughout the duration of tectonic activity, assuming that phases of compaction following extensions cause the pulsed release of more fluid. However it is hard to envisage how silica rich fluids continued to move from the fault, laterally 80m with no grain fracturing effects.

In the model of faults acting as barriers to fluid flow, the low permeability textures of the deformation bands and fault slip face, forming the fault damage zone, are proposed to retard cross-fault fluid flow and direct flowing compactional fluids horizontally or sub-vertically parallel to the main fault slip plane. This process may have been a single continuous process throughout basin extension and rapid compaction of Permian to Mid Jurassic sediment in the deep basin.

Integration of petrographic and stratigraphic data shows that the timing of fluid flow and cementation remains Late Jurassic in either case, indicating that the textural development of the fault planes is a crucial local mechanism. If periodic dilatancy can occur the faults have the potential to act as conduits, if following initial displacement textures are permanently reduced in permeability they will act as fluid barriers.

Previous observations of deformation bands suggests quartz cementation only occurs in significant quantity following burial to 2.7km (>70°C) (e.g. Fisher *et al.*, 2000). Observations here from oxygen isotope data show authigenic quartz precipitation from cool, meteoric fluids, indicating that the quartz precipitated in the deformation bands at burial depths <1km. This suggests that permeability reduction was a consequence of movement on the fault and that the deformation bands acted as low permeability fluid barriers after displacement occurred.

Observation that microfracture and Q2 cements consist of a single cathodoluminescence (CL) phase strongly suggests they precipitated from one fluid event. However, multiple episodes of precipitation from the same fluid cannot be completely ruled out on CL evidence alone, because multiple pulses of fluid may have a similar source. The oxygen isotope and fluid inclusion data suggest that Q2 cement grew from a single continuous period of fluid cooling and mixing. If the Q2 cement had alternatively precipitated from multiple episodes of fluid injection over time it may be considered that these fluid events were likely to differ in scale and fluid composition, leading to increased heterogeneity in the pattern of quartz cement volume and fluid inclusion distribution, which is not observed. The well-defined pattern of fluid mixing and cooling, creating an oxygen isotopic 'mixing line', both through time and spatially away from the faults, suggests a single fluid injection event and prolonged precipitation during mixing. Multiple fluid injections and cooling of the basinal fluid adjacent to the fault planes is likely to lead to rapid precipitation of authigenic quartz, with

little influence from meteoric pore fluids. Mass balance calculations (Appendix G) show that a basin-scale volume of fluid is required to flow into the Hopeman Sandstone to precipitate the observed amount of quartz. Periodic, short-lived dilatancy of the deformation bands during fault activity is proposed to be unfeasible for transporting such significant volumes of fluid into the sandstone.

The measurement of hot fluid inclusions within microfractures indicates that deep to shallow Inner Moray Firth fluid flow was a rapid process. The association of quartz cement with sub-vertical fault planes in the Hopeman Horst block at the basin margin suggests localised lateral or vertical fluid flow led to increased residence time and more rapid cooling, as basinal fluid mixed laterally in permeable shallow Hopeman Sandstone. The inference of this is that only minor quantities of silica precipitated as the fluid ascended toward the basin margin because fluid temperature and composition remained largely unaffected by interaction with the surrounding rock.

The inferred wider cement zone created from extrapolation of measured data surrounding the larger-scale Burghead Fault suggests that fault scale controls the amount of fluid and consequently the amount of quartz cementation. It is speculated that fluids may pass more easily around the fault tips, and at transfer zones between individual fault strands, meaning authigenic quartz may be further concentrated toward the centre of faults.

The asymmetric distribution of quartz cement around the Clashach and Burghead Faults is proposed to be a consequence of the basinward fluid flow towards the footwall. Channelling of compactional basinal fluid flow horizontally and sub-vertically along the fault zones restricted cementation to the footwall. Although deformation bands acted as permeability baffles, the main fault slip face, which accommodates the major displacement, was the lowest permeability feature in the system. The hanging walls appear to have acted as 'shadow zones' in which there is no significant fluid infiltration. Fluid ascended into the footwalls of faults because of their situation on the basinward side of the basin. The lack of any 'shadow zones' in the basin margin side of the deformation bands suggests that the fault slip face acted as the lowest permeability barrier, and the single biggest control on fluid flow in the fault system. The data in chapter 5 suggests that there is an increased volume of quartz cement in hanging wall sandstones immediately adjacent to the faults (<1m). This may represent slow seepage of siliceous fluid across the Clashach Fault slip face through time.

Alternately heat conduction from the hot fluids in the footwall, through the fault plane, may have created a local thermal aureole and caused local internal silicification. Although cementation represents a single continuous period, the maximum timescale for fluid expulsion and silica supply can be considered to be the period of Late Jurassic extension, 20Ma.

The constrained narrow spatial zones of Q2 cementation around the two faults suggests that the hot fluid did not penetrate significantly far from the fault plane. Isotope and inclusion data show a relatively narrow zone of fluid mixing and cooling in the footwalls. Thirty-two metres from the Clashach Fault authigenic quartz records precipitation from dominantly cool, meteoric fluids. If lateral flow from the faults was more extensive it may have resulted in a more homogeneous distribution of cement through the sandstone, as the fluid cooled and mixed with a larger volume. The influx of basin scale volumes of hot fluid, with a temperature of ~166°C, into a sandstone with a cool burial temperature of ~ 20°C to 40°C, means that a significant amount of heat must dissipate locally. The width of the Q2 cement zone is a product of the lateral distance through which the fluid penetrated and cooled. It is hypothesised that the shallow Hopeman Sandstone may have been acting as an aquifer with meteoric fluid flowing parallel to the fault planes. This flow of cool fluid may have acted to buffer the zone of hot fluid adjacent to the fault. This controlled the lateral extent of penetration and cooling of the basinal fluid, creating the observed narrow zones of cement which display precipitation through a continuum of cooling temperatures.

The lack of an internal silica source means that Q2 cement must have precipitated entirely from cooling of the hot basinal fluids, with no local contribution. This presents two hypotheses for the flow behaviour of the basinal fluid in the Hopeman Sandstone. The fluid could have entered the sandstone and cooled adjacent to the fault with little movement, precipitating Q2 whilst locally mixing with the meteoric porefluid. This requires that the basinal fluids cooled entirely in the observed Q2 cement zone by mixing with meteoric fluids, and through conduction of heat into the surrounding rock. Alternately, the basinal fluid may have been flowing laterally or vertically along the fault, with cement precipitation from the incremental cooling, and mixing, of renewed volumes of hot fluid entering the system. This involves precipitation of smaller volumes of silica caused by a small temperature drop of the hot fluid adjacent to the fault. The continuing influx of hot fluids, led to significant quantities of silica being precipitated. Whilst both of these processes are

considered possible, both also contain a number of unknown factors. For example, it may be unrealistic that a basinal volume of fluid does not laterally dissipate over a wide area of the sandstone. Further, complete cooling from 166°C to <60°C without fluid movement from the fault involves significant local re-distribution of heat which may control further temperature-fluid interactions in the rock. For the second hypothesis it is difficult to reconcile incremental cooling, and cementation from a continued flow of hot basinal fluid, with fluid inclusion evidence for cool precipitation during later overgrowth precipitation. Further, this process also requires that a significantly higher volume of fluid passed through the sandstone than that calculated from the mass balance (Appendix G). Further work is required to resolve which may be more realistic

As a comparison to known hot fluid-precipitation processes, the fluid system was a hydrothermal mineral spring which did not reach the surface, a "blind hot spring".

## 7.3 Implications for sedimentary basin evolution

The results of the Hopeman Sandstone case study are used in this section to provide some new insights into the wider understanding of the four principles of sedimentary geology discussed in the thesis introduction: quartz cementation, porosity and permeability evolution, faults as hydrocarbon seals, and mass transfer and basin fluid flow.

### 7.31 Quartz cementation

Quartz cementation sourced from the import of silica into a sandstone has frequently been ruled out as a mechanism for widespread cementation because of the low solubility of silica. In this study it has been shown that silica can be imported into a sandstone by fluid flow, and produce authigenic quartz. Current software models used to predict quartz cementation in sandstone hydrocarbon reservoirs assume an entirely closed diagenetic system of quartz cementation (e.g. Lander and Walderhaug 1999). Several implications for these models arise from the papers presented in this thesis

Cementation in a closed system involves gradual quartz precipitation during increasing burial temperature from 70°C. Hopeman Sandstone Q2 cement was precipitated from a discrete hot

fluid event at shallow burial depth, with a background temperature of 20-40°C. The process was not initiated by gradual burial temperature sandstone reactions, but by the onset of basin wide deformation and large-scale fluid movement. Whilst internal quartz cementation may be triggered by such phases of basin development and consequent deeper burial, the process of cementation occurs on a local scale with silica transport on a scale of 1m. The distribution of cement in this internal model is thought to be controlled by the availability of precipitation sites on clean detrital quartz grains (e.g. Worden *et al.*, 1998). Consequently variation in cement distribution throughout a given sandstone is related to micro-scale relationships such as the occurrence of grain-coating clays, clay laminae and grain size distribution. The distribution of imported quartz cement in the Hopeman Sandstone is primarily related to the position of the faults in the sandstone, which acted as zones of longer fluid residence. The availability of nucleation sites is a secondary control on cement distribution, as demonstrated by the effect of the palaeo-carbonate cement in the footwall of the Clashach Fault which predated quartz cement and prevented its nucleation. Also the quartz cement uniformly affects all sub-facies of the sandstone and is not controlled by any grain coating.

The conclusion that imported quartz cement in the Hopeman Sandstone is related to an individual event in basin development shows that this type of quartz cementation is more likely to occur in particular geological settings. The kilometre scale of fluid flow required to precipitate the observed volume of quartz cement along the Clashach and Burghead Faults indicates that fault-related quartz cementation is not likely to occur along all of the faults of a given basin. Faults and sandstones on basin margins, which may be structurally high 'exit windows' for large volumes of basinal fluid, are more likely locations for this process to occur. The link between fluid expulsion and basin extension indicates that it is also more probable for this quartz cement to occur in pre-rift margin sediments. Within the Inner Moray Firth, and particularly the Hopeman Horst, this suggests that exotic quartz cementation may be present in sediments from Permian to Triassic in age. The pre-rift Lower Jurassic is formed by mudstone which is likely to have acted as a top seal to the fluid flow system, and could not have acted as a significant sink for siliceous fluids. Sediments deposited following major extension will inevitably post-date the associated large-scale fluid expulsion and associated cementation.

The regional North Sea basin continued to develop through a phase of significant extension and burial in the Late Jurassic. This suggests that the large-scale fluid expulsion within the

Inner Moray Firth may have been a regional rift-related event, which also occurred in the Central and Northern North Sea basins. These sub-basins are broadly graben structures and contain many oilfields in pre-rift sediments located in faulted structural highs. If the fluid flow event occurred throughout the North Sea, it may have resulted in the precipitation of quartz cements around the Central and Northern North Sea graben margins.

The global implication of this documented quartz cementation process, is that if it occurs outwith the IMF basin, the timing of development, and the stratigraphic and structural occurrence of the quartz cement are broadly predictable. In the context of current attempts to model quartz cementation this predictability allows bounds to be set on the probability of occurrence of this type of quartz cementation. Further studies may help ascertain whether this process is restricted to the Inner Moray Firth Basin, or is more frequent but undetected, in shallow basin margin sandstones.

## 7.32 Permeability and porosity evolution.

The shallow burial depth of the Q2 cement produces anomalously low porosity and permeability zones within the footwalls of the two observed faults. Clean quartzose sandstones typically show a predictable reduction in porosity, and permeability, with increasing burial depth (e.g. Paxton *et al.*, 2002). At the maximum burial depth of the Hopeman Sandstone, 2.4km, porosity would be predicted to be c.25%, reduced from depositional values of 40-50% principally through mechanical compaction. Chemical compaction and quartz cementation are typically not predicted to occur at depths shallower than this 2.4km threshold. Importing exotic silica means this relationship does not apply uniformly through the sandstone, and porosity and permeability are reduced adjacent to fault planes at shallow burial. The shallow, 500m-1.25km, cementation reduces porosity to <1% adjacent to the fault at Burghead, and permeability to <1mD from predicted values for this depth of >30% and >800mD respectively, for uncemented quartzose sandstones.

As well as anomalously reducing porosity and permeability at this shallow depth the cement arrests further compaction in the most intensively cemented zones, preserving a high intergranular volume (IGV), and so bulk rock volume. Typical shallow sandstone cements are carbonates, which preserve high IGV, but commonly dissolve during deeper burial, as in

the footwall of the Clashach Fault, creating a positive secondary porosity and permeability anomaly with high IGV. Dissolution of significant volumes of authigenic quartz is uncommon. This means that, unlike carbonate cements, shallow authigenic quartz is likely to lead to irreversible porosity and permeability loss. Conversely, at increasing distance from fault planes where quartz cement volume decreases toward background levels, increased porosity may be preserved. Cement precipitated at grain boundaries prior to deep burial, and significant mechanical compaction, may assist in forming a rigid framework to resist the effects of mechanical compaction and pressure solution between detrital grains, at a given depth. The projected zone of cementation in the Burghead Fault footwall is 80m suggesting that although porosity and permeability are significantly reduced adjacent to the fault, a positive porosity anomaly may have been preserved at increased distance from the fault in a deeply buried analogue.

## 7.33 Faults as hydrocarbon traps

Faults in clean sandstones act as baffles and traps to fluid flow by forming low permeability features composed of poorly sorted, crushed, grains and, usually at deeper burial, cements. At shallow depths these faults may act to baffle and control fluid flow on short timescales, but are unlikely to trap fluids for geological lengths of time. At deeper burial faults have been observed to develop quartz cement preferentially to the undeformed sandstone creating significant barriers to fluid flow. The shallow cementation surrounding the Clashach and Burghead Faults onshore shows that the zone surrounding these faults can have permeability <1mD immediately adjacent to the main slip face, in contrast to >800mD at distance from the faults. Such shallow depth permeability loss will cause the footwall zones around the faults to act as fluid barriers and compartmentalise a reservoir on production timescales. Faults in analogous settings in the subsurface would not be predicted to affect fluid to such a degree because they have not reached the typical burial depth for enhanced cementation. The inference for hydrocarbon reservoirs is that fault-related cementation can act to trap hydrocarbons and compartmentalise sandstones, at a shallower burial depth than expected, during oilfield production. Faulted sandstone which may be proposed to act as carrier beds that allow hydrocarbons to flow through them may be affected by such cementation. Fluid flow on a basin scale may also be affected, reducing the possibility of further cementation sourced from regional fluid flows.

The oxygen isotopes analysed within a deformation band showed that quartz cement developed under cool conditions prior to precipitation of the shallow fault-related Q2 authigenic quartz. Previous studies have shown that quartz cement precipitates in deformation bands under typical burial temperature conditions for internal quartz growth (Fisher *et al.*, 2000), however the data in this study indicates that the deformation band cement grew at a cooler temperature than this, at <60°C. The deformation bands appear heavily cemented. Throughout the sandstone only minor (<5%) Q3 burial quartz cementation is present, showing that although the deformation band cements grew at a lower than typically expected temperature, they precipitate prior to burial quartz in the undeformed sandstone. The observation of shallow deformation band quartz cementation is significant for predicting the behaviour of faults as hydrocarbon seals. Many shallow faults may be ruled out as seals because it may not be considered that they have been buried to a sufficient depth, and so temperature, for quartz cement growth. Shallow fault cements may also act to baffle fluids and compartmentalise hydrocarbon reservoirs at depths less than presently predicted.

There is no evidence that the deformation band authigenic quartz is genetically related to the subsequent Q2 and Q3 quartz cement, suggesting that cementation was an independent, local, closed system diagenetic process. The probability of quartz cementation in deformation bands at shallow depths in other porous sandstones is therefore high.

## 7.34 Mass transfer and basinal fluid flow regimes.

Diagenetic models of basinal fluid flow are traditionally divided into two categories, those favouring a slow and gradual porefluid movement as basins subside and fill with sediment (e.g. Giles *et al.*, 1992, Bjorlykke 1994), and those where fluid flow events occur periodically on a regional scale transferring large amounts of solutes for precipitation (e.g. Burley *et al.*, 1989, Hippler 1993). Quartz cementation is a volumetrically significant diagenetic cement in sedimentary basins and so insights into silica mobility provide information on basinal fluid regimes.

The proposal in this thesis of silica transport by basin scale fluid expulsion suggests that basin scale fluid flow does occur within hydrocarbon basins. In contrast, the model of internal quartz cementation implies closed hydrologic systems with no, or only minor, mass transfer between sedimentary units. Whilst this process of quartz cementation, and hydrologic regime, is well documented for many deeply buried sandstones in the North Sea and globally, by the nature of oilfield studies the datasets are taken from deeply buried sandstones typically avoiding structural features. The case for a closed hydrologic regime is primarily based upon such studies. However, the well documented case for basin scale fluid flow presented here shows that such closed porefluid systems can be punctuated by periods of large scale fluid movement, and mass transfer, relating to regional tectonic events. This thesis also suggests that this process may have remained undetected in many basins because the principal diagenetic products are probably silica cements which, even with such extensive fluid flows, are volumetrically small. The calculation here of the amount of fluid required to precipitate cement along well-exposed small and medium scale faults shows that the physical evidence of this fluid flow will be difficult to detect in the subsurface. It also indicates that studies of deep basin structures may have found no diagenetic evidence for fault-fluid interaction because the fluid flow and mass transfer process occurs on the basin scale. Regional geologically rapid compactional fluid flow involves hot solute rich fluids flowing to shallower levels where the lack of temperature and chemical equilibrium between cool porefluids and hot evolved basinal fluids acts as a drive for precipitation. In this case quartz cement is produced. The link made between basin extension, sediment burial and fluid flow suggests that phases of major basin development cause regional scale fluid flow and mass transfer. Outwith these periods more gradual compaction is likely to produce slow vertical porefluid movement. Fluids moving in this gradual manner are closer to equilibrium with local conditions and so cannot transport significant amounts of solute.

The proposal that Q2 cementation in this case is the product of a fluid which cooled more rapidly during local migration, than it cooled during rapid lateral migration from the basin, indicates that the process of mass transfer can involve rapid transport of solute from one set of end member conditions to another. This may mean that only minor precipitation of material occurs within the transport pathway. In other cases, where fluid from a wide basin region is not focussed through a single structural feature, cements may be expected to be more widespread, forming a broad margin zone of diagenetic material.

Lead-zinc, Mississippi-Valley Type (MVT), mineral deposits also present within the Hopeman Horst, and documented in chapter 5, show that the peninsula acted as a window for fluid expulsion later in the basin history, potentially during regional Palaeocene uplift. Petrographic evidence shows that MVT fluids post-date Q2 quartz cementation. This mineralisation occurs throughout the Lossie Peninsula, and is not found elsewhere in the basin (Naylor *et al.*, 1989). This suggests a similar large-scale fluid flow event occurred and was focused toward the basin margin and into the Hopeman Horst. This second, proposed event, transported lead, zinc and fluorine. MVT deposits are typically found on basin margins in carbonates, but also in sandstones (Bjorlykke 1980), formed from large-scale up-dip fluid migration. Within the basin the Top Triassic chert is a silicified carbonate palaeosol (Naylor *et al.*, 1989) which is situated directly below the Lower Jurassic mudstones. Silicification of the chert has previously been interpreted as a burial cement (Naylor *et al.*, 1989). It is proposed here that the chert may have been silicified by the same fluid flow process that resulted in exotic authigenic quartz in the underlying Hopeman Sandstone. The basinwide extent of the Top Triassic horizon suggests that the Stotfield Chert represents the uppermost unit in this fluid flow system and that the Triassic sandstones may also be silicified in close proximity to structural features. This idea is reinforced by the presence of lead-zinc mineralisation within the Lower Triassic and Stotfield Chert in the Lossie Peninsula.

The proposal of basin-scale fluid flow on this scale is not considered unusual in this mineralisation context. The model of macro-scale diagenetic fluid flow in a hydrocarbon basin, combined with the observation of an MVT fluid flow event in the same basin, shows there may be a genetic structural link between the two processes, and the two 'types' of basin. Basin dimensions and structural development are proposed to form the major control on fluid flow and mass transfer. The geometry of small to medium sized half-graben basins such as the Inner Moray Firth may possess optimum dimensions to contain sufficient fluid and a focused pathway to precipitate the observed volumes of cements and minerals.

This page left blank

# Chapter 8.

# Conclusions and Future Work

This thesis presents the results of field and laboratory investigations into quartz cementation in porous sandstones. These studies have been used to further understand several areas of sedimentary geology; quartz cementation, porosity and permeability evolution, faults as hydrocarbon seals and mass transfer and basinal fluid flow.

## 8.1 Conclusions

- The Inner Moray Firth Basin developed through a series of Late Jurassic extensional faults which characteristically trend ENE-WSW and E-W. The Clashach and Burghead Faults are exposed onshore within the Lossie Peninsula, on the southern basin margin, where they displace U. Permian Hopeman Sandstone. These two faults are Late Jurassic extensional structures analogous to offshore faults in the basin. Displacement across the Clashach Fault is <50m and across the Burghead Fault is >100m. Integration of offshore seismic survey data with geological measurements of onshore exposures has allowed the Lossie Peninsula to be interpreted as a Late Jurassic horst block, bound by the Blind Zone fault offshore to the north, and the Spynie Fault to the south. This structural feature is named the Hopeman Horst and the Clashach and Burghead Faults form intra-horst features.

- Shallow burial depth (<1.25km) quartz cementation occurs in an asymmetrical pattern across the Clashach and Burghead Faults. Hanging wall sandstones contain a mean quartz cement of <5%. Moving through the fault planes, footwall sandstones display a pattern of decreasing quartz cement with increasing distance from the fault plane. Authigenic quartz volumes decrease from >25% adjacent to the fault planes to background levels of <5% at >32m at the Clashach Fault, and >80m at the Burghead Fault. Footwall quartz cementation is likely to be regionally extensive. Porosity is reduced by >20% adjacent to the faults and rises with increasing distance from the fault planes. Permeability in poorly cemented hanging wall sandstones is 100-1000mD and is reduced to 0.1-10mD in heavily cemented footwall sandstones. The Hopeman Sandstone acts as an analogue to offshore hydrocarbon reservoirs. The fault-associated quartz cement acts to enhance reservoir compartmentalisation and to create low permeability zones around faults which may retard fluid flow. The scale of the footwall cement zone increases positively with fault size, and at the Clashach Fault is 0.8 x fault throw. At the Burghead Fault the cement zone is 0.5 x fault throw.

- Two fluid inclusion assemblages are present in Clashach and Burghead Fault footwall sandstones. A set of 2-phase, liquid and vapour, inclusions found within quartz-cemented microcracks yielded a mean homogenisation temperature of 166°C. These microcracks are interpreted to be a product of local movement on the fault planes and record the presence of hot fluids in the shallow buried Sandstone. A set of single phase, aqueous inclusions, were observed in footwall quartz overgrowths, representing cementation from cool fluids, <60°C. The cathodoluminescence signature between the microcrack and overgrowth cements is continuous. Combined with the fluid inclusion data authigenic quartz oxygen isotope ratios ($^{18}O/^{16}O$) record growth from hot basinal fluids adjacent to the two fault planes. Isotope values become increasingly positive moving through the footwall, away from the fault plane, recording mixing of the hot basinal fluids with cool meteoric pore fluid. In the hanging wall, quartz cement oxygen isotopes record growth from evolved meteoric fluids, following precipitation of the cementation phase around the fault planes. Positive $\delta^{18}O$ values within deformation band authigenic quartz reveal cementation from meteoric fluids at shallow depth (<500m).

- Many previous workers have predicted that quartz cement development occurs through deep burial (to >70°C), and that intra-sandstone distribution is controlled by textural and detrital variation. Quartz cementation in the Hopeman Sandstone is localised around extensional fault planes, cross-cuts facies, and was emplaced at shallow burial depth (<1.25km). Such shallow cementation causes a reduction in porosity and permeability at depths below that currently predicted by many diagenetic models, and has an increased effect at larger-scale faults. The Hopeman Sandstone crops out in the Hopeman Horst and acts as a sedimentological and structural analogue to many buried hydrocarbon reservoirs. In such reservoirs the fault-related quartz cementation would act to reinforce structural compartmentalisation, and as a fluid seal during production of hydrocarbons. Predictions of quartz cementation also need to account for structural setting and basin history, as well as internal sandstone characteristics and burial history. The extensive quantitative dataset of fault-related cementation effects presented here can be used in reservoir models where a similar phase is thought to be present.

- The case study presented in this thesis has shown that quartz cementation can develop within an open diagenetic system. The recorded cooling of advecting deep basinal fluids at shallow depth shows that fluid flow, and mass transfer of silica on a basin scale, can occur. Extensional cataclastic faults can become quartz cemented, even at shallow depths, forming baffles to regional fluid flows and affecting flow pathways. Fluids can move between faults, and also where segments of individual structures meet. Locally fluid flow is focused in a fault parallel direction, but in shallow basin margin locations flow may be sub-vertical. Rapid large-scale fluid expulsion, caused by extension-related compaction, may lead to the concentration of diagenetic phases in similar basin margin settings.

## 8.2 Future Work

- The geological data gathered on the origin of the fault-related cement, which precipitated at shallow burial depths from hot basinal fluids, provides well-

constrained parameters for detailed geochemical and heat flow modelling. Through such models the constraints placed on the basin-scale process of cementation can be tested. The geological data suggests fluid flow occurred at a very rapid rate, conserving heat during transport. Estimates of the possible timing and duration of this process will allow further understanding of the geological model, particularly in relation to fluid sources and flow pathways.

- Local-scale modelling could make an interesting future step. Two hypotheses were proposed in Chapter 7 concerning the behaviour of the hot basinal fluid following entry into the Hopeman Sandstone. Comparative computer modelling of these processes may show the predicted cementation patterns expected to result from each case. The effect of different flow rates and local fluid pathways can be investigated and compared to the geological data presented here. It may also give some further insights into the questions relating to heat dissipation at shallow burial.

- Mississippi-Valley type lead-zinc mineralisation within the Hopeman Sandstone can be investigated further. Petrographic data shows that the mineralisation post-dates fault-associated quartz cement, but appears to be localised around faults, and in fractures, within the Lossie Peninsula. Geochemical investigations and modelling projects may reveal whether this represents a second basin scale fluid flow event, perhaps occurring during regional Tertiary exhumation.

- Wider geographical investigations are required to determine if the process of quartz cementation documented within the Inner Moray Firth was a localised basin-specific event, or alternatively, whether it may be characteristic of basin margin settings in extensional rift basins. Documenting additional cases of similar cementation will assist in characterising the conditions under which fluid flow and mass transfer can occur in sedimentary basins.

- Broader integration of studies in petroleum and mineral basins needs to be considered as an important future direction. The process of basin-scale fluid flow is more typically proposed in mineralised basin settings. Utilising data relating to the fluid regimes in mineral basins may assist in unravelling many diagenetic features of petroleum basins, and aid in a more thorough understanding of the mechanisms of mass transfer.

This page left blank

# Appendix A – Onshore to offshore structural integration

Projection of offshore Top Triassic seismic horizon to outcrop onshore

**Aim:** To calculate the position at which the seismic Top Triassic should outcrop onshore, assuming no structural control in the blind zone between the edge of the seismic data and the onshore exposures.

**Method:** Calculation of the Top Triassic dip and burial depth at the southern edge of the seismic lines directly offshore; imf97-201, 202, 203. Three seismic velocities were used to account for variability in the true value; theoretical values used were 2000m/s and 3000m/s. The mean calculated Lower –Mid Jurassic seismic velocity, 3600m/s, from Beatrice wells 11/30-1 and 11/30-2 was also used. Mean dip was calculated, for each velocity, over a significant length of the southernmost portion of each seismic line. This was used to project the height above sea level that each horizon would crop out onshore.

**Example calculation for seismic line 201.**

Data gathered from seismic line:

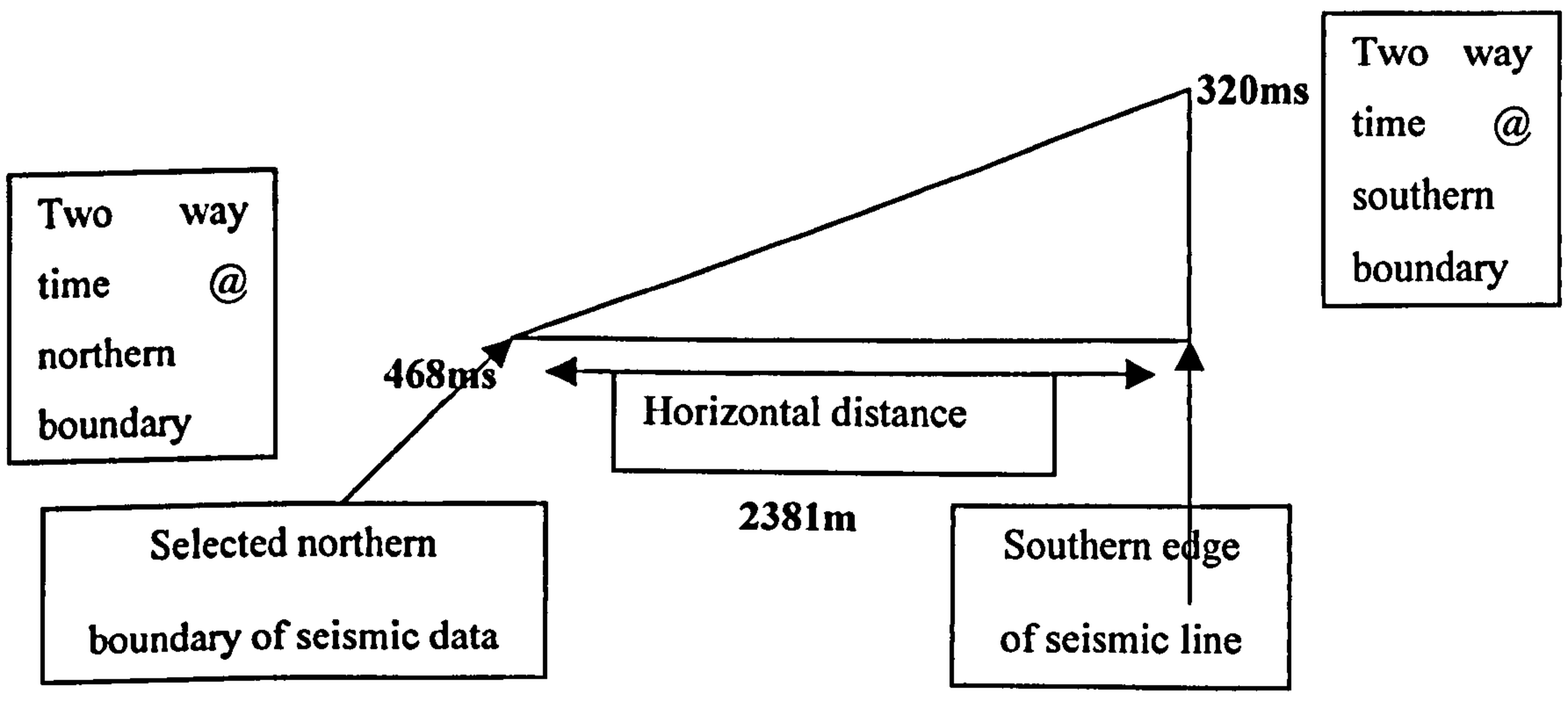

Step 1 – Calculation of Top Triassic burial depth on seismic data.

Burial depth at southern edge seismic = 320ms (TWT) /2 = 160ms (one-way time)

160/1000 =0.16secs *seismic velocity (m/s)

*2000m/s *3000m/s *3600m/s

**=320m = 480m = 576m**

Burial depth at selected northern boundary of utilised seismic data
= 468ms (TWT)/2 = 234ms

234/1000 =0.234secs*seismic velocity (m/s)

*2000m/s *3000m/s velocity *3600m/s

**=468m =702m =842m**

***Step 2 – Calculation of the dip of the Top Triassic horizon for each velocity.***

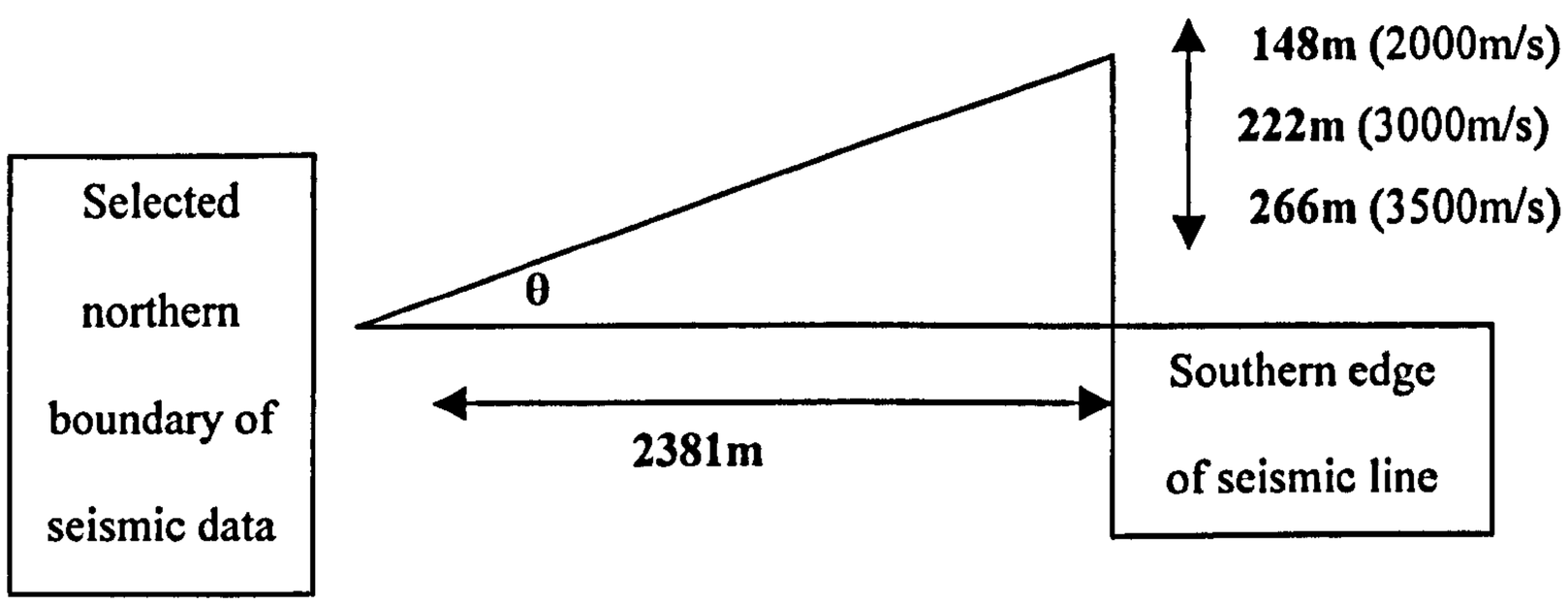


Top Triassic dip =

Tan θ = <u>depth between northern and southern edge of seismic data (m)</u>
horizontal traverse (m).

| For 2000m/s | For 3000m/s | For 3600m/s |
|---|---|---|
| Tan θ = 148m/2381m | Tan θ = 222m/2381m | Tan θ = 266m/2381m |
| Tan-1*(148/2381) | Tan –1* (222/2381) | Tan-1*(266/2381) |
| Dip = 3.6° | Dip = 5.3° | Dip = 6.3° |

<u>Step 3</u> – Calculation of the projected onshore outcrop of the seismic Top Triassic

The aim is to project the horizontal distance from the southern edge of the seismic line to its outcrop position onshore, at 60-80m above sea level, using Top Triassic dip and burial depth for each of the 3 seismic velocities.

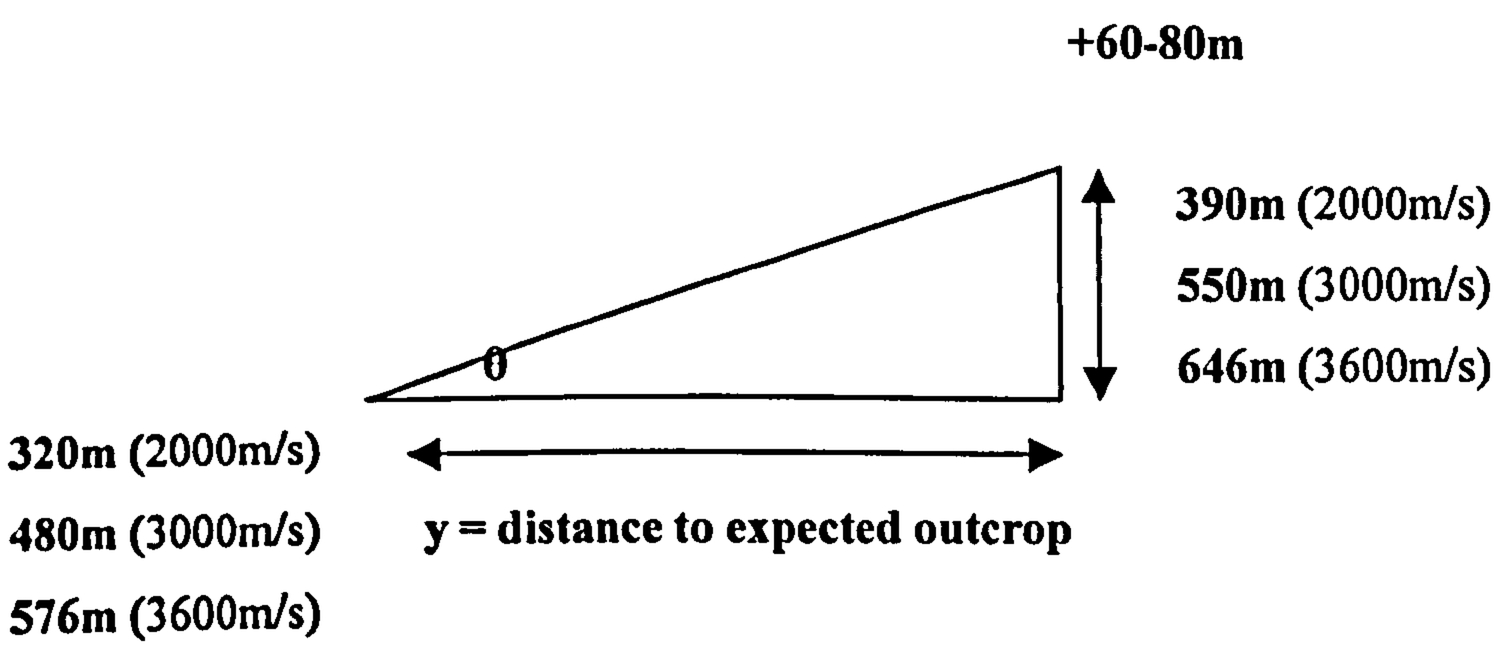


where **θ = 3.6°** (2000m/s), **5.3°** (3000m/s) **and 6.3°** (3600m/s)

y (distance to expected outcrop from southern edge of seismic line) :

For 2000m/s For 3000m/s For 3600m/s

**θ = 3.6°** **θ = 5.3°** **θ = 6.3°**

Tan 3.6 =390/ y Tan 5.3 = 550/y Tan 6.3 = 646/y

y =390/tan 3.6 y = 550/tan 5.3 y = 646/tan6.3

**y = 6199m** **y = 5928m** **y = 5851m**

***<u>Step 4</u> – Calculation for lines 202 and 203.***

The same methodology was used for lines 202 and 203 to produce an equivalent set of values, which were used in constructing scaled cross-sections in Chapter 4.

| seismic line | velocity (m/s) | depth (north) (m) | depth (south) (m) | mean dip | (y) distance to outcrop (m) |
|---|---|---|---|---|---|
| 202 | 2000 | 348 | 268 | 4.4° | 4080 |
| | 3000 | 522 | 402 | 6.5° | 3932 |
| | 3600 | 626 | 482 | 7.8° | 3854 |
| 203 | 2000 | 310 | 248 | 5° | 3326 |
| | 3000 | 465 | 372 | 7.4° | 3195 |
| | 3600 | 558 | 446 | 8.9° | 3123 |

# Appendix B – Calculation of 'Blind Zone' fault throw

**Calculation of displacement on Blind Zone fault.**

**Aim:** To quantify the displacement of the northern Hopeman Horst, 'Blind Zone' fault, to allow determination of the horst block scale and to test the sensitivity of the model.

**Method:** Compare the depth of the Top Triassic horizon projected from onshore to offshore (as measured from cross –sections, chapter 4), with the burial depth of the Top Triassic on seismic data on the southern edge of seismic survey coverage.

**Example calculation for seismic line 201.**

Data gathered from seismic line:

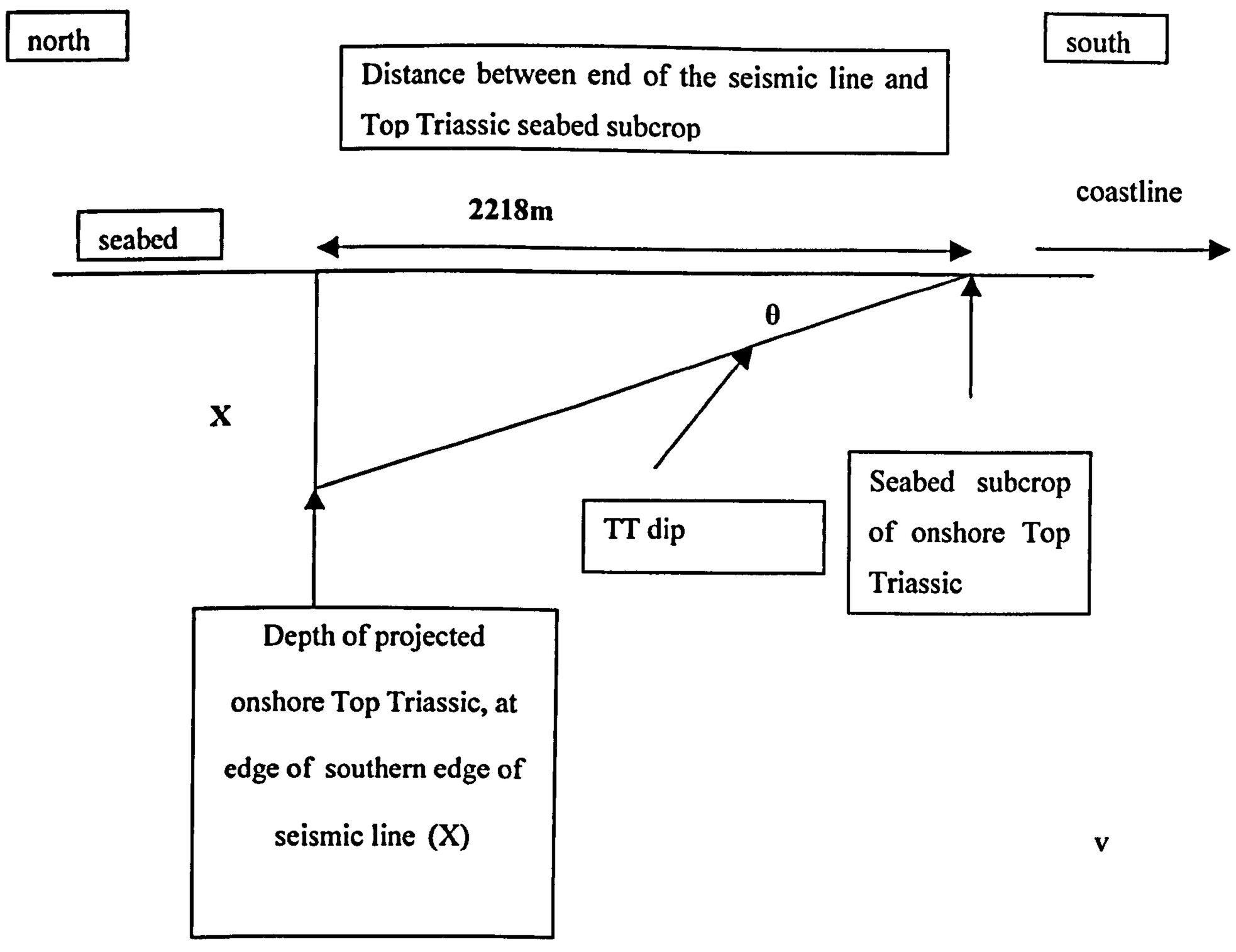


v

**<u>Step 1</u> -Depth of projected onshore Top Triassic at the southern edge of seismic line:**

Burial depth of onshore Top Triassic along profile of line 201(X) =

| For 2000m/s | For 3000m/s | For 3600m/s |
|---|---|---|
| **θ = 3.6°** | **θ = 5.3°** | **θ = 6.3°** |
| **Tan 3.6 =X/2218** | **Tan 5.3 = x/2218** | **Tan 6.3 =x/2218** |
| **X = tan3.6*2218** | **X = tan5.3*2218** | **X = tan6.3*2218** |
| **X=140m** | **X=206m** | **X=245m** |

True burial depth of Top Triassic at the southern edge of seismic data (Appendix A)=

| For 2000m/s | For 3000m/s | For 3600m/s |
|---|---|---|
| **=320m** | **=480m** | **=576m** |

True vertical (fault) displacement, calculated for each velocity, equals true total burial depth (from seismic data) - depth of projected onshore Top Triassic at the edge of the seismic line:

| For 2000m/s | For 3000m/s | For 3600m/s |
|---|---|---|
| =320-140m | =480-206m | =576-245 |
| **=180m** | **=274m** | **=331m** |

***<u>Step 2</u> - Calculation for lines 202 and 203.***

The same methodology was used for lines 202 and 203 to produce an equivalent set of values, which were used in constructing scaled cross-sections in Chapter 4.

| seismic line | velocity (m/s) | (X) onshore depth (m) | seismic depth (m) | fault displacement (m) |
|---|---|---|---|---|
| 202 | 2000 | 146 | 268 | 122 |
| | 3000 | 217 | 402 | 185 |
| | 3600 | 260 | 482 | 222 |
| 203 | 2000 | 161 | 248 | 87 |
| | 3000 | 239 | 372 | 133 |
| | 3600 | 288 | 446 | 158 |

# Appendix C – Sample location surveying method

**Aim:** To convert the raw data collected from the TopCon 'total station' surveyor into the true perpendicular distance of each sample from the fault plane in Clashach Quarry.

**<u>Step A</u> – Raw field data.**

The TopCon instrument is placed at a fixed base station position for the entire set of surveying. This represents a point of origin from which the instrument measures the true distance (m) to the sample point along 3 planes, in x,y,z, and the horizontal angle from the origin (Fig. C1).

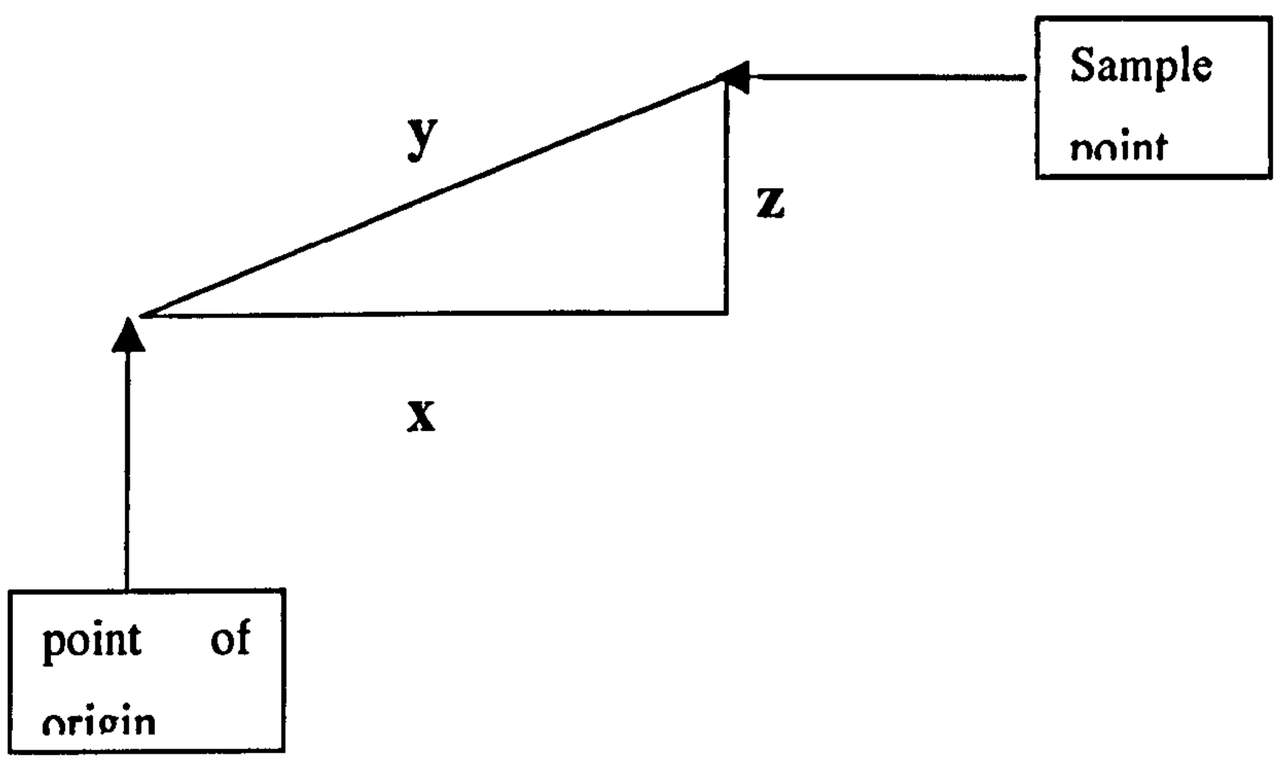

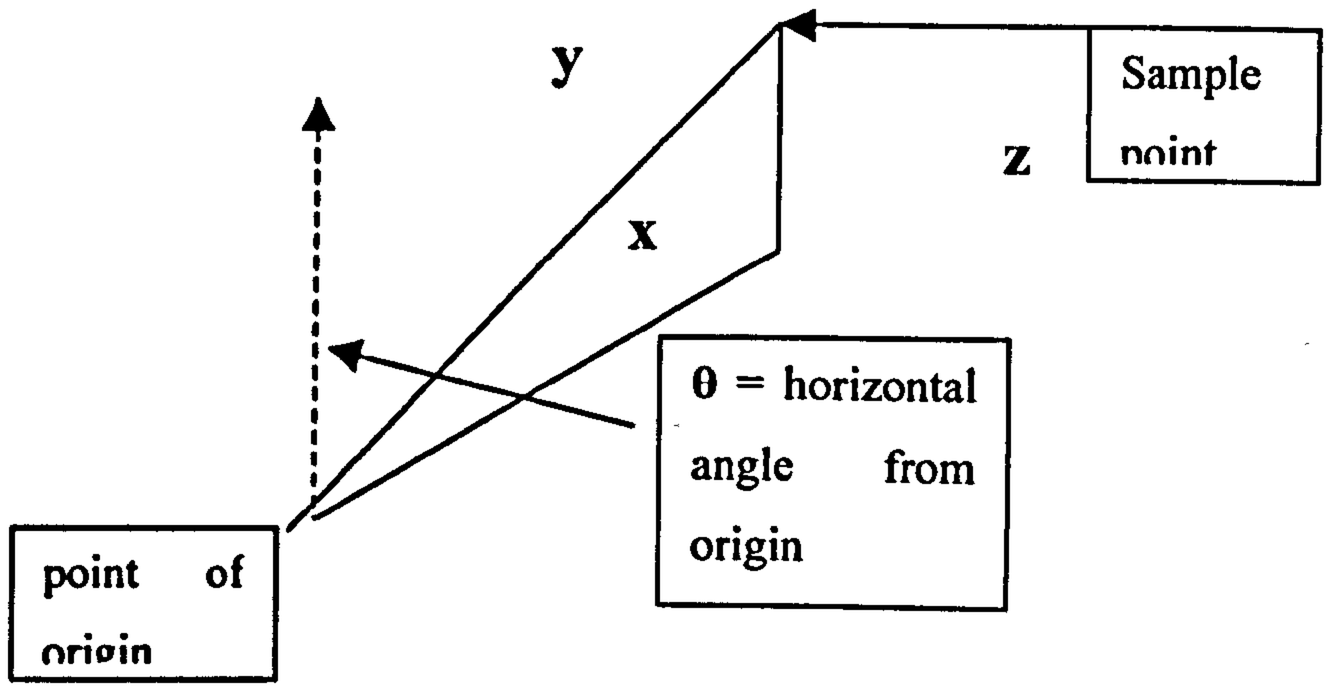


**Fig. C1.** Diagrams representing data collected by the TopCon surveying instrument.

***<u>Step B</u> – Convert the raw distance data to a set of cartesian co-ordinates ($x^1$,$y^2$,$z^3$).***

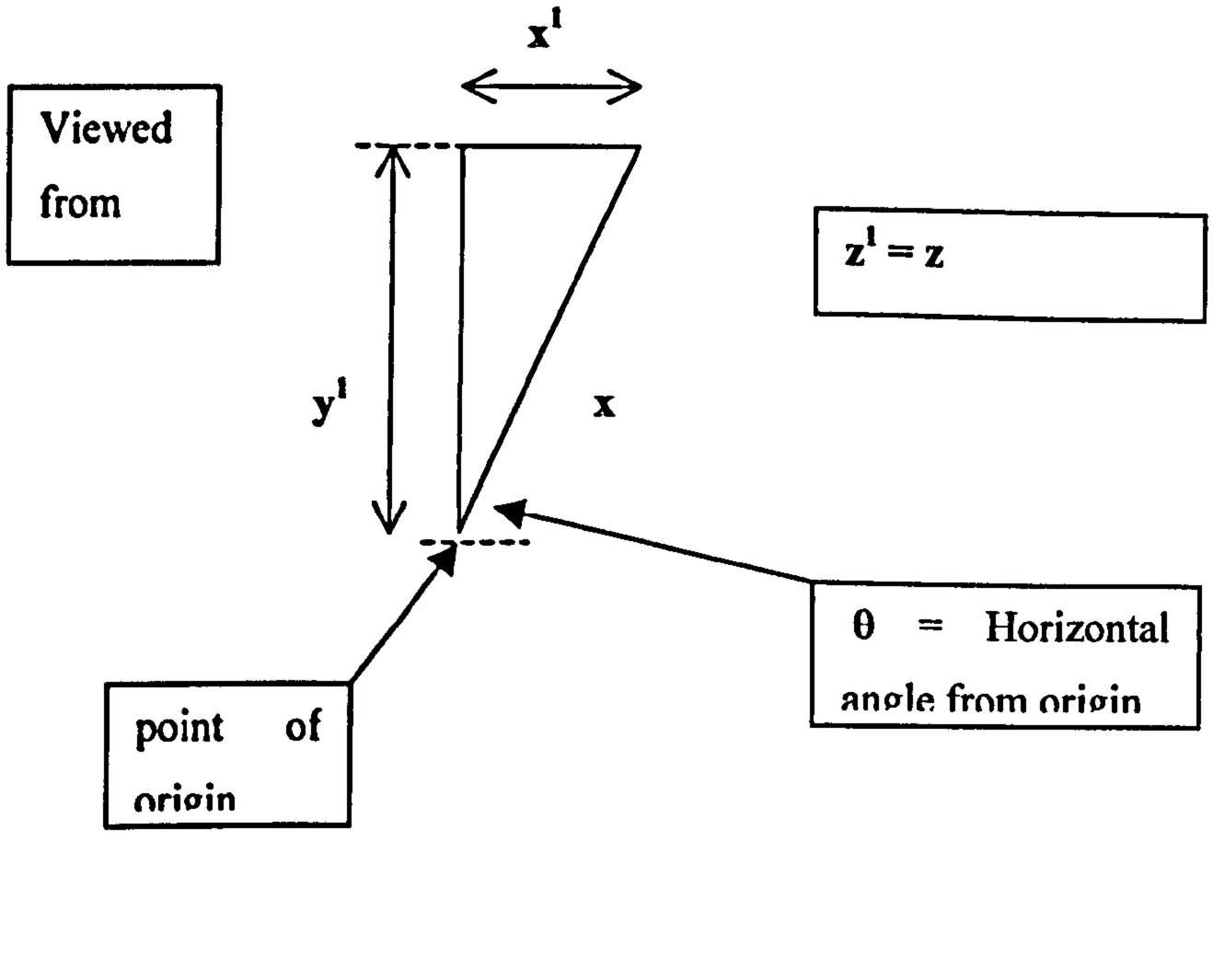

$\underline{X^1}$

$X = \sin \theta$

$\mathbf{X^1 = X \sin\theta}$

**So each x value is multiplied by sin θ.**

**Calculations were done in Microsoft Excel, which uses radians.**

**As an example, for point C1:**

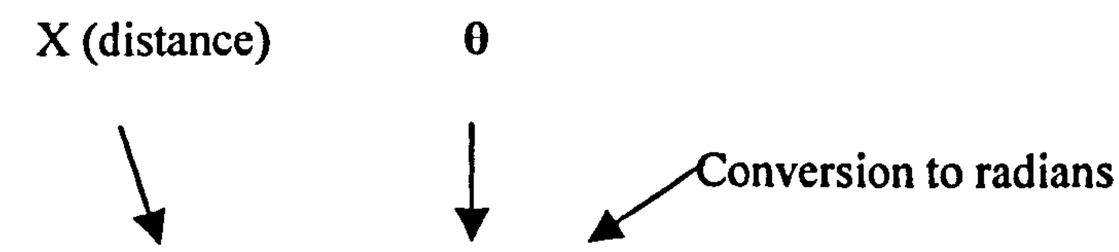


$X^1 = 70.177(\text{Sin}((47.240 \text{x} 0.01743)))$

$X^1 = 51.524$

$\underline{Y^1}$

$Y = \cos \theta$

$\mathbf{Y^1 = X \cos\theta}$

**For C1:**

$Y^1 = 70.177(\text{Cos}((47.240 \text{x} 0.01743)))$

$\mathbf{Y^1 = 47.646}$

Step C – Calculate the position of the Clashach Fault plane by computing the equation of 3 points which were surveyed on the exposed fault plane. Fault plane survey points were measured directly adjacent to the sample sites, allowing an accurate surface orientation to be calculated.

The equation of a plane through:

$(x_1, y_1, z_1)$, $(x_2,y_2,z_2)$, and $(x_3,y_3,z_3)$

in determinant form:

$$\begin{vmatrix} x-x_1 & y-y_1 & z-z_1 \\ x_2-x_1 & y_2-y_1 & z_2-z_1 \\ x_3-x_1 & y_3-y_1 & z_3-z_1 \end{vmatrix} = 0$$

to evaluate the determinant:

$$\begin{vmatrix} a_1 & b_1 & c_1 \\ a_2 & b_2 & c_2 \\ a_3 & b_3 & c_3 \end{vmatrix} \text{ is } (a_1[b_2c_3-c_2b_3] - b_1[a_2c_3-c_2a_3] + c1[a_2b_3-b_2a_3]) = 0$$

which for this case is:

$$\begin{aligned} &(x-x_1)[(y_2-y_1)(z_3-z_1)-(z_2-z_1)(y_3-y_1)] \quad (=a_1) \\ &-(y-y_1)[(x_2-x_1)(z_3-z_1)-(z_2-z_1)(x_3-x_1)] \quad (=b_1) \qquad = 0 \\ &+(z-z_1)[(x_2-x_1)(y_3-y_1)-(y2-y_1)(x_3-x_1)] \quad (=c_1) \end{aligned}$$

which simplifies to:

$$(x-x_1)a^1 -(y-y_1)b^1+(z-z_1)C^1 \qquad = 0 \qquad (1)$$

the equation needs to be in the form:

$$ax+by+cz+d = 0$$

Re-casting **(1)**:

$$a^1x-a^1x_1-b^1y+b^1y_1+c^1z-c^1z_1= 0$$

$$a^1x-b^1y+c^1z-[a^1x_1-b^1y_1+c^1z_1] = 0$$

a1, b1, c1, and x1, y1, z1 are known for each point on the fault plane:

$$a = 5.44646$$

$$b = -21.274$$

$$c =-68.404$$

---

***Step D – The formula which expresses the perpendicular distance from sample point coordinates x1,y1,z1 to the fault plane.***

ax+by+cz+d = 0 is

$$\left| \frac{ax1+by1+cz1+d}{\sqrt{a2+b2+c2}} \right|$$

The value of this expression is the perpendicular distance to the fault plane.

Given x,y,z, for each of the sample points in Cartesian coordinates and knowing a,b,c and d from the fault plane equation allows the perpendicular distance from each sample to the fault plane to be calculated

# Appendix D – Petrographic Techniques

## A - SEM-CL point count method

Scanning Electron Microscopy (SEM) allows high magnification (up to 100 000x) imaging of objects which is not achievable with traditional optical microscopes. The SEM used in this study was a Phillips XL-30. The basic operation of the SEM involves generation of electrons in an electron gun which are accelerated across a vacuum forming a beam. This beam is focused using electromagnetic lenses and is scanned across the sample surface.

Images are formed by the emission of electrons from the sample. Two types of electron are emitted; low energy secondary electrons and high energy backscattered electrons (BSE). The electron beam also creates Cathodoluminescence (CL) and X-rays. Each of these emitted signals can be collected by individual detectors, allowing a number of different images to be formed. High magnification images are produced using both secondary (SE) and backscatter electrons (BSE). Backscattered electrons can be detected separately. CL images are produced using a specific luminescence detector attached to the SEM, which collects CL light emitted during interaction of the normal electron beam on the sample surface. CL images allow phases with different luminescence to be identified accurately, but can mask textural features. However, both CL and SE images can be combined in any proportion to produce a mixed CL-SE image.

In this study CL, SE and mixed CL-SE images were produced of each sandstone thin section. Quartz overgrowths can be difficult to quantify accurately with optical microscopy (Evans *et al.*, 1992). CL signatures are thought to be controlled by trace element variations and crystal lattice defects (Zinkernagel 1978). Authigenic and detrital quartz typically have different CL signatures, which may be related to aluminium variation (England and Kelly pers. comm. 2004), and allowing highly accurate identification of each.

Two to four images of each thin section were taken and printed off on a high quality inkjet printer. A grid was constructed on transparent material, A4 paper size, which contained 450

points. This grid was overlain on each printed SEM-CL/SE image and the material under each point recorded using a manual point count machine. Point count categories were: detrital quartz, detrital K-feldspar, rock fragments, iron mineralisation, authigenic quartz, authigenic feldspar and porosity. Minor secondary porosity is a minor component (1-2%).

**B- Calculation of CEPL, COPL and Intergranular volume**

Point count data was used to calculate the percentage of porosity lost to cementation (CEPL) and the amount to compaction (COPL).

CEPL and COPL were calculated using the method of Ehrenberg (1995):

(1) $$COPL = \frac{OP - (100*IGV) - (OP*IGV)}{(100-IGV)}$$

(2) $$CEPL = (OP- COPL) *CEM/IGV.$$

Where,

OP = Original porosity; IGV = Intergranular volume; CEM = volume percent intergranular cement.

Cementational porosity loss is simple to quantify because it is a direct measurement of a present-day phase. Compactional porosity loss is more difficult to quantify and is prone to 3 major sources of error (Ehrenberg 1995); (1) choice of original porosity, (2) point count categories and operator error, (3) grain dissolution and reprecipitation.

(1) Choice of original porosity can be based upon either published values of natural sands, or laboratory experiments of packing spheres. The chosen value of original porosity widely affects the value of porosity loss attributed to compaction. The solution is to choose a suitable OP for the particular sandstone being examined. In this study a value of 40% was chosen for

all samples, based upon natural observations of clean, aeolian sandstones, and laboratory experiments (Beard and Weyl 1973). This is likely to represent a minimum for clean aeolian dune sandstones and so all figures quoted for COPL represent a minimum.

(2) Operator bias and point count categories lead to error because some intergrain and grain categories are easily confused, such as patchy carbonate cements surrounding grain moulds and some authigenic clays which may appear detrital. This error is considered small in this study because the sandstone contains no clay and is minerallogicaly simple. Collapse and deformation of soft rock fragments may also cause difficulty in differentiating between pore space and volumes occupied by detrital material. This is also considered a minor issue in this study because of the simple mineralogy. Ehrenberg (1995) highlights the differentiation between authigenic and detrital quartz as a source of error, but this is discounted here because of the use of the SEM-CL point counting technique.

(3) Grain dissolution and reprecipitation. Grain moulds produced when whole detrital grains are dissolved, and not identified as such can increase the measured IGV. In this study dissolution on this scale was not observed. Minor intra-grain feldspar dissolution could be identified as such. Pressure solution between detrital quartz grains reduces IGV and is difficult to quantify. Where pressure solution is widespread, IGV and COPL must be taken as a minimum. For the Hopeman Sandstone in this study grain contacts and pressure solution are poorly developed suggesting measured IGV is accurate.

The most significant error on COPL and CEPL calculations is the error from counting statistics associated with point counting. This error is ~3% ($2\sigma$) for 900 counts per section, and ~2% ($2\sigma$) for 1800 counts per section (Van der Plas and Tobi 1965).

Quoted IGV values represent pore space plus porosity plus matrix. The clean Hopeman Sandstone is matrix free meaning in this study IGV is an equivalent term to minus-cement porosity.

# Appendix D - Point count dataset

Full point counted data (volume %) for each petrographic sample in this thesis. Key data on authigenic quartz and porosity was also presented in Chapter 5.

| Sample Index | Detrital quartz | Detrital K-feldspar | Rock fragments | Iron minerals | Authigenic quartz | Authigenic K-feldspar | Porosity | IGV | CEPL | COPL |
|---|---|---|---|---|---|---|---|---|---|---|
| 0.5 | 70.6 | 2 | 0.2 | 0 | 4.2 | 0 | 23 | 27.2 | 4.8 | 17.6 |
| 1.7 | 65.7 | 1 | 0.3 | 0.5 | 7.9 | 0 | 24.3 | 32.2 | 8.2 | 11.5 |
| 2.2 | 71.3 | 0.9 | 0 | 0 | 4.6 | 0.1 | 22.6 | 27.3 | 4.7 | 17.5 |
| 2.3 | 68.9 | 1.5 | 0.5 | 0 | 4.1 | 0.1 | 25.3 | 29.5 | 4.3 | 14.9 |
| 2.4 | 69.9 | 3 | 2 | 0 | 4.2 | 0 | 20.7 | 24.9 | 4.2 | 20.1 |
| 2.9 | 70.3 | 1.3 | 1 | 0 | 6.1 | 0 | 21.1 | 27.2 | 6.1 | 17.6 |
| 2.9 | 69.9 | 0.8 | 2.5 | 0 | 15.7 | 0.2 | 10.8 | 26.7 | 16.0 | 18.1 |
| 3.0 | 68.1 | 1.8 | 0 | 0 | 6.9 | 0 | 24.1 | 31.0 | 7.1 | 13.0 |
| 3.1 | 66.5 | 2.5 | 3.4 | 0 | 9.1 | 0.8 | 17.7 | 27.6 | 10.0 | 17.1 |
| 3.2 | 62 | 1.3 | 1.9 | 0.2 | 7.3 | 0 | 27.2 | 34.5 | 7.7 | 8.4 |
| 3.4 | 66.4 | 0.9 | 0 | 0 | 6.6 | 0.2 | 25.8 | 32.6 | 7.1 | 11.0 |
| 3.8 | 62.7 | 1.2 | 5.6 | 0 | 13.4 | 0.2 | 16.6 | 30.2 | 13.9 | 14.0 |
| 4.2 | 64.6 | 2.2 | 2.5 | 0.6 | 10.5 | 0.1 | 19.2 | 29.8 | 10.8 | 14.6 |

| | | | | | | | | | | |
|---|---|---|---|---|---|---|---|---|---|---|
| 6.5 | 63.6 | 2.2 | 1.2 | 0 | 11.6 | 0.3 | 20.7 | 32.6 | 12.4 | 11.0 |
| 8.9 | 63 | 2.7 | 2.5 | 0.2 | 15.8 | 0.2 | 15.4 | 31.4 | 16.5 | 12.5 |
| 10.9 | 67 | 2.1 | 4.2 | 0.6 | 17.2 | 0.1 | 11.5 | 28.8 | 17.6 | 15.7 |
| 13.4 | 64 | 6.9 | 1.3 | 0.4 | 19.9 | 6.2 | 6.7 | 32.8 | 21.4 | 12.5 |
| 13.8 | 59.4 | 2.1 | 0 | 2 | 26.5 | 3 | 9.9 | 39.4 | 33.5 | 8.0 |
| 14.2 | 67.7 | 0.5 | 1.8 | 0 | 20 | 0.1 | 9.8 | 29.9 | 20.6 | 14.4 |
| 58.3 | 4.4 | 2 | 0.4 | 21.7 | 0.8 | 12 | 34.5 | 23.9 | 8.4 | |
| 17.5 | 68.5 | 0.7 | 0 | 0 | 16.5 | 0.2 | 14.1 | 30.8 | 17.2 | 13.3 |
| 18.7 | 64.1 | 1.8 | 0.6 | 1.2 | 18.3 | 0.2 | 13.5 | 32 | 19.2 | 11.8 |
| 19.2 | 59.7 | 5 | 2.1 | 0.5 | 18.4 | 1.6 | 13.3 | 33.3 | 21.0 | 10.0 |
| 19.6 | 65.3 | 4.8 | 0.5 | 0 | 16.7 | 1.2 | 12.1 | 30 | 18.4 | 13.7 |
| 20.1 | 66.9 | 2.7 | 1.5 | 0 | 17.5 | 0.8 | 10.6 | 28.9 | 18.6 | 15.6 |
| 20.7 | 55.9 | 4.2 | 0.6 | 0 | 23.5 | 0.7 | 15.1 | 39.3 | 26.5 | 3.8 |
| 21.5 | 68.1 | 0.7 | 0.2 | 0 | 15.3 | 0.2 | 15.5 | 31 | 15.9 | 14.3 |
| 21.7 | 70.8 | 0.5 | 0.7 | 0.5 | 11.1 | 0 | 16.3 | 27.4 | 11.3 | 16.2 |
| 24.3 | 59.8 | 5.4 | 0 | 0.8 | 15.3 | 2 | 16.7 | 34 | 18.3 | 9.1 |
| 26.3 | 64.8 | 3.4 | 1.1 | 0 | 13.6 | 0.6 | 16.4 | 30.6 | 14.6 | 13.5 |
| 27.3 | 64.4 | 4.3 | 1.5 | 0.4 | 17.6 | 0.8 | 10.9 | 29.3 | 18.8 | 15.1 |
| 27.3 | 70.2 | 0.7 | 0.1 | 0.1 | 12.9 | 0.1 | 15.9 | 28.9 | 13.2 | 15.6 |
| 28.0 | 63.0 | 3 | 1.7 | 0.4 | 13.7 | 0.8 | 17.3 | 31.8 | 15.0 | 12.0 |
| 29.7 | 69.1 | 1.9 | 1.2 | 0 | 6.4 | 0.1 | 21.1 | 27.6 | 6.6 | 17.1 |
| 29.9 | 60.7 | 2.9 | 1.7 | 0 | 15.7 | 0.5 | 18 | 34.2 | 17.1 | 8.8 |

| | | | | | | | | | | |
|---|---|---|---|---|---|---|---|---|---|---|
| 30.4 | 64.8 | 2.9 | 2.4 | 0.3 | 11.6 | 0.9 | 16.7 | 29.2 | 12.7 | 15.3 |
| 30.9 | 65.3 | 2.5 | 1.6 | 0 | 6 | 0.2 | 24.3 | 30.5 | 6.4 | 13.7 |
| 31.1 | 66.9 | 1.8 | 3.2 | 0 | 5.6 | 0 | 22.3 | 27.9 | 7.0 | 16.9 |
| 31.3 | 68.7 | 2.6 | 0.6 | 0.3 | 6.6 | 0.3 | 20.9 | 27.8 | 5.6 | 19.0 |
| 31.7 | 66.2 | 2.7 | 2 | 0.5 | 9.2 | 0.4 | 18.6 | 28.2 | 9.7 | 17.6 |
| 40.0 | 68 | 3.8 | 3.5 | 0.8 | 3.3 | 0 | 20.6 | 23.9 | 3.3 | 20.1 |
| 42.0 | 65.6 | 1 | 1.2 | 1 | 4.9 | 0.6 | 25.7 | 31.2 | 5.6 | 15.3 |
| 44.0 | 62 | 2.4 | 1.3 | 4.1 | 3.9 | 0.6 | 25.7 | 30.2 | 4.6 | 16.4 |
| -2.2 | 63.2 | 4.2 | 2.4 | 0 | 4.8 | 2 | 23.3 | 30.1 | 7.0 | 14.2 |
| -2.3 | 62.3 | 6.2 | 2.3 | 0 | 4.8 | 0.6 | 23.8 | 29.2 | 5.6 | 11.5 |
| -4.2 | 64.7 | 4.2 | 2.2 | 0 | 2.8 | 0.6 | 25.5 | 28.9 | 3.5 | 15.6 |
| -9.9 | 72.2 | 0.8 | 0.4 | 0 | 1.3 | 0 | 25.3 | 26.6 | 1.3 | 18.3 |
| -11.0 | 67.5 | 1.8 | 2.2 | 0 | 4.2 | 0.4 | 23.9 | 28.5 | 4.7 | 16.1 |
| -12.2 | 71 | 0.2 | 0.2 | 0 | 1.1 | 1.1 | 26.4 | 28.6 | 2.2 | 18.5 |
| -13.5 | 71.9 | 1.9 | 0.2 | 0 | 0.9 | 0.9 | 24.2 | 26 | 1.8 | 20.6 |
| -15.5 | 70.8 | 2.2 | 2.8 | 0.2 | 2 | 0 | 22 | 24 | 2.0 | 21.1 |
| -16.4 | 66.6 | 3.7 | 0 | 0.2 | 4.2 | 0 | 25.3 | 29.5 | 4.3 | 14.9 |
| -19.4 | 67.2 | 2.4 | 1.5 | 2 | 2.2 | 0.6 | 24.1 | 26.9 | 2.9 | 11.9 |
| -26.3 | 64 | 2.2 | 1.7 | 0 | 2.8 | 0.2 | 26.8 | 29.8 | 3.0 | 15.7 |
| -29.0 | 64.9 | 3.5 | 4.8 | 0.2 | 2.6 | 0.4 | 23.6 | 26.6 | 3.1 | 13.4 |
| -30.0 | 66.2 | 2.2 | 0.6 | 0 | 6.6 | 0.2 | 24.1 | 30.9 | 6.9 | 15.6 |
| 1 | 64.2 | 3.5 | 0.8 | 0 | 30.6 | 0 | 0.6 | 31.2 | 26.7 | 12.8 |
| 2 | 66.8 | 0.2 | 0 | 0 | 27.7 | 0 | 5.1 | 32.8 | 24.7 | 10.7 |

| | | | | | | | | | | | |
|---|---|---|---|---|---|---|---|---|---|---|---|
| 3.5 | 67.3 | 2 | 0 | 0 | 26 | 0 | 3.7 | 29.7 | 22.2 | 14.7 |
| 5 | 60.8 | 1.1 | 0.8 | 0 | 32 | 0.8 | 4.2 | 37 | 31.2 | 4.8 |
| 6 | 63.3 | 6 | 1.1 | 0 | 26.2 | 0.4 | 2.8 | 29.4 | 22.6 | 15.0 |
| 7 | 68 | 2.2 | 2.8 | 0 | 23.1 | 0 | 3.7 | 26.8 | 18.9 | 18.0 |
| 8 | 63.1 | 0.6 | 0.2 | 0 | 27.5 | 0 | 7.7 | 35.2 | 25.5 | 7.4 |
| 9.5 | 65.7 | 2.8 | 0.4 | 0 | 28.8 | 1.1 | 0.8 | 30.7 | 25.9 | 13.4 |
| 11 | 60.2 | 1.3 | 0 | 0 | 27.5 | 0 | 4.8 | 32.3 | 24.4 | 11.4 |
| 12 | 70.2 | 3.1 | 0 | 0 | 23.3 | 0.2 | 1.5 | 25 | 18.8 | 20.0 |
| 13 | 59.1 | 2.2 | 1.5 | 0 | 25.5 | 0.4 | 10.6 | 36.5 | 24.5 | 5.5 |

| Burghead Beds | Detrital quartz | Detrital K-feldspar | Rock fragments | Carbonate cement | Authigenic quartz | Authigenic K-feldspar | Porosity | IGV | CEPL | COPL |
|---|---|---|---|---|---|---|---|---|---|---|
| -5 | 48 | 8.9 | 6 | 13.9 | 5.2 | 0 | 18 | 37.1 | 10.5 | 20.1 |
| -2 | 59 | 7.9 | 11 | 5 | 3.1 | 0 | 14 | 22.1 | 11.7 | 17.6 |

# Appendix E – Permeability measurement technique

Permeability data was collected in the field using a portable mini-permeameter constructed in the Department of Petroleum Engineering, Heriot-Watt University, Edinburgh.

## A - Mini-permeametry background and theory

The mini-permeameter is a simple gas-flow measuring device designed to rapidly make a high number of permeability measurements. First proposed by Dykstra and Parsons (1950) the field permeameter was used by Weber *et al.* (1972) and has since become increasingly common for the geological characterisation of outcrop sediment permeability (e.g. Goggin *et al.*, 1988, Barton and Tyler 1993). Conventional methods of permeability measurement involve taking core plugs from oilfield samples, or natural outcrops, and conducting laboratory measurements. The advantage of the permeameter over these conventional methods is that although less accurate, it is non-destructive and allows rapid frequent spatial measurements to be made. This means that the detailed geological variation in permeability over a mm to cm scale can be recorded.

The permeameter operates by forcing compressed nitrogen gas to flow at a constant pressure through an injection tip which is pressed, and sealed, against the sample (Fig E1). Silicone rubber seals around the probe tip minimise gas leakage outwith the sample and mould around irregular outcrop rock surfaces. Prior to measurement flow rate is changed depending on the estimated permeability of the sample; high flow rates for low permeability material and lower flow rates for more permeable material. The instrument was calibrated by measuring core plug samples of known permeability in the laboratory.

For each field measurement gas pressure was constant and the variation in flow rate, compared with the start rate, was recorded once a steady state flow was reached (usually within 20 seconds). Values obtained from the permeameter relate to flow rate, which is controlled by permeability. These values are converted to permeability (darcys) using the analytical equation derived by Goggin *et al.* 1988;

$$K = \frac{2\mu P_1 Q_1}{(P^1_2 - P^2_2)G^a_o}$$

where;

K = permeability (Darcys)

$\mu$ = gas viscosity at atmospheric pressure (centipoises)

$P_1$ = injection pressure

$P_2$ = outflow pressure

$Q_1$ = volumetric rate at injection pressure $P_1$ (ml/sec)

$G_o$ = geometric factor (dimensionless)

a = radius of the seal area.

Known factors are $\mu$, $P_1$, $Q_1$, $G_0$ and a. $P_2$ is measured in the field.

Go, the geometric factor summarises all of the complexities associated with the flow geometry of the injected gas within the sample and is a function of tip-seal size and the sample dimensions and has been calculated using finite difference modelling. For outcrop studies sample dimensions are allowed to approach infinity. However the true geometry of flow paths in probe permeametry is largely unknown.

**B – Field measurements and conditions**

A series of measurements were taken in the field at Clashach Cove and around the Burghead Fault. Flow rate was recorded for each measurement, which was subsequently repeated on the same site as a check on accuracy. Occasional rough surfaces led to poor probe seals which was detected by the lack of measurement repeatability and not included in the dataset. Sites of measurement were restricted by access with the equipment. The permeameter weighs about 15kg and requires several tanks of nitrogen for a days analysis, restricting the number of locations at which the probe can be used.

The permeameter measures gas flow rate, and the conversion of this flow rate data to Darcy permeability does not account for the presence of fluid in the pore spaces of the material measured. Comparative field measurements on different sites are therefore constrained by the local conditions during fieldwork. In this study measurements were made over two consecutive days following several days of dry weather. The outcrops were visibly dry suggesting that true gas permeability was measured and the effects of two phase gas-fluid permeability were minor.

Weathering and surface effects on outcrops can also cause inaccurate measurements. Surfaces were gently cleaned with a soft brush prior to application of the probe to ensure true sandstone permeability was measured. Creation of dust flour and damage to surfaces was avoided by using this technique instead of more corrosive wire brushing and surface preparation. This effect is most important for highly permeable sites which can be more easily affected.

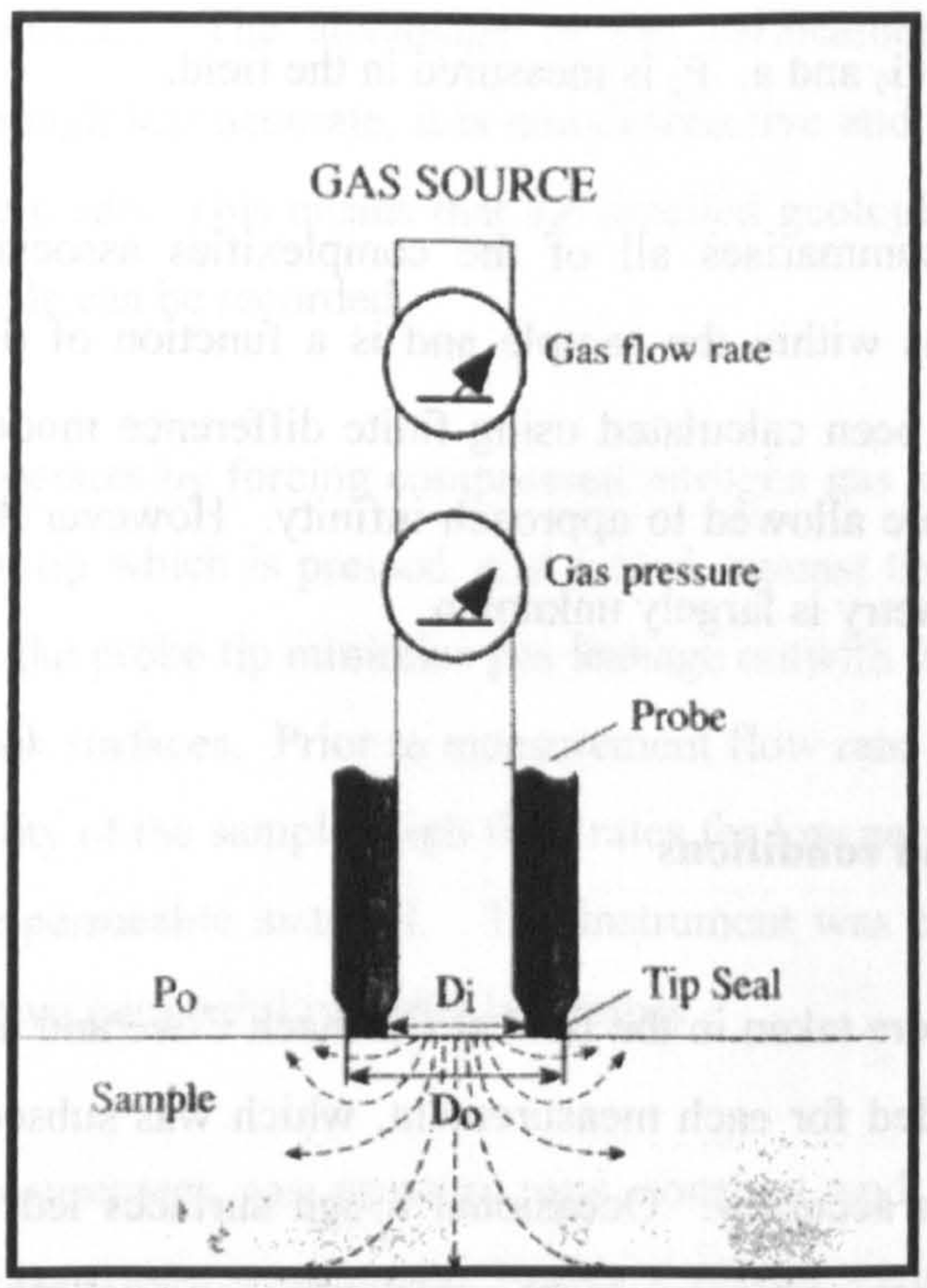


**Fig. E1.** Diagram of a steady-state probe permeameter. Di = internal diameter of seal, Do = external probe diameter, Po = atmospheric pressure. From Hurst and Goggin, 1995.

# Appendix F - Ion microprobe technique

Oxygen isotope values were analysed using an ion microprobe and a secondary ion mass spectrometer (SIMS). Many previous studies of oxygen isotopes in authigenic quartz have used conventional methods of isotopic analysis, but the ion probe has become increasingly utilised for diagenetic studies. The advantage of the probe over conventional analysis is the ability to target a specific zone on a thin section and measure different phases and positions of a quartz overgrowth. Conventional analyses involve crushing the sandstone and attempting to separate authigenic from detrital quartz. Whilst this technique is analytically more precise, it can only provide bulk figures for whole overgrowths. The ability to analyse specific locations within single overgrowths means the probe provides greater resolution of the variation in isotope ratios within a single overgrowth, although analytical error is larger (+/-1‰). The operating mechanism and parameters of the ion microprobe, and the raw data processing are detailed in this Appendix.

## A- The ion microprobe process

The ion microprobe used in this study was a Cameca ims-4f ion microprobe with a Charles Evans and Associates computer control, at the University of Edinburgh.

The ion microprobe allows measurement of isotopic ratios in rock thin sections with high spatial accuracy and good resolution. Samples are bombarded with a primary beam of charged particles which results in the ejection of charged particles, neutral particles and molecules from the surface of the sample. Ejected secondary ions are collected and analysed in a mass spectrometer.

A primary beam is created from two sources; a duoplasmatron and a Caesium gun. Generated primary ions are focused through a mass filter, apertures, lenses and deflection plates which can be altered to change the shape, size and intensity of the beam. Interaction of the beam with the sample surface causes the production of secondary ions which are removed

by the immersion lens, and transferred to the mass spectrometer (Fig. F1). Produced secondary ions have a wide range of energies with molecular species abundant at low energies and mono-atomic species at higher energies. The ions pass into an energy slit which allows only a small proportion of the total energy range to pass through, removing unwanted low-energy molecular species. The energy-filtered beam of mono-atomic species passes through a magnetic field which deflects different ions by different amounts allowing mass resolution and isolation, in this case, of $O^-$ ions.

The refined secondary ions are passed into one of four detectors on the ion probe; an electron multiplier, a Faraday cup, a resistive anode encoder or an image plate. The electron multiplier is used to quantify the magnitude of the secondary ion signal by producing a pulse of secondary electrons which is passed to a counting circuit.

Quartz acts as an insulating material, causing charge to build up on the sample surface during analysis. The use of a Cs+ primary beam, which interacts with negative oxygen ions, causes the sample surface to charge positively. A low energy electron gun was used to flood the surface with electrons to counter this build-up. A tungsten filament is held at ~4100V, emitting electrons which are focused onto the sample by a magnetic prism and an immersion lens. The sample surface is held at an equivalent voltage (~4100V) resulting in a cloud of low energy electrons above the sample surface.

***B – Data processing***

Data recorded by the ion probe includes a correction for instrument dead time. This dead time is a product of the time it takes for ions to enter the electron multiplier and produce a pulse of secondary electrons for measurement in the counting circuit. This dead time is calibrated prior to each analytical period and automatically accounted for in the quoted raw count data.

Raw count data is converted to $\delta^{18}O_{(SMOW)}$ by applying a number of corrections (Fig. F2). Raw data consists of the number of secondary ion counts on $\delta^{18}O^-$ and $\delta^{16}O^-$ per cycle. Eighty

cycles were made during each analysis (80 x [$\delta^{18}O^-$ 8secs; $\delta^{16}O^-$ 1sec]). The total number of counts for each isotope was converted to a count rate by using:

$$\textit{Count rate (CR) (counts/second)} = \frac{\textit{total number of counts}}{\textit{counting time}}$$

True isotope ratio (including the dead time correction) was calculated using;

$$\delta^{18}O/^{16}O = \frac{CR^{18}O}{CR^{16}O}$$

The mean and standard deviation of $^{18}O/^{16}O$ for each cycle in an analysis were calculated and any values outside 3σ from the mean were rejected. Instrumental drift through the days analyses was applied by plotting $^{18}O/^{16}O$ for all standards against analysis number. A least-squares regression through this data produced a correction for was used to predict the $^{18}O/^{16}O$ of the standard at the time of each unknown sample analysis using;

$$R_{std} = m(R_{unk}) + c$$

Where $R_{std}$ = $^{18}O/^{16}O$ of standard; $R_{unk}$ = $^{18}O/^{16}O$ of the unknown, m = gradient; c = y-intercept of the regression line.

All values of $^{18}O/^{16}O$ quoted in this thesis are in ‰ difference to SMOW ($\delta^{18}O_{SMOW}$), the standard mean ocean water ($2.00052 \times 10^{-3}$).

$\delta^{18}O_{SMOW}$ was calculated using;

$$\delta_{unk} = \left[\frac{(R_{unk})}{(R_{std})} \times (\delta_{std} + 1000)\right] - 1000$$

Errors on data from the ion probe are governed by Poisson counting statistics. The Poisson distribution shows the number of random, independent events (N), that occur over a specified period of measurement. For the probe N is the number of secondary ions counted by the detector during a single measurement period. Under Poisson conditions the precision of data for a single isotope and an isotope ratio depends only on the number of counts for each isotope of interest (Fitzsimons *et al.,* 1999).

Factors which reduce the precision of analyses are primary beam instability, sample charging, and heterogeneity within the scale of the analysis pit. This introduces non-random variation for a single isotope species, but comparison of species in a ratio largely cancels this out. The precision of isotope ratios is generally close to that predicted by counting statistics (Fitzsimons *et al.,* 1999).

Therefore analytical error (‰) for $^{18}O/^{16}O$ analyses (based on counting statistics alone) is;

$$\text{Error } (1\sigma) = \left[\frac{\sqrt{N}}{N}\right] \times 1000$$

Where N = total number of counts on 18O over the period of analysis.

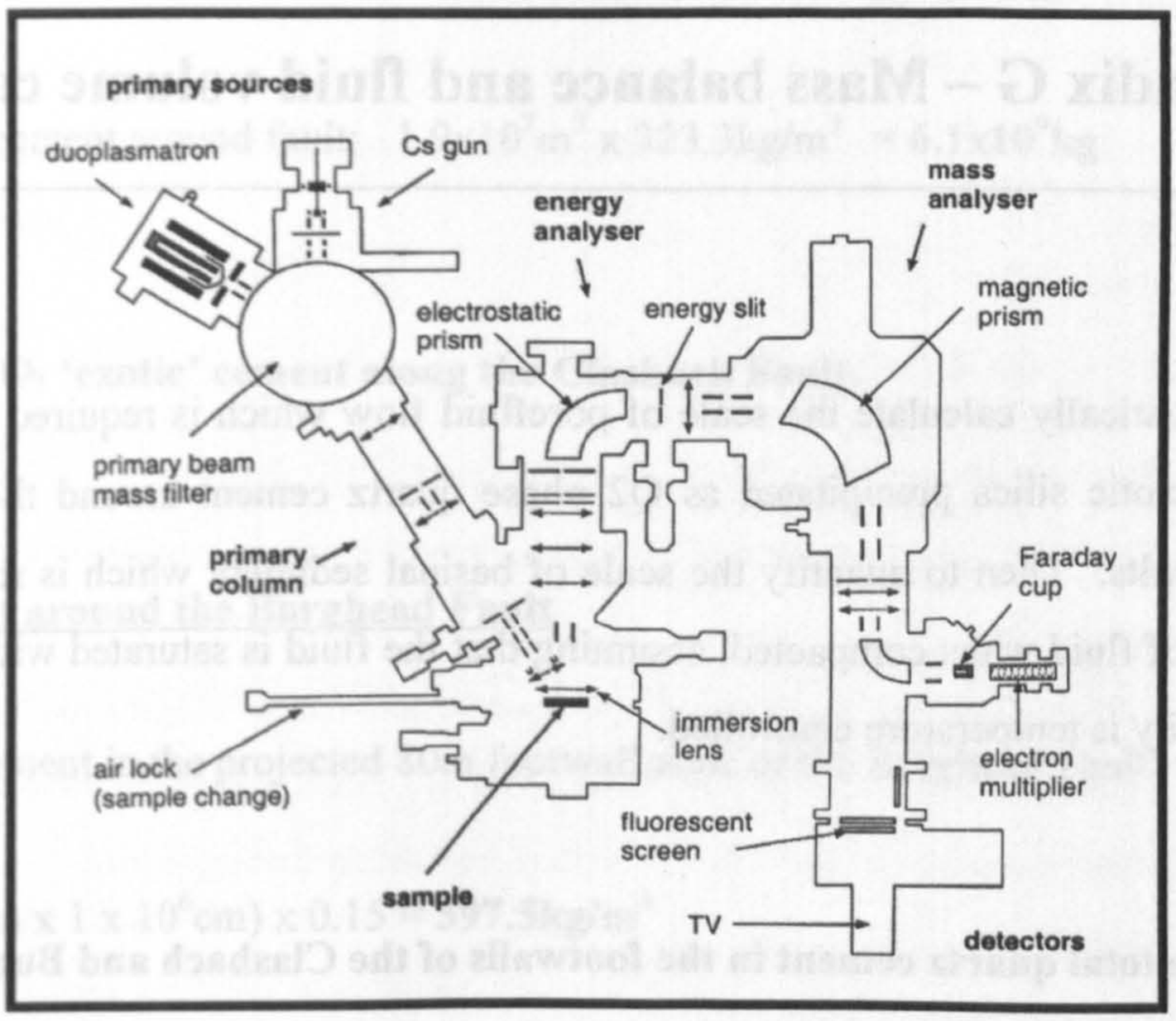


**Fig. F1.** Plane of the Cameca-ims 4f ion probe. From J.Craven (pers.comm).

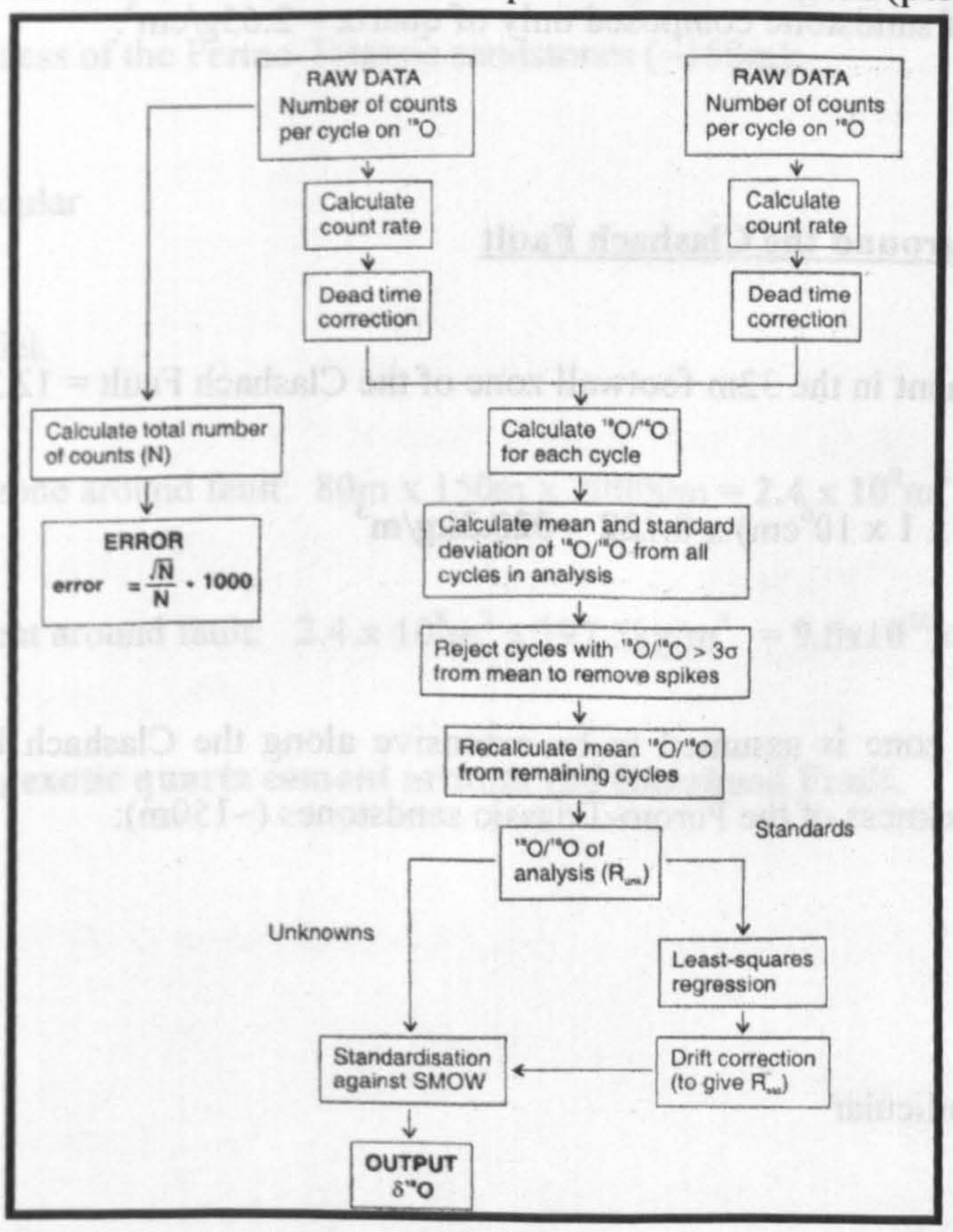


**Fig. E2.** Flow chart showing the processing of raw measured ion probe isotope data. From Lewis, PhD 1999.

# Appendix G – Mass balance and fluid volume calculation

**Aim:** Simplistically calculate the scale of porefluid flow which is required to transport the amount of exotic silica precipitated as Q2 phase quartz cement around the Clashach and Burghead Faults. Then to quantify the scale of basinal sediment which is required to expel this volume of fluid when compacted, assuming that the fluid is saturated with silica and that silica solubility is temperature controlled.

**<u>Step A</u> - The total quartz cement in the footwalls of the Clashach and Burghead Faults**

Density of $1m^3$ of sandstone composed only of quartz = $2.65g/cm^3$.

$1m^3 = 1x10^6cm$

**<u>Quartz cement around the Clashach Fault</u>**

Mean quartz cement in the 32m footwall zone of the Clashach Fault = 12.2%

$(2.65x10^{-3}kg/cm \times 1 \times 10^6cm) \times 0.122 = \mathbf{323.3kg/m^3}$

The Q2 cement zone is assumed to be extensive along the Clashach Fault 3-dimensional extent for the thickness of the Permo-Triassic sandstones (~150m):

Fault extent;

32m fault perpendicular

150m vertically

4000m fault parallel.

volume of cement zone around fault: 32m x 150m x 4000m = **1.9 x $10^7$m$^3$**

volume of Q2 cement around fault: 1.9x$10^7$m$^3$ x 323.3kg/m$^3$ = **6.1x$10^9$kg**

**= 6 x $10^9$ kg $SiO_2$ 'exotic' cement along the Clashach Fault.**

**<u>Quartz cement around the Burghead Fault</u>**

Mean quartz cement in the projected 80m footwall zone of the Burghead Fault = 15%

**(2.65x$10^{-3}$kg/cm x 1 x $10^6$cm) x 0.15 = 397.5kg/m$^3$**

The Q2 cement zone is assumed to be extensive along the Burghead Fault 3-dimensional extent for the thickness of the Permo-Triassic sandstones (~150m):

80m fault perpendicular
150m vertically
20000m fault parallel.

volume of cement zone around fault: 80m x 150m x 20000m = **2.4 x $10^8$m$^3$**

volume of Q2 cement around fault: 2.4 x $10^8$m$^3$ x 397.5kg/m$^3$ = **9.5x$10^{10}$kg**

**= 9.5 x $10^{10}$kg $SiO_2$ exotic quartz cement around the Burghead Fault.**

**<u>Step B -</u> The volume of compactional basinal fluid required to transport the calculated volume of silica.**

The calculation assumes that fluid which can transport silica from the deep basin is produced through compaction of sediment caused by burial during basin extension in the Late Jurassic.

For typical North Sea sandstones buried to ~5km a conservative original porosity of 40% will compact to <10% porosity. (Haszeldine et al., 2003). The calculation assumes that 30% of rock volume is lost through compaction and fluid expulsion during burial.

$1m^3 \times 30\% = 300{,}000cm^3/m^3$ fluid

$1cm^3 = 0.001$litres

$300{,}000cm^3 * 0.001 = 300$litres/$m^3$.

Silica solubility is assumed to be controlled by temperature. At basinal burial depths and temperatures, assuming a low geothermal gradient of 35°C/km.

5km burial depth = 175°C burial temperature.
Measured mean microfracture inclusion temperature is 166°C.

Silica solubility is ~100ppm at 175°C.

At precipitation depths and temperatures background sandstone is <60°C

Silica solubility is ~ 30ppm @60°C

Silica precipitation is caused by the temperature drop from 175°C to 60°C at the site of precipitation; 70ppm silica precipitates as a simple function of this temperature-solubility relationship.

1ppm = 1mg/litre

70ppm = 0.07g/litre

Therefore $1m^3$ of sediment which expels 300litres of silica saturated fluid at 175°C releases;
300litres * 0.07g/litre = $21g/m^3$ silica

Step C – Volume of sediment required to expel this amount of hot siliceous fluid during compaction.

Total $SiO_2$ around Clashach Fault = $2 \times 10^9$kg
Total Si within quartz is 47% (Si = 28, O = 16(*2))
= $2x10^9$kg *0.47 = $9.4x10^8$kg
Total Si transported and precipitated = $2.1 \times 10^{-2}$ kg/m$^3$

$\frac{9.4 \times 10^8 kg}{2.1 \times 10^{-2} kg/m3}$

= $4.5 \times 10^{10}$m$^3$ of sediment

Total $SiO_2$ around Burghead Fault = $9.5 \times 10^{10}$kg
Total Si within quartz is 47% (Si = 28, O = 16(*2))
= $9.5 \times 10^{10}$kg *0.47 = $4.5 \times 10^{10}$kg
Total Si transported and precipitated = $2.1 \times 10^{-2}$ kg/m$^3$

$\frac{4.5 \times 10^{10} kg}{2.1 \times 10^{-2} kg/m^3}$

= $2.1 \times 10^{12}$m$^3$ of sediment

Assuming expulsion of 30% of depositional volume as hot siliceous porefluid therefore requires 2.2 x $10^{12}m^3$ of sediment-source to account for the quartz cement surrounding both faults.

Notes:

This basic calculation shows within an order of magnitude the scale of fluid flow required to transport the quantity of silica required to produce the fault-related quartz cement around the Clashach and Burghead Faults. Parameters can be changed significantly but the amount of sediment required to release the volumes of fluid is essentially insensitive to variation in silica solubility and maximum fluid temperature within an order of magnitude.

---

# Appendix References


**Barton, M.D. and Tyler, N., 1993.** Quantification of permeability structure in distributary-channel deposits, Ferron Sandstone, Utah. In: (Chidsey, C.T (ed.) Geology of east-central Utah. Utah Geological Association Publication, 19, p.273-299.

**Beard, D.C. and Weyl, P.K., 1973.** Influence of texture on porosity and permeability of unconsolidated sand: American Association of Petroleum Geologists Bulletin, 57, p. 349-369.

**Dykstra, H. and Parsons, R.L., 1950.** The prediction of oil recovery by waterflood. In: Secondary recovery in the USA. American Petroleum Institute, New York, 2nd ed., p.160-174.

**Ehrenberg, S.N., 1995.** Measuring sandstone compaction from modal analyses of thin sections: how to do it and what the results mean. Journal of Sedimentary Research, 65A, 2, p.369-379.

**Electroscan Corporation, 1996.** Environmental Scanning Electron Microscopy – an introduction to ESEM. Robert Johnson Associates, El Dorado Hills, pp.55.

**England, G.L. and Kelly, N., 2004.** The role of aluminium in controlling cathodoluminescence in quartz cements. Personal Communication.

**Evans, J., Hogg, A.J.C., Hopkins, M.S. and Howarth, R.J., 1992.** Quantification of quartz cements using SEM, CL, and image analysis. Journal of Sedimentary Research, A64, 2, p.334-338.

**Fitzsimons, I.C.W., Harte, B. and Clark, R.M., 2000.** SIMS stable isotope measurement: Counting statistics and analytical precision. Mineralogical Magazine, 64, n.1, p.59-83.

**Goggin, D.J., Thrasher, R.L. and Lake, L.W., 1988a.** A theoretical and experimental analysis of mini-permeameter responses including gas slippage and high velocity flow effects. In Situ, 12, p.79-116.

**Hurst, A. and Goggin, D., 1995.** Probe permeametry; An overview and bibliography. American Association of Petroleum Geologists Bulletin, 79, p. 463-473.

**Lewis, S., 1999.** Metamorphic fluid flow and stable isotope modification in marble: n example from Naxos, Greece. Un published PhD, University of Edinburgh. pp. 349.

**Van der Plas, L. and Tobi, A.C., 1965.** A chart for judging the reliability of point counting results. American Journal of Science, 263, n.1, p.87-90.

**Weber, K.J., Eijpe, R., Leijnse, D. and Moens, C., 1972.** Permeability distribution in a Holocene distributary channel-fill near Leerdam (The Netherlands). Geologie an Mijnbouw, 51, p.53-62.

**Zinkernagel, U., 1978.** Cathodoluminescence of quartz and its application to sandstone petrology. Contributions to Sedimentology, Amsterdam, 8, pp.69.